Catalytic Water Oxidation Involving Ruthenium Polypyridyl Complexes

Jonah Wesley Jurss

"A dissertation submitted to the faculty of the University of North Carolina at Chapel Hill in partial fulfillment of the requirements for the degree of Doctor of Philosophy in the Department of Chemistry."

Chapel Hill
2011

Approved by:

Thomas J. Meyer

Joseph L. Templeton

Maurice S. Brookhart

Michel R. Gagné

Marcey L. Waters

ABSTRACT

Jonah Wesley Jurss: Catalytic Water Oxidation Involving
Ruthenium Polypyridyl Complexes
(Under the direction of Thomas J. Meyer and Joseph L. Templeton)

Light-driven water oxidation occurs in oxygenic photosynthesis in Photosystem II where reductive equivalents are produced to ultimately convert carbon dioxide into carbohydrates. This process effectively stores solar energy in the form of chemical bonds. Water oxidation is a key component in schemes for artificial photosynthesis, such as solar-driven water splitting into hydrogen and oxygen, $2H_2O \rightarrow O_2 + 2H_2$, which could provide much needed clean, renewable fuels.

The "blue dimer", *cis,cis*-$[(bpy)_2(H_2O)Ru^{III}ORu^{III}(OH_2)(bpy)_2]^{4+}$, is the first well characterized molecule known to catalyze water oxidation. It meets the stoichiometric requirements for water oxidation, $2H_2O \rightarrow O_2 + 4e^- + 4H^+$, by utilizing proton-coupled electron transfer (PCET) reactions in which both electrons and protons are transferred. In the key step, oxidation to the catalytically-active state, $[(O)Ru^{V}ORu^{V}(O)]^{4+}$, results in nucleophilic water attack to form the O-O bond, producing a peroxidic complex. The mechanism of blue dimer catalyzed water oxidation has been resolved to its clearest understanding yet, yielding new insights and opportunities for rational catalyst design.

Following this foray into the complexities of the blue dimer, a plethora of single-site (one aqua ligand) ruthenium monomers has been developed, each of which are capable of catalytic water oxidation, driven electrochemically or under acidic conditions using Ce(IV)

as a sacrificial oxidant. These homogeneous catalysts have been incorporated into devices by the synthesis of their phosphonic acid derivatized analogues to provide stable interfacial attachment to metal oxide surfaces. Low overpotentials for the electrocatalysis of water oxidation have been achieved with high turnover numbers.

Furthermore, a strategy for enhancing rates of water oxidation has been developed using a series of kinetically facile electron transfer mediators with varying thermodynamic driving force. Rate enhancements by factors of up to 30 have been obtained in solution and with surface-modified electrodes. An electrochemical kinetic analysis has been applied for homogeneous water oxidation with surface-modified electrodes.

The incorporation of catalysts with electron transfer mediators, which have been studied extensively as chromophores for excited state electron transfer reactions, has led to the design and synthesis of assemblies for electrocatalytic water oxidation, providing new insights into their application toward solar energy conversion. Another approach toward assemblies of this kind has been pursued by exploiting the pH dependence of phosphonic acid derivatized complexes by electrostatic association of cationic water oxidation catalysts to deprotonated, anionic redox mediator-chromophore adsorbates on electrode surfaces. This negates the need for difficult synthetic procedures and bridge design for attaching the necessary components for an artificial photosynthetic apparatus.

ACKNOWLEDGEMENTS

I am indebted to my advisors, Tom Meyer and Joe Templeton, for their guidance during graduate school. Their eager engagement with the research and valuable insight made my time at UNC exciting, productive, and primed for great intellectual growth. It has largely been their constructive criticism, timely encouragement, and praise that has helped shape my development as a chemist. To my benefit, their strengths in mentoring and directing research efforts complemented each other extremely well. It has been a pleasure to work with two such highly respected chemists, and even better people.

I am especially grateful for the friendships that have been made with members of the Meyer and Templeton research groups, in addition to many others of UNC Chemistry. I could not have asked for a better group of people to work with and spend so much time with over the last five years, inside and outside of the laboratory. There are too many friends and coworkers to list here, but a special thanks goes to Javier Concepcion. He has been a good friend from the beginning, great to work with, and his enthusiasm, optimism, and patient teaching in the laboratory have made a significant impact on me. Chris Gagliardi has also been a close friend from the beginning and one of the few people that always has me laughing. I also thank Jake Sprague for being a great friend and roommate for four years in Chapel Hill.

My parents, John and Diana, and sister, Jolene, have loved me and supported me my entire life. I would not be the person I am today without them. Mom and Dad instilled in us

the importance of education at an early age. To each of you and the rest of my family and friends, thank you: I love you dearly!

Finally, I praise God who "is before all things, and in [whom] all things hold together" (Colossians 1: 17). I thank God for my passion in the sciences, for curiosity and creativity. As Albert Einstein once said, "The more I learn of physics, the more I am drawn to metaphysics."

TABLE OF CONTENTS

LIST OF TABLES

LIST OF FIGURES

LIST OF SCHEMES

LIST OF SYMBOLS AND ABBREVIATIONS

A	ampere
A	area
AM	air mass
Appx.	Appendix
cm	centimeter
EPR	electron paramagnetic resonance
eV	electron-volt
G	global
HOMO	highest occupied molecular orbital
i	current
IR	infrared
ITO	tin-doped indium oxide
K	Kelvin
LUMO	lowest unoccupied molecular orbital
m	meter
M	molar
ms	millisecond
NHE	natural hydrogen electrode
nm	nanometer
r	radius
s	second
SCE	saturated calomel electrode

T	tesla
TW	terawatt
UV	ultraviolet
V	volt
Vis	visible
W	watt
XRD	x-ray diffraction
Å	angstrom
° or deg	degrees
ε	molar extinction coefficient
Γ	surface coverage
μA	microampere
μs	microsecond
ν	scan rate

CHAPTER 1

Solar Energy Conversion: Natural and Artificial Photosynthesis

The best candidate for an environmentally benign, sustainable replacement of fossil fuels is solar energy, an inexhaustible resource that supplies 120,000 TW of electromagnetic radiation to the earth per annum. Solar energy is most commonly converted into electricity using photovoltaic cells and dye-sensitized photoelectrochemical cells - the so-called Grätzel cells. Photons are captured with these cells as absorbed light excites electrons to create electron-hole pairs which are separated and driven in opposite directions to generate current. Lifetimes approaching 30 years and efficiencies of 15 to 20% have been obtained with first-generation photovoltaic cells made from expensive poly-crystalline silicon.[1] Although eighty-five percent of the commercial solar cell market is comprised of first-generation photovoltaics, their high manufacturing cost has prevented widespread implementation. More affordable materials have been pursued, such as amorphous or nanocrystalline Si,[2-5] CdTe,[6-8] and $CuInSe_2$.[9] However, these materials have been plagued by low efficiencies due to an observed decrease in device performance with lower material purity.

In photovoltaics, electron-hole pairs are formed by direct band gap excitation of the semiconductor. Subsequent charge separation is achieved with a p-n junction that is usually introduced by doping, or with a Schottky junction that utilizes differences in the work function of specific materials.[10-12] Consequently, an internal electric field is formed that directs conduction band electrons toward the n-type region, whereas a preference for valence holes is indicative of the p-type region. The photogenerated charges flow in opposite directions; the resulting asymmetry produces electrical current accompanied by a potential difference at the external electrodes, which can be applied to a load. One limitation of direct band gap excitation is the discrimination of absorbed light, such that only incident light of higher energy or matching the energy difference between the valence and conduction band

edges will be absorbed. Wavelengths of higher energy create “hot carriers” or “hot excitons” that relax through electron-phonon scattering modes in pico- to subpicosecond time regimes to release the excess kinetic free energy as heat.[13-15] A significant amount of the available light energy, ranging from 0.5 to 3.5 eV in the solar spectrum,[16] (Figure 1.1) is dissipated as heat in this manner, or not absorbed at all. Assuming comprehensive carrier cooling along with the narrow light selectivity of photovoltaics, a maximum thermodynamic efficiency of ~33% is possible.[17]

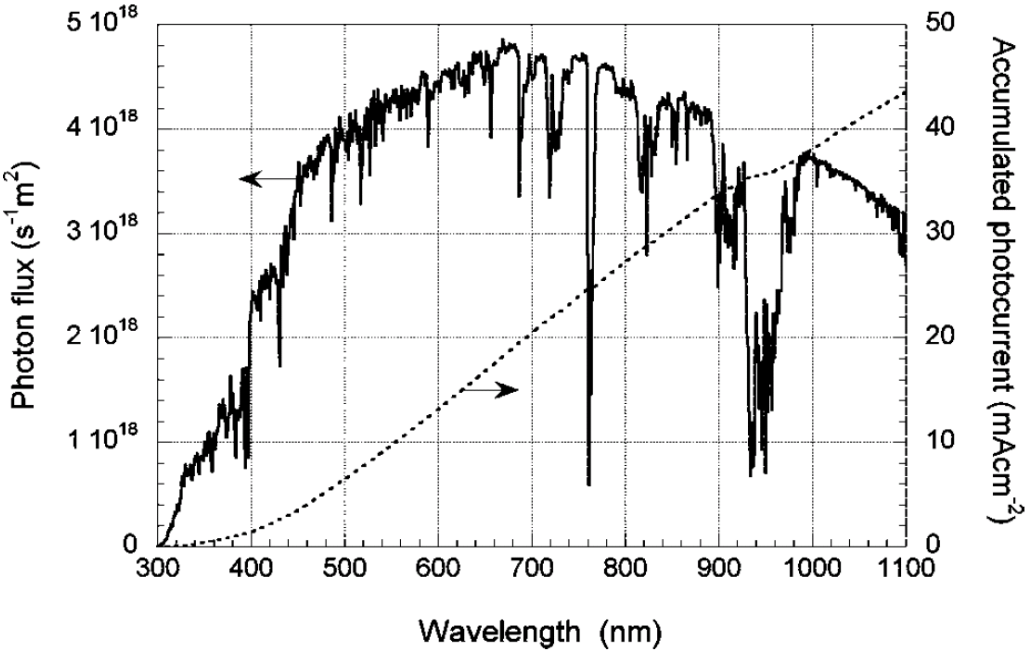

Figure 1.1.[18] Photon flux of the AM 1.5 G spectrum at 1000 W m^{-2} (ASTM G173-03), and calculated accumulated photocurrent.[18]

The thickness of the cell dictates the amount of light that will be absorbed, which decrees an optimal thickness for light harvesting and collection of electron-hole pairs. The constraint being that electron-hole pairs have a discrete lifetime before recombination occurs and, consequently, must diffuse to the electrical junction prior to this nonproductive process. In other words, cell thickness must be less than the exciton diffusion length. Impurities create

defects in the material that obstruct the separation of electron-hole pairs causing shorter lifetimes and a higher degree of charge recombination. To circumvent the expense of high purity materials, research is underway to reduce the necessary distance for charges to travel within the semiconductor by designing specifically-oriented, structural features, such as high aspect-ratio nanorods,[19-22] into the material morphology. The rods then maintain the thickness component of the semiconductor material to maximize light harvesting, but the electron-hole pairs can also reach the electrical junctions by traveling orthogonally to the long dimension of the rod and out radially along the short axis.[1] Structural features can also enhance light absorption by allowing incident photons to be reflected or diffracted back into the material for subsequent absorption rather than being lost by the same processes at a planar surface where such recycling is not possible.[22-25] Dye-sensitized photoelectrochemical (DS-PEC) cells represent another route toward a low-cost device for converting solar energy to electricity. These cells are commonly referred to as photogalvanic cells or Grätzel cells after Michael Grätzel who has pioneered their development over the last twenty years.[26-31]

DS-PEC cells are characterized by a mesoscopic, semiconducting metal oxide film in which a monolayer of dye has been attached to the surface by some functional group (such as carboxylic acids,[32-34] phosphonic acids,[35-39] siloxanes,[40-43] acetylacetonates,[44,45] amides,[46-48] or boronic acids[49]) imparting high stability in a range of appropriate media for these cells. This functionalized metal oxide film operates as a photoanode and is placed in contact with a redox active electrolyte or a hole conducting organic layer that bridges a gap to a separate counter electrode that is also connected to the photoanode by an external wire, thus completing a circuit, see Figure 1.2. Stable, wide band gap semiconductors are used in these systems, most notably TiO_2, although ZnO,[19,22,50] Nb_2O_5,[51-54] $SrTiO_3$,[55-57] and others have

also been studied.[29,58,59] Sensitization is the process of generating photocurrent with light energy that is less than the semiconductor band gap, and light-absorbing dyes used in this manner are called sensitizers. The dye absorbs light to form an excited state that undergoes reductive quenching, on the femto- to picosecond time-scale, via electron injection to the metal oxide conduction band.[14,60] A built-in inhibition to back electron transfer arises from the absence of energy levels in the semiconductor band gap.[61] Next, the oxidized dye is reduced by electron transfer from the electrolyte, typically the iodide/triiodide couple, eq. 1, in an organic solvent, such as acetonitrile.

$$I_3^- + 2e^- \leftrightarrow 3I^- \qquad (1)$$

Back electron transfer of the photo-injected electron to the oxidized sensitizer is avoided when regeneration of the dye occurs from iodide, I^-. The latter process is faster and exemplifies one of many favorable kinetic phenomena that operate in the Grätzel cell, Figure 1.2.[30,60] Subsequent reduction of the triiodide at the chemically-inert counter electrode, typically containing a catalytic amount of platinum, regenerates iodide after intervening electron migration through the external wire. The energy difference between the Fermi level of the photoanode and the redox potential of the electrolyte, I_3^-/I^- in this case, establishes an upper limit for the photovoltage produced by the system.[30]

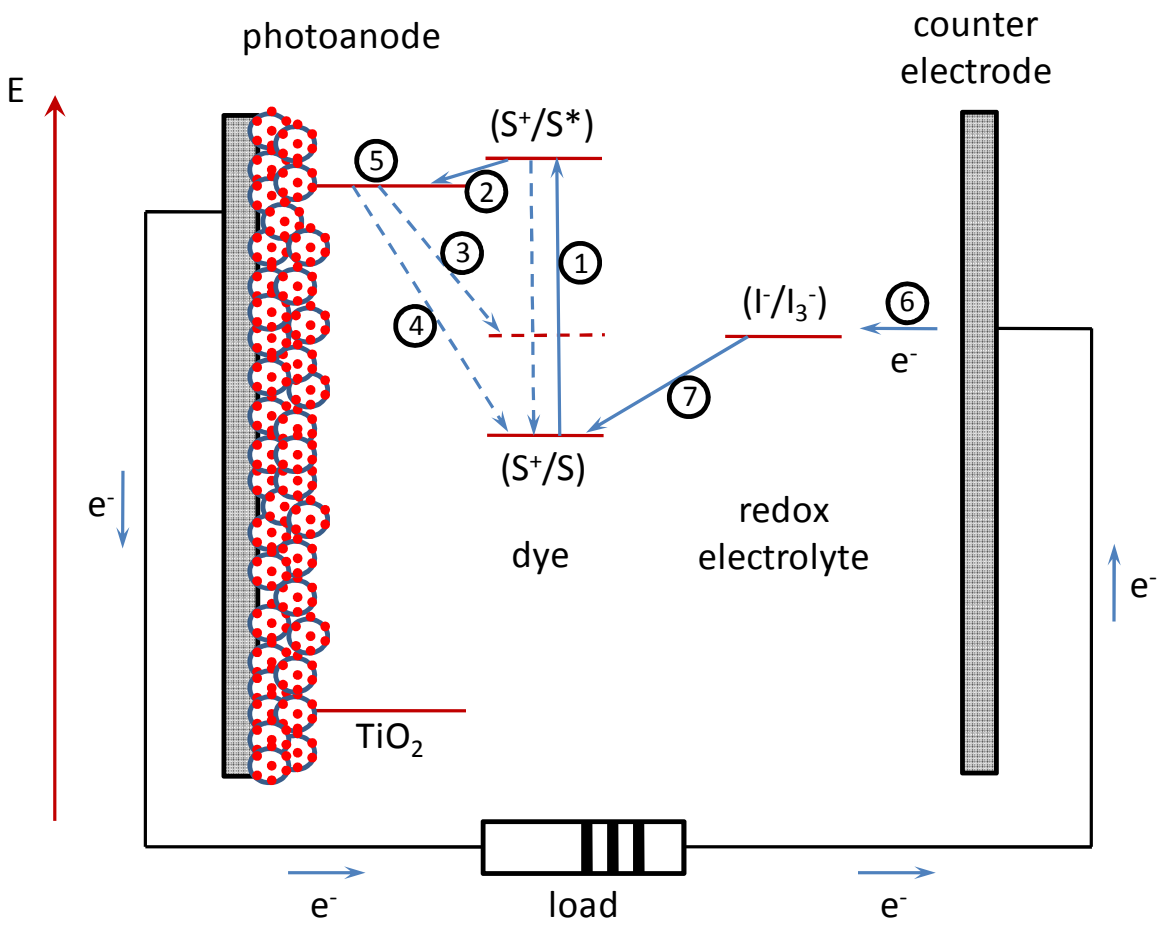

Figure 1.2. An illustration of a conventional dye-sensitized solar cell and its relative energetics, reaction kinetics, and electrode current densities. The processes are: (1) initial light absorption of the sensitizer, followed by (2) rapid excited-state electron injection into the TiO_2 conduction band with $k = 10^{10}$ - 10^{12} s^{-1} (3) back electron transfer to oxidized donors, I_3^- (4) charge recombination of injected electrons with oxidized sensitizers, $k = 10^6$ s^{-1} (5) electron migration through the TiO_2 film, $k = 10$ - 10^3 s^{-1} (6) reduction of triiodide at the counter electrode (7) regeneration of the oxidized dye by iodide with $k = 10^8$ s^{-1}. The current density at the photoanode is $j_0 = 10^{-11}$ - 10^{-9} A/cm^2 and at the counter electrode, $j_0 = 10^{-2}$ - 10^{-1} A/cm^2.[60,62] Competing processes are indicated by the dashed arrows.

Anatase TiO_2 nanocrystals of 20 nm diameter, that have shown the best performance, are spread on a conducting glass electrode and annealed at 450 °C in a short sintering process to establish an interconnected film of electronically-coupled particles.[63] The advent of sponge-like, nanostructured films of high surface area[26] was a substantial breakthrough in the early development of these cells because the amount of light absorbed by a monolayer dye

attached to a flat semiconductor surface is extremely low.[64] The optical density of a two-dimensional cross section of a standard DS-PEC cell relative to a planar metal oxide surface is $>10^2$ higher with typical values being ~5.0 x 10^{-8} mol/cm^2 and ~1.0 x 10^{-10} mol/cm^2, respectively.[65] Electron percolation through the TiO_2 network[66] is facilitated by charge compensating cations in the electrolyte.[67] Interpenetrating cations screen the negatively-charged electron by shadowing its migration through the film, thereby eliminating the internal field along with associated drift term that would appear in the relationship describing charge transport.[60] In the absence of this effect, movement of electrons throughout the material would be impeded where the Coulombic potential of percolating electrons is accompanied by an uncompensated local space charge. Electrons migrate rapidly through the TiO_2 layer with a diffusion coefficient of 10^{-4} cm^2 s^{-1}, which translates to a 10 ms traverse of a 10 μm thick film. Note that the electrochemical potential of the electron is maintained during diffusion.[30]

Electron injection from the excited state sensitizer is in competition with radiative as well as nonradiative deactivation pathways. This deleterious decay occurs with rapid kinetics ranging from 10^3 to 10^{10} s^{-1}.[15,60] Thus, injection kinetics need to be much faster so that a high quantum yield for electron transfer to the conduction band is obtained. The nature of the functional group providing surface attachment becomes a critical element in cell design as it relates to the degree of electronic coupling between the lowest unoccupied molecular orbital (LUMO) of the dye and the conduction band of the metal oxide.[15,35,60,68,69] Stability is also tied to this chemical interaction between the dye and exposed titanium atoms. For practical application, device performance should be consistent for at least twenty years, which amounts to over 50 million dye turnovers.[30]

A number of areas have been heavily researched to improve the efficiencies of Grätzel cells – new semiconductors,[29,58] sensitizers,[70-75] redox electrolytes,[76-83] functional groups for surface attachment.[18,31] However, energy storage is a lingering issue with these systems; sunlight is diffuse (~170 W m^{-2}) and intermittent, requiring its efficient storage before the sun can be used to power human civilization day and night, rain or shine.[1] The electrical output of solar cell technology can be coupled to catalysts for the production of solar fuels, but sequential conversion from solar energy to electrical energy to chemical energy is inundated by the cumulative device inefficiencies.[84] Commercial water electrolyzers that catalyze water splitting, i.e. $2H_2O \rightarrow 2H_2 + O_2$, operate at ~70% energy conversion efficiency, hence H_2 production can be achieved with an overall competence of ~12%.[85] Manufacturing costs along with inefficiencies in conversion and storage have to be reduced before large-scale fuel production becomes viable. Inexpensive, robust catalysts exhibiting low overpotentials and kinetically facile chemical transformations are required to improve these conversions toward far-reaching commercial expediency.[86] Solar fuel can also be generated from the reduction of CO_2 to generate chemicals such as methane, methanol, or higher order hydrocarbons. CO_2 also represents an abundant C1 substrate that can be exploited in value added synthesis as a cheap chemical feedstock; its utilization would inherently reduce its atmospheric concentration. In principle, the direct conversion from solar energy to solar fuels could be achieved with higher overall efficiencies by omitting the transitional step through electricity.[84] Nature has provided a blueprint for how one might go about this process.

In biology, the water-splitting reaction is accomplished by oxygenic photosynthesis. In the light-driven reaction of Photosystem II, Figure 1.3, of the natural photosynthetic

apparatus of green plants, molecular oxygen is released at the Oxygen Evolving Complex (OEC) according to the reaction in eq. 2.

$$2H_2O \rightarrow O_2 + 4H^+ + 4e^- \qquad (2)$$

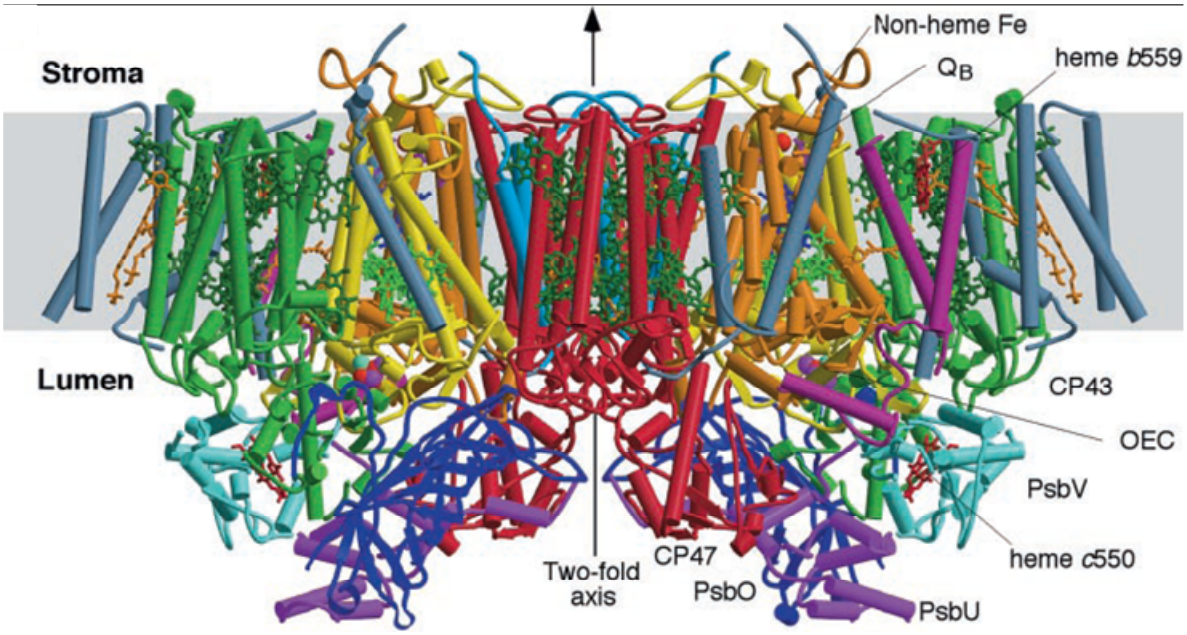

Figure 1.3.[87] Crystal structure of the Photosystem II dimer within the thylakoid membrane at 3.5 Å resolution. Helices are represented as cylinders. All protein subunits, and cofactors assigned by Ferreira and coworkers.[87]

Single-electron activation of the OEC transpires via the Kok cycle beginning with state S_0 and culminating with oxygen evolution from the transient S_4 state after $4e^-$ and $4H^+$ have been removed.[88] The reductive equivalents are used to drive the synthesis of adenosine triphosphate (ATP) and nicotinamide adenine dinucleotide phosphate (NADPH), by ATP synthase and Photosystem I, respectively. Chemical energy is thereby produced from solar energy; a subsequent reaction, spurred by ATP and NADPH, occurs to reduce CO_2 to carbohydrates, such as glucose, in the Calvin cycle. Together the two Photosystems store an

impressive 4.56 eV per cycle in two photogenerated NADPH molecules, in addition to seven equivalents of ATP with 7.5 kcal/mol stored/ATP.[84]

The machinery of photosynthesis is housed in organelles called chloroplasts; a single cell found in the leaves of green plants can have from 1 to 1000 of these. A phospholipid membrane provides the exterior shell of the ~5 μm ellipsoidal chloroplast structure, and within this casing, an aqueous fluid called the stroma is present. Long thylakoid "floors" called lamella are arranged within the stroma that allow flattened disc-like structures bound by a thylakoid membrane to stack into columns called grana, as shown in Figure 1.4.

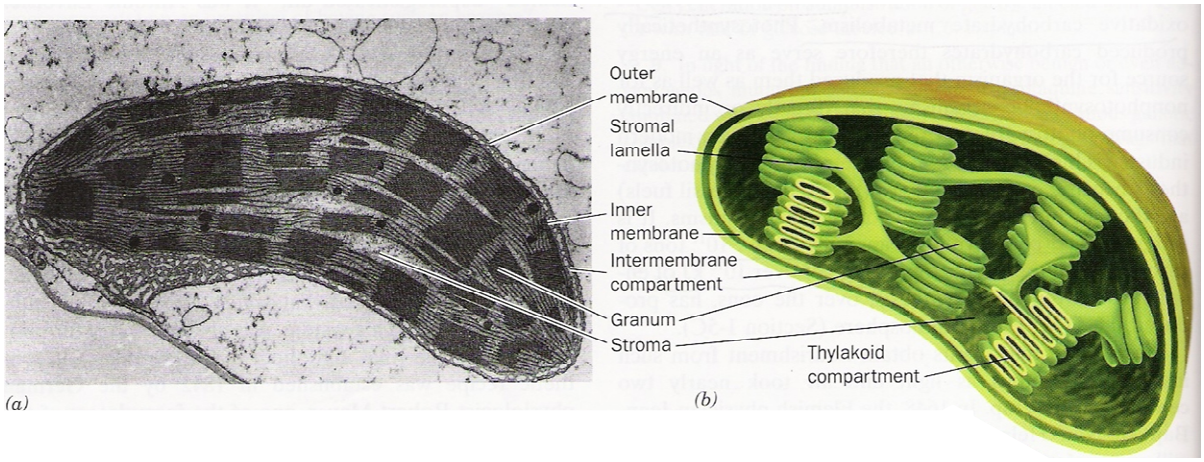

Figure 1.4.[89] Chloroplast from corn. (a) An electron micrograph. (b) Schematic diagram.[89]

Embedded within the thylakoid membrane are four major protein complexes: Photosystem I, Photosystem II, cytochrome b_6f, and ATP synthase. The thylakoid lumen is a fluid contained within the sac formed by the thylakoid membrane. Nearly 100% of the energy input for life on earth is provided by the solar fuel produced from this complex, three-dimensional photosynthetic architecture, Figure 1.5.

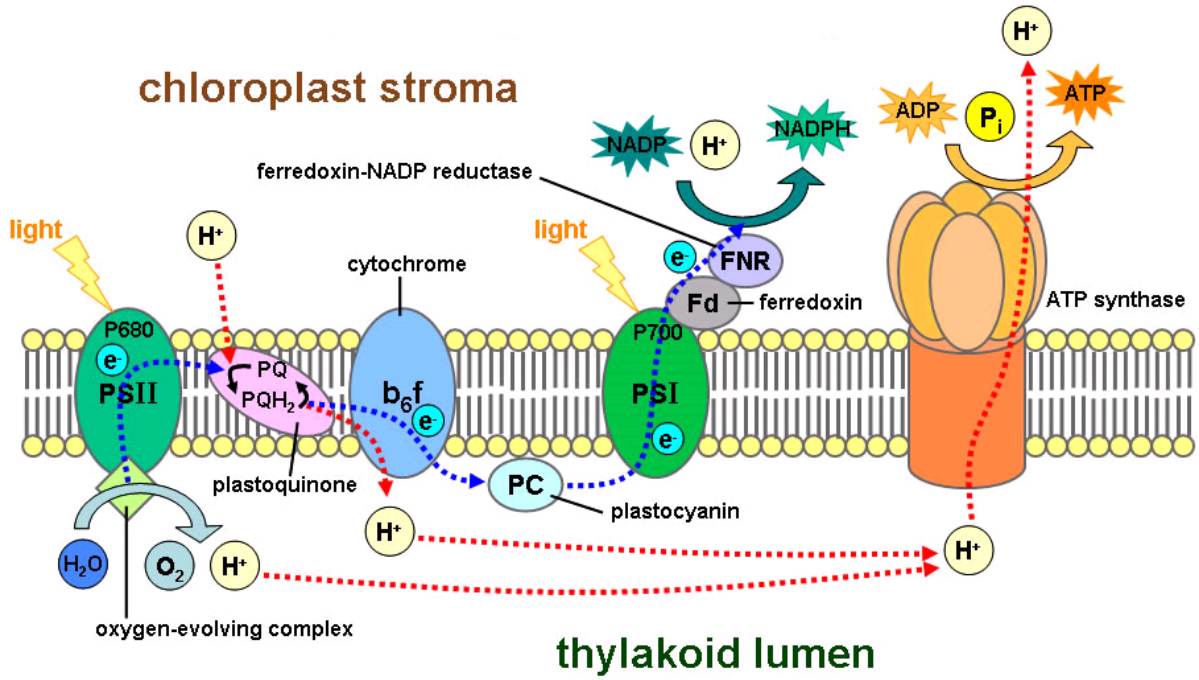

Figure 1.5. Schematic illustration showing the integrated components of oxygenic photosynthesis embedded in the thylakoid membrane.[90]

Shortly after nature was able to use water as a source of protons and electrons, oxygen-dependent life forms appeared on Earth.[91] This overall process is essential for life as we know it, providing oxygen as a metabolic oxidant and maintaining the earth's atmosphere in its current constitution.[92] Natural photosynthesis is initiated by light absorption by a chlorophyll pigment, P_{680}, that results in an excited state (P_{680}*). The excited electron is then quenched by a nearby electron acceptor molecule, pheophytin, and sent "downhill" toward Photosystem I on a wireless electron transport chain. Following pheophytin, the electron is shuttled to a neighboring benzoquinone acceptor, Q_A. The resulting charge separated state, P_{680}^{+} - $Q_A^{\bullet -}$, has a physical separation of ~17.5 Å and transiently stores ~1.4 eV of free energy, having been converted from the 1.8 eV of solar energy captured in the initial excited state. The electron transfers are driven by a free energy gradient through a series of finely-tuned molecules, each acceptor having a lower redox potential than its predecessor, in order

to increase the lifetime of the charge separated state. Recombination is in competition with using the energy for productive chemistry, where back electron transfer only produces local heating and wasted redox equivalents. The hole, or the oxidized chlorophyll P_{680}, is reduced on the donor side of P_{680} by long-range proton-coupled electron transfer oxidation of a tyrosine residue, Y_z, ~10 Å away. E°' of the (P_{680}^+/P_{680}) couple is 1.2 V vs. NHE; notice that it is a strong oxidant, thermodynamically capable of oxidizing water with E°' (O_2/H_2O) = 0.82 V at pH 7. This portion of the electron transport chain is necessarily shorter in this direction (between the chlorophyll pigment and the OEC), in order to maintain a thermodynamically-sufficient oxidizing hole. Tyrosine Y_z is hydrogen bonded through its phenolic hydrogen to the imidazole nitrogen of a histidine residue, His_{191}.[93,94] A scheme of the electron transport chain is shown in Figure 6. Oxidation of tyrosine Y_z by P_{680}^+ is relatively slow with $k \sim 10^7\ s^{-1}$, but highly effective with a per photon adsorbed efficiency of $\eta \sim 0.9$. Favoring this process is the much slower ($k \sim 7 \times 10^3\ s^{-1}$) back electron transfer recombination of the $P_{680}^+ - Q_A\bullet^-$ charge separated state. Back electron transfer is slowed dramatically by the long distance involved and the inverted region arising from the highly favorable ΔG°'.[84] In the inverted region, the sum of inner-sphere and outer-sphere reorganization energy ($\lambda = \lambda_i + \lambda_o$) is lower in energy than the driving force (ΔG°) for electron transfer, such that the rate of electron transfer and non-radiative decay actually slow down with increasing thermodynamic favor.[95] More will be said on this point later in the text.

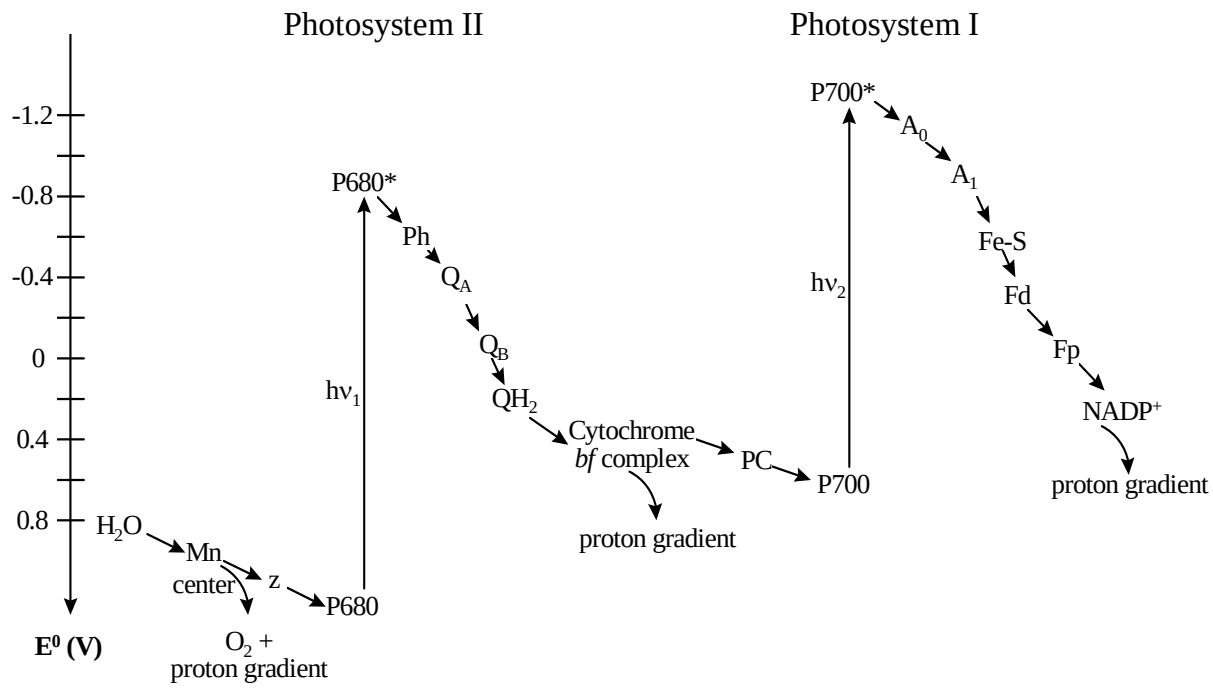

Figure 1.6. Detailed energy diagram (V vs. NHE) of electron transport chain, commonly referred to as the Z-scheme, of photosynthesis.[89]

Nevertheless, the oxidation of tyrosine, Y_z, increases the distance between redox equivalents to ~28 Å in the new charge separated state, $Y_z\bullet^+$ - $Q_A\bullet^-$. Recombination is further slowed to make sufficient time available for oxidative activation of the OEC, the water oxidizing reaction center of Photosystem II. The tyrosine, Y_z, is spatially separated from the nearest Mn ion of the [$CaMn_4$] cluster by around 7 Å.[94,96] This first electron transfer activation of the OEC by $Y_z\bullet^+$ initiates the Kok cycle for water oxidation. Activation of the OEC is relatively slow, ranging from 0.1 to 1 ms depending on the specific step within the Kok cycle, $S_0 \rightarrow S_1$, $S_1 \rightarrow S_2$,… as illustrated in Figure 1.7.

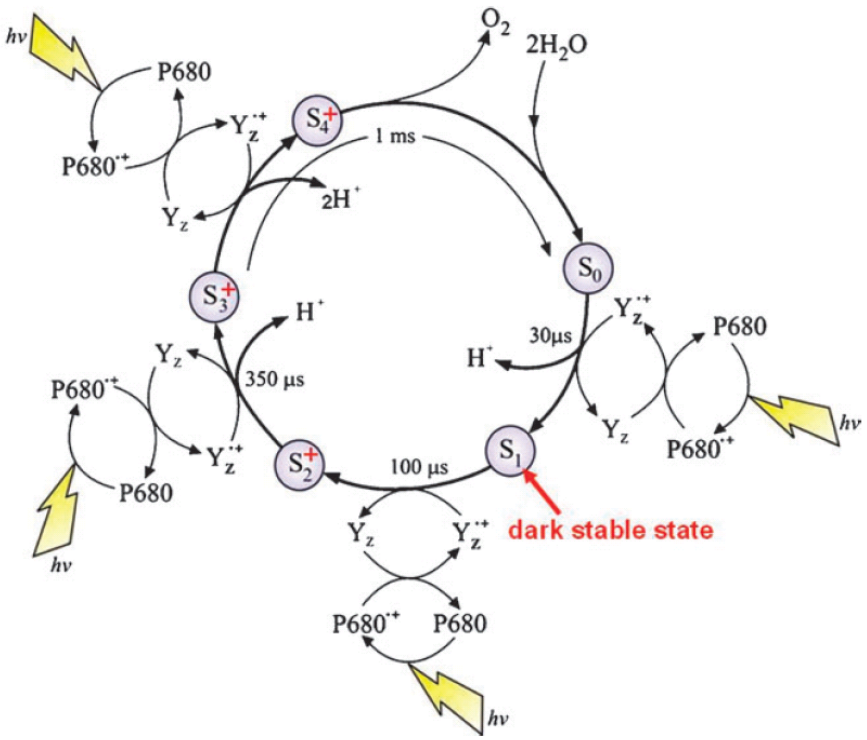

Figure 1.7.[97] The Kok cycle of Photosystem II showing the five steps involved in the four photon process of water oxidation, the proton loss in each transition, and the corresponding reaction half-times. Oxidation of the OEC is mediated by the redox active tyrosine Yz.[97]

Thus, $Q_A•^-$ reduces proximate electron acceptor, Q_B, a plastoquinone, to lengthen the charge separation to around 50 Å. A second reduction of $Q_B•^-$, accompanied by two protons originating from the stroma, takes place in the second stage, $S_1 \rightarrow S_2$, to give the reduced plastoquinol, H_2Q_B.This mobile electron-proton carrier then diffuses through the thylakoid membrane to the cytochrome b_6f complex (plastoquinol-plastocyanin reductase) where it is oxidized back to Q_B resulting in reduced Cu(I) plastocyanin.[84] The energy released in the thermodynamically favored electron transfer is used to translocate the protons supplied by H_2Q_B from the stroma into the lumen. In this manner, cytochrome b_6f acts as a proton pump, translocating protons across the thylakoid membrane, and precedes the electron transport

chain to Photosystem I via plastocyanin. This begins a process in which a proton gradient is established, which is ultimately used for the synthesis of ATP.

ATP synthase and cytochrome b_6f work in concert to generate ATP in a process called photophosphorylation. Electron transfer along the electron transport chain produces an electrochemical potential gradient ($\Delta\Psi$) that is coupled to the translocation of protons by cytochrome b_6f across the thylakoid membrane. As cytochrome b_6f pumps protons from the lumen to the stroma, the ensuing proton gradient (ΔpH) creates a proton-motive force (pmf) that is used to drive ATP synthase to form ATP from adenosine diphosphate (ADP) and inorganic phosphate (Pi). Electrical neutrality is avoided to allow the accumulation of $\Delta\Psi$ and ΔpH, both of which are needed to establish pmf. A key function of membrane compartmentalization in biological systems is maintaining these gradients, or imbalances. At the heart of bioenergetics is the coupling of a thermodynamically favorable reaction with a thermodynamically unfavorable reaction, such that the overall free energy of the system decreases, allowing the desired work to be accomplished. For example, a high-energy state transitions to a lower-energy state in order to afford uphill reactions such as charge separation and osmotic gradients.[85]

A continuous stream of protons is supplied to the lumen (~pH 4) from water oxidation at the OEC and is consumed in the terminal proton-coupled reduction of $NADP^+$ to NADPH. Electrons supplied, ultimately from water, to cytochrome b_6f and onto Photosystem I through the mobile, water-soluble plastocyanin culminate at chlorophyll, P_{700}. Subsequent light absorption takes places at P_{700} to enhance the reducing strength of the electrons prior to the reduction of $NADP^+$ to NADPH by ferredoxin: $NADP^+$ oxidoreductase. Once ATP and NADPH have been produced, the fixation of CO_2 takes place in the stroma through a process

known as the Calvin cycle. The overall conversion of solar energy to chemical energy executed in natural photosynthesis is given in eq. 3.

$$6CO_2 + 6H_2O + 24h\nu \rightarrow C_6H_{12}O_6 + 6O_2 \quad ; \quad \Delta G°' = 29.1 \text{ eV}, n = 24 \qquad (3)$$

A closer examination of chlorophyll reveals many pigment molecules arranged to form a light harvesting antenna that serves to increase the absorption cross section. Light absorption is then found to initiate an excited state that after a series of energy transfer steps is funneled to a reaction center where charge separation takes places. Covalent bonds arrange the pigments spatially to account for intermolecular distance, relative angles, and electronic coupling. Two different energy transfer mechanisms, identified as Dexter and Förster, are possible in any given system. Dexter energy transfer occurs between chromophores that have sufficient orbital overlap following van der Waals contact.[93] This is otherwise known as electron superexchange and bears a distance dependence that decays by e^{-2r} (where r equals radius) as the orbital overlap decreases. Förster energy transfer is a through-space mechanism with r^{-6} dependence that originates from nonradiative coupling of a donor emission dipole and an acceptor absorption dipole. Weaker distance dependence is observed in this mechanism, allowing Förster energy transfer to occur over much longer distances.[98] A lot of flexibility is offered between the two mechanisms for designing light harvesting arrays that can take advantage of bridging ligands and distance in order to direct excited state energy transfer to a specific location.

Recent spectroscopic studies and X-ray diffraction of Photosystem II reveals a complex structure that enables the management of protons and electrons exiting the active site.[87,99-103] The OEC consists of a Mn_3Ca cluster in a cubic arrangement with oxygen atoms at the corners and a fourth Mn attached by di-μ-oxo bridging and a bridging glutamate off a

Mn in the cluster. Oxygen is thought to evolve at this dangling Mn.[87,100,101,103,104] The OEC is an intricate structure that has been described as being "wired for protons".[94] A proton transport chain is directed away from the OEC to manage protons through their transfer along a series of Lewis basic amino acid residues that line a hydrophilic channel. In a matter of ~10 μs, protons navigate 30 Å along the proton exit channel to reach the lumen.[94] The lengths that photosynthesis goes to in establishing pmf explicate the importance of proton management. Furthermore, proton coupled electron transfer (PCET) plays an important role in the light-driven reactions of photosynthesis.[94]

PCET broadly refers to reactions in which both electrons and protons are transferred. This involves the stepwise reactions: proton transfer following by electron transfer (PT-ET) and electron transfer followed by proton transfer (ET-PT), as well as a third, mechanistically-distinct pathway characterized by the simultaneous movement of a proton and an electron. This concerted process is identified as coupled-electron proton transfer (EPT).[105-119] EPT is different from H-atom transfer (HAT) or hydride transfer in which both the electron and proton are transferred from the same chemical bond. Mechanistically, EPT is distinguished by electrons and protons transferring from different orbitals on the donor to different orbitals on the acceptor.[96] There are design elements to consider originating from the intrinsic mass difference between protons and electrons, and the required overlap of their respective donor-acceptor wavefunctions. Their coupled long-range transfer requires an architectural scaffold that facilitates this process. Protons can tunnel over a limited distance of only a few angstroms, whereas tens of angstroms can be tunneled by electrons. Therefore, nature couples long-range electron transfer to long-range proton transfer via a series of stepwise,

short-range proton transfers using hydrogen bonding.[85] This is clearly demonstrated in the proton transport channel trailing away from the OEC.

There are thermodynamic and kinetic implications associated with PCET. Kinetically inhibited pathways and high energy intermediates in reactions involving protons and electrons can be avoided when the concerted mechanism is available.[84,96,105,106] Charge accumulation is also avoided in PCET reactions as electrons and protons are lost. Consider the oxidation of $[Ru^{II}(bpy)_2(py)(OH_2)]^{2+}$ to $[Ru^{III}(bpy)_2(py)(OH)]^{2+}$ to $[Ru^{IV}(bpy)_2(py)(O)]^{2+}$ where the overall charge is maintained over two adjacent redox couples.[96,105] The separation between these redox couples is a mere 0.11 V. Adjacent metal couples in which charge build-up is observed typically have $\Delta E°'$ ranging from 0.5 to 1.5 V. The Ru(IV/III) and Ru(III)/II) couples in $Ru(bpy)_2Cl_2$ have $\Delta E°' = 1.7$ V.[84] "Redox potential leveling" is a term used to describe the occurrence of closely spaced redox couples that originate from PCET reactions.[106] PCET occurs due to the decreased electron content and its effect on the p*K*a properties of the molecule having acidic protons. The narrow potential range between redox couples in *cis*-$Ru(bpy)_2(py)(OH_2)^{2+}$ points to the significant stabilization of Ru(IV), which arises from proton loss and oxo formation. An orbital basis for this behavior is described in Figure 1.8. The multiple bonding Ru=O interaction is manifest by the overlap between $d\pi$ orbitals on Ru and the $2p\pi$ orbitals on oxygen. The sp_O and $p_{\pi,O}$ electron pairs on oxygen are available for electron donation and orbital interaction with the vacant $d\pi^*$ orbitals, which are largely $4d_{Ru}$ in character. The $d\pi_n$ orbitals are also largely $4d_{Ru}$ in nature, but are of the wrong symmetry to mix strongly with the oxygen orbitals, and are consequently nonbonding.[105]

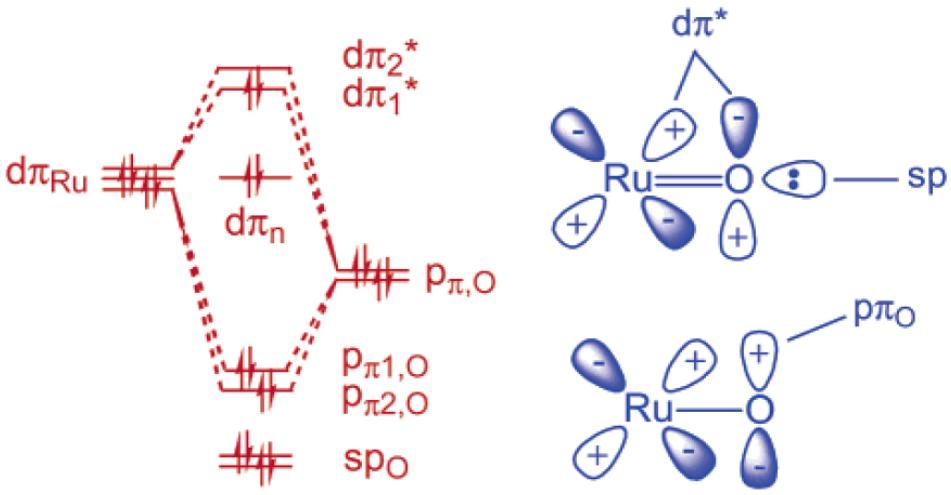

Figure 1.8.[105] $Ru^{IV}=O^{2+}$ schematic energy orbital diagram.[105]

Illustrated in Figure 1.9 is the comproportionation reaction of *cis*-$Ru^{II}(bpy)_2(py)(OH_2)^{2+}$ and *cis*-$Ru^{IV}(bpy)_2(py)(O)^{2+}$ (bpy = 2,2'-bipyridine and py = pyridine) to generate two equivalents of *cis*-$Ru^{III}(bpy)_2(py)(OH)^{2+}$.[120-122] Three possible mechanisms are described: (a) electron transfer followed by proton transfer, (b) proton transfer followed by electron transfer, and (c) concerted electron-proton transfer. The net reaction is the same in each case, but the energetics explain why the only observable pathway in the comproportionation reaction is the simultaneous transfer of the electron and proton. Specifically, the electron transfers from $d\pi_{Ru(II)}$ to $d\pi^*_{Ru(IV)}$ and the proton transfers from σ_{O-H} to $p\pi_O$ or $sp^2{}_O$. Reaction (a) is accessible, but is uphill by at least 0.55 eV because Ru^{III}-O^+ is formed and the estimated p*K*a for Ru^{III}-$OH_2{}^{2+}$ is >13. The experimental value of the reaction for $\Delta G^{\neq}$ is 0.44 eV, excluding any significant contribution of pathway (a). An even less favorable driving force (> 0.59 eV) is calculated for reaction (b) due to the low proton affinity of the oxo group. The EPT pathway (c) is the low-energy mechanism and dominates the reactivity as it is thermodynamically downhill with $\Delta G°'$ = -0.11 eV.[105]

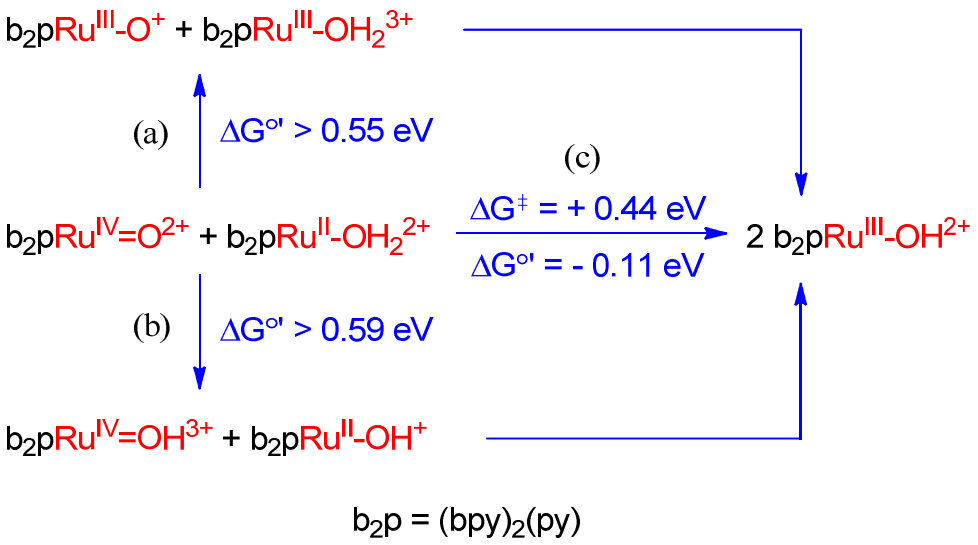

Figure 1.9. Reaction scheme describing the proton-coupled electron transfer comproportionation of *cis*-$Ru^{II}(bpy)_2(py)(OH_2)^{2+}$ and *cis*-$Ru^{IV}(bpy)_2(py)(O)^{2+}$. ΔG°' values are cited for each of the mechanistic possibilities (ET-PT, EPT, and PT-ET).[105]

PCET allows for the accumulation of multiple redox equivalents at a single site or cluster. It is used extensively throughout biology, and is of paramount consequence in small molecule activation and energy conversion. The proton-coupled electron transfer reaction of tyrosine Y_z with histidine His_{191} has been studied in detail, and plays an important role in the oxidative activation of the OEC.[94,123-125] Oxidation of tyrosine Y_z involves the transfer of a proton to His_{191}. Oxidation of Y_z is in competition with the charge recombination back reaction between P_{680}^+ and the reduced quinone $Q_A\bullet^-$, requiring rapid kinetics. At full speed Photosystem II can oxidize approximately 200 water molecules per second.[1] Thermodynamic values have been calculated showing the energetic advantage afforded by the coupled movement of protons and electrons, where the EPT pathway is favored over the nearest sequential pathway (ET-PT, PT-ET) by almost 0.5 eV. The p*K*a of 10 for the tyrosyl phenolic proton becomes significantly more acidic upon oxidation with p*K*a = -2.[94]

EPT is utilized at the OEC during oxidative activation as well as in the oxygen-oxygen bond forming step of water oxidation. Removal of the Ca ion from the coordination sphere of the OEC, Mn_4O_4Ca cluster, has been shown to inhibit the $S_2 \rightarrow S_3$ transition, where O···O coupling is thought to occur. This result, in conjunction with various spectroscopic measurements that have focused our view of the OEC, indicate the appended Mn ion and Ca ion are at the epicenter of water oxidation. Aqua ligands fill the coordination spheres of these ions and an aspartate residue, Asp170, is found in close proximity. As the electron density in the cluster decreases with each sequential oxidation, proton acidity increases, such that Mn^{IV}=O is formed and proton loss, enabled by Asp170, gives Ca-OH^-.[94] Again, removal of Asp170 disables the OEC toward water oxidation, emphasizing its contribution to the observed reactivity.[84] Nucleophilic attack by a lone electron pair of oxygen, originating from the native Ca-OH_2 group, on the electrophilic oxo substituent of the Mn^{IV} ion is proposed, Figure 1.10. It follows then that a high energy Mn-(HOOH) intermediate would be implicated after O-O bond formation without prior deprotonation of the Ca-OH_2 substituent. Asp170 provides an internal base, enabling a more energetically feasible pathway – deprotonation of Ca-OH_2 to Ca-OH^- prior to O-O coupling. While the carboxylate anion, $^-$OOC-Asp170 (p*K*a 4-5), appears to be too far away for direct proton transfer from Ca-OH_2, hydrogen bonding to Asp170 by a second aqua ligand at the Mn ion likely mediates proton transfer. Participation of Asp170 is further explained as alternative pathways invoking a water molecule acting as a proton transfer agent are unfavorable in light of its pK_a values, pK_a(H_2O) = 15.7 and pK_a(H_3O^+) = -1.74. Water is neither a good nucleophile nor a good electrophile. The Ca ion serves to make water a better nucleophile with a pK_a value for

Ca^{2+}(aq) equal to 9.7; conversely, oxidation of Mn^{II}-OH_2 to Mn^{IV}=O gives water more electrophilic character.[94]

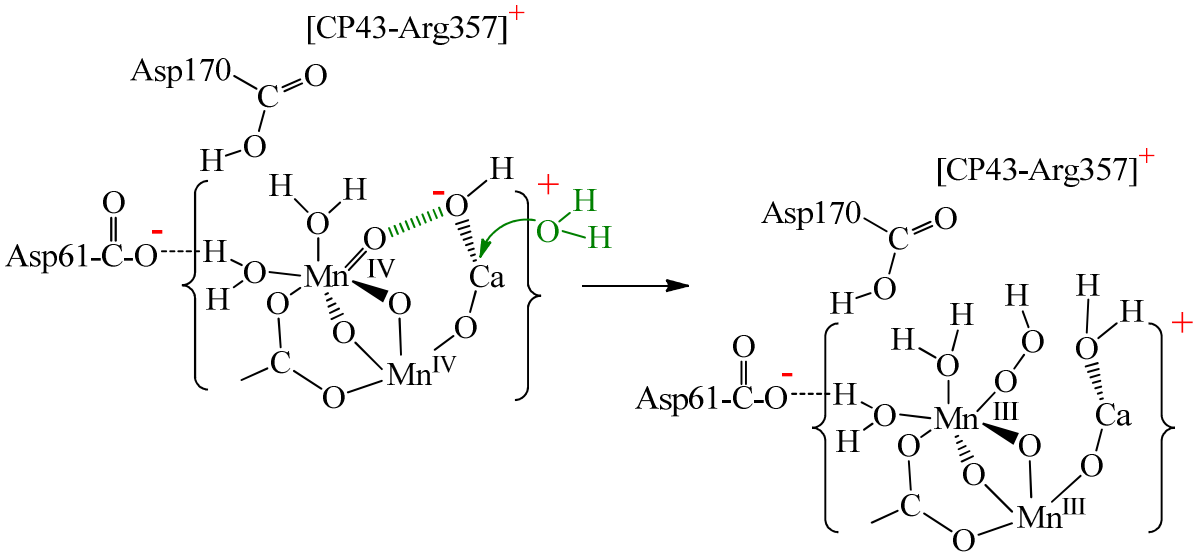

Figure 1.10. Reaction scheme detailing the proposed oxygen-oxygen bond forming step of water oxidation in the OEC.[94]

Using nature as a guide, key features and underlying concepts gleaned from natural photosynthesis can be implemented into strategies for the conversion of solar energy to chemical fuels. In a breakthrough experiment, a short-lived charge separated state was discovered in solution upon electron transfer quenching of excited state $[Ru(bpy)_3]^{2+}$* by methylviologen (MV^{2+}) and reduction of the resulting oxidized metal complex by triphenylamine (NPh_3).[126] A similar experiment is described in Figure 1.11 using 10-methylphenothiazine (10-MePTZ), in which visible light is used to drive an endoergic reaction.[61,95]

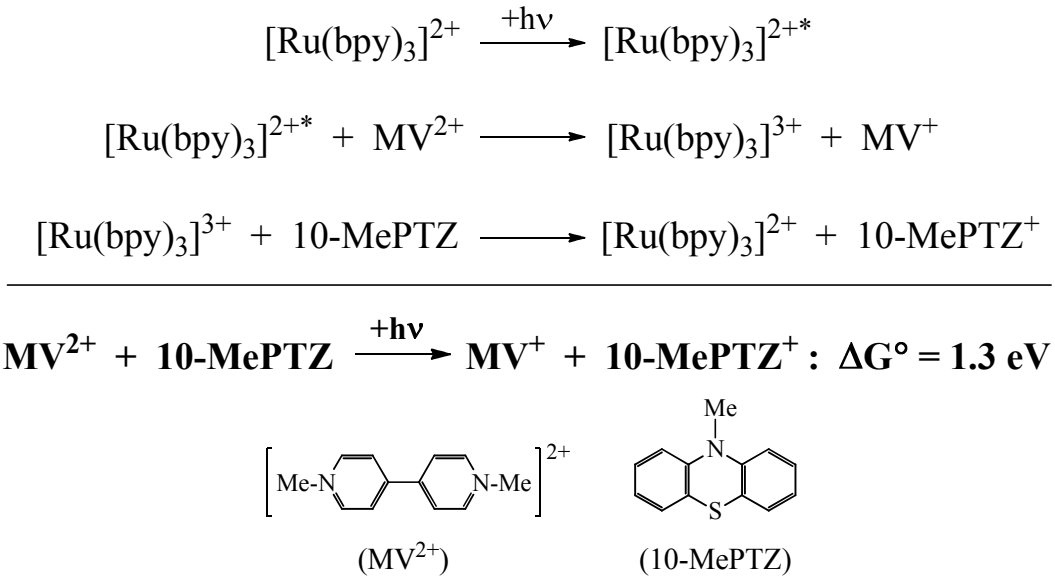

Figure 1.11. Reaction scheme depicting energy conversion via a charge separated state promoted by excited-state electron transfer quenching.[61]

The photogenerated electron transfer products allowed the transient storage of 1.3 eV of energy, but there was no directional control or molecular basis for storing or utilizing the redox equivalents before recombination. This initial experiment, however, provided the basis for a new field called artificial photosynthesis. Later a conceptual report outlining an integrated modular assembly was introduced[127] in order to emulate the fundamental steps required for natural photosynthesis: 1) light absorption, 2) excited state electron transfer quenching, 3) redox separation by electron transfer, 4) electron transfer activation of catalysts, 5) repetition of steps 1-4 to accumulate multiple redox equivalents at catalyst sites, and 6) subsequent reaction of the activated catalysts.[61]

Figure 1.12 illustrates two possible strategies toward the development of integrated modular assemblies, each bearing key components of an artificial photosynthetic apparatus. There are several significant differences between these two approaches.

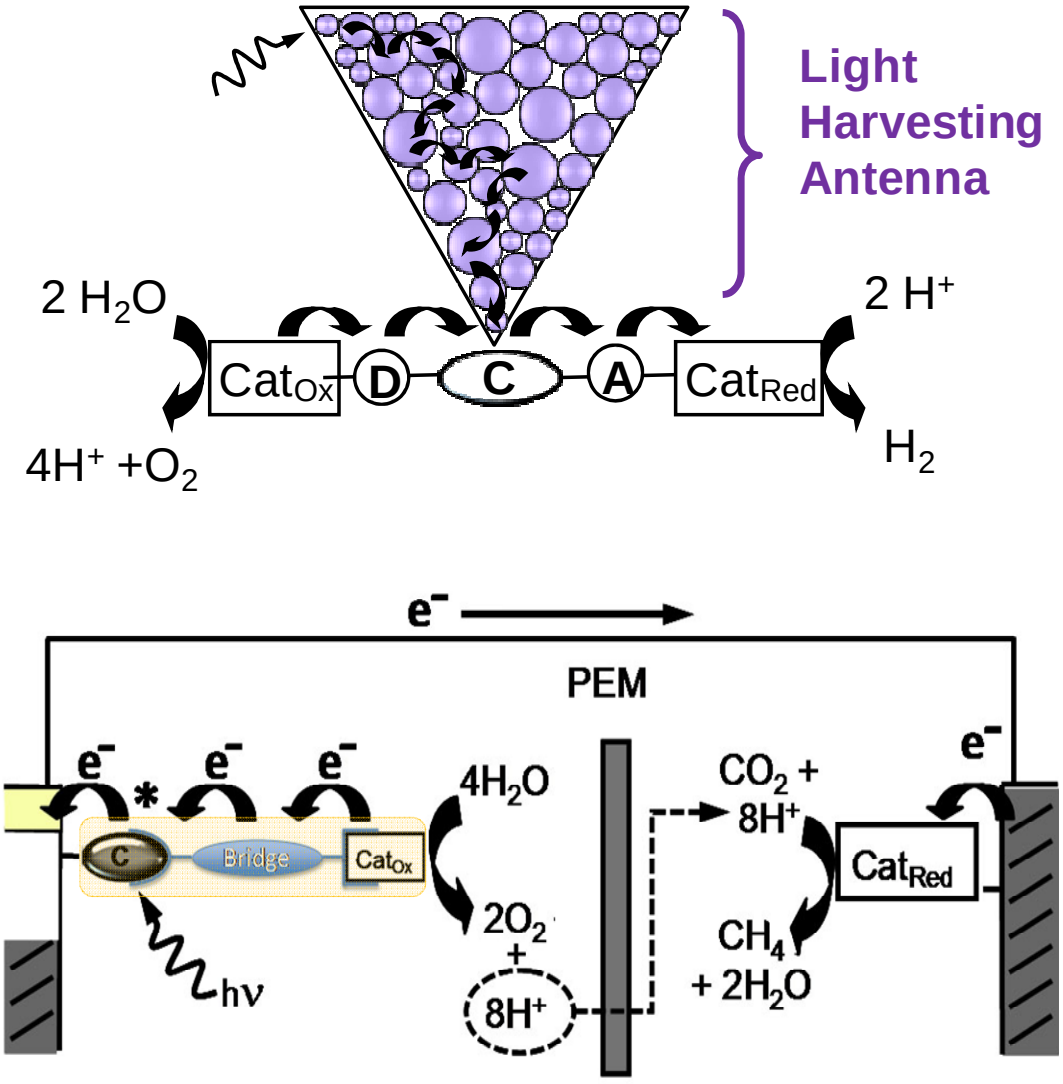

Figure 1.12. Diagrams showing key features of potential photosynthetic devices. (Top) Photochemical water splitting into H_2 and O_2 with an integrated modular assembly detailing electron transfer events after excitation of the light harvesting antenna.[61] (Bottom) A high surface area metal oxide has replaced the antenna array, and photochemical water oxidation is coupled to the reduction of CO_2 to methane. Abbreviations are: Cat_{Ox} = oxidation catalyst, Cat_{Red} = reduction catalyst, D = electron transfer donor, C = chromophore, A = electron transfer acceptor, and PEM = proton exchange membrane.[61]

In the top assembly, light absorption would likely require a light harvesting antenna to achieve efficient operation. Solar energy is diffuse and the absorption cross-section of a single molecule is low. Excitation of an antenna array followed by energy transfer

sensitization of a low-energy “reaction center” chromophore, C, would initiate charge separation. Semiconducting metal oxides are used in the lower assembly, analogous to the photogalvanic cells discussed earlier. Photosynthetic devices benefit in a number of ways by using metal oxide films: 1) high surface areas allow the absorption cross-section to be maximized, 2) facile diffusion of small molecule substrates and charge compensating ions can occur through the highly porous structure which is 50-70% void space, 3) easy, reversible tuning of unfilled acceptor states can be achieved, 4) efficient collection of injected electrons has been demonstrated, and 5) wide-band gap metal oxides offer high transparency from the visible to infrared regions of the electromagnetic spectrum.[128] The cross-section of the top assembly can be optimized by simply increasing the concentration in its respective medium; however, without the specific orientation allowed by surface attachment, inter-assembly electron transfer would be unavoidable and likely deleterious to its function. Synthetic demands are also simplified to some extent in the spatial separation of the two half reactions as in the lower assembly, reducing the covalent bridging and associated challenges by at least one.

Nonetheless, an integrated modular assembly is an approach that offers a significantly simplified route to artificial photosynthesis relative to the highly complex, intricate architecture that evolved over several billion years in nature. Compatible modules of the integrated assembly are needed that allow for their controlled sequential and spatial arrangement, possessing high general stability and a robust molecular framework to survive the activated catalysts and surrounding medium. Practical application would require an affordable, scalable synthesis with device stability on the order of $>10^8$ turnovers, corresponding to a ~20 year lifetime. Unlike the natural photosynthetic apparatus that self-

assembles and regenerates itself every ~30 minutes, an artificial system has to withstand the rigors of photochemistry and non-discriminating, potent reactivity. Natural photosynthesis utilizes elaborate light harvesting antennas, consisting of chlorophylls, carotenoids, and sometimes other pigment molecules as well. For example, a specific arrangement of ~90 chlorophyll molecules and 22 carotenoids is employed in Photosystem I to collect light and funnel excited state energy to the reaction center.[61,129] Singlet-singlet energy transfer dominates this concentration of solar energy. Triplet chlorophyll also forms with a quantum yield of ~3%, resulting in the generation of singlet oxygen, which is highly destructive to the photosynthetic apparatus. Carotenoids are thus strategically located to photoprotect the system by their efficient quenching of triplet chlorophyll.[130-141] Triplet-triplet energy transfer occurs through the Dexter superexchange mechanism due to the forbidden nature of the Forster dipole-dipole mechanism available in singlet-singlet energy transfer, meaning photoprotection relies on sufficient orbital overlap between the chlorophylls and caretonoids.[129] Protection mechanisms and self-healing capabilities may need to be developed and implemented in artificial systems in the absence of brute strength.[85,142]

Accumulating multiple redox equivalents at a single site or cluster presents significant challenges, affixed with the build-up of charge and reaction kinetics. Each subsequent removal or donation of an electron at a given catalyst becomes more difficult than the previous redox step, a natural consequence of increasing reactivity/instability. Charge accrual can be counterbalanced by EPT activation, such that redox potentials do not separate dramatically between adjacent couples. Yet as the reactivity increases with mounting redox equivalents, the catalyst is prone to behave as both an electron donor and an electron acceptor. More rapid electron transfer in the productive direction is needed to out-compete

the wasteful back electron transfer reaction.[143] A general understanding of the factors that dictate photophysics is a good starting point.

A classical treatment of electron transfer predicts that four parameters, including temperature, dictate the rate of electron transfer. Equation 4 provides a simple relationship describing the rate of nonadiabatic electron transfer. Orbital overlap between the reactant and the product states determines the electronic coupling, H_{rp}, parameter, while the driving force for the reaction, -ΔG°, and the reorganization energy, λ, account for the other two parameters. Reorganization energy amounts to the energy associated with the reactant and the product reaching their "activated" states by undergoing changes in their respective nuclear configurations, in addition to the specific rearrangement of solvent dipole interactions to compensate the electron transfer. The interplay between reorganization energy and reaction thermodynamics can be readily explained from equation 5, as well as the counterintuitive origin of the inverted region.[144]

$$k_{ET} = \frac{2\pi}{\hbar}\left|H_{rp}\right|^2 \frac{1}{\sqrt{4\pi\lambda k_b T}} \exp\left(\frac{-\Delta G^*}{k_b T}\right) \tag{4}$$

$$\Delta G^* = \frac{(\Delta G^\circ + \lambda)^2}{4\lambda} \tag{5}$$

The free energy-reaction coordinate curves in Figure 1.13 illustrate the three possible cases for simple electron transfer. The normal region where -ΔG° < λ (**I** and **A** in the plots) has an electron transfer barrier that decreases at -ΔG° approaches λ. The maximum rate of electron transfer occurs when -ΔG° = λ and the process becomes barrierless (**II** and **B**). When -ΔG° > λ, the rate begins to slow again; this is the inverted region (**III** and **C**).[61,145]

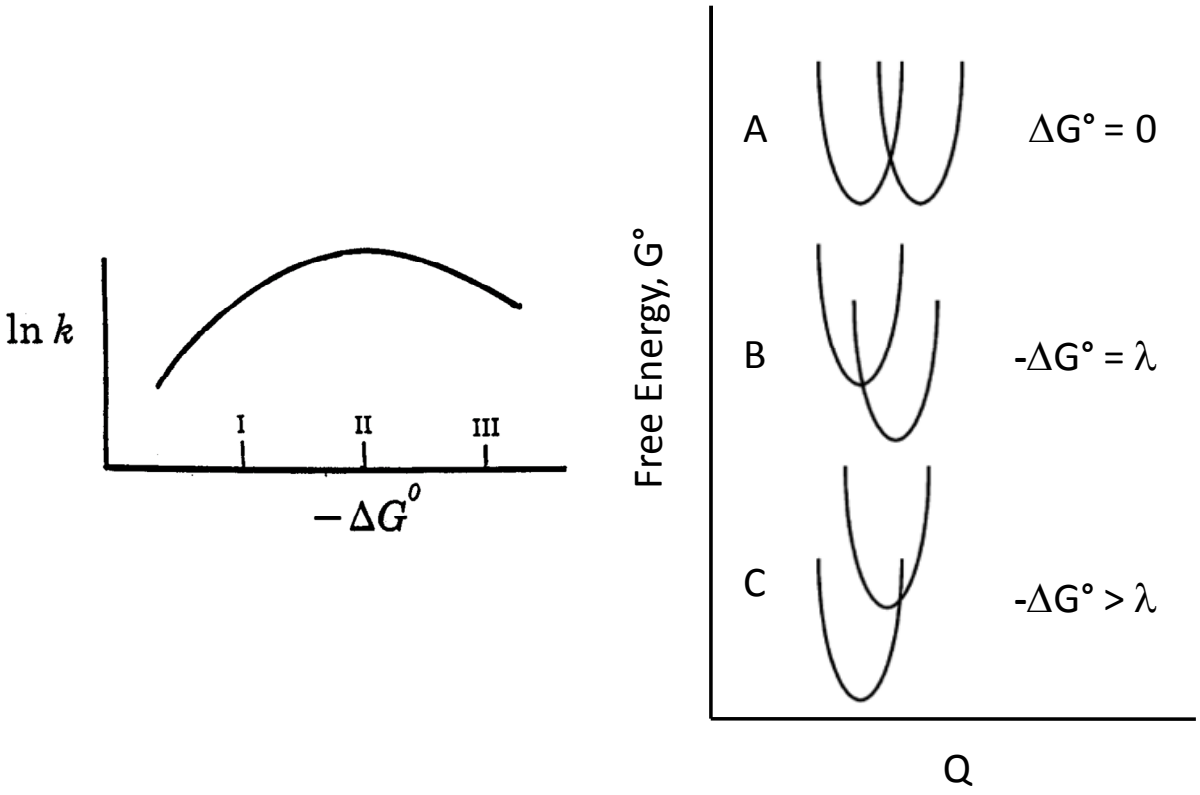

Figure 1.13. Left: Plot of ln *k* vs. -ΔG°.[145] Right: Free energy-reaction coordinate (Q) diagrams illustrating the dependence of the classical barrier to electron transfer on driving force, -ΔG°, at a fixed reorganizational energy, λ.[61]

Electron transfer rates depend heavily on the identity of the arbitrating medium, counter ions, and electronic coupling instilled by the donor-acceptor linkage chemistry as the intervening σ- and π-bonds mediate electron tunneling. Bridge stereochemistry has an additional affect on kinetics by dictating donor-acceptor orientation.[146] In order to design a successful DS-PEC for solar fuels generation, these considerations will have to be addressed.

Artificial photosynthesis is anticipated as one of the most promising routes toward clean energy alternatives.[61,127] In this strategy, photochemical water oxidation at an anode is coupled to a cathode reaction for reduction of protons to hydrogen or carbon dioxide to hydrocarbons or alcohols, as shown in eqs 6 and 7.

$$2H_2O + 4h\nu \rightarrow O_2 + 2H_2 \quad (6)$$

$$2H_2O + CO_2 + 8h\nu \rightarrow 2O_2 + CH_4 \quad (7)$$

Creating catalysts that can effect the multi-electron, multi-proton transformations associated with artificial photosynthesis is the most significant challenge facing the modular approach. Photon-driven, single-electron activation of multi-electron catalysis has to be available, and accessibile EPT pathways as needed. A necessary feature in order to avoid highly unfavorable intermediates, such as the direct $1e^-$ oxidation of water to give H_2O^+ has a redox potential of $E°'(H_2O^+/H_2O) = 2.9$ V, and the direct $1e^-$ reduction of CO_2 to give $CO_2^{\bullet -}$ has $E° = -1.9$ V; these steps introduce high energy intermediates and excessive overpotentials in route to desired products, O_2 and solar fuels such as methanol or methane (see Figure 1.14).

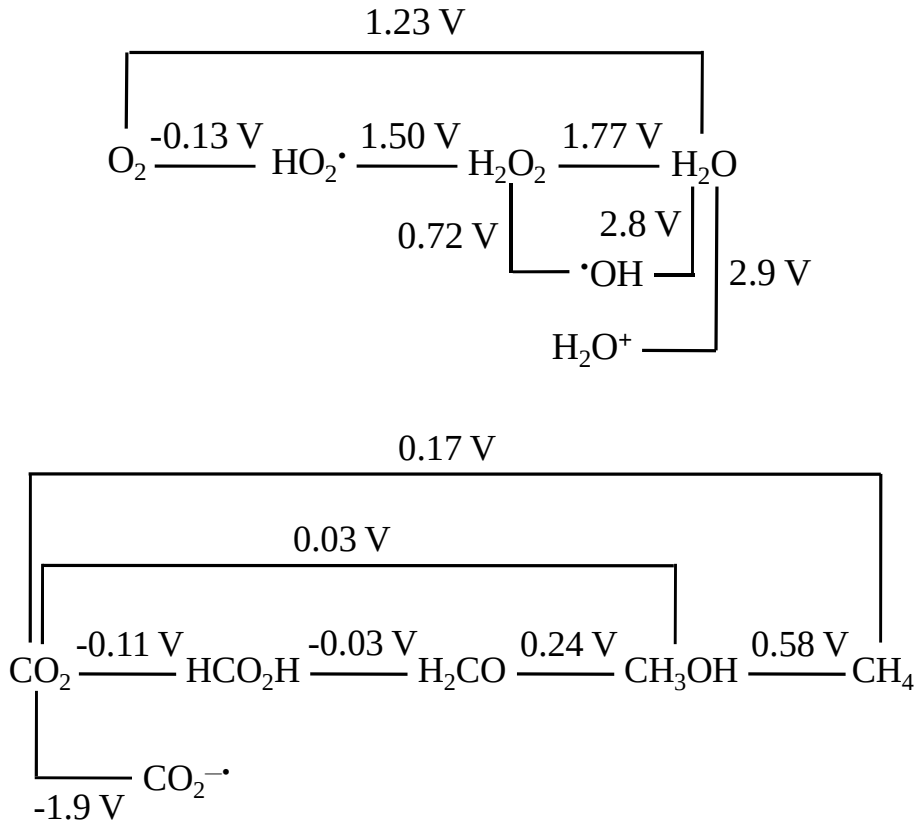

Figure 1.14. Latimer diagrams for (top) O_2/H_2O couple and (bottom) CO_2/CH_4 couple at pH = 0; redox potentials are in V vs. NHE.

Reaction rates and energetics have to be compatible with solar irradiance, such that catalysts can be driven by the available energy and at rates greater than or matching the solar flux. To maximize efficiency, turnover rates of ~1 ms per catalyst are needed to make emitted photons per unit time rate-limiting. Catalyst designs have to be amenable to incorporation into the final assembly and thermodynamically competent to drive the reaction.[61] Water oxidation is a fundamental half reaction that is present in both routes to solar fuel and a difficult chemical transformation for catalysis. The reaction is thermodynamically uphill by 1.23 V vs. NHE at pH = 0 ($\Delta G° = 4.92$ eV) and mechanistically demanding, requiring the loss of four protons and four electrons with the concomitant formation of an oxygen-oxygen bond.

The content of this dissertation will focus exclusively on the water oxidation half reaction of artificial photosynthesis as well as key components associated with light-driven and electrocatalytic water oxidation at metal oxide surfaces. Research projects discussed herein consist of the following chapters:

- *Electronic Structure of the Water Oxidation Catalyst, cis,cis-$[(bpy)_2(H_2O)Ru^{III}ORu^{III}(OH_2)(bpy)_2]^{4+}$. The Blue Dimer.*

The electronic structure of a catalyst is valuable in understanding reactivity, reaction kinetics, and the molecule's ability to accumulate multiple redox equivalents, which is highly beneficial in developing better catalysts. A detailed investigation into the electronic structure of the first synthetic catalyst for water oxidation is presented.

- *Mechanism of Water Oxidation by cis,cis-$[(bpy)_2(H_2O)Ru^{III}ORu^{III}(OH_2)(bpy)_2](ClO_4)_4$. The Blue Dimer.*

Mechanistic studies of the complex discussed in the previous chapter are reported. Reactivity and reaction kinetics have been used to elucidate a mechanism for stoichiometric and

catalytic water oxidation by the blue dimer, as well as unproductive side reactions associated with its redox chemistry.

- *One Site is Enough: Monomeric Water Oxidation Catalysts*

A family of new catalysts were developed following our mechanistic work on the blue dimer and insight gained from the proposed reaction mechanism of the OEC in Photosystem II. Mechanistic results and the role of thermodynamics on reactions kinetics are presented.

- *Diffusional and Surface Bound Electron Transfer Mediators*

Chromophore-redox mediators were employed to enhance reaction kinetics and to activate metal oxide electrodes toward electrocatalytic electron transfer of water oxidation catalysts in aqueous solution. These results are important in demonstrating the feasibility and application of these electron transfer mediators in DS-PEC cells for light-driven water oxidation at wide band gap metal oxides.

- *Electron Transfer Mediators-Chromophore/Catalyst Assemblies*

Components of the two previous chapters and ultimately of an apparatus for artificial photosynthesis were combined in a molecular assembly for water oxidation. The two assemblies reported were studied in electrocatalytic water oxidation at metal oxide surfaces with significant insight gained for future assemblies in photochemical applications.

- *pH Dependence of Phosphonic Acid Derivatized $[Ru(bpy)_3]^{2+}$ and Electrostatic Synthesis of Redox Mediator-Chromophore/Catalyst Assemblies*

The pH dependence of a series of phosphonic acid-substituted $[Ru(bpy)_3]^{2+}$ complexes was studied in solution and bound to electrode surfaces. From the observed deprotonation of the acidic phosphonate protons with p*K*a's around 2 and 6, the negatively charged chromophore-

electron transfer mediators were used to synthesize electrostatically-coupled assemblies with cationic catalysts. The synthesis, reactivity, and stability of these assemblies are reported.

REFERENCES

(1) Balzani, V.; Credi, A.; Venturi, M. *Chemsuschem* **2008**, *1*, 26.

(2) Yang, J.; Banerjee, A.; Guha, S. *Solar Energy Materials and Solar Cells* **2003**, *78*, 597.

(3) Shah, A.; Meier, J.; Vallat-Sauvain, E.; Wyrsch, N.; Kroll, U.; Droz, C.; Graf, U. *Solar Energy Materials and Solar Cells* **2003**, *78*, 469.

(4) Beaucarne, G. *Advances in OptoElectronics* **2007**.

(5) Shah, A. V.; Schade, H.; Vanecek, M.; Meier, J.; Vallat-Sauvain, E.; Wyrsch, N.; Kroll, U.; Droz, C.; Bailat, J. *Progress in Photovoltaics* **2004**, *12*, 113.

(6) In *Springer Handbook of Electronic and Photonic Materials*; Kasap, S., Capper, P., Eds.; Springer: 2007; Vol. XXXII, p 829.

(7) Khrypunov, G.; Romeo, A.; Kurdesau, F.; Batzner, D. L.; Zogg, H.; Tiwari, A. N. *Solar Energy Materials and Solar Cells* **2006**, *90*, 664.

(8) Bosio, A.; Romeo, N.; Mazzamuto, S.; Canevari, V. *Progress in Crystal Growth and Characterization of Materials* **2006**, *52*, 247.

(9) Powalla, M.; Bonnet, D. *Advances in OptoElectronics* **2007**.

(10) Saxena, V.; Steckl, A. J. *Sic Materials and Devices* **1998**, *52*, 77.

(11) Horvath, Z. J.; Adam, M.; Ducso, C.; Pinter, I.; Van Tuyen, V.; Barsony, I.; Gombia, E.; Mosca, R.; Makaro, Z. *Solid-State Electronics* **1998**, *42*, 221.

(12) Tove, P. A. *Vacuum* **1986**, *36*, 659.

(13) Benko, G.; Kallioinen, J.; Korppi-Tommola, J. E. I.; Yartsev, A. P.; Sundstrom, V. *Journal of the American Chemical Society* **2002**, *124*, 489.

(14) Wenger, B.; Gratzel, M.; Moser, J. E. *Journal of the American Chemical Society* **2005**, *127*, 12150.

(15) Watson, D. F.; Meyer, G. J. *Annual Review of Physical Chemistry* **2005**, *56*, 119.

(16) Nozik, A. J. *Physica E-Low-Dimensional Systems & Nanostructures* **2002**, *14*, 115.

(17) Nozik, A. J. *Nano Letters* **2010**, *10*, 2735.

(18) Hagfeldt, A.; Boschloo, G.; Sun, L.; Kloo, L.; Pettersson, H. *Chemical Reviews* **2010**, *ASAP*.

(19) Qurashi, A.; Hossain, M. F.; Faiz, M.; Tabet, N.; Alam, M. W.; Reddy, N. K. *Journal of Alloys and Compounds* **2010**, *503*, L40.

(20) Karak, S.; Ray, S. K.; Dhar, A. *Journal of Physics D-Applied Physics* **2010**, *43*.

(21) Bang, J. H.; Kamat, P. V. *Advanced Functional Materials* **2010**, *20*, 1970.

(22) Chang, C. J.; Kuo, E. H. *Colloids and Surfaces a-Physicochemical and Engineering Aspects* **2010**, *363*, 22.

(23) Isabella, O.; Krc, J.; Zeman, M. *Applied Physics Letters* **2010**, *97*.

(24) Zhao, L.; Zuo, Y. H.; Zhou, C. L.; Li, H. L.; Diao, H. W.; Wang, W. J. *Solar Energy* **2010**, *84*, 110.

(25) Dewan, R.; Knipp, D. *Journal of Applied Physics* **2009**, *106*.

(26) O'Regan, B.; Gratzel, M. *Nature* **1991**, *353*, 737.

(27) Nazeeruddin, M. K.; Kay, A.; Rodicio, I.; Humphrybaker, R.; Muller, E.; Liska, P.; Vlachopoulos, N.; Gratzel, M. *Journal of the American Chemical Society* **1993**, *115*, 6382.

(28) Hagfeldt, A.; Gratzel, M. *Accounts Of Chemical Research* **2000**, *33*, 269.

(29) Gratzel, M. *Nature* **2001**, *414*, 338.

(30) Gratzel, M. *Inorganic Chemistry* **2005**, *44*, 6841.

(31) Gratzel, M. *Accounts of Chemical Research* **2009**, *42*, 1788.

(32) Bae, E. Y.; Choi, W. Y.; Park, J. W.; Shin, H. S.; Kim, S. B.; Lee, J. S. *Journal of Physical Chemistry B* **2004**, *108*, 14093.

(33) Park, H.; Bae, E.; Lee, J. J.; Park, J.; Choi, W. *Journal of Physical Chemistry B* **2006**, *110*, 8740.

(34) Trammell, S. A.; Meyer, T. J. *Langmuir* **2003**, *19*, 6081.

(35) Gillaizeau-Gauthier, I.; Odobel, F.; Alebbi, M.; Argazzi, R.; Costa, E.; Bignozzi, C. A.; Qu, P.; Meyer, G. J. *Inorganic Chemistry* **2001**, *40*, 6073.

(36) Trammell, S. A.; Moss, J. A.; Yang, J. C.; Nakhle, B. M.; Slate, C. A.; Odobel, F.; Sykora, M.; Erickson, B. W.; Meyer, T. J. *Inorganic Chemistry* **1999**, *38*, 3665.

(37) Trammell, S. A.; Yang, P.; Sykora, M.; Fleming, C. N.; Odobel, F.; Meyer, T. J. *Journal of Physical Chemistry B* **2001**, *105*, 8895.

(38) Montalti, M.; Wadhwa, S.; Kim, W. Y.; Kipp, R. A.; Schmehl, R. H. *Inorganic Chemistry* **2000**, *39*, 76.

(39) Zabri, H.; Gillaizeau, I.; Bignozzi, C. A.; Caramori, S.; Charlot, M. F.; Cano-Boquera, J.; Odobel, F. *Inorganic Chemistry* **2003**, *42*, 6655.

(40) Gamble, L.; Jung, L. S.; Campbell, C. T. *Langmuir* **1995**, *11*, 4505.

(41) Kakiage, K.; Yamamura, M.; Fujimura, E.; Kyomen, T.; Unno, M.; Hanaya, M. *Chemistry Letters* **2010**, *39*, 260.

(42) Unno, M.; Kakiage, K.; Yamamura, M.; Kogure, T.; Kyomen, T.; Hanaya, M. *Applied Organometallic Chemistry* **2010**, *24*, 247.

(43) Armstrong, N. R.; Shepard, V. R. *Journal of Electroanalytical Chemistry* **1980**, *115*, 253.

(44) Heimer, T. A.; Darcangelis, S. T.; Farzad, F.; Stipkala, J. M.; Meyer, G. J. *Inorganic Chemistry* **1996**, *35*, 5319.

(45) McNamara, W. R.; Snoeberger, R. C.; Li, G.; Schleicher, J. M.; Cady, C. W.; Poyatos, M.; Schmuttenmaer, C. A.; Crabtree, R. H.; Brudvig, G. W.; Batista, V. S. *Journal of the American Chemical Society* **2008**, *130*, 14329.

(46) Moses, P. R.; Murray, R. W. *Journal of Electroanalytical Chemistry* **1977**, *77*, 393.

(47) Shepard, V. R.; Armstrong, N. R. *Journal of Physical Chemistry* **1979**, *83*, 1268.

(48) Fox, M. A.; Nobs, F. J.; Voynick, T. A. *Journal of the American Chemical Society* **1980**, *102*, 4036.

(49) Altobello, S.; Bignozzi, C. A.; Caramori, S.; Larramona, G.; Quici, S.; Marzanni, G.; Lakhmiri, R. *Journal of Photochemistry and Photobiology a-Chemistry* **2004**, *166*, 91.

(50) Yan, X. D.; Li, Z. W.; Zou, C. W.; Li, S.; Yang, J.; Chen, R.; Han, J.; Gao, W. *Journal of Physical Chemistry C* **2010**, *114*, 1436.

(51) Xia, J. B.; Masaki, N.; Jiang, K. J.; Yanagida, S. *Journal of Physical Chemistry C* **2007**, *111*, 8092.

(52) Chen, S. G.; Chappel, S.; Diamant, Y.; Zaban, A. *Chemistry of Materials* **2001**, *13*, 4629.

(53) Barros, D. D.; Abreu, P. P.; Werner, U.; Aegerter, M. A. *Journal of Sol-Gel Science and Technology* **1997**, *8*, 735.

(54) Guo, P.; Aegerter, M. A. *Thin Solid Films* **1999**, *351*, 290.

(55) Lenzmann, F.; Krueger, J.; Burnside, S.; Brooks, K.; Gratzel, M.; Gal, D.; Ruhle, S.; Cahen, D. *Journal of Physical Chemistry B* **2001**, *105*, 6347.

(56) Hod, I.; Shalom, M.; Tachan, Z.; Ruhle, S.; Zaban, A. *Journal of Physical Chemistry C* **2010**, *114*, 10015.

(57) Yang, S. M.; Kou, H. Z.; Wang, J. C.; Xue, H. B.; Han, H. L. *Journal of Physical Chemistry C* **2010**, *114*, 4245.

(58) Jose, R.; Thavasi, V.; Ramakrishna, S. *Journal of the American Ceramic Society* **2009**, *92*, 289.

(59) Bandara, J.; Weerasinghe, H. C. *Solar Energy Materials and Solar Cells* **2005**, *88*, 341.

(60) Ardo, S.; Meyer, G. J. *Chemical Society Reviews* **2009**, *38*, 115.

(61) Alstrum-Acevedo, J. H.; Brennaman, M. K.; Meyer, T. J. *Inorganic Chemistry* **2005**, *44*, 6802.

(62) Hagfeldt, A.; Gratzel, M. *Chemical Reviews* **1995**, *95*, 49.

(63) Barbe, C. J.; Arendse, F.; Comte, P.; Jirousek, M.; Lenzmann, F.; Shklover, V.; Gratzel, M. *Journal of the American Ceramic Society* **1997**, *80*, 3157.

(64) Gerischer, H.; Michel-Beyerle, M. E.; Rebentrost, F.; Tributsch, H. *Electrochimica Acta* **1968**, *13*, 1509.

(65) Meyer, T. J.; Meyer, G. J.; Pfennig, B. W.; Schoonover, J. R.; Timpson, C. J.; Wall, J. F.; Kobusch, C.; Chen, X. H.; Peek, B. M.; Wall, C. G.; Ou, W.; Erickson, B. W.; Bignozzi, C. A. *Inorganic Chemistry* **1994**, *33*, 3952.

(66) Blauch, D. N.; Saveant, J. M. *Journal of the American Chemical Society* **1992**, *114*, 3323.

(67) Staniszewski, A.; Ardo, S.; Sun, Y. L.; Castellano, F. N.; Meyer, G. J. *Journal of the American Chemical Society* **2008**, *130*, 11586.

(68) Jakubikova, E.; Snoeberger, R. C.; Batista, V. S.; Martin, R. L.; Batista, E. R. *Journal of Physical Chemistry A* **2009**, *113*, 12532.

(69) She, C. X.; Guo, J. C.; Irle, S.; Morokuma, K.; Mohler, D. L.; Zabri, H.; Odobel, F.; Youm, K. T.; Liu, F.; Hupp, J. T.; Lian, T. *Journal of Physical Chemistry A* **2007**, *111*, 6832.

(70) Walker, D.; Chappel, S.; Mahammed, A.; Brunschwig, B. S.; Winkler, J. R.; Gray, H. B.; Zaban, A.; Gross, Z. *Journal of Porphyrins and Phthalocyanines* **2006**, *10*, 1259.

(71) Nazeeruddin, M. K.; Pechy, P.; Renouard, T.; Zakeeruddin, S. M.; Humphry-Baker, R.; Comte, P.; Liska, P.; Cevey, L.; Costa, E.; Shklover, V.; Spiccia, L.; Deacon, G. B.; Bignozzi, C. A.; Gratzel, M. *Journal of the American Chemical Society* **2001**, *123*, 1613.

(72) Mayo, E. I.; Kilsa, K.; Tirrell, T.; Djurovich, P. I.; Tamayo, A.; Thompson, M. E.; Lewis, N. S.; Gray, H. B. *Photochemical & Photobiological Sciences* **2006**, *5*, 871.

(73) Wang, P.; Klein, C.; Moser, J. E.; Humphry-Baker, R.; Cevey-Ha, N. L.; Charvet, R.; Comte, P.; Zakeeruddin, S. M.; Gratzel, M. *Journal of Physical Chemistry B* **2004**, *108*, 17553.

(74) Schmidt-Mende, L.; Campbell, W. M.; Wang, Q.; Jolley, K. W.; Officer, D. L.; Nazeeruddin, M. K.; Gratzel, M. *Chemphyschem* **2005**, *6*, 1253.

(75) Wang, Q.; Carnpbell, W. M.; Bonfantani, E. E.; Jolley, K. W.; Officer, D. L.; Walsh, P. J.; Gordon, K.; Humphry-Baker, R.; Nazeeruddin, M. K.; Gratzel, M. *Journal of Physical Chemistry B* **2005**, *109*, 15397.

(76) Wang, M. K.; Chamberland, N.; Breau, L.; Moser, J. E.; Humphry-Baker, R.; Marsan, B.; Zakeeruddin, S. M.; Gratzel, M. *Nature Chemistry* **2010**, *2*, 385.

(77) Nakade, S.; Makimoto, Y.; Kubo, W.; Kitamura, T.; Wada, Y.; Yanagida, S. *Journal of Physical Chemistry B* **2005**, *109*, 3488.

(78) Stathatos, E.; Jovanovski, V.; Orel, B.; Jerman, I.; Lianos, P. *Journal of Physical Chemistry C* **2007**, *111*, 6528.

(79) Yang, C. H.; Ho, W. Y.; Yang, H. H.; Hsueh, M. L. *Journal of Materials Chemistry* **2010**, *20*, 6080.

(80) Suryanarayanan, V.; Lee, K. M.; Chen, J. G.; Ho, K. C. *Journal of Electroanalytical Chemistry* **2009**, *633*, 146.

(81) Cameron, P. J.; Peter, L. M.; Zakeeruddin, S. M.; Gratzel, M. *Coordination Chemistry Reviews* **2004**, *248*, 1447.

(82) Li, T. C.; Spokoyny, A. M.; She, C. X.; Farha, O. K.; Mirkin, C. A.; Marks, T. J.; Hupp, J. T. *Journal of the American Chemical Society* **2010**, *132*, 4580.

(83) Spokoyny, A. M.; Li, T. C.; Farha, O. K.; Machan, C. W.; She, C. X.; Stern, C. L.; Marks, T. J.; Hupp, J. T.; Mirkin, C. A. *Angewandte Chemie-International Edition* **2010**, *49*, 5339.

(84) Gagliardi, C. J.; Westlake, B. C.; Kent, C. A.; Paul, J. J.; Papanikolas, J. M.; Meyer, T. J. *Coordination Chemistry Reviews* **2010**, *254*, 2459.

(85) Hambourger, M.; Moore, G. F.; Kramer, D. M.; Gust, D.; Moore, A. L.; Moore, T. A. *Chemical Society Reviews* **2009**, *38*, 25.

(86) Concepcion, J. J.; Jurss, J. W.; Brennaman, M. K.; Hoertz, P. G.; Patrocinio, A. O. T.; Iha, N. Y. M.; Templeton, J. L.; Meyer, T. J. *Accounts of Chemical Research* **2009**, *42*, 1954.

(87) Ferreira, K. N.; Iverson, T. M.; Maghlaoui, K.; Barber, J.; Iwata, S. *Science* **2004**, *303*, 1831.

(88) Kok, B.; Forbush, B.; Mcgloin, M. *Photochemistry and Photobiology* **1970**, *11*, 457.

(89) Voet, D.; Voet, J. G. *Biochemistry*; Third Edition ed.; John Wiley & Sons, Inc., 2004.

(90) Taiz, L.; Zeiger, E. *Plant Physiology*; Fourth Edition ed.; Sinauer Associates, Inc., 2006.

(91) Barber, J. *Philosophical Transactions of the Royal Society a-Mathematical Physical and Engineering Sciences* **2007**, *365*, 1007.

(92) Ruttinger, W.; Dismukes, G. C. *Chemical Reviews* **1997**, *97*, 1.

(93) Herrero, C.; Lassalle-Kaiser, B.; Leibl, W.; Rutherford, A. W.; Aukauloo, A. *Coordination Chemistry Reviews* **2008**, *252*, 456.

(94) Meyer, T. J.; Huynh, M. H. V.; Thorp, H. H. *Angew. Chem., Int. Ed.* **2007**, *46*, 5284.

(95) Huynh, M. H. V.; Dattelbaum, D. M.; Meyer, T. J. *Coordination Chemistry Reviews* **2005**, *249*, 457.

(96) Liu, F.; Concepcion, J. J.; Jurss, J. W.; Cardolaccia, T.; Templeton, J. L.; Meyer, T. J. *Inorg. Chem. (Washington, DC, U. S.)* **2008**, *47*, 1727.

(97) Barber, J. *Chemical Society Reviews* **2009**, *38*, 185.

(98) Knight, T. E.; Guo, D.; Claude, J. P.; McCusker, J. K. *Inorganic Chemistry* **2008**, *47*, 7249.

(99) Zouni, A.; Witt, H. T.; Kern, J.; Fromme, P.; Krauss, N.; Saenger, W.; Orth, P. *Nature* **2001**, *409*, 739.

(100) Biesiadka, J.; Loll, B.; Kern, J.; Irrgang, K. D.; Zouni, A. *Physical Chemistry Chemical Physics* **2004**, *6*, 4733.

(101) Loll, B.; Kern, J.; Saenger, W.; Zouni, A.; Biesiadka, J. *Nature* **2005**, *438*, 1040.

(102) Kern, J.; Biesiadka, J.; Loll, B.; Saenger, W.; Zouni, A. *Photosynthesis Research* **2007**, *92*, 389.

(103) Yano, J.; Pushkar, Y.; Glatzel, P.; Lewis, A.; Sauer, K.; Messinger, J.; Bergmann, U.; Yachandra, V. *Journal of the American Chemical Society* **2005**, *127*, 14974.

(104) Barber, J. *Inorganic Chemistry* **2008**, *47*, 1700.

(105) Meyer, T. J.; Huynh, M. H. V. *Inorganic Chemistry* **2003**, *42*, 8140.

(106) Huynh, M.; Meyer, T. *Chemical Reviews* **2007**, *107*, 5004.

(107) Costentin, C.; Robert, M.; Saveant, J. M. *Journal of Electroanalytical Chemistry* **2006**, *588*, 197.

(108) Costentin, C. *Chem. Rev. (Washington, DC, U. S.)* **2008**, *108*, 2145.

(109) Hammes-Schiffer, S. *Hydrogen-Transfer React.* **2007**, *2*, 479.

(110) Hammes-Schiffer, S.; Soudackov, A. V. *J. Phys. Chem. B* **2008**, *112*, 14108.

(111) Navrotskaya, I.; Soudackov, A. V.; Hammes-Schiffer, S. *J. Chem. Phys.* **2008**, *128*, 244712/1.

(112) Venkataraman, C.; Soudackov, A. V.; Hammes-Schiffer, S. *J. Phys. Chem. C* **2008**, *112*, 12386.

(113) Edwards, S. J.; Soudackov, A. V.; Hammes-Schiffer, S. *Journal of Physical Chemistry A* **2009**, *113*, 2117.

(114) Hammes-Schiffer, S. *Acc Chem Res* **2009**.

(115) Navrotskaya, I.; Hammes-Schiffer, S. *J. Chem. Phys.* **2009**, *131*, 024112/1.

(116) Cukier, R. I. *Biochimica Et Biophysica Acta-Bioenergetics* **2004**, *1655*, 37.

(117) Chang, C. J.; Chang, M. C. Y.; Damrauer, N. H.; Nocera, D. G. *Biochimica Et Biophysica Acta-Bioenergetics* **2004**, *1655*, 13.

(118) Reece, S. Y.; Hodgkiss, J. M.; Stubbe, J.; Nocera, D. G. *Philos. Trans. R. Soc., B* **2006**, *361*, 1351.

(119) Reece, S. Y.; Nocera, D. G. *Annu. Rev. Biochem.* **2009**, *78*, 673.

(120) Binstead, R. A.; Meyer, T. J.; Moyer, B. A.; Samuels, G. J. *Abstracts of Papers of the American Chemical Society* **1980**, *180*, 265.

(121) Binstead, R. A.; Moyer, B. A.; Samuels, G. J.; Meyer, T. J. *Journal of the American Chemical Society* **1981**, *103*, 2897.

(122) Moyer, B. A.; Meyer, T. J. *Inorganic Chemistry* **1981**, *20*, 436.

(123) Hoganson, C. W.; Babcock, G. T. *Science* **1997**, *277*, 1953.

(124) Westphal, K. L.; Tommos, C.; Cukier, R. I.; Babcock, G. T. *Current Opinion in Plant Biology* **2000**, *3*, 236.

(125) McEvoy, J. P.; Brudvig, G. W. *Chem. Rev. (Washington, DC, U. S.)* **2006**, *106*, 4455.

(126) Young, R. C.; Meyer, T. J.; Whitten, D. G. *Journal of the American Chemical Society* **1975**, *97*, 4781.

(127) Meyer, T. J. *Acc. Chem. Res.* **1989**, *22*, 163.

(128) Meyer, G. J. *Inorganic Chemistry* **2005**, *44*, 6852.

(129) Gust, D.; Moore, T. A.; Moore, A. L. *Accounts of Chemical Research* **1993**, *26*, 198.

(130) Ariz, I.; Esteban, R.; Garcia-Plazaola, J. I.; Becerril, J. M.; Aparicio-Tejo, P. M.; Moran, J. F. *Journal of Plant Physiology* **2010**, *167*, 1038.

(131) Losciale, P.; Chow, W. S.; Grappadelli, L. C. *Journal of Experimental Botany* **2010**, *61*, 1177.

(132) Kirilovsky, D. *Photosynthesis Research* **2007**, *93*, 7.

(133) Ivanov, A. G.; Hurry, V.; Sane, P. V.; Oquist, G.; Huner, N. P. A. *Journal of Plant Biology* **2008**, *51*, 85.

(134) Martinez-Junza, V.; Szczepaniak, M.; Braslavsky, S. E.; Sander, J.; Nowaczyk, M.; Rogner, M.; Holzwarth, A. R. *Photochemical & Photobiological Sciences* **2008**, *7*, 1337.

(135) Ivanov, A. G.; Sane, P. V.; Hurry, V.; Oquist, G.; Huner, N. P. A. *Photosynthesis Research* **2008**, *98*, 565.

(136) Esteban, R.; Olascoaga, B.; Becerril, J. M.; Garcia-Plazaola, J. I. *Physiologia Plantarum* **2010**, *140*, 69.

(137) Mozzo, M.; Dall'Osto, L.; Hienerwadel, R.; Bassi, R.; Croce, R. *Journal of Biological Chemistry* **2008**, *283*, 6184.

(138) Mozzo, M.; Passarini, F.; Bassi, R.; van Amerongen, H.; Croce, R. *Biochimica Et Biophysica Acta-Bioenergetics* **2008**, *1777*, 1263.

(139) Bailey, S.; Grossman, A. *Photochemistry and Photobiology* **2008**, *84*, 1410.

(140) Ballottari, M.; Girardon, J.; Betterle, N.; Morosinotto, T.; Bassi, R. *Journal of Biological Chemistry* **2010**, *285*, 28309.

(141) Betterle, N.; Ballottari, M.; Hienerwadel, R.; Dall'Osto, L.; Bassi, R. *Arch Biochem Biophys* **2010**, *504*, 67.

(142) Kodis, G.; Terazono, Y.; Liddell, P. A.; Andreasson, J.; Garg, V.; Hambourger, M.; Moore, T. A.; Moore, A. L.; Gust, D. *Journal of the American Chemical Society* **2006**, *128*, 1818.

(143) Hammarstrom, L.; Styring, S. *Philosophical Transactions of the Royal Society B-Biological Sciences* **2008**, *363*, 1283.

(144) Falkenstrom, M.; Johansson, O.; Hammarstrom, L. *Inorganica Chimica Acta* **2007**, *360*, 741.

(145) Marcus, R. A. *Pure and Applied Chemistry* **1997**, *69*, 13.

(146) Wasielewski, M. R. *Chemical Reviews* **1992**, *92*, 435.

CHAPTER 2

Electronic Structure of the Water Oxidation Catalyst, *cis,cis*-$[(bpy)_2(H_2O)Ru^{III}ORu^{III}(OH_2)(bpy)_2]^{4+}$, The Blue Dimer

Introduction

The first designed catalyst for water oxidation was the ruthenium blue dimer, *cis,cis*-$[(bpy)_2(H_2O)Ru^{III}ORu^{III}(OH_2)(bpy)_2]^{4+}$.[1,2] It is oxidatively activated by proton coupled electron transfer (PCET) through a sequence of $1e^-$ intermediates, ultimately, to give the transient $[(bpy)_2(O)Ru^{V}ORu^{V}(O)(bpy)_2]^{4+}$. The latter undergoes rapid O-atom transfer to water to give a peroxidic intermediate which is further oxidized, resulting in oxygen release before re-entering the catalytic cycle. Recent summaries of water oxidation mechanism are available,[3-6] including a paper to follow.

The electronic properties of the blue dimer enabling water oxidation catalysis are obviously important but have been a source of controversy. There is clear chemical and spectroscopic evidence for strong cross-bridge electronic coupling which plays a significant role in providing access to the higher Ru(V) oxidation states at relatively low potentials, for example.[2-4,6-9] However, DFT calculations by Baik and co-workers[10] were predicated on weak electronic coupling with magnetic exchange across the μ-oxo bridge. Based on results of DFT (B3LYP) and complete active space self-consistent field (CASSCF) calculations,[11] Batista and Martin concluded that the ground state is a weakly antiferromagnetically coupled singlet state. They concluded that partial electronic delocalization occurs by mixing between dπ rather than by dδ orbitals as concluded by Baik and co-workers, Scheme 2.1.[10,12]

Scheme 2.1. Computational models of the blue dimer electronic structure.

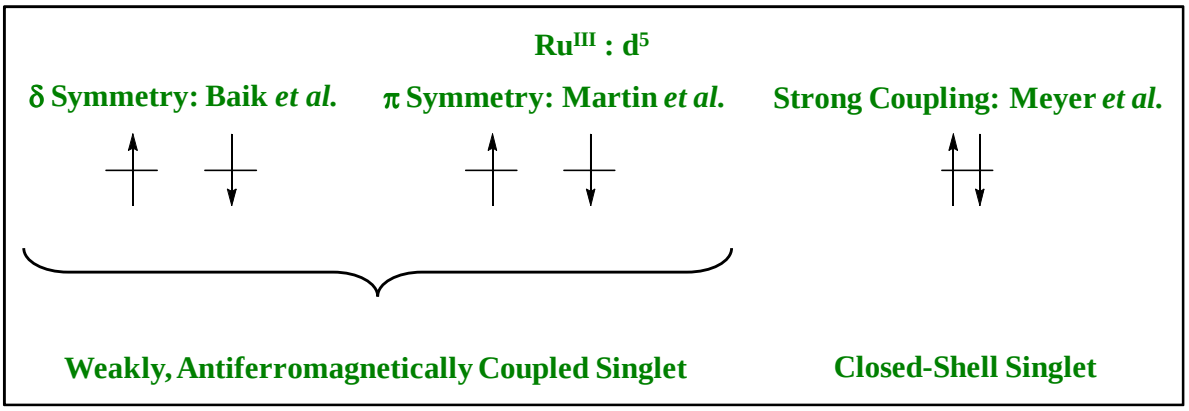

Molecular structures for both *cis,cis*-$[(bpy)_2(H_2O)Ru^{III}ORu^{III}(OH_2)bpy)_2]^{4+}$ and *cis,cis*-$[(bpy)_2(HO)Ru^{IV}ORu^{III}(OH_2)bpy)_2]^{4+}$ have been determined crystallographically, and structural information is available for a number of related blue dimer derivatives.[2,8,13,14] Electronic and molecular structures of the blue dimer[11] and its higher oxidation states[10,15] have been investigated by application of density functional theory (DFT). A detailed analysis of possible mechanisms of water oxidation has also been performed based on DFT calculations.[12]

We report here the results of an extensive series of experiments and results of DFT calculations that explore, in detail, the electronic and molecular structure of the blue dimer. The results unequivocally demonstrate that strong cross-bridge electronic coupling exists and that it has a profound influence on its properties.

Experimental

Jennifer M. Butler,[a] Kristin M. Omberg,[a] Luis M. Baraldo,[a] Darla Graff Thompson,[a] Estelle L. Lebeau,[a] Brooks Hornstein,[a] and Jon R. Schoonover[a] were responsible for the excitation dependent resonance Raman spectroscopy. Hershel Jude,[b] Joe D. Thompson,[b] Dana M.

Dattelbaum,[b] and Reginaldo C. Rocha[b] performed the temperature dependent magnetic measurements. Javier J. Concepcion and I provided the remaining experimental data and all of the computational results. [a]*Materials Science and Technology Division,* [b]*Materials Physics & Applications Division Los Alamos National Laboratory, Los Alamos, NM 87545.*

Materials: High purity water was further purified by a Millipure system. $RuCl_3 \bullet 3H_2O$ (Pressure Chemicals), $AgNO_3$, $NaClO_4$, $(NH_3)_2Ce(NO_3)_6$ (99.99+%, Aldrich), $(NH_4)_2Fe(SO_4)_2(H_2O)_6$ (≥ 99%, Aldrich), 2,2'-bipyridine (Aldrich), NaOH, $HClO_4$ (99.999%), HCl, H_2SO_4 and HNO_3 (Fisher) were all used as received. Na_2SO_4 was utilized as an internal standard in resonance Raman experiments and was purchased from Aldrich and also used as received.

Preparation of Complexes: The salts $[(bpy)_2(H_2O)Ru^{III}ORu^{III}(OH_2)(bpy)_2](ClO_4)_4$ and $[(bpy)_2(H_2O)Ru^{III}ORu^{IV}(OH)(bpy)_2](ClO_4)_4$ were synthesized as described earlier.[2] The hexafluorophosphate salt, i.e. $[(bpy)_2(H_2O)Ru^{III}ORu^{III}(OH_2)(bpy)_2](PF_6)_4$, was synthesized in analogous fashion, but isolated by addition of NH_4PF_6 to an aqueous solution of the ClO_4^- with the dimer pre-purified by chromatography on LH-20 Sephadex. The purity of the product was verified by comparison of electrochemical and electronic spectral features with literature results.[2]

Preparation of $[(bpy)_2(SO_4)Ru^{III}ORu^{IV}(SO_4)(bpy)_2](SO_4)_{0.5}$. Approximately 5 mL of a saturated $[(bpy)_2(H_2O)RuORu(OH_2)(bpy)_2](ClO_4)_4$ solution was prepared in 1.0 M H_2SO_4 to which 1 equivalent of $(NH_4)_2Ce(NO_3)_6$ was added via micropipette from a solution of known Ce(IV) concentration. The reaction vessel was shaken to promote mixing and was left for several days at room temperature to allow for crystallization to occur. UV-visible analysis of

the dissolved crystals and the remaining supernatant confirmed quantitative conversion to the desired product with λ_{max} = 468 nm.

Preparation of $[(bpy)_2(Cl)Ru^{III}ORu^{IV}(Cl)(bpy)_2](Ce(NO_3)_6)$. A 1 x 10^{-4} M solution of the ClO_4^- salt of the blue dimer was prepared in a 1:1 mixture of acetonitrile-0.1 M HNO_3 with 0.001 M $Ce(NO_3)_3$ and 0.01 M NaCl added. An aliquot corresponding to 2 equivalents of $(NH_4)_2Ce(NO_3)_6$ was added via micropipette from a solution of known Ce(IV) concentration. The reaction vessel was shaken to promote mixing and left for several days at room temperature to allow for crystallization to occur. The crystals were harvested and analyzed by x-ray diffraction (XRD).

***Measurements*:**

pH measurements were conducted by using a calibrated Accumet AB15 pH meter. UV-visible spectra were recorded on either an Agilent 8453 diode-array spectrophotometer or a Shimadzu UV-visible near-infrared spectrophotometer model UV-3600, both with 2 nm resolution.

Resonance Raman Measurements. Resonance Raman (RR) spectra were measured by using continuous wave excitation at 514.5, 501.7, 496.5, 465.8, and 457.9 nm from a Spectra-Physics 165 Ar^+ laser and at 676.4, 647.1, and 568.2 nm from a Coherent INNOVA 90K Kr^+ laser. The incident radiation was collected in a 135° backscattering geometry and dispersed by a Jobin-Yvon U1000 double monochromator with an 1800 grooves/mm grating. Slits were adjusted for each excitation wavelength to maintain a resolution of 4 cm^{-1}. The Raman signal was detected by a Hamamatsu R943-02 cooled photomultiplier tube with signal processing by an Instruments SA Spectra Link photon-counting system. Samples were prepared in nanopure water adjusted to pH = 1 with H_2SO_4. As noted above, 0.5 M Na_2SO_4

was used as an internal Raman standard. The concentration of *cis,cis*-$[(bpy)_2(H_2O)Ru^{III}ORu^{III}(OH_2)bpy)_2]^{4+}$ in water at pH = 1 was 0.2 mM for excitation at 568.2, 647.1, and 676.4 nm and 0.4 mM for the remaining excitation wavelengths. The difference in concentration was necessary due to the difference in absorbance at the different excitation wavelengths. Final spectra were the average of between 4 and 9 accumulations.

Spectra were corrected for detector response by using a 200 W Optronics Laboratory OL220M, M-447 quartz-halogen tungsten lamp operated at 65 A. Corrections for self-absorption of the scattered light were performed by using the method of Myers.[16] Spectral intensities (areas) were determined by using the fitting routines of GRAMS (Galactic Industries). Intensity values were normalized to the sulfate band at 982 cm^{-1}.

Magnetic Measurements. Magnetic measurements at H = 0.1 and 5 T over the temperature range of 2–350 K (with measurement on warming after cooling to 2 K in zero field) were made using a Quantum Design superconducting quantum interference device (SQUID) magnetometer. The dependence of magnetization on the magnetic field (H = 0–7 T) was also verified at 2, 10, 50, and 300 K (data available in Appendix A Figure S1). The powder sample was tightly packed between thin polymeric discs inside a plastic straw. Diamagnetic contributions to the magnetization from the discs and the straw were measured independently and subtracted from the total measured signal. The resulting estimated error in the sample magnetization is ±3%. The magnetic susceptibility, defined as the sample magnetization (M) divided by the applied magnetic field (H), was determined as a function of temperature. Effective magnetic moments were calculated as $\mu_{eff} = 2.828(\chi \cdot T)^{1/2}$, where χ is the magnetic susceptibility per formula unit. Susceptibility corrections for the underlying diamagnetism of sample constituents were made using tabulated Pascal's constants.

Computational Methods. DFT calculations were carried out by using Gaussian 03, revision C.02.[17] For Gaussian calculations, Becke's three-parameter hybrid functional with the LYP correlation functional (B3LYP) was used with Los Alamos effective core potential LanL2DZ basis set. Initial geometry optimizations were performed with Titan using Becke's 1988 functional with the Slater exchange and Perdew's 1986 gradient corrections along with his 1981 local correlation functional (BP86). The geometries obtained from Titan were used as input geometries for Gaussian, where full geometry optimizations were performed at B3LYP level. Molecular orbital (MO) diagrams were constructed for the fully optimized geometries in Gaussian. Franck-Condon vertical excitation energies and oscillator strengths were obtained with Time-Dependent Density Functional Theory (TD-DFT) as implemented in Gaussian. Solvent-specific interactions were modeled by explicitly adding hydrogen-bonded water molecules and chloride anions, respectively. The bulk of the solvent was modeled by means of the Integral Equation Formalism Polarizable Continuum Model (IEF-PCM), as implemented in Gaussian.

Results

X-ray Crystallography. The structures of the nominally mixed-valence $Ru^{IV}ORu^{III}$ cations, $[(bpy)_2(SO_4)RuORu(SO_4)(bpy)_2](SO_4)_{0.5}$ and $[(bpy)_2ClRuORuCl(bpy)_2](Ce(NO_3)_6)$, were determined by XRD and are shown in Figures 2.1 and 2.2, respectively. Each Ru center is approximately octahedral, coordinated by two bipyridine ligands (bpy), the bridging oxygen atom, and by one oxygen of a sulfate anion or by a chloride. The bpy ligands at each Ru center are arranged in the *cis* geometry.

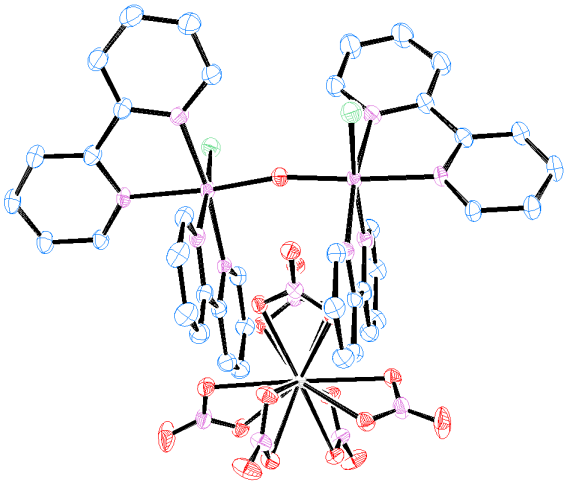

Figure 2.1. Crystal structure of *cis*,*cis*-$[(bpy)_2(Cl)Ru^{III}ORu^{IV}(Cl)(bpy)_2](Ce(NO_3)_6)$.

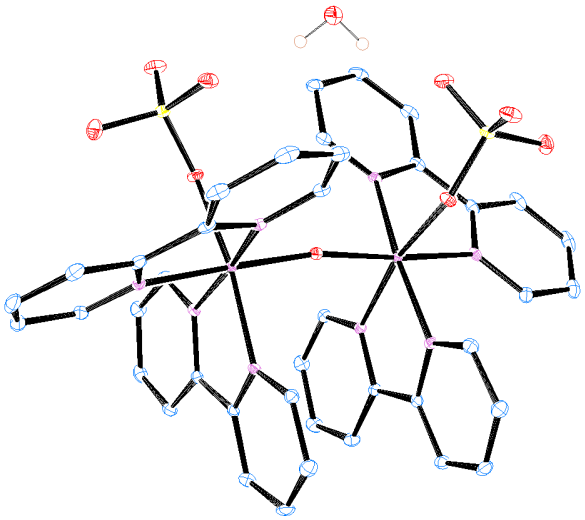

Figure 2.2. Crystal structure of *cis*,*cis*-$[(bpy)_2(SO_4)Ru^{IV}ORu^{III}(SO_4)(bpy)_2]\cdot H_2O(SO_4)_{0.5}$. The sulfate anion is not shown.

Selected structural parameters are listed in Table 2.1. Complete description of the parameters, structure solution and refinement conditions, atomic coordinates, bond distances and angles, and thermal parameters are provided in Appendix (Appx.) A.

Table 2.1. Crystallographic Data for the cations in the salts *cis,cis*-$[(bpy)_2(Cl)RuORu(Cl)(bpy)_2](Ce(NO_3)_6)$ and *cis,cis*-$[(bpy)_2(SO_4)RuORu(SO_4)(bpy)_2]\cdot H_2O(SO_4)_{0.5}$.

	$(Cl)RuORu(Cl)^{3+}$	$(SO_4)RuORu(O_4S)^{+}$
empirical formula	$Ru_2CeCl_2O_{19}N_{26}C_{64}H_{68}$	$Ru_2S_4O_{24}N_8C_{40}H_{47}$
formula weight	1918.60	1354.24
temperature, K	99(2)	100(2)
wavelength, Å	1.54178	1.54178
crystal system	monoclinic	monoclinic
space group	C 1 2/c 1	C2/c
a, Å	20.8445(9)	12.5581(3)
b, Å	23.98	20.4436(4)
c, Å	16.4296(8)	19.2993(4)
α, deg	90	90
β, deg	103.593	93.901(1)
γ, deg	90	90
volume, $Å^3$	7984.0(6)	4943.28(18)
Z	4	4
d_{calcd}, mg/cm^3	1.596	1.820
absorption coefficient, mm^{-1}	8.680	7.379
F(000)	3864	2748
crystal size, mm	0.10 x 0.10 x 0.25	0.20 x 0.10 x 0.05
θ range for data collection, °	2.85 to 66.57	4.14 to 67.5
index ranges	$-24 \le h \le 24$	$-14 \le h \le 14$
	$-28 \le k \le 28$	$-24 \le k \le 24$
	$-19 \le l \le 17$	$-18 \le l \le 22$
reflections collected	32539	18133
independent reflections	6996 [R(int) = 0.0378]	4260 [R(int) = 0.0277]
completeness to θ, %	99.2	98
absorption correction	mult-scan	numerical
max. and min. transmission	0.4773 and 0.2202	0.7092 and 0.3200
refinement method	full-matrix least-squares on F^2	
data / restraints / parameters	6996 / 117 / 521	4260 / 0 / 383
goodness-of-fit on F^2	1.056	1.084
final R indices [$I > 2\sigma(I)$]	R1 = 0.0501, wR2 = 0.1403	R1 = 0.0266, wR2 = 0.0611
R indices (all data)	R1 = 0.0519, wR2 = 0.1419	R1 = 0.0304, wR2 = 0.0626
largest diff. peak and hole, $eÅ^{-3}$	1.616 and -0.802	0.529 and -0.434

Important bond distances and angles are compared to analogous distances and angles in the related structures $[(bpy)_2(HO)Ru^{IV}ORu^{III}(OH_2)(bpy)_2](ClO_4)_4\bullet 2H_2O$ and $[(bpy)_2ClRu^{IV}ORu^{III}Cl(bpy)_2]\ (ClO_4)_3\bullet H_2O$ in Table 2.2.

Table 2.2. Comparison of important bond distances (Å) and angles (deg) in $[(bpy)_2(HO)Ru^{IV}ORu^{III}(OH_2)(bpy)_2](ClO_4)_4 \cdot 2H_2O$,[8] $[(bpy)_2ClRu^{III}ORu^{IV}Cl(bpy)_2](ClO_4)_3 \cdot H_2O$,[8] $[(bpy)_2ClRuORuCl(bpy)_2](Ce(NO_3)_6) \cdot H_2O$, and $[(bpy)_2(SO_4)RuORu(SO_4)(bpy)_2](SO_4) \cdot H_2O$.

	$(HO)Ru(2)^{IV}ORu(1)^{III}(OH_2)$	$ClRu(2)^{III}ORu(1)^{IV}Cl$[a]	$ClRuORuCl$[b]	$(SO_4)RuORu(SO_4)$
Distances				
M(1)-O	1.847(12)	1.845(9)	1.8365(5)	1.8400(3)
M(2)-O	1.823(12)	1.805(9)	1.8365(5)	1.8400(3)
L-M(1)	2.148(11) (L = OH_2)	2.357(4) (L = Cl^-)	2.3536(13) (L = Cl^-)	2.0435(18) (L = OSO_3^{2-})
M(2)-L'	1.978(14) (L' = OH^-)	2.339(4) (L' = Cl^-)	2.3536(13) (L' = Cl^-)	2.0435(18) (L = OSO_3^{2-})
L•••L'[c]	5.555(2) (H_2O•••OH)	5.777(5) (Cl•••Cl)	5.784 (Cl•••Cl)	5.005 (O_3SO•••OSO_3)
Angles				
L-M(1)-O	94.7(5) (L = OH_2)	95.1(3) (L = Cl^-)	94.74(9) (L = Cl^-)	93.83(7) (L = OSO_3^{2-})
O-M(2)-L'	99.2(5) (L' = OH^-)	93.6(3) (L' = Cl^-)	94.74(9) (L' = Cl^-)	93.83(7) (L = OSO_3^{2-})
M(1)-O-M(2)	170.0(7)	170.7(5)	168.32(3)	168.98(15)
L-M(1)-M(2)-L'[d]	117.2 (H_2O•••OH)	117.0 (Cl•••Cl)	111.51 (Cl•••Cl)	82.75 (O_3SO•••OSO_3)

a Asymmetric species. *b* Symmetric species. *c* Distance of separation between adjacent cis ligands across the μ-oxo bridge. *d* Torsional dihedral angle between the LM(1)O and LM(2)L' planes.

A structural asymmetry is observed in the $[(HO)Ru^{IV}ORu^{III}(OH_2)]^{4+}$ cation consistent with the difference in protonation at the two bridged sites. In the $Ru^{IV}ORu^{III}$ structures the bridge angle is increased relative to $Ru^{III}ORu^{III}$.[2,13,14] For example, <Ru-O-Ru angle = 165.4° in $[(H_2O)Ru^{III}ORu^{III}(OH_2)]^{4+}$ and 170.0° in $[(HO)Ru^{IV}ORu^{III}(OH_2)]^{4+}$.

The molecular formulas for the two different $[ClRuORuCl]^{3+}$ structures differ only in their respective counter ions, three perchlorate anions and a single $Ce(NO_3)_6^{3-}$ anion. There is a structural asymmetry across the bridge in $[ClRu^{IV}ORu^{III}Cl](ClO_4)_3$ with Ru-O bond distances of 1.805(9) and 1.845(9) Å, indicative of an asymmetric electronic distribution. The Ru-Cl bond distances are also different with the longer Ru-Cl bond (2.357(4) Å) at the Ru with the longer Ru-O bond, and the other at 2.339(4) Å.

Notably, the $[ClRu^{IV}ORu^{III}Cl]$ $(Ce(NO_3)_6)$ structure is symmetric across the bridge with equivalent Ru-O bond distances of 1.8365(5) Å and Ru-Cl bond distances of 2.3536(13) Å. The $Ce(NO_3)_6^{3-}$ anion is ion-paired within the cavity formed by the nearly parallel bpy ligands of each ruthenium. The arrangement of the three perchlorate anions in the $[ClRu^{IV}ORu^{III}Cl](ClO_4)_3$ structure is unsymmetrical with two associated more closely with one metal center than the other.

The mixed valence unit $[(SO_4)Ru^{IV}ORu^{III}(SO_4)]^+$ is also symmetric. The dianionic sulfate counter ion is located between two cationic units in the crystal lattice, providing the anionic charge for charge compensation. A hydrogen-bonded water molecule is positioned between the two coordinated sulfate ligands (shown, Figure 2.2).

Each of the nominally $[Ru^{IV}ORu^{III}]^{n+}$ structures is one of two enantiomers; the Λ,Λ forms are shown in Figures 2.1 and 2.2. There are equal amounts of each enantiomer in the crystals consistent with the centrosymmetric space groups. The symbol Λ is used to describe a left-handed propeller twist and the symbol Δ denotes a right-handed propeller twist. In addition to the enantiomers, a meso form is also present with coordination geometry at one ruthenium being Δ and at the other, Λ. The enantiomeric and meso forms of the blue dimer and its derivatives are chemically distinct.[6]

Steric interactions across the μ-oxo bridge lead to discrete rotamers within the same structural isomer that can differ significantly in energy. DFT calculations identified two low-energy rotamers, described here as “interior” and “exterior”, of the enantiomeric form of the blue dimer.[15] The “interior” label is used for blue dimer derivatives, $[(bpy)_2(X)RuORu(X)(bpy)_2]^{n+}$, with dihedral angles, X-Ru-Ru-X less than 90°. Analogous dihedral angles greater than 90° are described as belonging to the “exterior” category. The

dihedral angle describes the torsional difference between X(1) and X(2) along the direct Ru(1)-Ru(2) axis. The structure of the cation $[(bpy)_2(SO_4)Ru^{IV}ORu^{III}(SO_4)(bpy)_2]^+$ presents an "interior" rotamer with a SO_4-Ru-Ru-SO_4 dihedral angle of 82.75°. The remaining $Ru^{III}ORu^{IV}$ structures in Table 2.2 are "exterior" rotamers.

Magnetism

Variable-temperature magnetic susceptibility of the blue dimer in magnetic fields of 0.1 and 5.0 T exhibits a steady, approximately linear decrease at temperatures ranging from ~20 K up to 350 K (Figure 2.3). The steep increase in susceptibilities with decreasing temperature in the region below 20 K is typically associated with the presence of small amounts of paramagnetic impurities in the sample. The susceptibility is only slightly sensitive to the applied magnetic field above 100 K but converges at lower temperatures. The dependence of $1/\chi$ on temperature (Figure 2.3; inset) is essentially linear in the 250-350 K range, with $\theta = -270$ K (at $H = 5.0$ T).

As shown in Figure 2.4, the blue dimer is paramagnetic at room temperature with effective magnetic moments, μ_{eff}, of 2.11 μ_B/dimer ($\chi \cdot T = 0.559$ emu K mol^{-1}) for $H = 5.0$ and 2.23 μ_B/dimer ($\chi \cdot T = 0.622$ emu K mol^{-1}) for $H = 0.1$ T at 300 K. At room temperature, the blue dimer is also paramagnetic in solution, as observed earlier by ^{1}H NMR spectroscopy.[18] However, $\chi \cdot T$ is temperature-dependent and μ_{eff} decreases rapidly as the temperature is lowered below 100 K (Figure 2.4; inset). The residual magnetic moments of 0.30 μ_B/dimer ($\chi \cdot T = 1.2\times10^{-2}$ emu K mol^{-1}) at $H = 5.0$ T and 0.32 μ_B/dimer ($\chi \cdot T = 1.3\times10^{-2}$ emu K mol^{-1}) at $H = 0.1$ T indicate that the blue dimer is essentially diamagnetic at 2 K. Although it becomes gradually paramagnetic as the temperature increases, the extrapolated

number of unpaired electrons per dimer is between 1.4 and 1.5 even for the highest observed values of μ_{eff} and $\chi \cdot T$ at 350 K (Figure 2.4).

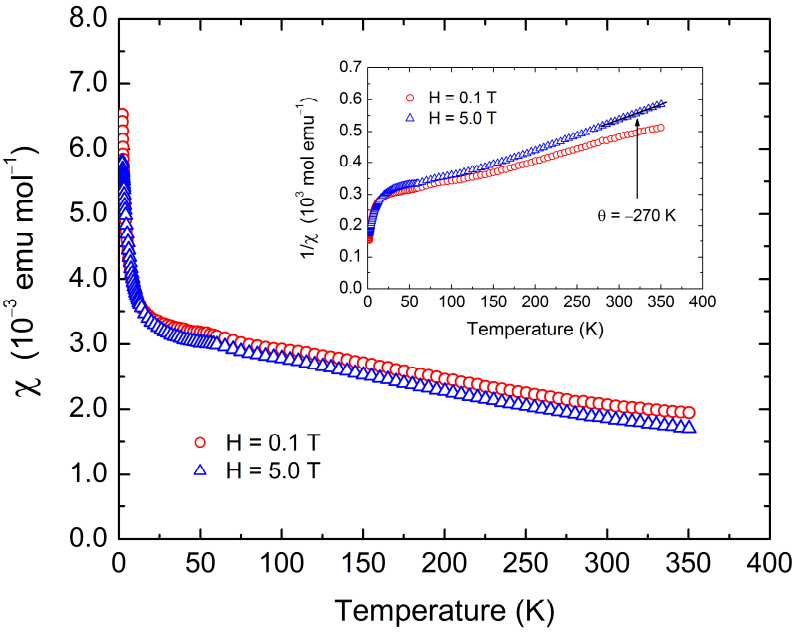

Figure 2.3. Temperature dependence of χ (magnetic susceptibility per formula unit) and $1/\chi$ (inset) for the blue dimer in magnetic fields of 0.1 T (red circles) and 5.0 T (blue triangles).

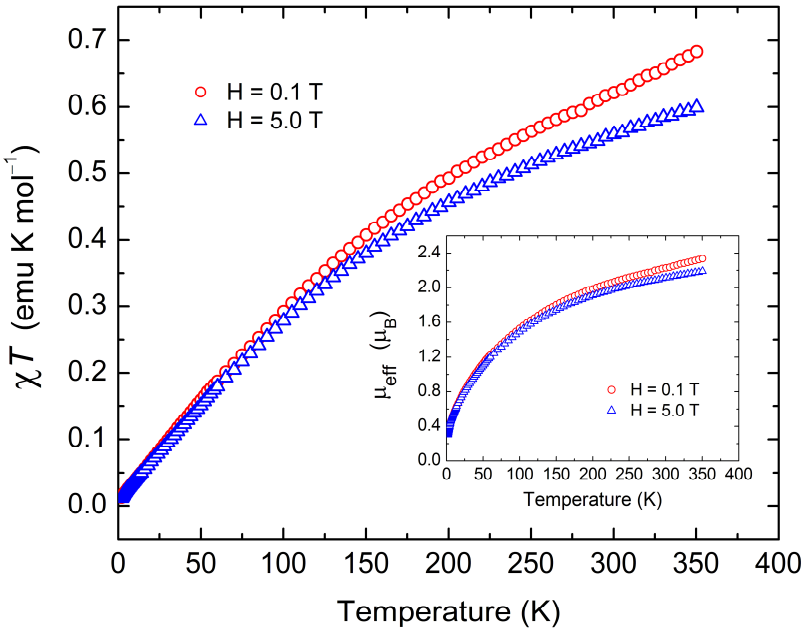

Figure 2.4. Temperature dependence of $\chi \cdot T$ and μ_{eff} (inset; magnetic moment per formula unit) for the blue dimer in magnetic fields of 0.1 T (red circles) and 5.0 T (blue triangles).

UV-visible-near IR Spectra.

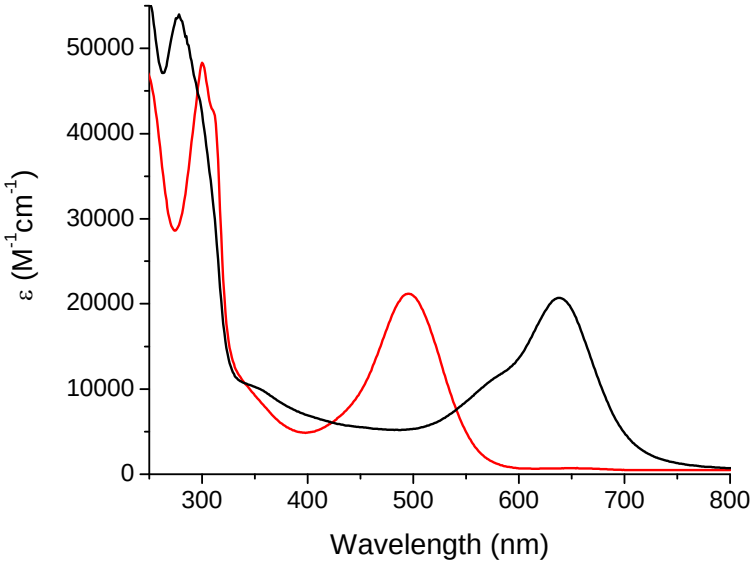

Figure 2.5. UV-visible spectra for $[(bpy)_2(H_2O)Ru^{III}ORu^{III}(OH_2)(bpy)_2]^{4+}$ (black) and $[(bpy)_2(HO)Ru^{IV}ORu^{III}(OH_2)(bpy)_2]^{4+}$ (red) in 0.1 M HNO_3.

As shown in Figure 2.5, the di-aqua Ru dimer, $[(H_2O)Ru^{III}ORu^{III}(OH_2)]^{4+}$, is blue in color with its most intense absorption band in the visible appearing at 637 nm at pH = 1. The spectrum is pH dependent with significant shifts in absorption occurring at higher pHs where the dominant forms become $[(H_2O)Ru^{III}ORu^{III}(OH)]^{3+}$ and $[(HO)Ru^{III}ORu^{III}(OH)]^{2+}$.[2]

The UV-visible spectra of *cis,cis*-$[(bpy)_2(H_2O)Ru^{III}ORu^{III}(OH_2)(bpy)_2]^{4+}$, *cis,cis*-$[(bpy)_2(Cl)Ru^{III}ORu^{III}(Cl)(bpy)_2]^{2+}$, and related μ-oxo-bpy complexes, are dominated by a manifold of intense $d\pi \rightarrow \pi^*(bpy)$ absorptions in the UV and intense bands in the low energy visible. For *cis,cis*-$[(bpy)_2(Cl)Ru^{III}ORu^{III}(Cl)(bpy)_2]^{2+}$ in acetonitrile, the visible λ_{max} appears at 672 nm (ε = 17,900 $M^{-1}cm^{-1}$).[7]

There is a shoulder on the high energy side of the high absorptivity absorption in these complexes that is readily apparent. The overlapping absorption features exhibit different solvent dependences. For *cis,cis*-$[(bpy)_2(Cl)Ru^{III}ORu^{III}(Cl)bpy)_2]^{2+}$, shifts are

observed in λ_{max} in nine solvents (water, ethanol, methanol, acetronitrile, propylene carbonate, dichloromethane, dimethyl sulfoxide, acetone, and benzyl alcohol) with the maximum variation from 654 nm in water to 674 nm in benzyl alcohol. Representative spectra are provided in Appx. A Figure S2. Assignments of the absorption features are assisted by Raman excitation profiles and are consistent with the results of DFT calculations, see below.

Analysis of intervalence transfer (IT) absorptions, typically appearing in the near-IR region, are a useful probe for assessing electron transfer barriers and the extent of delocalization in multinuclear transition metal systems.[19] Broad absorptions with low molar extinction coefficients are observed in the near-IR for the blue dimer and its higher oxidation state forms. These absorption bands are pH dependent and exhibit distinguishable shifts with changes in oxidation state or coordination environment which have proven useful in identifying intermediates and monitoring reactions in catalytic water oxidation cycles.[6]

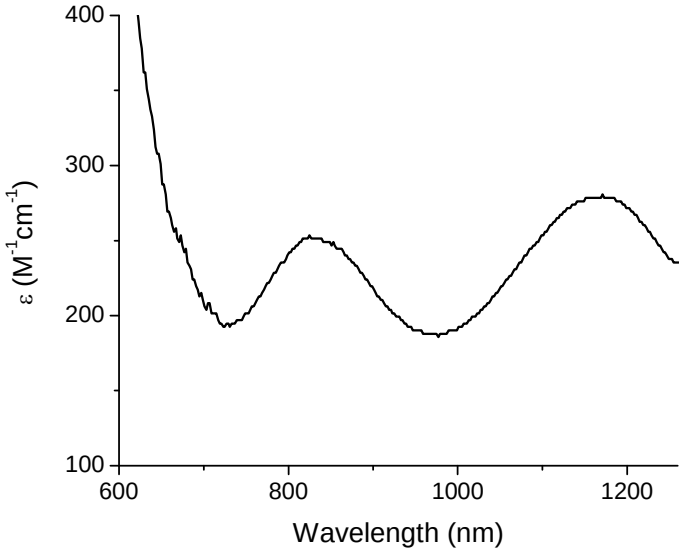

Figure 2.6. Near IR absorption of $[(HO)Ru^{IV}ORu^{III}(OH_2)]^{4+}$ in 0.1 M DNO_3.

Near-IR absorption band energies for $Ru^{III}ORu^{III}$ and $Ru^{IV}ORu^{III}$ forms of the blue dimer are listed in Table 2.3. Absorptions in this region appear from IT absorptions but, in this case, the bands are of low absorptivity. As discussed below, Interconfigurational (IC) bands are blue shifted by electronic coupling across the bridge.

Table 2.3. Near-IR absorption bands for $Ru^{III}ORu^{III}$ and $Ru^{IV}ORu^{III}$ forms of the blue dimer.

Complex Cation	nm (cm^{-1})	ε ($M^{-1}cm^{-1}$)
$[(H_2O)Ru^{III}ORu^{III}(OH_2)]^{4+}$	1133 (8830)	380
$[(H_2O)Ru^{III}ORu^{III}(OH)]^{3+}$	1103 (9070)	370
$[(H_2O)Ru^{IV}ORu^{III}(OH_2)]^{5+}$	840 (11900)	230
	1182 (8460)	300
$[(HO)Ru^{IV}ORu^{III}(OH_2)]^{4+}$	832 (12000)	250
	1164 (8590)	280

Excitation Dependent Resonance Raman.

Excitation dependent resonance Raman measurements were performed on *cis,cis*-$[(bpy)_2(H_2O)Ru^{III}ORu^{III}(OH_2)bpy)_2]^{4+}$ in pH = 1 aqueous medium at room temperature. The significance of the resonance enhancements for specific electronic transitions is that only those totally symmetric modes are enhanced for which there is a change in equilibrium displacement, $\Delta Q_{eq} \neq 0$. Analysis of the profiles can give quantitative information about the coupled displacements on a mode-by-mode basis, structural information about the excited state, and assist in assigning the origin of the underlying transition.[20-24]

From the match of excitation wavelengths with the blue dimer absorption spectrum, it is clear that the observed resonance enhancements are a consequence of a series of overlapping absorption bands which complicates any attempt at quantitative analysis of the

excitation profiles. Nonetheless, the trends in the enhancements with excitation wavelength are revealing as to the nature of the underlying electronic transitions.

Figure 2.7 shows a typical resonance Raman spectrum obtained with 514.5 nm excitation. Table 2.4 provides Raman band assignments in water at pH = 1. The bipyridine bands are labeled according to the nomenclature used in the normal coordinate analysis by Kincaid and coworkers for $[Ru(bpy)_3]^{2+}$.[25,26]

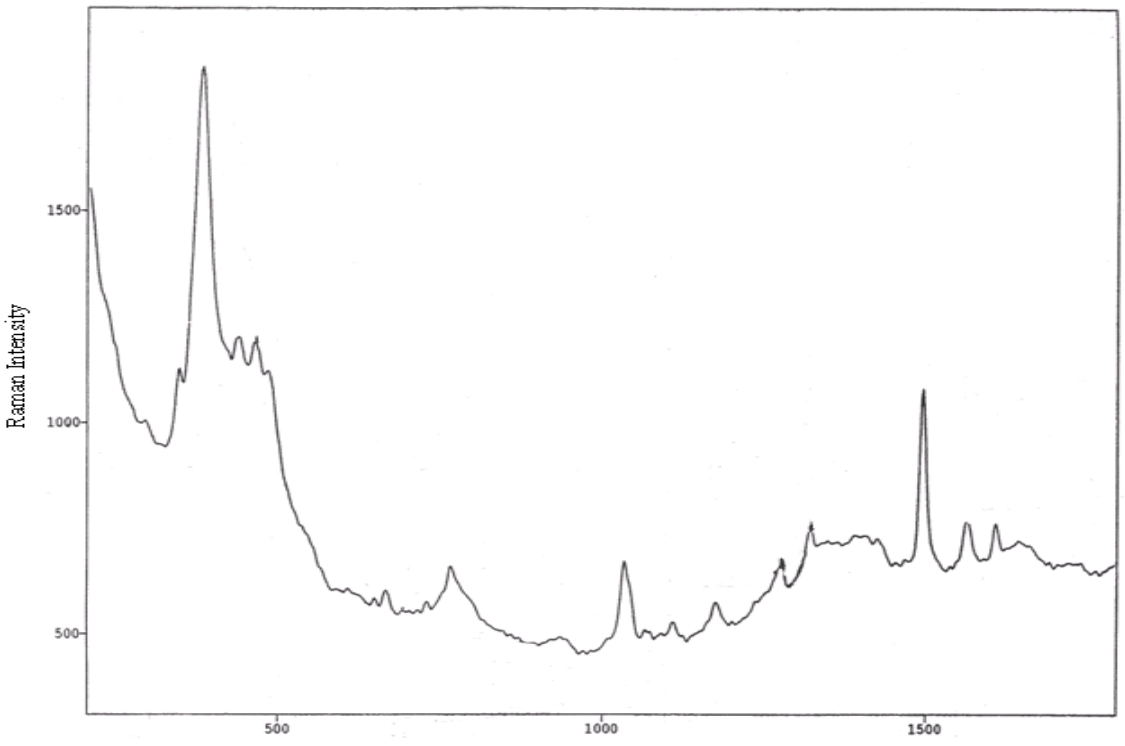

Figure 2.7. Resonance Raman spectrum of $[(bpy)_2(H_2O)Ru^{III}ORu^{III}(OH_2)bpy)_2]^{4+}$ in water at pH = 1 with 514.5 nm excitation.

Table 2.4. Raman band energies, polarizations (polarized, P, or depolarized, dp), and proposed assignments for $[(bpy)_2(H_2O)Ru^{III}ORu^{III}(OH_2)(bpy)_2]^{4+}$ in water at pH = 1.

Raman Shift (cm-1)	Polarization	Assignment
133	P	δ_{sym}(Ru-O-Ru)
170	dp	ν(bpy)
213	dp	
236	P	ν(Ru-N)
254		ν(bpy)
298	P	ν_{19}(bpy)
342	P	ν(bpy)
364		ν_{18}(bpy)
390	P	ν_{sym}(Ru-O-Ru)
419		
436	dp	
461	P	ν(bpy)
487	P	
551	P	ν_{sym}(Ru-O-Ru)+170
606		ν_{sym}(Ru-O-Ru)+254
666		ν_{17}(bpy)
728		ν_{sym}(Ru-O-Ru)+342
765		$2\nu_{sym}$(Ru-O-Ru); ν(bpy)
820		ν_{asym}(Ru-O-Ru)
1040		ν_{15}(bpy)
1111		ν_{13}(bpy)
1176		ν_{12}(bpy)
1278		ν_{10}(bpy)
1319		ν_{9}(bpy)
1494		ν_{7}(bpy)
1562		ν_{6}(bpy)
1604		ν_{5}(bpy)

Table 2.5. Differential Raman cross-sections at various excitation wavelengths for $[(bpy)_2(H_2O)Ru^{III}ORu^{III}(OH_2)bpy)_2]^{4+}$ in water at pH = 1.

Band (cm^{-1})	Laser Excitation Wavelength (nm)									
	457.6	465.8	476.5	488.0	496.5	501.7	514.5	568.2	647.1	676.4
298	16.4	15.8	34.4	45.8	36.7	19.4	6.6	0	24.5	0
342	77.1	135.0	187.7	211.1	229.8	81.4	14.1	0	182.4	80.0
364	0	0	0	0	0	0	26.6	0	2283	3087
390	939.5	252.7	1156	1158	1537	745.5	663.0	172.0	8556	2932
436	638.7	661.7	809.6	686.3	588.0	528.9	319.6	329.6	598.3	636.0
461	190.9	130.8	134.1	202.9	235.4	81.0	60.1	82.4	627.3	305.1
487	156.5	303.7	324.8	138.9	226.8	223.4	516.1	0	643.4	110.5
606	121.0	366.6	598.6	333.4	12.5	13.2	0	0	0	0
666	13.9	20.5	25.0	60.1	24.0	13.2	5.8	0	0	0
1040	307.1	293.0	275.4	289.0	215.5	163.7	124.3	0	661.0	286.0
1111	129.5	131.0	139.2	21.6	116.7	58.0	78.9	0	199.4	159.4
1176	59.2	54.5	52.4	32.7	48.8	22.8	19.6	0	176.0	225.2
1278	89.0	91.1	90.3	87.2	88.5	88.0	30.0	10.5	392.0	130.6
1319	78.8	72.5	0	0	92.4	38.1	48.0	0	40.0	41.9
1494	198.0	216.6	0	164.0	185.4	186.9	162.9	61.8	90.2	87.5
1562	65.5	105.9	95.0	41.9	62.8	60.0	76.1	0	96.3	0
1604	76.4	123.4	0	78.8	40.9	31.0	31.3	0	20.1	67.5

Features of note in these data include: <u>647.1 nm (15,400 cm^{-1}) excitation</u>: Excitation at this wavelength occurs within the absorption manifold of the intense band at 637 nm. In the 100-500-cm^{-1} region, the spectrum is dominated by an intense band near 385 cm^{-1} with 14 additional bands displaying enhancements as well. The 385-cm^{-1} band has been assigned to the symmetric Ru-O-Ru stretch of the bridge, ν_{sym}(Ru-O-Ru).[8] Above 500 cm^{-1}, overtones

and combinations appear of low intensity associated with a mixture of ν_{sym}(Ru-O-Ru) and a series of bands arising from ring vibrations of the bpy ligand. Note the band assignments in Table 2.4.

The vibrational mode ν_{18}(bpy) at 464 cm^{-1} and, to a lesser degree ν(bpy) bands at 436, 461, and 1040 cm^{-1}, are also resonantly enhanced. All of these low frequency ν(bpy) bands have significant Ru-N character. It is also notable that in a relative sense, medium frequency ν(bpy) ring stretching modes at 1111, 1176, and 1278 cm^{-1} are enhanced upon excitation at 647.1 and 674.1 nm.

514.5 nm (19,400 cm^{-1}) excitation: Upon 514.5 nm excitation, ν_{sym}(Ru-O-Ru) is also strongly enhanced. Absorption at this wavelength is dominated by the absorptions at 580 nm and 480 nm. Other bands are comparably enhanced, including bands of ν(bpy) origin, Table 2.5.

457.6 cm^{-1} (21,800 cm^{-1}) excitation: Absorption at this wavelength is also dominated by the absorption bands at 580 and 480 nm. In a relative sense, ν(bpy) bands at 1040, 1111, 1176, 1278, 1319, 1494, and 1562 cm^{-1} are increasingly enhanced as the excitation energy is increased from 514.5 nm to 457.6 nm. Resonance enhancement of these bands is reminiscent of enhancements found for Ru → bpy metal-to-ligand charge transfer (MLCT) excitation of molecules such as $[Ru(bpy)_3]^{2+}$.[27]

Figures 2.8a and 2.8b show Raman excitation profiles for representative bands at 364, 390, 461, 487 and 1040 cm^{-1}. Based on the Kincaid analysis, these bands are assigned to ν_{18}(bpy), ν_{sym}(Ru-O-Ru), ν(bpy), and ν_{15}(bpy). Differential Raman cross-sections for each Raman band at the different excitation wavelengths are listed in Table 2.5.

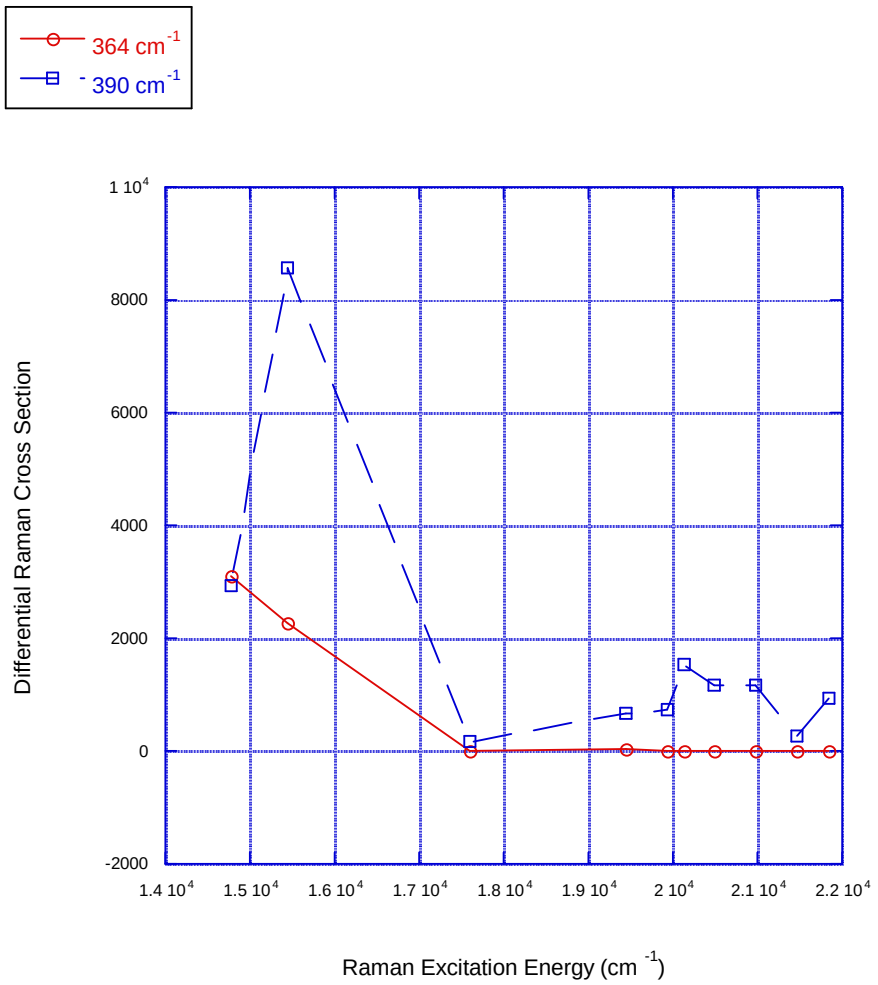

Figure 2.8a. Raman excitation profiles for *cis,cis*-$[(bpy)_2(H_2O)Ru^{III}ORu^{III}(OH_2)bpy)_2]^{4+}$ in water at pH = 2 vs. 0.5 M Na_2SO_4 for ν_{sym}(Ru-O-Ru) at 390 cm^{-1} and ν_{18}(bpy) at 364 cm^{-1}.

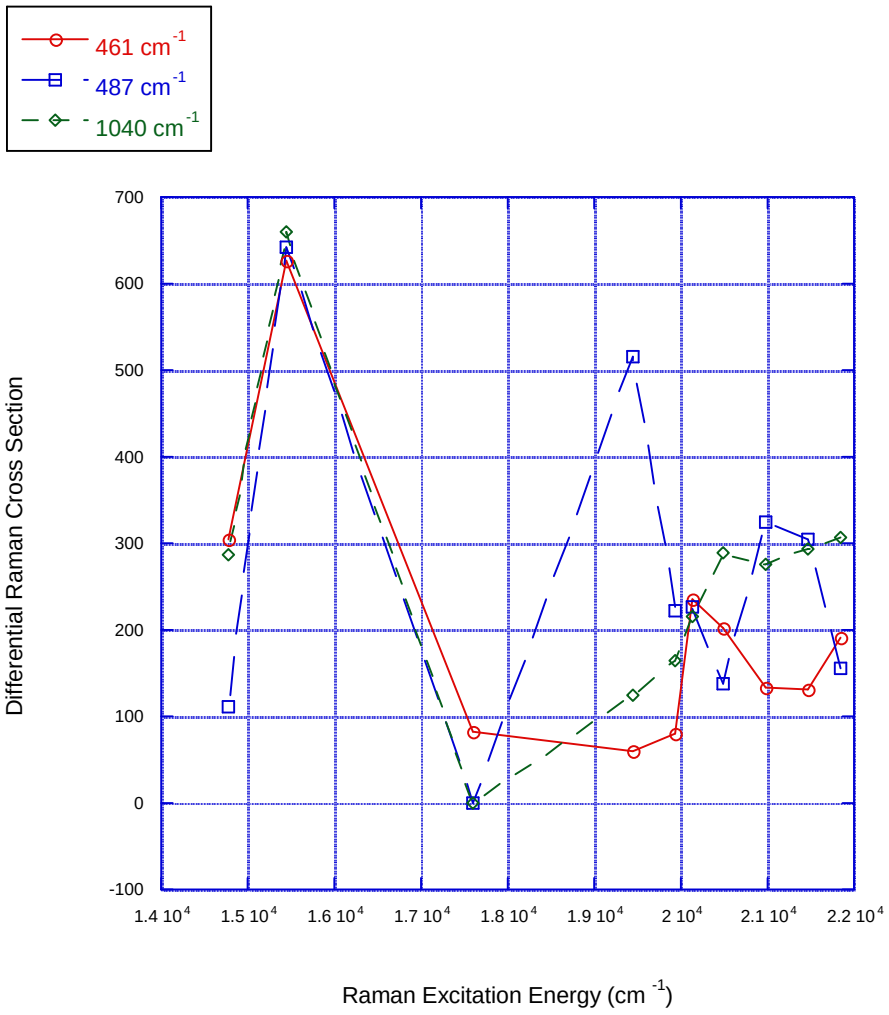

Figure 2.8b. Raman excitation profiles for *cis,cis*-$[(bpy)_2(H_2O)Ru^{III}ORu^{III}(OH_2)bpy)_2]^{4+}$ in water at pH = 2 vs. 0.5 M Na_2SO_4 for ν_{sym}(Ru-O-Ru) at 390 cm^{-1}, ν(bpy) at 461 cm^{-1}, and ν_{15}(bpy) at 1040 cm^{-1}. Note the band assignments in Table 2.4.

DFT Calculations.

The electronic structure of the blue dimer has been investigated theoretically by application of complete active space self-consistent field (CASSCF) calculations[11] and Density Functional Theory (DFT) with application of the broken symmetry approximation.[10,12] The results of these calculations suggest weak electronic coupling across the Ru-O-Ru bridge. However, these calculations are of limited value because they fail to account for the properties of the molecule. The results of preliminary DFT calculations[15]

have been extended here. They successfully account for chemical properties and electronic and molecular structure.

Geometries. *cis,cis*-$[(bpy)_2(H_2O)Ru^{III}ORu^{III}(OH_2)bpy)_2]^{4+}$: The coordinates from the X-ray structure of $[(bpy)_2(H_2O)Ru^{III}ORu^{III}(OH_2)bpy)_2]^{4+}$ (PDB file) were used as the input geometry for Gaussian. Although two geometric isomers are possible for the blue dimer, all the known X-ray structures for the family $[(bpy)_2(L)RuORu(L)bpy)_2]^{n+}$ (L = H_2O, Cl, NO_2, NH_3) are for the enantiomeric isomeric pair and all studies reported here will focus on that structure. The ground state was assumed to be a singlet, consistent with the magnetic properties, and the structure was optimized at DFT level (B3LYP, LANL2DZ) with no symmetry restrictions.

Tight convergence criteria were used for both the SCF and optimization itself. The calculation converged to a final C_2 symmetry, which was used to calculate the gas phase absorption spectrum and to build the structures with hydrogen-bonded water molecules and counterions. A delocalized model was first proposed by Dunitz and Orgel for $[Cl_5RuORuCl_5]^{4-}$ and later modified for the blue dimer.[7,28] A related analysis was reported for μ-oxo iron porphyrin dimers by Tatsumi and Hoffman.[29] We have extended our earlier DFT results based on a closed-shell singlet ground state by using the B3LYP functional and LANL2DZ basis set as implemented in Gaussian03.

Table 6 compares selected bond distances and angles for the reported X-ray structure of *cis,cis*-$[(bpy)_2(H_2O)Ru^{III}ORu^{III}(OH_2)bpy)_2](ClO_4)_4$ and optimized geometries for the cation in the gas phase, or with water molecules and/or chloride counter anions. cis,cis-$[(bpy)_2(H_2O)Ru^{III}ORu^{III}(OH_2)(bpy)_2]^{4+}\times 4H_2O$ (BD×$4H_2O$): Two water molecules were hydrogen-bonded to each of the two aqua ligands in the optimized gas phase structure

with a hydrogen-bond distance of 1.500 Å and the resulting "hydrate" was fully optimized under C_2 symmetry.

cis,cis-[(bpy)$_2$(H$_2$O)Ru^{III}ORu^{III}(OH$_2$)(bpy)$_2$]$^{4+}$×12H$_2$O (BD×12H$_2$O): Two additional water molecules were hydrogen-bonded to each of the four hydrogen-bonded water molecules in BD×4H$_2$O to complete a total of twelve hydrogen-bonded water molecules. The resulting structure was fully optimized under C_2 symmetry.

cis,cis-[(bpy)$_2$(H$_2$O)Ru^{III}ORu^{III}(OH$_2$)(bpy)$_2$](Cl)$_4$×4H$_2$O (BDCl$_4$×4H$_2$O): Four chloride anions were added to BD×4H$_2$O, each hydrogen-bonded to one of the aqua ligands with a hydrogen-bond distance of 1.700 Å. The resulting structure was fully optimized under C_2 symmetry.

Table 2.6. Significant bond distances and angles from the crystal structure and optimized geometries of the blue dimer with different numbers of water molecules and chloride ions in the outer coordination sphere.

Metric Feature	Exp.	BD	BD×4H$_2$O	BD×12H$_2$O	BDCl$_4$×4H$_2$O
d(Ru-O$_{oxo}$), Å	1.869	1.928	1.923	1.911	1.905
d(Ru-O$_{aquo}$), Å	2.137	2.236	2.157	2.127	2.112
d(Ru-N), Å	2.056	2.100	2.104	2.099	2.091
< (Ru-O-Ru)	165.5	158.3	162.2	160.9	162.3

The energy level diagram in Figure 2.9 is a result of the DFT calculations. In summary: (i) The highest filled level, dπ$_1$*, is antibonding, largely dπ in character, and arises dominantly from dπ-2p$_{\pi,O}$-dπ mixing. (ii) The lowest unoccupied level, dπ$_2$*, is similarly antibonding with regard to the Ru-O-Ru π interaction. (iii) The Ru-O-Ru π interaction also gives rise to filled bonding levels, not shown, which are largely 2p$_{\pi,O}$ in character and the non-bonding pair dπ$_1^n$, dπ$_2^n$. (iv) The remaining dπ orbitals, dδ or d$_{xy}$, are largely localized at

each Ru and have δ symmetry with regard to the Ru-μ-O bonding axes defined as the z axis at each Ru.

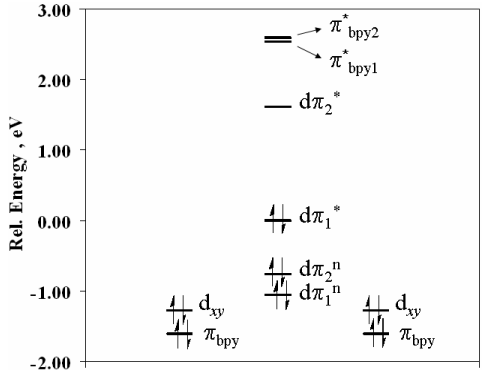

Figure 2.9. Energy level diagram for *cis,cis*-$[(bpy)_2(H_2O)Ru^{III}ORu^{III}(OH_2)(bpy)_2]^{4+}$ from DFT calculations based on the B3LYP functional and LANL2DZ basis set. A closed-shell singlet ground state was assumed. The energy levels are labeled to indicate their dominant orbital compositions with $d\pi_1$* and $d\pi_2$* largely antibonding dπ in character arising from dπ-$2p_{\pi,O}$-dπ mixing. Levels $d\pi_1^n$ and $d\pi_2^n$ are the corresponding nonbonding pair. The d_δ or d_{xy} (dπ) orbitals are largely localized at each Ru and have δ symmetry with regard to the Ru-μ-O bonds.

Time-dependent DFT calculations on the optimized structures provide an interpretation of the UV-visible absorption spectrum of the blue dimer. Introduction of hydrogen bonded water molecules and counter ions significantly improves excitation energies, although the overall shape of the absorption envelope is well accounted for with a polarizable continuum model for the solvent (Appx. A Figures S5,6). A spectrum recorded at pH = 1 and assignments based on the orbital diagram in Figure 2.9 are shown in Figure 2.10.

The visible absorption band that accounts for the blue color responsible for the blue in the blue dimer arises from overlapping dπ → π_{bpy}* (MLCT) and bridge-based dπ → dπ* transitions. The DFT calculations predict three low lying bands arising from transitions that have Interconfigurational (IC) dπ → dπ character. Low energy absorption features at 1205, 1125 and 915 nm (ε = 200-400 $M^{-1}cm^{-1}$) arise from Interconfigurational transitions within the

dπ orbital set, d_{xy},$d\pi_n \rightarrow d\pi_2^*$, Table 2.3. These three absorptions originate from two sets of d_{xy} orbitals which have δ symmetry with regard to the Ru-O-Ru bridge, and $d\pi_{1n}$, the higher energy nonbonding level arising from the through-bridge interaction, Figure 2.9. The acceptor level is $d\pi_2^*$, the second of two antibonding levels, largely dπ in character but mixed with $2p_O$. The oscillator strengths ($f \leq 0.0003$) are low for these bands consistent with considerable $d\pi \rightarrow d\pi$ character in the transitions.

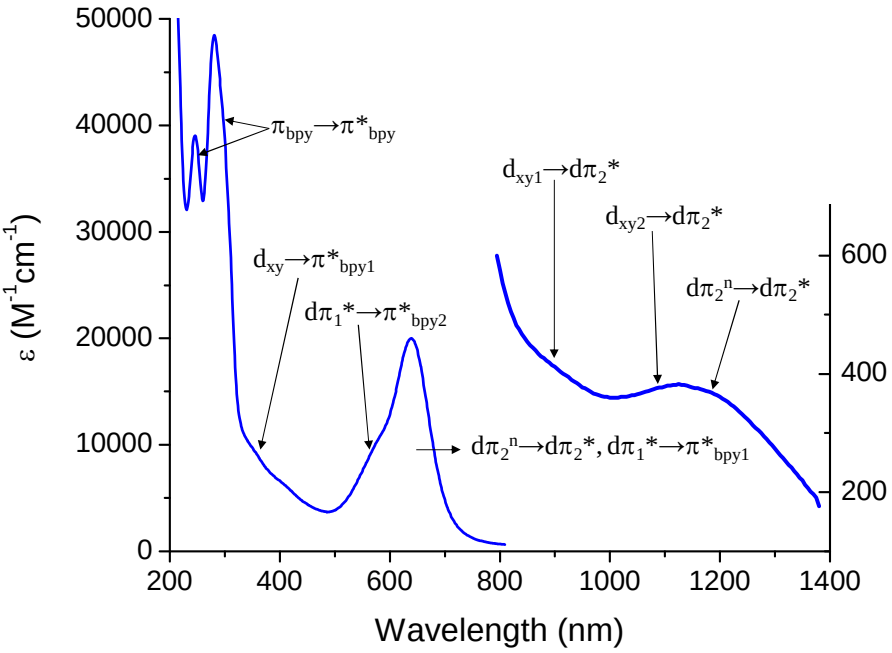

Figure 2.10. UV-Vis-near IR spectrum of *cis*,*cis*-$[(bpy)_2(H_2O)Ru^{III}ORu^{III}(OH_2)(bpy)_2]^{4+}$ in water at pH = 1. Band assignments are based on the bonding scheme in Figure 2.5. ε = 21,100 $M^{-1}cm^{-1}$ for the intense band at 637 nm.

Table 2.7. Absorption band energies and proposed assignments for *cis,cis*-$[(bpy)_2(H_2O)Ru^{III}ORu^{III}(OH_2)bpy)_2]^{4+}$ in water at pH = 1, see text.

Absorption Band (nm)	ε ($M^{-1}cm^{-1}$)	Assignment
271	39,846	$\pi \rightarrow \pi^*$(bpy)
280	50,310	$\pi \rightarrow \pi^*$(bpy)
375	26,700	$d\pi_1^*, d\pi_n \rightarrow \pi^*$(bpy) (MLCT)
410	24,400	$d\pi_2^n \rightarrow \pi^*$(bpy) (MLCT)
480	20,800	$\pi_1 \rightarrow d\pi_2^*$, $\pi_2 \rightarrow d\pi_2^*$ (LMCT)
580	16,200	$d\pi_2^n \rightarrow d\pi_2^*$, $d\pi_1^* \rightarrow \pi_2^*$ ($d\pi^n \rightarrow d\pi^*$; MLCT)
637	21,100	$d\pi_2^n \rightarrow d\pi_2^*$, $d\pi_1^* \rightarrow \pi_2^*$ ($d\pi^n \rightarrow d\pi^*$; MLCT)
1133	380	$d_{xy1} \rightarrow d\pi_2^*$, $d_{xy2} \rightarrow d\pi_2^*$, $d\pi_2^n \rightarrow d\pi_2^*$

Table 2.7 presents proposed UV-visible band assignments for $[(bpy)_2(H_2O)Ru^{III}ORu^{III}(OH_2)bpy)_2]^{4+}$ based on the orbital designations in Figure 2.11. The proposed assignments are consistent with the excitation dependent resonance Raman data and the results of the DFT calculations. Figure 2.11 illustrates molecular orbitals for $[(bpy)_2(H_2O)Ru^{III}ORu^{III}(OH_2)(bpy)_2]^{4+}$ involved in electron transitions in the near IR and visible.

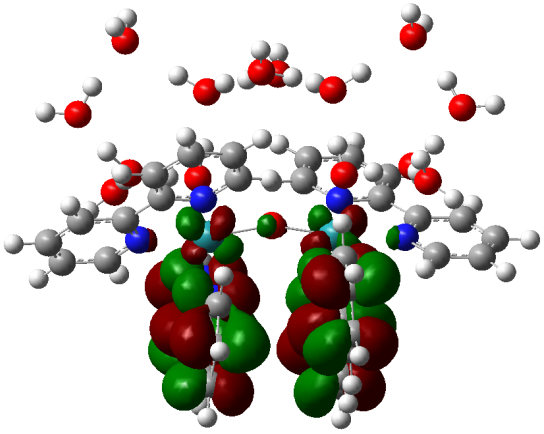

LUMO+2 (π^*_{bpy})

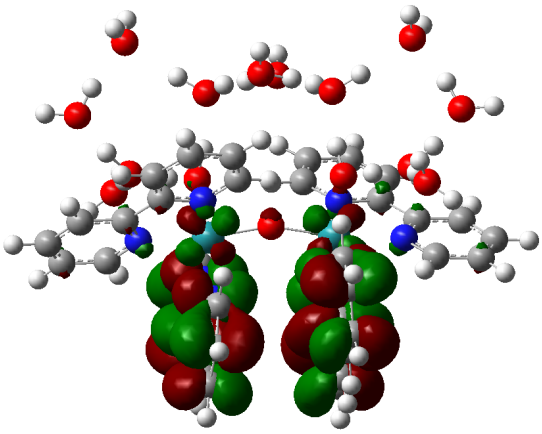

LUMO+1 (π^*_{bpy})

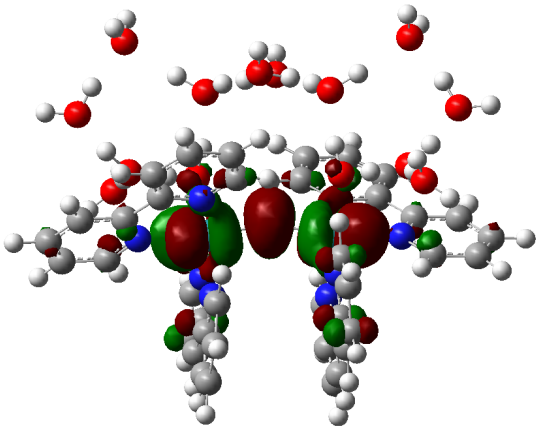

LUMO ($d\pi^*_2$)

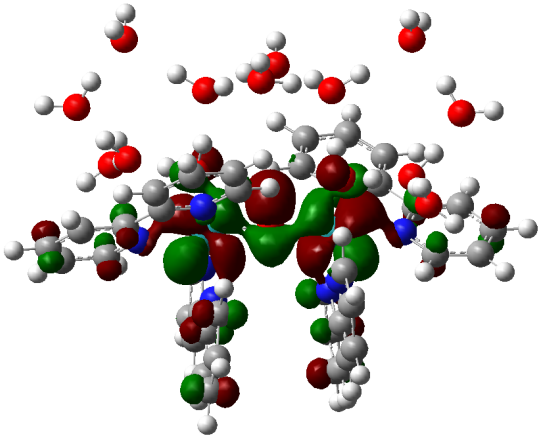

HOMO ($d\pi^*_1$)

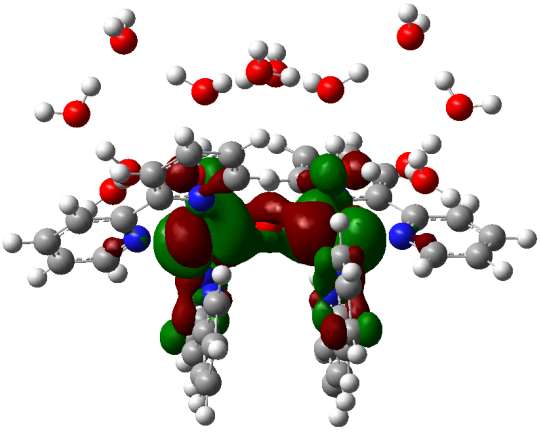

HOMO-1 ($d\pi_2$)

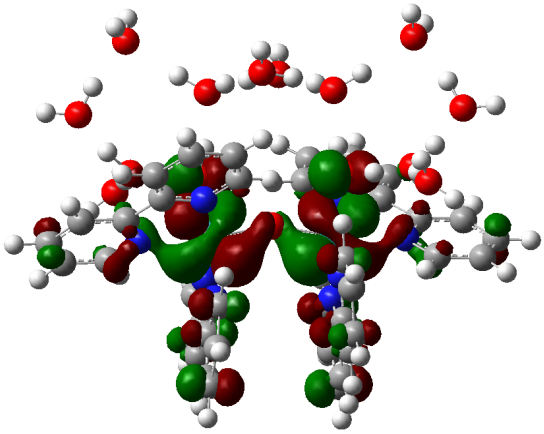

HOMO-2 ($d\pi_1$)

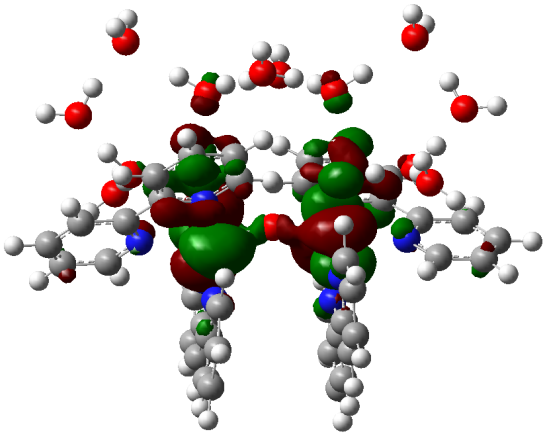

HOMO-3 (d_{xy})

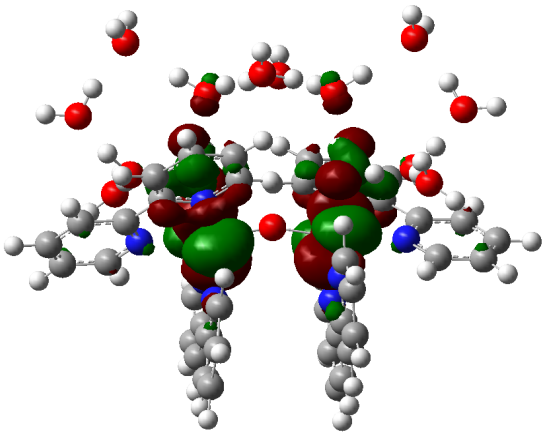

HOMO-4 (d_{xy})

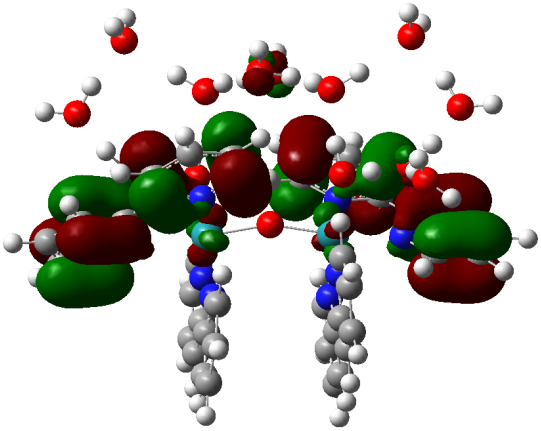

HOMO-5 (π_{bpy})

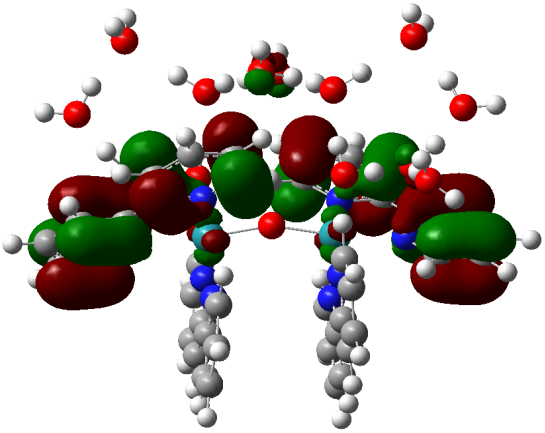

HOMO-6 (π_{bpy})

Figure 2.11. Molecular orbitals for $[(bpy)_2(H_2O)Ru^{III}ORu^{III}(OH_2)(bpy)_2]^{4+}$ involved in MLCT and bridge-based electronic transitions in the near IR-visible.

Both optimized geometries and electronic spectra for $[(bpy)_2(H_2O)Ru^{III}ORu^{III}(OH_2)(bpy)_2]^{4+}$ were obtained in the DFT calculations. Calculations based on C_2 symmetry accounted for the overall profile of the experimental spectrum (Appx. A Figure S5). The visible λ_{max} was red-shifted by ~70 nm for the gas phase spectrum relative to the experimental value at pH = 1. With the IEF-PCM model and acetonitrile as the solvent,

λ_{max} = 505 nm for the bridge-based band in the calculated spectrum matched well with the experimental λ_{max} = 513 nm (Appx. A Figure S9). Under conditions of the experiment, solvent exchange with the aqua ligands was slow.[9] A dramatic improvement in the calculated absorption spectrum is observed with the blue dimer when specific water molecules and counterions are included, or when non-hydrogen bonding solvents are used in the IEF-PCM model. Further illustration of this point is given in Appx. A Figure S10 where an exceptional match between the calculated and experimental absorption spectrum of *cis*-$Ru(bpy)_2Cl_2$ is observed. The IEF-PCM model with water as the solvent was employed. In this case, the molecule is void of sites for specific hydrogen bonding interactions and the associated difficulties of modeling water. Time-dependent DFT studies relating structure and solvent effects in calculated absorption spectra have been reported.[30-32]

Our DFT results also predict redox potentials well in non-hydrogen bonding solvents for non-PCET, one-electron couples. For the $[(bpy)_2(Cl)Ru^{IV}ORu^{III}(Cl)(bpy)_2]^{3+}/[(bpy)_2(Cl)Ru^{III}ORu^{III}(Cl)(bpy)_2]^{2+}$ couple, experimental[7] and calculated $E_{1/2}$ values (in CH_3CN, I = 0.1, vs. NHE) are 0.93 and 0.99, respectively (see Appx. A for details). Estimating redox potentials with DFT calculations is well-documented in the literature.[10,12,33]

Discussion

The blue dimer, $[(bpy)_2(H_2O)Ru^{III}ORu^{III}(OH_2)(bpy)_2]^{4+}$, was the first designed molecular catalyst for water oxidation.[1,2] The details by which it oxidizes water have been the subject of a series of investigations,[3-6] and will be the subject of a following paper. Oxidative activation of the blue dimer involves the stepwise oxidation through the series of

formal oxidation states $Ru^{III}ORu^{III}$, $Ru^{IV}ORu^{III}$, $Ru^{IV}ORu^{IV}$, $Ru^{V}ORu^{IV}$, $Ru^{V}ORu^{V}$. Oxidation with buildup of multiple oxidative equivalents by proton coupled electron transfer (PCET) meets the required $4e^-/4H^+$ demands of the oxygen/water half reaction, $2H_2O - 4H^+ - 4e^- \rightarrow O_2$. As noted above, both the blue dimer and the once-oxidized form, $[(bpy)_2(HO)Ru^{IV}ORu^{III}(OH_2)(bpy)_2]^{4+}$, have been characterized structurally. The intermediate $Ru^{IV}ORu^{IV}$ is a transient, unstable to disproportionation. $Ru^{V}ORu^{IV}$, as $[(bpy)_2(O)Ru^{V}ORu^{IV}(O)(bpy)_2]^{3+}$ by pH dependent electrochemical measurements,[2] exists as a discrete intermediate and undergoes slow water oxidation by a complex mechanism.[6]

The goal of this paper was to explore the electronic structure of the blue dimer which has been a source of controversy. In original DFT calculations by Baik and co-workers,[10] weak electronic coupling between Ru(III) sites across the μ-oxo bridge was assumed with magnetic exchange across the bridge. Based on results from DFT (B3LYP) and complete active space self-consistent field (CASSCF) calculations,[11] Batista and Martin concluded that the ground state is a weakly antiferromagnetically coupled single. They concluded that partial electronic delocalization occurs by mixing between dπ rather than by dδ orbitals as concluded by Baik and co-workers, Scheme 2.1.[10,11]

As shown below, with additional evidence summarized elsewhere,[6] there is clear evidence for strong coupling in the blue dimer which dominates its properties, distinguishes it from typical Ru(III) complexes, and is essential to understanding its reactivity.

Structure. Key intramolecular structural details for the cation *cis,cis*-$[(bpy)_2(H_2O)Ru^{III}ORu^{III}(OH_2)bpy)_2]^{2+}$ are listed in Table 2.8 where comparisons are made with the Ru-O-Ru units in $[(bpy)_2(H_3N)Ru^{III}ORu^{III}(NH_3)(bpy)_2](ClO_4)_4$ and $[(bpy)_2(O_2N)Ru^{III}ORu^{III}(NO_2)(bpy)_2](ClO_4)_2 \cdot 2H_2O$.

Table 2.8. Comparison of selected bond cistances (Å) and angles (deg) for the cations in $[(bpy)_2(H_2O)Ru^{III}ORu^{III}(OH_2)(bpy)_2](ClO_4)_4 \cdot 2H_2O$,[2] $[(bpy)_2(H_3N)Ru^{III}ORu^{III}(NH_3)(bpy)_2](ClO_4)_4 \cdot 2H_2O$,[14] and $[(bpy)_2(O_2N)Ru^{III}ORu^{III}(NO_2)(bpy)_2](ClO_4)_2 \cdot 2H_2O$.[13]

	$(H_2O)Ru^{III}ORu^{III}(OH_2)$	$(H_3N)Ru^{III}ORu^{III}(NH_3)$	$(O_2N)Ru^{III}ORu^{III}(NO_2)$
Distances			
M(1)-O	1.869(1)	1.8939(15)	1.876(6)
M(2)-O	1.869(1)	1.8939(15)	1.890(7)
L-M(1)	2.136(4) (L = OH_2)	2.126(6) (L = NH_3)	2.067(11) (L = NO_2)
M(2)-L'	2.136(4) (L' = OH_2)	2.126(6) (L' = NH_3)	2.034(8) (L = NO_2)
L•••L'[a]	4.725 (H_2O•••OH_2)	4.816 (H_3N•••NH_3)	5.518 (O_2N•••NO_2)
Angles			
L-M(1)-O	89.4(2) (L = OH_2)	92.8(3) (L = NH_3)	92.8(3) (L = NO_2)
O-M(2)-L'	89.4(2) (L' = OH_2)	92.8(3) (L' = NH_3)	92.5(3) (L = NO_2)
M(1)-O-M(2)	165.4(3)	158.2(4)	157.2(3)
L-M(1)-M(2)-L'[b]	65.7 (H_2O•••OH_2)	28.5 (H_3N•••NH_3)	115.9 (O_2N•••NO_2)

a Distance of separation between adjacent cis ligands across the μ-oxo bridge. *b* Torsional angle of L, L' along the direct M(1)-M(2) axis between the planes containing L-M(1)-O and O-M(2)-L'.

From the data in Table 2.8, Ru-O distances to the μ-oxo bridge in $[(H_2O)Ru^{III}ORu^{III}(OH_2)]^{4+}$ (1.869 Å) suggest considerable multiple bond character. The basis for π-bonding along the intersecting Ru-O-Ru bonding axes, as visualized, for example, in Figure 2.11, arises from π-bonding interactions between the p-orbitals of the bridging oxygen and dπ orbitals of the metal ions.

Terminal Ru-O bond lengths to the aqua ligands (2.136 Å) in the blue dimer are more consistent with those reported for Ru^{II}-OH_2 complexes (2.1053(16) - 2.188(6) Å) rather than for Ru^{III}-OH_2 (2.007(3) - 2.037(5) Å).[34-39] This is a significant observation consistent with electron content at the metal more nearly that of Ru(II) than Ru(III) and a consequence of considerable electron donation from the oxo bridge.

A comparison of Ru-O-Ru angles amongst the examples in Table 2.8 shows that the bis(aqua) complex (blue dimer) has the largest angle (165.4°), while the angles in the bis(ammine) (158.2°) and bis(nitro) (157.2°) cations are smaller. As noted elsewhere,[8] and

shown in Figure 2.9, bending along the Ru-O-Ru axis leads to electronic stabilization by removing the degeneracy of two half-filled antibonding $d\pi^*$ orbitals through Jahn-Teller stabilization to a doubly occupied lower energy state.

The effects of ligand-ligand repulsion can be seen in the magnitude of the dihedral angle between the planes containing L-M(1)-O and O-M(2)-L'. Even though the Ru-O-Ru bond angle for the bis(ammine) complex is only 1° larger than the bis(nitro) complex its H_3N-Ru-Ru-NH_3 dihedral angle is significantly smaller at 28.5° compared to 115.9°. The dihedral angle for the bis(aqua) complex is intermediate at 65.7°.

Localization vs. delocalization. Given the evidence for strong electronic coupling, the question of localization vs. delocalization in the mixed valence forms of the μ-oxo complexes is of considerable interest. Based on an original analysis by Hush, the transition from localized to delocalized and the extent of delocalization, are functions of the reorganization energy and the resonance energy arising from orbital mixing between sites.[40,41]

A number of experimental techniques have been applied to the question of localized vs. delocalized in mixed-valence materials, the most persuasive coming from XRD and IR measurements.[19,42-44] XRD results on the mixed-valence, nominally $Ru^{IV}ORu^{III}$, forms in Table 2.2 are revealing in this regard. In the coordinatively symmetrical salts, $[ClRuORuCl](Ce(NO_3)_6)$ and $[(SO_4)RuORu(SO_4)]SO_4$, the structures at the μ-oxo bridged sites are symmetrical, consistent with delocalization and an oxidation state description $Ru^{III.5}ORu^{III.5}$.

By contrast, there is a coordinative asymmetry in the ClO_4^- salt $[(Cl)Ru^{IV}ORu^{III}(Cl)](ClO_4)_3$. The asymmetry appears in differences in Ru-O (1.805(9) vs. 1.845(9) Å) and Ru-Cl bond lengths (2.357(4) vs. 2.339(4) Å) and in the asymmetric

disposition of the counter ions around the cation. The influence of extensive delocalization in the localized cation is evident in the structure in the Ru-Cl bond lengths. The difference in Ru-Cl bond lengths in $[ClRu^{IV}ORu^{III}Cl](ClO_4)_3$ is 0.018 Å which is considerably smaller than the average Ru-Cl bond difference of 0.102 Å, between $Ru^{II}(bpy)_2Cl_2$ (2.426 Å) and $[Ru^{III}(bpy)_2Cl_2]Cl$ (2.322 and 2.328 Å).[45]

The change from localization to delocalizatioin between different salts is a remarkable observation. As noted above, localization or delocalization is dictated by the relative magnitudes of the total reorganization energy (intramolecular and medium) and the resonance energy. A detailed analysis for $[(bpy)_2ClRu^{IV}ORu^{III}Cl(bpy)_2]^{3+}$ is necessarily complicated given the multiple orbital interactions contributing to electronic delocalization and the multiple vibrations coupled to the structural difference between Ru(III) and Ru(IV) in $Ru^{IV}ORu^{III}$.

In the present comparison, the intramolecular reorganization energy should be the same between lattices and the transition between localized and delocalized dictated by the medium reorganization energy. The role of solvent and counter ions have been documented for mixed valence compounds in solution.[42,46-50] In the ionic lattice of the mixed-valence crystals, counter ion and molecular positions are frozen. A significant contribution to the medium barrier to electron transfer arises from counter ion placement with counter ions frozen with regard to large amplitude translational displacements.

In the structure of the salt $[(bpy)_2ClRu^{IV}ORu^{III}Cl(bpy)_2](ClO_4)_3$, the ClO_4^- counter ions are unsymmetrically disposed creating a local electrostatic gradient favoring the localized isomer $[ClRu^{IV}ORu^{III}Cl]^{3+}$. In the $Ce(NO_3)_6^{3-}$ salt the counter anion is symmetrically disposed, presumably induced by the electrostatics of crystal formation. In this

crystal electrostatic symmetrization and loss of counter ion placement as a contributor to the reorganization energy is apparently sufficient to induce the transition from localized to delocalized, $[ClRu^{IV}ORu^{III}Cl]^{3+} \rightarrow [ClRu^{III.5}ORu^{III.5}Cl]^{3+}$.

The importance of electrostatic effects and symmetrization also appear in the structure of *cis,cis*-$[(bpy)_2(SO_4)RuORu(SO_4)(bpy)_2](SO_4)_{0.5}\bullet H_2O$. In this case, the charge compensating counter dianion appears as an electrostatic bridge between $[(O_4S)Ru^{III.5}ORu^{III.5}(SO_4)]^+$ cations and the mixed-valence core is delocalized.

A point of additional interest is the proximity of the $Ce(NO_3)_6^{3-}$ anion in the salt $[(bpy)_2(Cl)Ru^{IV}ORu^{III}(Cl)(bpy)_2](Ce(NO_3)_6)$ with respect to the cation and its penetration well into an intramolecular cavity created by the bpy ligands, Figure 2.1. As alluded to above, a major debilitating factor in the use of the blue dimer in water oxidation catalysis is its tendency to undergo anion coordination (anation) triggered by oxygen evolution and creation of open coordination sites.[3,6] The ligand-based structural pockets may play a role in structurally poising normally weakly coordinating anions such as ClO_4^- to capture coordination sites opened by oxygen loss.

***Magnetism*.** The blue dimer is essentially diamagnetic at 2K consistent with a ground state singlet. This result is consistent with reported low-temperature EPR measurements and the absence of a measurable EPR resonance at 4-5 K.[51] Magnetic properties are temperature dependent with paramagnetism increasing as the temperature increases. Even for the highest observed values of μ_{eff} and $\chi \cdot T$ at 350 K, the extrapolated number of unpaired electrons per dimer is still only ~1.4-1.5. Two unpaired electrons would be expected for non-interacting or weakly coupled low-spin Ru^{III} ($d\pi^5$) ions. The magnetic data provide clear evidence for

strongly coupled Ru(III) sites with the paramagnetism arising from thermal population of a low-lying magnetic state or states which are also delocalized.

The magnetic susceptibility data are unusual in that a prominent maximum is not found in the χ-T plot in Figure 2.3. In antiferromagnetically coupled dimeric systems, such maxima are typical and used to obtain the exchange coupling parameter J ($2J$ is the energy splitting between a singlet ground state and low-lying triplet excited state). Not surprisingly, attempted fits of the magnetic data by use of the Bleaney-Bowers expression[52,53] for two interacting sites each with one-electron local spins (i.e. $S_a = S_b = ½$; $\mathbf{H} = -2J \cdot \mathbf{S}_a \cdot \mathbf{S}_b$) was unable to simulate the temperature dependent data.

In a previous study,[7] the magnetic behavior of the nitro analog $[(bpy)_2(O_2N)Ru^{III}ORu^{III}(NO_2)(bpy)_2](PF_6)_2$ exhibited a more typical temperature dependence from 77-275 K with a maximum appearing in the χ-T plot at ~155 K. In this case, fitting of the data to the Bleaney-Bowers equation gave $2J = -173$ cm^{-1} (with $g = 2.48$).[20] Possible interpretations of the data were a moderate antiferromagnetic interaction between sites or strong electronic coupling. The latter was favored based on ancillary evidence- structure, electronic, and chemical properties.

The room temperature magnetic moment of the nitro derivative is 1.8 μ_B per Ru^{III}, the expected value for one unpaired electron. The difference in magnetic behavior between the blue dimer and this derivative is likely due to differences in structure and electronic properties and how they influence electronic coupling. Recall that the XRD determined Ru–O–Ru angle is 157.2º for the *di*cationic nitro analog and 165.4º for the *tetra*cationic blue dimer.

In the strongly coupled interpretation of the magnetic data for the blue dimer, Figure 2.9, there is a delocalized diamagnetic, singlet ground state of electronic configuration $[d\pi_1^*]^2$. In this model, the temperature dependent paramagnetism arises from a thermally populated, delocalized triplet state of configuration $[d\pi_1^*]^1[d\pi_2^*]^1$.

UV-visible-Near IR Spectra. The appearance of MLCT transitions in the visible region of the spectrum is a common feature for Ru(II) polypyridyl complexes,[54-57] but these bands typically appear in the UV for Ru(III).[39] For example, the MLCT λ_{max} for the most intense low energy feature for $Ru(bpy)_3^{2+}$ appears at λ_{max} ~460 nm, while the MLCT λ_{max} for $Ru(bpy)_3^{3+}$ is masked by intense, bpy-based $\pi \rightarrow \pi^*$ transitions between 200 to 300 nm.[58]

As a consequence, appearance of MLCT bands at relatively low energy, ~580 nm, in the blue dimer is a significant observation, an important consequence of strong Ru-O-Ru coupling across the μ-oxo bridge. The energies of MLCT transitions are directly related to electron content at the metal with transition energies increased due to stabilization of the Ru(III) $d\pi^5$ core. The dramatic shift to lower energy compared to related monomers arises from Ru-O-Ru electronic coupling and $d\pi$-$2p_O$ mixing across the μ-oxo bridge. This interaction increases the energy of nonbonding, largely $d\pi$ levels that are the origin of the low energy MLCT transitions, shifting them into the visible.[59,60]

There is a significant difference in solvent dependence for the overlapping MLCT and RuORu bridge-centered transitions. For MLCT transitions, where there is a significant difference in dipole character between ground and excited states, absorption band energies are highly solvent dependent.[46,50,61-65] A far smaller solvent dependence is predicted for the bridge-based $d\pi \rightarrow d\pi^*$ transition given its centrosymmetric origin. A solvent dependence is

predicted, arising from the bent Ru-O-Ru bridge and the resulting asymmetric change in electronic distribution between ground and excited states.

Low energy bands of low absorptivity appear in the near IR for both the $Ru^{III}ORu^{III}$ and $Ru^{IV}ORu^{III}$ forms of the blue dimer, Table 2.3. They arise from $d\pi_{xy} \rightarrow d\pi_2^*$, nominally Interconfigurational (IC) transitions which are analogous to Interconfigurational $d\pi \rightarrow d\pi$ transitions within the $d\pi^5$ cores of Ru^{III} complexes. IC bands are observed in related Ru(III) d^5 monomers but with low absorptivities and transition energies. The corresponding absorptions appear in the infrared, typically below 3000 cm^{-1}. Their allowedness is due to low symmetry and spin orbit coupling induced mixing of the $d\pi$ orbitals. The significant increase in energy and absorptivity for the $d\pi_n \rightarrow d\pi_{xy}$ bands in the dimers is an additional consequence of extensive Ru-O-Ru mixing across the μ-oxo bridge. The "IC" transitions in this case arise from transitions from largely localized d_{xy} orbitals to $d\pi_2^*$.

Resonance Raman excitation profiles. Analysis of the excitation dependent resonance Raman profiles provides additional insight into the electronic origin of the absorption bands in the blue dimer spectrum consistent with the DFT analysis.

637 nm: Based on the DFT assignments in Table 2.7, the experimental band at 637 nm arises from overlapping, bridge-based $d\pi_{2n} \rightarrow d\pi_2^*$ and $d\pi_1^* \rightarrow \pi^*(bpy_1)$ MLCT transitions with the intensity dominated by the former. Oscillator strengths for the two are 0.3430 and 0.0588, respectively. (Additional oscillator strengths are included in Appx. A.)

This assignment is consistent with the observed resonance enhancements of both ν_{sym}(Ru-O-Ru) and ν(bpy)-based modes, Table 2.5. As shown by the large intensity enhancement for ν_{sym}(Ru-O-Ru) there is a significant change in polarization between ground and excited states with strong coupling and a large displacement change for this mode. A

large displacement is qualitatively predicted based on the nature of the transition and excitation of an electron into $d\pi_2*$ which is antibonding with regard to the Ru-O-Ru interaction. Given its oscillator strength, this transition is strongly dipole allowed in contrast to $d\pi_{2n} \rightarrow d\pi_2*$. The change in electronic distribution for the transition is illustrated in Figure 2.11.

As noted above, the bent nature of the Ru-O-Ru bridge results in an asymmetrical change in electronic distribution in the $d\pi_{2n} \rightarrow d\pi_1*$ transition. Consistent with this conclusion, and a contribution from the overlapping MLCT component, there is a solvent dependence for this band in *cis,cis*-$[(bpy)_2(Cl)Ru^{III}ORu^{III}(Cl)bpy)_2]^{2+}$ as noted in a previous section.

580 nm: From the assignments in Table 2.7, the band at 580 nm is dominated by a second set of $d\pi_{2n} \rightarrow d\pi_1*$ ($d\pi \rightarrow d\pi*$) and MLCT transitions, one of which, $d\pi_1* \rightarrow \pi_2*(bpy_1)$, occurs at the same energy. The other two arise from the MLCT transitions $d\pi_1* \rightarrow \pi_1*(bpy_1)$ and $d\pi_1* \rightarrow \pi_1*(bpy_2)$. There is a lesser contribution from a $\pi_2(bpy_2) \rightarrow d\pi_2*$ Ligand-to-Metal Charge Transfer (LMCT) transition. The combined $d\pi \rightarrow d\pi*$, charge transfer origin for these transitions is consistent with the observed pattern of resonance enhancements for ν_{sym}(Ru-O-Ru) and ν(bpy).

The appearance of overlapping MLCT and LMCT bands and their underlying transitions is a novel feature arising from the μ-oxo bridge and the impact on the dπ orbitals of strong Ru-O-Ru electronic coupling. Electrochemical measurements show that the dimers are reduced with $E_{1/2}$ = 0.42 V vs SCE for the one-electron reduction of *cis,cis*-$[(bpy)_2(H_2O)Ru^{III}ORu^{III}(OH_2)bpy)_2]^{4+}$ to *cis,cis*-$[(bpy)_2(H_2O)Ru^{III}ORu^{II}(OH_2)bpy)_2]^{3+}$. The

relative low potential for reduction is consistent with the appearance of LMCT bands at relatively low energies in the visible.

480 nm: From Table 2.7, the intensity of this band is dominated by overlapping $\pi(bpy) \rightarrow d\pi*$ LMCT transitions, $\pi_1(bpy_1) \rightarrow d\pi_2*$, $\pi_2(bpy_1) \rightarrow d\pi_2*$. This assignment is consistent with the observed resonance enhancement of medium frequency ν(bpy) modes.

410 and 375 nm: Based on the assignments in Table 2.7, the bands at 410 nm, at 400 nm in $[(bpy)_2(Cl)Ru^{III}ORu^{III}(Cl)bpy)_2]^{2+}$, and 375 nm can similarly be assigned to a series of overlapping $d\pi \rightarrow \pi^*(bpy)$ MLCT bands.

Density Functional Theory – Optimized Geometries

Previous reports by Baik *et al.* concluded that the ground state for the blue dimer is a weakly antiferromagnetically coupled AF singlet, based on DFT calculations.[10,12] This conclusion was based on a comparison between calculated and experimental redox potentials. Notably, values calculated based on an AF singlet state were in better agreement with experimental values than values calculated based on a triplet state even though the DFT calculations predict a ground state triplet. In the Complete Active Space Multiconfiguration SCF (MC-SCF) calculations of Martin, et.al., a singlet ground state was calculated ~1000 cm^{-1} below the triplet.[11] The dπ orbitals were used as the active space, with 10 electrons distributed within the orbital set.

In the Baik calculations, a polarizable continuum model (PCM) was used to model the solvent (water) in the calculation of solvation energies without explicitly considering specific solvent interactions. For *cis,cis*-$[(bpy)_2(H_2O)Ru^{III}ORu^{III}(OH_2)bpy)_2]^{4+}$ and, its oxidized forms, strong hydrogen-bonding interactions of the aqua and hydroxo ligands with

protic solvents (such as water) are expected. A solvent model neglecting specific solvent interactions is probably inadequate.

Table 2.9 lists key geometric features calculated by using different DFT models and compares the results with the actual features from the x-ray structure. (See Appx. A for details.) Both weak coupling models significantly overestimate the Ru-O bridge distance and Ru-O-Ru angle as expected for weak electronic coupling. As shown in the table, features calculated by assuming strong coupling are in better agreement with the XRD results.[2]

Table 2.9**.** Comparison between experimental and calculated geometries for *cis,cis*-$[(bpy)_2(H_2O)Ru^{III}ORu^{III}(H_2O)(bpy)_2]^{4+}$.

Metric Feature →	Ru-μ-O, Å	<(RuORu), °	d(Ru-OH_2), Å
Martin *et al.*[11]	1.950	173.5	2.235
Baik *et al.*[10,12]	1.942	172.5	2.255
Bartolotti *et al.*[15]	1.874	151.6	2.164
This work	1.905	162.3	2.112
X-ray[2]	1.869	165.4	2.137

The orbital energy diagram in Figure 2.9, derived from the current DFT calculations, is qualitatively consistent with changes that occur upon oxidation or reduction and with the electronic absorption spectrum of *cis,cis*-$[(bpy)_2(H_2O)Ru^{III}ORu^{III}(OH_2)(bpy)_2]^{4+}$. Reduction occurs at antibonding level $d\pi_2^*$ resulting in loss of the Ru-O-Ru bridge, $[(bpy)_2(H_2O)Ru^{III}ORu^{III}(OH_2)(bpy)_2]^{4+} + H_2O \xrightarrow{+2e^-/2H^+} 2\ [Ru^{II}bpy)_2(H_2O)_2]^{2+}$.[8] Oxidation and proton loss give asymmetrical *cis,cis*-$[(bpy)_2(HO)Ru^{IV}ORu^{III}(OH_2)(bpy)_2]^{4+}$ in which the Ru-μ-O bond lengths decrease to 1.823 and 1.847 Å consistent with loss of an electron from antibonding $d\pi_1^*$.

The average Ru-μ-O distance is 1.882 Å in the series $[(bpy)_2(L)Ru^{III}ORu^{III}(L)(bpy)_2]^{n+}$ (L is H_2O, NH_3 or NO_2^-; n = 2 or 4),[2,13,14] 1.835 Å in [(phen)(py-ph)(Cl)$Ru^{III}ORu^{IV}$(py-ph)(phen)]$^+$ (phen is 1,10-phenanthroline; py-ph is 2-(2-pyridyl)phenyl),[66] and 1.836 Å in $[(bpy)_2(Cl)Ru^{III}ORu^{IV}(Cl)(bpy)_2]^{3+}$. In $[(Cl)_5Ru^{IV}ORu^{IV}(Cl)_5]^{4-}$,[67] $[(CH_3CN)_2(Cl)_3Ru^{IV}ORu^{IV}(Cl)_3(CH_3CN)_2]$,[68] [(OEP)(Cl)$Ru^{IV}ORu^{IV}$(Cl)(OEP)] (OEP is octaethylporphyrinato),[69] and [(PPP)(Cl)$Ru^{IV}ORu^{IV}$ (Cl)(PPP)] (PPP is 5,10,15,20-tetrakis(pentafluorophenyl)porphyrinato),[70] the average Ru-O bridge distance is 1.793 Å.

From these results there is an average decrease of Δ(Ru-μ-O) = -0.092 Å between the III,III and IV,IV oxidation states. Structural data are not available for the higher oxidation state forms of the blue dimer. From earlier gas phase calculations on one rotamer of $[(bpy)_2(O)Ru^{V}ORu^{V}(O)(bpy)_2]^{4+}$, Ru-μ-O = 1.856 Å, < Ru-O-Ru = 177.6°, and d(Ru=O) = 1.723 Å for the terminal oxo groups.[15]

Resonance Raman Energies and Structural Trends. Characteristic symmetric and asymmetric stretches appear for the Ru-O-Ru core for $Ru^{III}ORu^{III}$ appearing near 400 cm^{-1} and 800 cm^{-1}. In a series of $Fe^{III}OFe^{III}$ dimers a correlation has been found between the Fe-O-Fe bond angle and $\bar{\nu}_{sym}(Fe^{III}OFe^{III})$ band energies.[71] In this series, $\bar{\nu}_{sym}(Fe^{III}OFe^{III})$ decreases as the Fe-O-Fe angle increases with $\bar{\nu}_{sym}(Fe^{III}OFe^{III})$ varying from 550 cm^{-1} at 120° to 380 cm^{-1} at 180°. Based on data from the same series, $\bar{\nu}_{asym}(Fe^{III}OFe^{III})$ increases from 750 cm^{-1} at 120° to 850 cm^{-1} at 180°. Table 2.10 summarizes structural, magnetic, and spectroscopic data for a series of μ-oxo Ru complexes.

Table 2.10. Structural, magnetic, and spectrocoscopic data for Ru-O-Ru complexes.

No.	Complex	Angle (°) RuORu	Mag[a]	Ru-O (Å)[b]	$\bar{\nu}_{sym}$ (Ru^{III}-O-Ru^{III})	$\bar{\nu}_{asym}$ (Ru^{III}-O-Ru^{III})	$\bar{\nu}_{max}$ [c] (cm^{-1})	ε [c] ($M^{-1}cm^{-1}$)
1	$[(tpy)(C_2O_4)Ru\text{-}O\text{-}Ru(C_2O_4)(tpy)]$[72]	148.5	D	1.843	467	780	15700	10,500
2	$[(tpm)Ru]_2O(O_2P(O)(OH)]$[73]	124.6	D	1.870			17400	16,200
3	$[(bpy)_2(NO_2)Ru\text{-}O\text{-}Ru(NO_2)(bpy)_2]^{2+}$ [7]	157.2	P	1.883			15800	25,700
4	$[(tmtcan)$[d]$(acac)$[e]$Ru\text{-}O\text{-}Ru(acac)(tmtcan)]^{2+}$ [74]	180	P	1.913	333		16800	12400
5	$[[(py)_6Ru]_2(O)(CH_3CO_2)_2]^{2+}$ [75]	122.2		1.857	597		17000	10,000
6	$[[(tmtcan)_2Ru]_2(O)(CH_3CO_2)_2]^{2+}$ [76]	119.7	D	1.884			18400	6100
7	$[[(1\text{-}MeIm)$[f]$_3Ru]_2(O)(CH_3CO_2)_2]^{2+}$ [77]	122.3					20000	3600
8	$[(bpy)_2(NH_3)Ru\text{-}O\text{-}Ru(OH)(bpy)_2]^{3+}$ [14]	153.8		1.878	384	766		
9	$[(bpy)_2(H_2O)Ru\text{-}O\text{-}Ru(H_2O)(bpy)_2]^{4+}$ [2]	165.4	P	1.869	382	810	15700	25,000
10	$[(bpy)_2(NH_3)Ru\text{-}O\text{-}Ru(H_2O)(bpy)_2]^{4+}$ [14]	155.9		1.890	378	765		
11	$[(bpy)_2(NH_3)Ru\text{-}O\text{-}Ru(NH_3)(bpy)_2]^{4+}$ [8,14]	158.2	P	1.894	384	767	15800	37,300

a. Room temperature magnetism: paramagnetic (P) or diamagnetic (D).
b. Ru-μ-oxo bond length.
c. ν_{max} in cm^{-1} and molar extinction coefficient in $M^{-1}cm^{-1}$ for the intense absorption band in the visible.
d. tmtcan = 1,4,7-trimethyl-1,4,7-triazacyclononane
e. acac = acetylacetonate
f. 1-MeIm = 1-methylimidazole

As shown in Figure 2.12, structure-band energy correlations found in the $Fe^{III}OFe^{III}$ series also exists for the $Ru^{III}ORu^{III}$ dimers in Table 2.10. In this series, $\bar{\nu}_{sym}(Ru^{III}ORu^{III})$ varies from 597 cm^{-1} at 122° to 333 cm^{-1} at 180° while $\bar{\nu}_{asym}(Ru^{III}ORu^{III})$ varies from 780 cm^{-1} at 148° to 810 cm^{-1} at 165°. An unambiguous linear trend is seen when plotting $\bar{\nu}_{sym}$ vs. <Ru-O-Ru (Figure 2.12a).

Qualitatively, the magnitude of <MOM and the bending away from linearity and 180° represents a balance between electron stabilization and ligand-based electron-electron repulsion. The bending is a Jahn-Teller distortion which results in electronic stabilization

from the lifting of degeneracy in the doubly occupied $d\pi_1^*$, $d\pi_2^*$ levels, Figure 2.9. As the M-O-M angle becomes more acute, ligand-ligand repulsion increases. The final structures are a compromise between the two.

The energy separation between ground state singlet, $(d\pi_1^*)^2$, and excited triplet $(d\pi_1^*)^1(\pi_2^*)^1$ states depends on the exchange energy and the energy difference between $d\pi_1^*$ and $d\pi_2^*$. The latter is highly sensitive to <Ru-O-Ru as can be seen in the data in Table 2.10. Although the data are limited, a cut off between diamagnetic and paramagnetic ground states appears to occur at ~150^o. Below this angle the energy separation between $d\pi_1^*$ and $d\pi_2^*$ is increased and the ground state is diamagnetic. Above this angle the energy separation is decreased and the complexes are paramagnetic. The change from diamagnetic to paramagnetic in these molecules is a consequence of a smaller energy separation between singlet and triplet electronic states relative to the electron pairing energy of $(d\pi_1^*)^2$, behavior expected by Hund's rule and closely spaced orbitals. Arguably, a transition is illustrated in Figure 2.12b, where two clusters of data are observed in plotting the energy of the low energy visible absorption band vs. <RuORu.

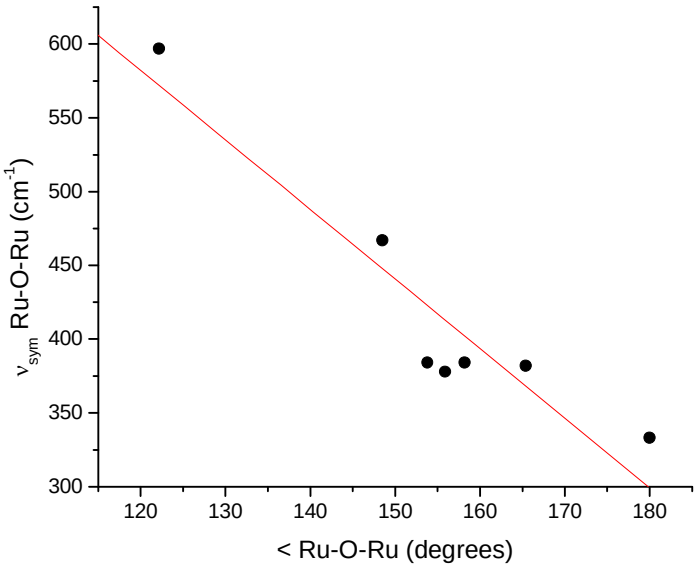

Figure 2.12a. Plot of ν_{sym}(Ru-O-Ru) vs. < Ru-O-Ru for complexes in Table 2.10.

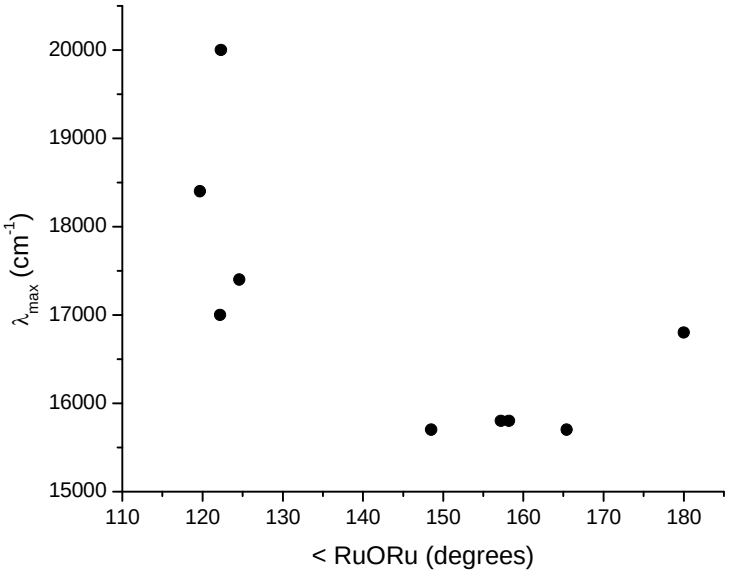

Figure 2.12b. As in Figure 2.12a variation in the energy of the intense, low energy visible absorption band with <RuORu.

X-ray Photoelectron Spectroscopy. $Ru(3d_{5/2})$ XPS binding energies have been reported for blue dimer analogs, $[(bpy)_2ClRu^{III}ORu^{III}Cl(bpy)_2](PF_6)_2$, $[(bpy)_2(O_2N)Ru^{III}ORu^{III}(NO_2)(bpy)_2](ClO_4)_2$, and mixed valence $[(bpy)_2ClRuORuCl(bpy)_2](PF_6)_3$. Comparisons with binding energies for related monomers, $Ru^{II}(bpy)_2Cl_2$ and $[Ru^{III}(bpy)_2Cl_2]Cl$ are revealing. Both $Ru^{III}ORu^{III}$ dimers have $Ru(3d_{5/2})$ binding energies of 280.5 eV, closer to the value expected for Ru(II) (279.9 eV for $Ru(bpy)_2Cl_2$) than Ru(III) (281.9 eV for $[Ru(bpy)_2Cl_2]Cl$. In the XPS spectrum of the mixed valence salt there is a single $Ru(3d_{5/2})$ binding energy of 282.3 eV,[20] consistent with the delocalized description $[ClRu^{III.5}ORu^{III.5}Cl]^{3+}$ found for the $[Ce(NO_3)_6]^{3-}$ salt.

Electrochemistry. Based on an analysis by Taube and Richardson, the comproportionation constant among three adjacent oxidation states for a mixed valence system- K_C, Scheme 2.2 - provides a measure of stabilization of the mixed valence form. It is determined by the difference in potentials between adjacent $1e^-$ couples, E_1 and E_2, with $\log(K_C) = 16.9(E_2 - E_1) = 16.9\Delta E$ at 25 ^oC.[78]

Scheme 2.2. Comproportionation in a mixed valence system.

$$[II\text{-}II] + [III\text{-}III] = 2\,[II\text{-}III]$$

$$[III\text{-}III] + [IV\text{-}IV] = 2\,[III\text{-}IV]$$

Table 2.11. Electrochemical data for adjacent $1e^-$ redox couples for Ru-O-Ru bridged complexes and calculated comproportionation constants - K_C, Scheme 2.2 - shown below the reduction potentials; *i* is irreversible.

	Reduction Potential (V vs. NHE)			
Compound	$E°_1$ [IV-IV]/ [III-IV]	$E°_2$ [III-IV]/ [III-III]	$E°_3$ [III-III]/ [II-III]	$E°_4$ [II-III]/ [II-II]
$[(HCO_2)(NH_3)_4Ru\text{-}O\text{-}Ru(NH_3)_4(O_2CH)]^{3+}$ [79,a]	1.17	0.00	~0.40 *i*	-
	6.0×10^{19}			
$[(Cl)(NH_3)_4Ru\text{-}O\text{-}Ru(NH_3)_4(Cl)]^{3+}$ [79,a]	1.03	0.18	~0.18 *i*	-
	2.3×10^{14}			
$[(NH_3)_5Ru\text{-}O\text{-}Ru(NH_3)_5]^{3+}$ [79,b]	1.91	0.56	-1.74	-
	6.6×10^{22}			
$[(tpa)ClRu\text{-}O\text{-}RuCl(tpa)]^{2+}$ [80,c]	1.99	0.75	-	-
	9.2×10^{20}			
$[(bpy)_2ClRu\text{-}O\text{-}RuCl(bpy)_2]^{2+}$ [7,c]	2.15	0.92	-0.08	-0.76 *i*
	6.2×10^{20}		3.1×10^{11}	
$[(bpy)_2(O_2N)Ru\text{-}O\text{-}Ru(NO_2)(bpy)_2]^{2+}$ [7,c]	~2.44 *i*	1.18	0.09	~ -0.51 *i*
	2.0×10^{21}		1.4×10^{10}	
$[(bpy)_2(py)Ru\text{-}O\text{-}Ru(NCCH_3)(bpy)_2]^{4+}$ [81,d]	-	1.51	0.42	-0.45 *i*
			5.1×10^{14}	
$[(bpy)_2(py)Ru\text{-}O\text{-}Ru(OH_2)(bpy)_2]^{4+}$ [81,d]	1.60	1.18	-	-
	1.3×10^{7}			
$[(bpy)_2(py)Ru\text{-}O\text{-}Ru(py)(bpy)_2]^{4+}$ [81,d]	-	1.50	0.45	-0.47 *i*
			3.6×10^{15}	
$[(bpy)_2(H_2O)Ru\text{-}O\text{-}Ru(OH_2)(bpy)_2]^{4+}$ [3,e]	>1.45	1.04	0.30 *i*	-
	$> 10^{7}$			
$[(bpy)_2(HO)Ru\text{-}O\text{-}Ru(OH)(bpy)_2]^{2+}$ [82,f]	0.67	0.46	-	-
	3.5×10^{3}			

a) 0.1 M LiCl, aqueous, various pHs; b) 0.1 M $LiClO_4$, acetonitrile; c) 0.1 M NBu_4PF_6, acetonitrile; d) 0.1 M NEt_4ClO_4, acetonitrile; e) 0.1 M CF_3SO_3H; f) 1.0 M NaOH

Although K_C is a measure of the degree of stabilization of the mixed valence forms of these couples, it includes the effects of electrostatic interactions, solvation effects, and redox asymmetry as well as electronic delocalization.[83] In the absence of any interactions, $K_C = 4$ for a complex with equivalent redox sites with large values observed for complexes with strong electronic coupling.[47-49]

Table 2.11 lists E and ΔE values for adjacent μ-oxo bridged IV-IV/IV-III and IV-III/III-III couples and for III-III/III-III-II and III-II/II-II couples where the data are available. The substantial values of K_C for the equilibrium, IV-IV + III-III = 2 IV-III, of up to $6.6x10^{22}$ are an impressive demonstration of highly stabilized mixed valence forms of the complexes. They are a far cry from $K_C = 4$ for non-interacting sites and inconsistent with weak electronic coupling.

Measurements on the equilibrium, III-III + II-II = 2 III-II, are complicated by instability of the reduced complexes toward loss of the μ-oxo bridge due to reduction at antibonding dπ* orbitals, Figure 2.9. This results in irreversible reduction. Nonetheless, from the limited data in Table 2.11, K_C values of up to 3.6×10^{15} show the importance of electronic coupling for this equilibrium as well.

As discussed elsewhere, additional electrochemical and pK_a comparisons reveal the profound influence of cross-bridge electronic coupling in the blue dimer and related complexes.[6]

Water Exchange Rates

The impact of electronic coupling appears in substitution rates.[9] The rate constant for water exchange in $[(bpy)_2(H_2O)Ru^{III}ORu^{III}(OH_2)(bpy)_2]^{4+}$ 23 °C is $k = 7 \times 10^{-3}$ s^{-1}. This is comparable to water exchange in other Ru(II) aqua complexes with $k = \sim 2 \times 10^{-2}$ s^{-1} for $Ru(OH_2)_6^{2+}$ with substitution at Ru(III) slower with $k \sim 4 \times 10^{-6}$ s^{-1} for $Ru(OH_2)_6^{3+}$.

Conclusions

In contrast to conclusions reached earlier based on DFT and CASSCF calculations,[10,11] the accumulated experimental evidence proves that strong, cross-bridge electronic coupling plays a major role in $[(bpy)_2(H_2O)Ru^{III}ORu^{III}(OH_2)(bpy)_2]^{4+}$:

- Structural comparisons show that multiple Ru-O bonding exists in the μ-oxo bridge. Ru-OH_2 bond distances are more characteristic of Ru(II) than Ru(III).
- Comproportionation constants for the equilibria, IV-IV + III-III = 2 IV-III, with $K_C > 10^{22}$, and III-III + II-II = 2 III-II, with $K_C > 10^{15}$, show that there is strong coupling between sites.
- Electrochemical reduction results in facile cleavage of the μ-oxo bridge consistent with reduction occurring at delocalized, antibonding dπ* orbitals of the μ-oxo bridge.
- Magnetic measurements are consistent with a delocalized diamagnetic singlet ground state with a low-lying, delocalized triplet explaining the temperature dependent paramagnetism.
- Electrochemical, pK_a, and water exchange rate comparisons all point to Ru sites with electron content more closely resembling Ru(II) than Ru(III). This conclusion is reinforced by XPS binding energy comparisons.
- The electronic absorption spectrum can be assigned quantitatively by DFT by assuming a delocalized model and singlet ground state but only by including specific H-bonding interactions with surrounding solvent water molecules. The visible spectrum is dominated by an intense, $d\pi_n \rightarrow d\pi^*$ Ru-O-Ru transition overlapped with a $d\pi \rightarrow \pi^*$(bpy) MLCT transition.

- A $Ru^{III} \rightarrow$ bpy MLCT transition appears in the visible while MLCT transitions in related Ru(III) complexes appear in the UV.
- The delocalized electronic structural model is consistent with resonance Raman excitation profiles and resonant enhancement of the ν_{sym} and ν_{asym}(Ru-O-Ru) modes upon excitation into Ru-O-Ru centered transitions, for example.
- Interconfiguration (IC) bands appear at significantly higher energies compared to related Ru(III) monomers, due to electronic delocalization and destabilization of $d\pi$ acceptor orbitals as $d\pi_2^*$.
- In structures of salts nominally containing the mixed valence $[Ru^{IV}ORu^{III}]^{n+}$ unit, *cis,cis*-$[(bpy)_2(SO_4)RuORu(SO_4)(bpy)_2]\bullet H_2O(SO_4)_{0.5}$ and $[(bpy)_2(Cl)RuORu(Cl)(bpy)_2](Ce(NO_3)_6)$, the Ru sites are equivalent consistent with electronic delocalization and the description $[Ru^{III.5}ORu^{III.5}]^{n+}$.

Additional observations of note have appeared in the analysis. The observation of counter ion dependent symmetrization in $[Ru^{IV}ORu^{III}]^{n+}$ salts is a notable result with asymmetrical placement of ClO_4^- in $[(bpy)_2(Cl)RuORu(Cl)(bpy)_2](ClO_4)_3$ an example of electrostatically induced localization.

Magnetic properties are sensitive to <Ru-O-Ru. Bending away from 180^o is a Jahn-Teller effect lifting the degeneracy of the triplet state $(d\pi_1^*)^1(d\pi_2^*)^1$ by stabilizing the $(d\pi_1^*)^2$ ground state. The equilibrium angle is a compromise between the associated stabilization energy, which increases with decreasing <Ru-O-Ru, and ligand-ligand repulsion.

The impact on electronic and chemical properties of bridge-based electronic coupling is profound playing a crucial role in the oxidative activation and subsequent reactivity of the blue dimer water oxidation catalyst as will be discussed in a following publication.

Acknowledgments

Funding by the Chemical Sciences, Geosciences and Biosciences Division of the Office of Basic Energy Sciences, U.S. Department of Energy Grant DE-FG02-06ER15788, and UNC EFRC: Solar Fuels and Next Generation Photovoltaics, an Energy Frontier Research Center funded by the U.S. Department of Energy, Office of Science, Office of Basic Energy Sciences under Award Number DE-SC0001011, is gratefully acknowledged. The work at LANL was supported by the U.S. Department of Energy through the Laboratory Directed Research & Development (LDRD) program.

Appendix A: Details of DFT calculations (excited states, oscillator strengths, Cartesian coordinates), comparisons between calculated and experimental absorption spectra, crystallographic data, experimental absorption spectra of $[(bpy)_2ClRuORuCl(bpy)_2](PF_6)_2$ in various solvents, a plot showing magnetic field dependence of magnetization for the blue dimer.

REFERENCES

(1) Gersten, S. W.; Samuels, G. J.; Meyer, T. J. *Journal of the American Chemical Society* 1982, *104*, 4029.

(2) Gilbert, J. A.; Eggleston, D. S.; Murphy, W. R.; Geselowitz, D. A.; Gersten, S.W.; Hodgson, D. J.; Meyer, T. J. *Journal of the American Chemical Society* 1985, *107*, 3855.

(3) Binstead, R. A.; Chronister, C. W.; Ni, J. F.; Hartshorn, C. M.; Meyer, T. J. *Journal of the American Chemical Society* 2000, *122*, 8464.

(4) Yamada, H.; Siems, W. F.; Koike, T.; Hurst, J. K. *Journal of the American Chemical Society* 2004, *126*, 9786.

(5) Hurst, J. K.; Cape, J. L.; Clark, A. E.; Das, S.; Qin, C. Y. *Inorganic Chemistry* 2008, *47*, 1753.

(6) Liu, F.; Concepcion, J. J.; Jurss, J. W.; Cardolaccia, T.; Templeton, J. L.; Meyer, T. J. *Inorganic Chemistry* 2008, *47*, 1727.

(7) Weaver, T. R.; Meyer, T. J.; Adeyemi, S. A.; Brown, G. M.; Eckberg, R. P.; Hatfield, W. E.; Johnson, E. C.; Murray, R. W.; Untereker, D. *Journal of the American Chemical Society* 1975, *97*, 3039.

(8) Schoonover, J. R.; Ni, J. F.; Roecker, L.; Whiter, P. S.; Meyer, T. J. *Inorganic Chemistry* 1996, *35*, 5885.

(9) Yamada, H.; Koike, T.; Hurst, J. K. *Journal of the American Chemical Society* 2001, *123*, 12775.

(10) Yang, X. F.; Baik, M. H. *Journal of the American Chemical Society* 2004, *126*, 13222.

(11) Batista, E. R.; Martin, R. L. *Journal of the American Chemical Society* 2007, *129*, 7224.

(12) Yang, X.; Baik, M. H. *Journal of the American Chemical Society* 2006, *128*, 7476.

(13) Phelps, D. W.; Kahn, E. M.; Hodgson, D. J. *Inorganic Chemistry* 1975, *14*, 2486.

(14) Ishitani, O.; White, P. S.; Meyer, T. J. *Inorganic Chemistry* 1996, *35*, 2167.

(15) Bartolotti, L. J.; Pedersen, L. G.; Meyer, T. J. *International Journal of Quantum Chemistry* 2001, *83*, 143.

(16) Myers, A. B. *Accounts of Chemical Research* 1997, *30*, 519.

(17) Frisch, M. J.; Trucks, G. W.; Schlegel, H. B.; Scuseria, G. E.; Robb, M. A.; Cheeseman, J. R.; Montgomery, J., J. A.; Vreven, T.; Kudin, K. N.; Burant, J. C.; Millam, J. M.; Iyengar, S. S.; Tomasi, J.; Barone, V.; Mennucci, B.; Cossi, M.; Scalmani, G.; Rega, N.; Petersson, G. A.; Nakatsuji, H.; Hada, M.; Ehara, M.; Toyota, K.; Fukuda, R.; Hasegawa, J.; Ishida, M.; Nakajima, T.; Honda, Y.; Kitao, O.; Nakai, H.; Klene, M.; Li, X.; Knox, J. E.; Hratchian, H. P.; Cross, J. B.; Bakken, V.; Adamo, C.; Jaramillo, J.; Gomperts, R.; Stratmann, R. E.; Yazyev, O.; Austin, A. J.; Cammi, R.; Pomelli, C.; Ochterski, J. W.; Ayala, P. Y.; Morokuma, K.; Voth, G. A.; Salvador, P.; Dannenberg, J. J.; Zakrzewski, V. G.; Dapprich, S.; Daniels, A. D.; Strain, M. C.; Farkas, O.; Malick, D. K.; Rabuck, A. D.; Raghavachari, K.; Foresman, J. B.; Ortiz, J. V.; Cui, Q.; Baboul, A. G.; Clifford, S.; Cioslowski, J.; Stefanov, B. B.; Liu, G.; Liashenko, A.; Piskorz, P.; Komaromi, I.; Martin, R. L.; Fox, D. J.; Keith, T.; Al-Laham, M. A.; Peng, C. Y.; Nanayakkara, A.; Challacombe, M.; Gill, P. M. W.; Johnson, B.; Chen, W.; Wong, M. W.; Gonzalez, C.; Pople, J. A.; Gaussian, Inc.: Wallingford, CT, 2004.

(18) Dobson, J. C.; Sullivan, B. P.; Doppelt, P.; Meyer, T. J. *Inorganic Chemistry* 1988, *27*, 3863.

(19) Demadis, K. D.; Hartshorn, C. M.; Meyer, T. J. *Chemical Reviews* 2001, *101*, 2655.

(20) Heller, E. J. *Accounts of Chemical Research* 1981, *14*, 368.

(21) Myers, A. B.; Mathies, R. A. *Biological Applications of Raman Spectrscopy*; Wiley and Sons: New York, 1988.

(22) Myers, A. B.; Mathies, R. A.; Tannor, D. J.; Heller, E. J. *Journal of Chemical Physics* 1982, *77*, 3857.

(23) Li, B. L.; Myers, A. B. *Journal of Physical Chemistry* 1990, *94*, 4051.

(24) Thompson, D. G.; Schoonover, J. R.; Timpson, C. J.; Meyer, T. J. *Journal of Physical Chemistry A* 2003, *107*, 10250.

(25) Mallick, P. K.; Danzer, G. D.; Strommen, D. P.; Kincaid, J. R. *Journal of Physical Chemistry* 1988, *92*, 5628.

(26) Strommen, D. P.; Mallick, P. K.; Danzer, G. D.; Lumpkin, R. S.; Kincaid, J. R. *Journal of Physical Chemistry* 1990, *94*, 1357.

(27) Omberg, K. M.; Schoonover, J. R.; Treadway, J. A.; Leasure, R. M.; Dyer, R. B.; Meyer, T. J. *Journal of the American Chemical Society* 1997, *119*, 7013.

(28) Dunitz, J. D.; Orgel, L. E. *Journal of Physics and Chemistry of Solids* 1957, *3*, 318.

(29) Tatsumi, K.; Hoffmann, R. *Journal of the American Chemical Society* 1981, *103*, 3328.

(30) Fodor, L.; Lendvay, G.; Horvath, A. *Journal of Physical Chemistry A* 2007, *111*, 12891.

(31) Lu, Z. A.; Zhang, Q. L.; Xu, Y. S.; Wang, M. L.; Liu, J. H. *Journal of Theoretical & Computational Chemistry* 2009, *8*, 631.

(32) Charlot, M. F.; Aukauloo, A. *Journal of Physical Chemistry A* 2007, *111*, 11661.

(33) Baik, M. H.; Friesner, R. A. *Journal of Physical Chemistry A* 2002, *106*, 7407.

(34) Bernhard, P.; Burgi, H. B.; Hauser, J.; Lehmann, H.; Ludi, A. *Inorganic Chemistry* 1982, *21*, 3936.

(35) Sauaia, M. G.; Tfouni, E.; Santos, R. H. D.; Gambardella, M. T. D.; Del Lama, M.; Guimaraes, L. F.; da Silva, R. S. *Inorganic Chemistry Communications* 2003, *6*, 864.

(36) Qvortrup, K.; McKenzie, C. J.; Bond, A. D. *Acta Crystallographica Section E-Structure Reports Online* 2007, *63*, M1400.

(37) Jude, H.; White, P. S.; Dattelbaum, D. M.; Rocha, R. C. *Acta Crystallographica Section E-Structure Reports Online* 2008, *64*, M1388.

(38) Concepcion, J. J.; Jurss, J. W.; Norris, M. R.; Chen, Z. F.; Templeton, J. L.; Meyer, T. J. *Inorganic Chemistry* 2010, *49*, 1277.

(39) Durham, B.; Wilson, S. R.; Hodgson, D. J.; Meyer, T. J. *Journal of the American Chemical Society* 1980, *102*, 600.

(40) Hush, N. S. In *Progress in Inorganic Chemistry*; John Wiley & Sons, Inc.: 1967; Vol. 8, p 391.

(41) Hush, N. S. *Electrochimica Acta* 1968, *13*, 1005.

(42) Concepcion, J. J.; Dattelbaum, D. M.; Meyer, T. J.; Rocha, R. C. *Philosophical Transactions of the Royal Society a-Mathematical Physical and Engineering Sciences* 2008, *366*, 163.

(43) D'Alessandro, D. M.; Keene, F. R. *Chemical Society Reviews* 2006, *35*, 424.

(44) D'Alessandro, D. M.; Keene, F. R. *Chemical Reviews* 2006, *106*, 2270.

(45) Eggleston, D. S.; Goldsby, K. A.; Hodgson, D. J.; Meyer, T. J. *Inorganic Chemistry* 1985, *24*, 4573.

(46) Neyhart, G. A.; Timpson, C. J.; Bates, W. D.; Meyer, T. J. *Journal of the American Chemical Society* 1996, *118*, 3730.

(47) Neyhart, G. A.; Hupp, J. T.; Curtis, J. C.; Timpson, C. J.; Meyer, T. J. *Journal of the American Chemical Society* 1996, *118*, 3724.

(48) Barriere, F.; Camire, N.; Geiger, W. E.; Mueller-Westerhoff, U. T.; Sanders, R. *Journal of the American Chemical Society* 2002, *124*, 7262.

(49) D'Alessandro, D. M.; Keene, F. R. *Dalton Transactions* 2004, 3950.

(50) Chen, P. Y.; Meyer, T. J. *Chemical Reviews* 1998, *98*, 1439.

(51) Lei, Y. B.; Hurst, J. K. *Inorganic Chemistry* 1994, *33*, 4460.

(52) Kahn, O. *Molecular Magnetism*; VCH, 1993.

(53) Bleaney, B.; Bowers, K. D. *Proc. Roy. Soc. (London) Ser. A* 1952, *214*, 451.

(54) Anderson, P. A.; Deacon, G. B.; Haarmann, K. H.; Keene, F. R.; Meyer, T. J.; Reitsma, D. A.; Skelton, B. W.; Strouse, G. F.; Thomas, N. C.; Treadway, J. A.; White, A. H. *Inorganic Chemistry* 1995, *34*, 6145.

(55) Zhang, G.; Zong, R.; Tseng, H. W.; Thummel, R. P. *Inorganic Chemistry* 2008, *47*, 990.

(56) Sens, C.; Rodriguez, M.; Romero, I.; Llobet, A.; Parella, T.; Benet-Buchholz, J. *Inorganic Chemistry* 2003, *42*, 8385.

(57) Ross, H. B.; Boldaji, M.; Rillema, D. P.; Blanton, C. B.; White, R. P. *Inorganic Chemistry* 1989, *28*, 1013.

(58) Demadis, K. D.; Dattelbaum, D. M.; Kober, E. M.; Concepcion, J. J.; Paul, J. J.; Meyer, T. J.; White, P. S. *Inorganica Chimica Acta* 2007, *360*, 1143.

(59) Hudson, A.; Kennedy, M. J. *Journal of the Chemical Society a -Inorganic Physical Theoretical* 1969, 1116.

(60) Bhattacharya, S.; Ghosh, P.; Chakravorty, A. *Inorganic Chemistry* 1985, *24*, 3224.

(61) North, A. M.; Pethrick, R. A.; Kryszewski, M.; Nadolski, B. *Acta Physica Polonica A* 1978, *54*, 797.

(62) Nadolski, B.; Uznanski, P.; Kryszewski, M. *Journal of Macromolecular Science-Physics* 1984, *B23*, 221.

(63) Moya, M. L.; Rodriguez, A.; Sanchez, F. *Inorganica Chimica Acta* 1992, *197*, 227.

(64) Dodsworth, E. S.; Lever, A. B. P. *Inorganic Chemistry* 1990, *29*, 499.

(65) Dodsworth, E. S.; Lever, A. B. P. *Coordination Chemistry Reviews* 1990, *97*, 271.

(66) Ryabov, A. D.; Le Lagadec, R.; Estevez, H.; Toscano, R. A.; Hernandez, S.; Alexandrova, L.; Kurova, V. S.; Fischer, A.; Sirlin, C.; Pfeffer, M. *Inorganic Chemistry* 2005, *44*, 1626.

(67) Efimenko, I. A.; Balakaeva, T. A.; Kurbakova, A. P.; Gorbunova, Y. E.; Mikhailov, Y. N. *Koordinatsionnaya Khimiya* 1994, *20*, 294.

(68) Tyrlik, S. K.; Kisielinska, M.; Huffman, J. C. *Transition Metal Chemistry* 1995, *20*, 413.

(69) Masuda, H.; Taga, T.; Osaki, K.; Sugimoto, H.; Mori, M.; Ogoshi, H. *Bulletin of the Chemical Society of Japan* 1982, *55*, 3887.

(70) Zhang, J. L.; Che, C. M. *Chemistry-a European Journal* 2005, *11*, 3899.

(71) Mukherjee, R. N.; Stack, T. D. P.; Holm, R. H. *Journal of the American Chemical Society* 1988, *110*, 1850.

(72) Lebeau, E. L.; Adeyemi, S. A.; Meyer, T. J. *Inorganic Chemistry* 1998, *37*, 6476.

(73) Llobet, A.; Curry, M. E.; Evans, H. T.; Meyer, T. J. *Inorganic Chemistry* 1989, *28*, 3131.

(74) Sudha, C.; Mandal, S. K.; Chakravarty, A. R. *Inorganic Chemistry* 1993, *32*, 3801.

(75) Cipriano, C.; Clark, R. J. H.; Oprescu, D.; Withnall, R. *Journal of the Chemical Society-Dalton Transactions* 1995, 2417.

(76) Neubold, P.; Wieghardt, K.; Nuber, B.; Weiss, J. *Inorganic Chemistry* 1989, *28*, 459.

(77) Schneider, R.; Weyhermuller, T.; Wieghardt, K.; Nuber, B. *Inorganic Chemistry* 1993, *32*, 4925.

(78) Richardson, D. E.; Taube, H. *Coordination Chemistry Reviews* 1984, *60*, 107.

(79) Emerson, J.; Clarke, M. J.; Ying, W. L.; Sanadi, D. R. *Journal of the American Chemical Society* 1993, *115*, 11799.

(80) Koshi, C.; Umakoshi, K.; Sasaki, Y. *Chemistry Letters* 1997, 1155.

(81) Doppelt, P.; Meyer, T. J. *Inorganic Chemistry* 1987, *26*, 2027.

(82) Kutner, W.; Gilbert, J. A.; Tomaszewski, A.; Meyer, T. J.; Murray, R. W. *Journal of Electroanalytical Chemistry* 1986, *205*, 185.

(83) Browne, W. R.; Hage, R.; Vos, J. G. *Coordination Chemistry Reviews* 2006, *250*, 1653.

CHAPTER 3

Mechanism of Water Oxidation by the Blue Dimer, *cis,cis*-$[(bpy)_2(H_2O)RuORu(OH_2)(bpy)_2](ClO_4)_4$

Introduction

Shortly after nature was able to use water as an electron source, oxygen-dependent life forms appeared on Earth.[1] In the light-driven reaction of Photosystem II of the natural photosynthetic apparatus found in green plants, dioxygen is released at the Oxygen Evolving Complex (OEC) according to the reaction, $2H_2O \rightarrow O_2 + 4H^+ + 4e^-$. The reductive equivalents are used in Photosystem I for the reduction of CO_2 to sugars, or in other words, the conversion of solar energy to chemical energy. This overall process is essential for life as we know it, providing oxygen as a metabolic oxidant and maintaining the Earth's atmosphere in its current constitution.[2] The OEC consists of a Mn_3Ca cluster with a fourth Mn attached by di-μ-oxo bridging and a bridging glutamate, at which oxygen is thought to evolve.[3-7] Recent results and mechanistic analysis of water oxidation at the OEC reveal similarities of water oxidation with that of the blue dimer.[8,9] Research in the area of water oxidation[10,11] has increased dramatically as the imminent need to develop renewable and sustainable energy sources as an alternative to fossil fuels is realized, especially with regard to solar energy conversion which is widely considered the only long-term solution.[12] Artificial photosynthesis is anticipated as one of the most promising routes toward clean energy alternatives.[13,14] In this strategy, photochemical water oxidation at an anode is coupled to a cathode reaction for reduction of protons to hydrogen or carbon dioxide to hydrocarbons or alcohols, i.e. $2H_2O + 4h\nu \rightarrow O_2 + 2H_2$; $2H_2O + CO_2 + 8h\nu \rightarrow 2O_2 + CH_4$. Water oxidation is a key half reaction that is present in both. A lack of molecular catalysts has hampered progress in this area.

Water oxidation is a difficult reaction for catalysis. The reaction is thermodynamically uphill by 1.23 V vs. NHE at pH = 0 ($\Delta G° = 4.92$ eV) and mechanistically

demanding, requiring the loss of four protons and four electrons with the concomitant formation of an oxygen-oxygen bond. Water itself is neither a good nucleophile nor a good electrophile and the high molecular complexity of the reaction has previously left mechanistic insight at a loss. The first designed, well-defined molecule known to function as a catalyst for water oxidation is the "blue dimer", *cis,cis*-$[(bpy)_2(H_2O)Ru^{III}ORu^{III}(OH_2)(bpy)_2](ClO_4)_4$.[15,16] No consensus reaction mechanism exists to date for the mechanism of water oxidation by the blue dimer.[8,17] Identifying the underlying reaction mechanism for existing catalysts is fundamental for the rational development of superior catalysts that are robust and efficient. We report herein on the mechanism of water oxidation by the blue dimer and the origin of deleterious anated intermediates that impede its activity long term.

Experimental

Robert A. Binstead provided old data and analysis that were collected previously in the Meyer laboratory. He was also a great asset in utilizing SPECFIT. Feng Liu and Javier J. Concepcion performed the redox and pH titrations of the intermediate at 455 nm, and some of the excess Ce(IV) consumption in 1.0 M acids. I collected and analyzed the remaining data.

Preparation of Complexes: The salts $[(bpy)_2(H_2O)Ru^{III}ORu^{III}(OH_2)(bpy)_2](ClO_4)_4$ and $[(bpy)_2(H_2O)Ru^{III}ORu^{IV}(OH)(bpy)_2](ClO_4)_4$ were synthesized as described earlier.[16]

Materials: High purity water was purified by a Millipure system. Triflic acid (HSO_3CF_3, 99+%, Aldrich) was distilled under vacuum with a small amount of $[(bpy)_2(H_2O)Ru^{III}ORu^{III}(OH_2)(bpy)_2](ClO_4)_4$ and an excess of $(NH_4)_2Ce(NO_3)_6$ added and was stored as a 2.0 M aqueous solution before use. NaOCl was obtained as an aqueous

reagent (10-13%) from Aldrich and its concentration was determined iodometrically by reacting with an excess of iodide in acidic solution. The iodine produced was titrated with a standard sodium thiosulfate solution. $RuCl_3 \bullet 3H_2O$ (Pressure Chemicals), $AgNO_3$, $NaClO_4$, $(NH_3)_2Ce(NO_3)_6$ (99.99+%, Aldrich) (Ce(IV)), $(NH_4)_2Fe(SO_4)_2(H_2O)_6$ ($\geq$ 99%, Aldrich) (Fe(II)), 2,2'-bipyridine (Aldrich), NaOH, $HClO_4$ (99.999%), HCl, H_2SO_4 and HNO_3 (Fisher) were used as received. Ce(IV) and Fe(II) solutions were made daily to ensure proper stoichiometry for mixing experiments by weighing and dissolving in the acid and concentration of choice.

Measurements: pH measurements were conducted by using an Accumet AB15 pH meter. UV-visible spectra were recorded on an Agilent 8453 diode-array spectrophotometer, a Shimadzu UV-visible near-infrared spectrophotometer model UV-3600, or a Hi-Tech SF-61MX stopped-flow/diode array spectrophotometer with 0.001 ms time resolution, each instrument has 2 nm spectral resolution. Photoreduction of the higher oxidation states of the blue dimer by the Xenon light source (Hi-Tech instrument) were avoided by attenuation of the lamp source (10% transmission filter and a 360 nm cut-off filter. The slower reactions at pH 1 also employed further attenuation with neutral density glass filters. The integration time of the diode array detection in stopped-flow experiments was increased proportionally: pH 0 (13 ms), pH 1 (125 ms). A 400 nm cut-off filter was often used in experiments with the other spectrophotometers except when following Ce(IV) consumption at 360 nm. Kinetic studies were limited to 25 °C using a water bath to thermostat the stopped-flow mixing apparatus, or to room temperature, 23 ± 2 °C as indicated in the text.

Kinetic measurements were made by recording UV-visible spectra vs. time and data were processed by use of the program SPECFIT/32 Global Analysis System (SPECTRUM

Software Associates), or by monitoring absorbance changes at a single wavelength following the growth or decay of an intermediate containing the blue dimer in known concentrations. First order or pseudo-first-order rate constants, k_{obs}, were calculated from a least-squares fit of the data to the relation $\ln(A_t - A_\infty) - \ln(A_0 - A_\infty) = -k_{obs}t$, where A_0 and A_∞ are the initial and final absorbances at the monitoring wavelength, respectively. A_t is the absorbance at time t. The second-order rate constants obtained from pseudo-first-order conditions were obtained from slopes of plots of k_{obs} (s^{-1}) vs. dimer concentration at the catalytic steady state. The rate constants for second order, equal concentration kinetics (e.g. disproportionation reactions) were obtained from a least squares fit of the data plotted to the relation $(A_0 - A_\infty)/C_0(A_t - A_\infty) = kt$. In experiments with 2 eq. of Ce(IV) added, absorbance-time changes were fit to the the second-order, unequal concentration expression, $\ln [0.5(C_0/C_t + 1)] = C_0 \times kt$, with C_0 and C_t the initial dimer concentration and dimer concentration at time t, respectively. Zero-order kinetic traces were fit to the expression $C_t - C_0 = kt$, with C_0, C_t and defined previously with plots of $A_t/\varepsilon b$ vs. time (s). The molar extinction coefficient is highly dependent on the nature and concentration of acid being used.

Cyclic voltammograms were obtained with a Bioanalytical Systems, Inc. 100B/W series potentiostat. Voltammetric measurements were made with a glassy carbon working electrode, a platinum wire auxiliary electrode and a saturated Ag/AgCl, 4 M potassium chloride reference electrode. IR measurements were obtained with a Shimadzu IRPrestige-21 Fourier Transform Infrared Spectrophotometer.

Oxygen measurements were conducted using an oxygen electrode (Model MI-730) from Microelectrodes. The electrode was calibrated by standard oxygen in nitrogen (1%, 2%, and 6%) gas mixtures obtained from Alltech. It was interfaced to a pH meter or a Keithley

6517A electrometer for data output. The measurements were made on solutions in a locally designed airtight electrochemical cell that had been purged with argon until the digital readout had stabilized. Water oxidation was initiated by adding acidic Ce(IV) solutions through a septum to the closed cell. An initial and final O_2 evolution measurement was recorded, and the amount of dioxygen produced was calculated based on the known headspace volume and the expected stoichiometry, $2H_2O \rightarrow O_2 + 4e^- + 4H^+$.

I. pH Dependence, Disproportionation, Dominant Forms

Based on earlier structural and pH dependent electrochemical measurements, the various oxidation state forms of *cis,cis*-$[(bpy)_2(H_2O)Ru^{III}ORu^{III}(OH_2)(bpy)_2]^{4+}$, from $Ru^{III}ORu^{III}$ to $Ru^{V}ORu^{V}$, vary in proton composition (containing coordinated H_2O, OH^-, or O^{2-}) depending on oxidation state and pH of the solution. For example, the first two pK_a values for the blue dimer occur at 5.9 and 8.3 (I = 0.1 M; 25 °C) and, depending on the pH, its dominant forms are $[(bpy)_2(H_2O)Ru^{III}ORu^{III}(OH_2)(bpy)_2]^{4+}$, $[(bpy)_2(H_2O)Ru^{III}ORu^{III}(OH)(bpy)_2]^{3+}$, or $[(bpy)_2(HO)Ru^{III}ORu^{III}(OH)(bpy)_2]^{2+}$. Similarly, the first two p*K*a values for $[(bpy)_2(H_2O)Ru^{IV}ORu^{III}(OH_2)(bpy)_2]^{5+}$ are $pK_{a,1} = 0.4$ and $pK_{a,2} = 3.2$.[16] Furthermore, the $[(bpy)_2(H_2O)Ru^{III}ORu^{III}(OH_2)(bpy)_2]^{4+}$ and $[(bpy)_2(HO)Ru^{IV}ORu^{III}(OH_2)(bpy)_2]^{4+}$ perchlorate salts are easily isolated as stable solids, and have been characterized crystallographically.[16,18]

For purposes of simplification, the abbreviations $Ru^{III}ORu^{III}$, $Ru^{IV}ORu^{III}$, $Ru^{IV}ORu^{V}$, $Ru^{V}ORu^{V}$, and so forth, will be used to summarize oxidation states. Proton and coordination sphere compositions will be abbreviated in the manner described by the following example: $[(bpy)_2(H_2O)Ru^{III}ORu^{III}(OH_2)(bpy)_2]^{4+} = [(H_2O)Ru^{III}ORu^{III}(OH_2)]^{4+}$

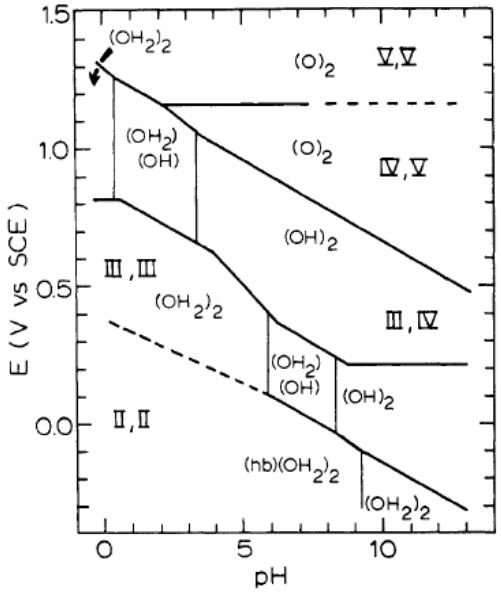

Figure 3.1.[16] $E_{1/2}$-pH diagram for *cis,cis*-$[(bpy)_2(H_2O)Ru^{III}ORu^{III}(OH_2)(bpy)_2]^{4+}$ at 25 °C, I = 0.1 M, vs. SCE (0.241 V vs. NHE). The vertical dotted lines correspond to pK_a values for the lower oxidation state of the couple, e.g., p$K_{a,1}$ = 5.9 and p$K_{a,2}$ = 8.3 for $[(H_2O)Ru^{III}ORu^{III}(OH_2)]^{4+}$. Oxidation state distributions, with III,III an abbreviation for $Ru^{III}ORu^{III}$, for example, and proton compositions of the sixth ligands, O, OH, or OH_2, are indicated in the potential-pH regions in which they dominate. For example III,III $(OH_2)_2$ is an abbreviation for $[(H_2O)Ru^{III}ORu^{III}(OH_2)]^{4+}$.[16]

As shown in the $E_{1/2}$-pH diagram in Figure 3.1, the acid-base properties of the complexes result in complex, pH-dependent redox potential behavior. In summary: (i) There are five thermodynamically stable oxidation states, $Ru^{II}ORu^{II}$, $Ru^{III}ORu^{III}$, $Ru^{IV}ORu^{III}$, $Ru^{IV}ORu^{V}$, and $Ru^{V}ORu^{V}$. (ii) The complex $E^{o\prime}$-pH dependence in Figure 3.1 arises largely from the acid base behavior of coordinated H_2O in $Ru^{III}ORu^{III}$ and $Ru^{IV}ORu^{III}$. (iii) Proton Coupled Electron Transfer (PCET) in which there is gain or loss of both electrons and protons is responsible for the appearance of closely spaced $E^{o\prime}$ values and the buildup of multiple redox equivalents required for multi-electron transfer catalysis.[8] (iv) The oxidation states $Ru^{II}ORu^{III}$ and $Ru^{IV}ORu^{IV}$ are "missing" due to their instability toward disproportionation, e.g., 2 $Ru^{IV}ORu^{IV} \rightarrow Ru^{IV}ORu^{V} + Ru^{IV}ORu^{III}$. This instability arises

from PCET and closely spaced E^{o}' values, electronic stabilization of adjacent oxidation states by electronic effects such as oxo formation, and differences in pH dependence between adjacent couples. The instability of $Ru^{II}ORu^{III}$ is due to strong electronic coupling across the bridge resulting in electrons being added to anti-bonding, bridge-based orbitals.[16] (v) Below pH = 2, $Ru^{V}ORu^{IV}$ is unstable with respect to disproportionation into $Ru^{IV}ORu^{IV}$ and $Ru^{V}ORu^{V}$. There is spectrophotometric evidence for protonation of $Ru^{IV}ORu^{V}$ from the acid-base equilibrium, $[(O)Ru^{V}ORu^{IV}(OH)]^{4+} \rightleftharpoons [(O)Ru^{V}ORu^{IV}(O)]^{3+}$ with pK_a(23 °, I = 1) = ~0.3.[8] (vi) All three higher oxidation states, $Ru^{V}ORu^{V}$, $Ru^{V}ORu^{IV}$, and $Ru^{IV}ORu^{IV}$ are thermodynamically capable of water oxidation with $Ru^{IV}ORu^{IV}$ the strongest oxidant of the three.[16] $Ru^{IV}ORu^{IV}$ is formulated as $[(HO)Ru^{IV}ORu^{IV}(OH)]^{4+}$ based on the results of a density functional theory calculation and electrochemical measurements in highly basic media.[19,20]

Spectrophotometric monitoring was used to follow the course of events that occurs following Ce(IV) addition to acidic solutions containing $Ru^{III}ORu^{III}$ or $Ru^{IV}ORu^{III}$. These spectra are complex with multiple overlapping absorption bands. For example, $[(bpy)_2(H_2O)Ru^{III}ORu^{III}(OH_2)(bpy)_2]^{4+}$ has 6 absorptions in the visible and near IR which have recently been assigned based on a DFT theoretical analysis.[21] Visible spectra are dominated by intense absorptions which characterize the species involved. A structured absorption appears at λ_{max} = 637 nm which arises from overlapping metal-to-ligand charge transfer (MLCT) and Ru-O-Ru bridge-based $d\pi \rightarrow d\pi^*$ transitions. In addition, low energy, low intensity bands appear in the near IR, at 915, 1125, and 1205 for the blue dimer, arising from interconfiguration $d\pi \rightarrow d\pi^*$ transitions.

In order to simplify interpretation of spectral changes in the sections that follow, absorption maxima that dominate the visible and near IR regions of the spectra are listed in Table 3.1. This listing includes the different oxidation states and coordination spheres of the blue dimer and intermediates identified in the remaining text. As can be seen in the data, in some cases there is significant overlap in spectral features between species. This requires application of spectral deconvolution procedures to ascertain the presence of multiple species and their relative importance. There are additional complications due to the co-existence of different acid-bases forms of intermediates in pH regions where both are present. Inspection of the data in Table 3.1 reveals that unique spectral characterization of the various species is possible by spectral monitoring.

Table 3.1: Characteristic visible and near-infrared absorption bands of various oxidation and protonation states of the blue dimer and intermediates that appear in its catalytic cycle, ± 2 nm.

Complex	λ_{max}, nm	ε, $M^{-1}cm^{-1}$	medium
$[(bpy)_2(H_2O)Ru^{III}ORu^{III}(OH_2)(bpy)_2]^{4+}$	637	22,500	pH 1 $HClO_4$
	1133	380	
$[(bpy)_2(H_2O)Ru^{IV}ORu^{III}(OH_2)(bpy)_2]^{5+}$	445	22,500	1.0 M $HClO_4$
	840	230	
	1182	300	
$[(bpy)_2(HO)Ru^{IV}ORu^{III}(OH_2)(bpy)_2]^{4+}$	495	22,000	0.01 M CF_3SO_3H
	832	250	
	1164	280	
$[(bpy)_2(HO)Ru^{IV}ORu^{III}(OH)(bpy)_2]^{3+}$	492	22,000	pH 6 phosphate buffer, 5 ^oC

$[(bpy)_2(HO)Ru^{IV}ORu^{IV}(OH_2)(X)(bpy)_2]^{4+}$	448	-	1.0 M CF_3SO_3H
$[(bpy)_2(HO)Ru^{IV}ORu^{IV}(OH_2)(X)(bpy)_2]^{4+}$	448		1.0 M $HClO_4$
$[(bpy)_2(HO)Ru^{IV}ORu^{IV}(OH)(X)(bpy)_2]^{3+}$	493	-	0.1 M CF_3SO_3H
$[(bpy)_2(O)Ru^{V}ORu^{IV}(OH)(bpy)_2]^{4+}$	478	14,500	1.0 M CF_3SO_3H
	750	600	
$[(bpy)_2(O)Ru^{V}ORu^{IV}(O)(bpy)_2]^{3+}$	488	14,000	0.1 M HNO_3
	710	1620	
$[(bpy)_2(O)Ru^{V}ORu^{IV}(O)(bpy)_2]^{3+}$	490	9,700	pH 6 phosphate buffer, 5 ^{o}C
$[(bpy)_2(O)Ru^{V}ORu^{V}(O)(bpy)_2]^{4+}$	406	-	1.0 M $HClO_4$, 5 ^{o}C
	588	-	
	750	-	
$[(bpy)_2(HOO)Ru^{IV}ORu^{IV}(OH)(bpy)_2]^{3+}$	451	-	1.0 M CF_3SO_3H
$[(bpy)_2(HOO)Ru^{III}ORu^{V}(O)(bpy)_2]^{3+}$	482	13,500	0.1 M HNO_3
	705	-	
	880	-	
$[(bpy)_2(HOO)Ru^{III}ORu^{IV}(OH)(bpy)_2]^{3+}$	488	-	0.1 M HNO_3
	735	-	
$[(bpy)_2(HOO)Ru^{III}ORu^{IV}(OH_2)(bpy)_2]^{4+}$	451	-	1.0 M HNO_3
	810	-	
$[(bpy)_2(O_2NO)Ru^{IV}ORu^{IV}(OH)(bpy)_2]^{4+}$	455	21,000	1.0 M HNO_3
	825		
	1173		

$[(bpy)_2(O_2NO)Ru^{III}ORu^{V}(O)(bpy)_2]^{3+}$	492	21,000	0.01 M HNO_3

II. Mixing and Kinetic Experiments.

A series of mixing and kinetic experiments were conducted to follow the oxidation of $[(bpy)_2(H_2O)Ru^{III}ORu^{III}(OH_2)(bpy)_2]^{4+}$ by Ce(IV) with spectrophotometric monitoring. All measurements were made at 23 ± 2 ^{o}C in quartz cuvettes with the strong acids HNO_3, CF_3SO_3H (triflic acid), $HClO_4$, and H_2SO_4. The results of these experiments reveal a remarkable sensitivity to both the nature and concentration of added acid. Mixing experiments with Ce(IV) are restricted to strongly acidic conditions in order to maintain its oxidizing strength which is greatly diminished as a result of complex hydrolysis above pH 1.[22] A simple depiction of catalyzed water oxidation by Ce(IV) is given in Scheme 3.1.

Scheme 3.1. Generic scheme of catalyzed Ce(IV)-driven water oxidation.

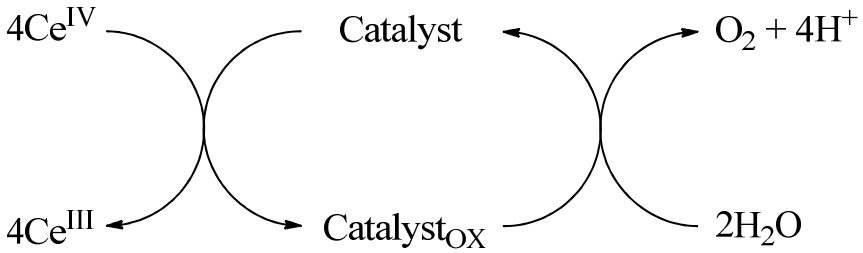

II.1. Oxidation of $[(H_2O)Ru^{III}ORu^{III}(OH_2)]^{4+}$ to $[Ru^{IV}ORu^{III}]^{n+}$. Due to the well-defined nature of the native $Ru^{III}ORu^{III}$ blue dimer and the once oxidized $Ru^{IV}ORu^{III}$ state, this is a good place to start. The reaction was previously studied in detail at pH 0 and pH 1 perchloric and triflic acid media.[23] However, incorrect rate constants were reported at pH 0, presumably just typographical errors as each of the rates were off by a factor of 10. The same data for experiments performed with $HClO_4$ media were re-examined. UV-visible stopped-flow, diode array kinetic spectroscopy was utilized with a concentration of

$[(H_2O)Ru^{III}ORu^{III}(OH_2)]^{4+}$ greater than [Ce(IV)] in order to avoid oxidation beyond $[Ru^{IV}ORu^{III}]^{n+}$. This concern is manifest in experiments with greater Ce(IV) addition by measurably slower rate constants arising from the presence of slower subsequent reactions taking place. Representative spectra vs. time traces of the partial oxidation of $[(H_2O)Ru^{III}ORu^{III}(OH_2)]^{4+}$ (λ_{max} = 637 nm) to $[(H_2O)Ru^{IV}ORu^{III}(OH_2)]^{5+}$ (λ_{max} = 445 nm) with < 1 eq. of Ce(IV) are given in Appendix (Appx.) B Figure S1. Figure 3.2 below illustrates complete oxidation of $Ru^{III}ORu^{III}$; however, this experiment was not used to determine kinetics for this reaction.

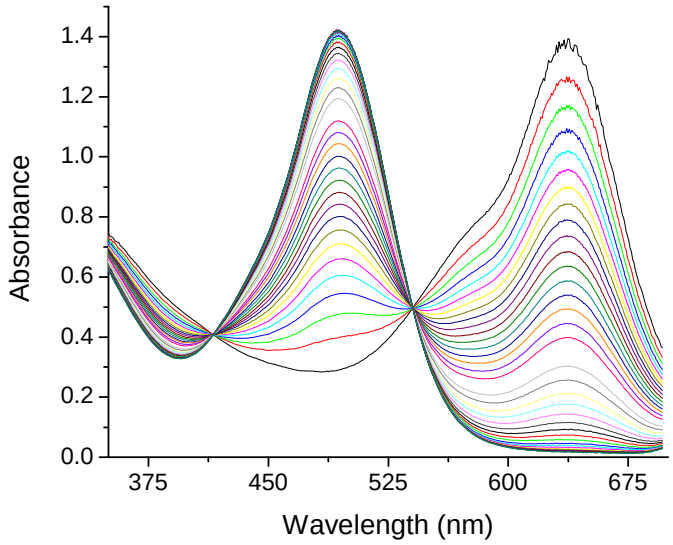

Figure 3.2. Addition of 1.95 x 10^{-4} M Ce(IV) to 6.5 x 10^{-5} M $[(H_2O)Ru^{III}ORu^{III}(OH_2)]^{4+}$ in 0.1 M $HClO_4$ at 25 °C. Data is truncated to show exclusively the one electron oxidation to $[(HO)Ru^{IV}ORu^{III}(OH_2)]^{4+}$.

A simple kinetic model was sufficient to fit the data: A + B → C + D, for which the initial concentration of $[(H_2O)Ru^{III}ORu^{III}(OH_2)]^{4+}$ must be well known. Kinetic measurements were also made in deuterated solvent to determine the kinetic isotope effect (KIE) of this reaction. Data for the triflic acid experiments were not found, but we have assumed the typographical error extends to the 1.0 M triflic acid rate constant as well,

consistent with the rate constants measured in $HClO_4$ and comparable rates measured in HNO_3. Corrected rate constants and KIE values are summarized in Table 3.2. Each rate constant is the average of multiple experiments (N ~ 10).

Table 3.2. Rate constants for Ce(IV) oxidation of $[(H_2O)Ru^{III}ORu^{III}(OH_2)]^{4+}$ at 25 °C.

Medium	k ($M^{-1}s^{-1}$)	k_H/k_D
1.0 M $HClO_4$	1.57 (±0.05) x 10^4	0.65
1.0 M CF_3SO_3H	1.8 x 10^4	0.87
0.1 M $HClO_4$	625 (±48)	0.86
0.1 M CF_3SO_3H	720	0.82

II.2. Generation and Reactivity of $Ru^{V}ORu^{IV}$.

$Ru^{V}ORu^{IV}$ can be prepared by controlled potential electrolysis (CPE) of $Ru^{IV}ORu^{III}$ at $E_{app} > E_{1/2}$ ($Ru^{V}ORu^{IV}/Ru^{IV}ORu^{III}$) in acetate or phosphate buffer solutions (pH 3 - 6) at 5 ° C.[23] The self-reduction process is slow, taking several hours for completion. The proton content of $Ru^{V}ORu^{IV}$ at these pHs is $[(O)Ru^{V}ORu^{IV}(O)]^{3+}$ based on its pH-dependent electrochemistry (Figure 3.1) and measured ν(Ru=O) stretch in resonance Raman spectra.[24] Shown in Figure 3.3 is the decay of $[(O)Ru^{V}ORu^{IV}(O)]^{3+}$ at 25 °C, pH 5.8 phosphate buffer. The decomposition proceeds with second-order equal concentration kinetics, k = 5.35 $M^{-1}s^{-1}$, consistent with rate-limiting disproportionation. (Details inAppx. B Figures S2-4.)

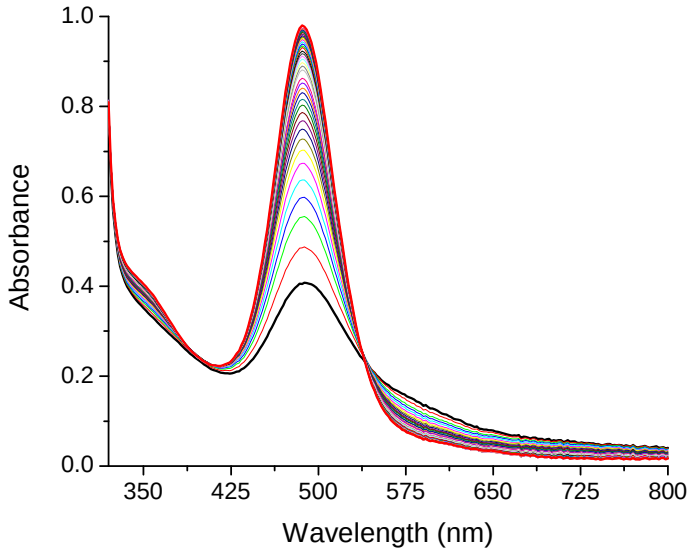

Figure 3.3. Decay of electrolytically-prepared 5.0 x 10^{-5} M $[(O)Ru^{V}ORu^{IV}(O)]^{3+}$ in 0.1 M pH 5.8 phosphate buffer at 25 °C. Black trace is at time = 0 s, red trace at time = 10,800 s with 240 s between spectra.

Addition of 2 eq. of Ce(IV) to the $Ru^{IV}ORu^{III}$ ion in 0.1 M HNO_3 produces $Ru^{V}ORu^{IV}$ cleanly, λ_{max} = 488 nm. Its decay kinetics were studied by monitoring the re-appearance of $[(HO)Ru^{IV}ORu^{III}(OH_2)]^{4+}$ at 495 nm, Appx. B Figure S5. The second order rate constants over a broad range of concentrations had modest variations from 1.4 $M^{-1}s^{-1}$ to 10.5 $M^{-1}s^{-1}$. $Ru^{V}ORu^{IV}$ decay kinetics were also studied at pH = 0 by mixing $Ru^{V}ORu^{IV}$ solutions generated by CPE at ~pH 6 with the appropriate amount of acid in a "pH jump" experiment, Figure 3.4. An initial spectroscopic shift in the visible λ_{max} from 490 nm to 484 nm ensued with $t_{1/2}$ < 10 ms, followed by a complex sequence of coupled reaction steps culminating in water oxidation.[25] The initial spectral change is likely protonation of the Ru^{IV}=O moiety to give Ru^{IV}-OH with a pK_a at ~0.3.

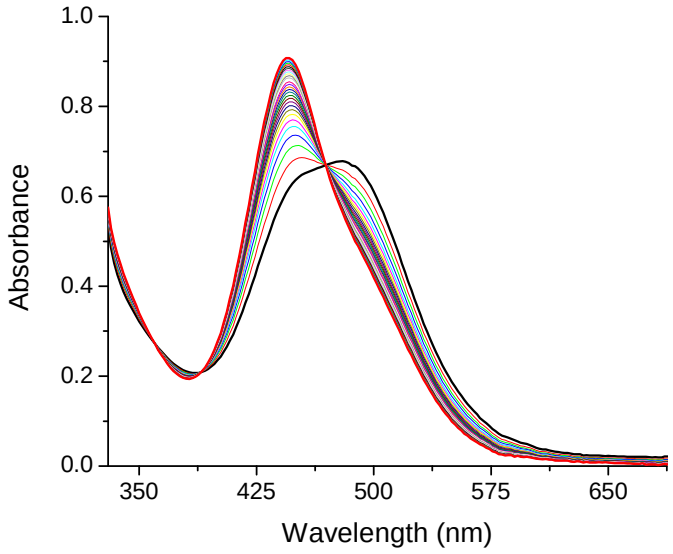

Figure 3.4. Decay of 5.0 x 10^{-5} M electrolytically prepared $[(O)Ru^{V}ORu^{IV}(O)]^{3+}$ at pH 6, acidified to pH = 0 with 2.0 M HOTf. First spectrum (black) at time = 0, last spectrum (red) = 7200 s. Scans are 240 s apart.

Decay kinetics of $Ru^{V}ORu^{IV}$ at pH = 0 were moderately faster than those observed at pH 1 and pH 6. Rate constants of 22 $M^{-1}s^{-1}$ gave satisfactory fits of the kinetic data.[23] While the self-reduction of $Ru^{V}ORu^{IV}$ is dominated by second order kinetics, the high number of coupled reactions involved in its complete conversion to $Ru^{IV}ORu^{III}$ introduces some mixing (error) in the observed kinetics. However, the relatively small range found in the rates from pH 0 to pH 6 is strongly against our previous assertion that the reaction is highly pH-dependent.[8]

The kinetic behavior of Ce(IV) oxidation of $Ru^{V}ORu^{IV}$ was investigated at pH 0 with $HClO_4$ and CF_3SO_3H by multi-mixing experiments in which $Ru^{V}ORu^{IV}$, presumably $[(O)Ru^{V}ORu^{IV}(OH)]^{4+}$, was generated prior to added aliquots of 2-10 eq. of Ce(IV), as described previously.[23] These experiments revealed the rapid generation of a species similar to that of $[(H_2O)Ru^{IV}ORu^{III}(OH_2)]^{5+}$ (λ_{max} = 445 nm), but with λ_{max} at 448 nm (Figure 3.5).

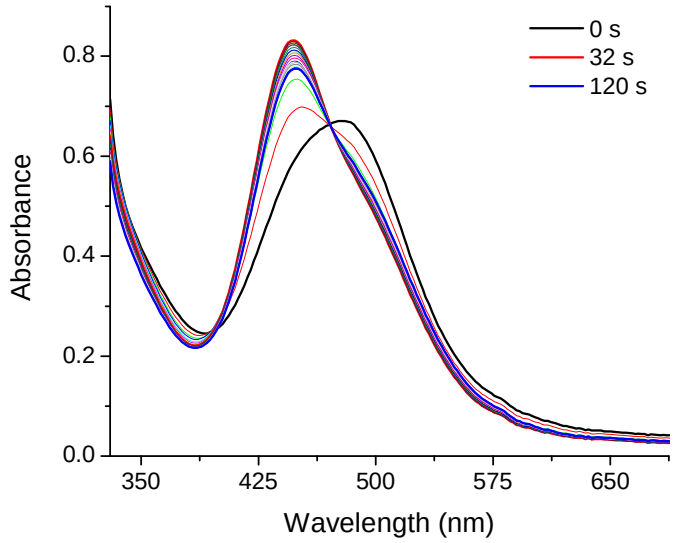

Figure 3.5. Addition of 4 eq. of Ce(IV) to electrolytically prepared $[(O)Ru^{V}ORu^{IV}(O)]^{3+}$, acidified to pH = 0. Scans are 4 s apart.

Additional experimental observations on the nature of intermediates shown in Figure 3.5 will be given in Sections II.6 and II.7, and subsequent discussion below.

II.3. Ce(IV) consumption in 0.1 M CF_3SO_3H, HNO_3, and $HClO_4$. In 0.1 M H_3O^+, $Ru^{IV}ORu^{III}$ exists as $[(bpy)_2(HO)Ru^{IV}ORu^{III}(OH_2)(bpy)_2]^{4+}$ (λ_{max} = 495 nm; ε = 22,000 $M^{-1}cm^{-1}$). Addition of 1 eq. of Ce(IV) to $Ru^{IV}ORu^{III}$ in 0.1 M H_3O^+ results in partial conversion to $Ru^{V}ORu^{IV}$ with λ_{max} = 488 nm. There is no clear evidence for an intermediate, consistent with the rapid disproportionation of the $Ru^{IV}ORu^{IV}$ oxidation state observed in electrochemical measurements. An apparent rate constant, k(0.1 M HNO_3, 23 ^{o}C) = 4.5 x 10^3 $M^{-1}s^{-1}$, was measured for this reaction with 5.0 x 10^{-5} M blue dimer.[26] However, spectral monitoring by rapid mixing, stopped-flow kinetics reveals a more complex mechanism following stoichiometric addition of Ce(IV). Spectra vs. time are given in Figure 3.6.

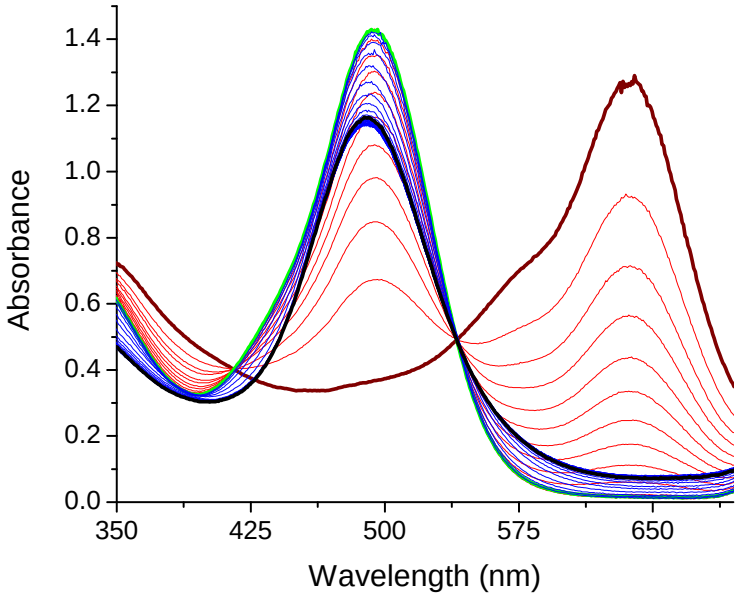

Figure 3.6. Addition of 3 eq. of Ce(IV) to 6.5 x 10^{-5} M $[(H_2O)Ru^{III}ORu^{III}(OH_2)]^{4+}$ in 0.1 M $HClO_4$. Legend: wine = 0.56 s, green = 27.6 s, black = 117.6 s after mixing.

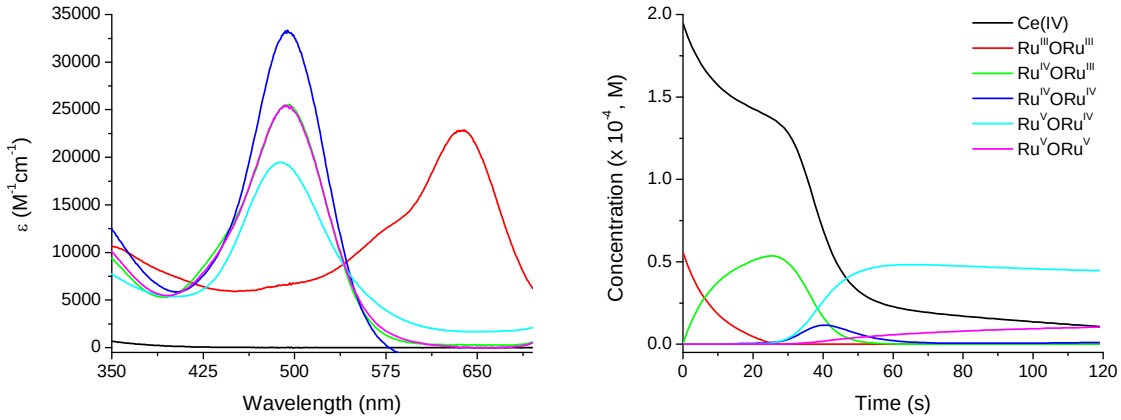

Figure 3.7. Calculated spectra and concentration profiles extracted from singular value deconvolution from the data shown in Figure 6: addition of 3 eq. of Ce(IV) to 6.5 x 10^{-5} M $[(H_2O)Ru^{III}ORu^{III}(OH_2)]^{4+}$ in 0.1 M $HClO_4$.

A kinetic analysis resulted in rate constants or estimates of rate constants for each step. Details of global fitting can be found in Appx. B Figures S6,7. A summary of the reaction steps and associated rate constants is given in Table 3.3.

Table 3.3. Summary of initial oxidative activation of blue dimer in 0.1 M $HClO_4$.

a	$Ru^{III}ORu^{III}$ + Ce(IV) → $Ru^{IV}ORu^{III}$ + Ce(III)	$k_1 = 625\ M^{-1}s^{-1}$
b	$Ru^{IV}ORu^{III}$ + Ce(IV) → $Ru^{IV}ORu^{IV}$ + Ce(III)	$k_2 = 3.24\ M^{-1}s^{-1}$
c	$Ru^{IV}ORu^{IV}$ + Ce(IV) → $Ru^{V}ORu^{IV}$ + Ce(III)	$k_3 = 7500\ M^{-1}s^{-1}$
d	$Ru^{V}ORu^{IV}$ + Ce(IV) → $Ru^{V}ORu^{V}$ + Ce(III)	$k_4 = 200\ M^{-1}s^{-1}$
e	$Ru^{V}ORu^{V}$ → $Ru^{III}ORu^{III}$	$k_5 = 5\ s^{-1}$
f	$Ru^{III}ORu^{III}$ + $Ru^{V}ORu^{IV}$ → $Ru^{IV}ORu^{III}$ + $Ru^{IV}ORu^{IV}$	$k_6 = 1.0 \times 10^5\ M^{-1}s^{-1}$
g	$Ru^{IV}ORu^{III}$ + $Ru^{V}ORu^{IV}$ → $2Ru^{IV}ORu^{IV}$	$k_7 = 6.0 \times 10^4\ M^{-1}s^{-1}$
h	$2Ru^{IV}ORu^{IV}$ → $Ru^{IV}ORu^{III}$ + $Ru^{V}ORu^{IV}$	$k_{-7} = 6.0 \times 10^4\ M^{-1}s^{-1}$
i	$Ru^{IV}ORu^{IV}$ + $Ru^{V}ORu^{V}$ → $2Ru^{V}ORu^{IV}$	$k_8 = 0.055\ M^{-1}s^{-1}$
j	$2Ru^{V}ORu^{IV}$ → $Ru^{IV}ORu^{IV}$ + $Ru^{V}ORu^{V}$	$k_{-8} = 0.055\ M^{-1}s^{-1}$

Kinetic behavior by the blue dimer under catalytic conditions is dominated by cross reactions. The cross reaction between $[(O)Ru^{V}ORu^{IV}(O)]^{4+}$ and $[(H_2O)Ru^{III}ORu^{III}(OH_2)]^{4+}$ was previously studied by direct mixing and spectral monitoring, step f.[23] $Ru^{V}ORu^{IV}$ was prepared by Ce(IV) oxidation and subsequently reacted with $Ru^{III}ORu^{III}$. A lower limit on the rate constant of $10^6 - 10^7\ M^{-1}s^{-1}$ was calculated as the reaction was instantaneous on the stopped-flow time-scale (< 1.25 ms), generating $Ru^{IV}ORu^{III}$ as the only observable product.[23] In Table 3.3, the rate constant for this reaction is supreme, compatible with the experimental data.

As described in Table 3.3, the rate constants for the steps $[(HO)Ru^{IV}ORu^{III}(OH_2)]^{4+}$ to $[(HO)Ru^{IV}ORu^{IV}(OH)]^{4+}$ and $[(HO)Ru^{IV}ORu^{IV}(OH)]^{4+}$ to $[(O)Ru^{V}ORu^{IV}(O)]^{3+}$ are kinetically-coupled, producing second-order autocatalysis. This assessment is analogous to the kinetics reported in 1.0 M $HClO_4$.[23] For oxidation of $Ru^{IV}ORu^{III}$ to $Ru^{IV}ORu^{IV}$ (step b), a

range of values from 3 to 20 $M^{-1}s^{-1}$ can be expected with compensating changes in the other kinetically-coupled rate constants. Similarly, for oxidation of $Ru^{IV}ORu^{IV}$ to $Ru^{V}ORu^{IV}$ (step c), values from 2,000 to 8,000 $M^{-1}s^{-1}$ give equally good fits, with compensating changes in the other rate constants. Values from 100 to 200 $M^{-1}s^{-1}$ represent the acceptable range for oxidation of $Ru^{V}ORu^{IV}$ to $Ru^{V}ORu^{V}$ (step d).

Oxidation of the blue dimer to $[(O)Ru^{V}ORu^{IV}(O)]^{4+}$ at pH 1 can be further summarized by eqs 1 and 2 in which rate limiting oxidation of $[(HO)Ru^{IV}ORu^{III}(OH_2)]^{4+}$ to $[(HO)Ru^{IV}ORu^{IV}(OH)]^{4+}$ occurs followed by its rapid oxidation to $[(O)Ru^{V}ORu^{IV}(O)]^{3+}$. An equilibrium exists between the disproportionation of $Ru^{IV}ORu^{IV}$, eq 2, and the comproportionation back reaction, step g of Table 3.3. This is a consequence of the closely spaced redox couples for the $Ru^{IV}ORu^{IV}/Ru^{IV}ORu^{III}$ and $Ru^{V}ORu^{IV}/Ru^{IV}ORu^{IV}$ waves (unresolved 2-electron and 3-electron steps in acidic media). The reversible disproportionation-comproportionation steps best model the data when their equilibrium constant is close to unity. As $Ru^{V}ORu^{IV}$ accumulates in solution, it reacts with $Ru^{IV}ORu^{III}$ to generate two $Ru^{IV}ORu^{IV}$ ions, faster than Ce(IV) oxidation of $Ru^{IV}ORu^{III}$, and hence, the reaction becomes autocatalytic due to the rapid oxidation of $Ru^{IV}ORu^{IV}$ by Ce(IV).

$$[(HO)Ru^{IV}ORu^{III}(OH_2)]^{4+} + Ce(IV) \rightarrow [(HO)Ru^{IV}ORu^{IV}(OH)]^{4+} + Ce(III) \qquad (1)$$

$$[(HO)Ru^{IV}ORu^{IV}(OH)]^{4+} + Ce(IV) \xrightarrow{rapid} [(O)Ru^{V}ORu^{IV}(O)]^{3+} + Ce(III) \qquad (2)$$

Overlapping absorption bands and rapid kinetics make deconvoluting the electronic spectrum of each intermediate difficult, as illustrated by the $Ru^{IV}ORu^{IV}$ and "$Ru^{V}ORu^{V}$" spectra being essentially matched in Figure 3.7. This is a consequence of not having enough colorimetric data associated with these intermediates to accurately distinguish their spectroscopic contribution to the measured absorption. For example, $Ru^{IV}ORu^{IV}$ never

accumulates appreciably during the catalytic cycle at pH 1. In 0.1 M $HClO_4$, the presence of a precipitant is discernable by the rise in the spectral baseline occurring after oxidation beyond $Ru^{IV}ORu^{III}$, Figure 3.6. Similarly, following addition of 3 eq. of Ce(IV) to $[(H_2O)Ru^{IV}ORu^{III}(OH_2)]^{5+}$ in cold, 1.0 M $HClO_4$, a black precipitate forms having a resonance Raman band at 816 cm^{-1}, assigned to ν(Ru=O).[23] An experimentally determined spectrum, thought to belong to the catalytically-active $[(O)Ru^{V}ORu^{V}(O)]^{4+}$ species is given in Figure 3.8.

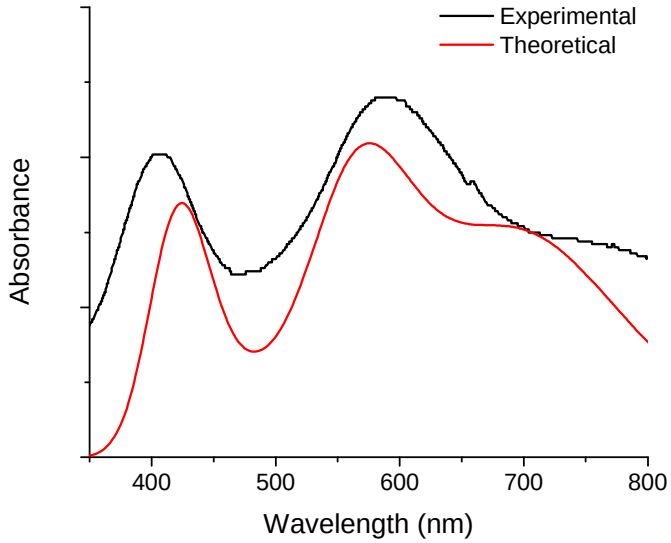

Figure 3.8. Experimental and calculated absorption spectra of $[(O)Ru^{V}ORu^{V}(O)]^{4+}$. Calculated with B3LYP functional and LanL2DZ basis set, gas phase, triplet electronic state. Details on the calculation are provided in Appx. B.

While the spectrum was gleaned by singular value deconvolution (SVD) using SPECFIT and tentatively identified as the elusive $Ru^{V}ORu^{V}$, it is supported by the theoretical spectrum produced by time-dependent density functional theory calculations on the optimized $[(O)Ru^{V}ORu^{V}(O)]^{4+}$ geometry. There is a dramatically different shape to the calculated spectrum of $[(O)Ru^{V}ORu^{V}(O)]^{4+}$ relative to other blue dimer oxidation states and intermediates calculated in the same manner. On this basis, there is no clear spectroscopic

data at pH 1 for $[(O)Ru^{V}ORu^{V}(O)]^{4+}$ during catalysis, consistent with the experiments at pH 0.[23] However, oxidation to the putative $Ru^{V}ORu^{V}$ and its subsequent reactivity are at the crux of establishing the mechanism of water oxidation by the blue dimer. What happens when the blue dimer is oxidized to the $[(O)Ru^{V}ORu^{V}(O)]^{4+}$ state?

The complexity of the system makes it difficult to obtain unique sets of rate constants, but the best estimates so far come from fits to stopped-flow data starting at the $[(HO)Ru^{IV}ORu^{III}(OH_2)]^{4+}$ state, *vide infra*. Concentration vs. time profiles are shown in Figure 3.9, corresponding to a mixing experiment in which ~3 eq. of Ce(IV) are added to $[(HO)Ru^{IV}ORu^{III}(OH_2)]^{4+}$ in 0.1 M $HClO_4$.

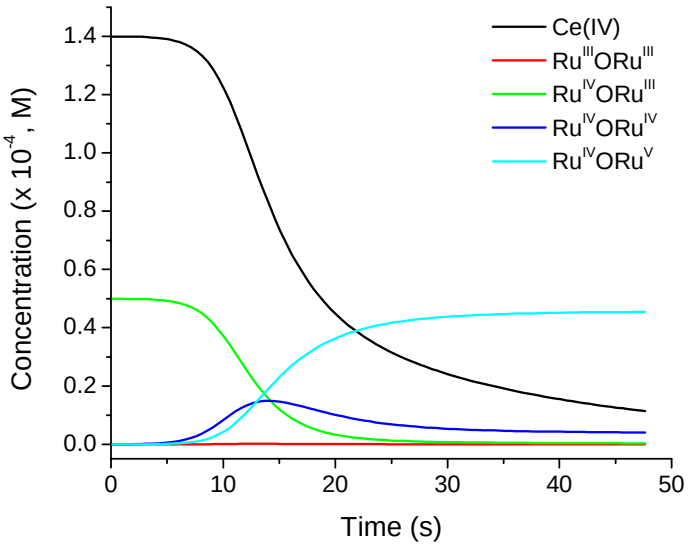

Figure 3.9. Addition of 2.8 eq. (1.4×10^{-4} M) of Ce(IV) to 5.0×10^{-5} M $[(HO)Ru^{IV}ORu^{III}(OH_2)]^{4+}$ in 0.1 M $HClO_4$. Details provided in Appx. B Figures S8-10.

The concentration profiles are similar to those in Figure 3.7, where $[(H_2O)Ru^{III}ORu^{III}(OH_2)]^{4+}$ was the starting point. Sluggish oxidation of $Ru^{III}ORu^{III}$ to $Ru^{IV}ORu^{III}$, followed by slow oxidation of $Ru^{IV}ORu^{III}$ prior to the autocatalytic portion of its disappearance alter the desired stoichiometry for clean conversion to a single intermediate. The Ce(IV) concentration profiles in Figures 3.7 and 3.9 illustrate this point. Single

wavelength data fits are given in Appx. B. Beginning from $Ru^{IV}ORu^{III}$, however, both in modeling the reaction and in practice (as they should be), allows for quantitative conversion to the higher oxidation states, $Ru^{V}ORu^{IV}$ and $\{Ru^{V}ORu^{V}\}$ at pH 1. Absent in Figure 3.9 is the appearance of "$Ru^{V}ORu^{V}$" toward the end of the reaction, as depicted in Figure 3.7, an over oxidation considering the stoichiometry of added Ce(IV).

Shown by the spectra in Figure 3.10, addition of 3 eq. of Ce(IV) to $[(HO)Ru^{IV}ORu^{III}(OH_2)]^{4+}$ ultimately results in oxidation to $\{Ru^{V}ORu^{V}\}$ and the appearance of an intermediate characterized by λ_{max} = 482, ~850 nm, Table 1.

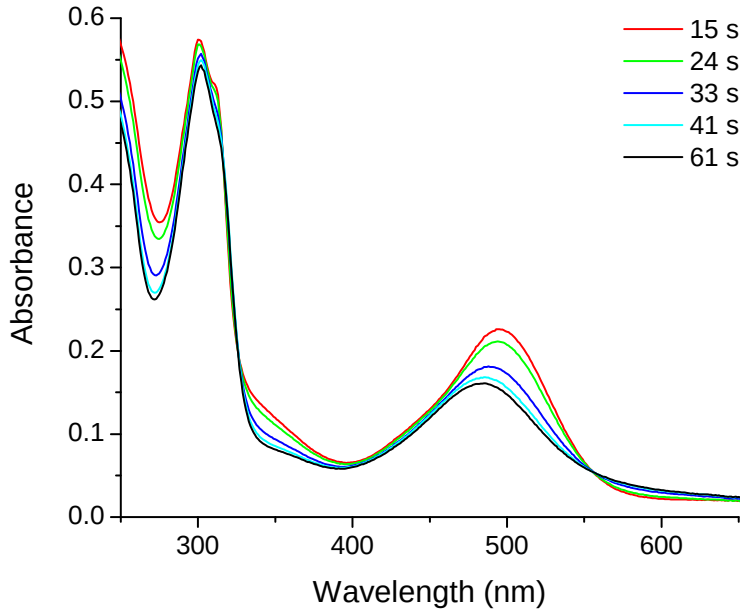

Figure 3.10. Addition of 3 eq. of Ce(IV) to 1.25 x 10^{-5} M $[(HO)Ru^{IV}ORu^{III}(OH_2)]^{4+}$ in 0.1 M HNO_3.

This intermediate appears with kinetics that are first order in Ce(IV) and first order in $Ru^{V}ORu^{IV}$ with k(0.1 M HNO_3, 23 ^{o}C) ~ 220 $M^{-1}s^{-1}$.[23,26] Acidification of the 482 nm intermediate (**I**) generated at pH 1 with strong acid to pH 0 produced a new intermediate, λ_{max} = 451 nm, Figure 3.11. The spectral change is reversible with pH.

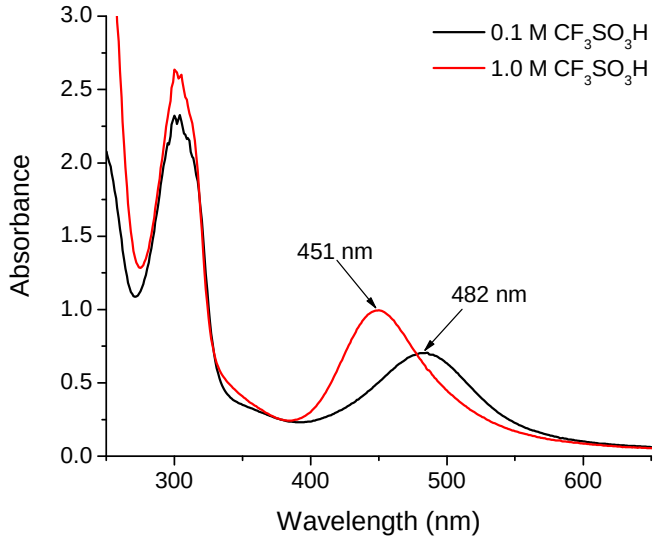

Figure 3.11. Acid-base forms of intermediate **I** in 1.0 M CF_3SO_3H (black) and in 0.1 M CF_3SO_3H (red).

A redox titration of intermediate **I** with λ_{max} = 482 nm is shown in Figure 3.12; sequential 1 eq. additions of aqueous Fe^{2+} were followed by spectral monitoring. A total of ~3.7 eq. of Fe^{2+} were needed to reduce the intermediate to $[(H_2O)Ru^{III}ORu^{III}(OH_2)]^{4+}$. As a reducing agent $Fe_{(aq)}^{2+}$ is known to reduce higher oxidation states of the blue dimer to $Ru^{III}ORu^{III}$ without further reduction on the time-scale of the experiment. The titration was reproduced with $[Os(phen)_3]^{2+}$ as the stoichiometric reductant, E°' = 0.83 V vs. NHE, and cross reactions were studied in which 3 eq. of $[(H_2O)Ru^{III}ORu^{III}(OH_2)]^{4+}$ were needed to reduce intermediate **I** to $[(HO)Ru^{IV}ORu^{III}(OH_2)]^{4+}$, Appx. B Figures S11-13.

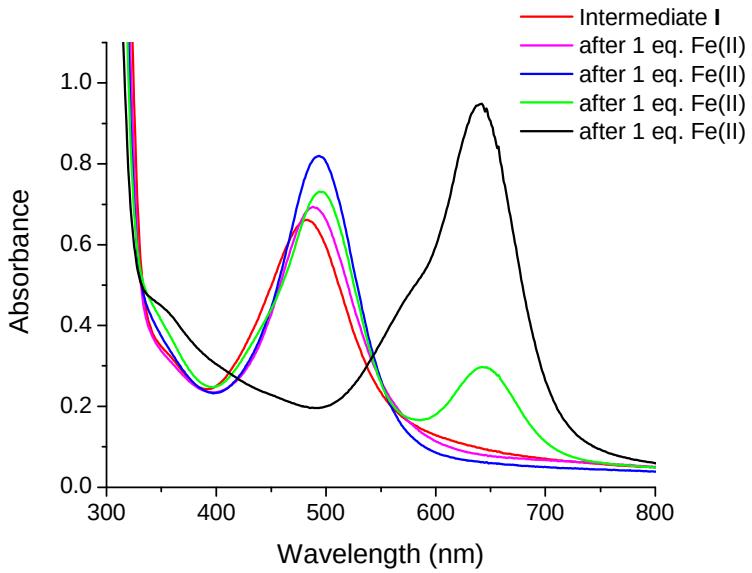

Figure 3.12. Redox titration with $Fe_{(aq)}^{2+}$ in 0.1 M HNO_3 after addition of 3 eq. of Ce(IV) to $[(HO)Ru^{IV}ORu^{III}(OH_2)]^{4+}$ to generate intermediate **I** at λ_{max} = 482 nm.

Intermediate **I** was generated by addition of 3 eq. of Ce(IV) to 5.0 x 10^{-5} M $[(HO)Ru^{IV}ORu^{III}(OH_2)]^{4+}$ in 0.1 M HNO_3; spectra vs. time for its quantitative decomposition back to $Ru^{IV}ORu^{III}$ are shown in Figure 3.13. Initial disproportionation of intermediate **I** is the first step in a series of reactions involved in this process The details of which will be discussed later in the text. In summary, intermediate **I** is four oxidative equivalents higher than $[(H_2O)Ru^{III}ORu^{III}(OH_2)]^{4+}$, pH-dependent, and appears following stoichiometric oxidation by Ce(IV) to the transient $Ru^{V}ORu^{V}$ while having a different absorption spectrum.

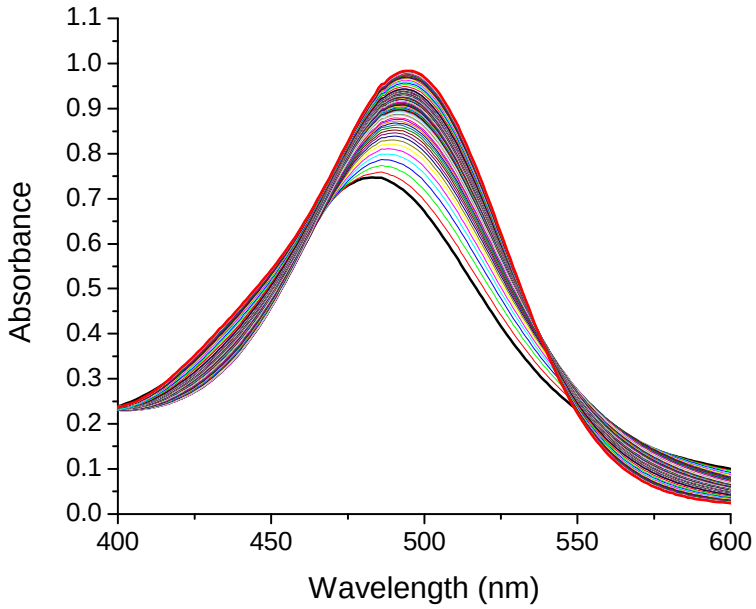

Figure 3.13. Decay of intermediate **I** (5 x 10^{-5} M), generated by adding 3 eq. of Ce(IV) to $[(HO)Ru^{IV}ORu^{III}(OH_2)]^{4+}$ in 0.1 M HNO_3. Black trace at time = 0 s, red trace = 50,000 s.

A pseudo-first order excess, 30 equivalents, of Ce(IV) was added to the blue dimer in 0.1 M H_3O^+ to initiate catalysis (Figure 3.14). The steady state intermediate at early times is intermediate **I**. As Ce(IV) is consumed, the visible absorption maximum shifts to λ_{max} = 488 nm, accompanied by a decrease in absorptivity. The shift in λ_{max} is adjunct with changes in the near IR from 705, 880 nm to 735 nm, respectively.

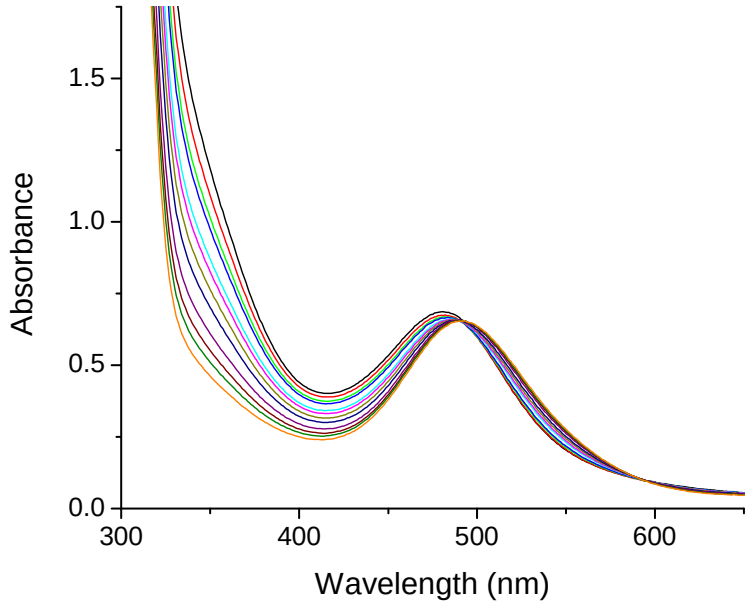

Figure 3.14. Addition of 30 eq. Ce(IV) to a concentration of 5.0 x 10^{-5} M blue dimer in 0.1 M HNO_3. Successive traces were recorded at 16 (black), 40 (red), 63 (green), 76 (blue), 110 (cyan), 126 (magenta), 150 (dark yellow), 180 (navy), 240 (purple), 300 (wine), 360 (olive), 480 s (orange) following Ce^{IV} addition.

Qualitatively similar behavior is observed with Ce(IV) consumption in pseudo-first order excess by 5.0 x 10^{-5} M blue dimer in 0.1 M $HClO_4$ and 0.1 M CF_3SO_3H, Appx. B Figure S14. The kinetics are consistent with rate-limiting oxidation of the steady state intermediate at λ_{max} = 482 nm, formed with excess Ce(IV) or by addition of 3 eq. of Ce(IV) to $[(HO)Ru^{IV}ORu^{III}(OH_2)]^{4+}$. Stoichiometric generation of intermediate **I** at high concentration produces qualitatively similar results to those observed during catalysis, Figure 3.15. In this case, the species rapidly shifts to a new species with a lower molar extinction coefficient and λ_{max} = 488 nm before subsequent reactions in its ultimate conversion back to $[(HO)Ru^{IV}ORu^{III}(OH_2)]^{4+}$ (λ_{max} = 495 nm) take place.

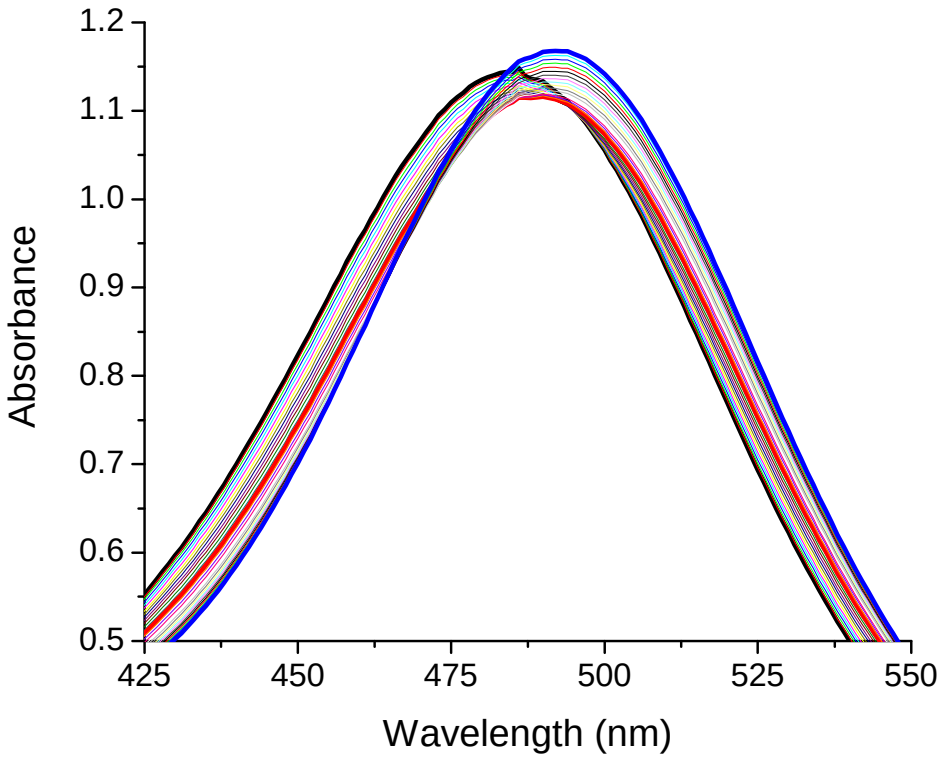

Figure 3.15. Addition of 3 eq. Ce(IV) to 0.94 mM $[(HO)Ru^{IV}ORu^{III}(OH_2)]^{4+}$ in 0.1 M HNO_3. Selected spectra: black = 3.9 s, λ_{max} = 483 nm; red = 10.9 s, λ_{max} = 488 nm; blue = 38.9 s after Ce(IV) addition. The full spectra are provided in Appx. B, Figure S15.

Ensuing characterization of this intermediate with λ_{max} = 488 nm (**II)** is given below. Acid-base forms of **II** are shown in Figure 3.16. Upon acidification of the species generated at pH 1 to pH = 0, the λ_{max} appears at 451 nm. A redox titration, Figure 3.17, with $Fe_{(aq)}^{2+}$ required ~2.7 eq. of the reductant to quantitatively form $[(H_2O)Ru^{III}ORu^{III}(OH_2)]^{4+}$. Interestingly, a shoulder appears in the absorption spectra following 1 and 2 eq. of total Fe^{2+} added with a λ_{max} ~ 455 nm.

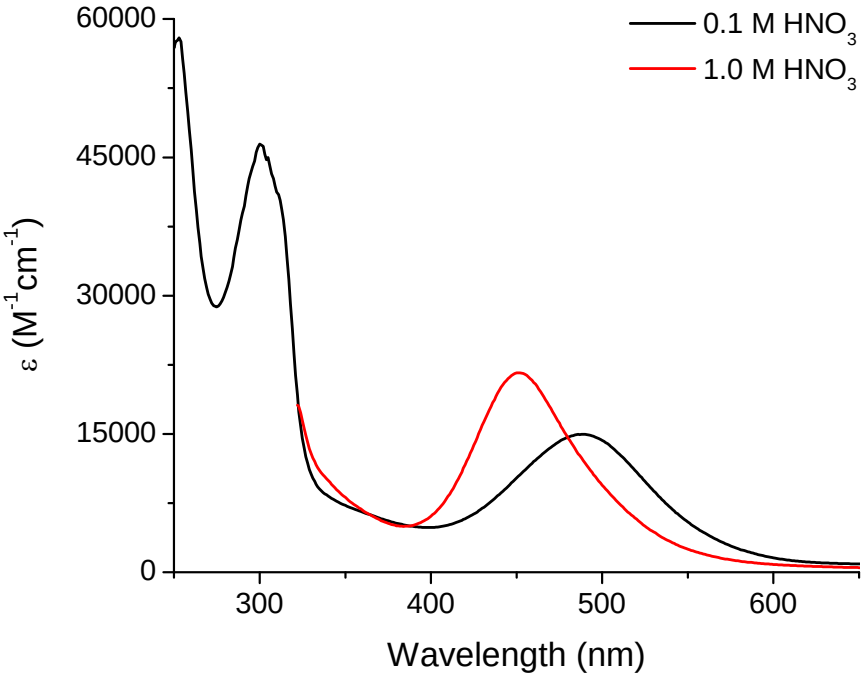

Figure 3.16. Acid-base forms of intermediate **II** in 0.1 M HNO_3 (black) and 1 M HNO_3 (red).

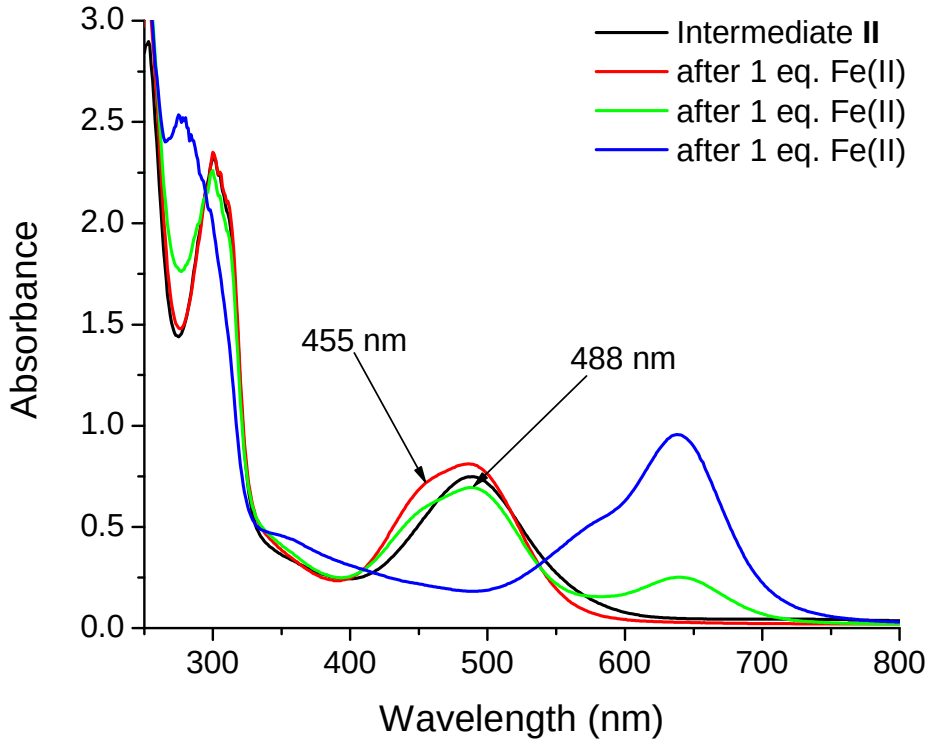

Figure 3.17. Redox titration with $Fe_{(aq)}^{2+}$ in 0.1 M HNO_3 after addition of 30 eq. Ce(IV) to $[(H_2O)Ru^{III}ORu^{III}(OH_2)]^{4+}$ to generate intermediate **II** at λ_{max} = 488 nm.

Spectra vs. time corresponding to the decay of intermediate **II**, Figure 3.18, reveal a similar distribution of species in the absorption profile when compared to the redox titration (Figure 3.17) with Fe^{2+}.

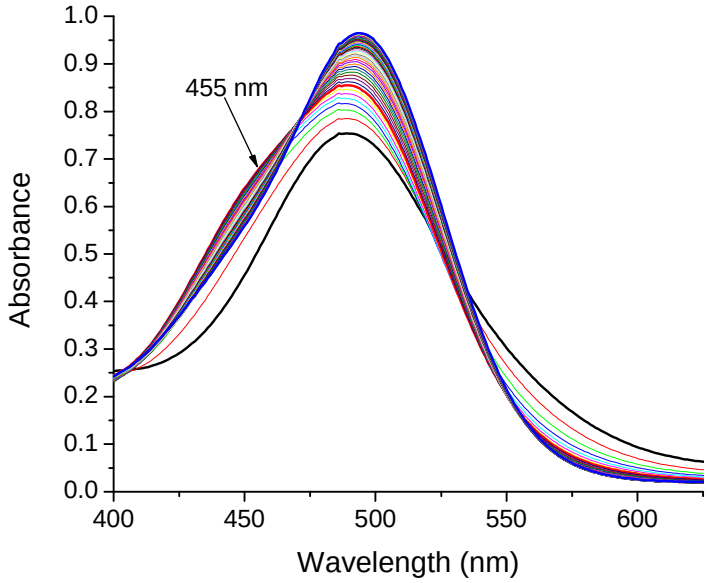

Figure 3.18. Decay of intermediate **II** with λ_{max} = 488 nm, generated after the consumption of 30 eq. Ce(IV) added to 5.0 x 10^{-5} M blue dimer in 0.1 M HNO_3.

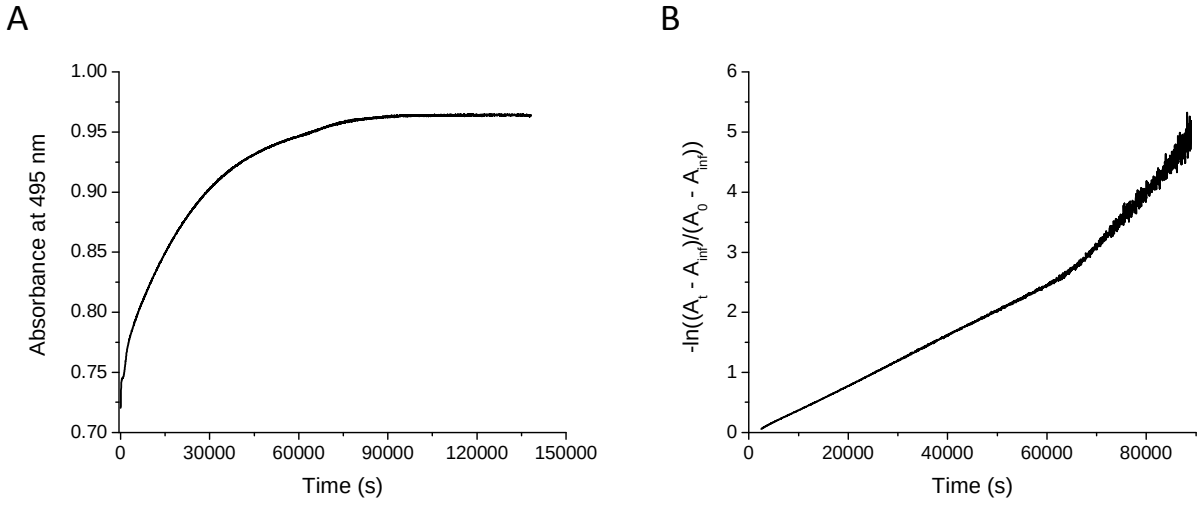

Figure 3.19. (A) Absorbance vs. time trace obtained from the spectral monitoring shown in Figure 17 following the decay of intermediate **II** by the appearance of $[(HO)Ru^{IV}ORu^{III}(OH_2)]^{4+}$ at its λ_{max}, 495 nm. (B) First order plot of kinetic trace in (A): $-\ln((A_t - A_\infty)/(A_0 - A_\infty))$ vs. time (s) for absorbance at 495 nm.

Linear fits of the two stages of first order decay are provided in Appx. B Figures S16. The first stage from 0 to ~60,000 seconds has k(0.1 M HNO_3, 23 °C) = 4 x 10^{-5} s^{-1}, and the second stage at longer times has a measured rate, k = 9 x 10^{-5} s^{-1}. Chemical reduction and self-reduction of intermediate **II** appears to indicate the presence of underlying cross reactions as evidenced by the mixture of products observed. Further support is deduced from the absence of multiple products during the implied decay of intermediate **II** in dilute solutions of blue dimer with excess Ce(IV) shown below, Figure 3.20.

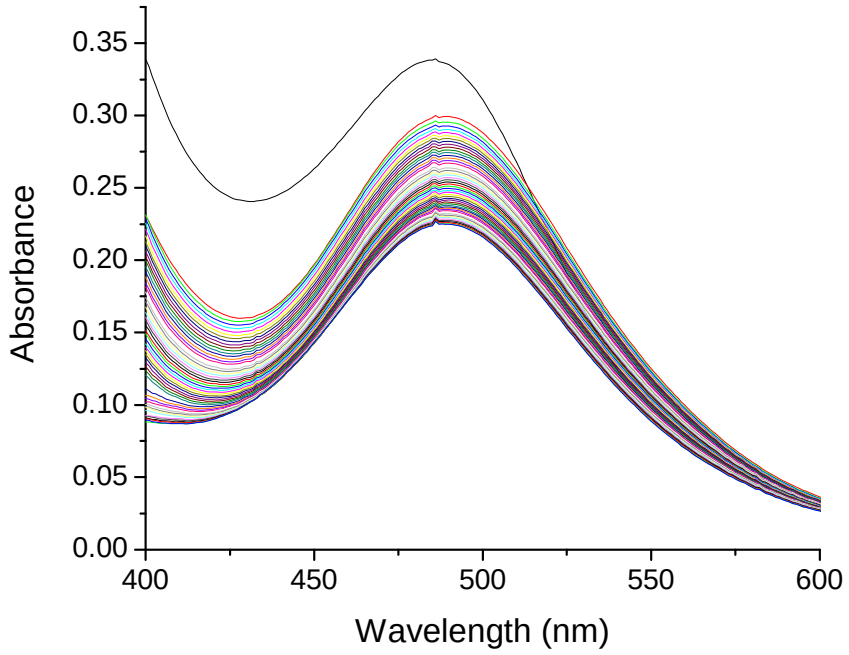

Figure 3.20. Addition of 75 eq. of Ce^{IV} to 2.0 x 10^{-5} M blue dimer in 0.1 M HNO_3. Note that the steady state species is intermediate **II** with λ_{max} = 488 nm for the bulk of Ce(IV) consumption.

In Figure 3.20, the first spectra after Ce(IV) addition has a λ_{max} at ~484 nm, which is likely a mixture of intermediate **I** (482 nm) and **II** (488 nm). The visible absorption λ_{max} then shifts to 488 nm, analogous to the spectra vs. time shown in Figure 3.14, and remains as the steady state intermediate for the bulk of Ce(IV) consumption.

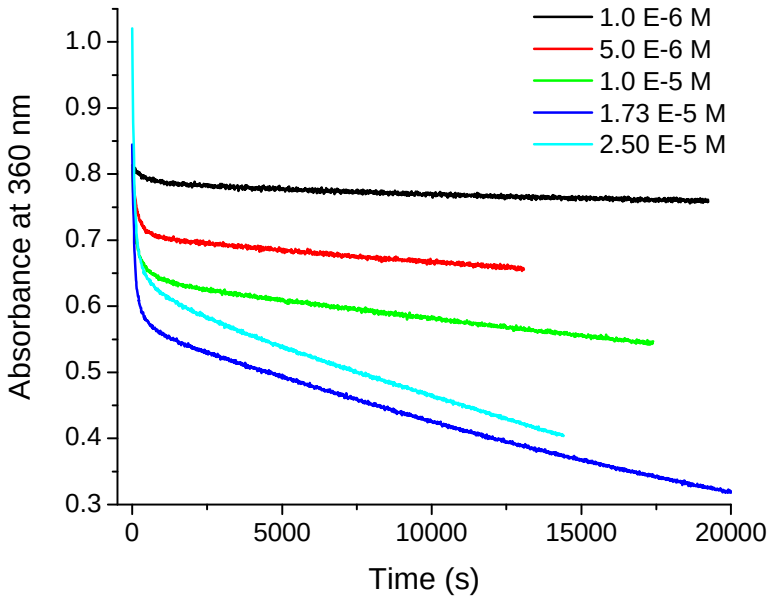

Figure 3.21. Absorbance vs. time traces monitoring Ce(IV) consumption at 360 nm following addition of 30 eq. of Ce(IV) added (with respect to 5.0 x 10^{-5} M catalyst) to low concentrations of the blue dimer. Spectral changes vs. time in each of these experiments matches that of Figure 3.20.

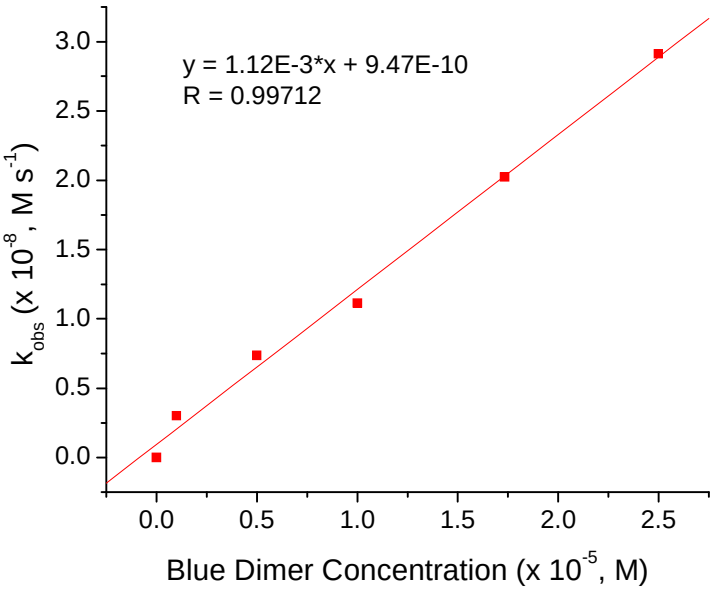

Figure 3.22. First order plot (k_{obs} vs. Blue Dimer Concentration (M)) of observed zero order rate constants obtained from linear fits of data shown in Figure 3.21 showing the first order dependence of Ce(IV) consumption on the concentration of catalyst. Fits are shown in Appx. B Figure S17.

Similar behavior to the experiment shown in Figure 3.14 is observed when excess Ce(IV) is added to low concentrations of the blue dimer. However, a noticeable difference is observed over long time periods in that Ce(IV) consumption quickly becomes zero order in Ce(IV) as indicated by the linear slope of the kinetic trace measured at 360 nm. Oxidation of intermediate **II** by Ce(IV) does not occur and it presumably decomposes by the first order kinetics shown in Figure 3.18. Noticeably absent in the spectral change vs. time in Figure 3.19 is the decomposition product with λ_{max} ~ 455 nm.

II.4. Intermediate **III** and Catalyst Deactivation.

Increasing the blue dimer concentration and maintaining a constant ratio of added Ce(IV) in the same medium (0.1 M HNO_3) produces different behavior. A series of absorption spectra vs. time for these mixing experiments is shown in Figure 3.23, in which a 400 nm light filter was utilized to avoid undesired photochemistry that occurs under incident UV light. High energy light (< 400 nm) was avoided or minimized whenever possible. Photoreduction of higher oxidation state intermediates and conversion to the 455 nm intermediate are enhanced in the presence of UV light. These photochemical pathways were not investigated further.

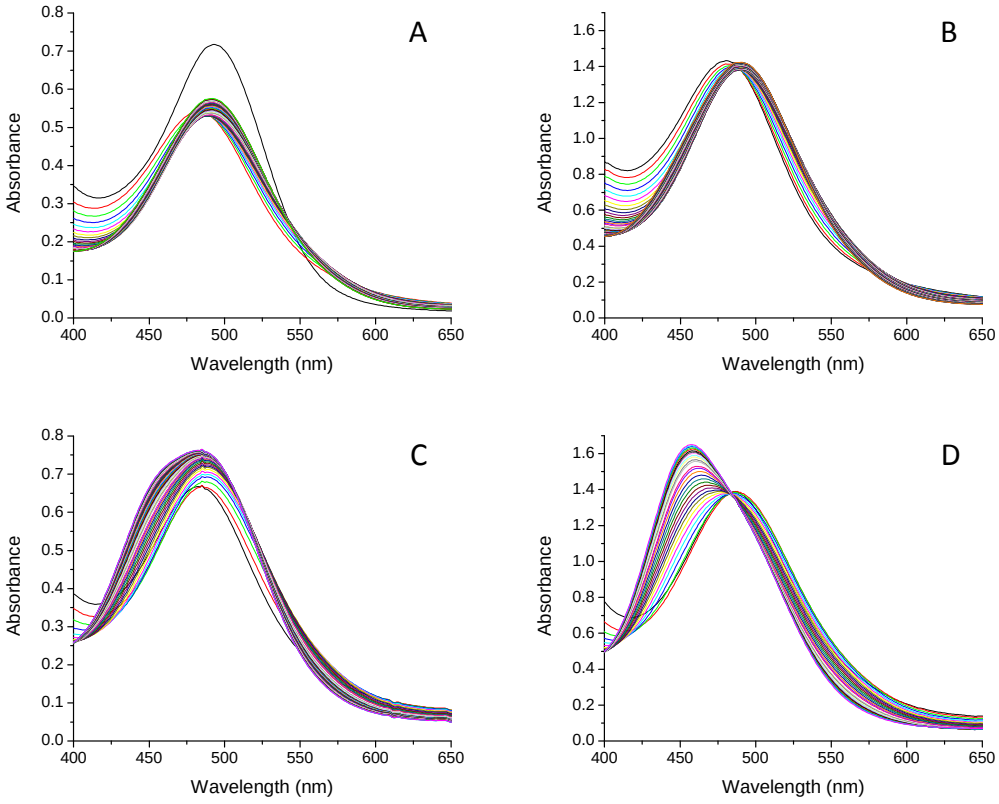

Figure 3.23. Addition of 30 eq. of Ce(IV) to different concentrations of $[(H_2O)Ru^{III}ORu^{III}(OH_2)]^{4+}$ in 0.1 M HNO_3 at 23 ± 2 °C. A 400 nm cut-off filter was used. (A) 1.5 x 10^{-3} M Ce(IV), 5.0 x 10^{-5} M blue dimer, (B) 3.0 x 10^{-3} M Ce(IV), 1.0 x 10^{-4} M blue dimer, (C) 0.015 M Ce(IV), 5.0 x 10^{-4} M blue dimer, (D) 0.03 M Ce(IV), 0.001 M blue dimer.

It appears that the conversion to the species with λ_{max} at 455 nm, intermediate **III,** intensifies with increasing blue dimer concentrations during catalysis. However, despite total number of turnovers being held constant (Figure 3.23) by the fixed ratio of Ce(IV) to blue dimer, the absolute concentration of each varies so no definitive conclusions can be drawn regarding the order of the reaction from these reactions. Importantly, once intermediate **III** is formed, it *cannot* be oxidized with Ce(IV), effectively deactivating the catalyst toward Ce(IV) consumption and water oxidation until its decay, Appx. B Figure S18. As noted in prior investigations, the presence of anated intermediates has been proposed.[23,27,28] The replacement of an aqua ligand with an anion would prevent oxo formation via PCET

oxidation of a ruthenium aqua center and end the associated advantages: redox potential leveling, charge compensation, etc.[8] Coordination of anions to the blue dimer during catalysis is perhaps not surprising. Open coordination sites in the blue dimer likely occur with O_2 evolution, and anions would be attracted to the high-valent, positively charged catalyst. We have undertaken a detailed investigated of these intermediates, *vide infra*.

A complication in assessing the experiment in Figure 3.23 is illustrated in Figure 3.24 where Ce(IV) and blue dimer concentrations are fixed and increasing concentrations of KNO_3 have been added. Both the rate and conversion to intermediate **III** are dependent on the concentration of nitrate. Our oxidant of choice, $(NH_4)_2Ce^{IV}(NO_3)_6$, brings with it a factor of 6 added NO_3^-. Delineating the dependence on rate and conversion to **III** with turnover number and NO_3^- concentration is thus problematic.

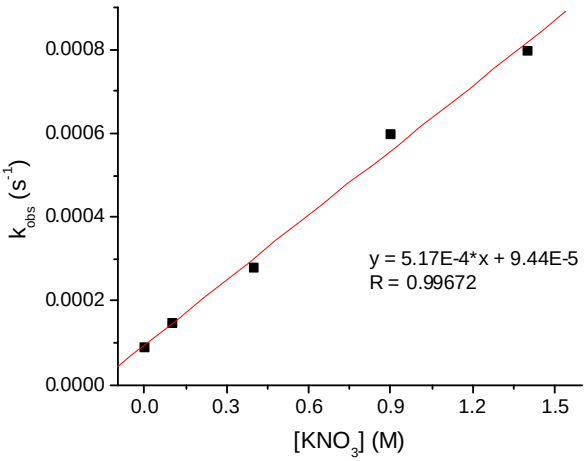

Figure 3.24. Linear relationship for k_{obs} (s^{-1}) vs. anion concentration for appearance of anated species at 455 nm. Addition of 30eq Ce(IV) to 5 x 10^{-5} M Blue Dimer in 0.1 M HNO_3 with increasing amounts of KNO_3. Spectra vs. time of the corresponding reactions are provided in Appx. B Figure S19.

With that said, the degree of conversion to intermediate **III** scales with Ce(IV) added. In Figure 3.25, increasing amounts of Ce(IV) were added to 0.001 M blue dimer in 0.1 M HNO_3.

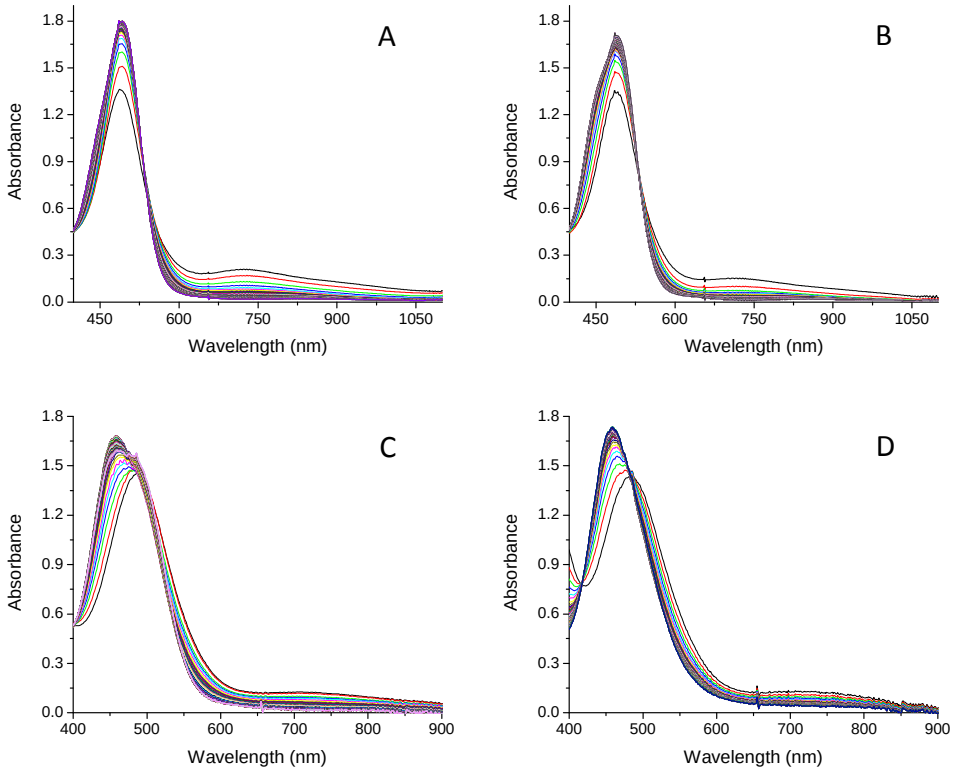

Figure 3.25. Addition of different amounts of Ce(IV) to 0.001 M $[(H_2O)Ru^{III}ORu^{III}(OH_2)]^{4+}$ in 0.1 M HNO_3. A 400 nm cut-off filter was used. (A) 7.5 x 10^{-3} M Ce(IV) – 7.5 eq. (B) 0.015 M Ce(IV) – 15 eq. (C) 0.03 M Ce(IV) – 30 eq. (D) 0.045 M Ce(IV) – 45 eq.

A plot of the absorbance at λ_{max} = 455 nm vs. [Ce(IV)] for the series of experiments represented by Figure 3.25 shows the linear dependence on added Ce(IV) in the conversion of blue dimer to intermediate **III**. Furthermore, the *rate* of appearance of **III** is first order in Ce(IV) and independent of blue dimer concentration, Appx. B Figures S20,21. The latter also holds true in 1.0 M HNO_3 (discussed later in the text). Given the available data, conversion to **III** has a dependence on catalyst concentration, despite the zero-order dependence regarding its rate of formation, indicating saturation kinetics are at play.

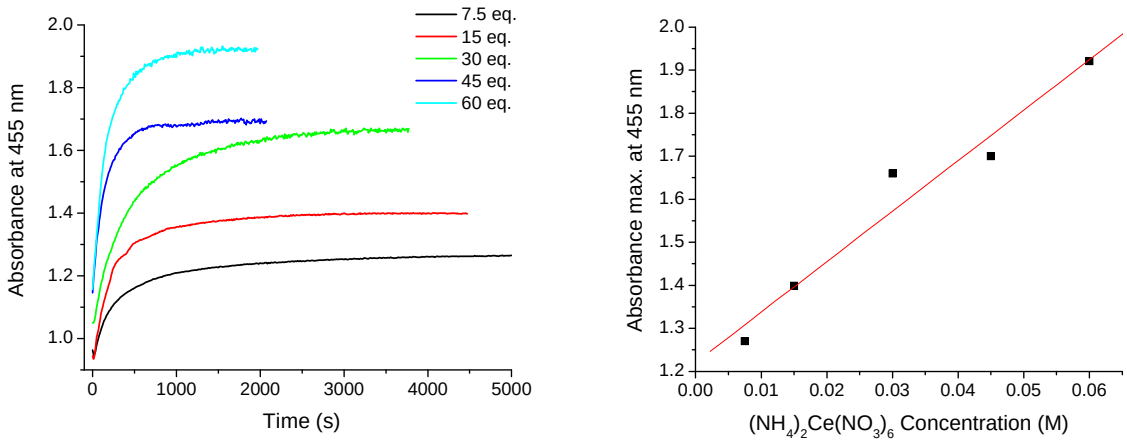

Figure 3.26. Addition of increasing amounts of Ce(IV) to 0.001 M blue dimer in 0.1 M HNO_3, representative spectra vs. time in Figure 3.25. (A) Monitoring the conversion to intermediate III at 455 nm. (B) Its associated absorption maximum plotted vs. [Ce(IV)].

Some characterization of intermediate **III** is provided in Figures 3.27 and 3.28. The net oxidation state composition of the intermediate was investigated by a spectrophotometric titration with added $Fe_{(aq)}^{2+}$. Incremental aqueous Fe^{2+} additions based on the initial concentration of blue dimer resulted in the spectral changes shown in Figure 3.27.

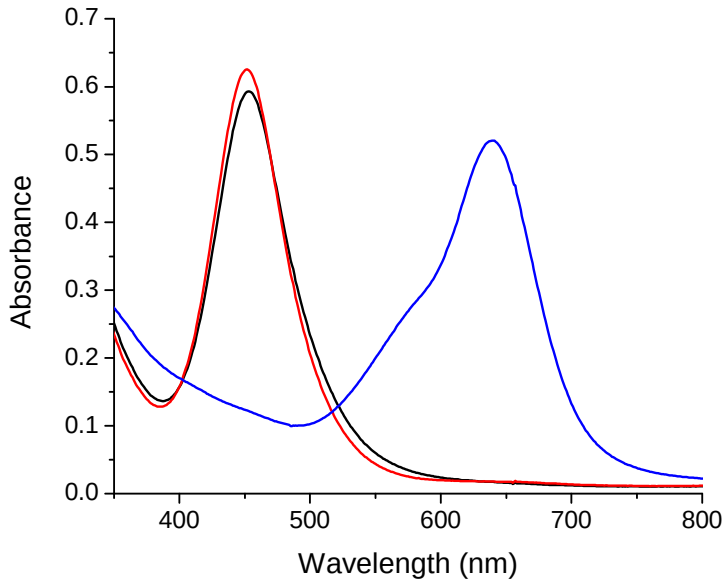

Figure 3.27. Redox titration with $Fe_{(aq)}^{2+}$. Addition of two sequential 1 eq. Fe^{2+} aliquots were required to reduce intermediate **III** to $[(H_2O)Ru^{III}ORu^{III}(OH_2)]^{4+}$. Black = intermediate **III** with λ_{max} = 455 nm, red = after 1 eq. of Fe^{2+}, and blue = $[(H_2O)Ru^{III}ORu^{III}(OH_2)]^{4+}$ after 2 eq. of Fe^{2+}.

Addition of 1 eq. of $Fe_{(aq)}^{2+}$ results in the appearance of a new species characterized by λ_{max} = 452 nm. Addition of a second aliquot of 1 eq. Fe^{2+}, for a total of 2 reductive equivalents, results in quantitative conversion of the intermediate to the blue dimer, $[(H_2O)Ru^{III}ORu^{III}(OH_2)]^{4+}$, at λ_{max} = 637 nm. This result is important in establishing that the intermediate is higher in oxidation state by 2 e^- compared to the blue dimer. The results of a spectrophotometric pH titration are shown in Figure 3.28. Increasing the pH of the solution above 2, by addition of NaOH, results in shifts in λ_{max} from 455 nm to 492 nm. The spectral shifts are reversible with pH.

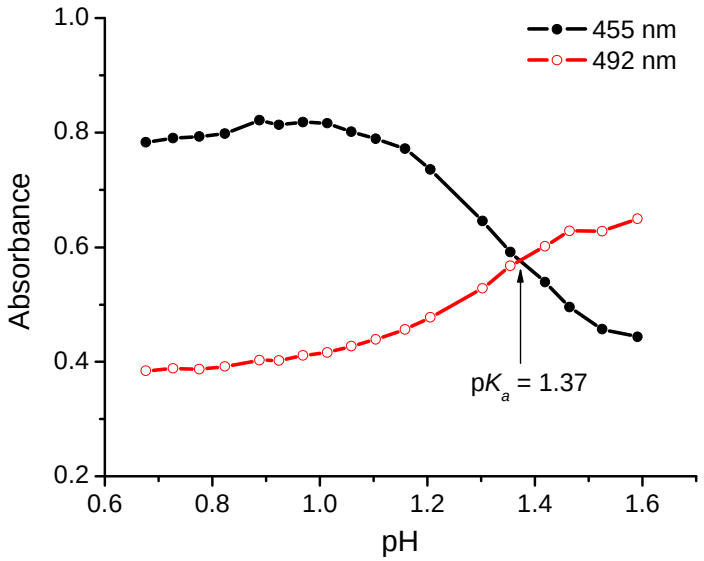

Figure 3.28. Absorbance vs. solution pH following titration of intermediate **III** in 1.0 M HNO_3 with 4.0 M NaOH, 23 ± 2 °C.

Based on the results of the redox and pH titrations and assuming the intermediate contains a bound NO_3^-, the p*K*a = 1.4 and the formal oxidation state of the anated intermediate is $Ru^{IV}ORu^{IV}$. These measurements are consistent with the acid-base equilibrium in eq 3.

$$[(bpy)_2(O_2NO)Ru^{IV}ORu^{IV}(OH)(bpy)_2]^{4+}\ (455\ nm) \rightleftharpoons \quad (3)$$

$$[(bpy)_2(O_2NO)Ru^{III}ORu^{V}(O)(bpy)_2]^{3+} + H^+\ (493\ nm)$$

The formulation of oxidation states is somewhat arbitrary but consistent with the known complex[29] $[(bpy)_2(py)Ru^{III}ORu^{V}(O)(bpy)_2]^{4+}$ and DFT results favoring $[(bpy)_2(HO)Ru^{IV}ORu^{IV}(OH)(bpy)_2]^{4+}$ over $[(bpy)_2(H_2O)Ru^{III}ORu^{V}(O)(bpy)_2]^{4+}$ for $Ru^{IV}ORu^{IV}$.[19]

Reappearance of $[(bpy)_2(HO)Ru^{IV}ORu^{III}(OH_2)(bpy)_2]^{4+}$. The slow return to $Ru^{IV}ORu^{III}$ was monitored in the visible at λ_{max} = 495 nm (ε = 22,000 $M^{-1}cm^{-1}$), Figure 3.29. Kinetics were first order in $[(NO_3^-)]$ and exhibited zero dependence on complex concentration. Catalytic activity is restored following the decay of $[(O_2NO)Ru^{IV}ORu^{IV}(OH)]^{4+}$, consistent with loss of anion and subsequent aquation.

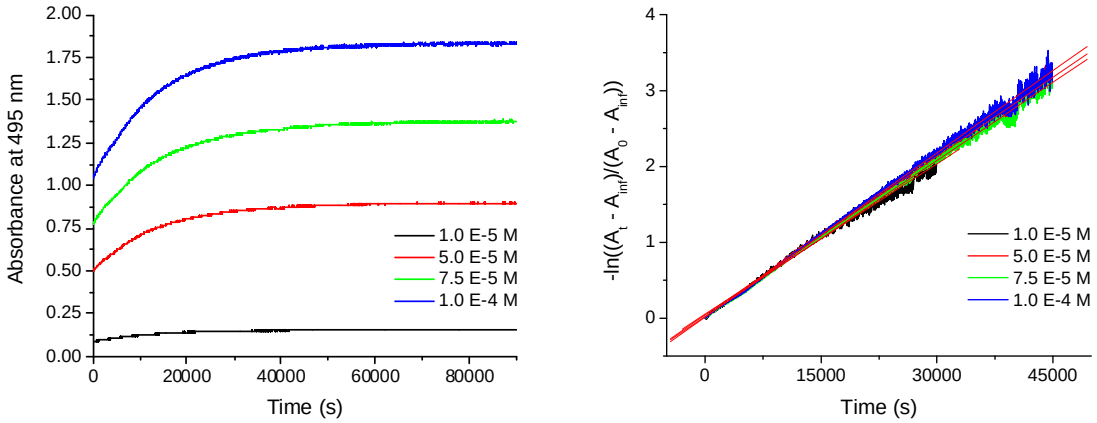

Figure 3.29. Decay of intermediate **III** in 0.1 M HNO_3 at different catalyst concentrations. Monitoring appearance of $[(HO)Ru^{IV}ORu^{III}(OH_2)]^{4+}$ at 495 nm. The first order rate constant for decay is 6.91 x 10^{-5} s^{-1}.

This rate constant is presumably aquation with rate limiting loss of NO_3^-, $k(-NO_3^-$, 0.1 M HNO_3) = 6.9 x 10^{-5} s^{-1} from the nitrato complex, $[(O_2NO)Ru^{IV}ORu^{IV}(OH)]^{4+}$ at this pH, to give $[(HO)Ru^{IV}ORu^{IV}(OH)]^{4+}$. Self-reduction to $[(HO)Ru^{IV}ORu^{III}(OH_2)]^{4+}$ ensues by a series of more kinetically facile reactions to be discussed later.

II.5. Ce(IV) consumption in 1.0 M HNO_3. *Catalysis, Oxidation by Ce(IV).* The 1 e^- oxidized form of $[(bpy)_2(H_2O)Ru^{III}ORu^{III}(OH_2)(bpy)_2]^{4+}$, $[(H_2O)Ru^{IV}ORu^{III}(OH_2)]^{5+}$, with λ_{max} = 445 nm (ε = 22,500 $M^{-1}cm^{-1}$) was generated *in situ* by adding 1 eq. of Ce(IV) to $Ru^{III}ORu^{III}$.

Spectral changes with time under catalytic conditions following the addition of 30 eq. of Ce(IV) to 5.0 x 10^{-5} M $Ru^{IV}ORu^{III}$ in 1.0 M HNO_3 are shown in Figure 3.30. Rapid oxidation of $Ru^{IV}ORu^{III}$ to $Ru^{V}ORu^{IV}$ occurs as shown by the shift in λ_{max} from 445 to ~482 nm, Section II.2. Similarly, in the near IR there are corresponding shifts in λ_{max} from 840, 1182 nm to 750 nm, Table 3.1.

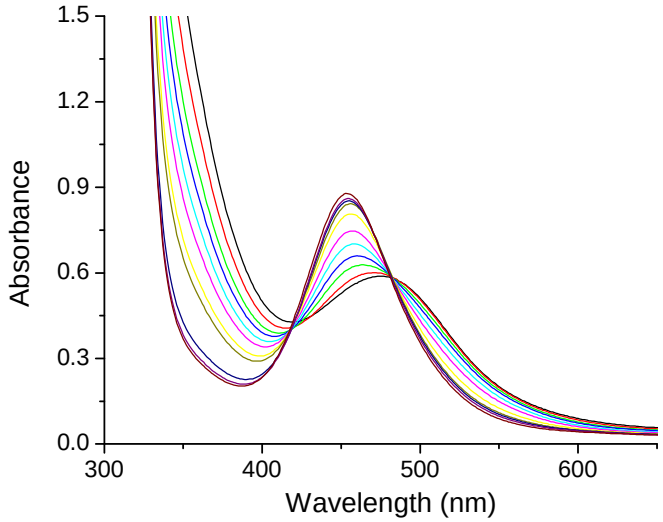

Figure 3.30. Absorbance-time traces following addition of 30 eq. of Ce(IV) to $[(bpy)_2(H_2O)Ru^{IV}O\ Ru^{III}(H_2O)(bpy)_2]^{5+}$ (5 x 10^{-5} M) in 1.0 M HNO_3. The black line trace is the spectrum 10 s after addition of Ce(IV). Successive traces were recorded at 30 (red), 62 (green), 97 (navy), 155 (cyan), 255 (magenta), 542 (yellow), 1030 (dark yellow), 2040 (purple), 3060 (brown), and 4340 s (maroon) following Ce(IV) addition.

Initial oxidation of $Ru^{IV}ORu^{III}$ to $Ru^{V}ORu^{IV}$, eq 1, is slow. However, as the reaction proceeds, disproportionation of the transient $Ru^{IV}ORu^{IV}$ intermediate, presumably as $[(HO)Ru^{IV}ORu^{IV}(OH)]^{4+}$,[19] catalyzes the reaction and the effective rate constant becomes rapid.[23] The slow step can be observed by rapid mixing and stopped flow analysis, analogous

to the kinetics previously discussed in 0.1 M $HClO_4$. The slow step is consistent with electrochemical measurements; oxidation of $Ru^{IV}ORu^{III}$ at electrode surfaces requires large overpotentials or surface modification to overcome or lower the activation barrier associated with direct oxidation.[30]

Observed kinetics are consistent with the mechanism in eq 1 with rate determining oxidation of $Ru^{IV}ORu^{III}$ followed by rapid oxidation of $Ru^{IV}ORu^{IV}$ to $Ru^{V}ORu^{IV}$. Analysis of the kinetics data gave k_{obs}(23 ^{o}C) = 2.0×10^3 M^{-1} s^{-1}. $Ru^{IV}ORu^{IV}$ has been reported as a kinetic intermediate in 1.0 M $HClO_4$ but is unstable toward disproportionation. The rate constant for oxidation of $[(HO)Ru^{IV}ORu^{III}(OH_2)]^{4+}$ to $Ru^{IV}ORu^{IV}$ by Ce^{IV} is 3.2 $M^{-1}s^{-1}$ in 0.1 M $HClO_4$. However, the effective rate of oxidation increases to ~10^3 $M^{-1}s^{-1}$ as the reaction proceeds and $[(O)Ru^{V}ORu^{IV}(O)]^{3+}$ appears in the solution. Autocatalysis occurs under these conditions as $Ru^{IV}ORu^{IV}$ is generated by comproportionation of $[(H_2O)Ru^{IV}ORu^{III}(OH_2)]^{5+}$ and $[(O)Ru^{V}ORu^{IV}(OH)]^{4+}$ and is oxidized rapidly by Ce(IV).[23]

$$[(H_2O)Ru^{III}ORu^{IV}(OH_2)]^{5+} + Ce(IV) \xrightarrow{k(III-IV\rightarrow IV-IV)} \{[(HO)Ru^{IV}ORu^{IV}(OH)]^{4+}\} + H^{+} + Ce(III) \quad (4)$$

$$\{[(HO)Ru^{IV}ORu^{IV}(OH)]^{4+}\} + Ce(IV) \xrightarrow{rapid} [(O)Ru^{V}Oru^{IV}(OH)]^{4+} + H^{+} + Ce(III) \quad (5)$$

At the first observation time in Figure 3.30, 10 s, ~35% of the initial Ce(IV) added is depleted as shown by absorbance changes in the UV. From the spectrum, $Ru^{V}ORu^{IV}$ is the dominant form of the catalyst during the catalytic cycle as Ce(IV) is consumed. This observation is consistent with rate limiting oxidation of $Ru^{V}ORu^{IV}$ to $Ru^{V}ORu^{V}$, eq 6. Once formed, $Ru^{V}ORu^{V}$ undergoes rapid oxidation of water and is subsequently oxidized back to $Ru^{V}ORu^{IV}$ with additional Ce(IV) consumption, eq 7. There is no spectral evidence for the

accrual of $Ru^{V}ORu^{V}$ as an intermediate. In an earlier study, evidence was summarized for its appearance as an unstable, black ClO_4^- salt upon oxidation at low temperature in $HClO_4$.

$$Ru^{IV}ORu^{V} + Ce(IV) \xrightarrow{k(V-IV \rightarrow V-V)} Ru^{V}ORu^{V} + Ce(III) \quad (6)$$

$$Ru^{V}ORu^{V} + 3\,Ce(IV) + 2\,H_2O \xrightarrow{rapid} Ru^{IV}ORu^{V} + 3\,Ce(III) + O_2 + 4\,H^+ \quad (7)$$

Pseudo-first order kinetics for Ce(IV) consumption were studied as a function of catalyst concentration, Figure 3.31.

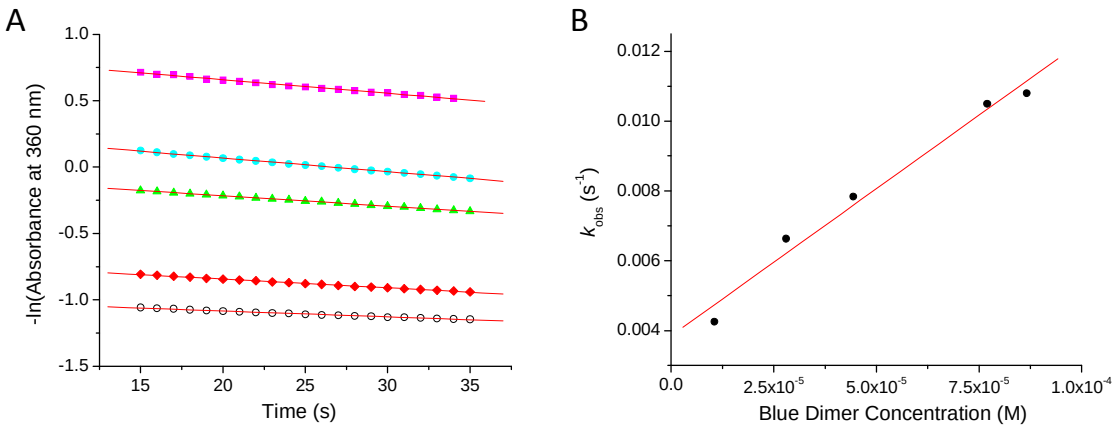

Figure 3.31. Pseudo-first order kinetics for excess Ce(IV) consumption. Addition of 30 eq. of Ce(IV) with respect to 5.0 x 10^{-5} M $[(HO)Ru^{IV}ORu^{III}(OH_2)]^{4+}$ in 1.0 M HNO_3. (A) Plot of -ln(absorbance at 360 nm) vs. time to determine k_{obs}. (B) k_{obs} (s^{-1}) vs. blue dimer concentration to establish first order dependence on catalyst, k = 80 $M^{-1}s^{-1}$. Legend: magenta = 8.66 x 10^{-5} M, cyan = 7.7 x 10^{-5} M, green = 4.44 x 10^{-5} M, red = 2.8 x 10^{-5} M, and white = 1.5 x 10^{-5} M blue dimer.

The kinetic traces observing loss of Ce(IV) at λ = 360 nm revealed that the reaction was first order in Ce(IV) and first order in added $Ru^{IV}ORu^{III}$, consistent with the rate law, -d[Ce(IV)]/dt = k[Ce(IV)][$Ru^{V}ORu^{IV}$] with k(1.0 M HNO_3, 23 °C) = 80 $M^{-1}s^{-1}$. A first order dependence on blue dimer was also observed at higher catalyst concentrations (8.0 x 10^{-4} M to 1.6 x 10^{-3} M), Appx. B Figure S22.

*Appearance of intermediate **III** at λ_{max} = 455 nm*. The spectrum evolves with time during catalysis with apparent conversion from λ_{max} = 482 nm for $Ru^{V}ORu^{IV}$ to $[(O_2NO)Ru^{IV}ORu^{IV}(OH)]^{4+}$ with λ_{max} = 455 nm and λ_{max} = 825, 1173 nm in the near IR. This species was verified as the same intermediate that builds up in 0.1 M HNO_3 with excess Ce(IV) consumption by the blue dimer. Absorbance vs. time profiles are given in Figure 3.32, where the absorbance at 455 nm was monitored to follow the appearance of the nitrato intermediate after the addition of excess Ce(IV) to different concentrations of blue dimer in 1.0 M HNO_3. Under the pseudo-first order kinetics afforded by the large excess of Ce(IV), apparent zero-order kinetics are observed with respect to catalyst concentration indicative of saturation kinetics. Quantitative conversion to intermediate **III** occurs at all catalyst concentrations given a pseudo-first order excess of oxidant in 1.0 M HNO_3; unlike in 0.1 M HNO_3, a consequence of the 10-fold increase in NO_3^-.

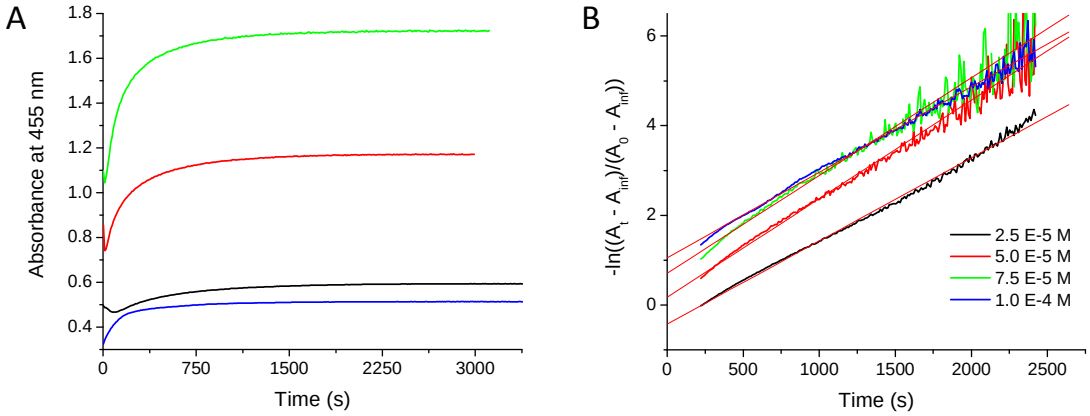

Figure 3.32. Addition of 30 eq. of Ce(IV) to different blue dimer concentrations in 1.0 M HNO_3, monitoring the growth of intermediate **III**, $[(O_2NO)Ru^{IV}ORu^{IV}(OH)]^{4+}$, at its λ_{max} of 455 nm.

On a still longer time scale (~1100 min, $t_{1/2}$ = ~145 min), these features disappear accompanied by the quantitative reappearance of $Ru^{IV}ORu^{III}$ at λ_{max} = 445 nm and 840, 1182

nm in the near-IR. A first order kinetic plot monitoring the decay of the nitrato intermediate in 1.0 M HNO_3 by measuring the re-appearance of $Ru^{IV}ORu^{III}$ is provided in Appx. B Figure S23. Clean first order kinetics were observed with k(1.0 M HNO_3) = 8.0 x 10^{-5} s^{-1}. The rate constant for anion loss and aquation is slower in 1.0 M HNO_3, relative to 0.1 M HNO_3.

Oxygen evolution in 1.0 M HNO_3. The evolution of O_2 with time was measured under catalytic conditions with 30 eq. of Ce(IV) added to 0.001 M $[(H_2O)Ru^{III}ORu^{III}(OH_2)]^{4+}$ in 1.0 M HNO_3. The amount of O_2 produced (7.5 eq.) was stoichiometric based on the amount of Ce(IV) added. A trace of O_2 evolution vs. time is shown in Figure 3.33. Qualitatively, O_2 continued to evolve *slowly* from the solution over an extended period until the reappearance of $Ru^{IV}ORu^{III}$ at λ_{max} = 445 nm, as observed spectrophotometrically.

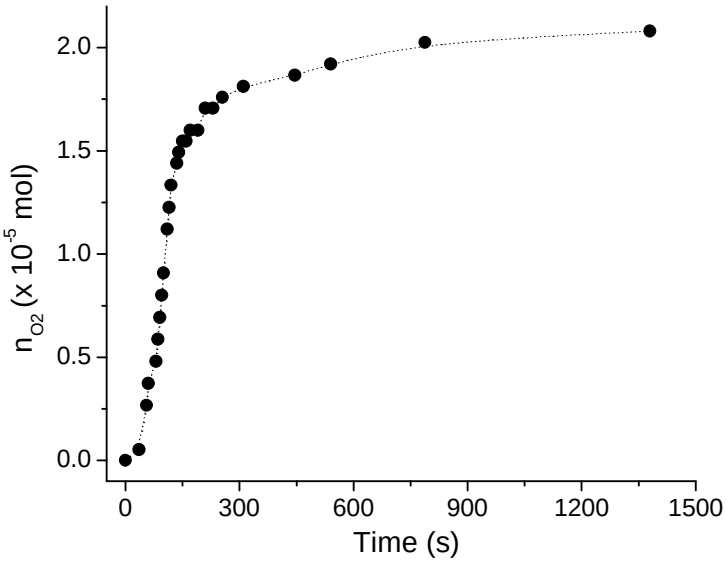

Figure 3.33. Oxygen evolution following addition of 30 eq. of Ce(IV) to 0.001 M $[(H_2O)Ru^{III}ORu^{III}(OH_2)]^{4+}$ in 1.0 M HNO_3 at 23 °C.

II.6. Ce(IV) consumption in 1.0 M CF_3SO_3H. UV-visible absorbance-time traces with 30 eq. of Ce(IV) added to 5.0 x 10^{-5} M $Ru^{IV}ORu^{III}$ in 1.0 M CF_3SO_3H are shown in Figure 3.34.

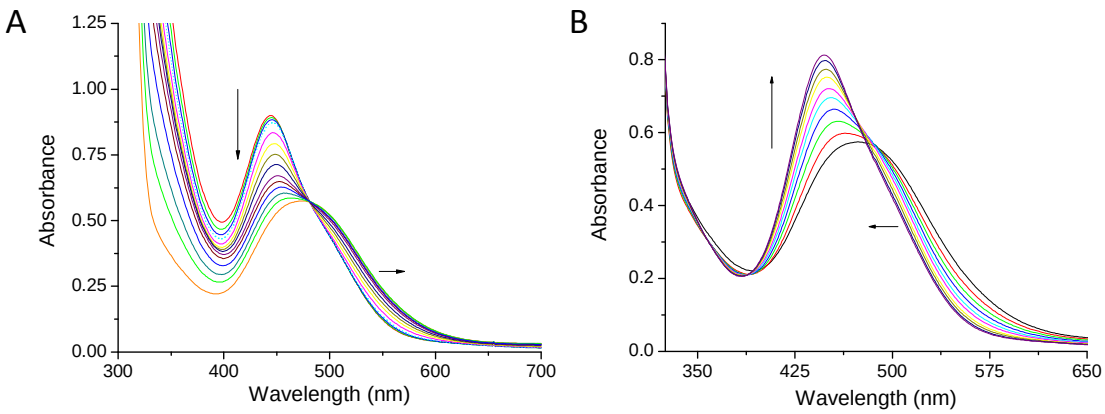

Figure 3.34. Addition of 30 eq. of Ce(IV) to 5.0 x 10^{-5} M $[(H_2O)Ru^{IV}ORu^{III}(OH_2)]^{5+}$ in 1.0 M CF_3SO_3H. (A) Ce(IV) consumption. The first spectrum (red) is 14 s after Ce(IV) addition and the last (orange) is at 1612 s. (B) After Ce(IV) consumption, decay of oxidized catalyst to back to $[(H_2O)Ru^{IV}ORu^{III}(OH_2)]^{5+}$ with λ_{max} = 445 nm. The first spectrum (black) is 1612 s and the last spectrum is 6545 s.

Kinetics of Ce(IV) loss were monitored during the catalytic cycle by absorbance-time measurements at 360 nm, Figure 3.35. Two regions of Ce(IV) loss were observed, both display kinetics that are zero order in Ce(IV). The faster, first process coincides with loss of ~65% of the initial Ce(IV) added with the remainder being consumed in the second stage. A species was a similar absorption spectrum to $[(H_2O)Ru^{IV}ORu^{III}(OH_2)]^{5+}$ is the steady state intermediate at early times. This species, intermediate **IV**, has a λ_{max} at 448 nm and is in acid-base equilibrium with its deprotonated form at λ_{max} = 493 nm, pH 1. Conversion to **IV** also occurs by addition of 1 eq. of Ce(IV) to $Ru^{IV}ORu^{III}$ in 1.0 CF_3SO_3H, a redox titration then required 2 eq. of $Fe(aq)^{2+}$ to reduce the intermediate to $[(H_2O)Ru^{III}ORu^{III}(OH_2)]^{4+}$. These results indicate that intermediate **IV** is a pH dependent $Ru^{IV}ORu^{IV}$ species.

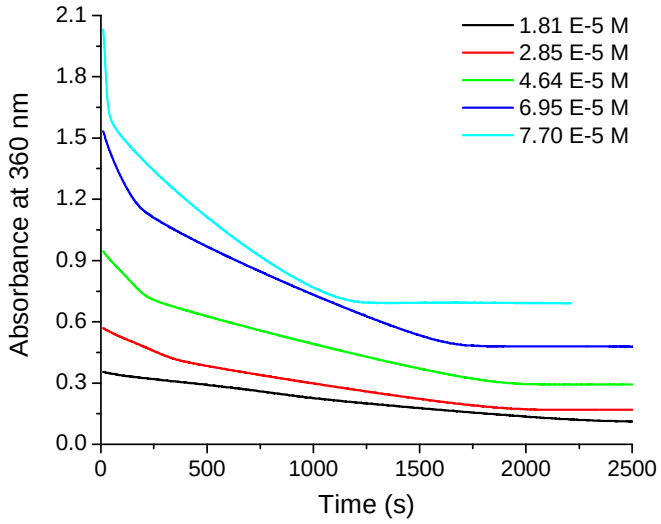

Figure 3.35. Following Ce(IV) consumption at 360 nm, addition of 30 eq. Ce(IV) with respect to 5.0 x 10^{-5} M blue dimer to different concentrations of $[(H_2O)Ru^{III}ORu^{III}(OH_2)]^{4+}$ in 1.0 M CF_3SO_3H.

The zero order dependence on Ce(IV) is obvious from the linear Ce(IV) decay observed at 360 nm. The second order dependence on blue dimer, however, is not. Figure 3.36 provides the linear fits to the faster, first stage of Ce(IV) consumption and the linear plot of k_{obs} (M s^{-1}) determined from these slopes vs. the square of blue dimer concentration. A rate constant of 1.15 x 10^3 $M^{-1}s^{-1}$ is measured for the first stage of Ce(IV) loss which lasts for the first ~100 s. First order kinetics for this process, k = 4 x 10^{-2} s^{-1}, were reported incorrectly in a previous publication.[8]

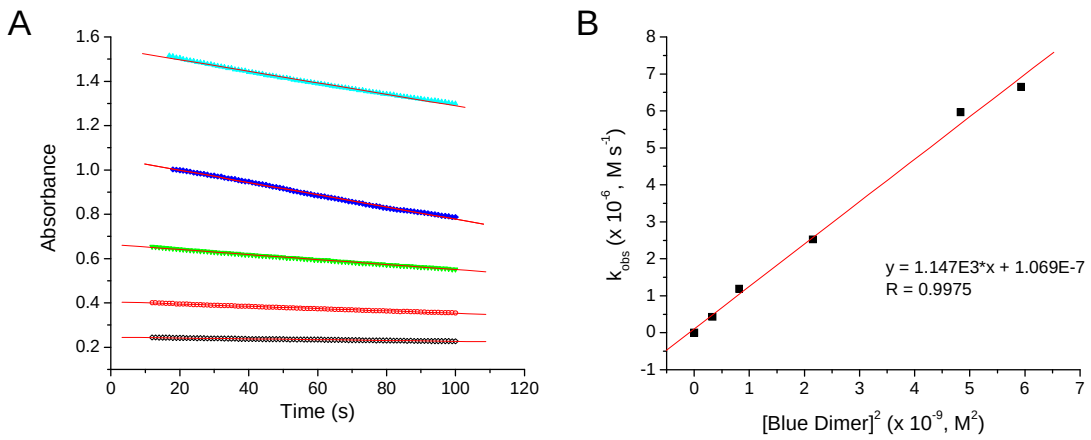

Figure 3.36. (A) Linear fits of first kinetic stage of Ce(IV) consumption in 1.0 M CF_3SO_3H, zero order in Ce(IV). (B) Plot of k_{obs} (x 10^{-6}, M s^{-1}) (from (A)) vs. [Blue Dimer]^2 (x 10^{-9}, M^2), k = 1.15 x 10^3 $M^{-1}s^{-1}$. Legend: Teal = 7.70 x 10^{-5} M, Blue = 6.95 x 10^{-5} M, Green = 4.64 x 10^{-5} M, Red = 2.85 x 10^{-5} M, Black = 1.81 x 10^{-5} M.

The remaining ~35% of Ce(IV) is also consumed in kinetics that are zero order in Ce(IV) but at a rate that is first order in blue dimer. Linear fits and a plot of k_{obs} (M s^{-1}) vs. blue dimer are given in Appx. B Figure S24. This slower process occurs with k(23 °C) = 0.012 s^{-1} (note: this value was reported ~2 times slower in a previous publication,[8] because the wrong value for the molar extinction coefficient of Ce(IV) was used) and coincides with a spectral shift from λ_{max} = 448 nm (**IV**) in the first stage of Ce(IV) consumption to a broad maximum at ~476 nm.

Kinetics of Ce(IV) consumption were investigated at higher dimer concentrations to further understand the second order dependence on catalyst. Pseudo-zero order Ce(IV) consumption is observed when monitoring Ce(IV) loss at 360 nm, shown in Figure 3.37A. Mixed kinetics and convoluted absorption spectra vs. time occur at these concentrations. It appears that a mixture of intermediate **IV** and the species with λ_{max} at 488 nm are present at the catalytic steady state. A second order rate constant, k = 1.5 $M^{-1}s^{-1}$, is calculated from Figure 3.37B. Reasonable linear fits of the absorption vs. time traces are provided in Appx. B

Figure S25. A greater percentage of the anated species, $[(CF_3O_2SO)Ru^{IV}ORu^{IV}(OH)]^{4+}$, was also present at the end of Ce(IV) consumption in these experiments. Thus, the cited rate constant is complicated by mixed kinetics and formation of the anated species.

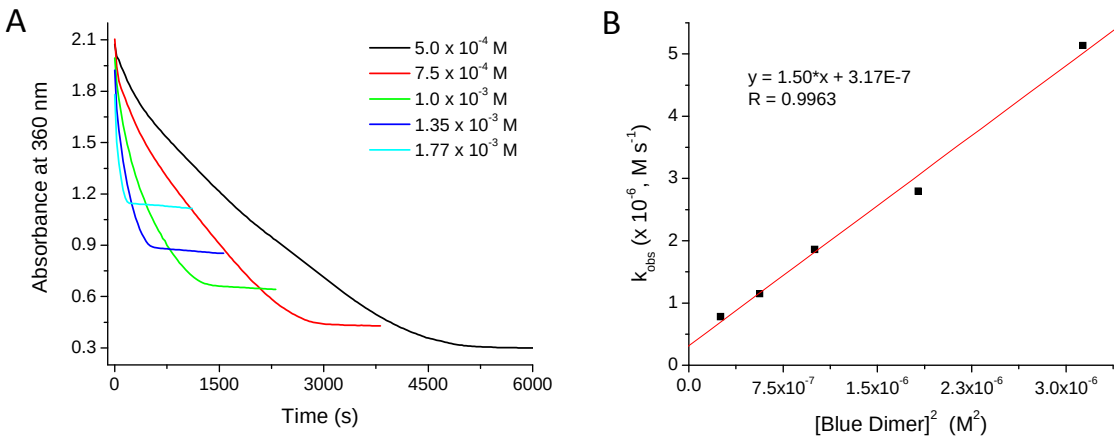

Figure 3.37. (A) Ce(IV) consumption followed at 360 nm. Addition of 30 eq. of Ce(IV) with respect to 0.001 M blue dimer was added to different catalyst concentrations, ranging from 5.0 x 10^{-4} M to 1.77 x 10^{-3} M. (B) A plot of k_{obs} (M s^{-1}) vs. the concentration of blue dimer squared (M^2).

Reappearance of $Ru^{IV}ORu^{III}$. Following the appearance of the mixture of $[(O)Ru^{IV}ORu^{V}(O)]^{3+}$ and $[(F_3CO_2SO)Ru^{IV}ORu^{IV}(OH)]^{4+}$, absorption spectral changes with time over a period of ~90 min gave quantitative reappearance of $Ru^{IV}ORu^{III}$ with λ_{max} = 445 nm. Observations in 1.0 M CF_3SO_3H were similar to those in 0.1 M HNO_3. When monitored at 1100 nm in the near IR, where only $Ru^{IV}ORu^{III}$ absorbs, k(23 °C) = 2.0 x 10^{-3} s^{-1}. (Kinetics are shown in Appx. B, Figure S26.) This rate constant is presumably the sum of rate constants for decomposition of the species at 488 nm and for aquation of the triflato intermediate, both concomitant with water oxidation/O_2 evolution.

II.7. Ce(IV) consumption in 1.0 M $HClO_4$.

Kinetics for Ce(IV) consumption in 1.0 M $HClO_4$ were similar to those measured in 1.0 M CF_3SO_3H, with some important differences to note. Shown in Figure 3.38 are spectra vs. time for the addition of 30 eq. of Ce(IV) to 5.0 x 10^{-5} M $[(H_2O)Ru^{IV}ORu^{III}(OH_2)]^{5+}$ in 1.0 M $HClO_4$.

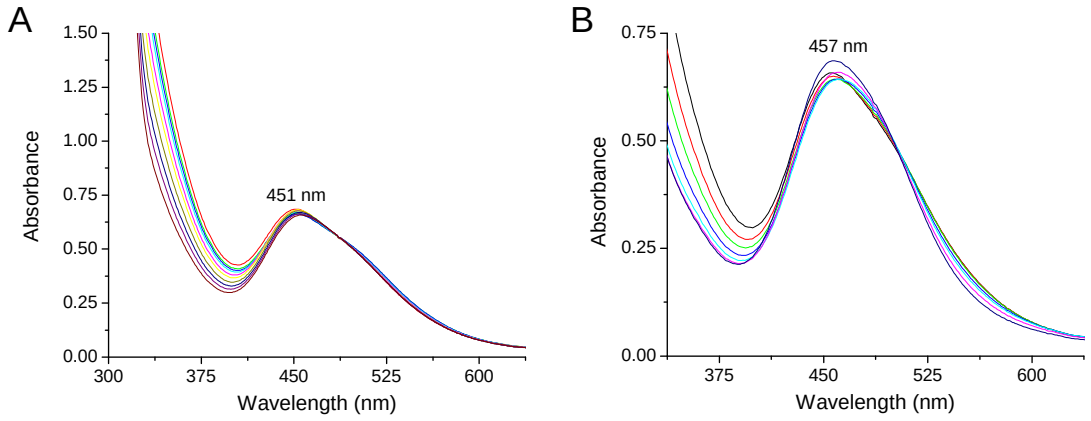

Figure 3.38. Addition of 30 eq. of Ce(IV) to 5.0 x 10^{-5} M blue dimer in 1.0 M $HClO_4$. (A) First spectrum (red) at time = 12 s after adding Ce(IV), last spectrum – 420 s. (B) Same experiment, time: 420 s to 920 s. Complete decay back to $Ru^{IV}ORu^{III}$ is provided in Appx. B Figure S27.

Monitoring at 360 nm revealed two stages of Ce(IV) consumption, both zero-order with respect to Ce(IV), and shown in Figures 3.39,40 and Appx. B Figure S28. The catalytic oxidation of water was investigated by addition of 17-100 eq. of Ce(IV) to solutions of $Ru^{IV}ORu^{III}$ (3.0 x 10^{-5} – 8.0 x 10^{-4} M) in 1.0 M $HClO_4$. A species analogous to intermediate **IV** with λ_{max} = 448 nm appears to be the steady state species at very early times following Ce(IV) addition. In retrospect, oxidation of $Ru^{V}ORu^{IV}$ in 1.0 M $HClO_4$ with an excess of Ce(IV), Figure 3.5, produced this species. Rapidly, however, the steady state intermediate ends up, as shown in Figure 3.37A, with λ_{max} = 451 nm. This is in contrast to the much

longer lived steady state intermediate **IV** in 1.0 M CF_3SO_3H and associated Ce(IV) loss. Recall from Figure 3.11, the acidic form of intermediate **I** also has a λ_{max} at 451 nm.

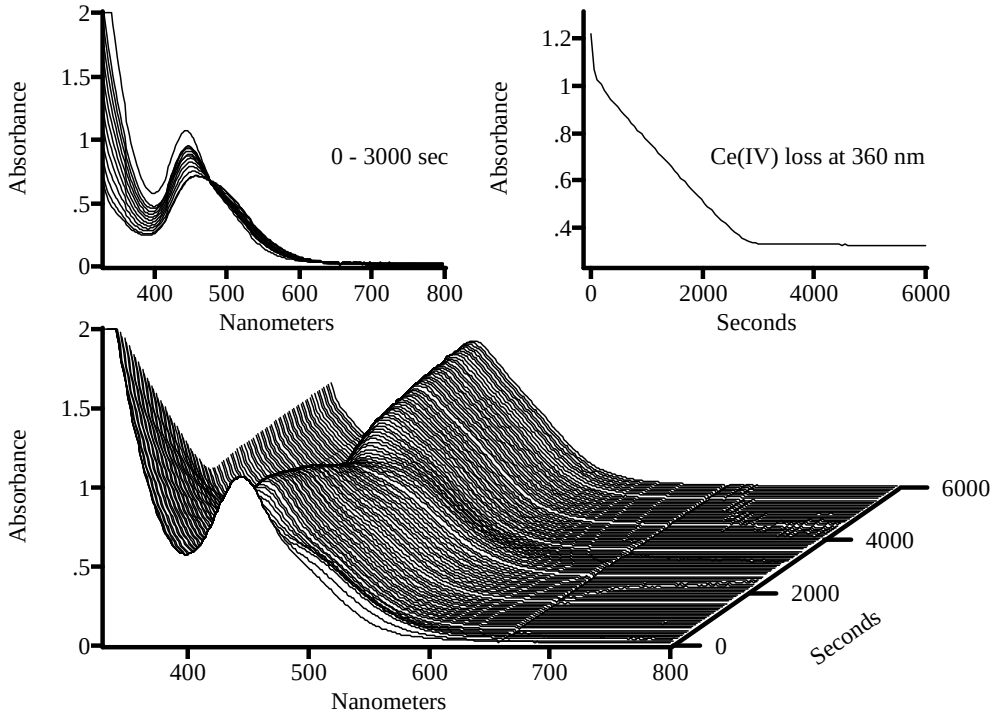

Figure 3.39. Addition of 39 eq. of Ce(IV) to 5.0 x 10^{-5} M $[(HO)Ru^{IV}ORu^{III}(OH_2)]^{4+}$ in 1.0 M $HClO_4$ and following the decay of the intermediate after Ce(IV) has been consumed.

The mixture of species generated after all Ce(IV) was consumed is shown in Figures 3.36B,37. With a λ_{max} at ~455 nm, this is presumably the perchlorate analogue, $[(ClO_4)Ru^{IV}ORu^{IV}(OH)]^{4+}$, of intermediate **III**, discussed earlier with coordinate nitrate or triflate. The decay of these oxidized blue dimer intermediates occurs as previously seen in 1.0 M CF_3SO_3H.

Linear fits of the second stage of Ce(IV) consumption are shown in Figure 3.38, and the associated kinetics correspond to a first order dependence on blue dimer. The first stage of Ce(IV) consumption can be found in Appx. B Figure S28. However, this first stage of Ce(IV) consumption is faster than in 1.0 M CF_3SO_3H and too few data points were collected

to accurately determine the dependence on catalyst concentration. Given the similarity between the steady state species and kinetics of Ce(IV) consumption, it is probable that the first stage in 1.0 M $HClO_4$ also has a second order dependence on blue dimer, i.e. Figure 3.36.

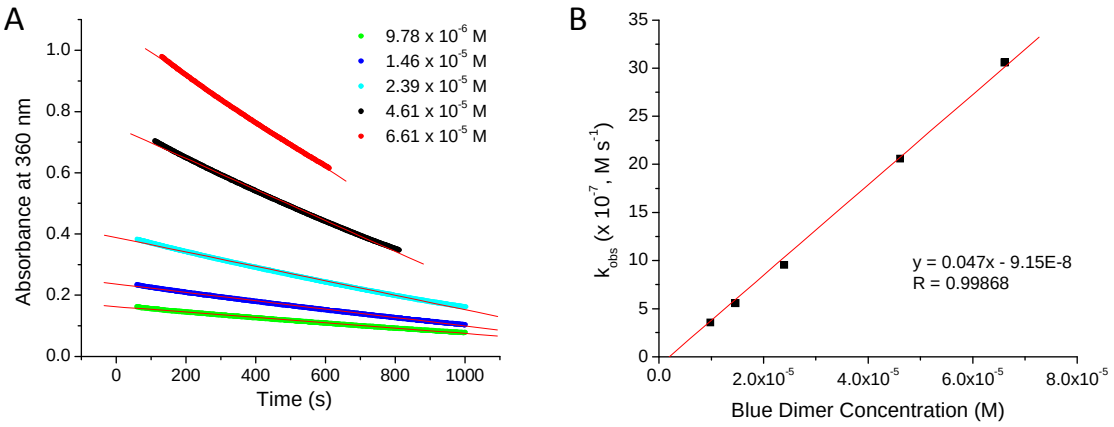

Figure 3.40. Second stage of zero-order Ce(IV) consumption in 1.0 M $HClO_4$, monitoring the absorbance at 360 nm. (A) Addition of 30 eq. of Ce(IV) with respect to 5.0 x 10^{-5} M blue dimer to different catalyst concentrations. Linear fits are shown. (B) A plot of k_{obs} (M s^{-1}), obtained from linear fits shown in (A), vs. Blue Dimer concentration (M). k = 0.047 s^{-1}.

Lei and Hurst report pseudo-zero order slopes at pH 0 for a second stage of Co(III) consumption by the blue dimer with rate constants of 0.01 s^{-1} (CF_3SO_3H) and 0.025 s^{-1} ($HClO_4$) that were linearly dependent on [dimer].[31] This precludes the effect originating from an interaction between the catalyst and Ce(IV). Rate constants measured using Ce(IV) are 0.012 s^{-1} (CF_3SO_3H) and 0.047 s^{-1} ($HClO_4$) in this report, qualitatively consistent with those reported by Hurst.

II.8. Anion involvement. Water oxidation with added CF_3SO_3Li in 0.1 M CF_3SO_3H. It is clear than anions are heavily involved, often to the detriment of catalyst activity, in water oxidation by the blue dimer. First order kinetics (zero order in Ce(IV)) were not observed in

1.0 M or 0.1 M HNO_3, nor with added KNO_3. Catalytic water oxidation under these conditions, as well as in 0.1 M $HClO_4$ and 0.1 M CF_3SO_3H, occurred instead by second order kinetics (first order in Ce(IV)). In each of these cases, anion involvement was limited to intermediate **III**, $[(X)Ru^{IV}ORu^{IV}(OH)]^{4+}$, with λ_{max} ~ 455 nm and X = NO_3^-, $CF_3SO_3^-$, or ClO_4^-. On the other hand, zero-order kinetics in Ce(IV) and the appearance of intermediate **IV**, λ_{max} = 448 nm, dominates at early times in 1.0 M CF_3SO_3H and 1.0 M $HClO_4$. To explore the possible role of anation, as well as the dependence on the nature of the anion, blue dimer catalyzed Ce(IV) water oxidation was studied in 0.1 M CF_3SO_3H with added CF_3SO_3Li (analogous to the KNO_3 experiments, Appx. B Figure S19). The reactions with added lithium triflate are provided in Appx. B Figure S29. Figure 3.39 shows the absorbance vs. time traces following Ce(IV) consumption at 360 nm.

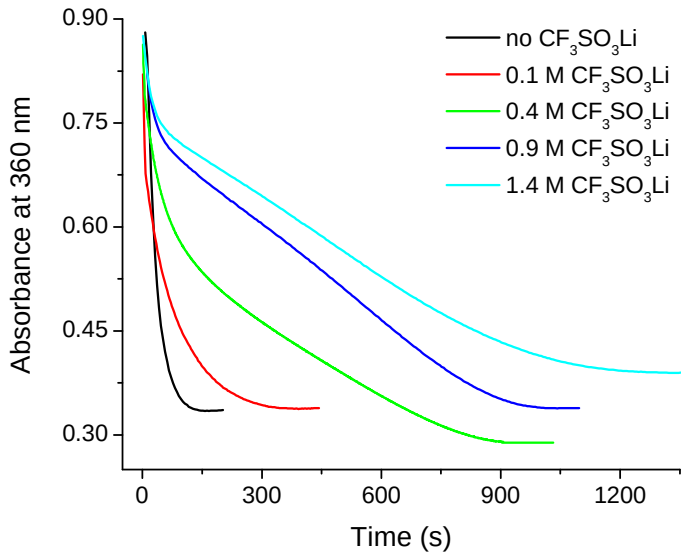

Figure 3.41. Addition of 30 eq. of Ce(IV) to 5 x 10^{-5} M blue dimer in 0.1 M CF_3SO_3H with increasing amounts of CF_3SO_3Li, monitoring Ce(IV) consumption at 360 nm.

Two stages of Ce(IV) consumption are observed, each zero-order with respect to Ce(IV), and only at high concentrations of added CF_3SO_3Li.

Significant interaction between oxidized blue dimer species and $Ce^{III}(NO_3)_6^{3-}$.

The rate of anation was shown to have a first order dependence on $[NO_3^-]$. In an attempt to unravel the contribution to anation of the blue dimer by anions associated with the Ce(IV), water oxidation was studied in the presence of added $Ce^{III}(NO_3)_6^{3-}$. The trianion is produced following oxidation of the blue dimer by $(NH_4)Ce^{IV}(NO_3)_6$. To allow comparison to the earlier study with added KNO_3, a proportional concentration of Ce(III) was added with respect to NO_3^-, i.e. 0.1 M KNO_3 is to 0.0167 M $Ce^{III}(NO_3)_6^{3-}$, 1.4 M KNO_3 is to 0.233 M $Ce^{III}(NO_3)_6^{3-}$, etc. Spectra vs. time are shown in Figure 3.42 for the addition of 30 eq. of Ce(IV) to 5.0 x 10^{-5} M blue dimer in 0.1 M HNO_3 and 0.233 M $Ce^{III}(NO_3)_6^{3-}$ added. Additional experiments with added Ce(III) are provided in Appx. B Figure S30.

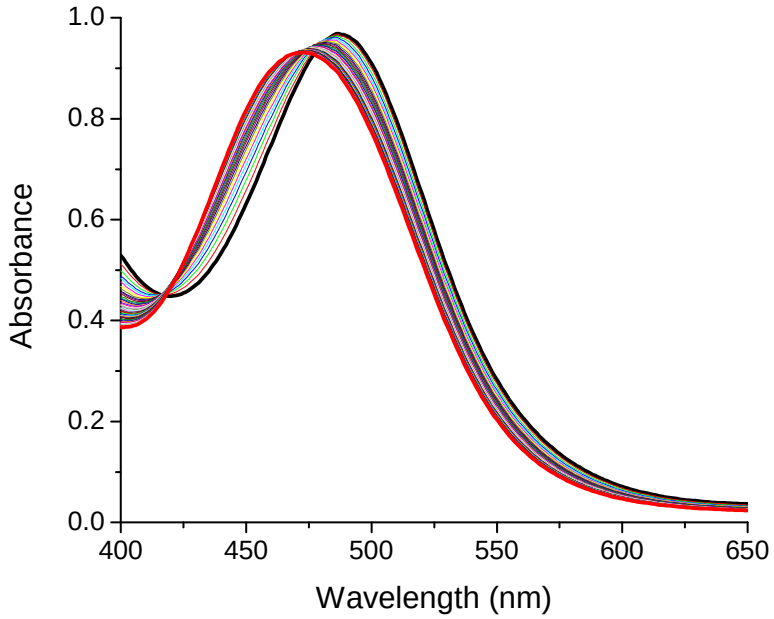

Figure 3.42. Addition of 30 eq. of Ce(IV) to 5.0 x 10^{-5} M $[(H_2O)Ru^{III}ORu^{III}(OH_2)]^{4+}$ in 0.1 M HNO_3 with 0.233 M added $Ce^{III}(NO_3)_6^{3-}$, spectra from 10 s after Ce(IV) addition to 16520 s, 330 s between spectra.

Soon after the addition of Ce(IV), a steady state intermediate appears with λ_{max} = 488 nm. Ce(IV) consumption is significantly slower relative to the analogous experiment without

added Ce(III). The rate slows with added Ce(III) until saturation kinetics are observed. Kinetics for Ce(IV) consumption exhibited mixed kinetics, but the same rate was measured with 0.15 M added Ce(III) compared to 0.233 M Ce(III). Intermediate **III**, $[(O_2NO)Ru^{IV}ORu^{IV}(OH)]^{4+}$, was not readily apparent. In Figure 3.42, the first spectrum has a λ_{max} at 488 nm and the last spectrum is broad with λ_{max} = 472 nm. Formation of the rate-limiting species at 488 nm occurred after several water oxidation cycles as determined by unsuccessful efforts to generate the intermediate with increasing amounts of stoichiometric Ce(IV) additions.

Additional evidence for anation.

The evidence for anion coordination is inferential but similar observations are made under catalytic water oxidation conditions in HNO_3, CF_3CSO_3H, and $HClO_4$. The appearance of intermediates containing nominally non-coordinating anions is a kinetic phenomenon. They are unstable on the long term toward anion loss and water oxidation and do not form spontaneously in solution. There is precedence for anion coordination with other anions in stable species identified crystallographically with NO_2^-, SO_4^{2-}, and Cl^-.[18,21,32] The mono- and di-substituted complexes, $[(H_2O)Ru^{III}ORu^{III}(Cl)]^{3+}$ and $[(Cl)Ru^{III}ORu^{III}(Cl)]^{2+}$ have been reported.[27,33]

Electron transfer induced anation by SO_4^{2-}. Absorption spectra of $[(H_2O)Ru^{III}ORu^{III}(H_2O)]^{4+}$ (λ_{max}= 638 nm) in 1 M H_2SO_4 are stable indefinitely without spectral change. Since this complex is known to be relatively substitutionally lable with $t_{1/2}$ ~ 100 s for water exchange,[34] this points to a small formation constant for SO_4^{2-} anation with the equilibrium in eq 8 lying to the left.

$$[(bpy)_2(H_2O)Ru^{III}ORu^{III}(OH_2)(bpy)_2]^{4+} + SO_4^{2-} \rightleftharpoons$$

$$[(bpy)_2(H_2O)Ru^{III}ORu^{III}(OSO_3)(bpy)_2]^{2+} + H_2O \quad (8)$$

Under the same conditions in solutions containing $[(H_2O)Ru^{IV}ORu^{III}(OH_2)]^{5+}$, slow spectral changes occur on a time scale of minutes consistent with slow anation.

Addition of $Ru^{III}ORu^{III}$ in small amounts to $[(H_2O)Ru^{IV}ORu^{III}(OH_2)]^{5+}$ causes the λ_{max} to shift at a measurable rate from 446 nm to 468 nm with a clear isosbestic point at 454 nm, Appx. B Figure S31. As described in Chapter 3.2, the structure of the species which appears at λ_{max}= 468 nm has been determined by XRD to be the bis-sulfato complex, $[(bpy)_2(SO_4)Ru^{IV}ORu^{III}(SO_4)(bpy)_2]^{+}$.

The appearance of the bis-sulfato complex follows a rate law that is first order in $Ru^{III}ORu^{III}$ and first order in sulfate with k(23 °C) = 1.2×10^{-3} $M^{-1}s^{-1}$ but independent of $[Ru^{IV}ORu^{III}]$. These observations are consistent with rate limiting substitution by SO_4^{2-} in $Ru^{III}ORu^{III}$, eq 9,

$$[(bpy)_2(H_2O)Ru^{III}ORu^{III}(OH_2)(bpy)_2]^{4+} + SO_4^{2-} \xrightarrow{k(SO_4^{2-})}$$

$$[(bpy)_2(H_2O)Ru^{III}ORu^{III}(SO_4)(bpy)_2]^{2+} + H_2O \quad (9)$$

followed by electron transfer to give the $Ru^{IV}ORu^{III}$ mono-sulfato complex, eq 10,

$$[(bpy)_2(H_2O)Ru^{III}ORu^{III}(SO_4)(bpy)_2]^{2+} + [(bpy)_2(HO)Ru^{IV}ORu^{III}(OH_2)(bpy)_2]^{4+} + H^+$$

$$\xrightarrow{rapid} [(bpy)_2(H_2O)Ru^{III}ORu^{IV}(SO_4)(bpy)_2]^{3+} +$$

$$[(bpy)_2(H_2O)Ru^{III}ORu^{III}(OH_2)(bpy)_2]^{4+} \quad (10)$$

Given the influence of anation on potentials for the $Ru^{IV}ORu^{III}/Ru^{III}ORu^{III}$ couple, the electron transfer reaction is spontaneous. For example $E^{o\prime}$ for the $Ru^{IV}ORu^{III}/Ru^{III}ORu^{III}$ couple of $[(bpy)_2(py)Ru^{III}ORu^{III}(py)(bpy)_2]^{4+}$ is ~0.6 V more positive than for $[(bpy)_2(Cl)Ru^{III}ORu^{III}(Cl)(bpy)_2]^{2+}$ in CH_3CN.[29]

The final product is the disulfato complex with no sign of buildup of the mono-sulfato complex as an intermediate. This shows that there is a second even more rapid catalyzed reaction involving addition of a second SO_4^{2-}, eq 11.

$$[(bpy)_2(H_2O)Ru^{III}ORu^{IV}(SO_4)(bpy)_2]^{3+} + SO_4^{2-} \rightarrow [(bpy)_2(SO_4)Ru^{III}ORu^{IV}(SO_4)(bpy)_2]^{+} + H_2O \quad (11)$$

There was no sign of electron transfer induced anation for non-coordinating anions, NO_3^-, ClO_4^- and $SO_3CF_3^-$ under similar conditions. This adds mechanistic significance to the observation that anated intermediates such as $[(O_2NO)Ru^{IV}ORu^{IV}(OH)]^{4+}$ appear late in catalytic cycles following addition of excess Ce(IV), as described in the sections above.

II.9. Rate constant summary. In order to facilitate discussion of the results obtained in the mixing experiments, a summary of rate constants obtained in the study are listed in Table 3.4.

Table 3.4. Summary of rate constants in addition to Table 3.3 (23 ± 2 °C).

Reaction	*k*	Medium
$2\ Ru^{IV}ORu^{IV}\text{-}X \rightarrow Ru^{IV}ORu^{III} + Ru^{V}ORu^{IV} + 2\ X^-$	$1.15 \times 10^3\ M^{-1}s^{-1}$	1.0 M CF_3SO_3H
second region of Ce(IV) consumption	$0.012\ s^{-1}$	1.0 M CF_3SO_3H
second region of Ce(IV) consumption	$0.047\ s^{-1}$	1.0 M $HClO_4$
$2\ [(O)Ru^{V}ORu^{IV}(O)]^{3+} \rightarrow \{Ru^{IV}ORu^{IV}\} + \{Ru^{V}ORu^{V}\}$	$5.34\ M^{-1}s^{-1}$	0.1 M pH 5.8 PBS
$2\ [(O)Ru^{V}ORu^{IV}(O)]^{3+} \rightarrow \{Ru^{IV}ORu^{IV}\} + \{Ru^{V}ORu^{V}\}$	$5.95\ M^{-1}s^{-1}$ (avg.)	0.1 M HNO_3
$[(O)Ru^{V}ORu^{IV}(O)]^{3+} + Ce(IV) \rightarrow \{Ru^{V}ORu^{V}\} + Ce(III)$	$220\ M^{-1}s^{-1}$	0.1 M HNO_3
$[(O)Ru^{V}ORu^{IV}(OH)]^{4+} + Ce(IV) \rightarrow \{Ru^{V}ORu^{V}\} + Ce(III)$	$80\ M^{-1}s^{-1}$	1.0 M HNO_3
$[(O_2NO)Ru^{IV}ORu^{IV}(OH)]^{4+} \rightarrow \{Ru^{IV}ORu^{IV}\}$	$8.0 \times 10^{-5}\ s^{-1}$	1.0 M HNO_3
$[(O_2NO)Ru^{IV}ORu^{IV}(OH)]^{4+} \rightarrow \{Ru^{IV}ORu^{IV}\}$	$6.91 \times 10^{-5}\ s^{-1}$	0.1 M HNO_3
$[(HOO)Ru^{III}ORu^{IV}(OH)]^{3+} \rightarrow [(L)Ru^{III}ORu^{IV}(OH)]^{4+} + H_2O_2$	$4.0 \times 10^{-5}\ s^{-1}$	0.1 M HNO_3

III.1. Electrochemistry.

There has long been a discrepancy in the sequence of observable redox states reported in the oxidative activation of the blue dimer. As described above, blue dimer mixing experiments with Ce(IV) as the chemical oxidant have revealed the presence of an intermediate between the $[Ru^{IV}ORu^{III}]^{n+}$ and $[Ru^{V}ORu^{IV}]^{n+}$ states. Scheme 3.2 illustrates the detectable redox states of the blue dimer as reported by Hurst in 0.5 M CF_3SO_3H.

Scheme 3.2. $E_{1/2}$ potentials in 0.5 M CF_3SO_3H, given in V vs. Ag/AgCl.

$$\{3,3\} \xrightarrow[0.87\ V]{-1e^-} \{3,4\} \xrightarrow[1.32\ V]{-1e^-} \{4,4\} \xrightarrow[1.39\ V]{-2e^-} \{5,5\}$$

This is in contrast to the electrochemical behavior depicted in the $E_{1/2}$-pH diagram, Figure 3.1, in which oxidation to $[(O)Ru^{V}ORu^{V}(O)]^{4+}$ below pH ~2.5 proceeds through a $1e^-$ oxidation step ($Ru^{IV}ORu^{III}/Ru^{III}ORu^{III}$) followed by a $3e^-$ process ($Ru^{V}ORu^{V}/Ru^{IV}ORu^{III}$), and at pH > ~2.5, a 1:2:1 electron transfer sequence is observed with {4,4} unstable with respect to disproportionation. There is no reason to doubt that a genuine $Ru^{V}ORu^{V}/Ru^{V}ORu^{IV}$ redox couple is observed above pH ~2.5, measured as a pH-independent wave with an average value of 1.22 V vs. Ag/AgCl.[16,27]

Substantial spectroscopic and kinetic evidence for an anated $Ru^{IV}ORu^{IV}$ state explains the seemingly contradictory results. The accumulation of $Ru^{V}ORu^{IV}$ as a metastable intermediate in mixing experiments with Ce(IV) is primarily a concentration effect where typical dimer concentrations studied by absorption spectroscopy (x 10^{-5} M) are two orders of magnitude lower than those used in electrochemical studies (x 10^{-3} M). These high concentrations result in rapid disproportionation. The closely spaced redox couples make it difficult to observe well-defined waves or to generate a single intermediate electrolytically.

Furthermore, slow electron transfer kinetics associated couples involving PCET, e.g. oxidation of $Ru^{IV}ORu^{III}$ (k(0.1 M $HClO_4$) = 3.24 $M^{-1}s^{-1}$, Table 3.3), can introduce skewed redox waves and large overpotentials.[16,30,35,36]

Despite these challenges, a numerical simulation of the reported redox potentials reconciles the two electrochemical studies. Converting Hurst's potentials[37,38] to the SCE reference scale (+0.83, +1.28, +1.35 V) for ease of comparison with the original CVs from the Meyer lab and redefining the oxidation sequence to successive $1e^-$ steps, we can then add the Meyer lab's measured $Ru^{V}ORu^{V}/Ru^{V}ORu^{IV}$ pH-independent $1e^-$ wave[16,27] (+1.17 V) to complete the $4e^-$ activation. Note: there is agreement on the nature of the $Ru^{IV}ORu^{III}/Ru^{III}ORu^{III}$ couple and its redox potential. Inputting the simulation parameters in DigiSim, accounting for Hurst's conditions (pH 0.3), and calculating the cyclic voltammogram for a scan rate of 20 mV/s produces a CV, Figure 3.43, just where it should be based on the pourbaix diagram. See Figure 3.44 for an experimentally determined cyclic voltammogram in strong acid.

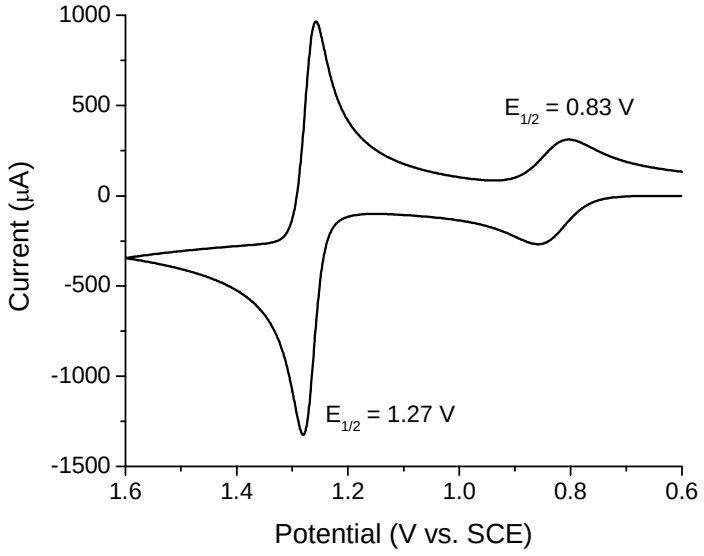

Figure 3.43. A simulated cyclic voltammogram of the blue dimer at pH 0.3, scan rate = 20 mV/s. Details of the simulation, using DigiSim, are available in Appx. B Figure S32.

There is excellent agreement between the two sets of electrochemical data obtained in different ways. The Hurst and Meyer lab results are complementary and self-consistent with each other. In fact, Hurst and coworkers recently came to the same conclusion in fitting a redox titration curve obtained from a rapid controlled potential electrolysis technique at low pH (< 2). The titration curve for the apparent 3 e^- wave from $Ru^{IV}ORu^{III}$ to $Ru^{V}ORu^{V}$ was non-Nernstian and could only be fit by assuming that two closely-spaced redox steps are involved "whose redox potentials [differ] by less than 60 mV".[24]

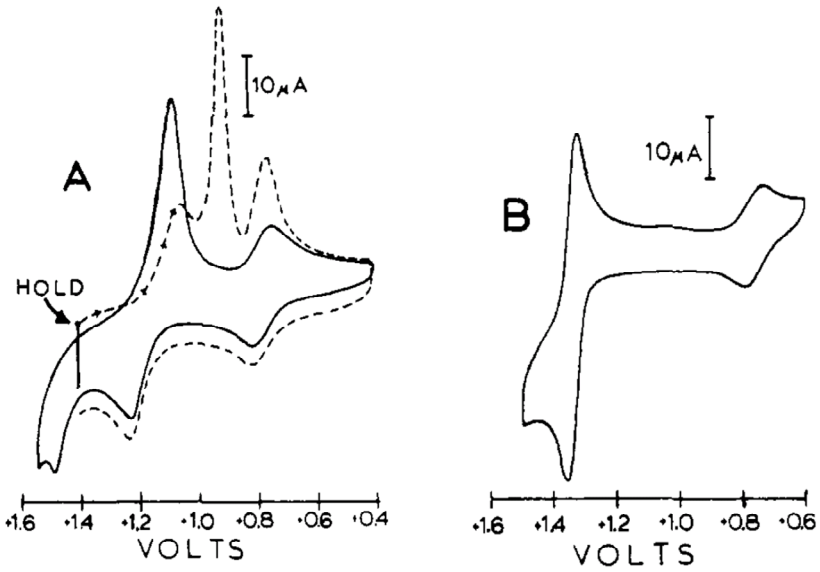

Figure 3.44.[16] Cyclic voltammograms of the blue dimer (8 x 10^{-4} M) in (A) 0.1 M $HClO_4$ (the dashed curve was measured after holding the potential at 1.4 V for 3 minutes, then scanning reductively) and (B) 3 M $HClO_4$. The scan rate is 20 mV/s for each CV.[16]

Figure 3.44A provides evidence of a new intermediate forming upon oxidation through the 3e^- wave. In one of the CVs (dashed line), the potential is first held at 1.4 V for 180 s before scanning reductively. The irreversible nature of the CV is obvious, and the three reductive peaks must originate from a new intermediate that has formed. In the other CV (solid line), an irreversible wave appears *after* the 3e^- wave at ~1.45 V that points to catalytic

oxidation of a new intermediate barring the unlikelihood of a $Ru^{VI}ORu^{V}/Ru^{V}ORu^{V}$ couple.[16] There has been no evidence for a thermodynamically accessible oxidation state beyond $Ru^{V}ORu^{V}$ in optical or resonance Raman spectroelectrochemical flow-cell experiments.[37] Oxidation to $[(O)Ru^{VI}ORu^{V}(O)]^{5+}$ is unattractive considering oxo formation has already occurred, charge compensating proton loss is no longer possible, and based on the known instability of *cis*-Ru^{VI} bis-oxo complexes.[8,39-42] In $[(H_2O)_2(tpy)Ru\text{-}O\text{-}Ru(tpy)(OH_2)_2]^{4+}$ (where tpy is 2,2':6',2"-terpyridine), for example, cleavage of the μ-oxo bridge is observed after oxidation to Ru^{VI} (accessible due to two aqua ligands at each metal center) and electronic considerations favoring isomerization to Ru^{VI} *trans* di-oxo.[43]

The redox titration with $Fe_{(aq)}^{2+}$ is ambiguous in distinguishing intermediate **I** from $[(O)Ru^{V}ORu^{V}(O)]^{4+}$, and even the pH dependence is not definitive as Hurst and coworkers have proposed protonation of this species at the μ-oxo bridge at pH 0, which they identify as the $Ru^{V}ORu^{V}$.[44,45] What then is the mechanistic fate of the catalytically-active $[(O)Ru^{V}ORu^{V}(O)]^{4+}$ species in water oxidation?

III.2. Catalytic water oxidation by $[(O)Ru^{V}ORu^{V}(O)]^{4+}$. Shown in Figure 3.45 are proposed pathways of water oxidation by the $Ru^{V}ORu^{V}$ blue dimer.

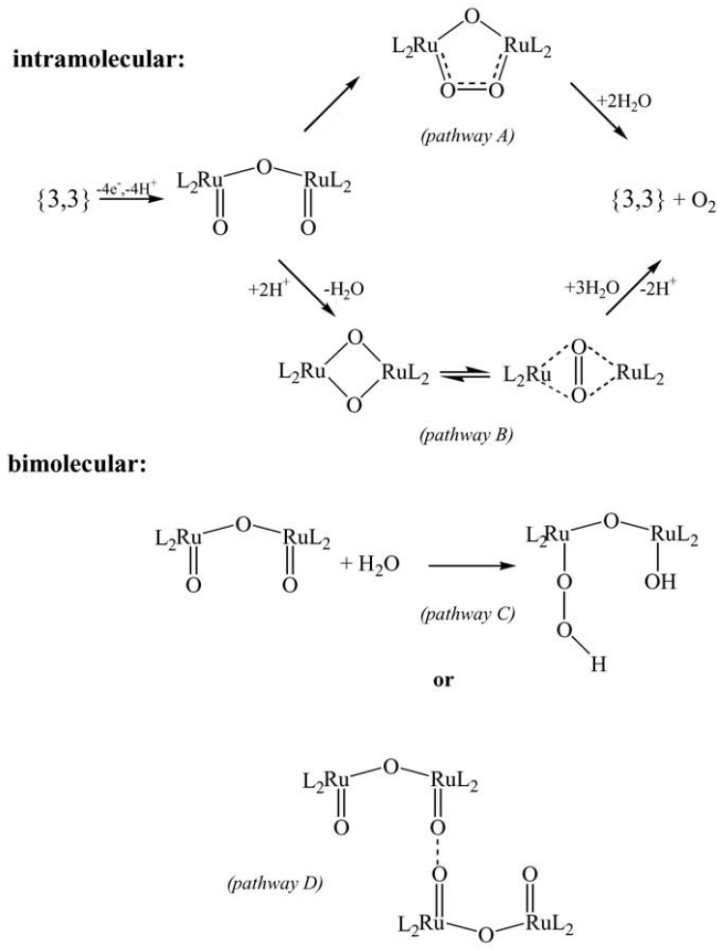

Figure 3.45.[38] Possible pathways for water oxidation by $[(O)Ru^{V}ORu^{V}(O)]^{4+}$.

Critical questions regarding the mechanistic details of the key O··O bond forming step (or steps) have been explored by ^{18}O isotopic labeling studies.[44,46-48] In these experiments, $[(H^{18}O)Ru^{IV}ORu^{III}(^{18}OH_2)]^{4+}$ was prepared, it has a slow rate of ligand substitution,[34] and oxidized with Ce(IV) in water of normal isotopic composition before H_2O exchange with solvent had occurred. A number of intramolecular and bimolecular oxo-oxo coupling pathways have been considered (Figure 3.45), as well as nucleophilic solvent attack at Ru^{V}=O, reminiscent of the O··O coupling step proposed in the Oxygen Evolving Complex of natural photosynthesis (see Chapter 1).

Hurst and coworkers established that there is no isotopic exchange at the μ-oxo bridge site under catalytic conditions using Ce(IV).[37,45] This eliminates *path b* from contention. Analyses of the isotopic distributions of dioxygen following the experiments showed that pathways in which both oxygens originate from the coordination sphere of the catalyst are negligible, *paths a* and *d*. Interestingly, the results indicate that two pathways may exist: one, in which one oxygen originates from solvent and the other from the catalyst, and a second, where both oxygens come from the solvent. The former constitutes the dominant pathway in the blue dimer, consistent with *path c*.

Concerns regarding potential oxygen atom transfer pathways involving cerium ions have also addressed.[48] Hydrolysis of aqueous Ce ions could allow oxygen-oxygen bond formation to occur between a blue dimer peroxo complex and a ceric-coordination water ligand, for example, to account for dioxygen in which two solvent waters were incorporated. Hurst and coworkers dismissed this possibility by ^{18}O labeling studies in photochemically-driven water oxidation by the blue dimer. The measured ratio of $^{32}O_2/^{34}O_2$ was identical within experimental error between the Ce(IV)-driven reactions and the photochemical system employing $[Ru(bpy)_3]^{2+}$ and $S_2O_8^{2-}$.[48]

Nucleophilic solvent attack at a single $Ru^V{=}O$ results in the formation of a peroxidic intermediate. Earlier mechanistic studies concluded that the catalytically-active state must be higher than Ru^VORu^{IV},[23,31] that there is no spectroscopic evidence for the buildup of $[(O)Ru^VORu^V(O)]^{4+}$ except under certain conditions where it can be observed as a black precipitate,[49,50] and that O_2 evolves with first order kinetics.[31,47,51] Also, first order kinetics for the reactivity of $[(O)Ru^VORu^V(O)]^{4+}$ have been reported following its generation from the disproportionation of Ru^VORu^{IV}.[25] These observations are compatible with nucleophilic

solvent attack to form a peroxo complex, where water is in pseudo-first order excess. On this basis, we identify intermediate **I** with λ_{max} = 482 nm as a peroxidic intermediate, the result of rapid reactivity with water by $[(O)Ru^{V}ORu^{V}(O)]^{4+}$. The stoichiometric experiments with added Ce(IV) show that the intermediate is $3e^-$ oxidized relative to $Ru^{IV}ORu^{III}$ and thus $4e^-$ relative to $Ru^{III}ORu^{III}$. This oxidative stoichiometry is consistent with the redox titration with $Fe_{(aq)}^{2+}$ in which 4 equivalents of Fe^{2+} are required to reduce the intermediate to $[(H_2O)Ru^{III}ORu^{III}(OH_2)]^{4+}$ (2 eq. for the metal centers and 2 eq. for the coordinated peroxo). The intermediate could be $[(O)Ru^{V}ORu^{V}(O)]^{4+}$ although its spectroscopic signatures at λ_{max} = 482 and ~850 nm are significantly different from those observed for the black suspension of the ClO_4^- salt, Figure 3.8.

Kinetic evidence also strongly supports its assignment as a peroxo complex capable of further oxidation rather than a long-lived $[(O)Ru^{V}ORu^{V}(O)]^{4+}$ with slow first order kinetics for reaction with water. For instance, the use of electron transfer agents of faster electron transfer kinetics than Ce(IV) result in significant rate enhancements for catalytic water oxidation, intermediate **I** remains as the steady state species in these reactions; similar enhancements are observed electrochemically.[26,30] Consistent with the available evidence, intermediate **I** is a peroxidic intermediate, $[(HO_2)Ru^{III}ORu^{V}(O)]^{3+}$ at pH 1. Based on measurements in 1.0 and 0.1 M CF_3SO_3H, this intermediate is in acid-base equilibrium with its protonated form, presumably $[(HO_2)Ru^{IV}ORu^{IV}(OH)]^{4+}$, eq 12.

$$[(HO_2)Ru^{IV}ORu^{IV}(OH)]^{4+}\ (451\ nm) \rightleftharpoons [(HO_2)Ru^{III}ORu^{V}(O)]^{3+}\ (482\ nm) + H^+ \qquad (12)$$

The oxo formulation is consistent with the appearance of a ν(Ru=O) stretch at 818 cm^{-1} in CF_3SO_3H as observed by Hurst *et al.*[37] The intensity of this band in resonance Raman

spectra of electrolytically-prepared {(O)$Ru^{V}ORu^{V}(O)^{4+}$}, identified as the $Ru^{V}ORu^{V}$ by Hurst and coworkers, identified here as a peroxidic intermediate, eq 12, was "markedly suppressed at acidities below 0.1 M" CF_3SO_3H. From pH titrations of intermediate **I** (λ_{max} = 482 nm), an approximate p*K*a of 0.1 was measured. The acid-base equilibrium shown in eq 12 is consistent with losing intensity of the band assigned to the Ru=O moiety rather than protonation of $[(O)Ru^{V}ORu^{V}(O)]^{4+}$ at the μ-oxo bridge as proposed by Hurst.[44,45]

First order rate constants for disappearance of the intermediate, *k*(0.5 M CF_3SO_3H, 23 ^{o}C) = 9.5 × 10^{-3} s^{-1},[37,47] and *k*(0.1 M HNO_3, 23 C) = 2 x 10^{-3} s^{-1} have been reported.[8] When generated under stoichiometric conditions, the peroxidic intermediate disappears with quantitative conversion to $Ru^{IV}ORu^{III}$. Complex kinetics, however, are clearly involved with the decomposition of this species, Figure 3.13,15. Upon further investigation with rapid mixing techniques to "catch" the full reaction, especially at high dimer concentrations, it was unequivocally determined that the decomposition has multiple kinetic components that dominate the reaction at different times.

The results of an SVD global analysis of the spectra vs. time shown in Figure 3.13 are given in Figures 3.46,47. Intermediate **I** with λ_{max} at 482 nm was generated by addition of 3 eq. of Ce(IV) to $[(HO)Ru^{IV}ORu^{III}(OH_2)]^{4+}$ in 0.1 M HNO_3. Its decay proceeds with a continual growth and shift in λ_{max} of the absorption band at 482 nm back to $[(HO)Ru^{IV}ORu^{III}(OH_2)]$ at λ_{max} = 495 nm, with no obvious intermediates. Simple first and second order kinetic models did not adequately account for the spectral changes vs. time. The same experiment at higher concentrations provides evidence of intermediates between $[(HOO)Ru^{III}ORu^{V}(O)]^{3+}$ and $[(HO)Ru^{IV}ORu^{III}(OH_2)]^{4+}$. Shown in Appx. B Figure S33 is the second order plot exhibiting linear behavior of single wavelength absorbance vs. time data

following the decay of 0.0012 M intermediate **I** in the visible and near IR. A dominant second order process is clearly present in the decay profile at high concentrations.

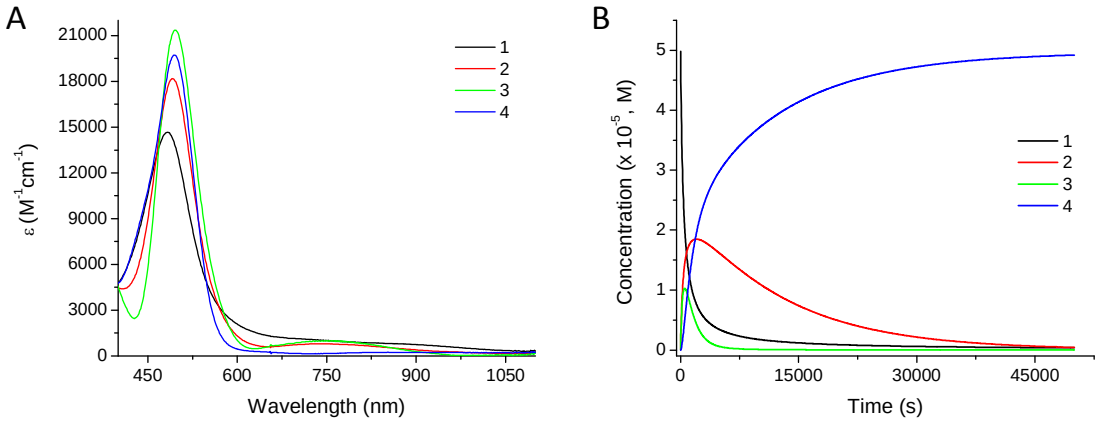

Figure 3.46. Calculated spectra and concentration profiles extracted from singular value deconvolution from the data shown in Figure 3.13: decay of the peroxidic intermediate generated by addition of 3 eq. of Ce(IV) to 5.0 x 10^{-5} M $[(HO)Ru^{IV}ORu^{III}(OH_2)]^{4+}$ in 0.1 M HNO_3.

The kinetic model used to fit the data is initial disproportionation, followed by rate-limiting first order decay of each of the disproportionation products, consistent with the mechanism described in eqs 13-15. Initial disproportion of the peroxidic intermediate occurs, eq 13,

$$2\ [(HOO)Ru^{III}ORu^{V}(O)]^{3+} \rightarrow [(HOO)Ru^{III}ORu^{IV}(OH)]^{3+} + [(^{-}OO)Ru^{IV}ORu^{V}(O)]^{3+} \quad (13)$$

followed by rate limiting first order decay of the resulting species, eq 14 and 15,

$$[(HOO)Ru^{III}ORu^{IV}(OH)]^{3+} + H_2O \rightarrow [(HO)Ru^{IV}ORu^{III}(OH_2)]^{4+} + H_2O_2 \quad (14)$$

$$[(^{-}OO)Ru^{IV}ORu^{V}(O)]^{3+} \rightarrow [(HO)Ru^{IV}ORu^{III}(OH_2)]^{4+} + O_2 \quad (15)$$

Single wavelength fits of the data are given in Figure 3.47.

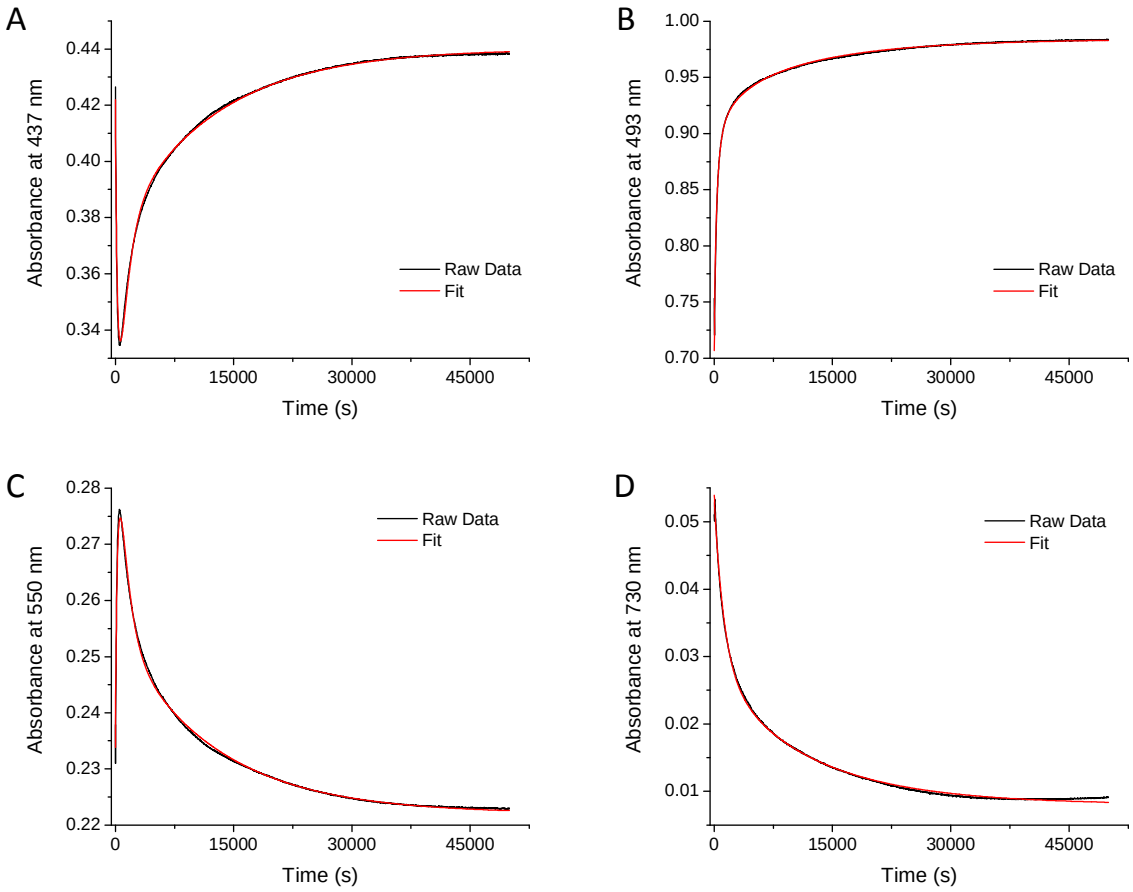

Figure 3.47. Single wavelength fits for data shown in Figure 3.13, using the model described in eqs 15-17. Details of the model can be found in Appx. B Figure S34.

Details of the same reaction with 4.0 x 10^{-4} M blue dimer, modeled with the same mechanism/kinetic processes, are in Appx. B Figures S35-37. The decomposition of reduced peroxide is likely more complex. Intermediate **II**, λ_{max} = 488 nm, is presumably the same intermediate. It builds up over the course of Ce(IV) consumption in 0.1 M H_3O^+ and requires 3 eq. of $Fe_{(aq)}^{2+}$ to be reduced to $[(H_2O)Ru^{III}ORu^{III}(OH_2)]^{4+}$. The pH dependence of this intermediate is presumably, eq 16,

$$[(HOO)Ru^{III}ORu^{IV}(OH_2)]^{4+}\ (451\ nm) \rightleftharpoons [(HOO)Ru^{III}ORu^{IV}(OH)]^{3+}\ (488\ nm) \quad (16)$$

Based on the ligand substitution rates observed for $[(HO)Ru^{IV}ORu^{III}(OH_2)]^{4+}$, $k \leq 10^{-5}$ s^{-1}, oxygen evolution from $[(^{-}OO)Ru^{IV}ORu^{V}(O)]^{3+}$ would be considerably faster allowing $[(HOO)Ru^{III}ORu^{IV}(OH)]^{3+}$ to accumulate in solution during catalytic water oxidation. The distribution of products resulting from its self-reduction to $[(HO)Ru^{IV}ORu^{III}(OH_2)]^{4+}$ are consistent with a lack of necessary oxidative equivalents to enable the release of O_2 cleanly. Rate limiting release of O_2 and replacement with water in the open coordination site would give $[(H_2O)Ru^{III}ORu^{II}(OH_2)]^{3+}$ which would be oxidized rapidly by another $[(HOO)Ru^{III}ORu^{IV}(OH)]^{3+}$ complex due to the instability of $Ru^{III}ORu^{II}$, setting off a series of complex cross reactions. Another possibility is substitution of the coordinated peroxide by an anion or water and subsequent oxidation of the dimer by H_2O_2 in solution to produce the corresponding anated species, $[(X)Ru^{IV}ORu^{IV}(OH)]^{4+}$ and $[(HO)Ru^{IV}ORu^{III}(OH_2)]^{4+}$. There is not enough kinetic information, due to the slow rate-limiting first order decay kinetics of this intermediate, Figures 3.18,19.

Conversion to intermediate **II** (λ_{max} = 488 nm) appears to originate from intermediate **I**, $[(HOO)Ru^{III}ORu^{V}(O)]^{3+}$ during catalysis as well as from the stoichiometric generation of **I**. It is three oxidative equivalents higher than $Ru^{III}ORu^{III}$, meaning that it has to have a coordinated peroxo ligand or that it is a $Ru^{V}ORu^{IV}$ species. The associated decay kinetics of intermediate **II** are not consistent with $[(O)Ru^{V}ORu^{IV}(O)]^{3+}$, nor the distribution of products following its self-reduction or chemical reduction with Fe^{2+}. Furthermore, the slow consumption of Ce(IV), zero-order in Ce(IV), by intermediate **II** (Figure 3.20) is not characteristic of $[(O)Ru^{V}ORu^{IV}(O)]^{3+}$ which consumes Ce(IV) with k(0.1 M HNO_3, 23 °C) ~ 200 $M^{-1}s^{-1}$. An anated $Ru^{V}ORu^{IV}$ could explain these slow kinetics by rate-limiting release of coordinated anion, but intermediate **III**, e.g. $[(O_2NO)Ru^{IV}ORu^{IV}(OH)]^{4+}$, cannot be oxidized

by Ce(IV) to $[(O_2NO)Ru^{IV}ORu^{V}(O)]^{3+}$, see Appx. B Figure S18. We are not sure how an oxidized anated species of this sort could form otherwise, and the redox titration after 1 eq. of Fe(II) would have presumably converted such an intermediate cleanly to $[(O_2NO)Ru^{IV}ORu^{IV}(OH)]^{4+}$ (λ_{max} = 455 nm), but this was not so.

Experiments with added Ce(III) provide strong evidence for an ion-pairing interaction involving the trianion Ce(III) and intermediate **II** (λ_{max} = 488 nm). The intermediate forms after several water oxidation cycles, which is also complicated by the increased in Ce(III) concentration following oxidation of the blue dimer by Ce(IV) in experiments were Ce(III) was not intentionally added to the reaction mixture. Three equivalents of Fe^{2+} are required to reduce this species to $[(H_2O)Ru^{III}ORu^{III}(OH_2)]^{4+}$; however, addition of 2 eq. of Ce(IV) to $[(HO)Ru^{IV}ORu^{III}(OH_2)]^{4+}$ in the presence of excess Ce(III) does not generate the same species. This does not completely rule out the possibility of an ion-paired $[(O)Ru^{V}ORu^{IV}(O)]^{3+}\bullet Ce^{III}(NO_3)_6^{3-}$ species that accumulates during catalysis and behaves differently from $Ru^{V}ORu^{IV}$ generated by stoichiometric Ce(IV) addition. Ion-pairing or binding of cerium ions to the blue dimer has been proposed before based on concentration-dependent resonance Raman spectra of frozen solutions of blue dimer with added Ce(IV).[37]

Finally, the accompanied zero-order Ce(IV) loss kinetics following generation of intermediate **II**, Figures 3.21,22, are only observed in very dilute solutions of blue dimer. This is consistent with slow oxidation of $Ru^{IV}ORu^{III}$ to $Ru^{IV}ORu^{IV}$, generally speaking and described above, Section II.3. Without accumulation of $Ru^{V}ORu^{IV}$ and the necessary comproportionation reaction with $Ru^{IV}ORu^{III}$ to initiate autocatalysis, oxidation is not observed at these concentrations. The Ce(IV) decay profile, absorbance at 360 nm, appears to be exponential even at moderately higher concentrations of catalyst, i.e. 5.0 x 10^{-5} M, but is

complicated by the formation of intermediate **III** which is not oxidized further in the presence of Ce(IV). Another consideration for the identity of intermediate **II**, barring a $Ru^{V}ORu^{IV}$ species, is an anated peroxo complex, such as $[(HOO)Ru^{III}ORu^{IV}(ONO_2)]^{3+}$. Reduction of the coordinated peroxide with Fe^{2+}, for example, would give $[(O_2NO)Ru^{IV}ORu^{IV}(OH)]^{4+}$.

A final point regarding the decomposition of intermediate **I**, $[(HOO)Ru^{III}ORu^{V}(O)]^{3+}$, is the apparently coincidental λ_{max} for species, $[(HOO)Ru^{III}ORu^{IV}(OH)]^{3+}$ and $[(^{-}OO)Ru^{IV}ORu^{V}(O)]^{3+}$, following disproportionation. The observed λ_{max} for $[(O)Ru^{V}ORu^{IV}(O)]^{3+}$ is 488 nm; a similar λ_{max} for a $Ru^{V}ORu^{IV}$ peroxo species is plausible. Additionally, the λ_{max} for $[(HO)Ru^{IV}ORu^{III}(OH)]^{3+}$ is 486 nm, a significant shift from its protonated form, $[(HO)Ru^{IV}ORu^{III}(OH_2)]^{4+}$, with λ_{max} = 495 nm. Given the coordination environment of the reduced form of the peroxo complex, $[(HOO)Ru^{III}ORu^{IV}(OH)]^{3+}$, a λ_{max} at ~488 nm seems reasonable. Dramatically different kinetics following the disproportionation of intermediate **I** at high catalyst concentrations vs. the kinetics of $[(HOO)Ru^{III}ORu^{IV}(OH)]^{3+}$ made after pseudo-first order Ce(IV) consumption and its accumulation during catalysis are consistent with a singular species in the latter.

III.3. Formation of $[(X)Ru^{IV}ORu^{IV}(OH)]^{4+}$ (X = ClO_4^-, $CF_3SO_3^-$, NO_3^-) during catalysis.

Formation of the anated intermediate, **III** with λ_{max} = 455 nm, appears to require a catalytic amount of Ce(IV). Stoichiometric oxidation of the blue dimer to higher oxidation states, including $\{(O)Ru^{V}ORu^{V}(O)^{4+}\}$, and subsequent decomposition back to $[(HO)Ru^{IV}ORu^{III}(OH_2)]^{4+}$ did not produce an observable amount of **III**. Conversion to the anated species, $[(X)Ru^{IV}ORu^{IV}(OH)]^{4+}$ (X = ClO_4^-, $CF_3SO_3^-$, NO_3^-), is dependent on turnover

number, indicating that only a fraction of the catalyst is converted to intermediate **III** during each water oxidation cycle.

The rate of formation, as well as the degree of conversion, to **III** is first order in $[NO_3^-]$. While more experiments are needed to unequivocally establish the dependence of anation on catalyst concentration, it appears that conversion to intermediate **III** increases with increasing dimer concentration. An earlier observation monitoring the rate of oxygen evolution as a function of catalyt concentration is consistent with an intermolecular deactivation pathway.[51] A second order dependence on [blue dimer] is consistent with disproportionation of the intermediate **I**, $[(HOO)Ru^{III}ORu^{V}(O)]^{3+}$, and rapid oxygen evolution from $[(^-OO)Ru^{IV}ORu^{V}(O)]^{3+}$. At lower concentrations, direct oxidation of intermediate **I** by Ce(IV) may be in competition with disproportionation, or faster. The presence of $Ce^{IV/III}$ in close proximity to the peroxidic intermediate may deter anion coordination following O_2 evolution. The buildup of intermediate **II** (λ_{max} = 488 nm) at lower concentrations and the lack of anated species (λ_{max} = 455 nm) is consistent with an intermolecular pathway for anation. Loss of catalytic activity appears to be induced by oxygen evolution and competitive anion capture of the open coordination site. Given the direct oxidation of intermediate **I** by Ce(IV) or an applied potential has been established, the tentative conclusion that anation is second-order in catalyst concentration implies that ion-pairing with the peroxidic intermediates plays an important role in the competitive binding of anions to the blue dimer.

Due to the sole use of $(NH_4)_2Ce^{IV}(NO_3)_6$ in this mechanistic study, and the proposed intermediates, $[(X)Ru^{IV}ORu^{IV}(OH)]^{4+}$ (X = ClO_4^-, $CF_3SO_3^-$, NO_3^-), could potentially be the nitrato species independent of the acidic medium employed. Additional studies using a

different oxidant would be needed to explore this further. However, coordination of a number of different anions has been definitively established, see Section II.8; the difference in intermediate **III** decay kinetics depending on the chosen medium indicates that the perchlorato and triflato analogues are in fact formed, consistent with rate-limiting loss of the coordinated anion.

III.4. Reappearance of $Ru^{IV}ORu^{III}$ from $[(O_2NO)Ru^{IV}ORu^{IV}(OH)]^{4+}$ in 0.1 M HNO_3. The decay of intermediate **III**, $[(O_2NO)Ru^{IV}ORu^{IV}(OH)]^{4+}$, was measured in HNO_3. On the longer timescale of ~1000 min, the absorption spectrum continues to evolve, ultimately with quantitative appearance of $Ru^{IV}ORu^{III}$ at λ_{max} = 495 nm. Under these conditions, spectral changes with time followed first order kinetics with k(23 °C) = 6.9 x 10^{-5} s^{-1}. First order decay kinetics are observed, independent of complex concentration, and dependent on anion concentration. This is presumably due to aquation via rate-limiting release of anion according to the equilibrium established with the concentration of anion in solution.

As described above, the intermediate at 455 nm appears to be $[(O_2NO)Ru^{IV}ORu^{IV}(OH)]^{4+}$. Given its $2e^-$ oxidized nature and the continued slow evolution of O_2 in Figure 3.33, the overall reaction for its return to $Ru^{IV}ORu^{III}$ can be summarized, eq 17.

$$4\,[(O_2NO)Ru^{IV}ORu^{IV}(OH)]^{4+} + 6\,H_2O \rightarrow$$
$$4\,[(HO)Ru^{IV}ORu^{III}(OH_2)]^{4+} + O_2 + 4\,NO_3^- \qquad (17)$$

Loss of anion generates $[(HO)Ru^{IV}ORu^{IV}(OH)]^{4+}$, a potent oxidant that is unstable with respect to disproportionation, eq 18,

$$2\,[(HO)Ru^{IV}ORu^{IV}(OH)]^{4+} \rightarrow [(HO)Ru^{IV}ORu^{III}(OH_2)]^{4+} +$$
$$[(O)Ru^{V}ORu^{IV}(O)]^{3+} \qquad (18)$$

followed by water oxidation by $Ru^{V}ORu^{IV}$, Section III.5. These latter steps are combined in eq 17.

$$[(O_2NO)Ru^{IV}ORu^{IV}(OH)]^{4+} + H_2O \xrightarrow{k(-NO_3^-)} [(HO)Ru^{IV}ORu^{IV}(OH)]^{4+} + NO_3^- + H^+ \quad (19)$$

$$4\,[(HO)Ru^{IV}ORu^{IV}(OH)]^{4+} + 2\,H_2O \xrightarrow{rapid} 4\,[(HO)Ru^{IV}ORu^{III}(H_2O)]^{4+} + O_2 \quad (20)$$

Water oxidation by the blue dimer $Ru^{III}ORu^{III}$ is highly complex since it involves stepwise proton-coupled four-electron oxidation from $Ru^{III}ORu^{III}$ to $Ru^{V}ORu^{V}$, during which comproportation and disproportionation reactions of oxidation states further complicate the mechanism. There are additional complexities from anation induced by oxygen evolution.

Given the dilute solutions used and the sensitivity of the O_2 measuring technique, it is difficult to verify the implied stoichiometry with regard to oxygen in eq 17. However, including the final increment provided in the net oxidation of water by excess Ce(IV), this is consistent with the observed results at a variety of Ce(IV)/ $Ru^{IV}ORu^{III}$ ratios.[44,46-48]

III.5. Water Oxidation by $[(O)Ru^{V}ORu^{IV}(O)]^{3+}$. As noted in previous sections, at the end of catalytic cycles induced by Ce(IV) oxidation, the dominant form of the catalyst, depending on the acid, is $[(O)Ru^{V}ORu^{IV}(O)]^{3+}$, the anated complexes, $[(X)Ru^{IV}ORu^{IV}(OH)]^{4+}$ (X = NO_3^-, $CF_3SO_3^-$, ClO_4^-), or a mixture of the two. Based on stoichiometry studies, both ultimately result in oxygen evolution and return to $Ru^{IV}ORu^{III}$. $Ru^{V}ORu^{IV}$ by eq 21 at pH = 0,

$$2\,[(O)Ru^{V}ORu^{IV}(O)]^{3+} + 4\,H^+ + 2\,H_2O \rightarrow 2\,[(H_2O)Ru^{IV}ORu^{III}(OH_2)]^{5+} + O_2 \quad (21)$$

The kinetics of water oxidation by $[(O)Ru^{V}ORu^{IV}(O)]^{3+}$ were investigated both here and in previous studies.[23,25] Results obtained from a variety of studies under different

conditions are summarized in Table 3.3. $[(O)Ru^{V}ORu^{IV}(O)]^{3+}$ is thermodynamically unstable with respect to disproportionation. The disproportionation reaction is shown in eq 22.

$$3\,[(O)Ru^{V}ORu^{IV}(O)]^{3+} + 4\,H^{+} \xrightarrow{k(V-IV,dis)} [(H_2O)Ru^{IV}ORu^{III}(OH_2)]^{4+} + 2\,[(O)Ru^{V}ORu^{V}(O)]^{4+} \quad (22)$$

The kinetics of disproportionation have been studied in 1.0 M HNO_3 and found to be second order in $[Ru^{V}ORu^{IV}]$ with k(25 °C) = 22 $M^{-1}s^{-1}$.[23] Under these conditions the mechanism for water oxidation presumably involves initial disproportionation, eq 23,

$$2\,[(O)Ru^{V}ORu^{IV}(O)]^{3+} \xrightarrow{k(V-IV,dis)} [(O)Ru^{V}ORu^{V}(O)]^{4+} + [(HO)Ru^{IV}ORu^{IV}(OH)]^{4+} \quad (23)$$

Disproportionation gives $Ru^{V}ORu^{V}$ with re-entry into the cycle for water oxidation by $Ru^{V}ORu^{V}$, see below. The net reaction for water oxidation by $[(HO)Ru^{IV}ORu^{IV}(OH)]^{4+}$ was shown in eq 20.

III.6. Ligand-centered Oxygen-Oxygen Bond Formation? Non-innocent ligand involvement in catalytic water oxidation by the blue dimer has been proposed by Hurst and coworkers to explain an apparent pathway for O··O bond formation in which both O atoms are obtained from solvent.

In this proposed mechanism,[38,52] concerted addition of water to the catalytically-active $[(O)Ru^{V}ORu^{V}(O)]^{4+}$ species occurs with coordination of an OH fragment to the 6 position of bipyridine and a one-electron reduction-protonation of the adjacent metal center to give Ru^{IV}-OH. A second reaction with water is proposed at the 5 position of the same pyridine ring to generate a $Ru^{IV}ORu^{IV}$ diol derivative. Internal electron transfer and oxygen-oxygen coupling at the hydrated ligand could occur to form a dioxetane intermediate followed by O_2 evolution to return to $[(H_2O)Ru^{III}ORu^{III}(OH_2)]^{4+}$. While experimental data

provide indirect evidence that such a pathway could be operable, Hurst and coworkers note that "support for this pathway rests entirely upon the isotope labeling results".[48] The mechanism is shown in Scheme 3.3.[38]

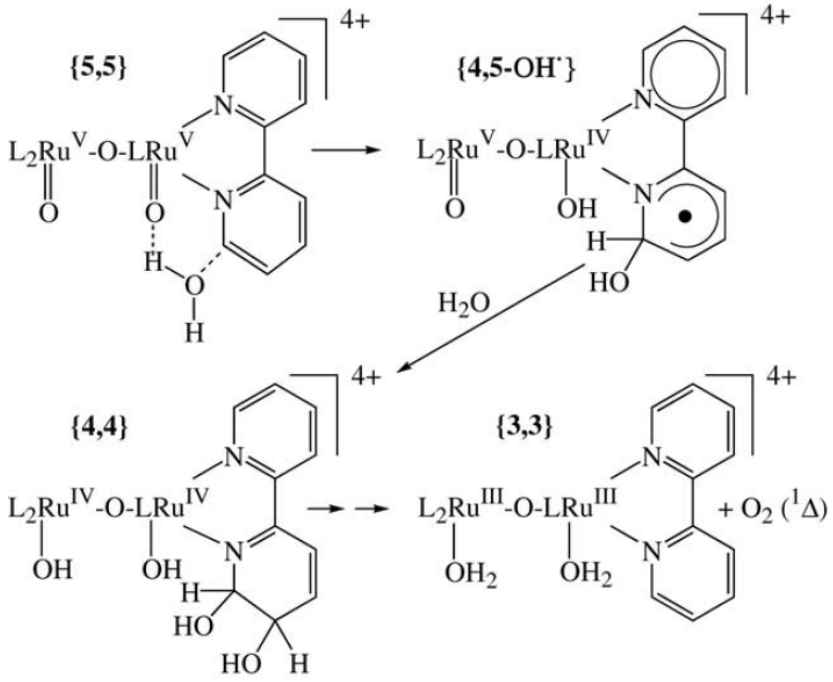

Scheme 3.3.[38] Proposed mechanism involving covalent hydration and a transient ligand radical in blue dimer catalyzed water oxidation.

Reduction of group 8 tris 2,2'-bipyridine trivalent ions to their corresponding M(II) ions (where M is Fe, Ru, or Os) is of particular interest in solar energy research and has been studied extensively, often in basic aqueous conditions.[53-61] Specifically, the sensitizer, $[Ru(bpy)_3]^{2+}$, is thermodynamically capable of the photoreduction of water to H_2 with formation of Ru(III) and subsequent oxidation of water to evolve dioxygen resulting in reduction of the metal to Ru(II).[59,61] The self-reduction of the $[M(bpy)_3]^{3+}$ species is complex and a number of mechanisms have been proposed to explain the reaction. Initially outer-sphere electron transfer oxidation of OH^- to OH• was suggested, but dismissed on energetic

grounds and incompatibility with the observed reaction dynamics. Furthermore, no effect on the decomposition kinetics was produced with addition of radical scavengers to the reaction medium.[38]

Another hypothesis that has been considered involves covalent hydration or pseudobase formation at the ligand, but this mechanism has been disputed.[60,61] Claims of covalent hydration and psuedobase formation have largely been on the basis of kinetic studies and few definitive measurements have been made to prove the point. Equally valid alternative mechanisms and intermediates have been proposed to account for the experimental observations. For example, recent results in reactions of $[Pt(bpy)_2]^{2+}$ with OH^- or CN^- have demonstrated that an associated mechanism occurs in which the nucleophile attacks the Pt(II) metal center.[60]

Reduction of $[Ru(bpy)_3]^{3+}$ was studied as a function of pH. The lifetime of $[Ru(bpy)_3]^{3+}$ in strongly acidic media is $\geq$ 25 h.[54] A first order dependence on $[OH^-]$ has been measured for the reduction, and in neutral to basic conditions, irreversible ligand oxidation has been established.[54] Ligand decomposition in acidic conditions was minimal, although a small amount of CO_2 was still measured. Importantly, in the photoreduction of $[Ru(bpy\text{-}d_8)_3]^{3+}$ in acidic media, no H-exchange in the deuterated ligands was observed.[54] It appears from these studies that covalent hydration of the bipyridine ligands in acidic media is extremely slow, irreversible, and not the dominant pathway for reduction of the trivalent complex.

Consistent with the available data, a mechanism involving nucleophilic attack of water at the metal ion has been proposed, initiating the reaction and forming a seven-coordinate intermediate. Ligand oxidation then occurs to generate N-oxides, followed by

disproportionation of the M(III) ions to M(II) and M(IV), and finally, O atom transfer from the N-oxide to M^{IV}=O takes place with subsequent liberation of O_2.[61] The presence of N-oxides has been verified as the major product of ligand oxidation in the decomposition of Fe(III).[55] However, Lay and Sasse note that the differences in ligand oxidation in Fe(III) and Ru(III) is most likely due the relative lability of the metal-ligand bonds, with the bidentate ligand remaining coordinated in Ru and dissociating in the case of Fe.[61] It should be noted that forming N-oxides in the Ru(III) case may not be necessary at all.

The reduction of $[M(bpy)_3]^{3+}$ ions has been shown to depend on the activity of water, analogous to the rate law for ligand substitution in $[Ru(NH_3)_6]^{3+}$. This is important since pseudobase formation is impossible in the hexaammine complex. Likewise, based on mechanistic studies, an associative-interchange mechanism is proposed in the water exchange reaction of $[Ru(OH_2)_6]^{6+}$. A seven-coordinate Fe(III) complex has also been characterized containing an aqua ligand, supporting the role of coordination expansion in the decomposition of $[M(bpy)_3]^{3+}$ rather than covalent hydration or pseudobase formation, at least in the absence of basic conditions.[61]

With regard to the blue dimer, a distorted pseudo-octahedral coordination geometry is observed, a consequence of multiple bonding with the μ-oxo bridge. Access to the metal center may be facilitated by the opening caused by this distorted coordination sphere. Refer to Chapter 2 for crystallographic data and discussion. Hurst disfavors a mechanism involving coordination expansion due to the lack of "facile exchange of the *cis*-ruthenyl oxygen atoms in {5,5} with solvent water."[38] However, oxo formation in the $[(O)Ru^{V}ORu^{IV}(O)]^{3+}$ and $[(O)Ru^{V}ORu^{V}(O)]^{4+}$ species, for example, would likely deactivate the coordination sphere to ligand substitution. Evidence for coordination expansion has been presented in the

involvement of anions during catalytic water oxidation in 1.0 M $HClO_4$ and 1.0 M CF_3SO_3H, as well as added CF_3SO_3Li, see below.

IV. Summary of Medium-dependent Water Oxidation.

In a previous paper, a mechanism of water oxidation was proposed based on kinetic studies and global analysis of UV-Visible measurements. Notable features of the mechanism include: (i) the water oxidation catalyst is $Ru^{V}ORu^{V}$. It does not build up in solution because it oxidizes water more rapidly than its formation. $Ru^{V}ORu^{V}$ reacts with water with $k \geq 1\ s^{-1}$. Evidence for the presence of $Ru^{V}ORu^{V}$ comes from resonance Raman studies on a highly explosive black microparticulate which precipitated from cold $HClO_4$ solutions following excess Ce^{IV} addition to $Ru^{IV}ORu^{III}$. (ii) $Ru^{V}ORu^{IV}$ is an observable intermediate which is unstable with respect to disproportionation, followed by water oxidation. At higher pHs, $Ru^{V}ORu^{IV}$ is more stable and could be generated electrolytically or by addition of stoichiometric HOCl to $Ru^{IV}ORu^{III}$ at pH 6. (iii) $Ru^{IV}ORu^{IV}$ is unstable with respect to disproportionation.

In this paper, we report kinetic and mixing measurements in different acidic environments that provide new insights into water oxidation by the blue dimer. Part of the sensitivity to medium arises from variations in the formal potential of the Ce(IV/III) couple. It is useful to keep in mind the dependence of the redox potential of Ce(IV/III) couple on the nature of the acid, Table 3.5.

Table 3.5. Selected Formal Potentials of Ce(IV/III) couple in Different Aqueous Acid Solutions at 25 °C in V vs. NHE.[62]

Redox Couple	Medium	Potential, V
$Ce^{IV} + e^- \Leftrightarrow Ce^{III}$	1 M HCl	1.28
	1 M H_2SO_4	1.44
	1 M HNO_3	1.61
	1 M $HClO_4$	1.70

IV.1. In 1.0 M HNO_3. The spectral changes with time in 1.0 M HNO_3 in Figure 3.30 are consistent with $Ru^{V}ORu^{IV}$ as the dominant form at the catalytic steady state. Under these conditions, water oxidation is rate limited by oxidation of $Ru^{V}ORu^{IV}$ to $Ru^{V}ORu^{V}$. $Ru^{V}ORu^{V}$ as a key intermediate for water oxidation does not appear in the catalytic steady state. Loss of Ce(IV) is in a reaction first order in both [Ce(IV)] and [$Ru^{V}ORu^{IV}$] with k(23 ^{o}C) = 80 ± 2 $M^{-1}s^{-1}$. This is due to $Ru^{V}ORu^{IV}$ existing as $[(O)Ru^{V}ORu^{IV}(OH)]^{4+}$ at this pH and having slower oxidation kinetics compared to $Ru^{V}ORu^{IV}$ at pH = 1, where it does not accumulate in solution, k($[(O)Ru^{V}ORu^{IV}(O)]^{3+}$, 0.1 M HNO_3) = 220 $M^{-1}s^{-1}$. We note that Ce(IV) consumption is rapid with ~35% reacted in 10 s after mixing. The time scale of catalytic water oxidation observed here is relatively rapid in contrast to 1.0 M $HClO_4$ and 1.0 M CF_3SO_3H.

After the majority of Ce^{IV} is consumed, there is evidence of a new intermediate absorbing at 455 nm, which decays to $Ru^{IV}ORu^{III}$ with first order kinetics on a long time scale, k(1.0 M HNO_3, 23 ^{o}C) = 8 x 10^{-5} s^{-1}. The oxidation state of the intermediate was investigated by titration by Fe^{2+} and was found to oxidize 2 eq. of Fe^{2+}. A separate titration by NaOH shows that the intermediate has a pK_a = 1.4 and its absorption maximum shifts to

492 nm when fully deprotonated. The process is reversible and most likely an acid-base equilibrium,

$$[(bpy)_2(HO)Ru^{IV}ORu^{IV}(NO_3)(bpy)_2]^{4+} \Leftrightarrow [(bpy)_2(O)Ru^{V}ORu^{III}(NO_3)(bpy)_2]^{3+} + H^+$$

The slow reaction of the intermediate to return to $Ru^{IV}ORu^{III}$ presumably involves aquation, followed by disproportionation and water oxidation.

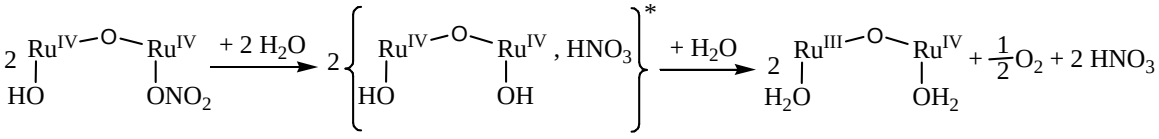

in which $[(HO)Ru^{IV}ORu^{IV}(OH)]^{4+}$ is favored by 16 kcal/mol over $[(O)Ru^{V}ORu^{III}(OH_2)]^{4+}$ based on theoretical gas phase DFT calculations.[19] The species in parenthesis is a transition state species.

<u>*IV.2. In 1.0 M CF_3SO_3H and 1.0 M $HClO_4$.*</u> Observations are different in *1.0 M CF_3SO_3H and 1.0 M $HClO_4$*. The results of our analysis of the available data are revealing as to how the blue dimer catalyzes the Ce(IV) oxidation of water. After surveying the results, the difficulties in analyzing this mechanism become apparent.

As a mechanistic summary: (i) The catalytically active form of the blue dimer is $[(bpy)_2(O)Ru^{V}ORu^{V}(O)(bpy)_2]^{4+}$, $Ru^{V}ORu^{V}$. It does not build up in solution as a discernible intermediate but undergoes a rapid reaction with water to form a peroxidic intermediate. (ii) $Ru^{V}ORu^{V}$ is reached by stepwise PCET oxidation of $Ru^{III}ORu^{III}$. In 1.0 M HNO_3 the slow step is Ce(IV) oxidation of $Ru^{V}ORu^{IV}$ to $Ru^{V}ORu^{V}$. (iii) In 1 M CF_3CSO_3H or $HClO_4$, $1e^-$ oxidation of $Ru^{IV}ORu^{III}$ is accompanied by anation to give an anated $Ru^{IV}ORu^{IV}$ species ($Ru^{IV}ORu^{IV}$-X) that presumably involves coordination expansion at one metal center. Disproportionation of $Ru^{IV}ORu^{IV}$-X occurs with subsequent buildup of the oxidized disproportionation product, $Ru^{V}ORu^{IV}$-X. (iv) Rate limiting loss of the anion to give the

protonated $[(O)Ru^{V}ORu^{IV}(OH)]^{4+}$ species results in Ce(IV) consumption that is zero-order in Ce(IV) and first order in catalyst. Early in the catalytic cycle in 0.1 M H_3O^+, Ce(IV) oxidation of $[(HO_2)Ru^{III}ORu^{V}(O)]^{3+}$ is rate limiting and catalysis is greatly accelerated compared to 1.0 M H_3O^+. (v) Anated intermediates, $[(bpy)_2(X)Ru^{IV}ORu^{IV}(OH)(bpy)_2]^{4+}$ (X = NO_3, CF_3SO_3, ClO_4), in acid-base equilibrium with their deprotonated forms $[(bpy)_2(X)Ru^{III}ORu^{V}(O)(bpy)_2]^{3+}$, appear under a variety of conditions: (a) accompanying $1e^-$ oxidation of $Ru^{IV}ORu^{III}$ in 1.0 M CF_3CSO_3H or $HClO_4$, (b) during catalytic cycles coupled to Ce(IV) oxidation of peroxidic intermediates, (c) decomposition of the reduced form of the peroxidic intermediate, $[(bpy)_2(HO_2)Ru^{III}ORu^{IV}(OH)(bpy)_2]^{3+}$. (vi) The anated intermediates subsequently undergo aquation followed by water oxidation via the transient $[(HO)Ru^{IV}ORu^{IV}(OH)]^{4+}$ species.

With this interpretation water oxidation by the blue dimer in its oxidized $Ru^{V}ORu^{V}$ form is rapid. A peroxidic intermediate is formed following nucleophilic water attack at a single Ru^{V}=O, a key mechanistic step in the catalytic cycle. In strongly acidic solutions, anated intermediates intervene deleteriously by tying up $Ru^{IV}ORu^{IV}$. A species that appears to be $Ru^{IV}ORu^{III}$ exists as the dominant form at the catalytic steady state. However, this is not $Ru^{IV}ORu^{III}$ as kinetic monitoring of Ce(IV) loss shows zero order kinetics with respect to Ce(IV) at the catalytic steady state. Our interpretation is that an intermediate appears in solution that coincidentally absorbs at a similar absorption maximum as that of $Ru^{IV}ORu^{III}$. Due the reversible binding of the anion, a seven-coordinate intermediate is proposed. This anated $Ru^{IV}ORu^{IV}$ is presumably, $[(bpy)_2(H_2O)(X)Ru^{IV}ORu^{IV}(OH)(bpy)_2]3+$ (λ_{max} = 448 nm), in acid-base equilibria with $[(bpy)_2(HO)(X)Ru^{IV}ORu^{IV}(OH)(bpy)_2]3+$ (λ_{max} = 492 nm at pH 1). Under these conditions, water oxidation is limited by a second order decomposition

of the intermediate with a rate constant of k = 1.15 x 10^3 $M^{-1}s^{-1}$. A second stage of Ce(IV) consumption also exists, with a rate corresponding to decomposition of the seven-coordination intermediate, $[(O)Ru^{V}ORu^{IV}(OH)(X)]^{3+}$. Conversion to the protonated $Ru^{V}ORu^{IV}$ occurs by rate-limiting first order kinetics, consistent with loss of coordinated anion. This mechanism in 1.0 M H_3O^+ is summarized in Scheme 3.4.

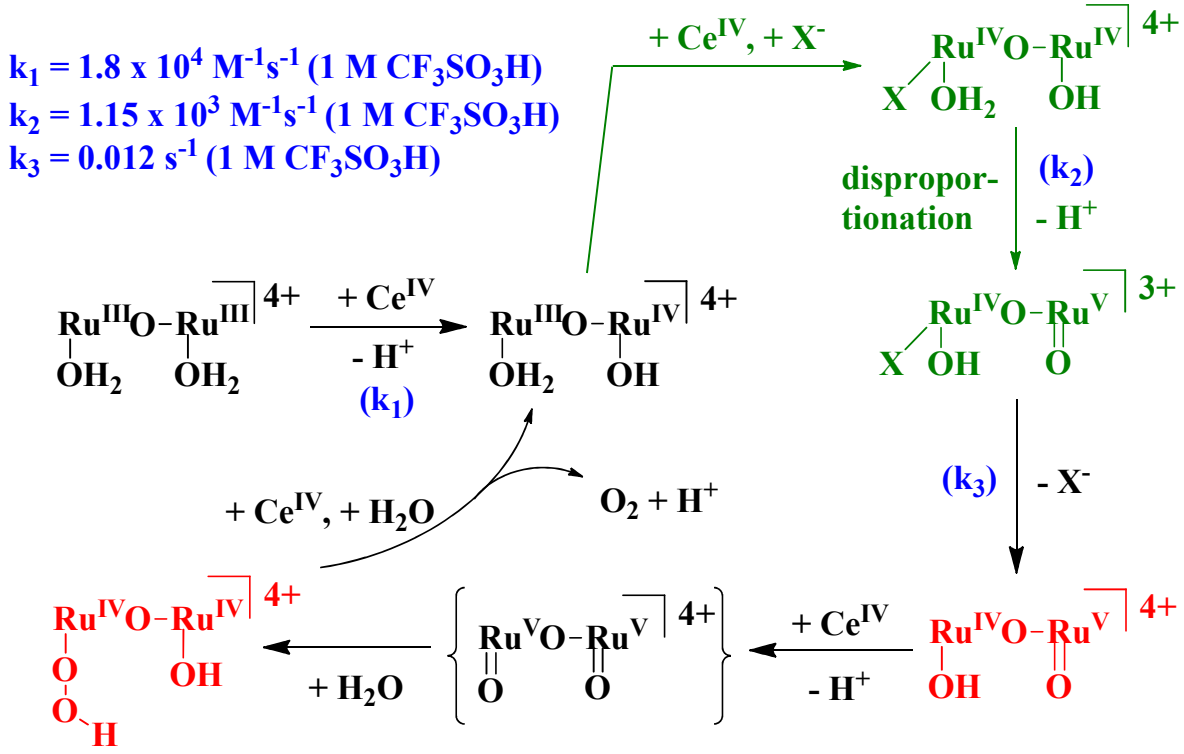

Scheme 3.4. Mechanism of Ce(IV)-driven water oxidation by the blue dimer in 1.0 M CF_3SO_3H (and 1.0 M $HClO_4$). The mechanism has been simplified following formation of $[(HOO)Ru^{IV}ORu^{IV}(OH)]^{4+}$. Species involving anions are denoted in green and species that are unstable with respect to disproportionation are in red (with the exception of $[(X)(H_2O)Ru^{IV}ORu^{IV}(OH)]^{4+}$ which also disproportionates). See Scheme 3.6 for a detailed summary of the oxidation and decomposition of the peroxidic intermediate.

Coordination expansion offers an important advantage in that the initial product of O_2 loss is the coordinatively stable complex $[(HO)Ru^{IV}ORu^{III}(X)]^{3+}$ rather than a coordinatively unsaturated intermediate. In d^4 Ru(IV) and d^3 Ru(V) there are orbital vacancies for electron pair donation and additional metal ligand bonding, although at the expense of orbital

coupling across the μ-oxo bridge. Coordination sphere expansion by associative substitution has been suggested as a pathway for water exchange in the blue dimer, Scheme 3.5. There is literature precedence for such pathways as well as seven coordinate metal complexes having lower d electron configurations.[63-67] Coordination expansion may also explain the ^{18}O labeling results.

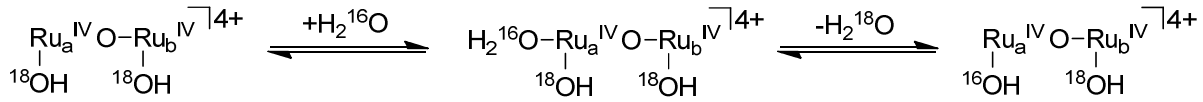

Scheme 3.5. Coordination expansion and ^{18}O labeling in $Ru^{IV}ORu^{IV}$. Ligand substitution is only illustrated at one metal center for the sake of simplicity.

IV.3. In 0.1 M HNO_3, 0.1 M $HClO_4$, 0.1 M CF_3SO_3H.

Shown in Scheme 3.6 is an outline of the mechanism of blue dimer catalyzed water oxidation. Oxidative activation from $[(H_2O)Ru^{III}ORu^{III}(OH_2)]^{4+}$ to $[(O)Ru^{V}ORu^{V}(O)]^{4+}$ occurs by autocatalytic kinetics where oxidation of $Ru^{IV}ORu^{III}$ is the slow step. As $Ru^{V}ORu^{IV}$ accumulates in solution, comproportionation with $Ru^{IV}ORu^{III}$ occurs to produce two equivalents of $Ru^{IV}ORu^{IV}$. $Ru^{IV}ORu^{IV}$ is rapidly oxidized to give $Ru^{V}ORu^{IV}$. Oxidation of $Ru^{V}ORu^{IV}$ by Ce(IV) in 0.1 M HNO_3 occurs with k = 220 $M^{-1}s^{-1}$ to $[(O)Ru^{V}ORu^{V}(O)]^{4+}$ which undergoes nucleophilic attack of water at a single Ru^{V}=O to give a species with λ_{max} = 482 nm, $[(HOO)Ru^{III}ORu^{V}(O)]^{3+}$. The peroxidic intermediate is unstable with respect to disproportionation to give $[(HOO)Ru^{III}ORu^{IV}(OH)]^{3+}$ and $[(^{-}OO)Ru^{IV}ORu^{V}(O)]^{3+}$. Both of these species decompose by first order kinetics to $Ru^{IV}ORu^{III}$.

$k_1 = 625\ M^{-1}s^{-1}$ (0.1M $HClO_4$)
$k_2 = 3.24\ M^{-1}s^{-1}$ (0.1M $HClO_4$)
$k_3 = 220\ M^{-1}s^{-1}$ (0.1M HNO_3)
$k_5 = 183\ M^{-1}s^{-1}$ (0.1M HNO_3)

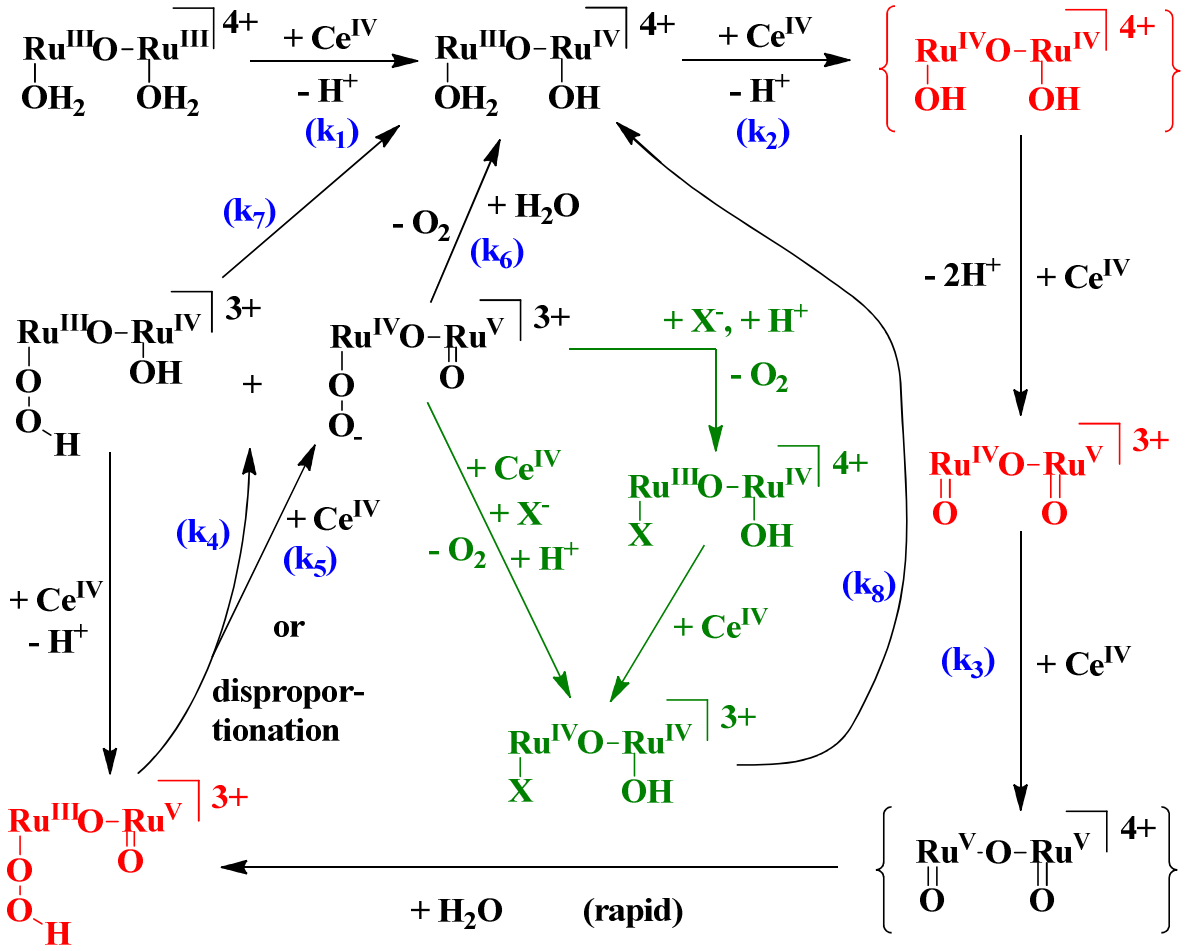

Scheme 3.6. Proposed mechanism of catalytic water oxidation by the blue dimer (protonation states of each intermediate are shown for pH 1 conditions). Competition between Ce(IV) oxidation and anion addition is shown. X^- is NO_3^-, $SO_3CF_3^-$, ClO_4^-.

REFERENCES

(1) Barber, J. *Philosophical Transactions of the Royal Society a-Mathematical Physical and Engineering Sciences* **2007**, *365*, 1007.

(2) Ruttinger, W.; Dismukes, G. C. *Chemical Reviews* **1997**, *97*, 1.

(3) Ferreira, K. N.; Iverson, T. M.; Maghlaoui, K.; Barber, J.; Iwata, S. *Science* **2004**, *303*, 1831.

(4) Biesiadka, J.; Loll, B.; Kern, J.; Irrgang, K. D.; Zouni, A. *Physical Chemistry Chemical Physics* **2004**, *6*, 4733.

(5) Loll, B.; Kern, J.; Saenger, W.; Zouni, A.; Biesiadka, J. *Nature* **2005**, *438*, 1040.

(6) Barber, J. *Inorganic Chemistry* **2008**, *47*, 1700.

(7) Yano, J.; Pushkar, Y.; Glatzel, P.; Lewis, A.; Sauer, K.; Messinger, J.; Bergmann, U.; Yachandra, V. *Journal of the American Chemical Society* **2005**, *127*, 14974.

(8) Liu, F.; Concepcion, J. J.; Jurss, J. W.; Cardolaccia, T.; Templeton, J. L.; Meyer, T. J. *Inorganic Chemistry* **2008**, *47*, 1727.

(9) Meyer Thomas, J.; Huynh My Hang, V.; Thorp, H. H. *Angew Chem Int Ed Engl* **2007**, *46*, 5284.

(10) Sala, X.; Romero, I.; Rodriguez, M.; Escriche, L.; Llobet, A. *Angewandte Chemie-International Edition* **2009**, *48*, 2842.

(11) Yagi, M.; Syouji, A.; Yamada, S.; Komi, M.; Yamazaki, H.; Tajima, S. *Photochemical & Photobiological Sciences* **2009**, *8*, 139.

(12) Lewis, N. S.; Nocera, D. G. *Proc. Nat. Acad. Sci.* **2006**, *103*, 15729.

(13) Meyer, T. J. *Acc. Chem. Res.* **1989**, *22*, 163.

(14) Alstrum-Acevedo, J. H.; Brennaman, M. K.; Meyer, T. J. *Inorganic Chemistry* **2005**, *44*, 6802.

(15) Gersten, S. W.; Samuels, G. J.; Meyer, T. J. *Journal of the American Chemical Society* **1982**, *104*, 4029.

(16) Gilbert, J. A.; Eggleston, D. S.; Murphy, W. R.; Geselowitz, D. A.; Gersten, S. W.; Hodgson, D. J.; Meyer, T. J. *Journal of the American Chemical Society* **1985**, *107*, 3855.

(17) Hurst, J. K.; Cape, J. L.; Clark, A. E.; Das, S.; Qin, C. Y. *Inorganic Chemistry* **2008**, *47*, 1753.

(18) Schoonover, J. R.; Ni, J. F.; Roecker, L.; Whiter, P. S.; Meyer, T. J. *Inorganic Chemistry* **1996**, *35*, 5885.

(19) Bartolotti, L. J.; Pedersen, L. G.; Meyer, T. J. *International Journal of Quantum Chemistry* **2001**, *83*, 143.

(20) Kutner, W.; Gilbert, J. A.; Tomaszewski, A.; Meyer, T. J.; Murray, R. W. *Journal of Electroanalytical Chemistry* **1986**, *205*, 185.

(21) Jurss, J. W.; Concepcion, J. J.; Butler, J. M.; Omberg, K. M.; Baraldo, L. M.; Thompson, D. G.; Lebeau, E. L.; Hornstein, B.; Schoonover, J. R.; Jude, H.; Thompson, J. D.; Dattelbaum, D. M.; Rocha, R. C.; Moonshiram, D.; Pushkar, Y.; Templeton, J. L.; Meyer, T. J. *Manuscript in Preparation.*

(22) Bondareva, T. N.; Stromberg, A. G. *Zhurnal Obshchei Khimii* **1955**, *25*, 666.

(23) Binstead, R. A.; Chronister, C. W.; Ni, J. F.; Hartshorn, C. M.; Meyer, T. J. *Journal of the American Chemical Society* **2000**, *122*, 8464.

(24) Cape, J. L.; Lymar, S. V.; Lightbody, T.; Hurst, J. K. *Inorganic Chemistry* **2009**, *48*, 4400.

(25) Raven, S. J.; Meyer, T. J. *Inorganic Chemistry* **1988**, *27*, 4478.

(26) Concepcion, J. J.; Jurss, J. W.; Templeton, J. L.; Meyer, T. J. *Proceedings of the National Academy of Sciences of the United States of America* **2008**, *105*, 17632.

(27) Vining, W. J.; Meyer, T. J. *Inorganic Chemistry* **1986**, *25*, 2023.

(28) Rotzinger, F. P.; Munavalli, S.; Comte, P.; Hurst, J. K.; Gratzel, M.; Pern, F. J.; Frank, A. J. *Journal of the American Chemical Society* **1987**, *109*, 6619.

(29) Doppelt, P.; Meyer, T. J. *Inorganic Chemistry* **1987**, *26*, 2027.

(30) Jurss, J. W.; Concepcion, J. C.; Norris, M. R.; Templeton, J. L.; Meyer, T. J. *Inorganic Chemistry* **2010**, *49*, 3980.

(31) Lei, Y. B.; Hurst, J. K. *Inorganica Chimica Acta* **1994**, *226*, 179.

(32) Phelps, D. W.; Kahn, E. M.; Hodgson, D. J. *Inorganic Chemistry* **1975**, *14*, 2486.

(33) Ellis, C. D.; Gilbert, J. A.; Murphy, W. R.; Meyer, T. J. *Journal of the American Chemical Society* **1983**, *105*, 4842.

(34) Yamada, H.; Koike, T.; Hurst, J. K. *Journal of the American Chemical Society* **2001**, *123*, 12775.

(35) Binstead, R. A.; Moyer, B. A.; Samuels, G. J.; Meyer, T. J. *Journal of the American Chemical Society* **1981**, *103*, 2897.

(36) Cabaniss, G.; Diamantis, A.; Murphy, W.; Linton, R.; Meyer, T. *Journal of the American Chemical Society* **1985**, *107*, 1845.

(37) Yamada, H.; Hurst, J. K. *Journal of the American Chemical Society* **2000**, *122*, 5303.

(38) Hurst, J. K. *Coordination Chemistry Reviews* **2005**, *249*, 313.

(39) Dobson, J. C.; Takeuchi, K. J.; Pipes, D. W.; Geselowitz, D. A.; Meyer, T. J. *Inorganic Chemistry* **1986**, *25*, 2357.

(40) Adeyemi, S. A.; Dovletoglou, A.; Guadalupe, A. R.; Meyer, T. J. *Inorganic Chemistry* **1992**, *31*, 1375.

(41) Dobson, J. C.; Meyer, T. J. *Inorganic Chemistry* **1988**, *27*, 3283.

(42) Collin, J. P.; Sauvage, J. P. *Inorganic Chemistry* **1986**, *25*, 135.

(43) Lebeau, E. L.; Adeyemi, S. A.; Meyer, T. J. *Inorganic Chemistry* **1998**, *37*, 6476.

(44) Hurst, J. K.; Zhou, J. Z.; Lei, Y. B. *Inorganic Chemistry* **1992**, *31*, 1010.

(45) Lei, Y. B.; Hurst, J. K. *Inorganic Chemistry* **1994**, *33*, 4460.

(46) Geselowitz, D.; Meyer, T. J. *Inorganic Chemistry* **1990**, *29*, 3894.

(47) Yamada, H.; Siems, W. F.; Koike, T.; Hurst, J. K. *Journal of the American Chemical Society* **2004**, *126*, 9786.

(48) Cape, J. L.; Siems, W. F.; Hurst, J. K. *Inorg Chem* **2009**, *48*, 8729.

(49) Okamoto, K.; Miyawaki, J.; Nagai, K.; Matsumura, D.; Nojima, A.; Yokoyama, T.; Kondoh, H.; Ohta, T. *Inorganic Chemistry* **2003**, *42*, 8682.

(50) Chronister, C. W.; Binstead, R. A.; Ni, J. F.; Meyer, T. J. *Inorganic Chemistry* **1997**, *36*, 3814.

(51) Nagoshi, K.; Yamashita, S.; Yagi, M.; Kaneko, M. *Journal of Molecular Catalysis a-Chemical* **1999**, *144*, 71.

(52) Cape, J. L.; Hurst, J. K. *Journal of the American Chemical Society* **2008**, *130*, 827.

(53) Creutz, C.; Sutin, N. *Proceedings of the National Academy of Sciences of the United States of America* **1975**, *72*, 2858.

(54) Ghosh, P. K.; Brunschwig, B. S.; Chou, M.; Creutz, C.; Sutin, N. *Journal of the American Chemical Society* **1984**, *106*, 4772.

(55) Nord, G.; Pedersen, B.; Bjergbakke, E. *Journal of the American Chemical Society* **1983**, *105*, 1913.

(56) Gillard, R. D. *Coordination Chemistry Reviews* **1975**, *16*, 67.

(57) Gil, V. M. S.; Gillard, R. D.; Williams, P. A.; Vagg, R. S.; Watton, E. C. *Transition Metal Chemistry* **1979**, *4*, 14.

(58) Arcesagues, J. A.; Gillard, R. D.; Lancashire, R. J.; Williams, P. A. *Journal of the Chemical Society-Dalton Transactions* **1979**, 193.

(59) Serpone, N.; Bolletta, F. *Inorganica Chimica Acta-Articles* **1983**, *75*, 189.

(60) Serpone, N.; Ponterini, G.; Jamieson, M. A.; Bolletta, F.; Maestri, M. *Coordination Chemistry Reviews* **1983**, *50*, 209.

(61) Lay, P. A.; Sasse, W. H. F. *Inorganic Chemistry* **1985**, *24*, 4707.

(62) Bard, A. J.; Faulkner, L. R. *Electrochemical Methods: Fundamentals and Applications*; Second Edition ed.; John Wiley & Sons, Inc., 2001.

(63) Tseng, H. W.; Zong, R.; Muckerman, J. T.; Thummel, R. *Inorganic Chemistry* **2008**, *47*, 11763.

(64) Herzmann, N.; Mudring, A. V.; Meyer, G. *Inorganic Chemistry* **2008**, *47*, 7954.

(65) Mattson, B. M.; Heiman, J. R.; Pignolet, L. H. *Inorganic Chemistry* **1976**, *15*, 564.

(66) Maddock, S. M.; Rickard, C. E. F.; Roper, W. R.; Wright, L. J. *Journal of Organometallic Chemistry* **1996**, *510*, 267.

(67) Given, K. W.; Mattson, B. M.; Pignolet, L. H. *Inorganic Chemistry* **1976**, *15*, 3152.

CHAPTER 4

One Site is Enough: Monomeric Water Oxidation Catalysts

Introduction

In natural photosynthesis, and many schemes for artificial photosynthesis, water oxidation, $2\ H_2O \rightarrow O_2 + 4\ e^- + 4\ H^+$, is a key half reaction.[1,2] A number of molecular catalysts have been reported for this reaction[2-8] but little mechanistic information is available. A detailed, medium dependent mechanism for water oxidation by the blue Ru dimer, *cis,cis*-$[(bpy)_2(H_2O)Ru^{III}ORu^{III}(OH_2)(bpy)_2]^{4+}$ (bpy is 2,2′-bipyridine), was described in the previous chapter. In 0.1 M HNO_3, under catalytic conditions with excess Ce(IV), rapid oxidation occurs through the intermediate $[(O)Ru^{V}ORu^{V}(O)]^{4+}$ to give a second intermediate tentatively identified as the peroxide, $[(bpy)_2(O)RuORu(OOH)(bpy)_2]^{4+}$.[2] A peroxidic intermediate has also been proposed in water oxidation at the Mn_4Ca cluster in the Oxygen Evolving Complex (OEC) of Photosystem II.[9,10]

A significant question remains as to whether or not dimeric or higher order structures are required to achieve catalytic water oxidation. Qualitative evidence for water oxidation by monomeric complexes of Ir and Ru has been presented by Bernhard *et al.* and by Thummel *et al.*, respectively.[4,7] We report here sustained catalytic water oxidation upon oxidation of the monomeric complexes, $[Ru(tpy)(bpm)(OH_2)]^{2+}$ and $[Ru(tpy)(bpz)(OH_2)]^{2+}$ (tpy is 2,2′:6′,2″-terpyridine; bpm is 2,2′-bipyrimidine; bpz is 2,2′-bipyrazine), by a well-defined mechanism involving Ru(V).

Experimental Section

Javier J. Concepcion and Michael R. Norris made the complexes described here and in Appendix C. Ligands were prepared by Javier, Michael, and I (Appx. C). Mixing experiments for UV-visible spectral analysis, electrochemical measurements, and their

corresponding interpretations were performed by Javier, Zoufeng Chen, and I. DFT calculations were completed by Javier. I measured evolved oxygen from each of the catalysts.

Materials. Distilled water was further purified using a Milli-Q Ultrapure water purification system. Stock solutions of Ce^{IV} for kinetic and stoichiometric measurements were prepared from $(NH_4)_2Ce(NO_3)_6$ (99.99+%, Aldrich). Nitric acid (Trace Metal Grade, 70%) was purchased from Fisher Scientific and perchloric acid (70%, purified by redistillation, 99.999% trace metals basis) was purchased from Aldrich. 2,2'-bipyrimidine (97%) and $RuCl_3 \times H_2O$ were purchased from Aldrich and used as received. 2,2'-bipyrazine,[11] $[Ru(tpy)Cl_3]$[12] and $[Ru(tpy)(C_2O_4)(OH_2)] \cdot 2H_2O$[13] were prepared as described in the literature. $[Ru(tpy)(L)(Cl)](ClO_4)$ (L is bpm or bpz) were prepared by a modification of the procedure reported for [Ru(tpy)(bpy)(Cl)]Cl.[14] All other reagents were ACS grade and used without additional purification. Elemental analyses were conducted by Atlantic Microlab, Inc., Atlanta, Georgia.

Methods. UV/Vis spectra and UV/Vis spectra *vs* time were recorded on an Agilent Technologies Model 8453 diode-array spectrophotometer. Data were processed by use of the program SPECFIT/32 Global Analysis System (SPECTRUM Software Associates). Kinetic measurements were also performed on a Shimadzu UV-Vis-NIR Spectrophotometer Model UV-3600 by monitoring the disappearance of Ce^{IV} at 360 nm.

Electrochemical measurements were performed on an EG&G Princeton Applied Research model 273A potentiostat/galvanostat. Voltammetric measurements were made with a planar EG&G PARC G0229 glassy carbon millielectrode, a platinum wire EG&G PARC K0266 counter electrode, and Ag/AgCl EG&G PARC K0265 reference electrode.

Oxygen measurements were performed with a calibrated O_2 electrode (YSI, Inc., Model 550A) or with a fluorescence-based YSI ProODO O_2 calibrated electrode. In a typical experiment, 30 equivalents of Ce^{IV} were added to stirred solutions containing 1.0-2.9×10^{-3} M ruthenium complex in 1.0 or 0.1 M HNO_3. The air-tight reaction cell was purged with argon prior to the addition of the Ce^{IV} until the digital readout had stabilized. O_2 evolution vs. time was recorded and the theoretical maximum was achieved within 3 %.

Results and Discussion

Reaction of $[Ru(tpy)(C_2O_4)(OH_2)]$[13] with bpz or bpm in 0.1 M $HClO_4$ or of $[Ru(tpy)(L)(Cl)]^+$ (L is bpm or bpz) with $AgNO_3$ in 1:1 H_2O:MeOH yields the corresponding aqua complexes $[Ru(tpy)(bpz)(OH_2)]^{2+}$ and $[Ru(tpy)(bpm)(OH_2)]^{2+}$. They are analogs of $[Ru(tpy)(bpy)(OH_2)]^{2+}$ and *cis*-$[Ru(bpy)_2(py)(H_2O)]^{2+}$ (py is pyridine) which, when oxidized to their Ru^{IV}=O forms, have an extensive stoichiometric and catalytic oxidative reactivity toward a variety of organic and inorganic molecules.[15]

As shown in Figure 4.1, the bpm complex shares with $[Ru(tpy)(bpy)(OH_2)]^{2+}$ multiple, pH-dependent oxidations in aqueous solutions. For $[Ru(tpy)(bpy)(OH_2)]^{2+}$, pH dependent Ru^{III}/Ru^{II} and Ru^{IV}/Ru^{III} couples appear separated by 92 mV over a broad pH range characteristic of closely spaced Ru(III/II) and Ru(IV/III) couples. The small potential separation between couples is a consequence of "redox potential leveling" and the PCET nature of the couple.[2,16] Protons are lost with no buildup of charge between couples and higher oxidation state Ru(IV) is stabilized by Ru=O bond formation. There is no evidence for further oxidation of this complex to the solvent limit at ~ 1.8 V vs. NHE.

For $[Ru(tpy)(bpm)(OH_2)]^{2+}$, Ru^{III} is a "missing" oxidation state.[2,15,16] A single $2e^-$ Ru^{IV}/Ru^{II} wave, as shown by peak current comparisons with the $[Ru(bpy)_3]^{3+/2+}$couple, is

observed from pH = 0 to pH = 14 with a change from the $[Ru^{IV}=O]^{2+} + 2e^- + 2\ H^+ \rightarrow [Ru^{II}\text{-}OH_2]^{2+}$ couple to $[Ru^{IV}=O]^{2+} + 2e^- + H^+ \rightarrow [Ru^{II}\text{-}OH]^{+}$, past $pK_{a,1} = 9.7$ (Appx. C - Figure S11). $E_{1/2}$ for the Ru^{IV}/Ru^{III} couple is lower than $E_{1/2}$ for the Ru^{III}/Ru^{II} couple due to bpm stabilization of Ru(II) by backbonding and stabilization of Ru(IV) (and Ru(V), see below) by σ donation.[17,18]

At higher potentials a pH-independent, $1e^-$ wave appears in the cyclic voltammogram (CV) at 1.65 V as a shoulder on the onset of a catalytic wave for water oxidation. The electrochemistry for $[Ru(tpy)(bpz)(OH_2)]^{2+}$ is similar to that for $[Ru(tpy)(bpm)(OH_2)]^{2+}$ with redox potentials for the corresponding Ru(IV/II) and Ru(V/IV) couples shifted to higher potentials (Appx. C - Figures S12 and S13).

Oxidation to Ru(V) triggers water oxidation both electrochemically and with added Ce(IV). Addition of 2 equivalents of Ce(IV) to a solution of $[Ru^{II}(tpy)(bpm)(OH_2)]^{2+}$ in 0.1 M HNO_3 (λ_{max} = 485 nm, 364 nm, 331 nm(sh) and 309 nm) results in formation of $[Ru^{IV}(tpy)(bpm)(O)]^{2+}$ (λ_{max} = 430 nm (sh), 353 nm (sh), 336 nm and 324 nm) with k(25 ºC) ~ 2400 $M^{-1}s^{-1}$, eqs 1 and 2.

$$[Ru^{II}\text{-}OH_2]^{2+} + Ce^{4+} \xrightarrow{k_1 \sim 2400\ M^{-1}s^{-1}} [Ru^{III}\text{-}OH]^{2+} + Ce^{3+} + H^+ \quad \text{(eq 1)}$$

$$[Ru^{III}\text{-}OH]^{2+} + Ce^{4+} \xrightarrow{\text{rapid}} [Ru^{IV}=O]^{2+} + Ce^{3+} + H^+ \quad \text{(eq 2)}$$

Further addition of 1 equivalent of Ce(IV) to $[Ru^{IV}=O]^{2+}$, or 3 equivalents of Ce(IV) to $[Ru^{II}(OH_2)]^{2+}$, results in formation of $[Ru^{V}=O]^{3+}$, k(25 ºC) ~ 5.0 $M^{-1}s^{-1}$, eq 3, but as a transient.

$$[Ru^{IV}=O]^{2+} + Ce^{4+} \xrightarrow{k_3 \sim 5.0\ M^{-1}s^{-1}} [Ru^{V}=O]^{3+} + Ce^{3+} \quad \text{(eq 3)}$$

As shown by UV-visible spectral changes over time, Appx. C - Figure S15, it undergoes a further reaction with water to give a second intermediate which we tentatively formulate as the peroxido complex, $[Ru^{III}(tpy)(bpm)(OOH)]^{2+}$ ($[Ru^{III}(OOH)]^{2+}$), eq 4. The peroxidic complex decomposes on a time scale of minutes to give $[Ru^{II}\text{-}OH_2]^{2+}$ and, presumably, O_2, Appx. C - Figure S16. In a redox titration between 2-3 equivalents of Fe_{aq}^{2+} were consumed per $[Ru^{III}(OOH)]^{2+}$ consistent with partial decomposition following its relatively slow formation by Ce(IV) oxidation. Both the decomposition reaction and further characterization of the intermediate are currently under investigation.

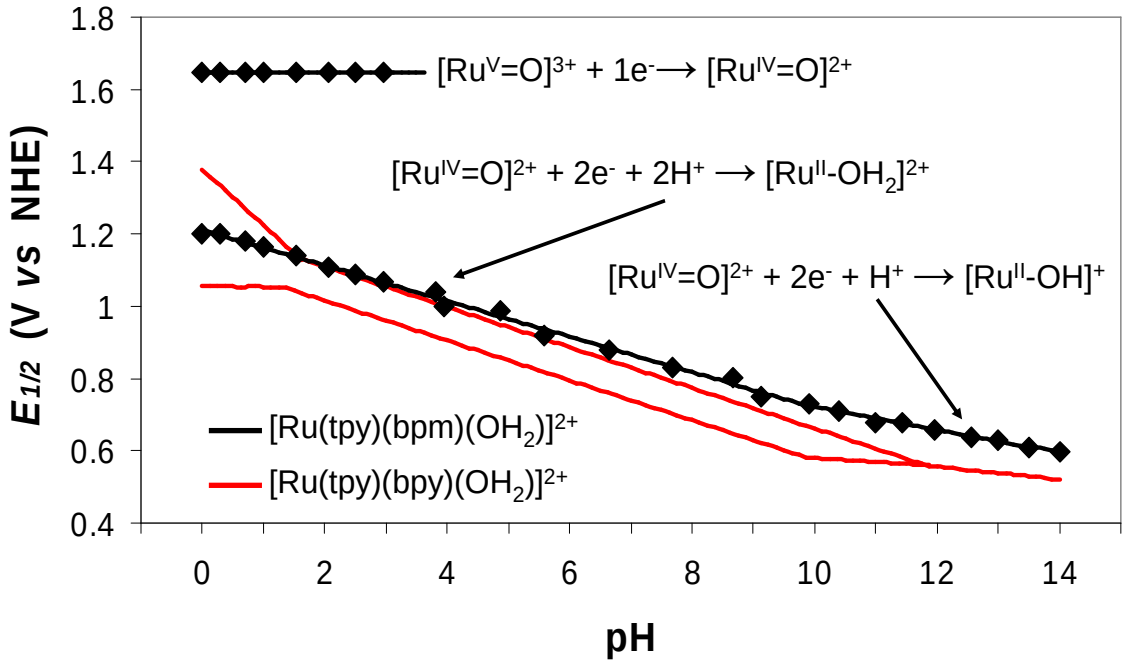

Figure 4.1. Plots of $E_{1/2}$ (V vs. NHE) vs. pH for the Ru(V/IV) and Ru(IV/II) redox couples of $[Ru(tpy)(bpm)(OH_2)]^{2+}$ and for the Ru(IV/III) and Ru(III/II) redox couples of $[Ru(tpy)(bpy)(OH_2)]^{2+}$ in aqueous solution (I = 0.1 M; T = 298 K; glassy carbon working electrode).

Under catalytic conditions with 30 equivalents of Ce^{IV} added, $[Ru^{III}(tpy)(bpm)(OOH)]^{2+}$ undergoes further oxidation to an additional intermediate which we tentatively assign as the Ru^{IV} peroxide $[Ru^{IV}(tpy)(bpm)(O_2)]^{2+}$($[Ru^{IV}OO]^{2+}$), eq 5.

$$[Ru^{V}(tpy)(bpm)(O)]^{3+} + H_2O \rightarrow [Ru^{III}(tpy)(bpm)(OOH)]^{2+} + H^{+} \quad (4)$$

$$[Ru^{III}(tpy)(bpm)(OOH)]^{2+} + Ce(IV) \rightarrow [Ru^{IV}(tpy)(bpm)(O_2)]^{2+} + Ce(III) + H^{+} \quad (5)$$

Based on the results of DFT calculations on $[Ru^{IV}(tpy)(bpm)(O_2)]^{2+}$, a seven-coordinate structure with a bidentate peroxido ligand is favored over a six-coordinated structure with a terminal peroxido ligand. All crystallographically characterized $[Ru^{IV}(O_2)]^{n+}$ complexes display this seven-coordinate structure.[19,20]

Under catalytic conditions with 30 equivalents of Ce(IV) in 0.1 M HNO_3, $[Ru^{IV}OO]^{2+}$, with λ_{max} = 436, 358(sh), 339(sh), 316(sh), and 286 nm, dominates at the catalytic steady state. Loss of Ce(IV) monitored at 360 nm is zero order in Ce(IV) and first order in complex with k(25 ºC) = 7.5×10^{-4} s^{-1} (Figure 4.2), consistent with decomposition of $[Ru^{IV}OO]^{2+}$ as the rate limiting step, eq 6.

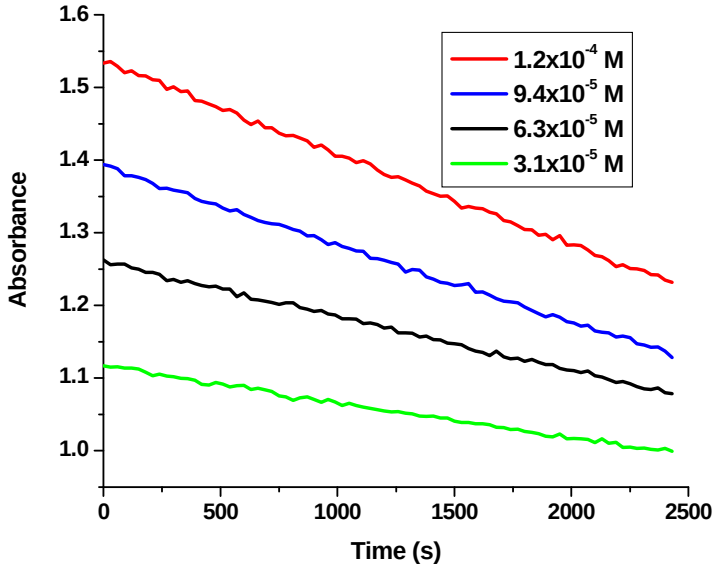

Figure 4.2. Monitoring Ce(IV) at 360 nm after addition of 30 equivalents of Ce(IV) to solutions of $Ru(tpy)(bpm)(OH_2)^{2+}$ at various concentrations in 0.1 M HNO_3.

Figure 4.3 shows a plot of zeroth-order rate constants obtained from the data shown in Figure 4.2 versus the concentration of the ruthenium complex. From the slope, a first order rate constant of 7.5×10^{-4} s^{-1} is obtained.

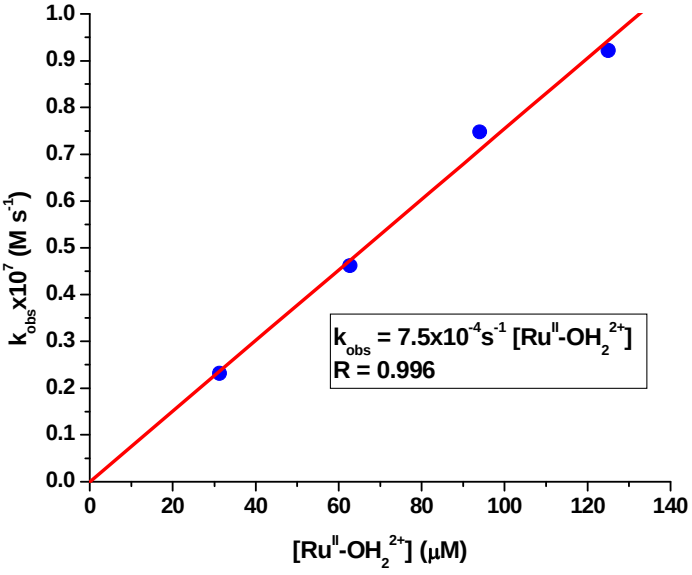

Figure 4.3. Plot of k_{obs} vs. concentration of Ru(tpy)(bpm)$(OH_2)^{2+}$. As can be seen from the plot, the kinetics for Ce(IV) disappearance are first order with respect to catalyst concentration.

In 1.0 M HNO_3 the kinetics of Ce(IV) loss are significantly enhanced and mixed first and second order in character. As shown in eq 7, this is consistent with further oxidation of $[Ru^{IV}OO]^{2+}$ by Ce(IV) competing with the first order pathway in eq 6. Subsequent water oxidation presumably occurs by eq 8 followed by re-oxidation of Ru(III). The appearance of the Ce(IV) pathway is a consequence of the enhanced E^{o}' for the Ce(IV/III) couple at higher acid concentrations.[21] Oxygen monitoring with an oxygen electrode in three separate experiments gave 100 (±3)% of the expected O_2 after 7.5 turnovers, Figure 4.4.

$$[Ru^{IV}(tpy)(bpm)(O_2)]^{2+} + H_2O \rightarrow [Ru^{II}(tpy)(bpm)(H_2O)]^{2+} + O_2 \quad (6)$$

$$[Ru^{IV}(tpy)(bpm)(O_2)]^{2+} + Ce(IV) \rightarrow [Ru^{V}(tpy)(bpm)(O_2)]^{3+} + Ce(III) \quad (7)$$

$$[Ru^{V}(tpy)(bpm)(O_2)]^{3+} + H_2O \rightarrow$$

$$[Ru^{III}(tpy)(bpm)(OH)]^{2+} + O_2 + H^+ \qquad (8)$$

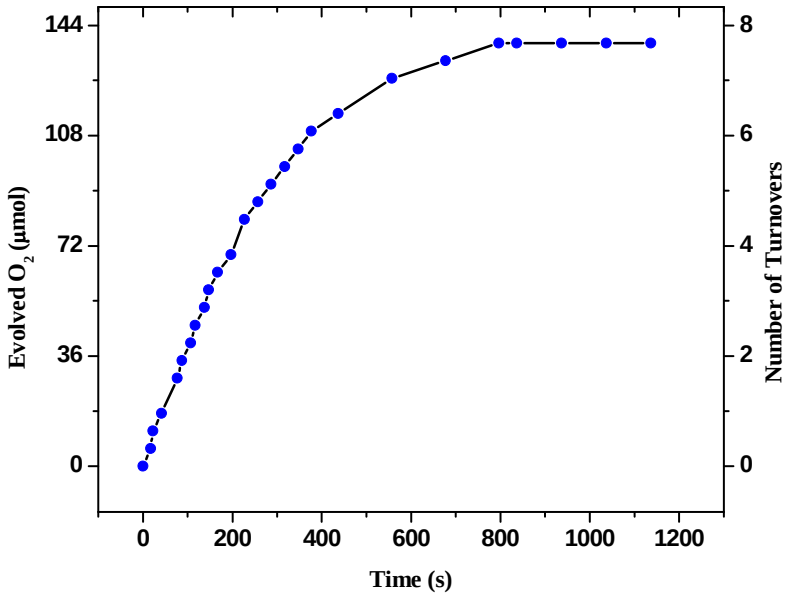

Figure 4.4. Oxygen evolution/turnover number vs. time plot for the addition of 30 equivalents of Ce(IV) (567 μmol) to 6.5 mL of 2.9×10^{-3} M $Ru(tpy)(bpm)(OH_2)^{2+}$ (18.9 μmol) in 1.0 M HNO_3. The experimental number of turnovers (7.68) is within 2.5 % of the expected number of turnovers (7.50).

Initial results under catalytic conditions in 0.1 M HNO_3 with $[Ru(tpy)(bpz)(OH_2)]^{2+}$ as the catalyst gave closely related results with evidence for a $[Ru^{III}\text{-}OOH]^{2+}$ intermediate and an intermediate building up at the catalytic steady state with λ_{max} = 385 (sh), 359(sh), 339(sh), 316 and 284(sh) nm. This intermediate is presumably the bpz analog $[Ru^{IV}(tpy)(bpz)(O_2)]^{2+}$. Under catalytic conditions loss of Ce(IV) is also zero order in Ce(IV) with $k(25\ ^{o}C) = 1.4\times10^{-3}\ s^{-1}$, eq 9. Based on redox potential measurements, water oxidation by $[Ru^{V}(tpy)(bpz)(O)]^{2+}$ is favored over the bpm complex with $E^{o\prime}(Ru^{V}{=}O^{3+}/Ru^{II}\text{-}OH_2{}^{2+})$ ~ 1.42 V (bpz) and 1.32 V (bpm) at pH = 1.

$$[Ru^{IV}(tpy)(bpz)(O_2)]^{2+} + H_2O \rightarrow [Ru^{II}(tpy)(bpz)(H_2O)]^{2+} + O_2 \quad (9)$$

The mechanism for water oxidation catalysis by $[Ru(tpy)(bpm)(OH_2)]^{2+}$ and $[Ru(tpy)(bpz)(OH_2)]^{2+}$ derived from our observations is shown in Figure 4.5. Notable is the use of single site catalysis and involvement of the $3e^-$ oxidized oxo complexes $[Ru^V(tpy)(bpm)(O)]^{3+}$ and $[Ru^V(tpy)(bpz)(O)]^{3+}$. Thermodynamically, use of the higher oxidation state is advantageous with $\Delta G^{o\prime} = -0.90$ eV for water oxidation by $[Ru^V(tpy)(bpm)(O)]^{3+}$, $2\ [Ru^V{=}O]^{3+} + 3\ H_2O \rightarrow 2\ [Ru^{II}\text{-}OH_2]^{2+} + 3/2\ O_2 + 2\ H^+$ compared to $\Delta G^{o\prime} = +0.04$ eV for oxidation by Ru(IV), $2\ [Ru^{IV}{=}O]^{2+} + 2\ H_2O \rightarrow 2\ [Ru^{II}\text{-}OH_2]^{2+} + O_2$ (pH=1). The appearance of peroxido intermediates is also a notable feature in the scheme. They are presumably high energy intermediates given $E^{o\prime} = 1.77$ V for the H_2O_2/H_2O couple and $E^{o\prime} = -0.39$ V for $[Ru^V(tpy)(bpm)(O)]^{3+}$ oxidation of H_2O to H_2O_2, $2\ [Ru^V{=}O]^{3+} + 6\ H_2O \rightarrow 2\ [Ru^{II}\text{-}OH_2]^{2+} + 3\ H_2O_2 + 2\ H^+$ at pH = 1.

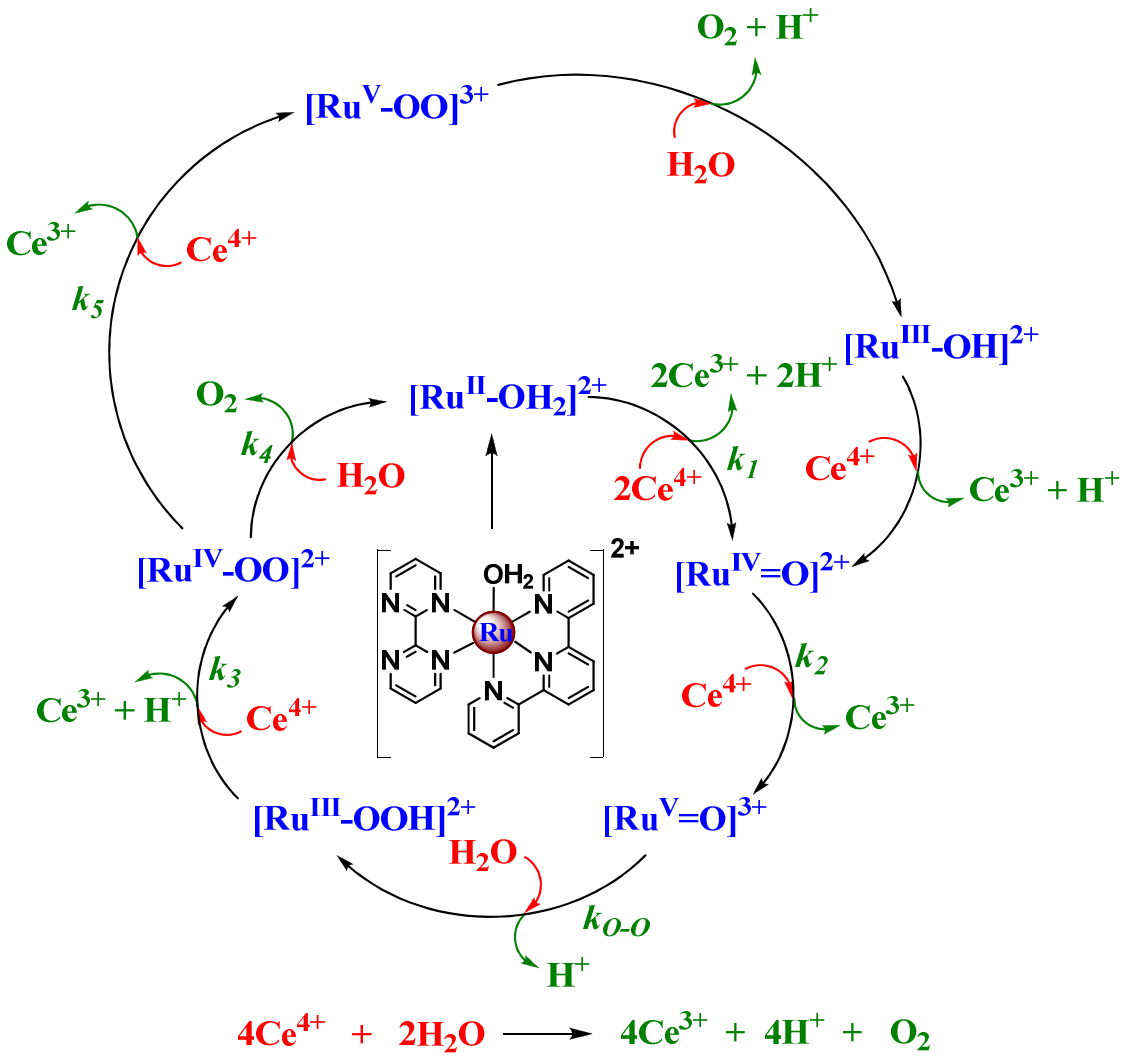

Figure 4.5. Single site mechanism for water oxidation by the monomers, $[Ru(tpy)(bpm)(OH_2)]^{2+}$ and $[Ru(tpy)(bpz)(OH_2)]^{2+}$.

These results are important in establishing detailed mechanistic insight into water oxidation at a single ruthenium site. In summary, mechanistic studies revealed a well defined, stepwise mechanism featuring Proton Coupled Electron Transfer (PCET),[9,16] a high oxidation state $Ru^{V}=O^{n+}$ intermediate, which undergoes O---O coupling with H_2O, and a series of peroxidic intermediates. The sequence of reactions is illustrated in Figure 4.5. With mechanistic details established, important questions remain. Is single site water oxidation

catalysis a general phenomenon as suggested by other recent reports?[22,23] What are the factors of molecular and electronic structure that maximize catalytic rates and turnover numbers?

Following the initial discovery of single site catalysts, $[Ru(tpy)(bpm)(OH_2)]^{2+}$ and $[Ru(tpy)(bpz)(OH_2)]^{2+}$, we developed a host of new single site Ru polypyridyl complexes capable of decomposing water. The diversity of ligand environments, their influence on rates and reaction thermodynamics, and the breadth of reactivity are remarkable. They point to a family of catalysts at the molecular scale with reactivity controllable by ligand variations which, by suitable modification, can be incorporated into molecular assemblies, nano-structured arrays, or at interfaces.

Generic structures are illustrated in Figure 4.6. They include the previously reported tpy complexes,[24] along with acetylacetonate (acac)[17] and carbene derivatives, a series of complexes based on the terdentate ligand 2,6-bis(1-methylbenzimidazol-2-yl)pyridine, Mebimpy, and a series of complexes of the type $Ru(DMAP)(NN)(OH_2)^{2+}$ (DMAP is 2,6-bis((dimethylamino)methyl)pyridine;[25] NN is 2,2'-bipyridine, bpy; 3-methyl-1-pyridylimidazol-2-ylidene, MeIm-py and 3-methyl-1-pyridylbenzimidazol-2-ylidene, Mebim-py, see Figure 4.6).

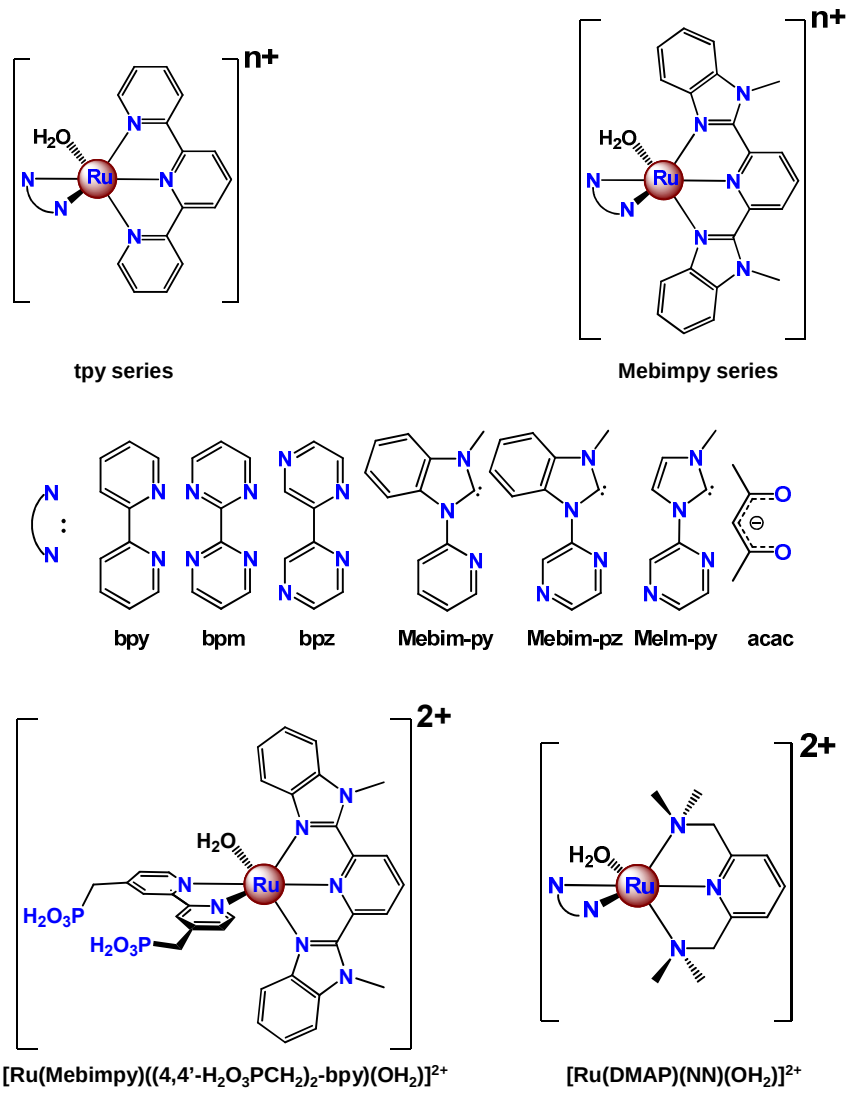

Figure 4.6. Single-site water oxidation catalysts.

A special case is Ru(Mebimpy)(4,4'-CH_2 PO_3H_2bpy)$(OH_2)^{2+}$ since phosphonic acid derivatization imparts aqueous stability on binding to metal oxide surfaces in acidic or neutral environments.

Synthesis and characterization of the series $[Ru(tpy)(NN)(OH_2)]^{n+}$ with NN= bpy, bpm, bpz and acac was described previously.[14,17,24,26] The synthesis of the series $[Ru(Mebimpy)(NN)(OH_2)]^{n+}$ with LL = bpy, bpm, bpz and acac was accomplished by

procedures similar to those used for the corresponding tpy complexes.[14,24,26] They involved isolation of $[Ru(Mebimpy)(NN)(Cl)]^{n+}$ followed by replacement of the chloro ligand in water assisted by added silver triflate or triflic acid. The *trans*-$[Ru(tpy)(NN)(OH_2)]^{2+}$, *trans*-$[Ru(Mebimpy)(NN)(OH_2)]^{2+}$, and *trans*-$[Ru(DMAP)(NN)(OH_2)]^{2+}$ (NN is 3-methyl-1-pyridylimidazol-2-ylidene, MeIm-py; 3-methyl-1-pyridylbenzimidazol-2-ylidene, Mebim-py; and 3-methyl-1-pyrazylbenzimidazol-2-ylidene, Mebim-pz) series were obtained by reaction of the monocationic carbene precursors with $Ru(tpy)Cl_3$,[12] $Ru(Mebimpy)Cl_3$[26] or $Ru(DMAP)Cl_3$[25] in ethyleneglycol at 150 ºC in the presence of NEt_3. In these cases aqua complexes rather than chloro complexes were obtained due to the *trans*-labilizing effect of the carbene on chloride ligand loss with the *trans* isomer the only product, see below. $[Ru(Mebimpy)(4,4'\text{-}((OH)_2OPCH_2)_2\text{-}bpy)(OH_2)]^{2+}$ was prepared by a modification of the procedure used to synthesize $[Ru(Mebimpy)(bpy)(OH_2)]^{2+}$ with an extra step required to hydrolyze the phosphonate esther groups. $Ru(DMAP)(bpy)(OH_2)^{2+}$ was prepared following a literature procedure.[25] All complexes were characterized by ^{1}H-NMR, elemental analysis, absorption spectroscopy and cyclic voltammetry (see Appendix C).

The crystal structure of *trans*-$[Ru(tpy)(Mebim\text{-}py)(OH_2)]^{2+}$ cation is shown in Figure 4.7.

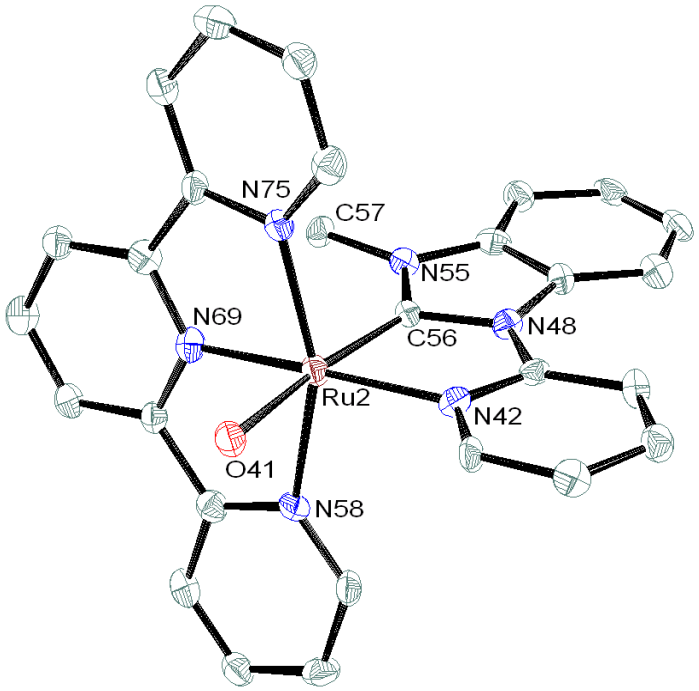

Figure 4.7. X-ray structure of the *trans*-$[Ru(tpy)(Mebim\text{-}py)(OH_2)]^{2+}$ cation in the salt *trans*-$[Ru(tpy)(Mebim\text{-}py)(OH_2)](ClO_4)_2$.

As noted above, only the *trans* isomer, was obtained. Notable features in the structure are the relatively short Ru-C distance (1.943 Å) indicative of multiple Ru-C bonding and the longer Ru-O distance (2.183 Å) compared to $Ru(tpy)(bpy)(OH_2)^{2+}$ (2.146 Å)[27] and $Ru(tpy)(phendione)(OH_2)^{2+}$ (2.127 Å, phendione is 1,10-phenanthroline-5,6-dione).[28] This labilizing effect might play an important role in the oxygen evolution step in the water oxidation catalytic cycle.

Representative cyclic voltammograms for $Ru(DMAP)(bpy)(OH_2)^{2+}$, *trans*-$[Ru(tpy)(Mebim\text{-}py)(OH_2)]^{2+}$, and the series $[Ru(Mebimpy)(NN)(OH^2)]^{2+}$ (LL = bpy, bpm, bpz), in 0.1 M HNO_3 are shown in Appx. C - Figure S18; analogous CVs for $Ru(tpy)(acac)(OH_2)]^{+}$ are in Appx. C - Figure S19. In these cyclic voltammograms, E^{o},

values for the $[Ru^{III}(Mebimpy)(NN)(OH/OH_2)]^{2+/3+}$/$[Ru^{II}(Mebimpy)(NN)(OH_2)]^{2+}$ and the $[Ru^{IV}(Mebimpy)(NN)(O)]^{2+}$/$[Ru^{III}(Mebimpy)(NN)(OH/OH_2)]^{2+/3+}$ couples vary systematically through the series from 0.82 to 1.13 V for the $Ru^{III/II}$ couple and from 1.24 to 1.48 V for the $Ru^{IV}/^{III}$ couple. E^{o}' values for the $Ru^{III/II}$ and for the $Ru^{IV}/^{III}$ couples vary from 0.51 to 1.18 V and from 0.74 to 1.54 V, respectively in the entire series (Tables 4.1 and 4.2).

Variations in E^{o}' are a consequence of the influence of σ-donor ligands in stabilizing higher oxidation states and π-acceptor ligands in stabilizing Ru(II).[17,18] Ligand variations also influence pKa's of Ru^{III}-OH_2^{3+} and Ru^{II}-OH_2^{2+} which, in turn, affect redox potentials due to the pH dependence of the $Ru^{III/II}$ and $Ru^{IV/III}$ couples. An additional $Ru^{V/IV}$, ligand-dependent wave appears as a shoulder from ~ 1.40 V to ~ 1.72 V at the onset of a catalytic water oxidation wave. Electrocatalytic waves well above background appear for all complexes past 1.3 V.

All complexes were screened as catalysts for net water oxidation by Ce(IV), $2H_2O + 4Ce^{4+} \rightarrow O_2 + 4H^+ + 4Ce^{3+}$, by adding 30 equivalents of Ce(IV) to 5.1×10^{-5} M complex in 0.1 M HNO_3. In these experiments loss of Ce(IV) was monitored spectrophotometrically at 360 nm, on the shoulder of λ_{max} = 318 nm for Ce(IV), ε = 3070 $M^{-1}cm^{-1}$. In all cases complete Ce(IV) consumption was observed on time scales from <100 s to 20000 s.
For the series $[Ru(tpy)(NN)(OH_2)]^{n+}$ (Table 4.1, NN is a bidentate ligand) and $[Ru(NNN)(bpy)(OH_2)]^{2+}$ (Table 4.2, NNN is tpy, Mebimpy, or DMAP) in 0.1 M HNO_3, absorbance-time measurements with Ce(IV) in pseudo first order excess, revealed two types of behavior. In one, the rate law was first order in complex, added initially as $Ru^{II}(OH_2)^{n+}$, and zero order in $[Ce^{IV}]$. The initial oxidation to $Ru^{IV}=O^{n+}$ is rapid. On the basis of Figure 4.5, this behavior is consistent with either rate limiting $Ru^{V}=O^{(n+1)+}$ oxo attack on H_2O, $k_{O\text{-}O}$,

or rate limiting O_2 loss from $Ru^{IV}(OO)^{n+}$, k_4. The latter is rate limiting for $[Ru(tpy)(bpm)(OH_2)]^{2+}$ and $[Ru(tpy)(bpz)(OH_2)]^{2+}$ catalyzed water oxidation.[24] In the second type of behavior, the rate law was first order in $[Ru^{II}(OH_2)^{n+}]$ and first order in $[Ce^{IV}]$. This limit is consistent with either rate limiting oxidation of $Ru^{IV}=O^{n+}$ to $Ru^{V}=O^{(n+1)+}$, k_2 in Figure 4.5,or rate limiting oxidation of $Ru^{IV}(OO)^{n+}$, k_5. Evidence for an additional pathway second order in complex was obtained at high concentrations of complex and will be discussed in a separate manuscript. $[Ru(tpy)(acac)(OH_2)]^{+}$ is a special case. Both pathways first and zero order in $[Ce^{IV}]$ compete in 0.1 M HNO_3 with the first order pathway dominating early in the catalytic cycle and the zero order pathway dominating as Ce(IV) is depleted.

Table 4.1. Water oxidation rate constants and $E_{1/2}$ (V vs. NHE) values for the $Ru^{III/II}$, $Ru^{IV/III}$ and $Ru^{V/IV}$ couples in the series $[Ru(tpy)(NN)(OH_2)]^{n+}$ in 0.1 M HNO_3.

NN	$Ru^{III/II}$	$Ru^{IV/III}$	$Ru^{V/IV}$	k_{O-O} *or* k_4 (s^{-1})	k_2 *or* k_5 ($M^{-1}s^{-1}$)	$t_{1/2}$ (s)
bpy	1.01	1.19	1.60	1.9×10^{-4}		3650
bpm	1.12	< 1.12[a]	1.65	7.5×10^{-4}		925
bpz	1.22	< 1.22[a]	1.69	1.4×10^{-3}		495
Mebim-py	1.11	1.49	1.70		33	410
Mebim-pz	1.18	1.54	1.72		170	80
acac	0.51	1.14	1.58	5.0×10^{-4}	515	1390, 26

[a] Half times ($t_{1/2}$) for net Ce(IV) consumption with $[Ce^{IV}] = 1.5 \times 10^{-3}$ M and $[RuOH_2]^{2+} = 5.1 \times 10^{-5}$ M at 23 ± 2 °C. Only $2e^-$ $Ru^{IV}=O^{2+}/Ru^{II}OH_2^{2+}$ couples are observed for $[Ru(tpy)(LL)(OH_2)]^{n+}$ (LL = bpm, bpz).

Table 4.2. As in Table 4.1 for the series $[Ru(NNN)(bpy)(OH_2)]^{2+}$.

NNN	$Ru^{III/II}$	$Ru^{IV/III}$	$Ru^{V/IV}$	k_4 (s^{-1})	k_2 *or* k_5 ($M^{-1}s^{-1}$)	$t_{1/2}$ (s)
tpy	1.01	1.19	1.60	1.9×10^{-4}	-	3650
Mebimpy	0.82	1.29	1.67	-	52	260
DMAP	0.54	0.88	1.40	-	4.1	3315

Tables 4.1 and 4.2 present $E_{1/2}$ values for the Ru(III/II), Ru(IV/III), and Ru(V/IV) couples as well as rate constants for the rate limiting steps in water oxidation catalysis by the series $[Ru(tpy)(NN)(OH_2)]^{n+}$ and $[Ru(NNN)(bpy)(OH_2)]^{2+}$. For comparisons among catalysts having different rate limiting steps, the half times $t_{1/2}$ for consumption of Ce(IV), with $[Ce^{IV}] = 1.5 \times 10^{-3}$ M initially and $[Ru(OH_2)]^{n+} = 5.1 \times 10^{-5}$ M, are also reported.

General trends emerge from the data in Tables 4.1 and 4.2. For the $Ru^{V/III}$ couples, of relevance in the O---O bond forming step (k_{O-O} in Figure 4.2), $E_{1/2}(Ru^{V/III}) = 1/2[(E_{1/2}(Ru^{V/IV}) + E_{1/2}(Ru^{IV/III})]$, is dictated largely by the $Ru^{IV/III}$ couple. It is highly tunable, ranging from 1.54 to 0.88 V because of its sensitivity to the σ-donor and π-acceptor properties of the ligands. The $Ru^{V/III}$ couple is pH dependent. $E^{o\prime}$ decreases by -118 mV/pH unit in strongly acidic solutions for the $Ru^{V}{=}O^{n+}/Ru^{III}\text{-}OH_2^{n+}$ couple and by -59 mV/pH unit for the $Ru^{V}{=}O^{n+}/Ru^{III}\text{-}OH^{(n-1)+}$ couple past pK_a for $Ru^{III}\text{-}OH_2^{n+}$, which is also ligand dependent (see Appx. C - Figures S25-S27 for representative $E_{1/2}$ vs. pH diagrams).

For representative complexes $[Ru(tpy)(bpm)(OH_2)]^{2+}$, $[Ru(tpy)(Mebim\text{-}py)(OH_2)]^{2+}$, $[Ru(Mebimpy)(bpy)(OH_2)]^{2+}$, and $[Ru(tpy)(Mebim\text{-}pz)(OH_2)]^{2+}$, oxygen evolution was measured by use of an O_2 electrode (Appx. C, Figures S21-S24). In all cases, the expected amount of oxygen, 7.5 eq/30 eq of Ce(IV), was observed, showing that water oxidation is

quantitative. As illustrated in cyclic voltammograms of $[Ru(tpy)(acac)(OH_2)]^+$, these complexes are also electrocatalysts with evidence for water oxidation triggered by oxidation of $Ru^{IV}=O^+$ to $Ru^{V}=O^{2+}$ at slow scan rates (Appx. C - Figure S19).

Conclusion

Our observations are remarkable in pointing to the generality of water oxidation catalysis by single site Ru complex catalysts. Water oxidation appears to occur by a common mechanism utilizing PCET oxidation to $Ru^{IV}=O^{(n-1)+}$, followed by further oxidation and oxo transfer from $Ru^{V}=O^{n+}$ to give Ru^{III}-$OOH^{(n-1)+}$. The O---O bond forming reaction is reminiscent of well documented O-atom transfer to sulfides, sulfoxides, phosphines, and olefins by $Ru(bpy)_2(py)(O)^{2+}$ and $Ru(tpy)(bpy)(O)^{2+}$.[15] Water oxidation catalysis appears to be general for polypyridyl aqua complexes with coordinated H_2O, which have oxidatively stable ligands, the ability to reach higher oxidation state Ru=O intermediates, and the driving force to carry out the reaction.

REFERENCES

(1) Alstrum-Acevedo, J. H.; Brennaman, M. K.; Meyer, T. J. *Inorganic Chemistry* **2005**, *44*, 6802.

(2) Liu, F.; Concepcion, J. J.; Jurss, J. W.; Cardolaccia, T.; Templeton, J. L.; Meyer, T. J. *Inorg. Chem. (Washington, DC, U. S.)* **2008**, *47*, 1727.

(3) Gersten, S. W.; Samuels, G. J.; Meyer, T. J. *Journal of the American Chemical Society* **1982**, *104*, 4029.

(4) McDaniel, N. D.; Coughlin, F. J.; Tinker, L. L.; Bernhard, S. *Journal of the American Chemical Society* **2008**, *130*, 210.

(5) Betley, T. A.; Wu, Q.; Van Voorhis, T.; Nocera, D. G. *Inorganic Chemistry* **2008**, *47*, 1849.

(6) Tagore, R.; Crabtree, R. H.; Brudvig, G. W. *Inorganic Chemistry* **2008**, *47*, 1815.

(7) Zong, R.; Thummel, R. P. *Journal of the American Chemical Society* **2005**, *127*, 12802.

(8) Deng, Z. P.; Tseng, H. W.; Zong, R. F.; Wang, D.; Thummel, R. *Inorganic Chemistry* **2008**, *47*, 1835.

(9) Meyer, T. J.; Huynh, M. H. V.; Thorp, H. H. *Angew. Chem., Int. Ed.* **2007**, *46*, 5284.

(10) Renger, G. *Photosynthesis Research* **2007**, *92*, 407.

(11) Rillema, D. P.; Allen, G.; Meyer, T. J.; Conrad, D. *Inorganic Chemistry* **1983**, *22*, 1617.

(12) Sullivan, B. P.; Calvert, J. M.; Meyer, T. J. *Inorganic Chemistry* **1980**, *19*, 1404.

(13) Adeyemi, S. A.; Dovletoglou, A.; Guadalupe, A. R.; Meyer, T. J. *Inorganic Chemistry* **1992**, *31*, 1375.

(14) Takeuchi, K. J.; Thompson, M. S.; Pipes, D. W.; Meyer, T. J. *Inorganic Chemistry* **1984**, *23*, 1845.

(15) Meyer, T. J.; Huynh, M. H. V. *Inorganic Chemistry* **2003**, *42*, 8140.

(16) Huynh, M.; Meyer, T. *Chemical Reviews* **2007**, *107*, 5004.

(17) Dovletoglou, A.; Adeyemi, S. A.; Meyer, T. J. *Inorganic Chemistry* **1996**, *35*, 4120.

(18) Masllorens, E.; Rodriguez, M.; Romero, I.; Roglans, A.; Parella, T.; Benet-Buchholz, J.; Poyatos, M.; Llobet, A. *Journal of the American Chemical Society* **2006**, *128*, 5306.

(19) Clemente, M. E. N.; Saavedra, P. J.; Vasquez, M. C.; Paz-Sandoval, M. A.; Arif, A. M.; Ernst, R. D. *Organometallics* **2002**, *21*, 592.

(20) Shen, J. Y.; Stevens, E. D.; Nolan, S. P. *Organometallics* **1998**, *17*, 3875.

(21) Bondareva, T. N.; Stromberg, A. G. *Zhurnal Obshchei Khimii* **1955**, *25*, 666.

(22) Tseng, H. W.; Zong, R.; Muckerman, J. T.; Thummel, R. *Inorganic Chemistry* **2008**, *47*, 11763.

(23) Hull, J. F.; Balcells, D.; Blakemore, J. D.; Incarvito, C. D.; Eisenstein, O.; Brudvig, G. W.; Crabtree, R. H. *Journal of the American Chemical Society* **2009**, *131*, 8730.

(24) Concepcion, J. J.; Jurss, J. W.; Templeton, J. L.; Meyer, T. J. *Journal of the American Chemical Society* **2008**, *130*, 16462.

(25) Welch, T. W.; Ciftan, S. A.; White, P. S.; Thorp, H. H. *Inorganic Chemistry* **1997**, *36*, 4812.

(26) Concepcion, J. J.; Tsai, M. K.; Muckerman, J. T.; Meyer, T. J. *Journal of the American Chemical Society* **2010**, *132*, 1545.

(27) Qvortrup, K.; McKenzie, C. J.; Bond, A. D. *Acta Crystallographica Section E-Structure Reports Online* **2007**, *63*, M1400.

(28) Fujihara, T.; Wada, T.; Tanaka, K. *Dalton Transactions* **2004**, 645.

CHAPTER 5

Diffusional and Surface-adsorbed Electron Transfer Mediators

Introduction

Water oxidation is a key reaction in photosynthesis, responsible for much of life as we know it.[1-8] It is also a central reaction in artificial photosynthesis, an example being solar-driven splitting of water into hydrogen and oxygen, $2H_2O \rightarrow O_2 + 2H_2$.[9-11] In natural photosynthesis, water oxidation occurs at Photosystem II (PSII) through the Kok cycle following absorption of four photons. Detailed insight into how this reaction occurs is emerging based on theoretical and spectroscopic studies, including recent x-ray diffraction and extended x-ray absorption fine structure results to 3.0 Å resolution.[12-14]

Given the demands of the half reaction, $2H_2O \rightarrow O_2 + 4H^+ + 4e^-$, with requirements for both $4e^-/4H^+$ loss and O---O bond formation, water oxidation is difficult to achieve at a single catalyst site or cluster. In addition to PSII, water oxidation is also catalyzed by the ruthenium "blue dimer" *cis,cis*-$[(bpy)_2(H_2O)Ru^{III}ORu^{III}(OH_2)(bpy)_2]^{4+}$ and structurally related derivatives.[15-21] Additional molecular catalysts based on iridium and ruthenium complexes and ruthenium-containing polyoxometalates have been reported recently.[22-29]

The low oxidation state $Ru^{III}ORu^{III}$ form of the ruthenium blue dimer undergoes oxidative activation by proton-coupled electron transfer (PCET) in which stepwise loss of electrons and protons occurs. Single electron activation of multi-electron catalysis has been shown to be viable in catalytic water oxidation. PCET is essential, because it allows for the buildup of multiple oxidative equivalents at a single site or cluster without building up positive charge or proceeding through high energy catalytic precursors.[21,30] As shown by the results of pH-dependent electrochemical studies,[16] loss of $4e^-/4H^+$ occurs to give a reactive, transient intermediate followed by O_2 evolution. In the absence of a serendipitous discovery, mechanistic knowledge is required for the design of robust, long-lived catalysts for water

oxidation. Such knowledge is also important for the microscopic reverse reaction, oxygen reduction to water, which occurs at the cathode in fuel cell applications.[31,32]

Mechanistic investigations of ruthenium blue dimer water oxidation with Ce(IV) as the net oxidant have resulted in seemingly contradictory observations and/or interpretations of data in different laboratories.[17-21] A theoretical analysis of mechanism based on a density functional theory calculations has also appeared.[33] We were recently able to reconcile the seemingly disparate experimental observations on water oxidation by the ruthenium blue dimer by a comprehensive series of chemical mixing experiments with spectral and electrochemical monitoring. These observations revealed a complex mechanism involving a series of pH-dependent intermediates.

A powerful method for studying the blue dimer oxidation mechanism is spectrophotometric monitoring of changes in the solution absorbance after addition of the potent chemical oxidant Ce(IV) with $E^{o'}$[Ce(IV/III)] = 1.74 V vs. NHE in 1.0 M $HClO_4$. The dimer and its various oxidation states all absorb light strongly in the visible because of a combination of Ru-O-Ru bridged-based and charge transfer absorptions.[21] The used of Ce(IV) is restricted to strongly acidic solutions to avoid the complex hydrolysis phenomena that occur above pH = 1.[34]

The mechanism of water oxidation in solutions dilute in blue dimer with Ce(IV) as oxidant, in catalytic excess, is shown in Scheme 5.1. It features oxidation to a transient intermediate $[(bpy)_2(O)Ru^{V}ORu^{V}(O)(bpy)_2]^{4+}$ which undergoes rapid reaction with water to give a transiently stable peroxidic intermediate. In 0.1 M $HClO_4$ the latter decomposes by first order kinetics and evolves oxygen, k_4.[21]

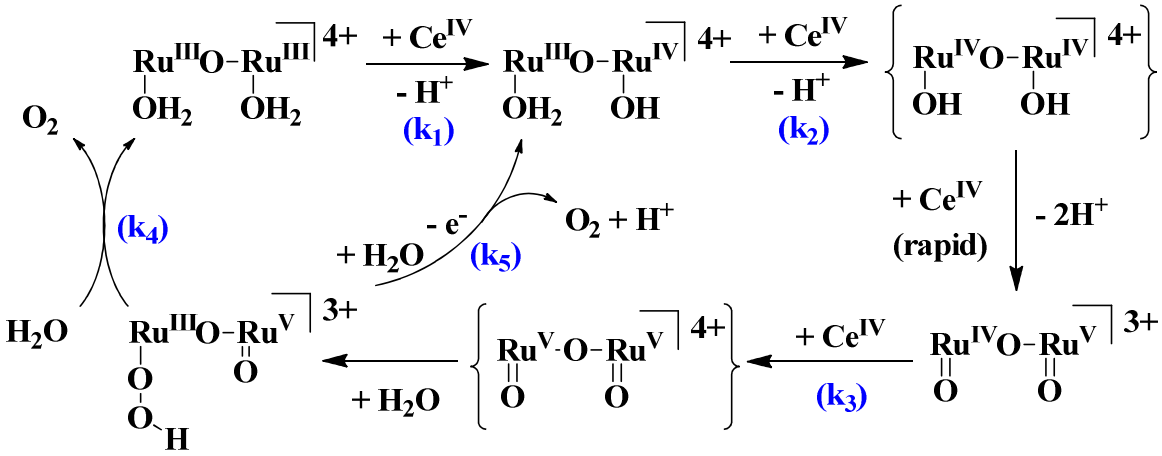

Scheme 5.1. Mechanism of Ce(IV) catalyzed water oxidation by the Blue Dimer at pH 1: k_1 = 630 $M^{-1}s^{-1}$, k_2 = 3.2 $M^{-1}s^{-1}$, k_3 = 2.0 x 10^2 $M^{-1}s^{-1}$, and k_4 = 2 x 10^{-3} s^{-1} (measured in 0.1 M $HClO_4$) at 23±2°C.

Addition of 1 equivalent of Ce(IV) to solutions containing $[(H_2O)Ru^{III}ORu^{III}(OH_2)]^{4+}$ in 0.1 M HNO_3 gives $[(H_2O)Ru^{III}ORu^{IV}(OH)]^{4+}$, eq. 1, with λ_{max} = 495, 1173 nm. Addition of another two equivalents of Ce(IV), eq. 2, gives previously characterized $[(O)Ru^{IV}ORu^{V}(O)]^{3+}$ with λ_{max} = 488, 710 nm. This reaction occurs in two steps with *k*(298 K,0.1 M HNO_3) = 4.5 x 10^3 $M^{-1}s^{-1}$ for the first step giving the intermediate Ru^{IV}-O-Ru^{IV}. It is unstable with respect to disproportionation and undergoes further, rapid oxidation to give $[(O)Ru^{IV}ORu^{V}(O)]^{3+}$.[21] The designation of localized oxidation states in this and related mixed-valence intermediates is a convenience. There is evidence for strong electronic coupling acrouss the m-oxo bridge, and the oxidation states may be delocalized, $[(O)Ru^{4.5}ORu^{4.5}(O)]^{3+}$.

$$[(H_2O)Ru^{III}ORu^{III}(OH_2)]^{4+} + Ce^{IV} \rightarrow [(H_2O)Ru^{III}ORu^{IV}(OH)]^{4+} + Ce^{III} + H^+ \qquad (1)$$

$$[(H_2O)Ru^{III}ORu^{IV}(OH)]^{4+} + 2Ce^{IV} \rightarrow [(O)Ru^{V}ORu^{IV}(O)]^{3+} + 2Ce^{III} + 3H^+ \qquad (2)$$

Oxidation past $[(O)Ru^{IV}ORu^{V}(O)]^{3+}$ by 1 equivalent of added Ce(IV) gives an intermediate (**I**) with λ_{max} = 482, 850 nm. The same intermediate appears after addition of 3 equivalents of Ce(IV) to $[(H_2O)Ru^{III}ORu^{IV}(OH)]^{4+}$. Redox titrations with addition of Fe^{2+}(aq) as a reducing agent show that addition of 4 equivalents of Fe^{2+}(aq) results in quantitative reduction of **I** to $[(H_2O)Ru^{III}ORu^{III}(OH_2)]^{4+}$. Increasing the acid concentration to 1.0 M HNO_3 results in absorption spectral shifts to λ_{max} = 451, 750 nm. The absorption changes with acid concentration are reversible and consistent with the acid-base equilibrium between **I** and a second, protonated form, **II,** shown in eq 4 with $0 < pK_a < 1$.

$$[(O)Ru^{IV}ORu^{V}(O)]^{3+} + Ce^{IV} \rightarrow \{[(O)Ru^{V}ORu^{V}(O)]^{4+}\} + Ce^{III}$$

$$\{[(O)Ru^{V}ORu^{V}(O)]^{4+}\} + H_2O \rightarrow [(HO_2)Ru^{III}ORu^{V}(O)]^{3+} + H^{+} \quad (3)$$

$$[(HO_2)Ru^{IV}ORu^{IV}(OH)]^{4+} \text{ (}\mathbf{II}\text{, } \lambda_{max} = 451, 750 \text{ nm)} \rightleftharpoons$$

$$[(HO_2)Ru^{III}ORu^{V}(O)]^{3+} + H^{+} \text{ (}\mathbf{I}\text{, } \lambda_{max} = 482, 850 \text{ nm)} \quad (4)$$

Appearance of the intermediate at λ_{max} = 482, 850 nm occurs rapidly following one electron oxidation of $[(O)Ru^{IV}ORu^{V}(O)]^{3+}$ to $[(O)Ru^{V}ORu^{V}(O)]^{4+}$. The latter does not build up as an observable transient but has been trapped as an unstable black ClO_4^- salt in ice-cold 1.0 M $HClO_4$.[17]

In eq 4, the intermediate is formulated as a terminal peroxide, $(HO_2)Ru^{III}ORu^{V}(O)^{3+}$. This formulation is consistent with the results of the redox titration and the acid-base equilibrium in eq 4. It is also consistent with the results of DFT calculations by Yang and Baik which predict a peroxidic intermediate.[33] The oxidation state distribution in

deprotonated form **I** is unknown but consistent with proton loss and stabilization by oxo formation in $Ru^{V}=O$.[35]

After addition of 30 equivalents of Ce(IV), the peroxidic intermediate is the dominant form in the catalytic steady state as shown by visible absorption measurements. Under these conditions, loss of Ce(IV), monitored at 360 nm, is first order in intermediate and first order in Ce(IV) with k(298 K,0.1 M HNO_3) = 183 $M^{-1}s^{-1}$. These observations point to rate limiting oxidation of $[(HO_2)Ru^{III}ORu^{V}(O)]^{3+}$ followed by rapid O_2 evolution, eqs 5 and 6, as the final steps in the oxidation cycle.

$$[(HO_2)Ru^{III}ORu^{V}(O)]^{3+} + Ce^{IV} \rightarrow \{[(HO_2)Ru^{IV}ORu^{V}(O)]^{4+}\} + Ce^{III} \quad (5)$$

$$\{[(HO_2)Ru^{IV}ORu^{V}(O)]^{4+}\} + H_2O \xrightarrow{rapid} [(H_2O)Ru^{III}ORu^{IV}(OH)]^{4+} + O_2 \quad (6)$$

On the basis of this mechanistic insight, we have devised a strategy for increasing rates of water oxidation catalysis by the blue dimer with added electron transfer mediators, $Ru(bpy)_2(L\text{-}L)^{2+}$ (L-L is 2,2'-bipyridine (bpy), 2,2'-bipyrimidine (bpm) and 2,2'-bipyrazine (bpz)) and $[Ru(bpm)_3]^{2+}$, that enhance the slow step in the overall catalytic cycle.

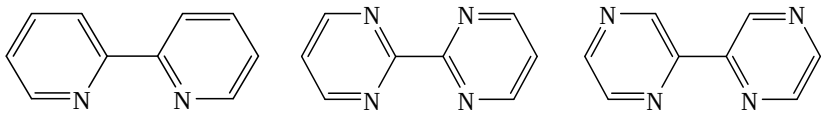

bpy bpm bpz

Experimental Section

Javier J. Concepcion synthesized the previously reported, diffusional redox mediators, and we performed the mixing experiments described herein with these complexes (Javier completing the bulk of the measurements in this case). We interpreted the data based on the mechanistic work I was involved in with the blue dimer. I synthesized the phosphonated bipyridine ligand and previously reported phosphonate-derivatized $[Ru(bpy)_3]^{2+}$ complex used in this study; Javier and Michael R. Norris developed its synthesis (see reference 46). I was responsible for oxygen measurements and all of the measurements associated with the surface catalyzed reactions.

Materials. Distilled water was further purified using a Milli-Q Ultrapure water purification system. Stock solutions of Ce^{IV} for kinetic and stoichiometric measurements were prepared from $(NH_4)_2Ce(NO_3)_6$ (99.99+%, Aldrich). Nitric acid (Trace Metal Grade, 70%) was purchased from Fisher Scientific and trifluoromethanesulfonic (HOTf) acid (Reagent Grade, 98%) from Aldrich. Trifluoromethanesulfonic acid was purified by addition of blue dimer and an excess of $(NH_4)_2Ce(NO_3)_6$ as solids to oxidize reducing impurities, followed by vacuum distillation. Purified HOTf was stored as 2.0 M stock solutions. 2,2'-bipyridine (97%), 4,4'-dimethyl-2,2'-bipyridine (99%), $RuCl_3 \times H_2O$, cerium(III) nitrate hexahydrate, and ammonium ferrous sulfate hexahydrate were purchased from Aldrich and used as received. *cis*-$[Ru(bpy)_2Cl_2]$ and *cis,cis*-$[(bpy)_2(H_2O)Ru^{III}ORu^{III}(OH_2)bpy)_2](ClO_4)_2$ were prepared as previously described.[16,36] 2,2'-bipyrimidine (97%) and $RuCl_3 \times H_2O$ were purchased from Aldrich and used as received. 2,2'-bipyrazine and $[Ru(bpy)_3](Cl)_2 \times 6H_2O$ were prepared as described in the literature.[37,38] $[Ru(bpm)_3](PF_6)_2$,[39] $[Ru(bpy)_2(bpz)](PF_6)_2$,[39] and $[Ru(bpy)_2(bpm)](PF_6)_2$ [40] were prepared as reported in the literature and converted to the

water-soluble chloride or nitrate salts by metathesis in acetone or acetonitrile with tetrabutylammonium chloride or nitrate. All other reagents were ACS grade and used without additional purification.

Methods. UV/Vis spectra vs. time was recorded on an Agilent Technologies Model 8453 diode-array spectrophotometer. Data were processed by use of the program SPECFIT/32 Global Analysis System (SPECTRUM Software Associates). Kinetic measurements were also performed on a Shimadzu UV-Vis-NIR Spectrophotometer Model UV-3600 by monitoring the disappearance of Ce^{IV} at 360 nm. Electrochemical measurements were performed on either a EG&G Princeton Applied Research model 273A potentiostat/galvanostat or a Bioanalytical Systems, Inc. 100B/W series potentiostat. Voltammetric measurements were made with one of the following working electrodes (1-3): **1)** a planar EG&G PARC G0229 glassy carbon millielectrode; **2)** planar ITO (In_2O_3:Sn); **3)** ITO electrode modified with $[Ru((4,4'\text{-}(HO_2)_2P(O)CH_2)_2bpy)_2(bpy)]^{2+}$; a platinum wire with attached platinum mesh counter electrode, and a Ag/AgCl Bioanalytical Systems, Inc. RE-5B reference electrode. Oxygen measurements were performed with a calibrated O_2 electrode (Microelectrodes, Inc. MI-730) or a calibrated O_2 electrode (YSI, Inc., Model ProODO). In a typical experiment using redox mediators in solution, 30 equivalents of Ce^{IV} were added to stirred solutions containing 3×10^{-4} M $Ru^{III}ORu^{III}$ blue dimer in 0.1 M HNO_3 with 6×10^{-4} M redox mediator. The air-tight reaction cell was purged with argon prior to the addition of the Ce^{IV} until the digital readout had stabilized. O_2 evolution vs. time was recorded and the theoretical maximum was achieved within 2 % for multiple runs with and without redox mediator. In the typical electrochemical experiment with surface modified electrodes, the air-tight reaction cell was purged with argon prior to holding at an applied potential and until the

digital readout had stabilized. An initial and final O_2 evolution measurement was recorded and the generated O_2 was within 5 % of the expected stoichiometry, $2H_2O \rightarrow O_2 + 4e^- + 4H^+$, based on the integrated current-time profile.

Results and Discussion

With these ligand variations of the added electron transfer mediators, reduction potentials for the corresponding Ru(III/II) couples ($E^{o'}$ vs NHE) are varied systematically: 1.27, 1.47, 1.40, and 1.69 V, respectively. Oxidation to their Ru(III) forms by Ce(IV) is spontaneous or nearly spontaneous with $E^{o'}$(Ce(IV/III)) = 1.60 V in 1 M HNO_3. These couples undergo facile electron transfer with self-exchange rate constants between the $Ru(bpy)_2(L)^{3+}$ and $Ru(bpy)_2(L)^{2+}$ forms on the order of 10^8-10^9 s^{-1}, while the self-exchange rate constant for the Ce(IV/III) couple is slower by orders of magnitude.[41]

Results obtained by monitoring Ce(IV) loss spectrophotometrically at 360 nm under catalytic conditions with 30 equivalents of added Ce(IV) and added mediator are summarized in Table 5.1.

Table 5.1. Rate constant data for oxidation of **I (**0.1 M HNO_3) or **II** (1 M HNO_3) at 298 K with $[(H_2O)Ru^{III}ORu^{III}(OH_2)^{4+}]$ = 1.25×10^{-5} M, [Redox Mediator] = 1.25×10^{-5} M and 30 equivalents of Ce(IV).

Redox Mediator	*k* (1.0 M HNO_3) $M^{-1}s^{-1}$	*k* (0.1 M HNO_3) $M^{-1}s^{-1}$
None	78	183
$[Ru(bpy)_3]^{2+}$	*	1862
$[Ru(bpy)_2(bpm)]^{2+}$	1044	5493
$[Ru(bpy)_2(bpz)]^{2+}$	1848	†
$[Ru(bpm)_3]^{2+}$	895	†

As monitored by Ce(IV) loss at 360 nm (see Appendix D).
Conditions: $[(H_2O)Ru^{III}ORu^{III}(OH_2)^{4+}]$ = 1.25 x 10^{-5} M, [redox mediator] = 1.25 x 10^{-5} M, and 30 eq of Ce(IV).
*No catalysis because oxidation of the protonated form of the peroxidic intermediate $[(HO_2)Ru^{IV}ORu^{IV}(OH)]^{4+}$ at pH = 0 by $Ru(bpy)3^{3+}$ is thermodynamically unfavorable and slow.
†No catalysis because oxidation of $[Ru(bpy)_2(bpz)]^{2+}$ or $[Ru(bpm)_3]^{2+}$ by Ce(IV) at pH = 1 is slow. $E^{o'}$(Ce(IV/III)) = 1.6 V in 1 M HNO_3, but this couple is highly medium-dependent.[34]

Under these conditions, the peroxidic intermediate, as **I** or **II** depending on acidity, still dominates at the catalytic steady state (Figure 5.1 and 5.2).

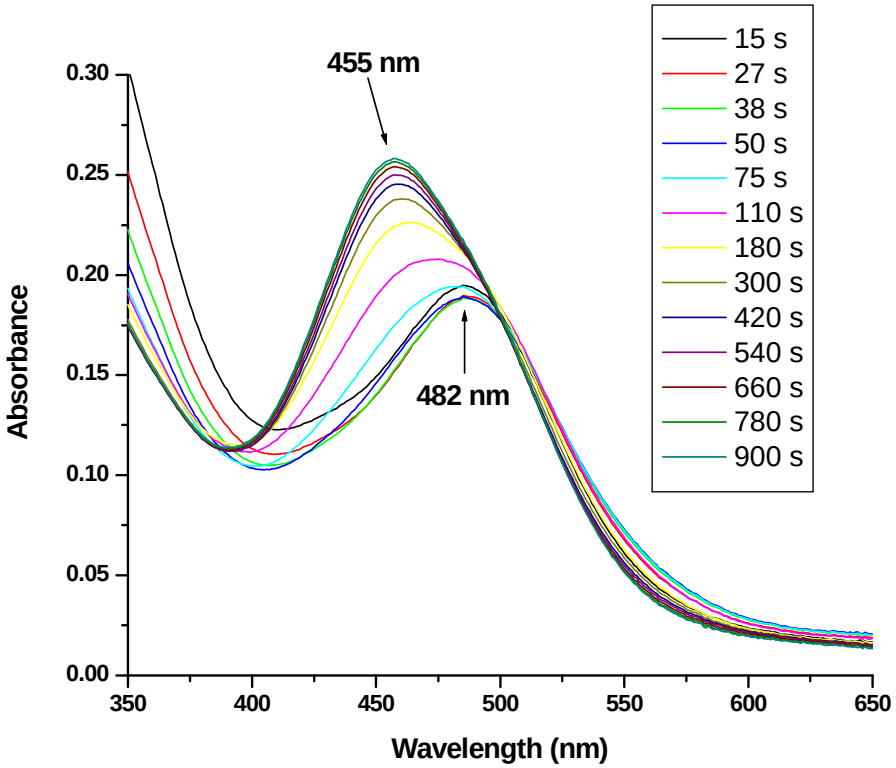

Figure 5.1. Spectral changes following the addition of 30 equivalents of Ce(IV) to a solution containing 1.25×10^{-5} M $(H_2O)Ru^{III}ORu^{III}(OH_2)^{4+}$ and 1.25×10^{-5} M $[Ru(bpy)_2(bpm)]^{2+}$ as redox mediator in 0.1 M HNO_3. Initially, the peroxidic intermediate $(HO_2)Ru^{III}ORu^{V}(O)^{3+}$ (λ_{max} = 482 nm) is the dominant species in solution because its oxidation by the redox mediator is the rate determining step. Once all the Ce(IV) has been consumed (~ 50 s) the anated species $(O_2NO)Ru^{IV}ORu^{IV}(OH)^{4+}$ (λ_{max} = 455 nm) begins to form and it is the dominant form of the dimer at the end of the experiment (~ 900 s).

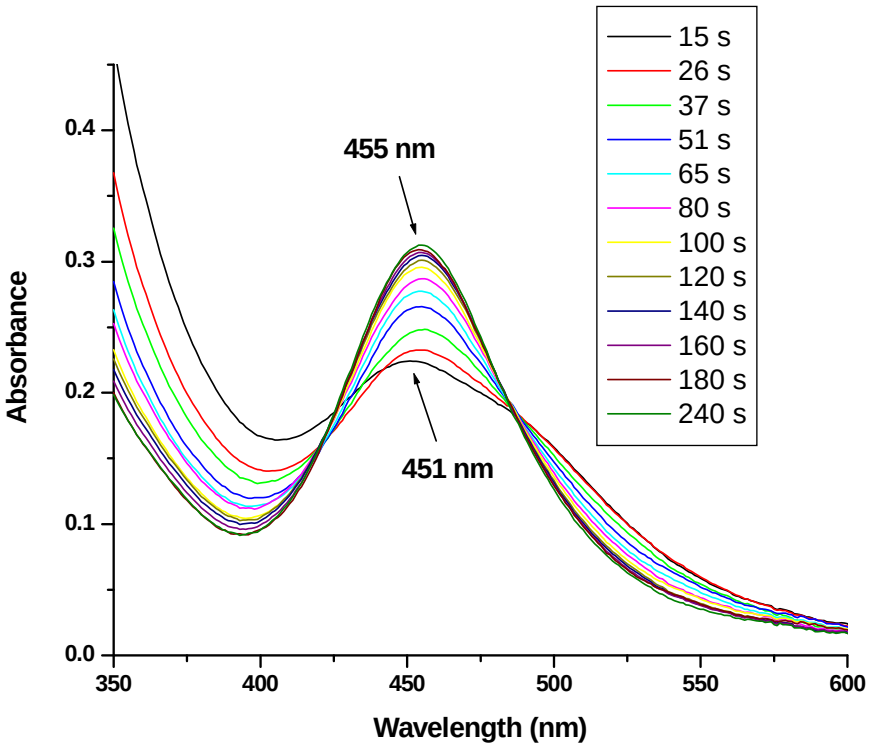

Figure 5.2. Spectral changes following the addition of 30 equivalents of Ce(IV) to a solution containing 1.25 x 10^{-5} M $(H_2O)Ru^{III}ORu^{III}(OH_2)^{4+}$ and 1.25 x 10^{-5} M $[Ru(bpy)_2(bpz)]^{2+}$ as redox mediator in 1.0 M HNO_3. Initially, the peroxidic intermediate $(HO_2)Ru^{IV}ORu^{IV}(OH)^{4+}$ (λ_{max} = 451 nm) is the dominant species in solution because its oxidation by the redox mediator is the rate determining step. Due to a higher anion concentration in this case (1.0 M NO_3^-), the anated species, $(O_2NO)Ru^{IV}ORu^{IV}(OH)^{4+}$ (λ_{max} = 455 nm), begins to form before all the Ce(IV) has been consumed (~ 180 s) and it is the dominant form of the dimer at the end of the experiment (~ 300 s).

The data in Table 5.1 demonstrate rate enhancements for water oxidation by factors of up to ~30 as a result of mediated oxidation of the peroxidic intermediate, eqs 7 and 8. The rate enhancements are attributable to an interplay between rate limiting oxidation of RuL_3^{2+} (eq 7) and rate limiting oxidation of the peroxidic intermediate (eq 8). For example, the rate constant for oxidation of $[Ru(phen)_3]^{2+}$ by Ce(IV) in 0.1 M HNO_3 (~10^5 $M^{-1}s^{-1}$)[42] is ~500 times more rapid than oxidation of $[(HO_2)Ru^{III}ORu^{V}(O)]^{3+}$ by $[Ru(bpy)_3]^{3+}$ (~1.9 x 10^3

$M^{-1}s^{-1}$). On the other hand, there is no catalysis by $[Ru(bpy)_2(bpz)]^{2+}$ in 0.1 M HNO_3 (Table 5.1) because of slow oxidation of RuL_3^{2+} by Ce(IV).

$$[RuL_3]^{2+} + Ce^{IV} \rightarrow [RuL_3]^{3+} + Ce^{III} \quad (7)$$

$$[(HO_2)Ru^{III}ORu^{V}(O)]^{3+} + [RuL_3]^{3+} \rightarrow \{[(HO_2)Ru^{IV}ORu^{V}(O)]^{4+}\} + [RuL_3]^{2+} \quad (8)$$

With added mediator, oxygen evolution occurs quantitatively as shown by oxygen electrode measurements. Addition of 30 equivalents of Ce(IV) resulted in appearance of the expected ~7.5 eq of O_2, consistent with the expected stoichiometry in eq 9 and the catalytic cycle in Scheme 5.2.

Scheme 5.2. Blue dimer catalyzed Ce(IV) water oxidation utilizing redox mediators.

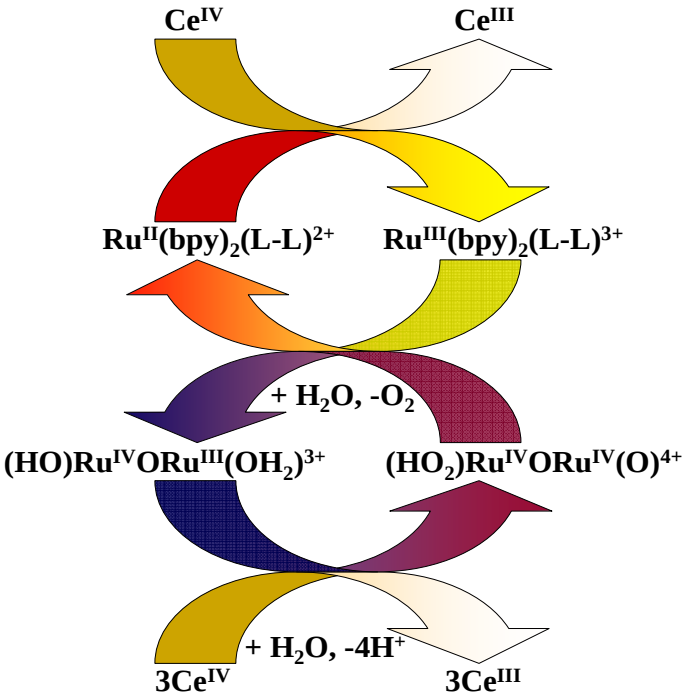

$$4\ Ce(IV) + 2\ H_2O \rightarrow 4\ Ce(III) + O_2 + 4H^+ \quad (9)$$

These results are important in further demonstrating and then exploiting the complex mechanistic details of water oxidation by the ruthenium blue dimer. They also add to the limited insight available for water oxidation and make a possible connection with water oxidation in PSII, in which a peroxido intermediate has also been proposed.[6,7] Preliminary electrochemical experiments in 0.1 M HNO_3 with a glassy carbon working electrode demonstrate that mediator-assisted electrocatalytic water oxidation (Scheme 5.3) is attainable, with a turnover number of 19 already achieved.

Scheme 5.3. Electrochemically driven water oxidation by the blue dimer with added redox mediators.

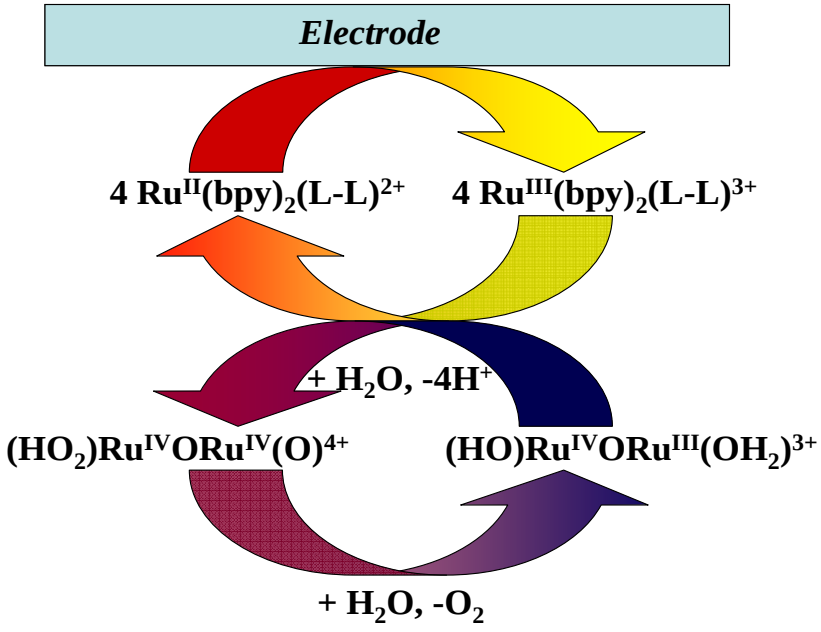

In the Reaction Center of PSII, light is harvested by an antenna array consisting of chlorophylls and organic pigments, which sensitize the lowest singlet excited state of chlorophyll P_{680} or a neighboring pheophytin$_{D1}$.[43] This excited state subsequently undergoes oxidative quenching, giving P_{680}^{+} by electron transfer to quinone Q_A. In the next step, P_{680}^{+}

oxidizes redox mediator tyrosine Tyr_Z (Y_Z), which in turn activates the oxygen evolving complex (OEC) by coupled electron-proton transfer (EPT).[6,30]

Cape and Hurst have shown that $[Ru(bpy)_3]^{3+}$ generated by persulfate oxidation of $[Ru(bpy)_3]^{2+*}$ can oxidize the blue dimer, which then oxidizes water. We believe that it should be possible to mimic the features of the reaction center in PSII in designed molecular assemblies on the surfaces of appropriately chosen semiconductor metal oxide electrodes with the ruthenium blue dimer or a derivative acting as an OEC analog.[21,44]

Translating the solution reactivity of mediated single electron activation of catalysts to electrode surfaces is a difficult challenge. For the blue dimer, *cis,cis*-$[(bpy)_2(H_2O)Ru^{III}ORu^{III}(H_2O)(bpy)_2]^{4+}$, the catalytically active intermediate $[(O)Ru^{V}ORu^{V}(O)]^{4+}$ is kinetically inaccessible at an unmodified metal oxide surface where the only available redox pathway is electron transfer. A remarkable surface activation of ITO (In_2O_3:Sn) electrodes toward catalytic water oxidation by the blue dimer can be achieved by surface phosphonate derivatization with $[Ru(4,4'\text{-}((HO)_2P(O)CH_2)_2bpy)_2(bpy)]^{2+}$. Surface binding dramatically improves the rate of surface oxidation of the blue dimer and induces water oxidation catalysis.

The multi-electron nature of water oxidation, $2H_2O \rightarrow O_2 + 4e^- + 4H^+$, poses significant mechanistic challenges. For example, mechanisms involving $1e^-$ oxidation and hydroxyl radical as an intermediate with $E^o(\bullet OH/H_2O) = 2.8$ V vs. NHE are too slow to be of interest which can be significantly inhibiting at electrode surfaces where the only available pathway is electron transfer.[45] We report a pronounced surface activation effect at Sn(IV)-doped In_2O_3 (ITO) electrodes modified by surface binding of a functionalized $[Ru(bpy)_3]^{2+}$ complex (bpy is 2,2'-bipyridine).

In cyclic voltammograms (CVs) of the blue dimer in 0.1 M triflic acid (HOTf), an electrochemically reversible, scan rate dependent, $1e^-$ wave appears at $E_{1/2}$ = 1.04 V vs. NHE, for the $[(H_2O)Ru^{III}ORu^{IV}(OH)]^{4+}/[(H_2O)Ru^{III}ORu^{III}(OH_2)]^{4+}$ couple, Figure 5.3A. A dramatically different response, Figure 5.3B, appears at ITO electrodes with chemically linked, phosphonate-derivatized $[Ru(4,4'\text{-}((HO)_2P(O)CH_2)_2bpy)_2(bpy)]^{2+}$ (**ITO-Ru^{2+}**) (4,4'-$((HO)_2P(O)CH_2)_2$bpy is 4,4'-bis-(methyl)phosphonato-2,2'-bipyridine).[46]

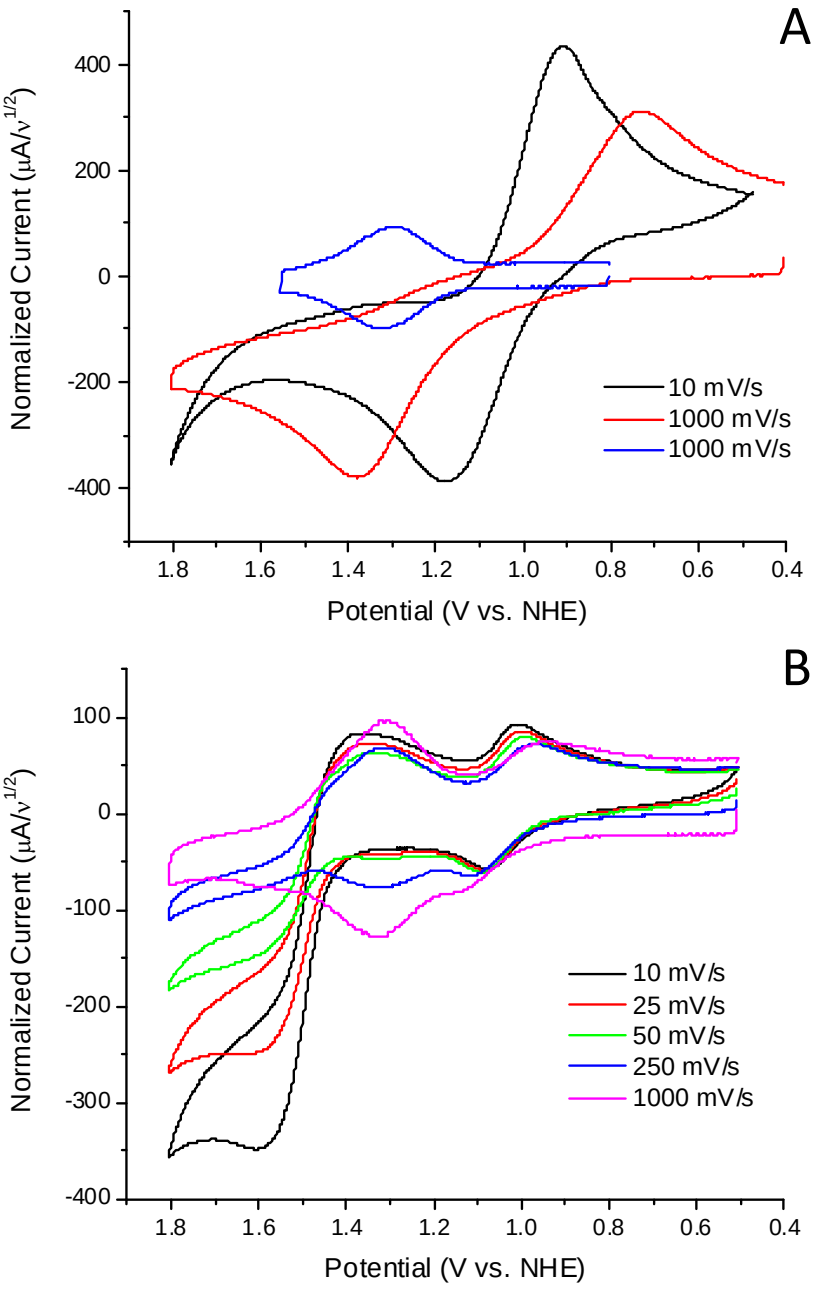

Figure 5.3. A). Scan rate normalized ($i_p/v^{1/2}$) cyclic voltammograms (CVs) of 1 mM Blue dimer in 0.1 M triflic acid (HOTf) at an ITO electrode (1.55 cm^2) at scan rates of 10 and 1000 mV/s, 23 ± 2 ^oC. A CV (i_p/v) of surface-adsorbed [Ru(4,4'-$((HO_2)_2P(O)CH_2)_2bpy)_2(bpy)]^{2+}$ on ITO (**ITO-Ru^{2+}**), Γ = 1.0 x 10^{-10} mol/cm^2, 1.55 cm^2, is shown in blue. B). CVs ($i_p/v^{1/2}$) of 1.0 x 10^{-4} M blue dimer in 0.1 M HOTf at **ITO-Ru^{2+}** (Γ = 1.0 x 10^{-10} mol/cm^2, 1.5 cm^2) at various scan rates.

Synthesis and characterization of the complex is described in Appendix D. It was added to ITO by soaking electrodes for extended periods in methanol solutions (at least 8 hours) containing the complex, Figure 5.4. The loaded surface was then rinsed with methanol and air dried. Surface coverages (Γ in mol/cm^2) were determined by integrating the cathodic peak area for the surface Ru(III/II) wave at $E_{1/2}$ = 1.31 V vs. NHE at pH = 1, Figure 5.3A, after background subtraction and converting coulombs to mol/cm^2 as described previously.[47] Surface coverages were controlled by the stock solution concentrations as shown in the isotherm in Figure 5.4. Maximum coverages of $\Gamma \sim 1 \times 10^{-10}$ mol/cm^2 were obtained.

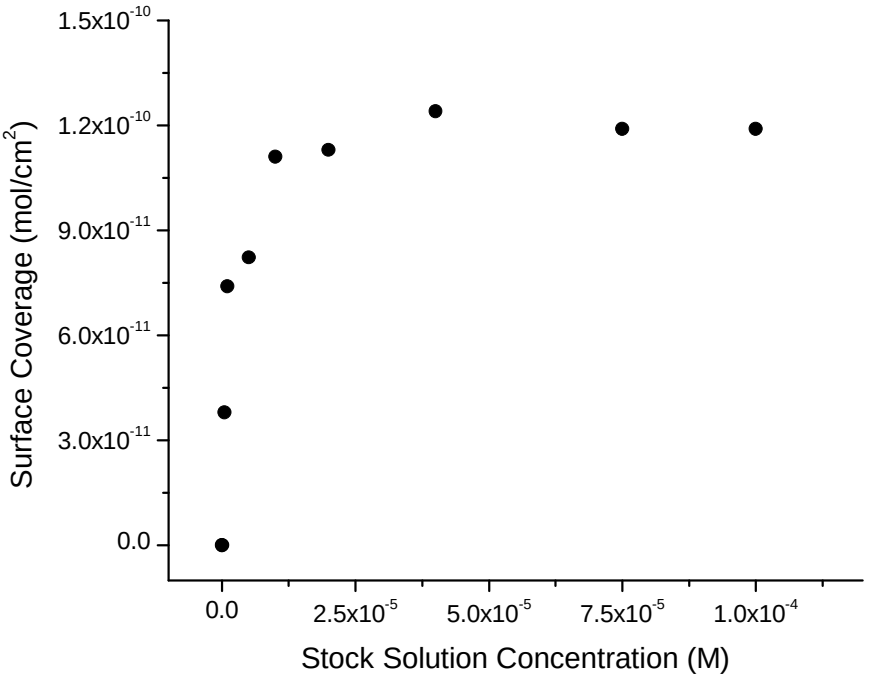

Figure 5.4. Surface coverage isotherm for surface-adsorbed [Ru(4,4'-$((HO_2)_2P(O)CH_2)_2bpy)_2(bpy)]Cl_2$ on ITO, determined by cyclic voltammetry in 0.1 M HNO_3 at 23 ± 2 ^oC.

Peak currents (i_p) for the surface Ru(III/II) wave vary linearly with scan rate (v) as expected for a surface-confined couple, Appx. D - Figures S1,2.[48] At the modified electrode

with added blue dimer, the $[(H_2O)Ru^{III}ORu^{IV}(OH)]^{4+}/[(H_2O)Ru^{III}ORu^{III}(OH_2)]^{4+}$ wave appears at $E_{1/2}$ = 1.04 V and an additional oxidative wave at $E_{p,a}$ = 1.57 V for the $3e^-/3H^+$ couple,[16] $[(H_2O)Ru^{III}ORu^{IV}(OH)]^{4+} \xrightarrow{-3e^-,-3H^+} [(O)Ru^{V}ORu^{V}(O)]^{4+}$. Peak currents for both waves vary with $v^{1/2}$ consistent with diffusional couples, Appx. D - Figures S3,4.[48]

The dramatic current enhancement for the $3e^-/3H^+$ wave at 1.57 V is due to an enhancement of rate limiting electron transfer oxidation of $[(H_2O)Ru^{III}ORu^{IV}(OH)]^{4+}$ to $Ru^{IV}ORu^{IV}$ (presumably as $[(HO)Ru^{IV}ORu^{IV}(OH)]^{4+}$ at this pH), eq 10a.[49] $Ru^{IV}ORu^{IV}$ is a kinetic intermediate unstable toward disproportionation with $E^o(Ru^{IV}ORu^{IV}/Ru^{III}ORu^{IV)} > E^o(Ru^{IV}ORu^{V}/ Ru^{IV}ORu^{IV)}$.[21] Once formed in the rate limiting step, it undergoes further $2e^-/2H^+$ oxidation to $[(O)Ru^{V}ORu^{V}(O)]^{4+}$ followed by water attack to give the peroxide, eq 10b. The rate constant for oxidation of $[(H_2O)Ru^{III}ORu^{IV}(OH)]^{4+}$ to $Ru^{IV}ORu^{IV}$ by Ce^{IV} is 3.2 $M^{-1}s^{-1}$ in 0.1 M $HClO_4$. However, the effective rate of oxidation increases to ~10^3 $M^{-1}s^{-1}$ as the reaction proceeds and $[(O)Ru^{IV}ORu^{V}(O)]^{3+}$ appears in the solution. Under these conditions $Ru^{IV}ORu^{IV}$ forms by comproportionation between $[(H_2O)Ru^{III}ORu^{IV}(OH)]^{4+}$ and $[(O)Ru^{IV}ORu^{V}(O)]^{3+}$ and is oxidized rapidly by Ce^{IV}.[17]

$$\text{ITO-Ru}^{3+} + [(H_2O)Ru^{III}ORu^{IV}(OH)]^{4+} \rightarrow \text{ITO-Ru}^{2+} + [(HO)Ru^{IV}ORu^{IV}(OH)]^{4+} + H^+ \qquad (10a)$$

$$[(HO)Ru^{IV}ORu^{IV}(OH)]^{4+} \xrightarrow{+H_2O,-2e^-,-3H^+} [(HOO)Ru^{III}ORu^{V}(O)]^{3+} \quad \text{(rapid)} \qquad (10b)$$

A mechanism related to Scheme 5.1 also holds for the surface mediated reaction. At even higher potentials, a catalytic water oxidation wave appears with an onset at ~1.7 V. Catalytic water oxidation at these potentials appears to be triggered by further oxidation of the peroxidic intermediate $[(HOO)Ru^{III}ORu^{V}(O)]^{3+}$ to $[(OO)Ru^{IV}ORu^{V}(O)]^{3+}$ (k_5 in Scheme 5.1 but at the electrode) followed by rapid oxygen release, eq 11. In CVs of this intermediate (generated by addition of x3 Ce(IV) to $[(H_2O)Ru^{III}ORu^{IV}(OH)]^{4+}$) at a mediator modified electrode (Figure 5.5), an irreversible oxidation wave appears at ~1.8 V on a catalytic background. The peroxidic intermediate is further characterized by λ_{max} = 482 nm (ε = 13,200 $M^{-1}cm^{-1}$)[21] and a wave for a $[(HOO)Ru^{III}ORu^{V}(O)]^{3+}/[(HOO)Ru^{III}ORu^{IV}(OH)]^{3+}$ couple at $E_{1/2}$ = 1.03 V vs. NHE.

$$[(HOO)Ru^{III}ORu^{V}(O)]^{3+} \xrightarrow{-e^-,-H^+} [(OO)Ru^{IV}ORu^{V}(O)]^{3+} \qquad (11a)$$

$$[(OO)Ru^{IV}ORu^{V}(O)]^{3+} \xrightarrow{+H_2O,+H^+} [(H_2O)Ru^{III}ORu^{IV}(OH)]^{4+} + O_2 \text{ (rapid)} \qquad (11b)$$

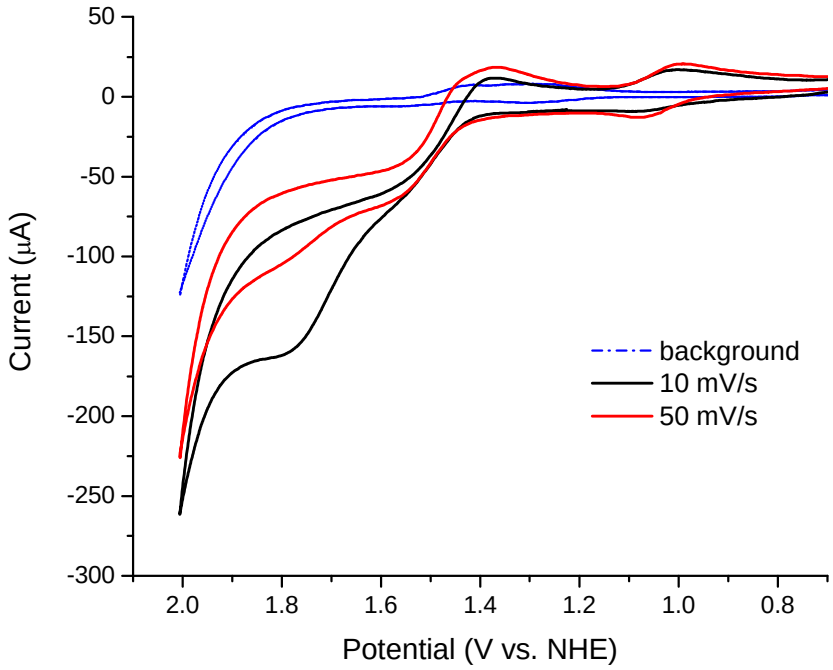

Figure 5.5. CVs of the peroxido intermediate formed by addition of x3 Ce(IV) to 1.0 x 10^{-4} M $[(H_2O)Ru^{III}ORu^{IV}(OH)]^{4+}$ in 0.1 M HOTf with surface adsorbed $[Ru(4,4'\text{-}((HO_2)_2P(O)CH_2)_2bpy)_2(bpy)]^{2+}$ on ITO (Γ = 1.0 x 10^{-10} mol/cm^2; 1.52 cm^2). The background is of 3.0 x 10^{-4} M Ce(III) in 0.1 M HOTf at the same electrode.

As noted below, holding the potential past $E^{o'}$ for the Ru(III/II) wave at 1.31 V leads to electrocatalytic water oxidation. Peak currents increase linearly with surface coverage of the mediator and with concentration of blue dimer in the external solution, Figure 5.6A and Appx. D - Figure S5. The rate constant for surface oxidation of blue dimer calculated from catalytic current measurements, Figure 5.6B, is k_{cat} = 2.1 x 10^3 $M^{-1}s^{-1}$. Catalysis is not observed at bare ITO electrodes. A comparable rate enhancement of blue dimer catalysis was observed with k_{cat} = 1.9 x 10^3 $M^{-1}s^{-1}$ for $[Ru(bpy)_3]^{3+}$ as the oxidant in solution.[50]

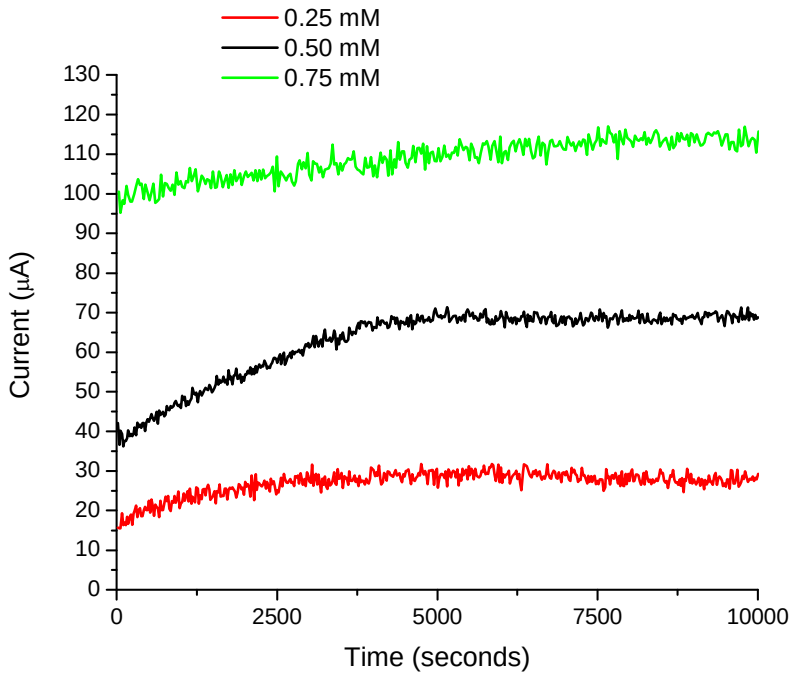

(A)

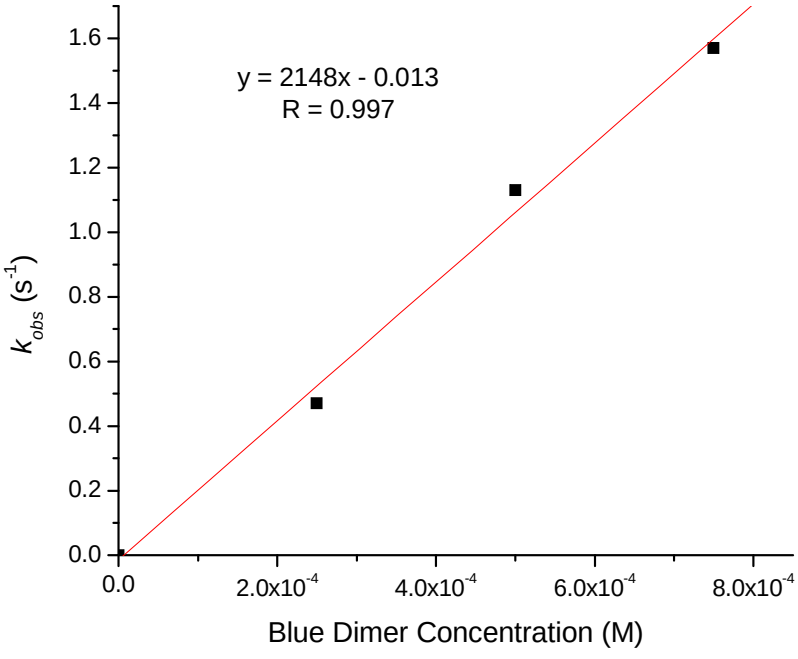

(B)

Figure 5.6. (A) Concentration dependence of limiting currents for water oxidation by controlled potential electrolysis in stirred solutions of 0.25 mM, 0.5 mM, and 0.75 mM $[(bpy)_2(H_2O)Ru^{III}ORu^{IV}(OH)(bpy)_2]^{4+}$ in 0.1 M HOTf with 2.5 x 10^{-5} M $[Ru(4,4'\text{-}((HO_2)_2P(O)CH_2)_2bpy)_2(bpy)]^{2+}$ in the external solution (4 ml total volume) at ITO-$[Ru(4,4'\text{-}((HO_2)_2P(O)CH_2)_2bpy)_2(bpy)]^{2+}$ (Γ ~ 1x10^{-10} mol/cm^2; with A = 1.55, 1.56, and 1.87 cm^2, respectively). The potential was held at 1.46 V versus NHE. The solutions were stirred by a magnetic stir bar at rates sufficient that i_{lim} was independent of stir rate. (B) $k_{obs} = k_{act}$ values calculated from the expression rate = $k_{cat}[(H_2O)Ru^{III}ORu^{IV}(OH)^{4+}] = i_{lim}/nF\Gamma A$ with i_{lim} the

limiting current, k_{cat} the catalytic rate constant, A the electrode surface area, and n = 4, the electrochemical stoichiometry.[51] For the electrode reaction, $k_{obs} = k_{cat} = k_{ET}K_A$, with k_{ET} the electron transfer rate constant and K_A the association complex constant between ITO-Ru^{2+} and $[(H_2O)Ru^{III}ORu^{IV}(OH)]^{4+}$.

A complication appears in CV data at higher blue dimer concentrations, especially in $HClO_4$, arising from adsorption/micro-precipitation of salts of $[(O)Ru^{V}ORu^{V}(O)]^{4+}$ on the electrode surface. Adsorption is characterized by a reductive spike in the current-potential profile at $E_{p,c}$ = 1.43 V in reverse scans, Appx. D - Figure S6,7. Under other conditions, a nearly reversible $3e^-/3H^+$ surface wave is observed, Figure 5.7.[16] A related effect has been reported for chemical oxidation of the blue dimer by x4 Ce(IV) in ice cold 1.0 M $HClO_4$.[17,52]

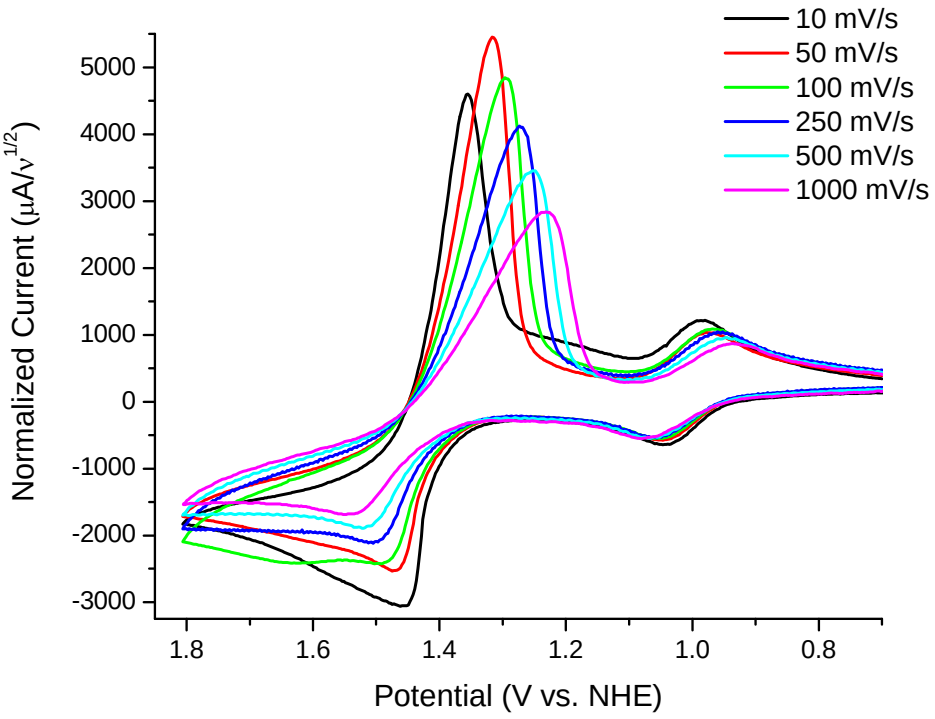

Figure 5.7. Scan rate normalized cyclic voltammograms of 1 mM Blue dimer in 0.1 M $HClO_4$ at ITO-$[Ru(4,4'\text{-}((HO_2)_2P(O)CH_2)_2bpy)_2(bpy)]^{2+}$ ($\Gamma \sim 1x10^{-10}$ mol/cm^2; 1.47 cm^2).

Depending on solution conditions, blue dimer adsorption causes slow loss of surface catalysis over time as the mediator is lost from the surface. Steady state surface loading was

maintained by adding 2.5 x 10^{-5} M $[Ru(4,4'\text{-}((HO_2)_2P(O)CH_2)_2bpy)_2(bpy)]^{2+}$ to the external solution to maintain a monolayer surface coverage, Figure 5.4.

Electrocatalytic water oxidation was investigated with 0.5 mM blue dimer in the external solution in 0.1 M HOTf at an applied potential of 1.46 V vs NHE, just past the Ru(III/II) surface couple at 1.31 V (Appx. D - Figure S8). Steady state, catalytic current densities of 44 $\mu A/cm^2$ were obtained for more than five hours under these conditions. At this potential, water oxidation is initiated by oxidation of the mediator with an overvoltage of ~0.3 V relative to the O_2/H_2O couple. Illustrating the importance of catalyst surface binding, there was no evidence for catalysis at an unmodified ITO electrode with 2.5 x 10^{-5} M $[Ru(bpy)_3]^{2+}$ in the external solution.

Evolved oxygen measurements in an air-tight electrochemical cell confirmed electrocatalytic production of oxygen. O_2 was measured by the difference in the initial reading of O_2 in the headspace of an airtight, degassed electrochemical cell and the final reading. The final reading was stable indefinitely. After 500 min of electrolysis at 1.46 V, 0.95 coulombs had passed producing 2.5 x 10^{-6} mol O_2, corresponding to 17,500 turnovers of the surface mediator, 1.25 turnovers of the blue dimer, and a Faradaic efficiency of 95 %.

Spectrophotometric monitoring revealed that the dominant form of the catalyst in the initial stages of the electrolysis was $[(H_2O)Ru^{III}ORu^{IV}(OH)]^{4+}$ (λ_{max} = 495 nm; ε = 22,000 $M^{-1}cm^{-1}$) consistent with its rate limiting oxidation to $Ru^{IV}ORu^{IV}$. As the electrolysis proceeds, the spectrum shifts to 492 nm consistent with earlier observations of anation and formation of $[(H_2O)Ru^{III}ORu^{IV}(OTf)]^{4+}$.[21] Anated intermediates inhibit catalysis because of the requirement to undergo aquation before re-entering the catalytic cycle.

Conclusion

Our results demonstrate that multi-electron transfer water oxidation catalysis can be accelerated by mediating interfacial electron transfer near the potential of the O_2/H_2O couple with relatively low overvoltages. There are potentially important implications for photodriven water oxidation as well.[53]

REFERENCES

(1) Tommos, C.; Babcock, G. T. *Accounts of Chemical Research* **1998**, *31*, 18.

(2) Nelson, N.; Yocum, C. F. *Annual Review of Plant Biology* **2006**, *57*, 521.

(3) Kern, J.; Biesiadka, J.; Loll, B.; Saenger, W.; Zouni, A. *Photosynthesis Research* **2007**, *92*, 389.

(4) Barber, J. *Biochemical Society Transactions* **2006**, *34*, 619.

(5) McEvoy, J. P.; Brudvig, G. W. *Chem. Rev. (Washington, DC, U. S.)* **2006**, *106*, 4455.

(6) Meyer, T. J.; Huynh, M. H. V.; Thorp, H. H. *Angew. Chem., Int. Ed.* **2007**, *46*, 5284.

(7) Renger, G. *Photosynthesis Research* **2007**, *92*, 407.

(8) Cady, C. W.; Crabtree, R. H.; Brudvig, G. W. *Coordination Chemistry Reviews* **2008**, *252*, 444.

(9) Alstrum-Acevedo, J. H.; Brennaman, M. K.; Meyer, T. J. *Inorganic Chemistry* **2005**, *44*, 6802.

(10) Gust, D.; Moore, T. A.; Moore, A. L. *Accounts of Chemical Research* **2001**, *34*, 40.

(11) Wasielewski, M. R. *Chemical Reviews* **1992**, *92*, 435.

(12) Ferreira, K. N.; Iverson, T. M.; Maghlaoui, K.; Barber, J.; Iwata, S. *Science* **2004**, *303*, 1831.

(13) Loll, B.; Kern, J.; Saenger, W.; Zouni, A.; Biesiadka, J. *Nature* **2005**, *438*, 1040.

(14) Yano, J.; Pushkar, Y.; Glatzel, P.; Lewis, A.; Sauer, K.; Messinger, J.; Bergmann, U.; Yachandra, V. *Journal of the American Chemical Society* **2005**, *127*, 14974.

(15) Gersten, S. W.; Samuels, G. J.; Meyer, T. J. *Journal of the American Chemical Society* **1982**, *104*, 4029.

(16) Gilbert, J. A.; Eggleston, D. S.; Murphy, W. R.; Geselowitz, D. A.; Gersten, S. W.; Hodgson, D. J.; Meyer, T. J. *Journal of the American Chemical Society* **1985**, *107*, 3855.

(17) Binstead, R. A.; Chronister, C. W.; Ni, J. F.; Hartshorn, C. M.; Meyer, T. J. *Journal of the American Chemical Society* **2000**, *122*, 8464.

(18) Yamada, H.; Siems, W. F.; Koike, T.; Hurst, J. K. *Journal of the American Chemical Society* **2004**, *126*, 9786.

(19) Hurst, J. K. *Coordination Chemistry Reviews* **2005**, *249*, 313.

(20) Hurst, J. K.; Cape, J. L.; Clark, A. E.; Das, S.; Qin, C. Y. *Inorganic Chemistry* **2008**, *47*, 1753.

(21) Liu, F.; Concepcion, J. J.; Jurss, J. W.; Cardolaccia, T.; Templeton, J. L.; Meyer, T. J. *Inorg. Chem. (Washington, DC, U. S.)* **2008**, *47*, 1727.

(22) McDaniel, N. D.; Coughlin, F. J.; Tinker, L. L.; Bernhard, S. *Journal of the American Chemical Society* **2008**, *130*, 210.

(23) Concepcion, J. J.; Jurss, J. W.; Templeton, J. L.; Meyer, T. J. *Journal of the American Chemical Society* **2008**, *130*, 16462.

(24) Concepcion, J. J.; Jurss, J. W.; Norris, M. R.; Chen, Z. F.; Templeton, J. L.; Meyer, T. J. *Inorganic Chemistry* **2010**, *49*, 1277.

(25) Sartorel, A.; Carraro, M.; Scorrano, G.; De Zorzi, R.; Geremia, S.; McDaniel, N. D.; Bernhard, S.; Bonchio, M. *Journal of the American Chemical Society* **2008**, *130*, 5006.

(26) Hull, J. F.; Balcells, D.; Blakemore, J. D.; Incarvito, C. D.; Eisenstein, O.; Brudvig, G. W.; Crabtree, R. H. *Journal of the American Chemical Society* **2009**, *131*, 8730.

(27) Zong, R.; Thummel, R. P. *Journal of the American Chemical Society* **2005**, *127*, 12802.

(28) Tseng, H. W.; Zong, R.; Muckerman, J. T.; Thummel, R. *Inorganic Chemistry* **2008**, *47*, 11763.

(29) Geletii, Y. V.; Botar, B.; Koegerler, P.; Hillesheim, D. A.; Musaev, D. G.; Hill, C. L. *Angewandte Chemie-International Edition* **2008**, *47*, 3896.

(30) Huynh, M.; Meyer, T. *Chemical Reviews* **2007**, *107*, 5004.

(31) Collman, J. P.; Devaraj, N. K.; Decreau, R. A.; Yang, Y.; Yan, Y.-L.; Ebina, W.; Eberspacher, T. A.; Chidsey, C. E. D. *Science (Washington, DC, U. S.)* **2007**, *315*, 1565.

(32) Chang, C. J.; Loh, Z. H.; Shi, C. N.; Anson, F. C.; Nocera, D. G. *Journal of the American Chemical Society* **2004**, *126*, 10013.

(33) Yang, X.; Baik, M. H. *Journal of the American Chemical Society* **2006**, *128*, 7476.

(34) Bondareva, T. N.; Stromberg, A. G. *Zhurnal Obshchei Khimii* **1955**, *25*, 666.

(35) Meyer, T. J.; Huynh, M. H. V. *Inorganic Chemistry* **2003**, *42*, 8140.

(36) Sullivan, B. P.; Salmon, D. J.; Meyer, T. J. *Inorganic Chemistry* **1978**, *17*, 3334.

(37) Boully, L.; Darabantu, M.; Turck, A.; Ple, N. *Journal of Heterocyclic Chemistry* **2005**, *42*, 1423.

(38) Broomhead, J. A.; Young, C. G. *Inorganic Syntheses* **1982**, *21*, 127.

(39) Rillema, D. P.; Allen, G.; Meyer, T. J.; Conrad, D. *Inorganic Chemistry* **1983**, *22*, 1617.

(40) Ji, Z.; Huang, S. D.; Guadalupe, A. R. *Inorganica Chimica Acta* **2000**, *305*, 127.

(41) Sigler, P. B.; Masters, B. J. *Journal of the American Chemical Society* **1957**, *79*, 6353.

(42) Miller, J. D.; Prince, R. H. *Journal of the Chemical Society a -Inorganic Physical Theoretical* **1966**, 1370.

(43) Holzwarth, A. R.; Muller, M. G.; Reus, M.; Nowaczyk, M.; Sander, J.; Rogner, M. *Proceedings of the National Academy of Sciences of the United States of America* **2006**, *103*, 6895.

(44) Treadway, J. A.; Moss, J. A.; Meyer, T. J. *Inorganic Chemistry* **1999**, *38*, 4386.

(45) Costentin, C.; Robert, M.; Saveant, J. M. *Journal of Electroanalytical Chemistry* **2006**, *588*, 197.

(46) Utilization of a previously published synthetic procedure for the surface catalyst, $[Ru(4,4'\text{-}(HO)_2P(O)CH_2)_2\text{-}bpy)_2(bpy)]Cl_2$,4b, gave CV surface enhancements but with qualitatively different wave forms (Figures S9-S11 in Appx. D). Currently under investigation, these preparations gave greater than monolayer coverages and the products appear to be oligomeric in nature. (b) Will, G.; Boschloo, G.; Rao, S. N.; Fitzmaurice, D. *J. Phys. Chem. B.* **1999**, *103*(38), 8067.

(47) Meyer, T. J.; Meyer, G. J.; Pfennig, B. W.; Schoonover, J. R.; Timpson, C. J.; Wall, J. F.; Kobusch, C.; Chen, X. H.; Peek, B. M.; Wall, C. G.; Ou, W.; Erickson, B. W.; Bignozzi, C. A. *Inorganic Chemistry* **1994**, *33*, 3952.

(48) Bard, A. J.; Faulkner, L. R. *Electrochemical Methods: Fundamentals and Applications*; Second Edition ed.; John Wiley & Sons, Inc., 2001.

(49) Bartolotti, L. J.; Pedersen, L. G.; Meyer, T. J. *International Journal of Quantum Chemistry* **2001**, *83*, 143.

(50) Concepcion, J. J.; Jurss, J. W.; Templeton, J. L.; Meyer, T. J. *Proceedings of the National Academy of Sciences of the United States of America* **2008**, *105*, 17632.

(51) Elliott, S. J.; McElhaney, A. E.; Feng, C. J.; Enemark, J. H.; Armstrong, F. A. *Journal of the American Chemical Society* **2002**, *124*, 11612.

(52) Cape, J. L.; Lymar, S. V.; Lightbody, T.; Hurst, J. K. *Inorganic Chemistry* **2009**, *48*, 4400.

(53) Concepcion, J. J.; Jurss, J. W.; Hoertz, P. G.; Meyer, T. J. *Angewandte Chemie-International Edition* **2009**, *48*, 9473.

CHAPTER 6

Electron Transfer Mediators-Chromophore/Catalyst Assemblies

Introduction

A plethora of new single-site catalysts for water oxidation have been established which operate by a well-defined mechanism via stepwise $3e^-$ oxidation to high valent ruthenium oxo complexes.[1,2] Additional single-site Ru catalysts have been identified by Thummel which may utilize a related mechanism.[3] These reactions appear to occur through key O---O bond forming steps and peroxido intermediates reminiscent of the proposed water oxidation mechanism of the Oxygen Evolving Complex (OEC) in Photosystem II (PSII)[4,5] and water oxidation by the blue Ru dimer, *cis,cis*-$[(bpy)_2(H_2O)Ru^{III}ORu^{III}(OH_2)(bpy)_2]^{4+}$ (bpy is 2,2′-bipyridine).[6] We have also described greatly enhanced rates of Ce(IV)-catalyzed water oxidation by the blue dimer by added redox mediators, $[Ru(bpy)_2(LL)]^{2+}$ (L-L is bpy, bpm, and bpz) and $[Ru(bpm)_3]^{2+}$.[7] Utilizing these results, robust water oxidation catalysis based on assemblies containing both the catalyst and redox mediator functions in solution and, notably, the methylenephosphonate derivatives for stable attachment to electrode surfaces have been developed.

Experimental Section

Javier J. Concepcion synthesized the complexes described in this chapter. Spectroscopic and electrochemical studies were completed by myself and Javier. I measured evolved oxygen.

Materials. Distilled water was further purified using a Milli-Q Ultrapure water purification system. Stock solutions of Ce^{IV} for kinetic and stoichiometric measurements were prepared from $(NH_4)_2Ce(NO_3)_6$ (99.99+%, Aldrich). Nitric acid (Trace Metal Grade, 70%) was purchased from Fisher Scientific and perchloric acid (70%, purified by redistillation, 99.999% trace metals basis) was purchased from Aldrich. 2,2'-bipyrimidine (97%) and $RuCl_3 \times H_2O$ were purchased from Aldrich and used as received. 2,6-bis(1-

methylbenzimidazol-2-yl)pyridine (Mebimpy) was prepared as reported for 2,6-bis(benzimidazol-2-yl)pyridine.[8] $[Ru(tpy)Cl_3]$[9] and $[Ru^{II}((4,4'\text{-}(EtO)_2OPCH_2)_2bpy)_2Cl_2]$[10] were prepared as described in the literature. $[Ru(LLL)(bpm)(Cl)](ClO_4)$ (LLL is tpy or Mebimpy) were prepared by a modification of the procedure reported for $[Ru(tpy)(bpm)(Cl)](PF_6)$.[11] All other reagents were ACS grade and used without additional purification. Detailed synthetic procedures are described in Appendix E.

Methods. UV/Vis spectra were recorded on an Agilent Technologies Model 8453 diode-array spectrophotometer. Stopped-flow experiments were performed on a Hi-Tech SF-61 DX2 double mixing stopped-flow system equipped with a diode array detector. The stopped volume was 100 μL and the initial concentrations in the syringes of **1** and Ce(IV) were 5×10^{-5} and 5×10^{-4} M, respectively. Kinetic measurements were also performed on a Shimadzu UV-Vis-NIR Spectrophotometer Model UV-3600 by monitoring the disappearance of Ce^{IV} at 360 nm. Data were processed by use of the program SPECFIT/32 Global Analysis System (SPECTRUM Software Associates). Electrochemical measurements were performed on an EG&G Princeton Applied Research model 273A potentiostat/galvanostat. Voltammetric measurements were made with a planar EG&G PARC G0229 glassy carbon millielectrode, a platinum wire EG&G PARC K0266 counter electrode, and Ag/AgCl EG&G PARC K0265 reference electrode. Oxygen measurements were performed with a calibrated O_2 electrode (YSI, Inc., Model 550A). In a typical experiment, 30 equivalents of Ce^{IV} were added to stirred solutions containing 2.9×10^{-3} M **1** or **2** in 1.0 M HNO_3. The air-tight reaction cell was purged with argon prior to the addition of the Ce^{IV} until the digital readout had stabilized. O_2 evolution vs. time was recorded and the theoretical maximum was achieved within 3 %.

Results and Discussion

The assemblies can be synthesized in two steps: (1) Reaction of $[Ru^{II}(bpy)_2Cl_2]\times 2H_2O$ with $[Ru^{II}(LLL)(bpm)Cl]^+$ in 1:1 EtOH:H_2O {bpy is 2,2'-bipyridine, bpm is 2,2'-bipyrimidine; LLL is tpy (2,2':6',2''-terpyridine) or Mebimpy (2,6-bis(1-methylbenzimidazol-2-yl)pyridine,[11,12] structures in Figure 6.1A}. 2) Removal of the chloro ligand and chloride counter ions in the resulting ligand-bridged assemblies $[(bpy)_2Ru^{II}(bpm)Ru^{II}(LLL)Cl]Cl_3$ by reaction with neat HOTf (OTf^- is trifluoromethanesulfonate anion) followed by displacement of OTf^- in water to give $[(bpy)_2Ru^{II}(bpm)Ru^{II}(tpy)(OH_2)]^{4+}$ (**1**) or $[(bpy)_2Ru^{II}(bpm)Ru^{II}(Mebimpy)(OH_2)]^{4+}$ (**2**). Purification was achieved by column chromatography (Sephadex LH-20) by using water as the eluant.

The corresponding methylenephosphonate ethyl esther derivatives were prepared by similar strategies by replacing $[Ru^{II}(bpy)_2Cl_2]\times 2H_2O$ with $[Ru^{II}((4,4'\text{-}(EtO)_2OPCH_2)_2bpy)_2Cl_2]$.[10] Hydrolysis of the methylenephosphonate ethyl esther derivatives in 4.0 M HCl gave the corresponding phosphonic acid derivatives which were treated in a similar fashion with neat triflic acid and water to give $[(4,4'\text{-}(HO)_2OPCH_2)_2bpy)_2Ru^{II}(bpm)Ru^{II}(tpy)(OH_2)]^{4+}$ (**1-(PO_3H_2)**) and $[(4,4'\text{-}(HO)_2OPCH_2)_2bpy)_2Ru^{II}(bpm)Ru^{II}(Mebimpy)(OH_2)]^{4+}$ (**2-(PO_3H_2)**). Purification was also achieved by column chromatography on Sephadex LH-20 by using water as the eluent. **1** and **2** were characterized by ^{1}H-NMR, UV-Vis spectroscopy, high resolution mass spectrometry and cyclic voltammetry and **1-(PO_3H_2)** and **2-(PO_3H_2)** by ^{31}P-NMR, UV-Vis spectroscopy, and cyclic voltammetry (Appx. E).

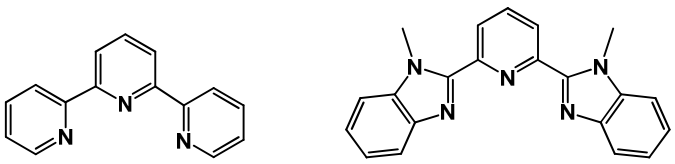

tpy Mebimpy

A

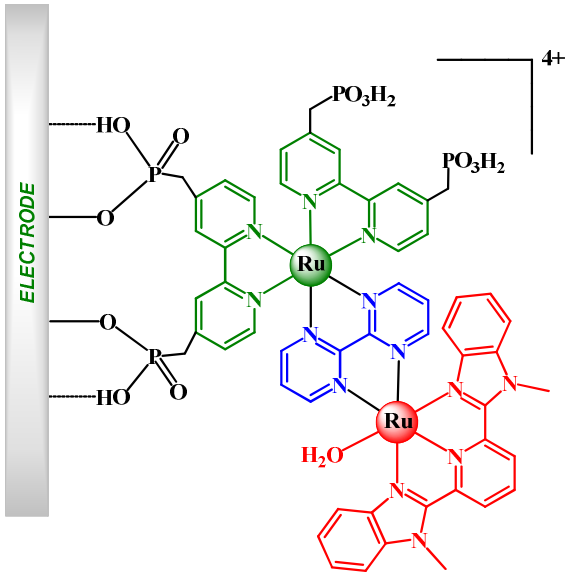

B

Figure 6.1. (A) Structures of tpy and Mebimpy. (B) Redox mediator-water oxidation catalyst assembly (**2-(PO_3H_2)**) anchored to a metal oxide electrode.

All four complexes display intense, pH-dependent MLCT absorptions in the visible. They are green in their aqua forms ($[(4,4'\text{-}(X)_2bpy)_2Ru^{II}(bpm)Ru^{II}(LLL)(OH_2)]^{4+}$ (X is $(HO)_2OPCH_2$ or H). For $[(bpy)_2Ru_1^{II}(bpm)Ru_2^{II}(tpy)(OH_2)]^{4+}$, a $d\pi(Ru_2)\rightarrow\pi^*(bpm)$ absorption occurs at λ_{max} = 610 nm (ε = 8800 $M^{-1}cm^{-1}$) and overlapping $d\pi(Ru_1,Ru_2)\rightarrow\pi^*(bpm)$, $d\pi(Ru_1)\rightarrow\pi^*(bpy)$, $d\pi(Ru_2)\rightarrow\pi^*(tpy)$ bands at 457 nm (shoulder, ε = 13,400 $M^{-1}cm^{-1}$) and 413 nm (ε = 27,300 $M^{-1}cm^{-1}$) at pH = 1.

Both **1** and **2** display multiple, pH-dependent oxidations in cyclic voltammograms collected in aqueous solutions. In 0.1 M HNO_3, **1** undergoes a two-electron oxidation at 1.21 V (vs. NHE) reminiscent of the two-electron oxidation of $[Ru(tpy)(bpm)(OH_2)]^{2+}$,[1] eq 2. At higher potentials, $Ru^{III}(bpm)Ru^{IV}=O^{5+}/Ru^{II}(bpm)Ru^{IV}=O^{4+}$ (1.47 V) and $Ru^{III}(bpm)Ru^{V}=O^{6+}/Ru^{III}(bpm)Ru^{IV}=O^{5+}$ (1.69V) waves are observed at the onset of a catalytic water oxidation wave, eqs 3 and 4.

$$[(bpy)_2Ru^{II}(bpm)Ru^{II}(tpy)(OH_2)]^{4+} - 2H^+ - 2e^- \rightarrow [(bpy)_2Ru^{II}(bpm)Ru^{IV}(tpy)(O)]^{4+} \qquad \text{(eq 2)}$$

$$[(bpy)_2Ru^{II}(bpm)Ru^{IV}(tpy)(O)]^{4+} - e^- \rightarrow [(bpy)_2Ru^{III}(bpm)Ru^{IV}(tpy)(O)]^{5+} \qquad \text{(eq 3)}$$

$$[(bpy)_2Ru^{III}(bpm)Ru^{IV}(tpy)(O)]^{5+} - e^- \rightarrow [(bpy)_2Ru^{III}(bpm)Ru^{V}(tpy)(O)]^{6+} \qquad \text{(eq 4)}$$

For **2** at pH = 1, there are separate $1e^-$ Ru(IV/III), Ru(III/II) waves at 1.30 V vs. NHE and 0.69 V with the $Ru^{IV}=O/Ru^{III}$-OH couple of the catalytic site overlapping with the $Ru^{III/II}$ couple of the redox mediator at 1.33 V. This $Ru^{III/II}$ couple is followed by a $Ru^{III}(bpm)Ru^{V}=O^{6+}/Ru^{III}(bpm)Ru^{IV}=O^{5+}$ wave at the onset of a wave for catalytic water oxidation at 1.57 V.

In Figure 6.2A is shown a stopped-flow absorbance-time trace illustrating the appearance of a series of intermediates in the catalytic oxidation of water by **1** as well as a fit

of the data to the kinetic model. The results of a series of studies in 0.1 M HNO_3, including rate constants for individual steps, are summarized in Scheme 1 with spectra of intermediates shown in Figure 6.2B. In summary: (a,b) Initial oxidation of $[(bpy)_2Ru^{II}(bpm)Ru^{II}(tpy)(OH_2)]^{4+}$ ($Ru_1^{II}Ru_2^{II}$-OH_2^{4+}) to $Ru_1^{II}Ru_2^{IV}=O^{4+}$ occurs with k_1 = 2.1×10^3 $M^{-1}s^{-1}$. The intermediate $Ru^{II}Ru^{III}$-OH^{4+} is unstable towards disproportionation and does not build up in solution. As shown by the green and red spectra in Figure 6.2B, formation of $Ru_1^{II}Ru_2^{IV}=O^{4+}$ is accompanied by loss of $Ru_2^{II}\rightarrow$tpy,bpy MLCT bands in the visible. (c) Oxidation of $Ru_1^{II}Ru_2^{IV}=O^{4+}$ to $Ru_1^{III}Ru_2^{IV}=O^{5+}$ (k_2 = 390 $M^{-1}s^{-1}$) results in disappearance of $Ru_2^{II}\rightarrow$bpm,bpy MLCT bands and appearance of low absorptivity features in the visible, Figure 6.2B. (d) Oxidation of $Ru^{III}Ru^{IV}O^{5+}$ to $Ru^{III}Ru^{V}=O^{6+}$ (k_3 = 104 $M^{-1}s^{-1}$) occurs with appearance of similar features possibly arising from a combination of ligand-to-metal charge transfer (LMCT) and mixed valence absorptions.

The fate of $Ru^{III}Ru^{V}=O^{6+}$ depends on the concentration of Ce(IV). When generated stoichiometrically, by adding 4 equivalents of Ce(IV) to $Ru^{II}Ru^{II}$-OH_2^{4+}, it disappears by pseudo first order kinetics with $k_{O\text{-}O}$ = 1.9×10^{-3} s^{-1} to give $Ru^{III}Ru^{III}$-OOH^{5+} as a discernible intermediate, eq (e), analogous to $[Ru^{III}(tpy)(bpm)(OOH)]^{2+}$.[1] This is the key O---O bond forming step. When generated in the presence of excess Ce(IV), $Ru^{III}Ru^{III}$-OOH^{5+} is oxidized rapidly, presumably to $Ru^{III}Ru^{IV}$-OO^{5+}, eq (f). With excess Ce(IV), disappearance of $Ru^{III}Ru^{IV}$-OO^{5+} becomes first order in Ce(IV) and first order in $Ru^{III}Ru^{IV}$-OO^{5+} with k_4 = 40 $M^{-1}s^{-1}$. As shown in Scheme 1, eq (g)-(h), further oxidation appears to give $Ru^{III}Ru^{V}$-OO^{6+} which does not build up in solution undergoing rapid oxygen evolution to give $Ru^{II}Ru^{IV}=O^{4+}$, closing the catalytic cycle.

Under catalytic conditions with 30 equivalents of Ce(IV) added, the Ru(IV) peroxo intermediate, $[(bpy)_2Ru^{III}(bpm)Ru^{IV}(LLL)(OO)]^{5+}$, dominates at the catalytic steady state. Loss of Ce(IV), monitored at 360 nm, is first order in Ce(IV) and first order in complex with k(25ºC) = 40 $M^{-1}s^{-1}$ for $[(bpy)_2Ru^{II}(bpm)Ru^{II}(tpy)(OH_2)]^{4+}$ (**1**) and 60 $M^{-1}s^{-1}$ for $[(bpy)_2Ru^{II}(bpm)Ru^{II}(Mebimpy)(OH_2)]^{4+}$ (**2**). Assembly **2** utilizes an analogous mechanism as shown by stopped flow measurements. Oxygen monitoring with an oxygen electrode in 0.1 M HNO_3 with 30 equivalents of Ce(IV) gave 100 ± 3 % of the expected oxygen for ~7 turnovers for both (**1**) and (**2**).

$$\mathrm{Ru^{II}Ru^{II}\text{–}OH_2^{4+}} + \mathrm{Ce^{4+}} \xrightarrow{k_1} \mathrm{\{Ru^{II}Ru^{III}\text{–}OH\}^{4+}} + \mathrm{Ce^{3+}} + \mathrm{H^+} \quad \text{(a)}$$

$$\mathrm{\{Ru^{II}Ru^{III}\text{–}OH\}^{4+}} + \mathrm{Ce^{4+}} \xrightarrow{\text{rapid}} \mathrm{Ru^{II}Ru^{IV}{=}O^{4+}} + \mathrm{Ce^{3+}} + \mathrm{H^+} \quad \text{(b)}$$

$$\mathrm{Ru^{II}Ru^{IV}{=}O^{4+}} + \mathrm{Ce^{4+}} \xrightarrow{k_2} \mathrm{Ru^{III}Ru^{IV}{=}O^{5+}} + \mathrm{Ce^{3+}} \quad \text{(c)}$$

$$\mathrm{Ru^{III}Ru^{IV}{=}O^{5+}} + \mathrm{Ce^{4+}} \xrightarrow{k_3} \mathrm{Ru^{III}Ru^{V}{=}O^{6+}} + \mathrm{Ce^{3+}} \quad \text{(d)}$$

$$\mathrm{Ru^{III}Ru^{V}{=}O^{6+}} + \mathrm{H_2O} \xrightarrow{k_{O\text{-}O}} \mathrm{\{Ru^{III}Ru^{III}\text{–}O_2H\}^{5+}} + \mathrm{H^+} \quad \text{(e)}$$

$$\mathrm{\{Ru^{III}Ru^{III}\text{–}O_2H\}^{5+}} + \mathrm{Ce^{4+}} \xrightarrow{\text{rapid}} \mathrm{Ru^{III}Ru^{IV}\text{-}O_2^{5+}} + \mathrm{Ce^{3+}} + \mathrm{H^+} \quad \text{(f)}$$

$$\mathrm{Ru^{III}Ru^{IV}\text{-}O_2^{5+}} + \mathrm{Ce^{4+}} \xrightarrow{k_4} \mathrm{\{Ru^{III}Ru^{V}\text{-}O_2\}^{6+}} + \mathrm{Ce^{3+}} \quad \text{(g)}$$

$$\mathrm{\{Ru^{III}Ru^{V}\text{-}O_2\}^{6+}} + \mathrm{H_2O} \xrightarrow{\text{rapid}} \mathrm{\{Ru^{III}Ru^{III}\text{–}OH\}^{5+}} + \mathrm{O_2} + \mathrm{H^+} \quad \text{(h)}$$

Scheme 6.1. Reactions and rate constants for water oxidation by $[(bpy)_2Ru^{II}(bpm)Ru^{II}(tpy)(OH_2)]^{4+}$ in 0.1 M HNO_3 at 25ºC. Oxidation of $Ru^{III}Ru^{IV}\text{-}O_2^{5+}$ to $\{Ru^{III}Ru^{IV}\text{-}O_2^{6+}\}$, eq (g), is rate limiting with **$Ru^{III}Ru^{IV}\text{-}O_2^{5+}$** dominant at the catalytic steady state.

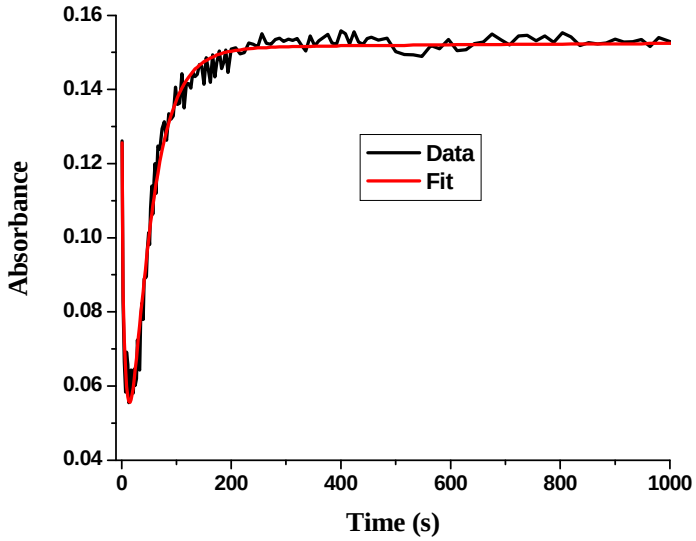

A

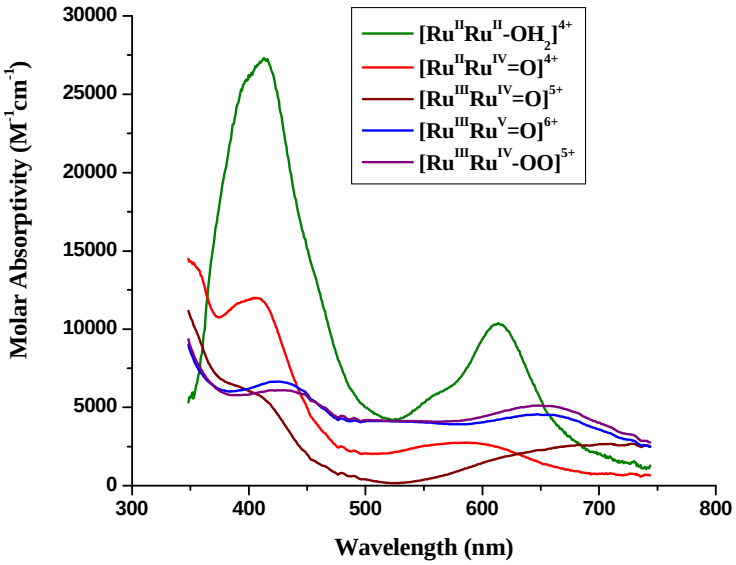

B

Figure 6.2. (A) Absorbance-time trace at 546 nm for **1** following addition of 10 equivalents of Ce(IV) to $[(bpy)_2Ru^{II}(bpm)Ru^{II}(tpy)(OH_2)]^{4+}$ in 0.1 M HNO_3 at 298 K. The fit of the absorbance-time trace to the mechanism in Scheme 1 is shown with $k_1 = 2.1\times10^3$ $M^{-1}s^{-1}$; $k_2 = 390$ $M^{-1}s^{-1}$; $k_3 = 104$ $M^{-1}s^{-1}$; $k_{O\text{-}O} = 1.9\times10^{-3}$ s^{-1} and $k_4 = 40$ $M^{-1}s^{-1}$. (B) As in A), spectra of intermediates obtained by stopped flow measurements during the course of the reaction.

The phosphonated versions of **1** and **2** can be anchored to metal oxide surfaces such as tin-doped indium oxide (ITO) and fluorine-doped tin oxide (FTO) from acidic aqueous solutions, Figure 6.1B. Surface electrochemical behavior is similar to that for the non-phosphonated complexes in solution with a pH-dependent two-electron wave appearing for **1-(PO_3H_2)** at $E_{1/2}$ (Ru^{IV}=O/Ru^{II}-OH_2) = 1.24 V (1.0 M $HClO_4$), followed by pH-independent waves at 1.47 V (Ru^{III}/Ru^{II}-redox mediator) and 1.69 V (Ru^{V}=O/Ru^{IV}=O). The latter appears at the onset of a catalytic water oxidation wave.

Electrolysis with **1-(PO_3H_2)** or **2-(PO_3H_2)** at 1.8 V (vs. NHE) anchored to FTO in 1.0 M $HClO_4$ resulted in sustained, constant catalytic currents for more than 20 hours with no sign of decrease in catalytic activity. In one set of experiments, Figure 6.3, **1-(PO_3H_2)** underwent 8,900 turnovers with a turnover frequency (TOF) of 0.3 s^{-1}. Under similar conditions, **2-(PO_3H_2)** underwent more than 28,000 turnovers over a 13 hour period with a turnover rate of 0.6 s^{-1} with no sign of reduction in catalytic activity.

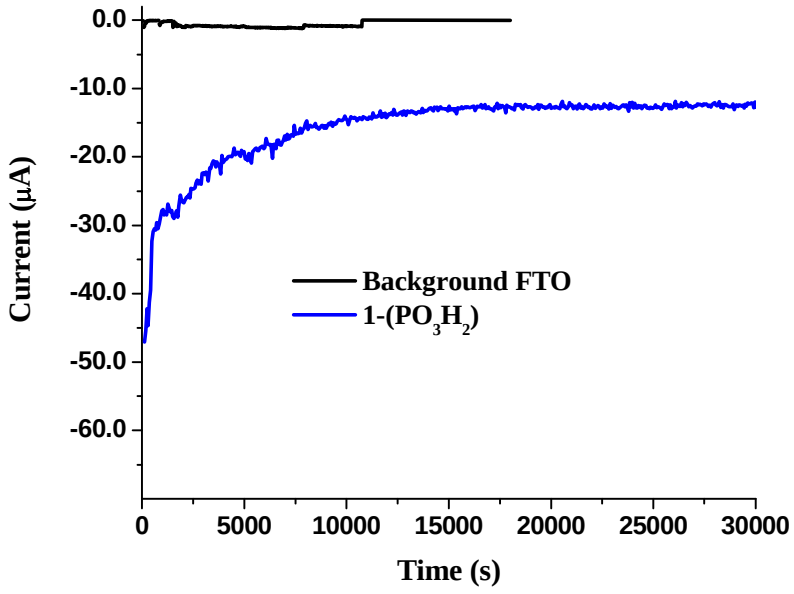

Figure 6.3. Electrolysis of **1-(PO_3H_2)** anchored to FTO at 1.8 V in 1.0 M $HClO_4$. Number of turnovers: 8,900; TOF = 0.3 s^{-1}; current density ~ 6.7 μA/cm^2; Γ ~ 7 x 10^{-11} mol/cm^2; A = 1.95 cm^2.

Conclusion

The robustness and turnover rates of these catalysts are encouraging. They oxidize water following well-defined, single site mechanisms similar to those previously reported[1,2] and offer promise in electrocatalytic and photoelectrocatalytic water oxidation.

REFERENCES

(1) Concepcion, J. J.; Jurss, J. W.; Templeton, J. L.; Meyer, T. J. *Journal of the American Chemical Society* **2008**, *130*, 16462.

(2) Concepcion, J. J.; Jurss, J. W.; Norris, M. R.; Chen, Z. F.; Templeton, J. L.; Meyer, T. J. *Inorganic Chemistry* **2010**, *49*, 1277.

(3) Tseng, H. W.; Zong, R.; Muckerman, J. T.; Thummel, R. *Inorganic Chemistry* **2008**, *47*, 11763.

(4) Meyer, T. J.; Huynh, M. H. V.; Thorp, H. H. *Angew. Chem., Int. Ed.* **2007**, *46*, 5284.

(5) Renger, G. *Photosynthesis Research* **2007**, *92*, 407.

(6) Liu, F.; Concepcion, J. J.; Jurss, J. W.; Cardolaccia, T.; Templeton, J. L.; Meyer, T. J. *Inorg. Chem. (Washington, DC, U. S.)* **2008**, *47*, 1727.

(7) Concepcion, J. J.; Jurss, J. W.; Templeton, J. L.; Meyer, T. J. *Proceedings of the National Academy of Sciences of the United States of America* **2008**, *105*, 17632.

(8) Xu, X. J.; Xi, Z. X.; Chen, W. Z.; Wang, D. Q. *Journal of Coordination Chemistry* **2007**, *60*, 2297.

(9) Sullivan, B. P.; Calvert, J. M.; Meyer, T. J. *Inorganic Chemistry* **1980**, *19*, 1404.

(10) Will, G.; Boschloo, G.; Rao, S. N.; Fitzmaurice, D. *Journal of Physical Chemistry B* **1999**, *103*, 8067.

(11) Swavey, S.; Fang, Z. L.; Brewer, K. J. *Inorganic Chemistry* **2002**, *41*, 2598.

(12) Takeuchi, K. J.; Thompson, M. S.; Pipes, D. W.; Meyer, T. J. *Inorganic Chemistry* **1984**, *23*, 1845.

CHAPTER 7

pH Dependence of Phosphonic Acid Derivatized $[Ru(bpy)_3]^{2+}$ and Electrostatic Synthesis of Redox Mediator-Chromophore/Catalyst Assemblies

Introduction

Solar radiation is the earth's most abundant source of energy, but its intermittent and geographically diffuse delivery requires its storage before the sun can be relied on to power the continuous and dynamic needs of society.[1] Artificial photosynthesis aims to couple light-driven water oxidation at one catalyst to reductive chemistry at another catalyst in order to store energy in chemical bonds.[2] We imagine the generation of a useful solar fuel with a dye-sensitized photoelectrochemical cell (DS-PEC) in which these redox catalysts are attached to electrode materials, enabling efficient electron harvesting through well-defined vectorial electron transfer.[3]

Recent progress has been made in developing catalysts for water oxidation and using facile electron transfer mediators to enhance reaction kinetics.[4,5] For optimal efficiency, matching the natural solar flux is necessary and requires catalyst turnover rates on the ~1 ms timescale.[3] The redox mediators previously reported also represent one of the most widely studied classes of compounds for light absorption to promote excited state electron transfer.[6] Phosphonate functionalities on catalyst or chromophore-redox mediator components of the DS-PEC provide stable attachment to metal oxide electrodes in acidic to neutral aqueous media while maintaining the complex's observed solution reactivity.[7,8] However, chemical modification of complexes with phosphonate substituents and binding of catalysts to appropriate chromophore-redox mediators (see Chapters 1 and 6) present considerable synthetic challenges and stringent bridge requirements that greatly affect device efficacy.

The nature of the linkage chemistry has been shown to have a significant impact on the efficiency of charge transfer sensitization at TiO_2 electrodes.[9,10] Several computational investigations have been reported regarding the interfacial phosphonate interaction with

various conclusions.[11] However, electronic coupling between the sensitizer and the metal oxide conduction band as mediated by the surface linkage appears to be a dominant factor dictating quantum yields for electron injection as well as electron transfer kinetics.[10,11] Surface stability is closely tied to the metal oxide to which the phosphonate functionality is bound, and further, to the conditions employed for establishing the metal oxide-phosphonate interaction. The current state of the literature on phosphonate binding is poorly resolved. Reported studies typically have multiple variations in the surface loading procedures and measurements to-date have not been definitive enough for a thorough or quantitative understanding of the interfacial interaction. Defining the specifics of phosphonate binding at metal oxide surfaces would allow a more comprehensive understanding of where the interfacial electron transfer dynamics and surface stability originate.

Figure 7.1 depicts the typical phosphonic acid adsorption modes proposed at metal oxide surfaces.[12] Phosphonate ester bonds are formed with metal ions in the material via a condensation mechanism involving metal-hydroxide surface sites. Phosphonate binding to the oxide framework in these materials is not believed to occur; however, hydrogen bonding at these sites is a strong possibility.[13] In any event, the specific binding mode (mono-, bi-, or tridentate) at a metal oxide surface is not easy to assess experimentally and may include multiple modes of binding within the same sample.

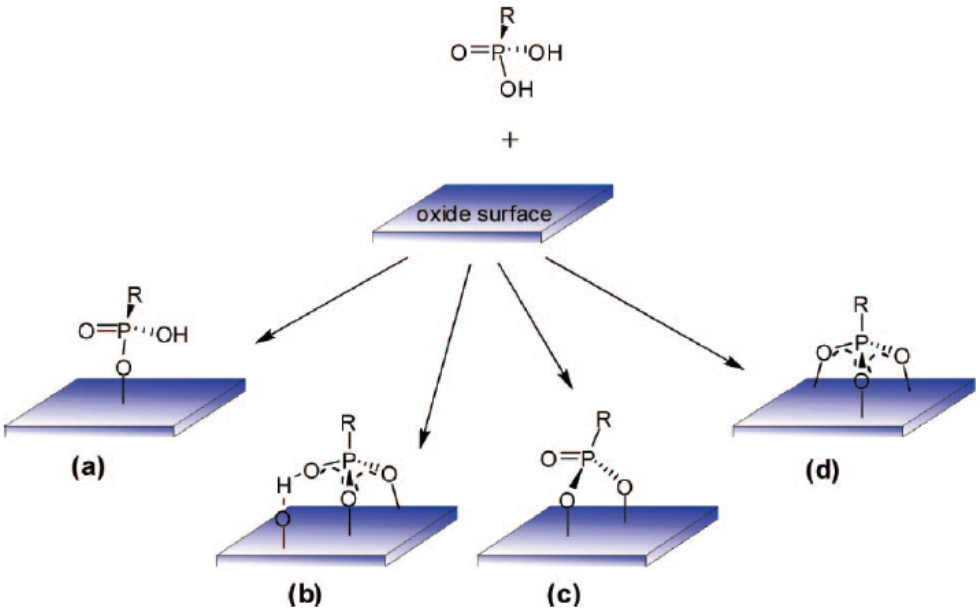

Figure 7.1.[12] Proposed surface binding modes of phosphonic acid groups at a metal oxide surface. (a) monodentate, (b) and (c) bidentate, and (d) tridentate.

We report herein a series of phosphonate-derivatized $[Ru(bpy)_3]^{2+}$ salts (where bpy = 2,2'-bipyridine) that have been used to systematically probe the surface binding interaction. A pH dependence associated with the phosphonic acid functionalities of these complexes has been observed and the resulting ions exploited in the synthesis of assemblies for electrocatalysis with important implications for solar energy conversion.

Experimental Section

Robert A. Binstead was a tremendous help with the pH titrations and corresponding data analysis. Javier J. Concepcion and Michael R. Norris synthesized the majority of phosphonate-derivatized complexes and the water oxidation catalyst, $[Ru(Mebimpy)(bpy)(OH_2)]^{2+}$. I synthesized phosphonated bipyridines and did some of the

synthesis of complexes described below. I performed all of the electrochemical measurements and analysis.

Materials. Distilled water was further purified using a Milli-Q Ultrapure water purification system. Nitric acid (99.999% Trace Metals Grade, 70%) was purchased from Fisher Scientific, phosphoric acid (99.99% Trace Metals Grade, 85%) and trifluoromethanesulfonic (CF_3SO_3H) acid (Reagent Grade, 98%) were obtained from Aldrich. Trifluoromethanesulfonic acid was further purified by addition of blue dimer and an excess of $(NH_4)_2Ce(NO_3)_6$ as solids to oxidize reducing impurities, followed by vacuum distillation. Purified CF_3SO_3H was stored as 2.0 M stock solutions. All other reagents were ACS grade and used without additional purification.

Methods. UV-visible spectra were recorded on an Agilent Technologies Model 8453 diode-array spectrophotometer. Data were processed by use of the program SPECFIT/32 Global Analysis System (SPECTRUM Software Associates). Electrochemical measurements were performed on a Bioanalytical Systems, Inc. 100B/W series potentiostat. Voltammetric measurements were made with ITO electrodes modified with a phosphonate-derivatized $[Ru(bpy)_3]^{2+}$ complex, a platinum wire with attached platinum mesh counter electrode, and a Ag/AgCl Bioanalytical Systems, Inc. RE-5B reference electrode. Spectrophotometric pH titrations were made using a Metrohm (Herisau, Switzerland) model 905 Titrando autotitrator in conjunction with the Agilent 8453 UV-visible spectrophotometer described above. The autotitrator was equipped with a 2 mL model 800 Dosino burette for liquid transfers through Agilent FEP tubing and an Agilent compact flow cell (1, 2, 5, or 10 mm path) for UV-visible measurements. Titrants were added to the sample solution (25-30 ml) via a 10 mL model 800 Dosino burette (1 μL resolution). A dual junction Metrohm pH electrode (3.0 M KCl

inner/3.0 M NaCl outer compartment) was employed for pH titrations (1<pH<11). Calibration of the pH electrode was performed with three Metrohm standards of pH 4, 7, and 9, respectively. The burettes, pH measurements, and spectrophotometer scans were controlled with Tiamo version 2.2 software supplied by Metrohm. Automated wavelength scans at each aliquot of titrant were triggered on the Agilent 8453 spectrophotometer via a Metrohm MSB Remote I/O controller connected to the GPIO and Remote I/O ports of the spectrophotometer.

Synthesis

4.4'-($Et_2O_3PCH_2)_2$-bpy (1). This ligand was synthesized with an important modification of a literature procedure that avoids use of column chromatography for purification. In a typical reaction, 2.58 g (7.5 mmol) 4,4'-($BrCH_2)_2$-bpy was dissolved in 6.6 mL (6.3 g, 37.7 mmol) triethylphosphite. The headspace was purged with argon for 15 minutes and then the reaction was heated to 80 °C for 12 h. The reaction mixture was then allowed to cool to room temperature and 30 mL of pentane were added to precipitate the product as an off-white solid. Product was collected by vacuum filtration and washed with pentanes to remove any excess triethylphosphite. Yield: 3.35 g (98%).

4,4'-($Et_2O_3P)_2$-bpy (2). This procedure was adapted from a literature preparation.[14] In a typical reaction, 4.00 g (8.84 mmol) 4,4'-trifluoromethanesulfonate-2,2'-bipyridine, 2.4 mL (2.6 g, 20.2 mmol) diethyl phosphite, 0.946 g (0.884 mmol) tetrakistriphenylphosphine palladium(0) and 21.5 g (88.4 mmol) triphenylphosphine were added to a flask and purged with argon. To the reagents, 2.6 mL triethylamine and 86 mL anhydrous toluene were added and the reaction was heated to 110 ºC for 16 h. The reaction was allowed to cool and was washed with 40 mL of a 15 % ammonium hydroxide solution followed by 50 mL of water.

The organic phase was collected and dried over magnesium sulfate. Solvent was removed under reduced pressure and a yellow oil resulted which was run down a silica column eluting first with ethylacetate, then dichloromethane, and finally 5 % methanol in dichloromethane to elute the product. Yield: 1.95 g (51%). ^{1}H NMR (400 MHz, $CDCl_3$): δ 8.81 (t, 2H), 8.75 (d, 2H), 7.70 (dd, 2H), 4.17 (m, 8H), 1.34 (t, 12H). ^{31}P NMR ($CDCl_3$): δ 14.73.

***cis*-Ru(bpy)$_2$Cl$_2$.** In a typical preparation, 969 mg (3.46 mmol) dichlororuthenium(II) cyclooctadiene polymer and 1.08 g (6.9 mmol) 2,2'-bipyridine were suspended in 40 mL *o*-dichlorobenzene. The reaction was heated to 190 °C under argon fro 30 min. The mixture was allowed to cool and a dark solid precipitated which was filtered and washed with diethyl ether. Yield: 1.51 g (90%). This product was used without further purification.

***cis*-Ru((Et$_2$O$_3$P)$_2$-bpy)$_2$Cl$_2$.** A suspension of $RuCl_3$ (1.00 mmol), **5** (2.00 mmol), and zinc powder (10.0 mmol) was heated at reflux in ethanol for 12 h. The reaction mixture was filtered hot and the solvent was removed from the filtrate under vacuum. The resulting dark purple solid was collected, washed with Et_2O and dried. This product was used without further purification.

[Ru(Bz)(bpy)Cl]Cl. (Bz is benzene) This complex was synthesized by modification of a literature preparation.[15] In a typical reaction, 1.00 g (2.33 mmol) 2,2'-bipyridine and 583 mg (1.17 mmol) $[Ru(Bz)Cl]_2Cl_2$ were suspended in 70 mL methanol. The reaction was heated under argon at reflux for 3 h. The reaction was then filtered hot to remove any unreacted material and the solvent was removed from the filtrate on a rotary evaporator. A dark solid resulted that was collected under diethyl ether and filtered. Yield: 1.49 g (94%). Product was used without further purification.

[Ru(Bz)(bpy)OTf]OTf. [Ru(Bz)(bpy)Cl]Cl (1.50 g, 2.30 mmol) were suspended in CH_2Cl_2 (50 mL) and the solution was degassed with argon. After adding a needle to vent the reaction, 1.5 mL (0.011 mmol) trifluoromethanesulfonic acid were added and the reaction was stirred for 2 h. Upon addition of 200 mL of Et_2O, a dark solid precipitated from solution. The solid was filtered and washed with Et_2O.

[Ru(Mebimpy)(bpy)(OH_2)](OTf)$_2$. This complex was synthesized as described in Appx. C.

General Procedure for Phosphonate-derivatized Ruthenium Complexes.

Method A. A solution of ligand (**1** or **2**) (1.03 mmol) and 500 mg (1.03 mmol) *cis*-$Ru(bpy)_2Cl_2$ in 40 mL of EtOH/H_2O (1:1, v:v) was heated at reflux under an atmosphere of argon. The reaction was monitored by UV-Vis spectroscopy and stopped when no more spectral changes were taking place (4-12 h.). The solvent was then removed on a rotary evaporator and the residue dissolved in 40 mL of 4 M HCl. The reaction was then heated at reflux for 48 h to hydrolyze the phosphonate-ester groups. Upon completion of the hydrolysis, the solvent was removed on a rotary evaporatory and the product was purified using size-exclusion chromatography (Sephadex LH-20/water or 0.1 M HCl depending on product solubility). Similar fractions were combined, the solvent removed, and the solid collected and rinsed with Et_2O.

Method B. A solution of [Ru(Bz)(bpy)OTf]OTf (0.50 mmol) and ligand (**1** or **2**) (1.00 mmol) were heated at refulx in 40 mL of H_2O/EtOH (1:1, v:v) solution under an atmosphere of argon for 5 h. The solvent was reduced to 5 mL on a rotary evaporator and the resulting solution was purified on a Sephadex LH-20 column. Similar fractions were combined, solvent removed, and the solid collected.

Method C. A suspension of $RuCl_3$ (1.00 mmol), ligand (**1** or **2)** (3.00 mmol), and zinc powder (10.0 mmol) was heated at reflux in ethanol for 30 h. The reaction mixture was filtered hot and the solvent was removed from the filtrate under vacuum. The resulting solid was collected, washed with Et_2O and dried. This product was used without further purification.

$[Ru(bpy)_2(4,4'\text{-}(H_2O_3PCH_2)_2\text{-}bpy)]Cl_2$. This complex was prepared as in Method A starting with *cis*-$Ru(bpy)_2Cl_2$ and **3**. ^{1}H NMR (400 MHz, D_2O): δ 8.51 (d, 4H), 8.45 (s, 2H), 8.01 (t, 4H), 7.88 (d, 2H), 7.81 (d, 2H), 7.69 (d, 2H), 7.34 (m, 4H), 7.26 (s, 2H), 3.29 (d, 4H). ^{31}P NMR (400 MHz, D_2O): δ 19.03.

$[Ru(bpy)(4,4'\text{-}(H_2O_3PCH_2)_2\text{-}bpy)_2](PF_6)(NO_3)$. This complex was prepared as described in Method B.

$[Ru(4,4'\text{-}(H_2O_3PCH_2)_2\text{-}bpy)_3]Cl_2$. This complex was prepared using Method C.

$[Ru(bpy)_2(4,4'\text{-}(H_2O_3P)_2\text{-}bpy)]Cl_2$. This complex was prepared as described in Method A starting with *cis*-$Ru(bpy)_2Cl_2$ and **3**. ^{1}H NMR (400 MHz, D_2O): δ 8.75 (d, 2H), 8.51 (d, 4H), 8.03 (t, 4H), 7.91 (m, 2H), 7.79 (dd, 4H), 7.55 (dd, 2H), 7.35 (t, 4H). ^{31}P NMR (400 MHz, D_2O): δ 6.78.

$[Ru(bpy)(4,4'\text{-}(H_2O_3P)_2\text{-}bpy)_2](PF_6)(Cl)$. ^{1}H NMR (400 MHz, D_2O): δ 8.51 (d, 2H), 8.04 (t, 2H), 7.88 (m, 4H), 7.74 (d, 2H), 7.56 (dd, 4H), 7.37 (t, 2H). ^{31}P NMR (400 MHz, D_2O): δ 6.74.

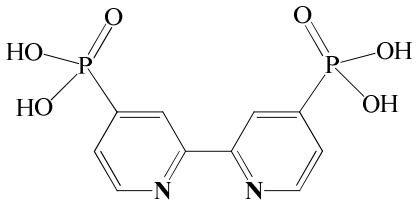

4,4'-$(H_2O_3P)_2$-bpy

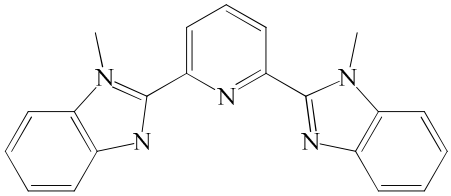

Mebimpy

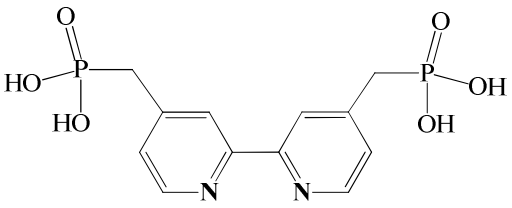

4,4'-$(H_2O_3PCH_2)_2$-bpy

Results

Tin-doped indium oxide (Sn^{IV}:In_2O_3, ITO) slides were loaded with phosphonic acid substituted $[Ru(bpy)_3]^{2+}$ complexes by a prolonged (~ 8 hours) soak at room temperature in stock solutions containing the complex dissolved in methanol or at pH 1 (HNO_3, $HClO_4$). Surface coverages in mol/cm^2 of the electroactive species were determined by cyclic voltammetry. The background subtracted reductive wave of the Ru(III/II) couple was integrated to find the area under the curve with units of A•V. Division of this value by the scan rate used to collect the cyclic voltammogram (in V/s) gives the number of coulombs associated with the redox process. Because the coulomb is the amount of charge transported in the given length of time at a given potential, it represents moles of electrons and can be divided by the surface area (cm^2) of the electrode to give mol/cm^2. Assuming a one electron couple, such as the Ru(III/II) couple of $[Ru(bpy)_3]^{2+}$, this is equal to the moles of complex per unit area.

Shown in Figure 7.2 is a representative surface loading isotherm for [Ru(4,4'-$(H_2O_3P)_2$-bpy)$_2$(bpy)]$^{2+}$ on ITO. Slides were loaded from stocks solutions of different

concentrations of complex in 0.1 M HNO_3 until monolayer (or saturated) surface coverage (Γ_0) was achieved. Surface binding constants, K, were calculated from the Langmuir model for surface adsorption, represented in eq 1, where θ is the fractional surface coverage (Γ/Γ_0) and [Ru^{II}] is concentration of complex in the stock solution.[16]

$$\theta = \frac{\mathbf{K\,[Ru^{II}]}}{\mathbf{1 + K[Ru^{II}]}} \qquad (1)$$

Additional isotherms for adsorption of phosphonate-derivatized $[Ru(bpy)_3]^{2+}$ complexes are given in Appendix (Appx.) F Figures S1-6. Equilibrium constants, K, for surface binding are listed in Table 7.1.

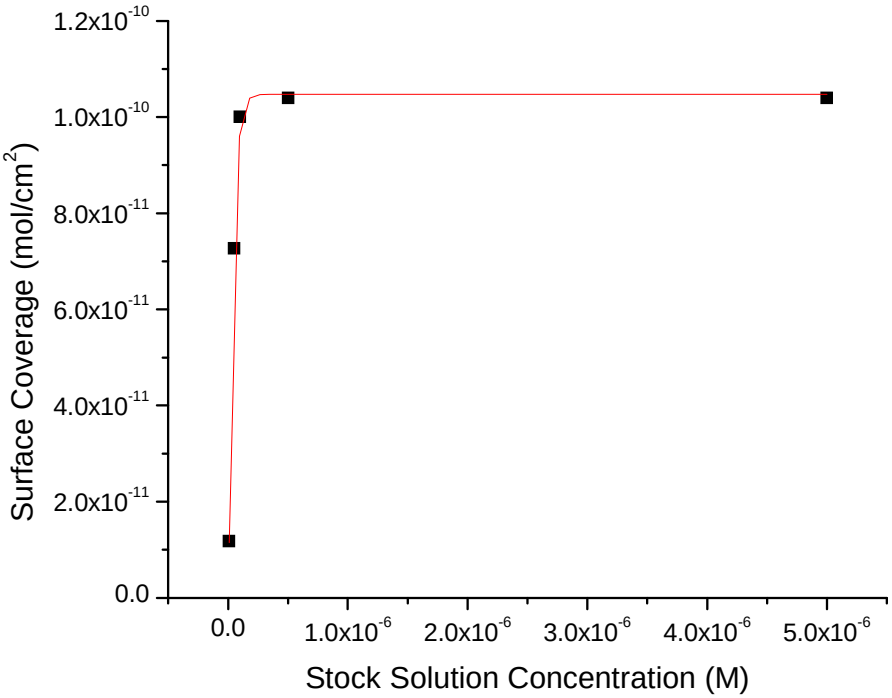

Figure 7.2. Isotherm - surface coverage (mol/cm^2) vs. concentration of stock solution (M) containing [Ru(4,4'-$(H_2O_3P)_2$-bpy)$_2$(bpy)]Cl_2 in 0.1 M HNO_3. Surface coverages determined from cyclic voltammograms obtained in 0.1 M $HClO_4$.

Binding constants were calculated using eq 1 and the experimental isotherms. Surface loading and subsequent quantification via electrochemistry were performed at room temperature (23 ± 2 °C), and errors associated with K are as high as a factor of 2.

Table 7.1. Surface loading isotherms for phosphonic acid derivatized $[Ru(bpy)_3]^{2+}$ complexes on ITO.

Surface Catalyst	Loading Conditions	K (M^{-1})
$[Ru(bpy)_2(4,4'\text{-}(H_2O_3P)_2\text{-}bpy)]^{2+}$	0.1 M HNO_3	3.15×10^7
$[Ru(4,4'\text{-}(H_2O_3P)_2\text{-}bpy)_2(bpy)]^{2+}$	0.1 M HNO_3	3.32×10^7
$[Ru(bpy)_2(4,4'\text{-}(H_2O_3PCH_2)_2\text{-}bpy)]^{2+}$	methanol	1.49×10^6
$[Ru(bpy)_2(4,4'\text{-}(H_2O_3PCH_2)_2\text{-}bpy)]^{2+}$	0.1 M HNO_3	1.95×10^7
$[Ru(4,4'\text{-}(H_2O_3PCH_2)_2\text{-}bpy)_2(bpy)]^{2+}$	methanol	1.38×10^6
$[Ru(4,4'\text{-}(H_2O_3PCH_2)_2\text{-}bpy)_2(bpy)]^{2+}$	0.1 M $HClO_4$	7.21×10^6
$[Ru(4,4'\text{-}(H_2O_3PCH_2)_2\text{-}bpy)_3]^{2+}$	0.1 M $HClO_4$	1.96×10^6

A variety of loading conditions were employed in order to optimize surface loading. Stock solutions of 0.1 M HNO_3 offered the most reproducible results and could be used with the entire series of complexes under investigation. Microcrystallization, or an explicit precipitation event, was observed over extended periods of soaking in 0.1 M $HClO_4$, Appx. F Figure S5. Exactly twice the expected monolayer surface coverage was measured (~2×10^{-10} mol/cm^2) with $[Ru(4,4'\text{-}(H_2O_3PCH_2)_2\text{-}bpy)_2(bpy)]^{2+}$. A similar result was obtained in 0.1 M $HClO_4$ with $[Ru(4,4'\text{-}(H_2O_3PCH_2)_2\text{-}bpy)_3]^{2+}$. Subsequent soaking of the slide for ~1 day in clean (no adsorbate) pH 1 aqueous solutions resulted in quantitative desorption of the precipitate to give monolayer coverage. Methanol was also used as a solvent in stock solutions. With complexes bearing a single phosphonated bipyridine, full monolayer surface loadings were not achieved however from methanol stock solutions. (See Appx. F Figure S6.) Monolayer surface coverages did occur using methanol with the $[Ru(bpy)(L)_2]^{2+}$

complexes, where L is either of the phosphonated bipyridine ligands. This is presumably due to the higher number of phosphonic acid groups and a stronger surface interaction. Additionally, $[Ru(4,4'\text{-}(H_2O_3PCH_2)_2\text{-}bpy)_3]^{2+}$ had little to no solubility in methanol, leaving this solvent with limited utility in the present study.

Surface loading vs. time is shown in Figure 7.3 for the series (mono, bis, tris) of complexes with 4,4'-$(H_2O_3PCH_2)_2$-bpy. Rapid binding to the surface is observed with saturated coverages occurring in less than 120 s in solutions of 1.0 x 10^{-4} M complex and independent of the stock solution solvent. These rapid binding kinetics were exploited in the surface catalysis of blue dimer water oxidation (Chapter 5) to maintain surface loading despite loss of the adsorbate during catalysis.[5]

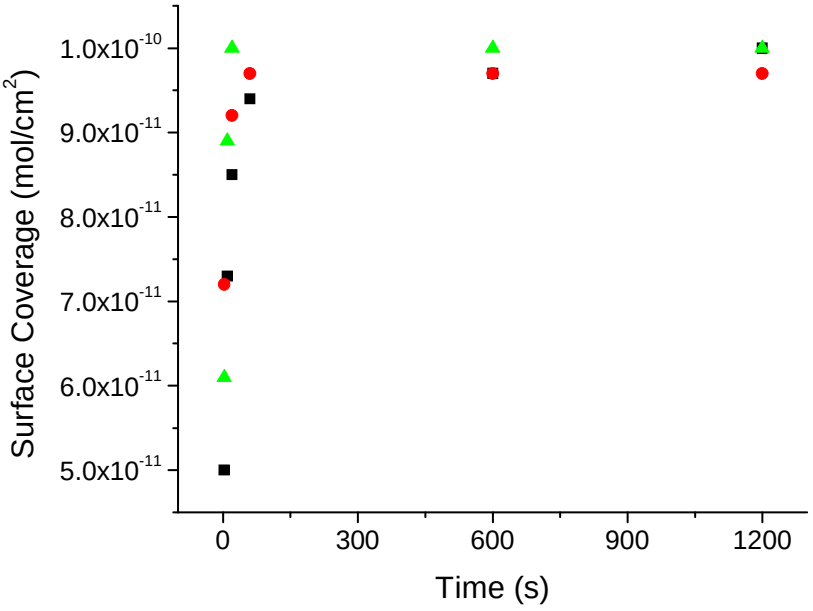

Figure 7.3. Surface loading (mol/cm^2) vs. time for the $[Ru(bpy)_3]^{2+}$ series with 4,4'-$(H_2O_3PCH_2)_2$-bpy on ITO. Legend: black squares – $[Ru(bpy)_2(4,4'\text{-}(H_2O_3PCH_2)_2\text{-}bpy)]^{2+}$, loaded from 1.0 x 10^{-4} M complex, 0.1 M HNO_3 stock solution; red diamonds – $[Ru(4,4'\text{-}(H_2O_3PCH_2)_2\text{-}bpy)_2(bpy)]^{2+}$, loaded from 1.0 x 10^{-4} M complex, methanol stock solution; green triangles – $[Ru(4,4'\text{-}(H_2O_3PCH_2)_2\text{-}bpy)_3]^{2+}$, loaded from 1.0 x 10^{-4} M complex, 0.1 M $HClO_4$ stock solution.

$E_{1/2}$ vs. pH diagrams of the Ru(III/II) couple were constructed to establish the pH dependence of the adsorbates. Constant ionic strength was maintained with 0.9 M $LiClO_4$ supporting electrolyte. Shown in Figure 7.4 are the $E_{1/2}$-pH (Pourbaix) diagrams for the 4,4'-$(H_2O_3PCH_2)_2$-bpy series. Additional Pourbaix diagrams can be found in Appx. F. The Nernst equation for an equilibrium at standard conditions, eq 2,

$$E_{1/2} = E^{o\prime} - \frac{mRT}{nF} \ln \frac{[red]}{[ox]} = E^{o\prime} - \frac{m}{n} 0.0592 \ln \frac{[red]}{[ox]} \quad (2)$$

predicts $E_{1/2}$ to vary by –59.2(*m*/*n*) mV/pH unit with *m* the number of protons transferred and *n* the number of electrons.[17] Given the high number of acidic protons at each phosphonate group, a slope (or slopes) having values of 59(*m*) was expected for the pH dependent $1e^-$ couple.

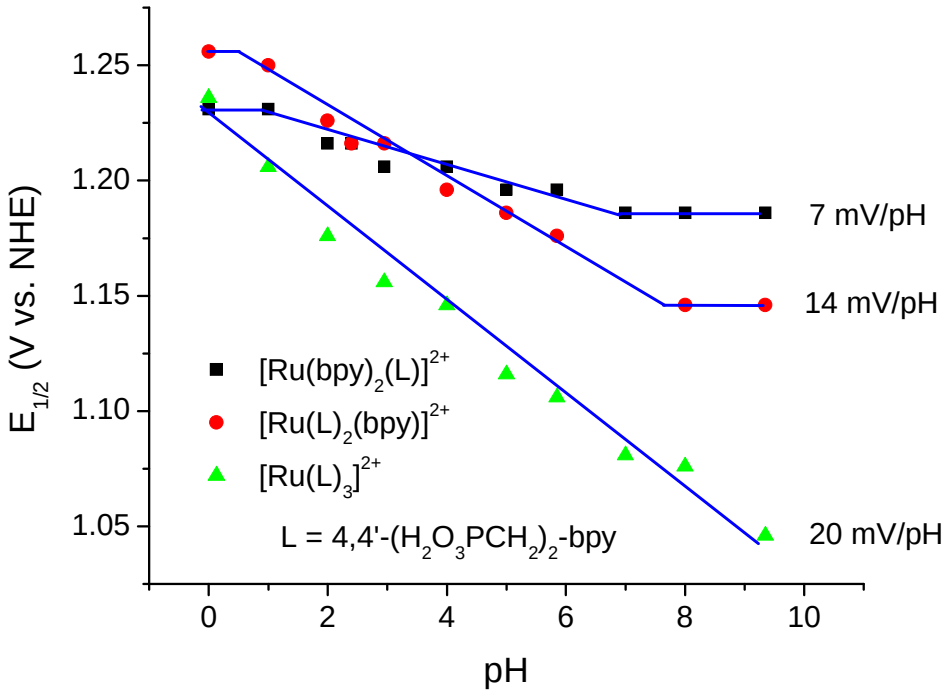

Figure 7.4. $E_{1/2}$-pH diagram of $[Ru(4,4'\text{-}(H_2O_3PCH_2)_2\text{-}bpy)_n(bpy)_{3-n}]^{2+}$ series on ITO, ionic strength was kept constant at1.0 M with $LiClO_4$, 23 °C, monolayer surface coverage (~1.0 x 10^{-10} mol/cm^2).

Clearly this expectation was not met as the slopes across the series range from only 7 mV/pH unit to as high as 20 mV/pH unit. A systematic increase is observed, however, in going from the *mono*, $[Ru(bpy)_2(4,4'\text{-}(H_2O_3PCH_2)_2\text{-}bpy)]^{2+}$, at 7 mV/pH unit to the *bis* (14 mV/pH unit) to the *tris* analogue, $[Ru(4,4'\text{-}(H_2O_3PCH_2)_2\text{-}bpy)_3]^{2+}$, with a slope of 20 mV/pH unit. An increased of ~7 mV/pH/4,4'-$(H_2O_3PCH_2)_2$-bpy. No clear breaks in the linear response of the Ru(III/II) $E_{1/2}$ value to pH were observed to indicate individual acid-base events. It should be noted that a significant loss of complex from the electrode surface occurred at basic pH values. The $E_{1/2}$ values at these pHs were measured with partially loaded slides experiencing rapid desorption of the surface bound complex.

A control experiment was performed with a pH-independent complex, $[Os(phen)_3](NO_3)_2$, where phen is 1,10-phenanthroline, at a bare ITO electrode, Appx. F Figure S7. Changes across a pH range of 1 to 10 were essentially negligible, resulting in a total change of ~15 mV. There is an upward trend in $E_{1/2}$ as the pH becomes more basic with an associated slope of ~1.5 mV/pH unit. This change is likely a surface effect due to the pK_as of the ITO surface hydroxyl sites of which an isoelectric point exists around pH 6 to 8, depending on the degree of doping and how the ITO is manufactured.[18] Kinetic effects also arise due to surface charge, as demonstrated in Appx. F Figure S8. The measured peak splitting for the $1e^-$ blue dimer, $[(bpy)_2(H_2O)Ru^{III}ORu^{III}(OH_2)(bpy)_2]^{4+}$, couple ($[(HO)Ru^{IV}ORu^{III}(OH_2)]^{4+}/[(H_2O)Ru^{III}ORu^{III}(OH_2)]^{4+}$) in 0.1 M HNO_3 varies by up to a factor of 2 at a bare ITO electrode relative to an ITO electrode coated with a monolayer of polystyrenesulfonate (PSS). PSS is an anionically charged polymer. The electrostatic attraction between PSS and the blue dimer reduces peak splitting, indicating faster interfacial electron transfer kinetics.

However, significant thermodynamic effects were observed in altering the nature of the supporting electrolyte as well as the ionic strength, Appx. F Figures S9-11. In changing from 1.0 M $LiClO_4$ to 1.0 M CF_3SO_3Na, a change of ~60 mV in $E_{1/2}$ was measured for $[Ru(bpy)_2(4,4'\text{-}(H_2O_3P)_2\text{-}bpy)]^{2+}$ on ITO, Figure S9. Effects of this nature have been previously reported.[19] The $E_{1/2}$-pH dependence was also affected. In neat 0.1 M phosphate buffers, a slope of ~35 mV/pH unit was determined, Figure S10, for $[Ru(4,4'\text{-}(H_2O_3P)_2\text{-}bpy)_2(bpy)]^{2+}$ on ITO. The slope associated with this same surface adsorbed complex with 1.0 M $LiClO_4$ supporting electrolyte was ~21 mV/pH unit, Figure S11. Finally, surface loading studies revealed that the pH-dependence in our electrochemical measurements is independent (within experimental error) of surface coverage, Figure S11.

Given the inconclusive results of the electrochemical measurements, spectrophotometric pH titrations were pursued to establish pK_as of the complexes in solution. The results of these studies are given below and in Appx. F. Each series of results provides the raw data – absorption spectra vs. pH, the calculated spectra of each contributing species, the speciation curves – concentration vs. pH profiles, and four examples of the fit at single wavelengths in the absorption vs. pH data. Following the figures are details of the model and the calculated formation constants associated with the protonation states of the complex. From these values, pK_as and relative errors can be determined. And, finally, the statistical parameters regarding the raw data and the fit are given in order to assess the validity of the extracted values.

SPECFIT global analysis software provides Durbin-Watson factors and the Relative Error of Fit percentage following spectral fitting procedures. The residuals of a least squares fit are tested for the presence of serial auto-correlation to produce the Durbin-Watson

statistic. This method appears to work well for the types of systematic misfit errors arising in titration experiments and kinetic measurements.[20] The Durbin-Watson factor is calculated as follows:

$$DW = \frac{\sum_{t=2}^{N} (r_t - r_{t-1})^2}{\sum_{t=1}^{N} (r^2)} \qquad (3)$$

where,

r = (y_t – Y_t) residual
y_t = experimental data point
Y_t = calculated data point
t = data series index

Successive residual errors are examined by this method to determine their tendency to be correlated. A Durbin-Waton statistic of 2.0, the mid-point value of its range of 0.0 to 4.0, indicates that the residuals are uncorrelated (i.e. no systematic misfit). When residuals (misfits to the model) contain sinusoidal-like variations about the fitted function values, a positive serial autocorrelation (DW << 2) occurs. Negative serial auto-correlation (DW >>2) is not likely given the experiments under examination, but occurs when an increase in an independent variable leads to a reduction in a dependent variable. The Durbin-Watson factor is an ideal statistical test in factor analytical data, especially when the noise in the data set is very low, in contrast to the χ^2 (Chi-squared) statistic.[20]

In addition, the Relative Error of Fit is a simple, reliable statistic for assessing the quality of a least squares fit. This statistic expresses the root mean squares of the data as a percentage (%), and has the advantage of being independent of scale and units of the experimental data. It is best, however, to use this method in conjunction with other statistics as this statistic is averaged over all of the data and is insensitive to systematic misfit between

the model and data set. To support the acceptance of a proposed model, the Durbin-Watson statistic combined with the Relative Error of Fit value can give an accurate assessment of the quality of a fit.[20] The Relative Error of Fit is calculated as follows:

$$RE = \sqrt{\frac{\sum_{i=1}^{N}(y_i - Y_i)^2}{\sum_{i=1}^{N} y_i^2}} \times 100\% \qquad (4)$$

where,

N = number of data points
yi = experimental observation at the (i-th) point
Yi = calculated function at the (i-th) point

According to the authors of SPECFIT, "As a general guide, a good fit should have a Relative Error of Fit < 1.0%, and preferably lower for titration data acquired on low noise spectrophotometers (i.e., with $\sigma \sim 0.0002$ absorbance units). However, data acquired on instruments with higher levels of random, photometric noise may exhibit relative errors > 1%. In such cases the Durbin-Watson statistic should be the primary method for assessing the quality of the fit."[20]

Figures 7.5 to 7.7 correspond to the spectrophotometric pH titration of 1.0×10^{-4} M $[Ru(bpy)_2(4,4'\text{-}(H_2O_3P)_2\text{-}bpy)]^{2+}$ in 0.1 M H_3PO_4 acidified to pH 1 with HNO_3 containing 0.9 M $NaClO_4$ supporting electrolyte (25 mL starting volume). Eleven milliliters of 0.66 M NaOH titrant was used.

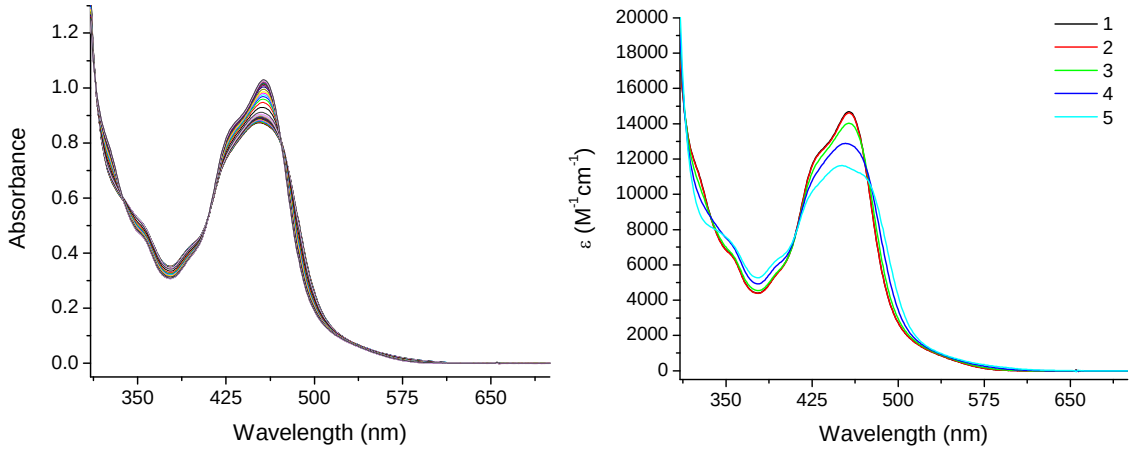

Figure 7.5. $[Ru(bpy)_2(4,4'\text{-}(H_2O_3P)_2\text{-}bpy)]^{2+}$ (1.0×10^{-4} M) in 0.1 M H_3PO_4 acidified to pH 1 with HNO_3 containing 0.9 M $NaClO_4$ supporting electrolyte. Left: dilution corrected raw data. Right: contributing species.

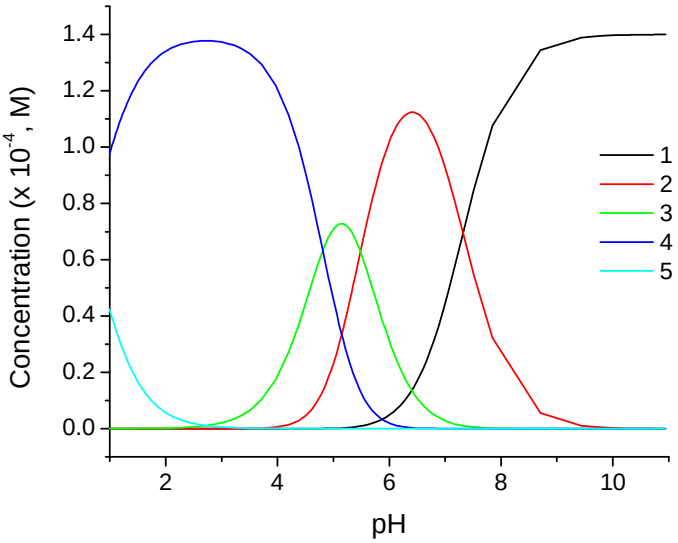

Figure 7.6. Concentration vs. pH curves for different acid-base forms of $[Ru(bpy)_2(4,4'\text{-}(H_2O_3P)_2\text{-}bpy)]^{2+}$ (1.0×10^{-4} M) in 0.1 M H_3PO_4 acidified to pH 1 with HNO_3 containing 0.9 M $NaClO_4$ supporting electrolyte.

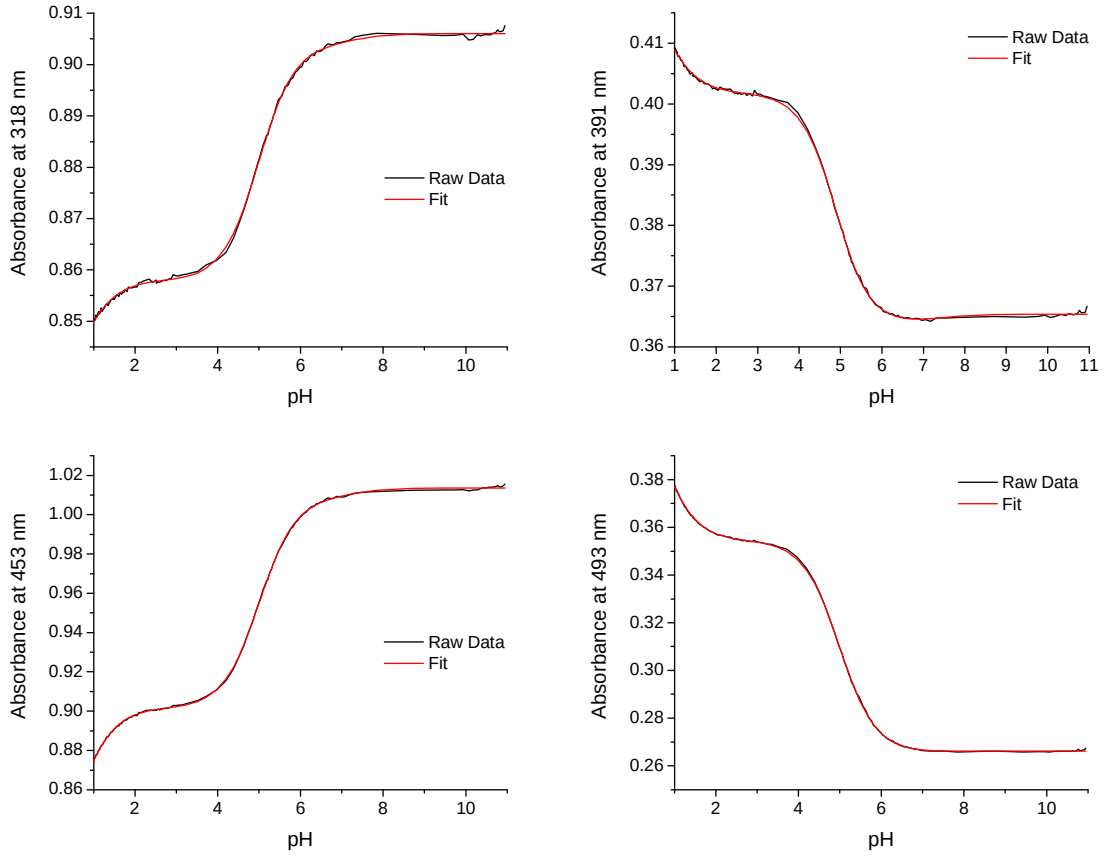

Figure 7.7. $[Ru(bpy)_2(4,4'\text{-}(H_2O_3P)_2\text{-}bpy)]^{2+}$ (1.0×10^{-4} M) in 0.1 M H_3PO_4 acidified to pH 1 with HNO_3 containing 0.9 M $NaClO_4$ supporting electrolyte. Single wavelength fits.

[SPECIES]	[FIXED]	[PARAMETER]		[ERROR]
1 0	True	0.00000E+00	+/-	0.00000E+00
1 1	False	7.31881E+00	+/-	6.67172E-02
1 2	False	1.28056E+01	+/-	7.14789E-02
1 3	False	1.76174E+01	+/-	7.54874E-02
1 4	False	1.82513E+01	+/-	7.88490E-02

[STATISTICS]
Experimental Noise = 1.047E-04
Relative Error Of Fit = 0.0604%
Durbin-Watson Factor = 0.8986
Goodness Of Fit, Chi^2 = 7.289E+00
Durbin-Watson Factor (raw data) = 1.0092

Fitting Report 7.1. $[Ru(bpy)_2(4,4'\text{-}(H_2O_3P)_2\text{-}bpy)]^{2+}$ (1.0×10^{-4} M) in 0.1 M H_3PO_4 acidified to pH 1 with HNO_3 containing 0.9 M $NaClO_4$ supporting electrolyte.

Figures 7.8 to 7.10 correspond to the spectrophotometric pH titration of 1.0 x 10^{-4} M $[Ru(4,4'\text{-}(H_2O_3P)_2\text{-}bpy)_2(bpy)]^{2+}$ in 0.1 M H_3PO_4 acidified to pH 1 with HNO_3 containing 0.9 M $NaClO_4$ supporting electrolyte (25 mL starting volume). Eleven milliliters of 0.66 M NaOH titrant was used.

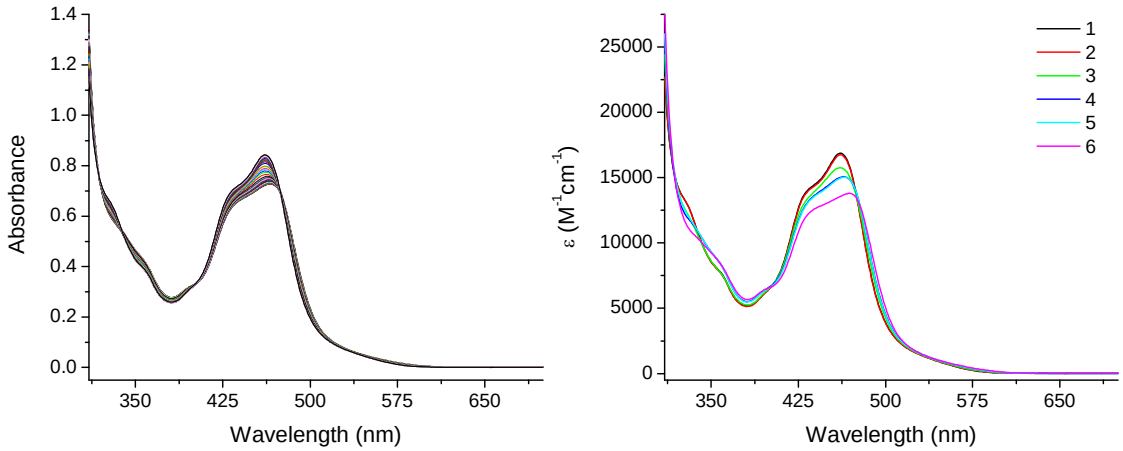

Figure 7.8. $[Ru(4,4'\text{-}(H_2O_3P)_2\text{-}bpy)_2(bpy)]^{2+}$ (1.0 x 10^{-4} M) in 0.1 M H_3PO_4 acidified to pH 1 with HNO_3 containing 0.9 M $NaClO_4$ supporting electrolyte. Left: dilution corrected raw data. Right: contributing species.

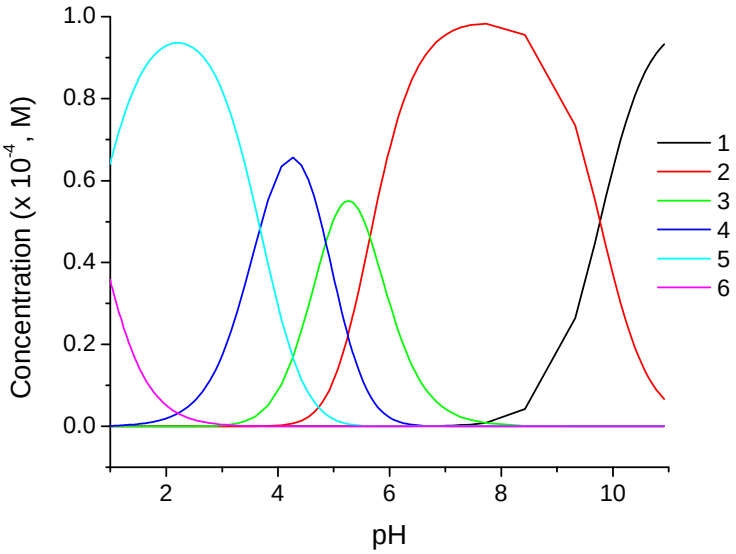

Figure 7.9. Concentration vs. pH curves for different acid-base forms of $[Ru(4,4'\text{-}(H_2O_3P)_2\text{-}bpy)_2(bpy)]^{2+}$ (1.0 x 10^{-4} M) in 0.1 M H_3PO_4 acidified to pH 1 with HNO_3 containing 0.9 M $NaClO_4$ supporting electrolyte.

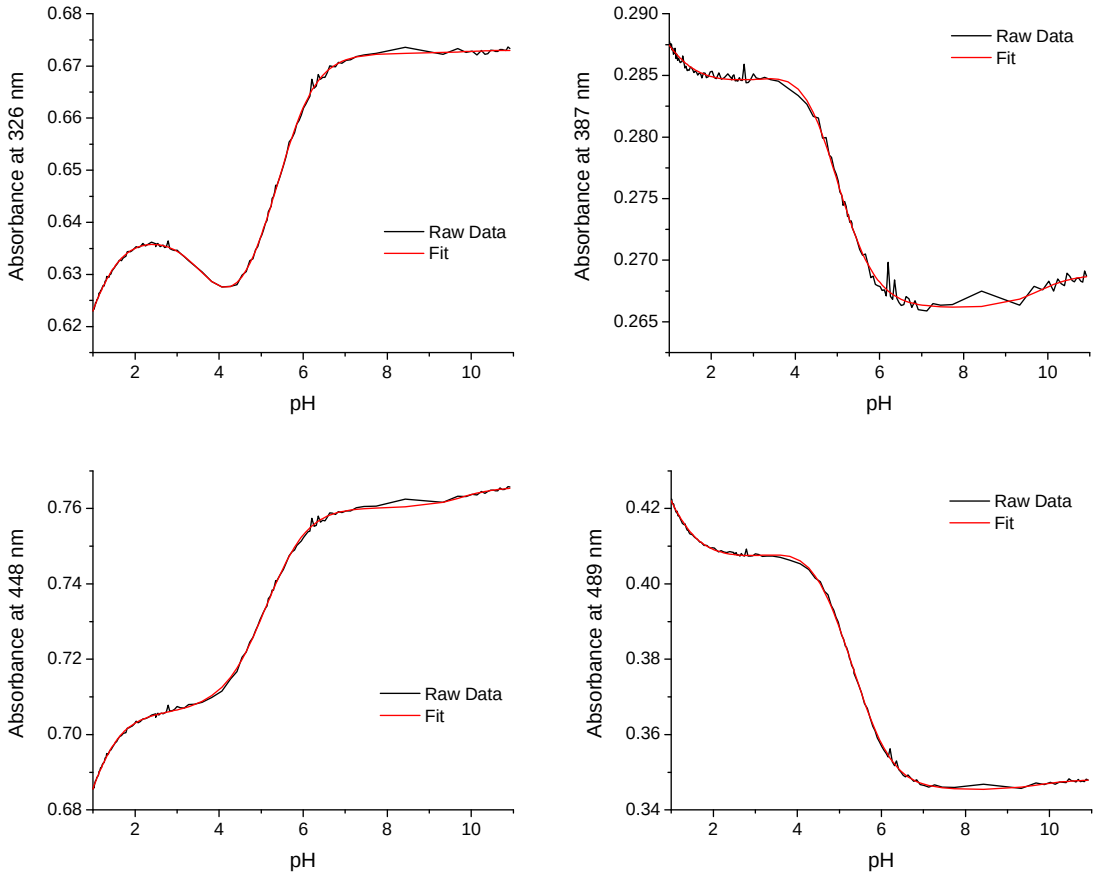

Figure 7.10. $[Ru(4,4'\text{-}(H_2O_3P)_2\text{-}bpy)_2(bpy)]^{2+}$ (1.0×10^{-4} M) in 0.1 M H_3PO_4 acidified to pH 1 with HNO_3 containing 0.9 M $NaClO_4$ supporting electrolyte. Single wavelength fits.

[SPECIES]	[FIXED]	[PARAMETER]		[ERROR]
1 0	True	0.00000E+00	+/-	0.00000E+00
1 1	False	9.77294E+00	+/-	7.67636E-02
1 2	False	1.54206E+01	+/-	8.11611E-02
1 3	False	2.02793E+01	+/-	9.01608E-02
1 4	False	2.39565E+01	+/-	9.91384E-02
1 5	False	2.46982E+01	+/-	1.03260E-01

[STATISTICS]
Experimental Noise = 9.530E-05
Relative Error Of Fit = 0.1125%
Durbin-Watson Factor = 2.0160
Goodness Of Fit, Chi^2 = 2.191E+01
Durbin-Watson Factor (raw data) = 2.0168

Fitting Report 7.2. $[Ru(4,4'\text{-}(H_2O_3P)_2\text{-}bpy)_2(bpy)]^{2+}$ (1.0×10^{-4} M) in 0.1 M H_3PO_4 acidified to pH 1 with HNO_3 containing 0.9 M $NaClO_4$ supporting electrolyte.

Figures 7.11 to 7.13 correspond to the spectrophotometric pH titration of 2.0×10^{-4} M $[Ru(bpy)_2(4,4'\text{-}(H_2O_3PCH_2)_2\text{-}bpy)]^{2+}$ in 0.1 M H_3PO_4 acidified to pH 1 with HNO_3 containing 0.9 M $NaClO_4$ supporting electrolyte (25 mL starting volume). Eleven milliliters of 0.66 M NaOH titrant was used.

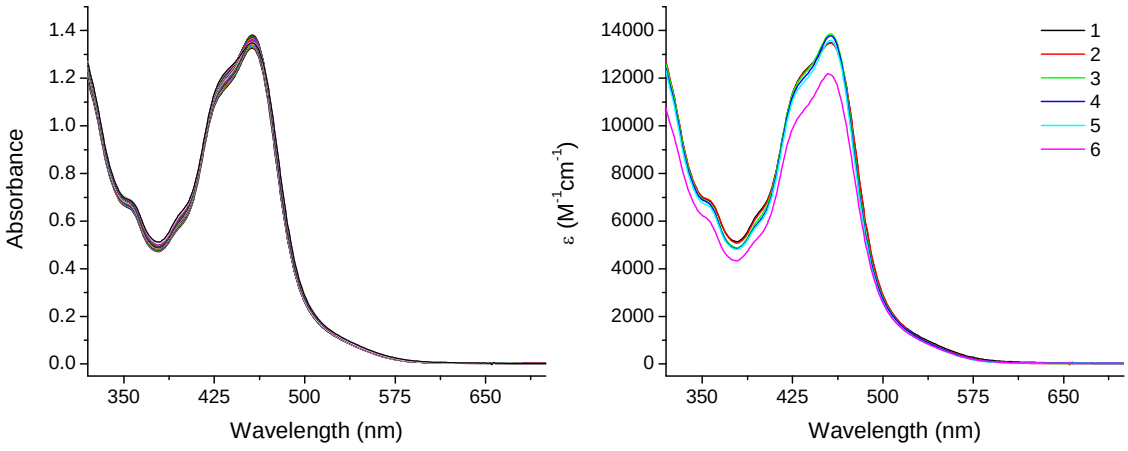

Figure 7.11. $[Ru(bpy)_2(4,4'\text{-}(H_2O_3PCH_2)_2\text{-}bpy)]^{2+}$ (2.0×10^{-4} M) in 0.1 M H_3PO_4 acidified to pH 1 with HNO_3 containing 0.9 M $NaClO_4$ supporting electrolyte. Left: dilution corrected raw data. Right: contributing species.

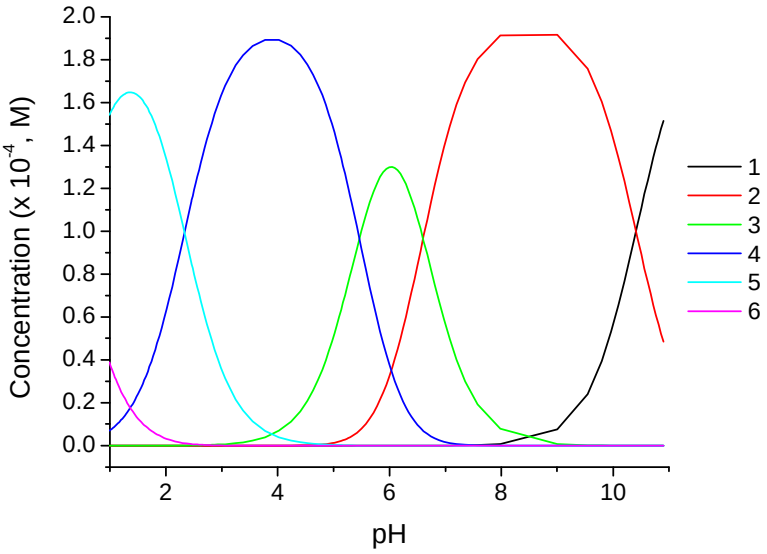

Figure 7.12. Concentration vs. pH curves for different acid-base forms of $[Ru(bpy)_2(4,4'-(H_2O_3PCH_2)_2\text{-}bpy)]^{2+}$ (2.0×10^{-4} M) in 0.1 M H_3PO_4 acidified to pH 1 with HNO_3 containing 0.9 M $NaClO_4$ supporting electrolyte.

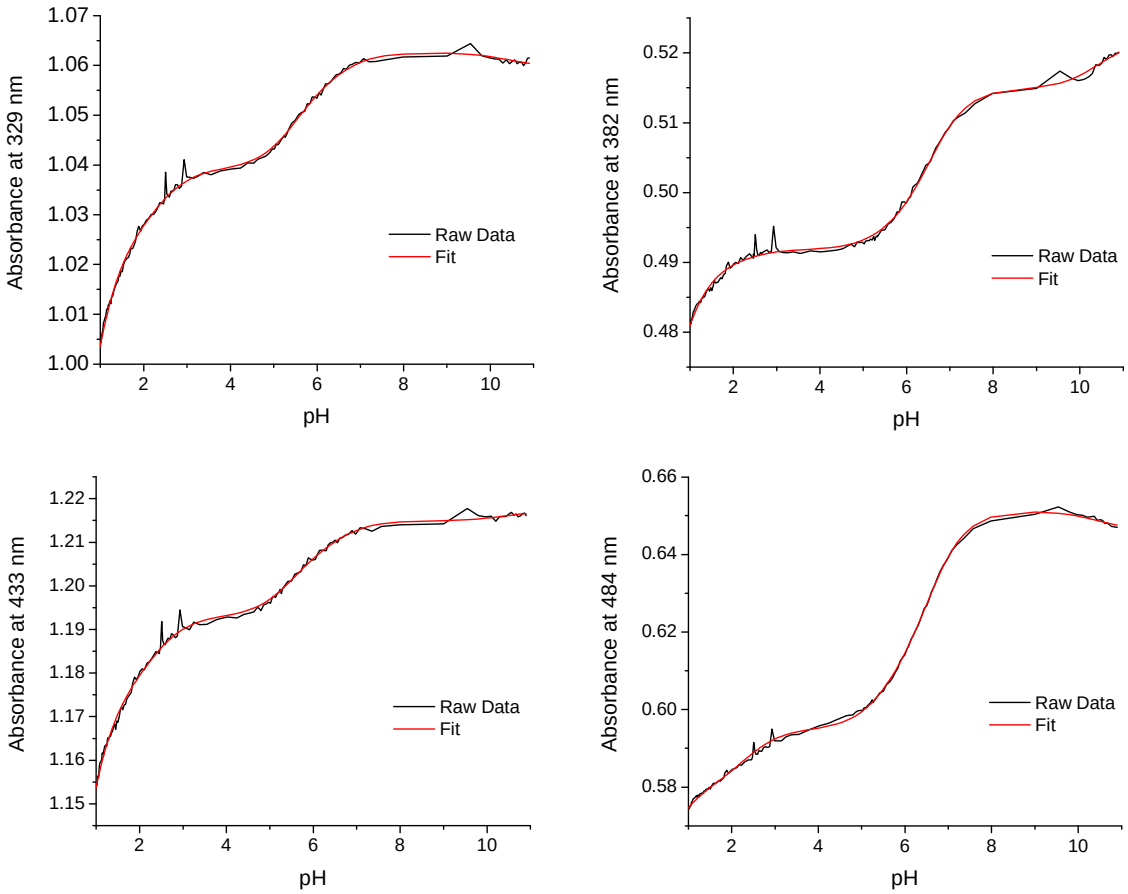

Figure 7.13. $[Ru(bpy)_2(4,4'\text{-}(H_2O_3PCH_2)_2\text{-}bpy)]^{2+}$ (2.0×10^{-4} M) in 0.1 M H_3PO_4 acidified to pH 1 with HNO_3 containing 0.9 M $NaClO_4$ supporting electrolyte.Single wavelength fits.

[SPECIES]	[FIXED]	[PARAMETER]		[ERROR]
1 0	True	0.00000E+00	+/-	0.00000E+00
1 1	False	1.04087E+01	+/-	9.57962E-02
1 2	False	1.70101E+01	+/-	9.69218E-02
1 3	False	2.24715E+01	+/-	1.02511E-01
1 4	False	2.48053E+01	+/-	1.08922E-01
1 5	False	2.51953E+01	+/-	1.54500E-01

[STATISTICS]
Experimental Noise = 1.713E-04
Relative Error Of Fit = 0.1057%
Durbin-Watson Factor = 1.1491
Goodness Of Fit, Chi^2 = 1.474E+01
Durbin-Watson Factor (raw data) = 1.1920

Fitting Report 7.3. $[Ru(bpy)_2(4,4'\text{-}(H_2O_3PCH_2)_2\text{-}bpy)]^{2+}$ (2.0×10^{-4} M) in 0.1 M H_3PO_4 acidified to pH 1 with HNO_3 containing 0.9 M $NaClO_4$ supporting electrolyte.

Figures 7.14 to 7.16 correspond to the spectrophotometric pH titration of 1.13×10^{-4} M $[Ru(4,4'\text{-}(H_2O_3PCH_2)_2\text{-}bpy)_2(bpy)]^{2+}$ in 0.1 M H_3PO_4 acidified to pH 1 with HNO_3 containing 0.9 M NaCl supporting electrolyte (25 mL starting volume). Eleven milliliters of 0.66 M NaOH titrant was used.

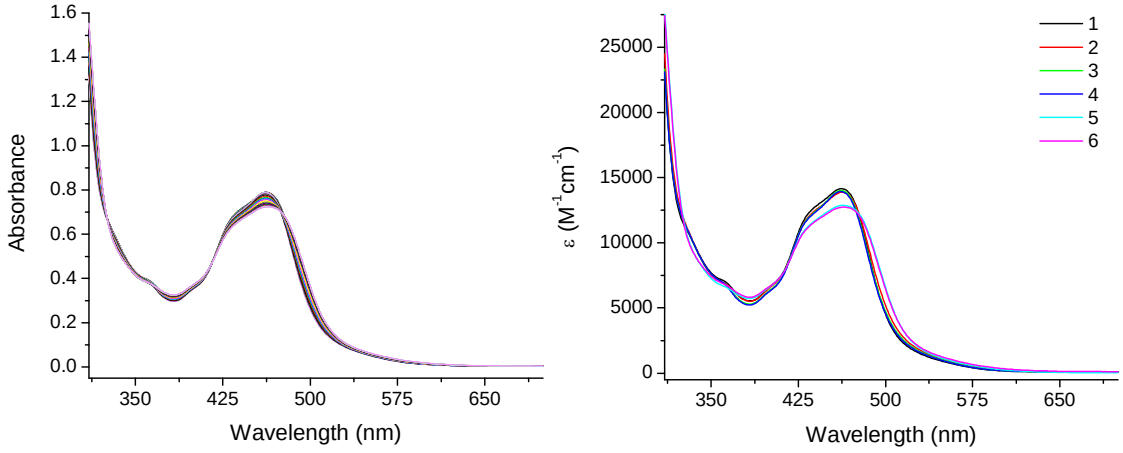

Figure 7.14. $[Ru(4,4'\text{-}(H_2O_3PCH_2)_2\text{-}bpy)_2(bpy)]^{2+}$ (1.13×10^{-4} M) in 0.1 M H_3PO_4 acidified to pH 1 with HNO_3 containing 0.9 M NaCl supporting electrolyte. Left: dilution corrected raw data. Right: contributing species.

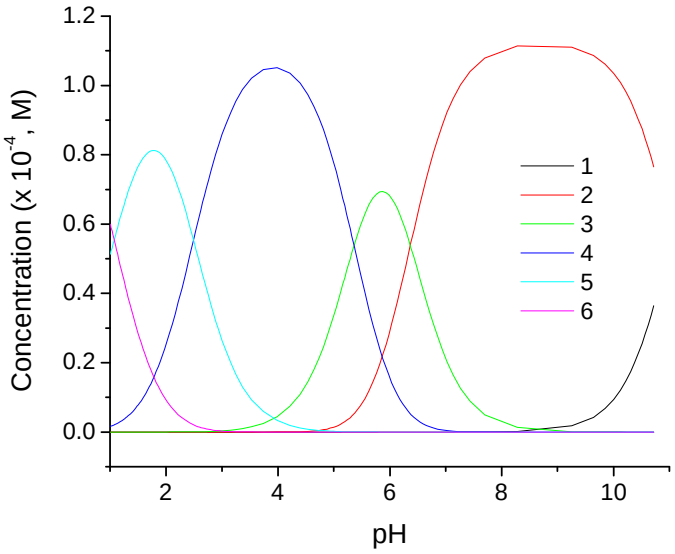

Figure 7.15. Concentration vs. pH curves for different acid-base forms of [Ru(4,4'-$(H_2O_3PCH_2)_2$-bpy)$_2$(bpy)]$^{2+}$ (1.13 x 10^{-4} M) in 0.1 M H_3PO_4 acidified to pH 1 with HNO_3 containing 0.9 M NaCl supporting electrolyte.

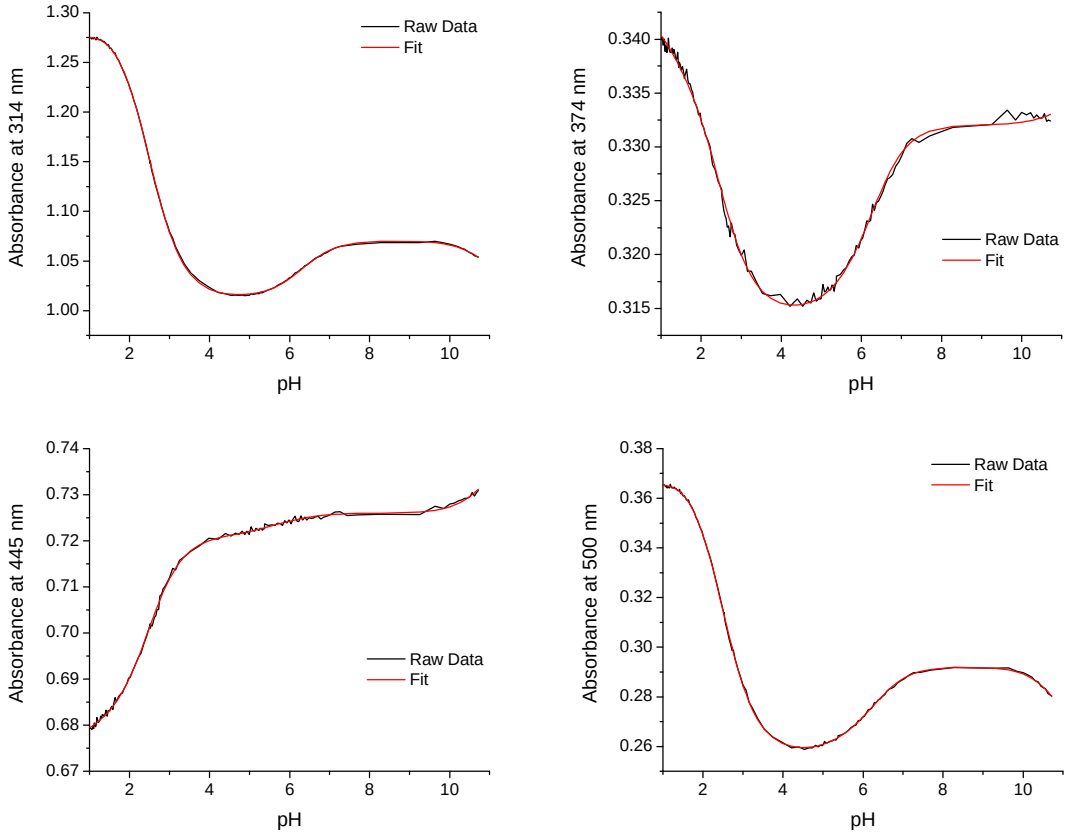

Figure 7.16. [Ru(4,4'-$(H_2O_3PCH_2)_2$-bpy)$_2$(bpy)]$^{2+}$ (1.13 x 10^{-4} M) in 0.1 M H_3PO_4 acidified to pH 1 with HNO_3 containing 0.9 M NaCl supporting electrolyte. Single wavelength fits.

[SPECIES]	[FIXED]	[PARAMETER]		[ERROR]
1 0	True	0.00000E+00	+/-	0.00000E+00
1 1	False	1.10430E+01	+/-	1.19529E-01
1 2	False	1.74106E+01	+/-	1.16538E-01
1 3	False	2.27712E+01	+/-	1.35055E-01
1 4	False	2.52629E+01	+/-	1.35065E-01
1 5	False	2.63355E+01	+/-	1.51208E-01

[STATISTICS]
Experimental Noise = 1.104E-04
Relative Error Of Fit = 0.1131%
Durbin-Watson Factor = 1.5129
Goodness Of Fit, Chi^2 = 1.828E+01
Durbin-Watson Factor (raw data) = 1.5327

Fitting Report 7.4. $[Ru(4,4'\text{-}(H_2O_3PCH_2)_2\text{-}bpy)_2(bpy)]^{2+}$ (1.13 x 10^{-4} M) in 0.1 M H_3PO_4 acidified to pH 1 with HNO_3 containing 0.9 M NaCl supporting electrolyte.

Figures 7.17 to 7.19 correspond to the spectrophotometric pH titration of 1.1 x 10^{-4} M $[Ru(4,4'\text{-}(H_2O_3PCH_2)_2\text{-}bpy)_3]^{2+}$ in 0.1 M H_3PO_4 acidified to pH 1 with HNO_3 containing 0.9 M $NaClO_4$ supporting electrolyte (25 mL starting volume). Eleven milliliters of 0.66 M NaOH titrant was used.

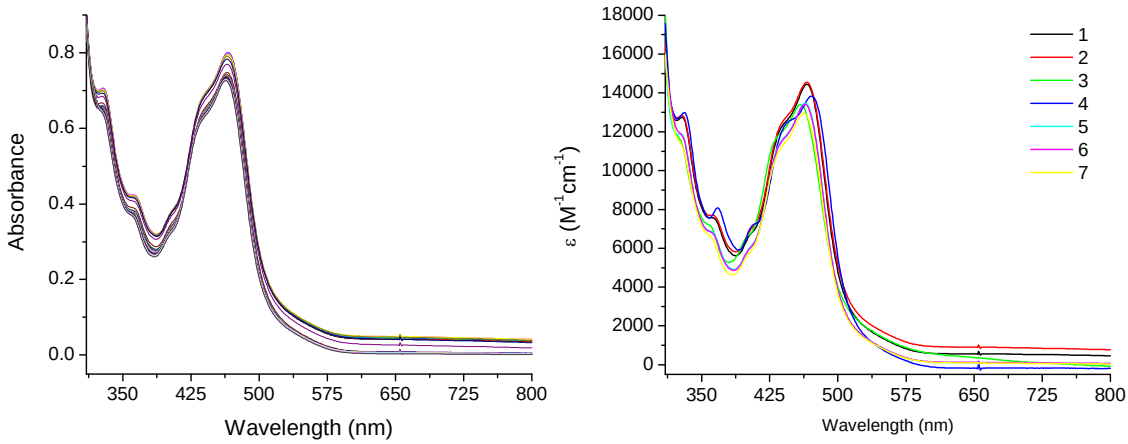

Figure 7.17. $[Ru(4,4'\text{-}(H_2O_3PCH_2)_2\text{-}bpy)_3]^{2+}$ (1.1 x 10^{-4} M) in 0.1 M H_3PO_4 acidified to pH 1 with HNO_3 containing 0.9 M $NaClO_4$ supporting electrolyte. Left: dilution corrected raw data. Right: contributing species.

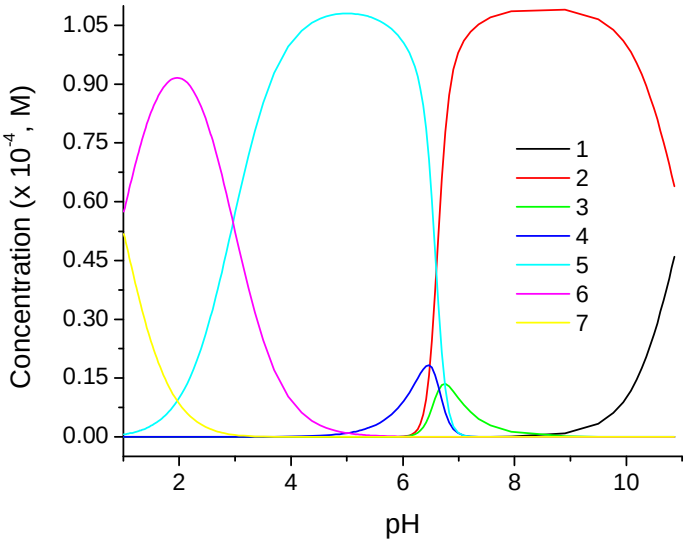

Figure 7.18. Concentration vs. pH curves for different acid-base forms of [Ru(4,4'-$(H_2O_3PCH_2)_2$-bpy)$_3$]$^{2+}$ (1.1 x 10^{-4} M) in 0.1 M H_3PO_4 acidified to pH 1 with HNO_3 containing 0.9 M $NaClO_4$ supporting electrolyte.

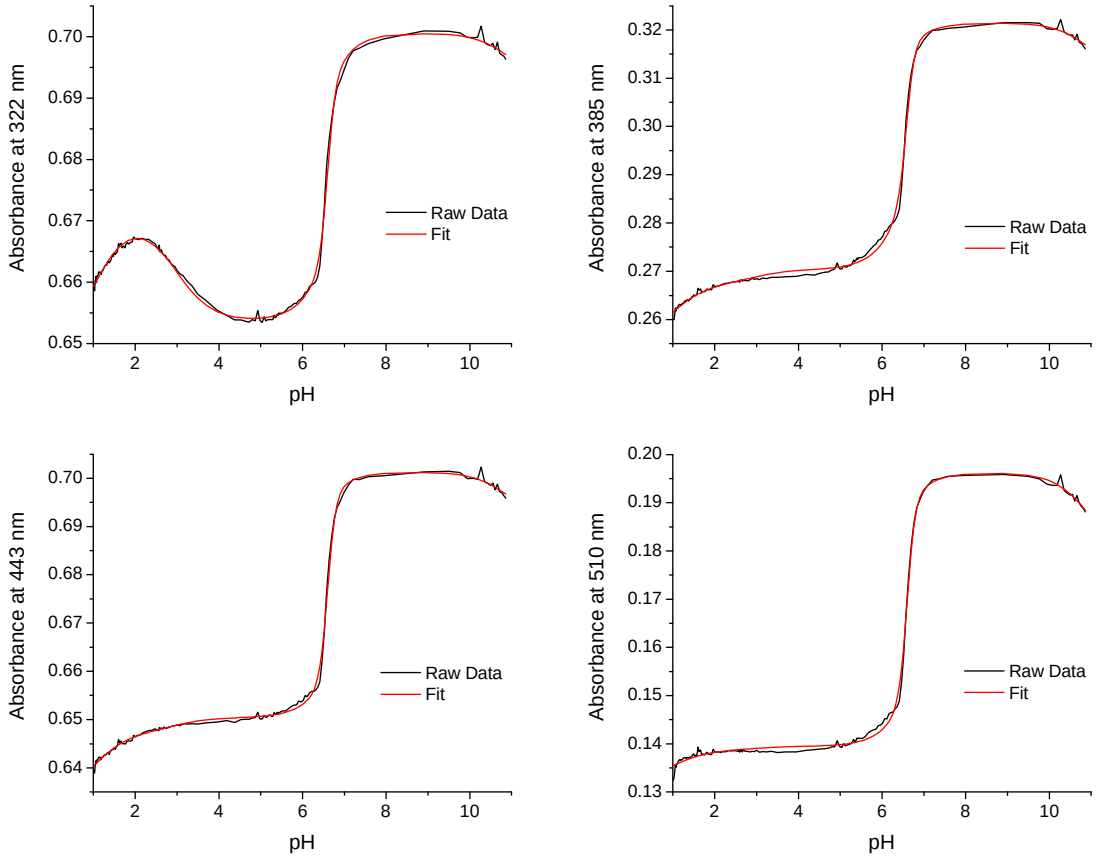

Figure 7.19. [Ru(4,4'-$(H_2O_3PCH_2)_2$-bpy)$_3$]$^{2+}$ (1.1 x 10^{-4} M) in 0.1 M H_3PO_4 acidified to pH 1 with HNO_3 containing 0.9 M $NaClO_4$ supporting electrolyte. Single wavelength fits.

[SPECIES]	[FIXED]	[PARAMETER]		[ERROR]
1 0	True	0.00000E+00	+/-	0.00000E+00
1 1	True	1.10000E+01	+/-	0.00000E+00
1 2	True	1.70000E+01	+/-	0.00000E+00
1 5	False	3.69432E+01	+/-	7.62612E-02
1 6	False	4.39991E+01	+/-	3.18635E-02
1 7	False	4.69636E+01	+/-	4.57861E-02
1 8	False	4.79295E+01	+/-	8.20244E-02

[STATISTICS]
Experimental Noise = 8.416E-05
Relative Error Of Fit = 0.2257%
Durbin-Watson Factor = 0.6523
Goodness Of Fit, Chi^2 = 8.043E+01
Durbin-Watson Factor (raw data) = 0.6657

Fitting Report 7.5. $[Ru(4,4'\text{-}(H_2O_3PCH_2)_2\text{-}bpy)_3]^{2+}$ (1.1×10^{-4} M) in 0.1 M H_3PO_4 acidified to pH 1 with HNO_3 containing 0.9 M $NaClO_4$ supporting electrolyte.

A summary of pK_a values measured from the above spectrophotometric pH titrations of phosphonate-derivatized $[Ru(bpy)_3]^{2+}$ complexes is provided in Table 7.2.

Table 7.2. pK_a values determined by spectrophotometric monitoring of absorbance changes vs. pH for phosphonate-derivatized $[Ru(bpy)_3]^{2+}$ complexes.

Complex	**p$K_{a,1}$**	**p$K_{a,2}$**	**p$K_{a,3}$**	**p$K_{a,4}$**	**p$K_{a,5}$**
$[Ru(bpy)_2(4,4'\text{-}(H_2O_3P)_2\text{-}bpy)]^{2+}$	0.63	4.81	5.49	7.32	-
$[Ru(4,4'\text{-}(H_2O_3P)_2\text{-}bpy)_2(bpy)]^{2+}$	0.74	3.68	4.86	5.65	9.77
$[Ru(bpy)_2(4,4'\text{-}(H_2O_3PCH_2)_2\text{-}bpy)]^{2+}$	0.39	2.33	5.46	6.60	10.41
$[Ru(4,4'\text{-}(H_2O_3PCH_2)_2\text{-}bpy)_2(bpy)]^{2+}$	1.07	2.49	5.36	6.37	11.04
$[Ru(4,4'\text{-}(H_2O_3PCH_2)_2\text{-}bpy)_3]^{2+}$	0.97	2.96	-	-	-

A spectrophotometric pH titration of $[Ru(bpy)_3]^{2+}$ was also performed as a control experiment using the method and conditions employed above (1.5×10^{-4} M complex, 0.1 M H_3PO_4 acidified to pH 1 with HNO_3, 0.9 M NaCl, 25 mL starting volume, titrated with 11

mL of 0.66 M NaOH). We expect this complex to be pH independent, having no titratable protons. A 1.7% increase in absorbance was observed. In the MLCT region, the increase in sample absorbance varies almost linearly with scan number, which is proportional to time. The only region that displays any real pH dependence is below 325 nm, where the absorption is dominated by intra-ligand transitions. It is reasonable to propose that these transitions are responding weakly to the changing anionic composition of the medium (0.1 M phosphate buffer). The experiment indicates a minor source of systematic error in our measurements as our sample likely experiences some loss to evaporation, despite our efforts to seal the top of our vessel in the absence of a properly machined cell top that can accommodate the various electrodes and tubing. The absorbance changes are much smaller than the rest of the complexes and it is safe to assume that there is nothing of any significance occurring in the pH titration of $[Ru(bpy)_3]^{2+}$.

It should also be noted that the ionic strength plays a significant role in these measurements as well. The effect of ionic strength in pH titrations, specifically with compounds in solution, is well-documented.[21] A second pH titration of $[Ru(4,4'\text{-}(H_2O_3PCH_2)_2\text{-}bpy)_3]^{2+}$ was performed that illustrates the importance of ionic strength. Notice in the raw data, Figure 7.17, that the baseline is unstable in the first titration. The jump in baseline occurs abruptly at pH 6.5, after which, the solution appeared slightly turbid indicating a change in sample solubility. Light scattering from the precipitate prevented any additional pK_as from being determined. It was hypothesized that the sodium salt of the deprotonated, anionic complex was not completely soluble. The 0.9 M $NaClO_4$ supporting electrolyte was removed in the second titration, details are located in Appx. F, to reduce the concentration of Na^+ in hopes of avoiding this problem. In this case, solubility did not

become an issue until pH 6.8, where the same jump in baseline was observed. However, in measuring the first two pK_a values, we found p$K_{a,1}$ equal to 1.65, and p$K_{a,2}$ at 6.9, which are much less acidic compared to the values of 0.97 and 2.96 (Table 7.2) measured with 0.9 M $NaClO_4$. Deprotonation of $[Ru(4,4'\text{-}(H_2O_3PCH_2)_2\text{-}bpy)_3]^{2+}$ in solution is stifled in the absence of a supporting electrolyte. Spectrophotometric pH titrations are currently underway for the complexes adsorbed to high surface area TiO_2 films on fluorine-doped tin oxide (FTO)-coated glass substrates.

Following an observation made during surface catalyzed blue dimer water oxidation at pH 4, it became apparent that a significant interaction between the blue dimer and the electrode surface was taking place, which did not noticeably occur at pH 1. After the electrode was removed from solutions containing the blue dimer and transferred to a clean solution for electrochemical measurements, the blue dimer waves were still present.

In acidic aqueous media, the surface charge on TiO_2 is positive as it has an isoelectric point of ~5.[22] In a previous report, the change in Zeta potential at pH 3 was monitored for the TiO_2 nanoparticles coated with increasing concentrations of phosphonate-derivatized $[Ru(bpy)_3]^{2+}$.[23] These experiments show that the surface charge becomes less positive as more complex is bound to the surface. In the case of surface-adsorbed $[Ru(4,4'\text{-}(H_2O_3P)_2\text{-}bpy)_3]^{2+}$, the Zeta potential actually becomes negative, presumably due to dangling, deprotonated phosphonic acid substituents.[23]

Consequently, ion-pairing measurements were studied in an effort to synthesize redox mediator/chromophore-catalyst systems via electrostatic self-assembly. Shown in Figure 7.20 is a representative cyclic voltammogram (CV) of such a system. An ITO slide with $[Ru(4,4'\text{-}(H_2O_3P)_2\text{-}bpy)_2(bpy)]^{2+}$ loaded to monolayer surface coverage was soaked for ~4 hours in a

0.025 M pH 5 acetate buffer solution containing 0.001 M $[Ru(Mebimpy)(bpy)(OH_2)](O_3SCF_3)_2$, a known water oxidation catalyst.[24] The slide was removed from the stock solution, rinsed with 0.1 M pH 5 acetate buffer solution, and allowed to air-dry. A scan rate of 100 mV/s was used for the CV in Figure 7.20, taken in a fresh solution of 0.1 M pH 5 acetate buffer (no catalyst in the external solution). Additional CVs at different scan rates (ν) are provided in Appx. F Figure S24.

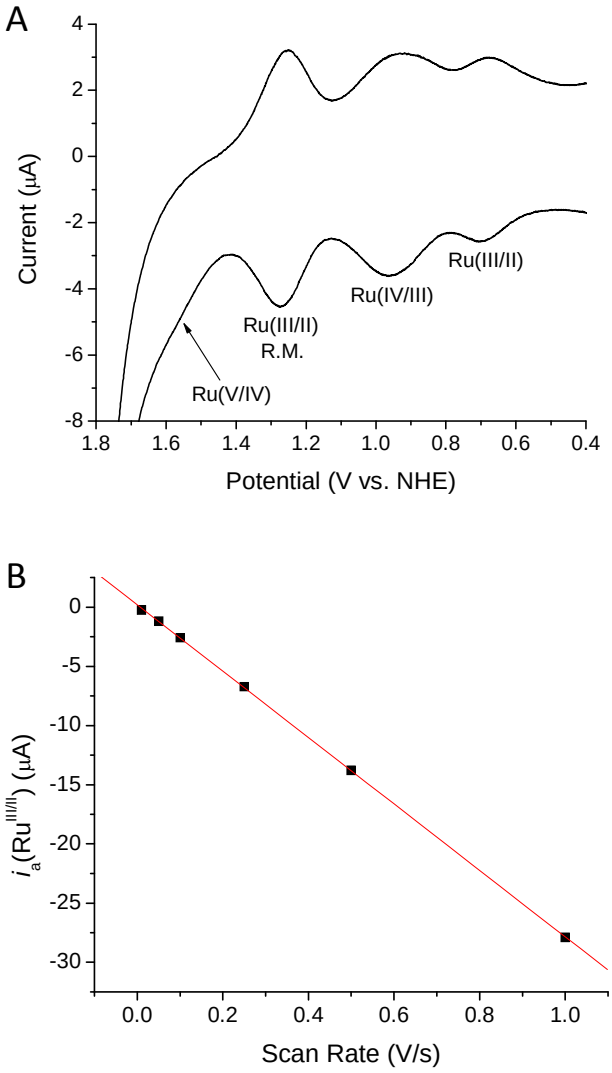

Figure 7.20. $[Ru(4,4'\text{-}(H_2O_3P)_2\text{-}bpy)_2(bpy)]^{2+}$ on ITO (Γ = 1.0 x 10^{-10} mol/cm^2), soaked in 0.001 M $[Ru(Mebimpy)(bpy)(OH_2)]^{2+}$ in 0.025 M pH 5 acetate buffer (~4 h).
CVs measured in clean 0.1 M pH 5 acetate buffer. (A) CV at scan rate = 100 mV/s. (B) Plot of oxidative current (i_a) of first Ru(III/II) wave vs. scan rate (V/s): R = 0.99996.

Labels denoting the redox couples associated with the molecular components of the ion-pair are shown in Figure 7.20A. Based on the independently determined redox potentials of the redox mediator, Appendix F Figures S10,11, and the catalyst, $[Ru(Mebimpy)(bpy)(OH_2)]^{2+}$, Appendix C Figure S25, the waves have been identified as follows: $E_{1/2}$ at 0.69 V, Ru(III/II) catalyst; $E_{1/2}$ at 0.95 V, Ru(IV/III) catalyst; $E_{1/2}$ at 1.26 V, Ru(III/II) redox mediator (R.M.); irreversible oxidation at 1.56 V, Ru(V/IV) catalyst.

Importantly, Figure 7.20B establishes the non-diffusional nature of the redox events. The oxidative peak current (in μA) for the catalyst Ru(III/II) couple is plotted vs. scan rate (V/s). Peak current scales linearly with scan rate for Nernstian adsorbates, whereas diffusional systems are proportional to the square root of the scan rate.[25] Further evidence can be gleaned in this regard from Figure 7.21 in which the cyclic voltammograms have been normalized vs. scan rate. The current-potential profile of the first three waves overlap as they ought, with exception to the CV measured at 10 mV/s due to electrocatalytic water oxidation.

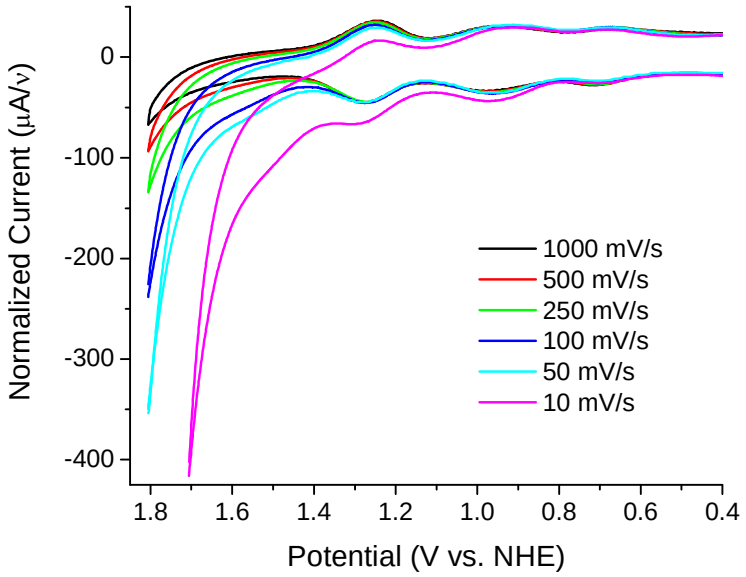

Figure 7.21. Normalized CVs (current divided by scan rate). $[Ru(4,4'\text{-}(H_2O_3P)_2\text{-}bpy)_2(bpy)]^{2+}$ on ITO (Γ = 1.0 x 10^{-10} mol/cm^2), soaked in 0.001 M $[Ru(Mebimpy)(bpy)(OH2)]^{2+}$ in 0.025 M pH 5 acetate buffer (~4 h). CVs measured in clean 0.1 M pH 5 acetate buffer. Scan rates are shown.

Following the initial CVs, a controlled potential electrolysis was performed at 1.71 V vs. NHE on the same slide, Appx. F Figure S25. While the measured current was modest, CVs taken of the slide after the CPE revealed the same series of waves, but the Ru(IV/III) wave had noticeably increased, Appx. F Figure S26. In Figure 7.22A, the normalized CVs are given. The catalyst Ru(III/II) couple appears to be scan rate dependent now. However, a plot of its oxidative peak current vs. scan rate shows this couple is still a Nernstian adsorbate, Figure 7.22B. Considering its non-diffusional nature, the apparent scan rate dependence is a kinetic phenomenon rather than a mass transport effect, since the molecule is adsorbed. This kinetic effect likely arises due to the large separation between the catalyst Ru(III/II) couple and that of the redox mediator. The slow kinetics cause the apparent disappearance of the Ru(III/II) couple at fast scan rates, a result of the mediator being too high in potential to facilitate the proton-coupled electron transfer event of the catalyst $[Ru^{III}\text{-}OH]^{2+}/[Ru^{II}\text{-}OH_2]^{2+}$ couple. Consequently, the catalyst in its Ru^{IV} oxidation state has accumulated on the surface. Thermodynamically, the catalyst Ru(V/IV) couple is uphill with respect to the redox mediator. This is presumably the rate-limiting step and allows for the Ru^{IV}=O species of the catalyst to exist at the steady state.

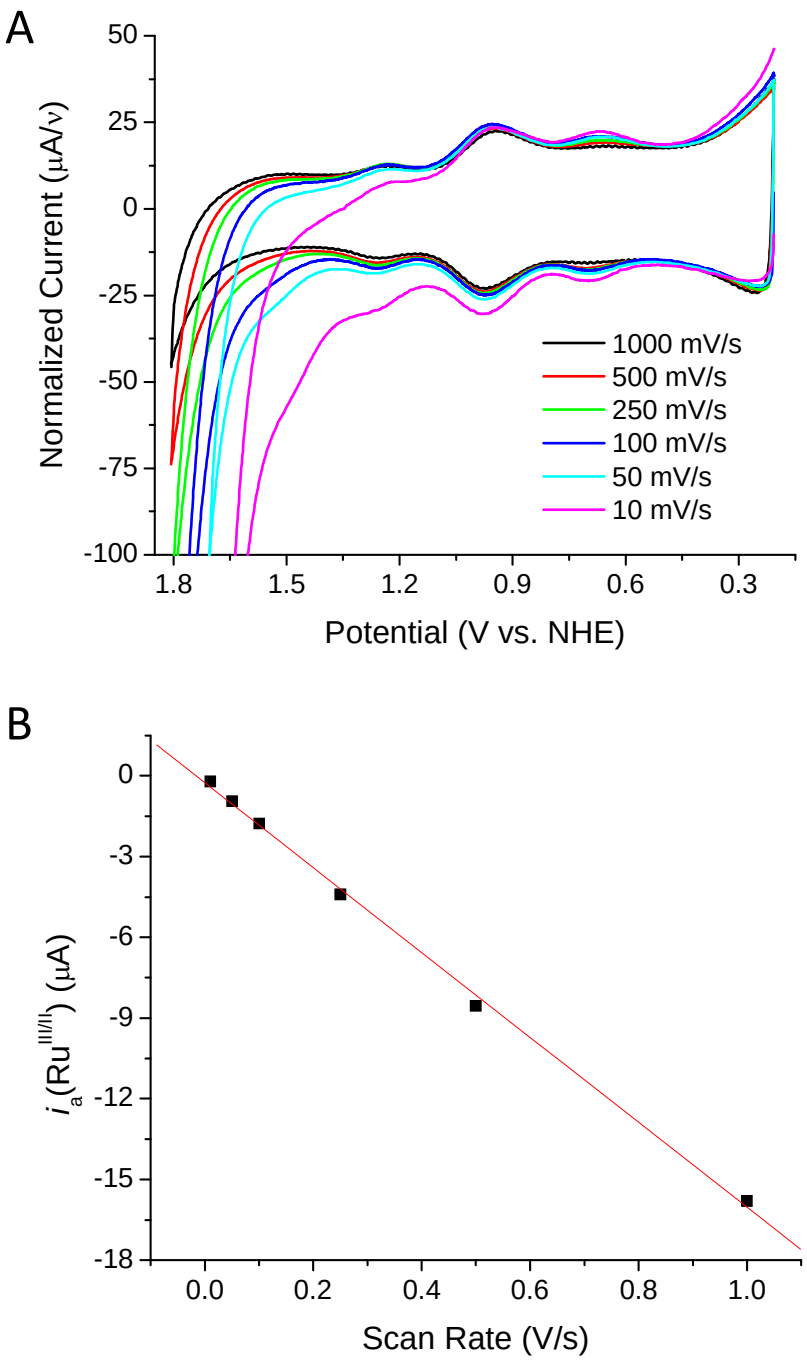

Figure 7.22. $[Ru(4,4'\text{-}(H_2O_3P)_2\text{-}bpy)_2(bpy)]^{2+}$ on ITO, soaked in 0.001 M $[Ru(Mebimpy)(bpy)(OH_2)]^{2+}$ in 0.025 M pH 5 acetate buffer (~4 h). CVs in 0.1 M pH 5 acetate buffer following a controlled potential electrolysis (CPE) at 1.71 V vs. NHE for ~3100 s. (A) Scan rate normalized CVs (current divided by scan rate). (B) A plot of the oxidative peak potential of the catalyst Ru(III/II) wave vs. scan rate.

On the same slide, another controlled potential electrolysis at 0 V vs. NHE, Appx. F Figure S27, was performed for ~2000 s. After which, the CVs in Figure 7.23 were measured (normalized vs. scan rate).

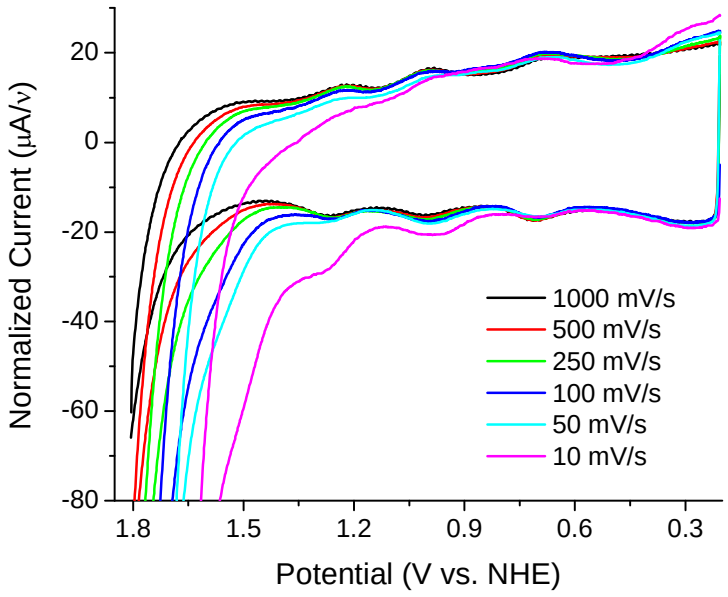

Figure 7.23. $[Ru(4,4'\text{-}(H_2O_3P)_2\text{-}bpy)_2(bpy)]^{2+}$ on ITO, soaked in 0.001 M $[Ru(Mebimpy)(bpy)(OH_2)]^{2+}$ in 0.025 M pH 5 acetate buffer (~4 h). CVs in 0.1 M pH 5 acetate buffer following a controlled potential electrolysis at 0.0 V vs. NHE for ~2000 s.

The waves become kinetically well-behaved after the reductive electrolysis. In all cases, the redox processes were due to an adsorbed species. Total current, however, dropped substantially from the first CVs of the ion-paired system to those of Figure 7.23.

During cyclic voltammograms of the phosphonate derivatized $[Ru(bpy)_3]^{2+}$, a new electrochemically reversible wave appears at ~0.9 V at the expense of the Ru(III/II) mediator couple. Each complex in the series was studied and found to have a similar decomposition product growing in with repeated CVs or during a controlled potential electrolysis (CPE) past the Ru(III/II) wave.

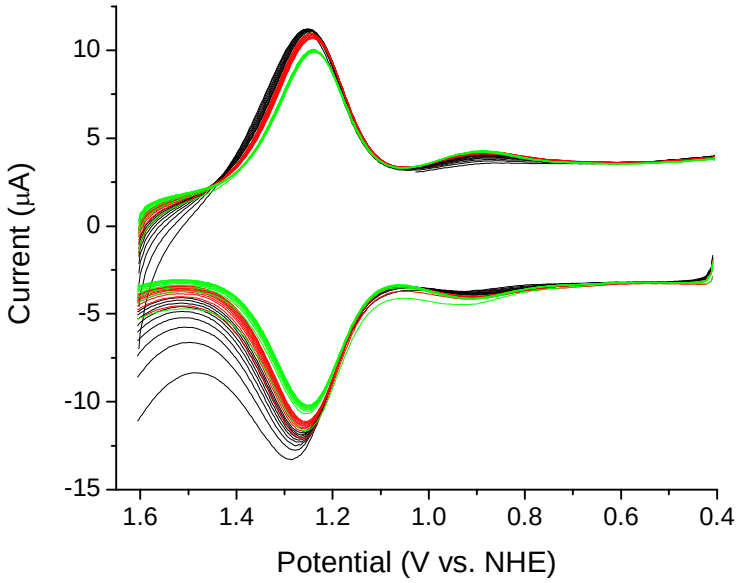

Figure 7.24. $[Ru(bpy)_2(4,4'\text{-}(H_2O_3P)_2\text{-}bpy)]^{2+}$ (Γ = 1.0 x 10^{-10} mol/cm^2) on ITO in 0.075 M CF_3SO_3Na and 0.025 M phosphate buffer. Repeated cyclic voltammograms were taken.

Discussion

A general discussion of the current state of the literature regarding phosphonic acid surface binding and its effect on charge injection, stability, and pH dependence is warranted. There are many conflicting reports due to the difficulty at measuring the surface binding interaction experimentally, and perhaps more significantly, the vast array of methods in which to load the substrates. In addition, ample evidence has established that phosphonates bind in different ways to different metal oxides. Due to the proposed condensation mechanism for the phosphonate ester bond formation at the surface, a form of heat treatment is often used to drive this reaction to completion.

Computational studies have also been reported regarding the nature of phosphonate binding to TiO_2 surfaces.[11,13,26] In a study by Ojamae and coworkers investigating phosphonic acid adsorption at the TiO_2 anatase (101) surface, they calculated monodentate and bidentate binding modes to be stable with calculated adsorption energies exceeding 40

kcal/mol. The best monodentate geometry was more stable than the best bidentate geometry by 2.6 kcal/mol. In contrast, a tridentate mode was also investigated. However, it was not preferred due to a bad geometrical match, in the sense that the distance to a third coordinatively unsaturated Ti is too long. No stable structure could therefore be found.[26] Their modeling may have a flaw in that instead of allowing the calculation to proceed by condensation to form the Ti-O-P bond and expelling H_2O, the residual proton is transferred to an under-coordinated surface oxygen. The less stable bidentate mode and the lack of a stable structure for a tridentate mode could be associated with poor proton management/mechanistic oversight. Perhaps this modeling is sufficient, but it does assume that bridging hydroxide groups, Ti-OH-Ti, can be generated. In terms of the 2.6 kcal/mol difference between monodentate and bidentate binding modes, Batista and coworkers report a difference of only 0.7 kcal/mol between investigated monodentate and bidentate binding modes which is "essentially identical at the level of theory being considered here".[11] In the Batista calculations, it is not clear if they optimized different binding modes, disregarding the condensation, and going straight to the final, assumed geometry and thus avoiding the need for proton management.

Luschtinetz and coworkers follow a similar model for optimization where dissociated protons end up at coordinately unsaturated O atoms on the TiO_2 surface. It appears that their calculations are more thorough and robust than those of Ojamae and coworkers. Their investigate found that a stable monodentate binding mode could be found with a calculated adsorption energy of 45 kcal/mol, and bidentate modes, all having fully dissociated phosphonic acids with the P=O bond involved in H-bonding to surface OH groups. The bidentate modes had calculated adsorption energies of 66 to 68 kcal/mol. In regards to a

tridentate binding mode, this type of adsorption could be realized on "clean" TiO_2 via a fully deprotonated (HPO_3^{2-}) with its three O atoms binding to three different surface Ti-5c atoms. However, no stable tridentate structure could be found for the clean anatase (101) surface nor the clean rutile (110) surface. On both surfaces, the rows of Ti-5c atoms are separated by rows of projecting O-2c atoms. Thus the third coordinatively unsaturated Ti is too far away and sterically hindered.[13] This is in agreement with Ojamae et al.

The matter of protonation of bridging, coordinatively-unsaturated O atoms at the surface of TiO_2 is not a trivial matter. As Luschtinetz et al. discuss further, O-vacancy defects are always present on natural TiO_2 surfaces. Water molecules dissociate at this sites to form bridging hydroxyl groups, filling the void. They propose that these specific sites could react with a phosphonic acid in a condensation mechanism, which extends the possibilities of surfacing binding/adsorption structures enormously – such that tridentate binding at TiO_2 could be stable.[13]

Bredas and coworkers report a theoretical and experimental study of phosphonate binding to tin-doped indium oxide (ITO). Unlike the other theoretical investigations, their geometry optimization were performed by generating a large number of intial geometries sampling the under-coordinated metal sites and surface hydroxyl groups which are expected to participate in binding. Optimizations were then performed for each initial configuration, allowing elimination of up to two water molecules to accompany phosphonic acid chemisorption. Stable geometries for bidentate and tridentate adsorption modes were obtained.[12]

In corroboration with the calculations of Bredas et al., n-octylphosphonic acid was loaded on ITO surfaces from ethanol followed by heating at 140 °C for 48 hours. Based on

XPS measurements and calculated binding energies, there was no hydrogen bonding or P-OH groups present on the surface.[12] The most prevalent surface modification procedures used in the literature involve some sort of heat treatment, either during or after the loading of the phosphonic acid substrate. By a number of reports, even with the heat treatment, residual P-OH groups exist. There is evidence that without the heat treatment, the tridentate mode does not form to a significant extent due to unfavorable geometric matching with coordinatively unsaturated metal sites. This means that a larger number of P-OH groups should persist. However, this does assume that bonds to bridging O atoms at the surface are not possible sites for covalent attachment.

The results presented herein establish that surface binding constants are higher than those measured for carboxylic acid-derivatized $[Ru(bpy)_3]^{2+}$ ($\sim 10^5$ M^{-1}) by more than an order of magnitude.[16,27,28] This is not surprising given the high affinity of the phosphonate groups to metal oxide surfaces, the rapid binding kinetics, and high stability in acidic aqueous conditions. Carboxylic acids are limited to organic solvents and can easily be exchanged with functionalized molecules in solution due to their weaker interaction and more dynamic surface equilibrium.[27]

A surprising result from the spectrophotometric pH titrations is the highly coupled nature of the pK_as. The separation between the first two pK_as and the separation between the third and fourth pK_as is indicative of this electronic effect. These two sets of pK_as are presumably from the first proton loss from the phosphonate groups, in two separate events due to electronic coupling, in the first pair, and likewise, proton loss associated with the second proton on the same phosphonate groups in the latter pair of pK_as. From previous pH titrations of two different ruthenium complexes dissolved in solution and bearing a single

4,4'-$(H_2O_3P)_2$-bpy ligand, the first pKa was ~1-2 and the second pKa is ~5-6.[29,30] These values are consistent with those of Table 2, despite the coarseness of their titrations. The level of precision in our data has allowed us to resolve the individual acid-base events. In an uncoupled system, the first proton from all phosphonate substituents would dissociate simultaneously, as was previously thought.

The last pK_a, measured in several of the complexes, around 10 or higher, appears to be a function of the high pH and possible decomposition of the complex in high concentrations of hydroxide. We have observed ligand substitution in complexes bearing the 4,4'-phosphonate-derivatized bipyridines, often in the form of ligand scrambling during synthetic procedures in the presence of a better ligand. This pK_a is in the typical range observed for Ru^{II}-OH_2/OH acid-base equilibria found for ruthenium polypyridyl aqua complexes,[17,24] indicating the decomposition product may have a coordinate aqua ligand following ligand substitution. More experiments are needed in order to characterize this species and the mechanism by which it forms.

A pH dependence on surface adsorbed complexes caused by the phosphonic acid groups is observed in the systematic increase in the $E_{1/2}$-pH diagram slopes of the series, $[Ru(4,4'\text{-}(H_2O_3PCH_2)_2\text{-}bpy)_n(bpy)_{3-n}]^{2+}$. However, slopes that could be deciphered in terms of proton content were not observed, based on expected Nernstian behavior. As shown by the high dependence on the ionic strength and the nature of the electrolyte, drawing too many conclusions from this data would be inappropriate until these effects are understood in more detail.

Significant differences in the acid-base properties of molecules have been observed when in solution or surface confined monolayers.[31] Field effects and solvation dynamics at

surfaces may be the cause of these observations. The protonation state of the surface may also have a significant influence on the acidity of the surface bound species. A number of groups have reported on the pH dependence of adsorbates at electrode surfaces using a variety of techniques.[31-36] There appears to be a significant interplay between the pH dependence of the molecule and the pH dependence of the surface itself.

Ion-pairing and solvation dynamics in the double layer of electrode materials will be strongly dependent on the nature and concentration of the supporting electrolyte in electrochemical experiments. The double layer will dependent heavily on the surface charge which is manifest in the protonation state of surface sites and the isoelectric point of the material in aqueous solutions. Furthermore, metal oxide band edges and the density of states in electrode materials can be tuned with the solution pH.[32,37] Kinetics of interfacial electron transfer for an array of redox active molecules have been studied in order to probe the importance of overlap between molecular energy levels and those of the electrode.[38] This effect may explain the subtle increase in $E_{1/2}$ of $[Os(phen)_3]^{2+}$ as a function of pH at ITO.

It can be assumed based on the solution titrations and the systematic change in slopes with increasing phosphonate groups that deprotonation of the more substituted $[Ru(bpy)_3]^{2+}$ complexes will produce an anionically charged molecule. For example, $[Ru(4,4'\text{-}(H_2O_3PCH_2)_2\text{-}bpy)_3]^{2+}$ will have dangling phosphonic acid groups based on the geometric impossible at a planar surface for all groups to bind. The deprotonation can be exploited in the synthesis of redox mediator/chromophore-catalysts assemblies via ion-pairing. The effect was readily observed at pH 5 by soaking the surface modified ITO slides with a cationic catalyst. Electrochemical behavior expected of a Nernstian adsorbate was obtained for the ion-paired catalyst.

Ion-pairing is supported by the lack of similar effects at low pH (< 2) where the phosphonic acid groups are still largely protonated, and the surface-bound redox mediator should be neutral or cationic. Distinguishing between ion pairing and precipitation is also demonstrated in “knocking off” the microprecipitate observed in loading surface mediators in 0.1 M $HClO_4$. Placing the slide in fresh solution resulted in complete removable of the second layer, as the equilibrium will favor loss to solution where the solution is free of complex.

Kinetic effects are seen in the ion-pairing experiments that we speculate can be changed by conditioning the electrode in holding the potential reductively for a short period of time. The Ru(III/II) wave had slow kinetics prior to the reductive electrolysis where the ion-paired catalyst presumably was able to rearrange to be in closer proximity to the electrode surface or form a better pairing interaction with the surface mediator. We have seen effects of this nature in which waves were not visible at all in the cyclic voltammetry prior to a reductive conditioning (electrolysis) of the electrode. Similar electrochemical results have been reported in which redox active molecules were incorporated into charged polymer films.[39,40]

Additional studies are needed to fully characterize these assemblies and to investigate further the decomposition product that grows from the surface-adsorbed redox mediator. Based on the preliminary results shown here, this appears to be an attractive route toward synthesizing chromophore/redox mediator-catalyst assemblies at metal oxide surfaces for potential application in light-driven catalysis. At the least, the stable ion-pairing interaction makes these systems useful for electrocatalysis.

Measurements are currently underway to translate the spectrophotometric pH titrations described above to high surface area metal oxides which can be monitored spectrophotometrically as a function of pH. This will potentially enable us to directly determine pK_a values of surface adsorbed phosphonate groups, revealing the number of titratable protons, and providing new insight into the surface binding interaction.

REFERENCES

(1) Lewis, N. S.; Nocera, D. G. *Proc. Nat. Acad. Sci.* **2006**, *103*, 15729.

(2) Meyer, T. J. *Acc. Chem. Res.* **1989**, *22*, 163.

(3) Alstrum-Acevedo, J. H.; Brennaman, M. K.; Meyer, T. J. *Inorganic Chemistry* **2005**, *44*, 6802.

(4) Concepcion, J. J.; Jurss, J. W.; Templeton, J. L.; Meyer, T. J. *Proceedings of the National Academy of Sciences of the United States of America* **2008**, *105*, 17632.

(5) Jurss, J. W.; Concepcion, J. C.; Norris, M. R.; Templeton, J. L.; Meyer, T. J. *Inorganic Chemistry* **2010**, *49*, 3980.

(6) Anderson, P. A.; Deacon, G. B.; Haarmann, K. H.; Keene, F. R.; Meyer, T. J.; Reitsma, D. A.; Skelton, B. W.; Strouse, G. F.; Thomas, N. C.; Treadway, J. A.; White, A. H. *Inorganic Chemistry* **1995**, *34*, 6145.

(7) Concepcion, J. J.; Jurss, J. W.; Hoertz, P. G.; Meyer, T. J. *Angewandte Chemie-International Edition* **2009**, *48*, 9473.

(8) Chen, Z. F.; Concepcion, J. J.; Jurss, J. W.; Meyer, T. J. *Journal of the American Chemical Society* **2009**, *131*, 15580.

(9) Gillaizeau-Gauthier, I.; Odobel, F.; Alebbi, M.; Argazzi, R.; Costa, E.; Bignozzi, C. A.; Qu, P.; Meyer, G. J. *Inorganic Chemistry* **2001**, *40*, 6073.

(10) She, C. X.; Guo, J. C.; Irle, S.; Morokuma, K.; Mohler, D. L.; Zabri, H.; Odobel, F.; Youm, K. T.; Liu, F.; Hupp, J. T.; Lian, T. *Journal of Physical Chemistry A* **2007**, *111*, 6832.

(11) Jakubikova, E.; Snoeberger, R. C.; Batista, V. S.; Martin, R. L.; Batista, E. R. *Journal of Physical Chemistry A* **2009**, *113*, 12532.

(12) Paramonov, P. B.; Paniagua, S. A.; Hotchkiss, P. J.; Jones, S. C.; Armstrong, N. R.; Marder, S. R.; Bredas, J. L. *Chemistry of Materials* **2008**, *20*, 5131.

(13) Luschtinetz, R.; Frenzel, J.; Milek, T.; Seifert, G. *Journal of Physical Chemistry C* **2009**, *113*, 5730.

(14) Monnereau, C.; Gomez, J.; Blart, E.; Odobel, F. *Inorganic Chemistry* **2005**, *44*, 4806.

(15) Freedman, D. A.; Evju, J. K.; Pomije, M. K.; Mann, K. R. *Inorganic Chemistry* **2001**, *40*, 5711.

(16) Meyer, T. J.; Meyer, G. J.; Pfennig, B. W.; Schoonover, J. R.; Timpson, C. J.; Wall, J. F.; Kobusch, C.; Chen, X. H.; Peek, B. M.; Wall, C. G.; Ou, W.; Erickson, B. W.; Bignozzi, C. A. *Inorganic Chemistry* **1994**, *33*, 3952.

(17) Liu, F.; Concepcion, J. J.; Jurss, J. W.; Cardolaccia, T.; Templeton, J. L.; Meyer, T. J. *Inorganic Chemistry* **2008**, *47*, 1727.

(18) Sun, J. K.; Velamakanni, B. V.; Gerberich, W. W.; Francis, L. F. *Journal of Colloid and Interface Science* **2004**, *280*, 387.

(19) Forster, R. J.; Pellegrin, Y.; Keyes, T. E. *Electrochemistry Communications* **2007**, *9*, 1899.

(20) Binstead, R. A.; Jung, B.; Zuberbuhler, A. D.; Version 3.0.40 for 32-bit Windows systems ed.; Spectrum Software Associates, Marlborough, MA, U.S.A.: 2007; Vol. SPECFIT/32 Global Analysis System.

(21) Sigel, H.; Zuberbuhler, A. D.; Yamauchi, O. *Analytica Chimica Acta* **1991**, *255*, 63.

(22) Connor, P. A.; Dobson, K. D.; McQuillan, A. J. *Langmuir* **1999**, *15*, 2402.

(23) Park, H.; Bae, E.; Lee, J. J.; Park, J.; Choi, W. *Journal of Physical Chemistry B* **2006**, *110*, 8740.

(24) Concepcion, J. J.; Jurss, J. W.; Norris, M. R.; Chen, Z. F.; Templeton, J. L.; Meyer, T. J. *Inorganic Chemistry* **2010**, *49*, 1277.

(25) Bard, A. J.; Faulkner, L. R. *Electrochemical Methods: Fundamentals and Applications*; Second Edition ed.; John Wiley & Sons, Inc., 2001.

(26) Nilsing, M.; Lunell, S.; Persson, P.; Ojamae, L. *Surface Science* **2005**, *582*, 49.

(27) Trammell, S. A.; Meyer, T. J. *Langmuir* **2003**, *19*, 6081.

(28) Trammell, S. A.; Meyer, T. J. *Journal of Physical Chemistry B* **1999**, *103*, 104.

(29) Montalti, M.; Wadhwa, S.; Kim, W. Y.; Kipp, R. A.; Schmehl, R. H. *Inorganic Chemistry* **2000**, *39*, 76.

(30) Zabri, H.; Gillaizeau, I.; Bignozzi, C. A.; Caramori, S.; Charlot, M. F.; Cano-Boquera, J.; Odobel, F. *Inorganic Chemistry* **2003**, *42*, 6655.

(31) Burgess, I.; Seivewright, B.; Lennox, R. B. *Langmuir* **2006**, *22*, 4420.

(32) Qu, P.; Meyer, G. J. *Langmuir* **2001**, *17*, 6720.

(33) vanderVegte, E. W.; Hadziioannou, G. *Journal of Physical Chemistry B* **1997**, *101*, 9563.

(34) Zaban, A.; Ferrere, S.; Sprague, J.; Gregg, B. A. *Journal of Physical Chemistry B* **1997**, *101*, 55.

(35) Zaban, A.; Ferrere, S.; Gregg, B. A. *Journal of Physical Chemistry B* **1998**, *102*, 452.

(36) Yan, S. G.; Hupp, J. T. *Journal of Physical Chemistry* **1996**, *100*, 6867.

(37) Gerischer, H. *Electrochimica Acta* **1989**, *34*, 1005.

(38) Ho, S. I.; Rajeshwar, K. *Journal of the Electrochemical Society* **1987**, *134*, 2491.

(39) Shigehara, K.; Oyama, N.; Anson, F. C. *Journal of the American Chemical Society* **1981**, *103*, 2552.

(40) Martin, C. R.; Rubinstein, I.; Bard, A. J. *Journal of the American Chemical Society* **1982**, *104*, 4817.

APPENDIX A

Electronic Structure of the Water Oxidation Catalyst, *cis,cis*-$[(bpy)_2(H_2O)RuORu(OH_2)(bpy)_2]^{4+}$, The Blue Dimer

Table of Contents

Table 1. Atomic coordinates and equivalent isotropic atomic displacement parameters ($Å^2$) for $[(bpy)_2ClRu^{IV}ORu^{III}Cl(bpy)_2](Ce(NO_3)_6)•H_2O$.

U(eq) is defined as one third of the trace of the orthogonalized U_{ij} tensor.

	x/a	y/b	z/c	U(eq)
Ru1	0.411119(16)	0.221135(14)	0.20467(2)	0.02910(12)
Cl1	0.41118(6)	0.16648(5)	0.08571(8)	0.0427(2)
O1	0.5	0.2134(2)	0.25	0.0338(10)
N2	0.3849(2)	0.15033(18)	0.2611(2)	0.0366(9)
C3	0.4279(2)	0.1142(2)	0.3074(4)	0.0471(13)
C4	0.4068(2)	0.0682(2)	0.3439(5)	0.063(2)
C5	0.3402(4)	0.0587(2)	0.3325(5)	0.068(2)
C6	0.2957(2)	0.0949(2)	0.2829(4)	0.0536(15)
C7	0.3188(2)	0.1407(2)	0.2482(2)	0.0387(11)
C8	0.2761(2)	0.1823(2)	0.1965(2)	0.0369(11)
C9	0.2080(2)	0.1804(2)	0.1783(2)	0.0426(11)
C10	0.1725(2)	0.2218(2)	0.1271(4)	0.0454(13)
C11	0.2052(2)	0.2630(2)	0.0942(2)	0.0434(11)
C12	0.2737(2)	0.2630(2)	0.1153(2)	0.0361(11)
N13	0.3084(2)	0.22370(17)	0.1660(2)	0.0317(9)
N14	0.4019(2)	0.27559(17)	0.2985(2)	0.0323(9)
C15	0.3924(2)	0.2606(2)	0.3734(2)	0.0383(11)
C16	0.3883(2)	0.2995(2)	0.4339(2)	0.0441(13)
C17	0.3927(2)	0.3551(2)	0.4164(2)	0.0457(13)
C18	0.4016(2)	0.3712(2)	0.3382(2)	0.0402(11)
C19	0.4063(2)	0.3307(2)	0.2800(2)	0.0340(10)
C20	0.4178(2)	0.3428(2)	0.1963(2)	0.0323(10)
C21	0.4227(2)	0.3961(2)	0.1662(2)	0.0376(11)
C22	0.4342(2)	0.4025(2)	0.0869(2)	0.0401(11)
C23	0.4412(2)	0.3561(2)	0.0406(2)	0.0382(11)
C24	0.4367(2)	0.3037(2)	0.0734(2)	0.0340(10)
N25	0.42452(18)	0.29679(16)	0.1498(2)	0.0288(8)
Ce1	0.0	0.087772(15)	0.25	0.03096(13)
O31	0.0405(2)	0.07091(16)	0.1137(2)	0.0472(9)
N32	0.0516(2)	0.0191(2)	0.1227(2)	0.0446(11)
O33	0.0434(2)	0.99775(14)	0.1916(2)	0.0409(8)
O34	0.0695(2)	0.9909(2)	0.0709(2)	0.0679(14)
O35	0.1298(2)	0.08564(16)	0.2802(2)	0.0488(10)
N36	0.1386(2)	0.0504(2)	0.3401(4)	0.0550(14)

	x/a	y/b	z/c	U(eq)
O37	0.0889(2)	0.03670(16)	0.3660(2)	0.0457(9)
O38	0.1936(2)	0.0310(2)	0.3699(5)	0.102(2)
O39	0.05224(17)	0.15909(14)	0.3716(2)	0.0393(8)
N40	0.0022(2)	0.19048(18)	0.3608(2)	0.0369(9)
O41	0.95217(17)	0.17715(14)	0.3028(2)	0.0407(8)
O42	0.0003(2)	0.23173(17)	0.4048(2)	0.0478(9)
N51	0.2300(5)	0.2789(7)	0.3249(10)	0.239(7)
C52	0.1762(7)	0.2787(5)	0.3232(9)	0.235(7)
C53	0.1106(5)	0.2911(9)	0.3057(11)	0.235(7)
N54	0.2601(4)	0.3749(2)	0.0088(5)	0.100(2)
C55	0.2692(5)	0.4161(4)	0.9825(7)	0.098(2)
C56	0.2934(5)	0.4590(4)	0.9444(7)	0.110(3)
N57	0.5851(13)	0.0177(8)	0.4932(13)	0.291(9)
C58	0.5940(9)	0.0091(9)	0.4301(14)	0.284(9)
C59	0.5860(15)	0.9958(9)	0.3477(14)	0.281(9)
N60	0.3596(10)	0.1596(7)	0.4881(13)	0.286(12)
C61	0.3057(10)	0.1564(5)	0.4848(15)	0.285(12)
C62	0.2448(10)	0.1375(9)	0.4884(14)	0.289(12)
N63	0.2595(10)	0.9043(7)	0.3070(11)	0.239(7)
C64	0.2660(11)	0.9245(5)	0.2484(13)	0.241(7)
C65	0.2772(11)	0.9340(9)	0.1711(13)	0.248(7)
N66	0.5122(18)	0.8591(13)	0.426(2)	0.410(18)
C67	0.4652(18)	0.8830(15)	0.4064(17)	0.411(18)
C68	0.4160(17)	0.9211(13)	0.403(2)	0.414(18)

Table 2. Bond lengths (Å) for $[(bpy)_2ClRu^{IV}ORu^{III}Cl(bpy)_2](Ce(NO_3)_6)\cdot H_2O$.

Ru1-O1	1.8365(5)	Ru1-N14	2.063(4)
Ru1-N2	2.070(4)	Ru1-N25	2.074(4)
Ru1-N13	2.087(4)	Ru1-Cl1	2.3536(13)
O1-Ru1#2	1.8365(5)	N2-C3	1.347(7)
N2-C7	1.363(7)	C3-C4	1.376(9)
C4-C5	1.375(10)	C5-C6	1.387(9)
C6-C7	1.375(8)	C7-C8	1.468(8)
C8-N13	1.361(7)	C8-C9	1.380(7)
C9-C10	1.397(8)	C10-C11	1.381(8)
C11-C12	1.387(7)	C12-N13	1.349(6)

N14-C15	1.341(7)	N14-C19	1.365(6)
C15-C16	1.380(8)	C16-C17	1.371(8)
C17-C18	1.396(8)	C18-C19	1.381(8)
C19-C20	1.479(7)	C20-N25	1.368(6)
C20-C21	1.383(7)	C21-C22	1.389(8)
C22-C23	1.375(8)	C23-C24	1.379(7)
C24-N25	1.348(6)	Ce1-O41#1	2.598(4)
Ce1-O41	2.598(4)	Ce1-O31	2.605(4)
Ce1-O31#1	2.605(4)	Ce1-O33	2.609(4)
Ce1-O33#1	2.609(4)	Ce1-O37#1	2.628(4)
Ce1-O37	2.628(4)	Ce1-O35#1	2.634(4)
Ce1-O35	2.634(4)	Ce1-O39	2.661(4)
Ce1-O39#1	2.661(4)	O31-N32	1.267(6)
N32-O34	1.212(6)	N32-O33	1.289(6)
O35-N36	1.277(6)	N36-O38	1.226(7)
N36-O37	1.253(6)	O39-N40	1.264(6)
N40-O42	1.231(6)	N40-O41	1.278(6)
N51-C52	1.114(9)	C52-C53	1.363(10)
N54-C55	1.113(9)	C55-C56	1.361(10)
N57-C58	1.114(9)	C58-C59	1.363(10)
N60-C61	1.114(9)	C61-C62	1.363(10)
N63-C64	1.115(9)	C64-C65	1.362(10)
N66-C67	1.115(9)	C67-C68	1.364(10)

Symmetry transformations used to generate equivalent atoms:

#1 -x, y, -z+1/2

#2 -x+1, y, -z+1/2

Table 3. Bond angles (°) for $[(bpy)_2ClRu^{IV}ORu^{III}Cl(bpy)_2](Ce(NO_3)_6)\cdot H_2O$.

O1-Ru1-N14	91.32(14)	O1-Ru1-N2	94.78(17)
N14-Ru1-N2	95.96(17)	O1-Ru1-N25	92.20(16)
N14-Ru1-N25	79.41(16)	N2-Ru1-N25	171.72(16)
O1-Ru1-N13	172.65(14)	N14-Ru1-N13	86.56(16)
N2-Ru1-N13	78.47(16)	N25-Ru1-N13	94.32(15)
O1-Ru1-Cl1	94.77(9)	N14-Ru1-Cl1	172.38(11)
N2-Ru1-Cl1	88.10(13)	N25-Ru1-Cl1	95.76(12)
N13-Ru1-Cl1	87.95(12)	Ru1#2-O1-Ru1	168.4(3)

C3-N2-C7	119.5(5)	C3-N2-Ru1	124.8(4)
C7-N2-Ru1	115.7(3)	N2-C3-C4	121.6(6)
C5-C4-C3	119.2(6)	C4-C5-C6	119.4(6)
C7-C6-C5	119.5(6)	N2-C7-C6	120.7(5)
N2-C7-C8	115.4(4)	C6-C7-C8	123.9(5)
N13-C8-C9	121.0(5)	N13-C8-C7	115.1(4)
C9-C8-C7	123.8(5)	C8-C9-C10	118.7(5)
C11-C10-C9	120.2(5)	C10-C11-C12	118.5(5)
N13-C12-C11	121.7(5)	C12-N13-C8	119.9(4)
C12-N13-Ru1	124.8(3)	C8-N13-Ru1	115.3(3)
C15-N14-C19	119.7(4)	C15-N14-Ru1	125.2(4)
C19-N14-Ru1	115.1(3)	N14-C15-C16	121.8(5)
C17-C16-C15	119.3(5)	C16-C17-C18	119.3(5)
C19-C18-C17	119.3(5)	N14-C19-C18	120.5(5)
N14-C19-C20	115.5(4)	C18-C19-C20	124.0(5)
N25-C20-C21	121.4(5)	N25-C20-C19	114.9(4)
C21-C20-C19	123.7(5)	C20-C21-C22	118.8(5)
C23-C22-C21	119.6(5)	C22-C23-C24	119.7(5)
N25-C24-C23	121.5(5)	C24-N25-C20	119.1(4)
C24-N25-Ru1	125.9(3)	C20-N25-Ru1	114.9(3)
O41#1-Ce1-O41	68.77(17)	O41#1-Ce1-O31	67.27(12)
O41-Ce1-O31	129.99(12)	O41#1-Ce1-O31#1	129.99(12)
O41-Ce1-O31#1	67.27(12)	O31-Ce1-O31#1	162.14(17)
O41#1-Ce1-O33	111.51(12)	O41-Ce1-O33	177.48(11)
O31-Ce1-O33	49.06(11)	O31#1-Ce1-O33	113.47(12)
O41#1-Ce1-O33#1	177.48(11)	O41-Ce1-O33#1	111.51(12)
O31-Ce1-O33#1	113.47(12)	O31#1-Ce1-O33#1	49.06(11)
O33-Ce1-O33#1	68.33(16)	O41#1-Ce1-O37#1	113.77(12)
O41-Ce1-O37#1	111.48(11)	O31-Ce1-O37#1	67.65(13)
O31#1-Ce1-O37#1	103.62(12)	O33-Ce1-O37#1	66.05(12)
O33#1-Ce1-O37#1	68.57(12)	O41#1-Ce1-O37	111.48(11)
O41-Ce1-O37	113.77(12)	O31-Ce1-O37	103.62(12)
O31#1-Ce1-O37	67.65(13)	O33-Ce1-O37	68.57(12)
O33#1-Ce1-O37	66.05(12)	O37#1-Ce1-O37	124.44(17)
O41#1-Ce1-O35#1	114.27(12)	O41-Ce1-O35#1	67.74(11)
O31-Ce1-O35#1	111.18(13)	O31#1-Ce1-O35#1	68.45(14)
O33-Ce1-O35#1	110.13(12)	O33#1-Ce1-O35#1	67.89(13)
O37#1-Ce1-O35#1	48.42(12)	O37-Ce1-O35#1	130.21(13)

O41#1-Ce1-O35	67.74(11)	O41-Ce1-O35	114.27(12)
O31-Ce1-O35	68.45(14)	O31#1-Ce1-O35	111.18(13)
O33-Ce1-O35	67.89(13)	O33#1-Ce1-O35	110.13(12)
O37#1-Ce1-O35	130.21(13)	O37-Ce1-O35	48.42(12)
O35#1-Ce1-O35	177.77(17)	O41#1-Ce1-O39	66.35(11)
O41-Ce1-O39	48.72(11)	O31-Ce1-O39	125.98(13)
O31#1-Ce1-O39	67.18(11)	O33-Ce1-O39	133.78(12)
O33#1-Ce1-O39	111.83(11)	O37#1-Ce1-O39	159.80(11)
O37-Ce1-O39	70.17(12)	O35#1-Ce1-O39	112.02(11)
O35-Ce1-O39	69.52(13)	O41#1-Ce1-O39#1	48.72(11)
O41-Ce1-O39#1	66.35(11)	O31-Ce1-O39#1	67.18(11)
O31#1-Ce1-O39#1	125.98(13)	O33-Ce1-O39#1	111.83(11)
O33#1-Ce1-O39#1	133.78(12)	O37#1-Ce1-O39#1	70.17(12)
O37-Ce1-O39#1	159.80(11)	O35#1-Ce1-O39#1	69.52(13)
O35-Ce1-O39#1	112.02(11)	O39-Ce1-O39#1	100.00(15)
N32-O31-Ce1	98.0(3)	O34-N32-O31	122.8(5)
O34-N32-O33	121.5(5)	O31-N32-O33	115.7(4)
N32-O33-Ce1	97.1(3)	N36-O35-Ce1	96.5(3)
O38-N36-O37	122.3(5)	O38-N36-O35	120.7(5)
O37-N36-O35	117.0(5)	N36-O37-Ce1	97.5(3)
N40-O39-Ce1	95.7(3)	O42-N40-O39	122.4(4)
O42-N40-O41	120.3(4)	O39-N40-O41	117.2(4)
N40-O41-Ce1	98.4(3)	N51-C52-C53	163.5(12)
N54-C55-C56	164.8(12)	N57-C58-C59	163.6(12)
N60-C61-C62	163.7(12)	N63-C64-C65	163.7(12)
N66-C67-C68	163.1(16)		

Symmetry transformations used to generate equivalent atoms:

#1 -x, y, -z+1/2

#2 -x+1, y, -z+1/2

Table 4. Torsion angles (°) for $[(bpy)_2ClRu^{IV}ORu^{III}Cl(bpy)_2](Ce(NO_3)_6)\cdot H_2O$.

N14-Ru1-O1-Ru1#2	-50.65(11)	N2-Ru1-O1-Ru1#2	-146.74(13)
N25-Ru1-O1-Ru1#2	28.80(11)	N13-Ru1-O1-Ru1#2	-123.7(13)
Cl1-Ru1-O1-Ru1#2	124.77(4)	O1-Ru1-N2-C3	-4.7(5)
N14-Ru1-N2-C3	-96.5(5)	N25-Ru1-N2-C3	-152.1(10)
N13-Ru1-N2-C3	178.2(5)	Cl1-Ru1-N2-C3	89.9(5)
O1-Ru1-N2-C7	176.1(4)	N14-Ru1-N2-C7	84.3(4)

N25-Ru1-N2-C7	28.7(13)	N13-Ru1-N2-C7	-1.0(4)
Cl1-Ru1-N2-C7	-89.3(4)	C7-N2-C3-C4	-1.6(10)
Ru1-N2-C3-C4	179.2(5)	N2-C3-C4-C5	0.4(12)
C3-C4-C5-C6	1.5(13)	C4-C5-C6-C7	-2.2(12)
C3-N2-C7-C6	0.9(9)	Ru1-N2-C7-C6	-179.9(5)
C3-N2-C7-C8	-179.6(5)	Ru1-N2-C7-C8	-0.4(6)
C5-C6-C7-N2	1.0(10)	C5-C6-C7-C8	-178.5(7)
N2-C7-C8-N13	2.3(7)	C6-C7-C8-N13	-178.2(6)
N2-C7-C8-C9	-178.3(5)	C6-C7-C8-C9	1.1(9)
N13-C8-C9-C10	0.5(8)	C7-C8-C9-C10	-178.8(5)
C8-C9-C10-C11	1.4(9)	C9-C10-C11-C12	-2.0(9)
C10-C11-C12-N13	0.8(9)	C11-C12-N13-C8	1.0(8)
C11-C12-N13-Ru1	-178.1(4)	C9-C8-N13-C12	-1.6(8)
C7-C8-N13-C12	177.7(5)	C9-C8-N13-Ru1	177.5(4)
C7-C8-N13-Ru1	-3.1(6)	O1-Ru1-N13-C12	157.9(12)
N14-Ru1-N13-C12	84.5(4)	N2-Ru1-N13-C12	-178.7(4)
N25-Ru1-N13-C12	5.5(4)	Cl1-Ru1-N13-C12	-90.2(4)
O1-Ru1-N13-C8	-21.2(15)	N14-Ru1-N13-C8	-94.5(4)
N2-Ru1-N13-C8	2.3(4)	N25-Ru1-N13-C8	-173.6(4)
Cl1-Ru1-N13-C8	90.7(4)	O1-Ru1-N14-C15	-85.8(4)
N2-Ru1-N14-C15	9.1(4)	N25-Ru1-N14-C15	-177.8(4)
N13-Ru1-N14-C15	87.1(4)	Cl1-Ru1-N14-C15	131.1(8)
O1-Ru1-N14-C19	94.1(3)	N2-Ru1-N14-C19	-171.0(3)
N25-Ru1-N14-C19	2.1(3)	N13-Ru1-N14-C19	-93.0(3)
Cl1-Ru1-N14-C19	-49.0(11)	C19-N14-C15-C16	-1.5(7)
Ru1-N14-C15-C16	178.4(4)	N14-C15-C16-C17	1.4(8)
C15-C16-C17-C18	-0.4(9)	C16-C17-C18-C19	-0.4(8)
C15-N14-C19-C18	0.6(7)	Ru1-N14-C19-C18	-179.2(4)
C15-N14-C19-C20	179.1(4)	Ru1-N14-C19-C20	-0.8(5)
C17-C18-C19-N14	0.3(8)	C17-C18-C19-C20	-178.1(5)
N14-C19-C20-N25	-1.9(6)	C18-C19-C20-N25	176.5(4)
N14-C19-C20-C21	179.0(4)	C18-C19-C20-C21	-2.6(8)
N25-C20-C21-C22	0.3(7)	C19-C20-C21-C22	179.3(5)
C20-C21-C22-C23	-0.5(8)	C21-C22-C23-C24	-0.2(8)
C22-C23-C24-N25	1.1(8)	C23-C24-N25-C20	-1.3(7)
C23-C24-N25-Ru1	176.3(4)	C21-C20-N25-C24	0.6(7)
C19-C20-N25-C24	-178.5(4)	C21-C20-N25-Ru1	-177.3(4)
C19-C20-N25-Ru1	3.6(5)	O1-Ru1-N25-C24	88.2(4)

N14-Ru1-N25-C24	179.2(4)	N2-Ru1-N25-C24	-124.3(11)
N13-Ru1-N25-C24	-95.2(4)	Cl1-Ru1-N25-C24	-6.8(4)
O1-Ru1-N25-C20	-94.1(3)	N14-Ru1-N25-C20	-3.1(3)
N2-Ru1-N25-C20	53.4(12)	N13-Ru1-N25-C20	82.5(3)
Cl1-Ru1-N25-C20	170.9(3)	O41#1-Ce1-O31-N32	155.1(4)
O41-Ce1-O31-N32	-174.6(3)	O31#1-Ce1-O31-N32	-11.2(3)
O33-Ce1-O31-N32	2.3(3)	O33#1-Ce1-O31-N32	-22.2(4)
O37#1-Ce1-O31-N32	-74.7(3)	O37-Ce1-O31-N32	47.3(4)
O35#1-Ce1-O31-N32	-96.5(3)	O35-Ce1-O31-N32	81.2(3)
O39-Ce1-O31-N32	122.5(3)	O39#1-Ce1-O31-N32	-151.7(4)
Ce1-O31-N32-O34	176.9(5)	Ce1-O31-N32-O33	-3.9(5)
O34-N32-O33-Ce1	-176.9(5)	O31-N32-O33-Ce1	3.9(5)
O41#1-Ce1-O33-N32	-29.2(3)	O41-Ce1-O33-N32	67.(3)
O31-Ce1-O33-N32	-2.3(3)	O31#1-Ce1-O33-N32	173.2(3)
O33#1-Ce1-O33-N32	153.5(4)	O37#1-Ce1-O33-N32	78.2(3)
O37-Ce1-O33-N32	-134.8(3)	O35#1-Ce1-O33-N32	98.7(3)
O35-Ce1-O33-N32	-82.4(3)	O39-Ce1-O33-N32	-106.5(3)
O39#1-Ce1-O33-N32	23.5(3)	O41#1-Ce1-O35-N36	157.5(4)
O41-Ce1-O35-N36	105.3(4)	O31-Ce1-O35-N36	-129.2(4)
O31#1-Ce1-O35-N36	31.6(4)	O33-Ce1-O35-N36	-76.1(4)
O33#1-Ce1-O35-N36	-21.1(4)	O37#1-Ce1-O35-N36	-99.6(4)
O37-Ce1-O35-N36	4.3(3)	O35#1-Ce1-O35-N36	-48.4(4)
O39-Ce1-O35-N36	85.5(4)	O39#1-Ce1-O35-N36	178.3(4)
Ce1-O35-N36-O38	172.1(7)	Ce1-O35-N36-O37	-7.6(6)
O38-N36-O37-Ce1	-172.0(7)	O35-N36-O37-Ce1	7.6(6)
O41#1-Ce1-O37-N36	-31.1(4)	O41-Ce1-O37-N36	-106.5(4)
O31-Ce1-O37-N36	39.5(4)	O31#1-Ce1-O37-N36	-156.9(4)
O33-Ce1-O37-N36	74.5(4)	O33#1-Ce1-O37-N36	149.5(4)
O37#1-Ce1-O37-N36	111.6(4)	O35#1-Ce1-O37-N36	173.3(3)
O35-Ce1-O37-N36	-4.4(3)	O39-Ce1-O37-N36	-84.2(4)
O39#1-Ce1-O37-N36	-20.6(6)	O41#1-Ce1-O39-N40	81.8(3)
O41-Ce1-O39-N40	-0.1(2)	O31-Ce1-O39-N40	114.7(3)
O31#1-Ce1-O39-N40	-79.2(3)	O33-Ce1-O39-N40	179.5(2)
O33#1-Ce1-O39-N40	-100.1(3)	O37#1-Ce1-O39-N40	-13.0(5)
O37-Ce1-O39-N40	-152.5(3)	O35#1-Ce1-O39-N40	-26.1(3)
O35-Ce1-O39-N40	155.7(3)	O39#1-Ce1-O39-N40	45.8(2)
Ce1-O39-N40-O42	178.7(4)	Ce1-O39-N40-O41	0.1(4)
O42-N40-O41-Ce1	-178.7(4)	O39-N40-O41-Ce1	-0.1(4)

O41#1-Ce1-O41-N40	-76.5(3)	O31-Ce1-O41-N40	-106.4(3)
O31#1-Ce1-O41-N40	79.0(3)	O33-Ce1-O41-N40	-173.(2)
O33#1-Ce1-O41-N40	100.8(3)	O37#1-Ce1-O41-N40	175.3(3)
O37-Ce1-O41-N40	28.4(3)	O35#1-Ce1-O41-N40	154.0(3)
O35-Ce1-O41-N40	-24.9(3)	O39-Ce1-O41-N40	0.1(2)
O39#1-Ce1-O41-N40	-129.5(3)		

Symmetry transformations used to generate equivalent atoms:

#1 -x, y, -z+1/2

#2 -x+1, y, -z+1/2

Table 5. Anisotropic atomic displacement parameters ($Å^2$) for $[(bpy)_2ClRu^{IV}ORu^{III}Cl(bpy)_2](Ce(NO_3)_6)\bullet H_2O$.

The anisotropic atomic displacement factor exponent takes the form: $-2\pi^2[h^2 a^{*2} U_{11} + ... + 2 h k a^* b^* U_{12}]$

	U_{11}	U_{22}	U_{33}	U_{23}	U_{13}	U_{12}
Ru1	0.0226(2)	0.0331(2)	0.0285(2)	0.00282(12)	-0.00033(13)	-0.00248(12)
Cl1	0.0398(5)	0.0434(5)	0.0407(7)	-0.0031(5)	0.0011(5)	-0.0004(5)
O1	0.031(2)	0.035(2)	0.032(3)	0	0.001(2)	0
N2	0.035(2)	0.037(2)	0.035(2)	0.0067(17)	0.0022(17)	-0.0036(17)
C3	0.036(3)	0.046(3)	0.055(4)	0.011(3)	0.003(2)	-0.001(2)
C4	0.051(4)	0.055(4)	0.077(5)	0.026(3)	0.001(3)	-0.003(3)
C5	0.057(4)	0.058(4)	0.084(5)	0.031(4)	0.008(4)	-0.013(3)
C6	0.041(3)	0.055(3)	0.063(4)	0.010(3)	0.009(3)	-0.010(3)
C7	0.033(3)	0.045(3)	0.037(3)	0.001(2)	0.005(2)	-0.008(2)
C8	0.036(3)	0.042(3)	0.031(3)	-0.002(2)	0.003(2)	-0.007(2)
C9	0.034(3)	0.056(3)	0.038(3)	0.001(2)	0.007(2)	-0.010(2)
C10	0.026(3)	0.065(4)	0.042(3)	0.001(3)	0.002(2)	-0.004(2)
C11	0.029(3)	0.058(3)	0.039(3)	0.008(2)	-0.001(2)	0.000(2)
C12	0.026(2)	0.044(3)	0.035(3)	0.004(2)	0.000(2)	-0.002(2)
N13	0.021(2)	0.041(2)	0.030(2)	0.0020(16)	0.0007(16)	-0.0031(15)
N14	0.025(2)	0.040(2)	0.029(2)	0.0025(16)	0.0003(16)	-0.0041(16)
C15	0.033(3)	0.042(3)	0.038(3)	0.003(2)	0.004(2)	-0.006(2)
C16	0.045(3)	0.057(3)	0.029(3)	-0.001(2)	0.008(2)	-0.012(3)
C17	0.050(3)	0.051(3)	0.035(3)	-0.007(2)	0.010(2)	-0.009(3)
C18	0.039(3)	0.041(3)	0.040(3)	-0.003(2)	0.008(2)	-0.003(2)
C19	0.027(2)	0.041(3)	0.031(2)	0.000(2)	0.002(2)	-0.003(2)
C20	0.024(2)	0.036(2)	0.033(3)	0.001(2)	0.000(2)	-0.0026(18)

	U_{11}	U_{22}	U_{33}	U_{23}	U_{13}	U_{12}
C21	0.038(3)	0.038(3)	0.034(3)	0.000(2)	0.003(2)	0.000(2)
C22	0.042(3)	0.040(3)	0.037(3)	0.009(2)	0.008(2)	-0.001(2)
C23	0.040(3)	0.043(3)	0.031(3)	0.004(2)	0.007(2)	-0.001(2)
C24	0.032(2)	0.041(3)	0.027(2)	0.000(2)	0.003(2)	0.000(2)
N25	0.0208(18)	0.033(2)	0.031(2)	0.0028(16)	0.0015(15)	-0.0010(15)
Ce1	0.0311(2)	0.0325(2)	0.0309(2)	0	0.01051(16)	0
O31	0.061(2)	0.040(2)	0.047(2)	0.0144(17)	0.025(2)	0.0124(18)
N32	0.056(3)	0.045(3)	0.040(3)	0.008(2)	0.025(2)	0.012(2)
O33	0.049(2)	0.039(2)	0.038(2)	0.0081(15)	0.0198(16)	0.0060(16)
O34	0.107(4)	0.057(3)	0.053(3)	0.010(2)	0.045(3)	0.032(3)
O35	0.042(2)	0.049(2)	0.055(3)	0.0208(18)	0.011(2)	-0.0053(17)
N36	0.037(3)	0.063(3)	0.060(3)	0.029(3)	0.003(2)	-0.003(2)
O37	0.044(2)	0.046(2)	0.048(2)	0.0112(17)	0.0120(17)	-0.0065(17)
O38	0.040(3)	0.129(5)	0.129(5)	0.088(5)	0.003(3)	-0.001(3)
O39	0.0355(18)	0.043(2)	0.038(2)	0.0052(15)	0.0057(15)	0.0016(15)
N40	0.041(2)	0.039(2)	0.032(2)	-0.0002(18)	0.0085(18)	-0.004(2)
O41	0.0315(18)	0.045(2)	0.043(2)	-0.0087(16)	0.0045(15)	-0.0010(15)
O42	0.050(2)	0.046(2)	0.045(2)	-0.0121(18)	0.0057(18)	0.0006(17)
N51	0.141(8)	0.336(14)	0.202(9)	-0.200(10)	-0.035(9)	0.056(11)
C52	0.137(8)	0.335(14)	0.200(9)	-0.195(10)	-0.028(9)	0.049(11)
C53	0.137(9)	0.337(15)	0.202(10)	-0.185(11)	-0.019(9)	0.039(12)
N54	0.085(4)	0.097(5)	0.105(5)	0.032(4)	-0.003(4)	-0.012(4)
C55	0.092(4)	0.090(4)	0.102(5)	0.028(4)	-0.001(4)	-0.015(4)
C56	0.109(5)	0.098(5)	0.111(6)	0.024(4)	-0.002(5)	-0.017(4)
N57	0.46(2)	0.187(11)	0.26(2)	0.117(16)	0.16(2)	0.070(13)
C58	0.46(2)	0.185(11)	0.25(2)	0.118(17)	0.17(2)	0.071(13)
C59	0.45(2)	0.188(11)	0.25(2)	0.116(17)	0.17(2)	0.073(13)
N60	0.55(4)	0.179(10)	0.197(10)	-0.072(8)	0.22(2)	-0.136(16)
C61	0.54(4)	0.182(10)	0.199(9)	-0.083(8)	0.23(2)	-0.133(16)
C62	0.54(4)	0.188(11)	0.207(10)	-0.096(9)	0.23(2)	-0.128(16)
N63	0.232(13)	0.212(13)	0.26(2)	0.090(12)	0.036(13)	-0.072(10)
C64	0.235(13)	0.211(12)	0.27(2)	0.093(12)	0.034(14)	-0.077(10)
C65	0.240(13)	0.214(13)	0.27(2)	0.091(12)	0.029(14)	-0.073(10)
N66	0.65(6)	0.23(3)	0.50(3)	0.02(2)	0.43(4)	0.03(2)
C67	0.65(6)	0.23(3)	0.50(3)	0.02(2)	0.43(4)	0.03(2)
C68	0.65(6)	0.23(3)	0.50(3)	0.03(2)	0.43(4)	0.03(2)

Table 6. Hydrogen atomic coordinates and isotropic atomic displacement parameters ($Å^2$) for $[(bpy)_2ClRu^{IV}ORu^{III}Cl(bpy)_2](Ce(NO_3)_6)•H_2O$.

	x/a	y/b	z/c	U(eq)
H3	0.4739	0.1205	0.3150	0.057
H4	0.4379	0.0433	0.3767	0.076
H5	0.3248	0.0277	0.3584	0.081
H6	0.2496	0.0881	0.2729	0.064
H9	0.1858	0.1515	0.2001	0.051
H10	0.1256	0.2217	0.1149	0.054
H11	0.1814	0.2906	0.0579	0.052
H12	0.2967	0.2914	0.0936	0.043
H15	0.3883	0.2222	0.3852	0.046
H16	0.3825	0.2879	0.4869	0.053
H17	0.3896	0.3825	0.4572	0.055
H18	0.4045	0.4095	0.3251	0.048
H21	0.4182	0.4278	0.1991	0.045
H22	0.4374	0.4387	0.0647	0.048
H23	0.4490	0.3601	-0.0138	0.046
H24	0.4423	0.2718	0.0415	0.041
H53A	0.1025	0.3254	0.2726	0.352
H53B	0.0967	0.2963	0.3582	0.352
H53C	0.0855	0.2604	0.2739	0.352
H56A	0.3133	0.4868	0.9864	0.166
H56B	0.2575	0.4761	0.9027	0.166
H56C	0.3270	0.4448	0.9168	0.166
H59A	0.5694	0.9575	0.3382	0.422
H59B	0.6285	0.9987	0.3322	0.422
H59C	0.5543	1.0215	0.3133	0.422
H62A	0.2418	0.1354	0.5469	0.434
H62B	0.2376	0.1004	0.4629	0.434
H62C	0.2110	0.1632	0.4577	0.434
H65A	0.2586	0.9703	0.1503	0.372
H65B	0.2563	0.9046	0.1326	0.372
H65C	0.3248	0.9341	0.1750	0.372
H68A	0.4173	0.9349	0.4594	0.622
H68B	0.3732	0.9035	0.3798	0.622
H68C	0.4223	0.9523	0.3671	0.622

Table 1A. Atomic coordinates (x 10^4) and equivalent isotropic displacement parameters ($Å^2$x 10^3) for $[(bpy)_2(SO_4)Ru^{IV}ORu^{III}(O_4S)(bpy)_2](SO_4)_{1/2}•H_2O$. U(eq) is defined as one third of the trace of the orthogonalized U^{ij} tensor.

	x	y	z	U(eq)
Ru(1)	3839(1)	3883(1)	1872(1)	9(1)
S(1)	2531(1)	2496(1)	2027(1)	14(1)
O(1)	5000	3797(1)	2500	11(1)
O(2)	3011(2)	3140(1)	2297(1)	14(1)
O(3)	1681(2)	2647(1)	1492(1)	22(1)
O(4)	2106(2)	2192(1)	2635(1)	22(1)
O(5)	3354(2)	2101(1)	1734(1)	21(1)
N(7)	4446(2)	4753(1)	1534(1)	12(1)
C(8)	5201(2)	4815(1)	1076(1)	13(1)
C(9)	5591(2)	5420(1)	904(2)	19(1)
C(10)	5194(2)	5975(1)	1205(2)	18(1)
C(11)	4401(2)	5914(1)	1665(2)	16(1)
C(12)	4040(2)	5292(1)	1826(1)	12(1)
C(13)	3225(2)	5177(1)	2323(1)	12(1)
C(14)	2661(2)	5662(1)	2634(1)	15(1)
C(15)	1918(2)	5492(1)	3101(2)	18(1)
C(16)	1753(2)	4842(1)	3254(2)	18(1)
C(17)	2338(2)	4375(1)	2925(1)	15(1)
N(18)	3048(2)	4534(1)	2469(1)	11(1)
N(19)	2721(2)	3945(1)	1031(1)	13(1)
C(20)	1815(2)	4301(1)	1018(2)	17(1)
C(21)	1107(2)	4315(1)	439(2)	21(1)
C(22)	1331(2)	3962(2)	-140(2)	24(1)
C(23)	2260(2)	3595(1)	-130(2)	19(1)
C(24)	2945(2)	3587(1)	464(1)	15(1)
C(25)	3925(2)	3193(1)	548(1)	14(1)
C(26)	4254(2)	2755(1)	57(2)	19(1)
C(27)	5162(2)	2386(1)	203(2)	21(1)
C(28)	5720(2)	2452(1)	840(2)	20(1)
C(29)	5363(2)	2896(1)	1312(2)	16(1)
N(30)	4488(2)	3263(1)	1171(1)	11(1)
S(2)	7506(1)	4070(1)	9915(1)	16(1)
O(31)	7567(2)	3765(1)	9253(1)	39(1)
O(32)	8572(2)	4180(1)	10205(1)	32(1)
O(33)	6938(2)	4675(1)	9826(1)	26(1)
O(34)	6948(2)	3662(1)	10376(1)	40(1)
O(35)	5000	1478(2)	2500	25(1)
O(36)	5551(2)	632(1)	1411(1)	29(1)

O(37)	9871(2)	3417(1)	3124(1)	28(1)
O(38)	1553(2)	2913(1)	3750(1)	29(1)

Table 2A. Bond lengths [Å] and angles [°] for $[(bpy)_2(SO_4)Ru^{IV}ORu^{III}(O_4S)(bpy)_2](SO_4)_{1/2}\bullet H_2O$.

Ru(1)-O(1)	1.8400(3)
Ru(1)-O(2)	2.0435(18)
Ru(1)-N(18)	2.058(2)
Ru(1)-N(7)	2.058(2)
Ru(1)-N(30)	2.062(2)
Ru(1)-N(19)	2.076(2)
S(1)-O(5)	1.456(2)
S(1)-O(4)	1.461(2)
S(1)-O(3)	1.466(2)
S(1)-O(2)	1.5262(18)
O(1)-Ru(1)#1	1.8400(3)
N(7)-C(8)	1.347(4)
N(7)-C(12)	1.353(3)
C(8)-C(9)	1.379(4)
C(9)-C(10)	1.384(4)
C(10)-C(11)	1.383(4)
C(11)-C(12)	1.392(4)
C(12)-C(13)	1.468(4)
C(13)-N(18)	1.366(3)
C(13)-C(14)	1.381(4)
C(14)-C(15)	1.385(4)
C(15)-C(16)	1.381(4)
C(16)-C(17)	1.384(4)
C(17)-N(18)	1.336(4)
N(19)-C(20)	1.348(4)
N(19)-C(24)	1.361(4)
C(20)-C(21)	1.380(4)
C(21)-C(22)	1.376(5)
C(22)-C(23)	1.386(4)
C(23)-C(24)	1.387(4)
C(24)-C(25)	1.471(4)
C(25)-N(30)	1.360(3)
C(25)-C(26)	1.387(4)
C(26)-C(27)	1.381(4)
C(27)-C(28)	1.379(4)
C(28)-C(29)	1.383(4)
C(29)-N(30)	1.343(3)
S(2)-O(31)	1.428(2)

S(2)-O(33)	1.432(2)
S(2)-O(32)	1.434(2)
S(2)-O(34)	1.436(2)
O(1)-Ru(1)-O(2)	93.83(7)
O(1)-Ru(1)-N(18)	94.84(7)
O(2)-Ru(1)-N(18)	88.70(8)
O(1)-Ru(1)-N(7)	89.88(9)
O(2)-Ru(1)-N(7)	168.15(8)
N(18)-Ru(1)-N(7)	79.76(9)
O(1)-Ru(1)-N(30)	92.42(8)
O(2)-Ru(1)-N(30)	92.36(8)
N(18)-Ru(1)-N(30)	172.58(8)
N(7)-Ru(1)-N(30)	98.74(9)
O(1)-Ru(1)-N(19)	169.76(7)
O(2)-Ru(1)-N(19)	91.35(8)
N(18)-Ru(1)-N(19)	94.10(9)
N(7)-Ru(1)-N(19)	86.82(8)
N(30)-Ru(1)-N(19)	78.53(9)
O(5)-S(1)-O(4)	112.57(12)
O(5)-S(1)-O(3)	110.25(12)
O(4)-S(1)-O(3)	111.58(12)
O(5)-S(1)-O(2)	109.69(11)
O(4)-S(1)-O(2)	104.45(11)
O(3)-S(1)-O(2)	108.05(11)
Ru(1)#1-O(1)-Ru(1)	168.98(15)
S(1)-O(2)-Ru(1)	134.79(12)
C(8)-N(7)-C(12)	120.0(2)
C(8)-N(7)-Ru(1)	125.55(18)
C(12)-N(7)-Ru(1)	114.45(18)
N(7)-C(8)-C(9)	121.3(3)
C(8)-C(9)-C(10)	119.4(3)
C(11)-C(10)-C(9)	119.4(3)
C(10)-C(11)-C(12)	119.1(3)
N(7)-C(12)-C(11)	120.8(3)
N(7)-C(12)-C(13)	116.1(2)
C(11)-C(12)-C(13)	123.1(2)
N(18)-C(13)-C(14)	120.4(3)
N(18)-C(13)-C(12)	114.8(2)
C(14)-C(13)-C(12)	124.7(2)
C(13)-C(14)-C(15)	119.4(3)
C(16)-C(15)-C(14)	119.9(3)
C(15)-C(16)-C(17)	118.3(3)
N(18)-C(17)-C(16)	122.3(3)
C(17)-N(18)-C(13)	119.7(2)
C(17)-N(18)-Ru(1)	125.58(18)
C(13)-N(18)-Ru(1)	114.51(18)

C(20)-N(19)-C(24)	119.7(2)
C(20)-N(19)-Ru(1)	124.90(19)
C(24)-N(19)-Ru(1)	115.42(18)
N(19)-C(20)-C(21)	121.6(3)
C(22)-C(21)-C(20)	119.4(3)
C(21)-C(22)-C(23)	119.4(3)
C(22)-C(23)-C(24)	119.4(3)
N(19)-C(24)-C(23)	120.5(3)
N(19)-C(24)-C(25)	115.1(2)
C(23)-C(24)-C(25)	124.4(3)
N(30)-C(25)-C(26)	120.8(3)
N(30)-C(25)-C(24)	114.8(2)
C(26)-C(25)-C(24)	124.4(2)
C(27)-C(26)-C(25)	119.5(3)
C(28)-C(27)-C(26)	119.4(3)
C(27)-C(28)-C(29)	119.0(3)
N(30)-C(29)-C(28)	122.0(3)
C(29)-N(30)-C(25)	119.3(2)
C(29)-N(30)-Ru(1)	124.40(18)
C(25)-N(30)-Ru(1)	116.10(18)
O(31)-S(2)-O(33)	108.97(14)
O(31)-S(2)-O(32)	108.19(15)
O(33)-S(2)-O(32)	110.85(14)
O(31)-S(2)-O(34)	111.10(17)
O(33)-S(2)-O(34)	108.41(14)
O(32)-S(2)-O(34)	109.33(14)

Symmetry transformations used to generate equivalent atoms:
#1 -x+1,y,-z+1/2

Table 3A. Anisotropic displacement parameters ($Å^2 x\ 10^3$) for $[(bpy)_2(SO_4)Ru^{IV}ORu^{III}(O_4S)(bpy)_2](SO_4)_{1/2}•H_2O$. The anisotropic displacement factor exponent takes the form: $-2\pi^2[h^2a^{*2}U^{11} + ... + 2\ h\ k\ a^*\ b^*\ U^{12}]$

	U^{11}	U^{22}	U^{33}	U^{23}	U^{13}	U^{12}
Ru(1)	10(1)	8(1)	8(1)	0(1)	0(1)	0(1)
S(1)	16(1)	11(1)	14(1)	-1(1)	1(1)	-2(1)
O(1)	13(1)	10(1)	11(1)	0	2(1)	0
O(2)	18(1)	13(1)	11(1)	1(1)	1(1)	-4(1)
O(3)	19(1)	28(1)	19(1)	-3(1)	-4(1)	-2(1)
O(4)	32(1)	15(1)	19(1)	-2(1)	7(1)	-5(1)
O(5)	25(1)	13(1)	24(1)	-1(1)	6(1)	1(1)
N(7)	13(1)	10(1)	11(1)	2(1)	-2(1)	1(1)

C(8)	14(1)	14(1)	12(1)	1(1)	1(1)	1(1)
C(9)	19(2)	21(2)	16(2)	1(1)	3(1)	-2(1)
C(10)	23(2)	13(1)	19(2)	7(1)	3(1)	-4(1)
C(11)	21(2)	13(1)	14(2)	2(1)	2(1)	2(1)
C(12)	13(1)	11(1)	11(1)	1(1)	-3(1)	2(1)
C(13)	12(1)	14(1)	10(1)	1(1)	-3(1)	-1(1)
C(14)	18(1)	12(1)	15(2)	0(1)	-2(1)	2(1)
C(15)	17(1)	20(1)	17(2)	-4(1)	0(1)	7(1)
C(16)	17(1)	21(2)	17(2)	-2(1)	6(1)	1(1)
C(17)	18(1)	14(1)	14(2)	1(1)	1(1)	-2(1)
N(18)	12(1)	12(1)	10(1)	-1(1)	0(1)	2(1)
N(19)	15(1)	11(1)	12(1)	3(1)	-2(1)	-4(1)
C(20)	15(1)	15(1)	21(2)	6(1)	0(1)	-1(1)
C(21)	15(1)	23(2)	24(2)	11(1)	-3(1)	-5(1)
C(22)	20(2)	31(2)	19(2)	11(1)	-7(1)	-13(1)
C(23)	25(2)	22(2)	11(2)	3(1)	-3(1)	-11(1)
C(24)	17(1)	15(1)	13(2)	2(1)	0(1)	-6(1)
C(25)	19(1)	13(1)	9(1)	2(1)	4(1)	-7(1)
C(26)	28(2)	18(1)	11(2)	-2(1)	4(1)	-9(1)
C(27)	29(2)	15(1)	22(2)	-7(1)	14(1)	-6(1)
C(28)	21(2)	13(1)	27(2)	-1(1)	10(1)	-1(1)
C(29)	18(1)	12(1)	18(2)	0(1)	2(1)	-3(1)
N(30)	15(1)	10(1)	9(1)	-2(1)	3(1)	-3(1)
S(2)	13(1)	18(1)	17(1)	2(1)	2(1)	1(1)
O(31)	36(1)	44(2)	36(2)	-13(1)	-5(1)	17(1)
O(32)	18(1)	40(1)	38(1)	3(1)	0(1)	-3(1)
O(33)	24(1)	23(1)	32(1)	1(1)	6(1)	3(1)
O(34)	27(1)	39(1)	56(2)	24(1)	7(1)	-1(1)
O(35)	23(2)	21(2)	30(2)	0	-3(1)	0
O(36)	24(1)	38(1)	24(1)	-1(1)	3(1)	0(1)
O(37)	26(1)	31(1)	28(1)	-3(1)	4(1)	-2(1)
O(38)	23(1)	40(1)	24(1)	-10(1)	1(1)	-1(1)

Table 4A. Hydrogen coordinates (x 10^4) and isotropic displacement parameters ($Å^2$x 10^3) for $[(bpy)_2(SO_4)Ru^{IV}ORu^{III}(O_4S)(bpy)_2](SO_4)_{1/2}•H_2O$.

x	y	z	U(eq)
H(8)	5471	4434	866	16
H(9)	6126	5455	581	22
H(10)	5464	6395	1098	22
H(11)	4107	6291	1867	19
H(14)	2781	6109	2529	18
H(15)	1522	5822	3316	22
H(16)	1251	4718	3577	22
H(17)	2230	3926	3028	18
H(20)	1662	4547	1416	20
H(21)	470	4565	441	25
H(22)	853	3970	-543	28
H(23)	2427	3351	-528	23
H(26)	3857	2709	-377	23
H(27)	5401	2089	-132	26
H(28)	6340	2197	952	24
H(29)	5748	2942	1750	19
H(35)	4550(30)	1737(16)	2355(19)	28(10)
H(36A)	5420(40)	900(20)	1750(20)	56(14)
H(36B)	5980(30)	780(20)	1220(20)	39(14)
H(37A)	10420(40)	3250(20)	3380(20)	49(13)
H(37B)	9400(40)	3120(30)	3220(30)	90(19)
H(37C)	10000	3420(30)	2500	80(20)
H(38A)	2060(30)	3070(20)	4000(20)	44(12)
H(38B)	1840(30)	2640(20)	3450(20)	43(12)

Table 5A. Torsion angles [°] for $[(bpy)_2(SO_4)Ru^{IV}ORu^{III}(O_4S)(bpy)_2](SO_4)_{1/2}\bullet H_2O$.

O(2)-Ru(1)-O(1)-Ru(1)#1	-139.00(5)
N(18)-Ru(1)-O(1)-Ru(1)#1	-49.98(6)
N(7)-Ru(1)-O(1)-Ru(1)#1	29.73(6)
N(30)-Ru(1)-O(1)-Ru(1)#1	128.48(6)
N(19)-Ru(1)-O(1)-Ru(1)#1	100.8(5)
O(5)-S(1)-O(2)-Ru(1)	55.82(18)
O(4)-S(1)-O(2)-Ru(1)	176.70(15)
O(3)-S(1)-O(2)-Ru(1)	-64.39(18)
O(1)-Ru(1)-O(2)-S(1)	-121.70(16)
N(18)-Ru(1)-O(2)-S(1)	143.53(16)
N(7)-Ru(1)-O(2)-S(1)	130.4(3)
N(30)-Ru(1)-O(2)-S(1)	-29.12(16)
N(19)-Ru(1)-O(2)-S(1)	49.46(16)
O(1)-Ru(1)-N(7)-C(8)	81.6(2)
O(2)-Ru(1)-N(7)-C(8)	-170.1(3)
N(18)-Ru(1)-N(7)-C(8)	176.5(2)
N(30)-Ru(1)-N(7)-C(8)	-10.8(2)
N(19)-Ru(1)-N(7)-C(8)	-88.7(2)
O(1)-Ru(1)-N(7)-C(12)	-96.88(17)
O(2)-Ru(1)-N(7)-C(12)	11.5(5)
N(18)-Ru(1)-N(7)-C(12)	-1.93(17)
N(30)-Ru(1)-N(7)-C(12)	170.70(17)
N(19)-Ru(1)-N(7)-C(12)	92.82(18)
C(12)-N(7)-C(8)-C(9)	1.3(4)
Ru(1)-N(7)-C(8)-C(9)	-177.13(19)
N(7)-C(8)-C(9)-C(10)	-0.3(4)
C(8)-C(9)-C(10)-C(11)	-1.1(4)
C(9)-C(10)-C(11)-C(12)	1.6(4)
C(8)-N(7)-C(12)-C(11)	-0.7(4)
Ru(1)-N(7)-C(12)-C(11)	177.84(19)
C(8)-N(7)-C(12)-C(13)	-179.6(2)
Ru(1)-N(7)-C(12)-C(13)	-1.1(3)
C(10)-C(11)-C(12)-N(7)	-0.7(4)
C(10)-C(11)-C(12)-C(13)	178.1(2)
N(7)-C(12)-C(13)-N(18)	5.2(3)
C(11)-C(12)-C(13)-N(18)	-173.7(2)
N(7)-C(12)-C(13)-C(14)	-174.9(2)
C(11)-C(12)-C(13)-C(14)	6.2(4)
N(18)-C(13)-C(14)-C(15)	0.5(4)
C(12)-C(13)-C(14)-C(15)	-179.3(2)
C(13)-C(14)-C(15)-C(16)	0.4(4)
C(14)-C(15)-C(16)-C(17)	-0.6(4)
C(15)-C(16)-C(17)-N(18)	-0.1(4)
C(16)-C(17)-N(18)-C(13)	1.0(4)

C(16)-C(17)-N(18)-Ru(1)	-172.9(2)
C(14)-C(13)-N(18)-C(17)	-1.2(4)
C(12)-C(13)-N(18)-C(17)	178.7(2)
C(14)-C(13)-N(18)-Ru(1)	173.36(19)
C(12)-C(13)-N(18)-Ru(1)	-6.8(3)
O(1)-Ru(1)-N(18)-C(17)	-92.0(2)
O(2)-Ru(1)-N(18)-C(17)	1.7(2)
N(7)-Ru(1)-N(18)-C(17)	179.0(2)
N(19)-Ru(1)-N(18)-C(17)	93.0(2)
O(1)-Ru(1)-N(18)-C(13)	93.82(18)
O(2)-Ru(1)-N(18)-C(13)	-172.45(17)
N(7)-Ru(1)-N(18)-C(13)	4.82(17)
N(19)-Ru(1)-N(18)-C(13)	-81.19(18)
O(1)-Ru(1)-N(19)-C(20)	-153.6(5)
O(2)-Ru(1)-N(19)-C(20)	86.0(2)
N(18)-Ru(1)-N(19)-C(20)	-2.8(2)
N(7)-Ru(1)-N(19)-C(20)	-82.3(2)
N(30)-Ru(1)-N(19)-C(20)	178.1(2)
O(1)-Ru(1)-N(19)-C(24)	27.1(6)
O(2)-Ru(1)-N(19)-C(24)	-93.24(18)
N(18)-Ru(1)-N(19)-C(24)	177.96(18)
N(7)-Ru(1)-N(19)-C(24)	98.48(19)
N(30)-Ru(1)-N(19)-C(24)	-1.11(18)
C(24)-N(19)-C(20)-C(21)	-0.4(4)
Ru(1)-N(19)-C(20)-C(21)	-179.6(2)
N(19)-C(20)-C(21)-C(22)	-0.5(4)
C(20)-C(21)-C(22)-C(23)	0.5(4)
C(21)-C(22)-C(23)-C(24)	0.3(4)
C(20)-N(19)-C(24)-C(23)	1.3(4)
Ru(1)-N(19)-C(24)-C(23)	-179.5(2)
C(20)-N(19)-C(24)-C(25)	-177.0(2)
Ru(1)-N(19)-C(24)-C(25)	2.2(3)
C(22)-C(23)-C(24)-N(19)	-1.2(4)
C(22)-C(23)-C(24)-C(25)	176.9(3)
N(19)-C(24)-C(25)-N(30)	-2.5(3)
C(23)-C(24)-C(25)-N(30)	179.3(3)
N(19)-C(24)-C(25)-C(26)	174.7(2)
C(23)-C(24)-C(25)-C(26)	-3.5(4)
N(30)-C(25)-C(26)-C(27)	0.2(4)
C(24)-C(25)-C(26)-C(27)	-176.9(3)
C(25)-C(26)-C(27)-C(28)	0.9(4)
C(26)-C(27)-C(28)-C(29)	-1.1(4)
C(27)-C(28)-C(29)-N(30)	0.2(4)
C(28)-C(29)-N(30)-C(25)	0.9(4)
C(28)-C(29)-N(30)-Ru(1)	175.1(2)
C(26)-C(25)-N(30)-C(29)	-1.0(4)

C(24)-C(25)-N(30)-C(29)	176.3(2)
C(26)-C(25)-N(30)-Ru(1)	-175.8(2)
C(24)-C(25)-N(30)-Ru(1)	1.6(3)
O(1)-Ru(1)-N(30)-C(29)	10.1(2)
O(2)-Ru(1)-N(30)-C(29)	-83.8(2)
N(7)-Ru(1)-N(30)-C(29)	100.3(2)
N(19)-Ru(1)-N(30)-C(29)	-174.7(2)
O(1)-Ru(1)-N(30)-C(25)	-175.47(18)
O(2)-Ru(1)-N(30)-C(25)	90.59(18)
N(7)-Ru(1)-N(30)-C(25)	-85.23(19)
N(19)-Ru(1)-N(30)-C(25)	-0.31(18)

Symmetry transformations used to generate equivalent atoms:
#1 -x+1,y,-z+1/2

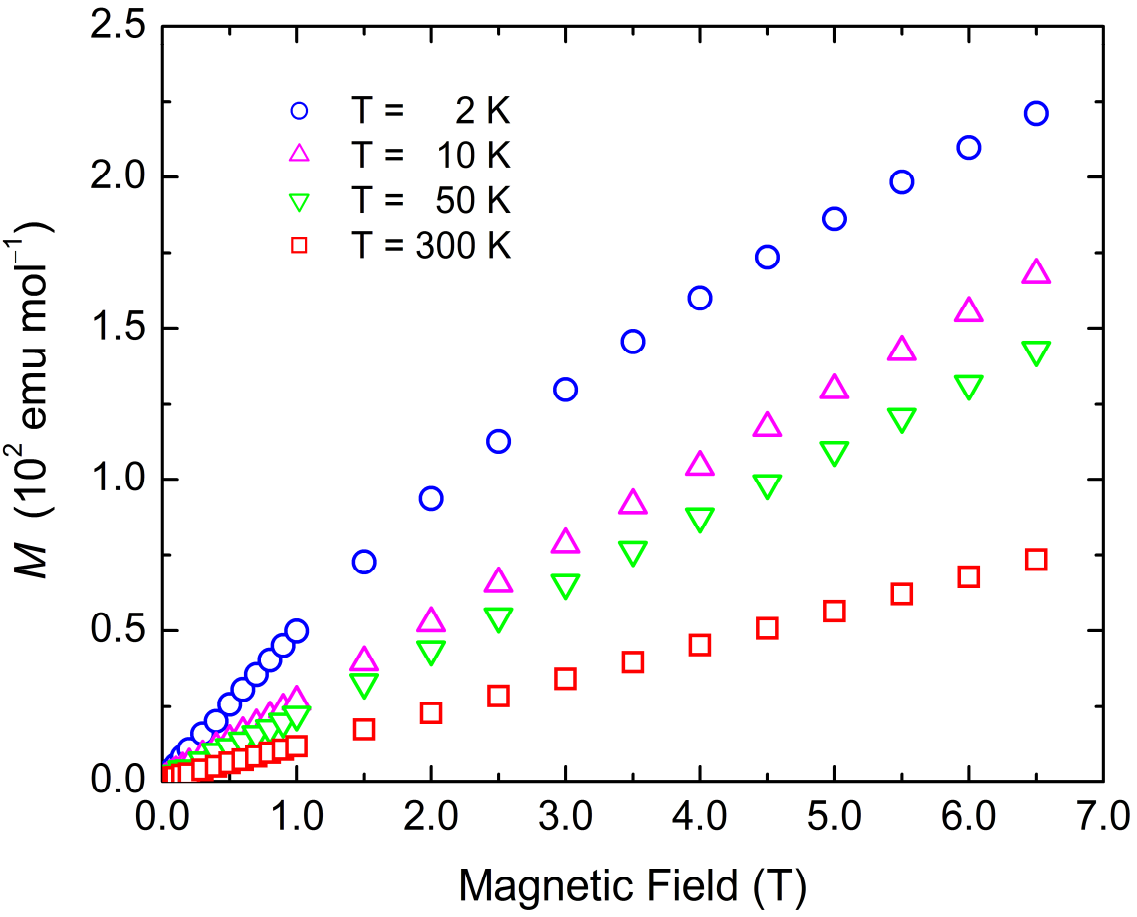

Figure S1. Field dependence of the magnetization for the blue dimer at various temperatures.

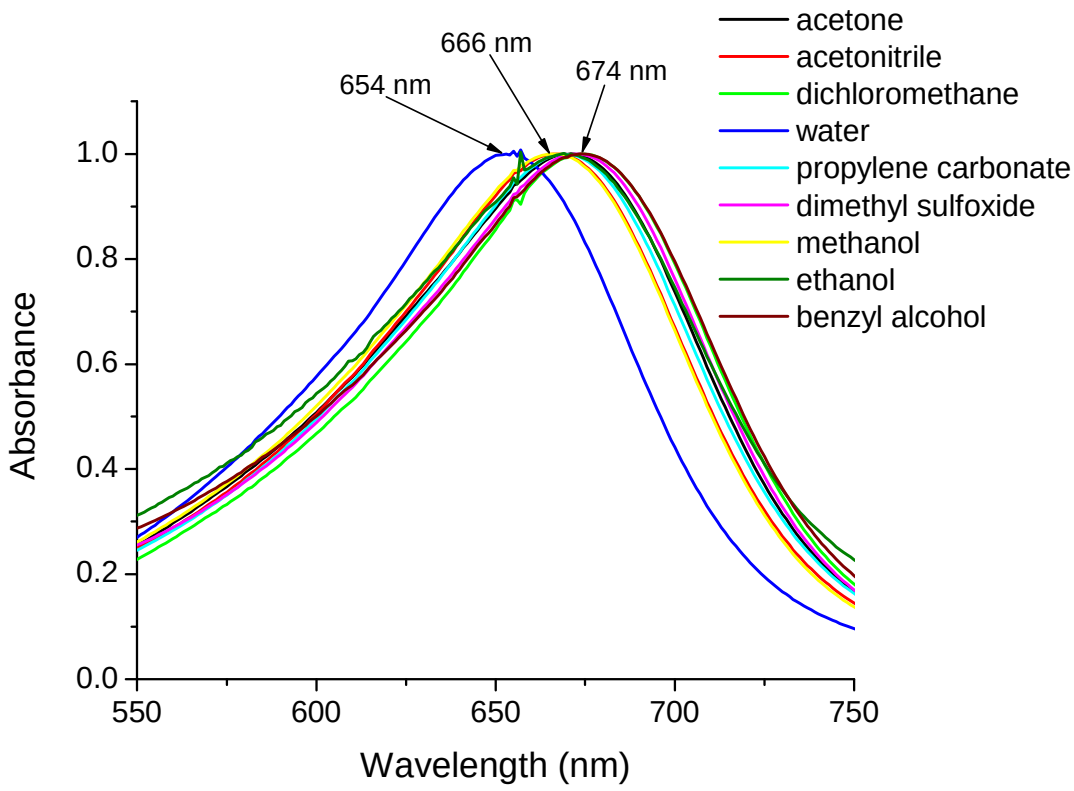

Figure S2. Solvent dependence on visible absorption band for *cis,cis*-$[(bpy)_2ClRuORuCl(bpy)_2](PF_6)_2$.

Computational Methods

Theoretical calculations were carried out by using Density Functional Theory (DFT) as implemented in Gaussian03, revision D.02.[1] Becke's three-parameter hybrid functional[2-5] with the LYP correlation functional[6] (B3LYP) was used with Los Alamos effective core potential LanL2DZ basis set. Frequency calculations were performed in the optimized geometries to ensure that the geometries correspond to a minimum in the potential energy surface. Franck-Condon vertical excitation energies and oscillator strengths were obtained with non-equilibrium Time-Dependent Density Functional Theory (TD-DFT)[7-9] as implemented in Gaussian03. Solvent-specific interactions and counterion effects were modeled by explicitly adding hydrogen-bonded water molecules and chloride anions, respectively. The bulk of the solvent was modeled by means of the Integral Equation Formalism Polarizable Continum Model (IEF-PCM)[12-15], as implemented in Gaussian03. Pauling's radii were used in all cases. The electronic spectra were modeled as the convolution of gaussian bands associated with each transition.[16] Estimation of redox potentials with DFT calculations is well documented in the literature.[17-19]

Geometries

Closed-shell singlets.

***cis,cis*-$[(bpy)_2(H_2O)Ru^{III}ORu^{III}(OH_2)bpy)_2]^{4+}$ (BD)**: The coordinates of the x-ray structure[20] of $[(bpy)_2(H_2O)Ru^{III}ORu^{III}(OH_2)bpy)_2]^{4+}$ were used as input geometry in Gaussian03. Although three isomers are possible for the blue dimer (enantiomeric pair and meso), all the known x-ray structures for the family $[(bpy)_2(L)RuORu(L)bpy)_2]^{n+}$ (L: H_2O, Cl, NO_2, NH_3)[20-23] contain only the enantiomeric pair and all studies reported here focus on a single enantiomers with the enantiomer chosen (D,D or L,L) irrelevant to the results. The ground state was assumed to be a closed-shell singlet and the structure was optimized at DFT level (B3LYP, LANL2DZ) with no symmetry restrictions. Tight convergence criteria were used for both the SCF and the optimization itself. The calculation converged to a final C_2 symmetry, which was used to calculate the gas phase absorption spectrum and to build the structures with hydrogen-bonded water molecules and counterions.

***cis,cis*-$[(bpy)_2(H_2O)Ru^{III}ORu^{III}(OH_2)(bpy)_2]^{4+}\times 4H_2O$ (BD×4H_2O)**: Two water molecules were hydrogen-bonded to each of the two aquo ligands of the optimized gas phase structure with a hydrogen-bond distance of 1.500 Å and the resulting "hydrate" was fully optimized under C_2 symmetry.

***cis,cis*-$[(bpy)_2(H_2O)Ru^{III}ORu^{III}(OH_2)(bpy)_2](Cl)_4\times 4H_2O$ (BDCl_4×4H_2O)**: Four chloride anions were added to BD×4H_2O, each hydrogen-bonded to one of the hydrogen-bonded water molecules with a hydrogen-bond distance of 1.700 Å. The resulting structure was fully optimized under C_2 symmetry.

Broken symmetry singlet.

BS-BD: For the broken symmetry state, we used the geometry of the closed-shell singlet as the starting point. The methodology described in the Gaussian official website was employed (http://www.gaussian.com/g_news/sum05/newsletter_g03_tips.htm). Martin *et al.*[24] were unable to optimize the structure of the broken symmetry state using the LANL2 relativistic effective core potential with the corresponding uncontracted basis set for Ru. We were able to optimize the structure of the broken symmetry state using the LANL2DZ basis set. The resulting structure was used for the comparison shown in Table1.

$Ru^{IV}ORu^{III}$ structures containing coordinated aqua or chloride ligands were optimized as a ground state doublet with strong coupling. The Ru-μ-O bond distances were shorter in this oxidation state relative to their $Ru^{III}ORu^{III}$ analogues as expected.

Energies. As previously reported by Baik *et al.*[19] and Martin *et al.*[24], the results from DFT calculations place the triplet state as the lowest in energy for the blue dimer, followed by the broken symmetry state, and the closed-shell singlet is the highest in energy. In our work, we disregard the energy ordering obtained from the calculations and we focused our attention in the comparison of calculated *vs* experimental properties for the different electronic configurations.

Geometries. Tables S12 through S21 contain the Cartesian coordinates for the different structures. Figures S1 and S2 show the optimized structures for $BD{\times}4H_2O$ and $BDCl_4{\times}4H_2O$, respectively. Some significant features are also shown in the figures.

Spectra. Figure S6 shows a comparison between the experimental absorption spectrum for the blue dimer in H_2O at pH 7 and the calculated spectrum for $BDCl_4{\times}4H_2O$. Figures S5 to S10 show calculated and experimental absorption spectra for complexes discussed in the manuscript. Tables S7 to S11 show selected excitation energies and oscillators strengths of transitions from time-dependent DFT calculations.

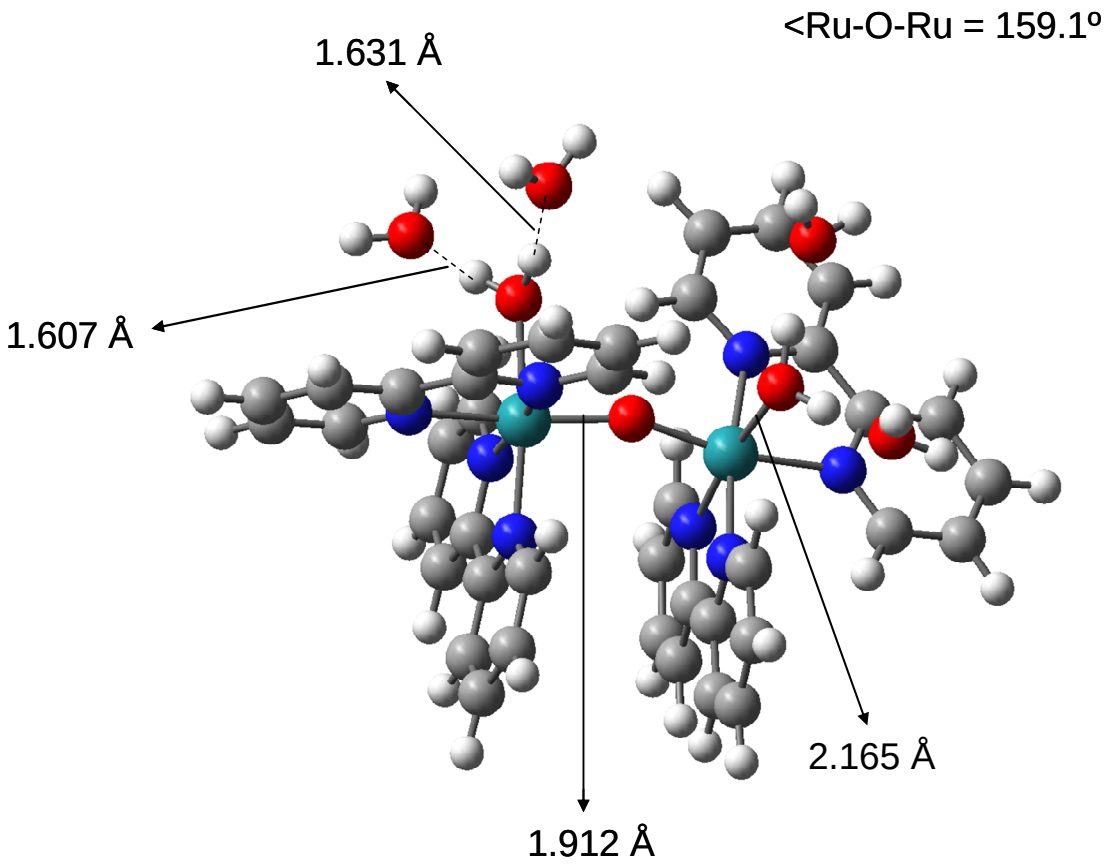

Figure S3. Optimized structure for BD×4H_2O.

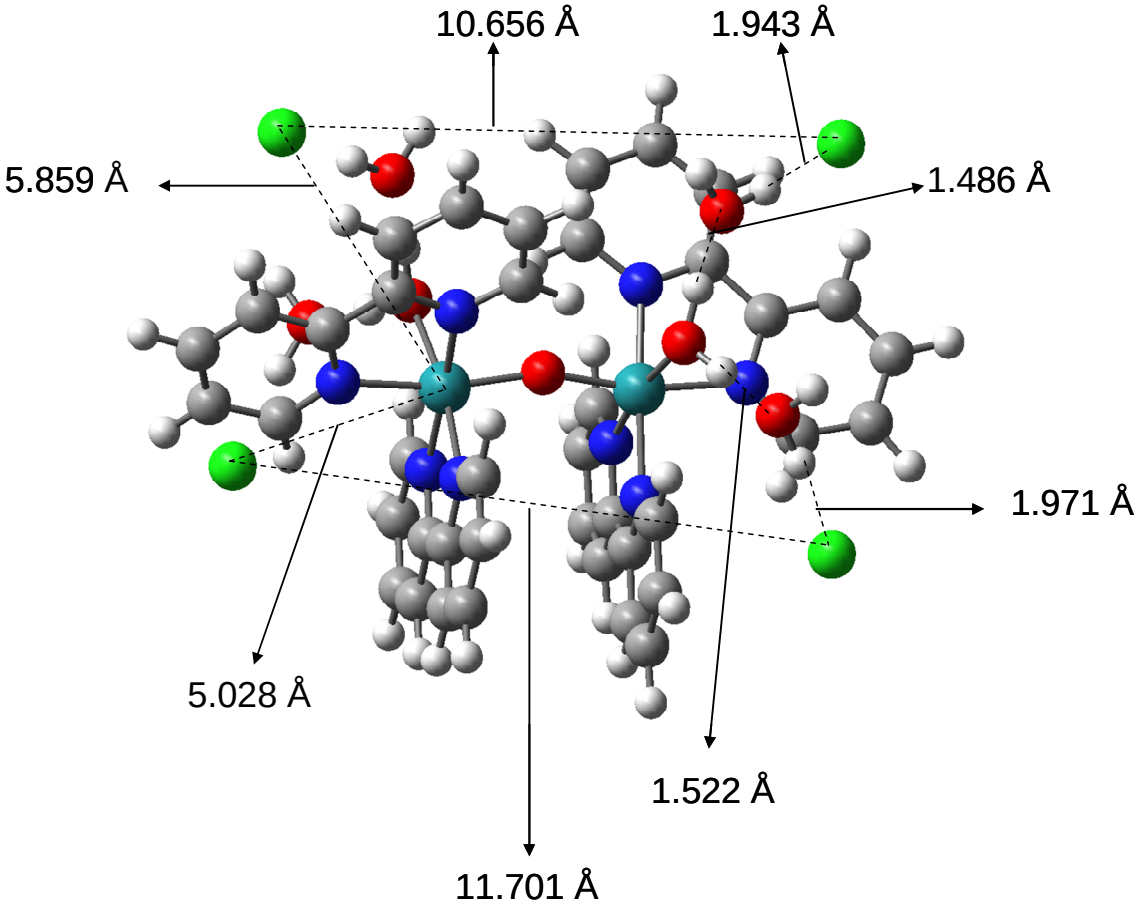

Figure S4. Optimized structure for $BDCl_4 \times 4H_2O$.

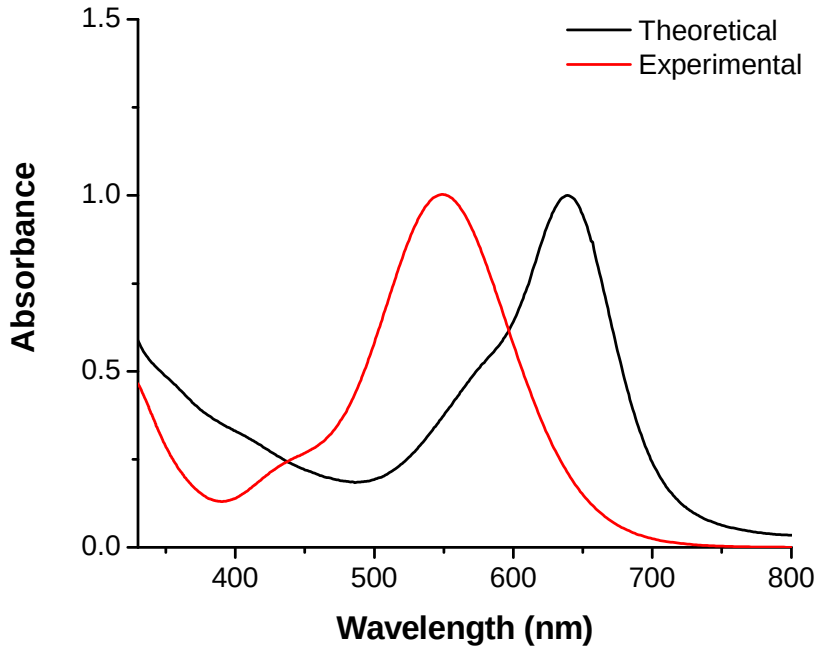

Figure S5. Comparison between calculated (strong coupling, BD) and experimental absorption spectra for the blue dimer.

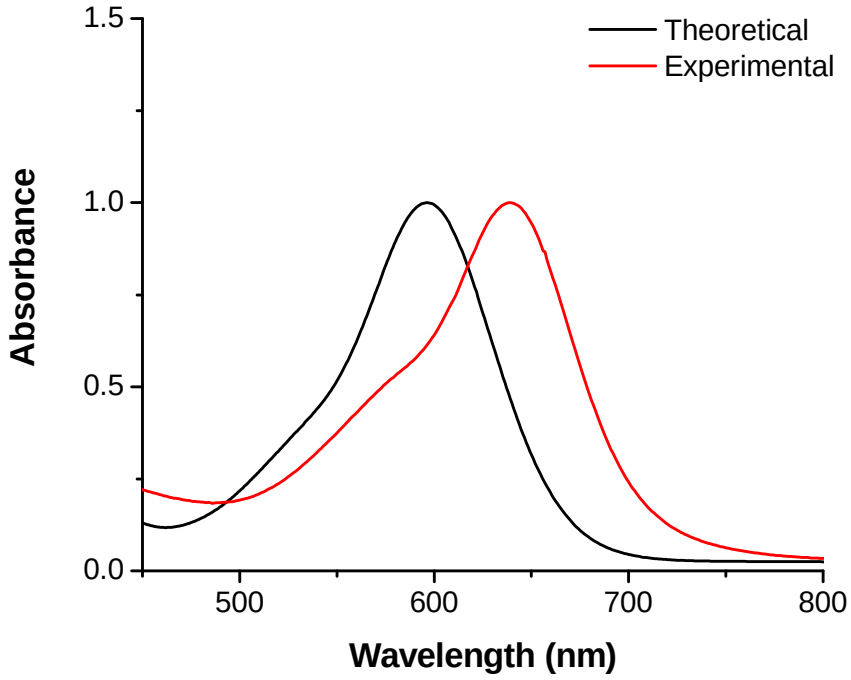

Figure S6. Comparison between calculated (strong coupling, $BDCl_4 \times 4H_2O$) and experimental absorption spectra for the blue dimer.

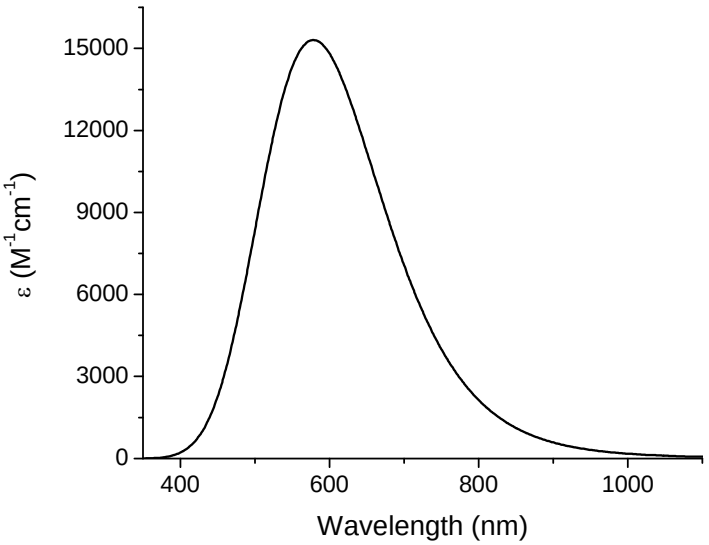

Figure S7. Calculated broken-symmetry absorption spectra for the blue dimer (BS-BD).

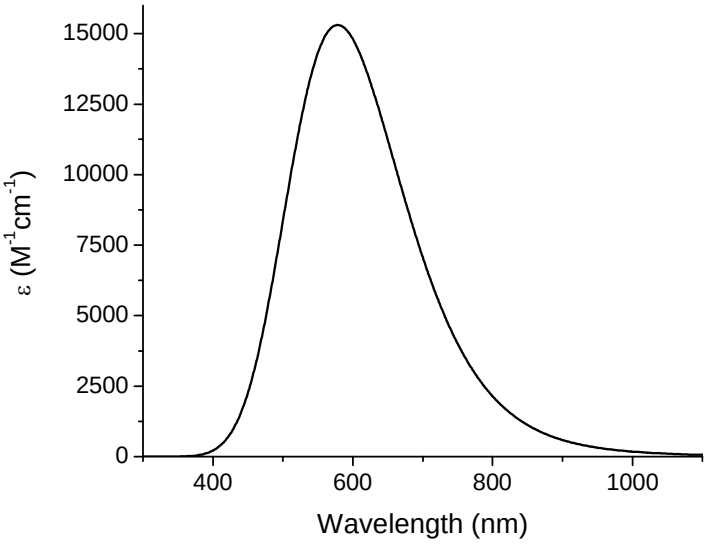

Figure S8. Calculated absorption spectra for optimized blue dimer in triplet electronic state.

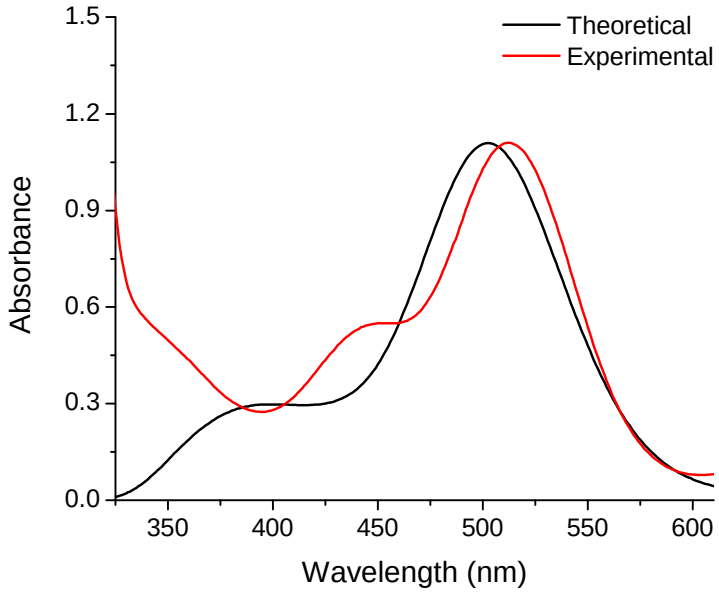

Figure S9. Comparison between calculated and experimental absorption spectra for $[(HO)Ru^{IV}ORu^{III}(OH_2)]^{4+}$ in acetonitrile and with IEF-PCM (acetonitrile).

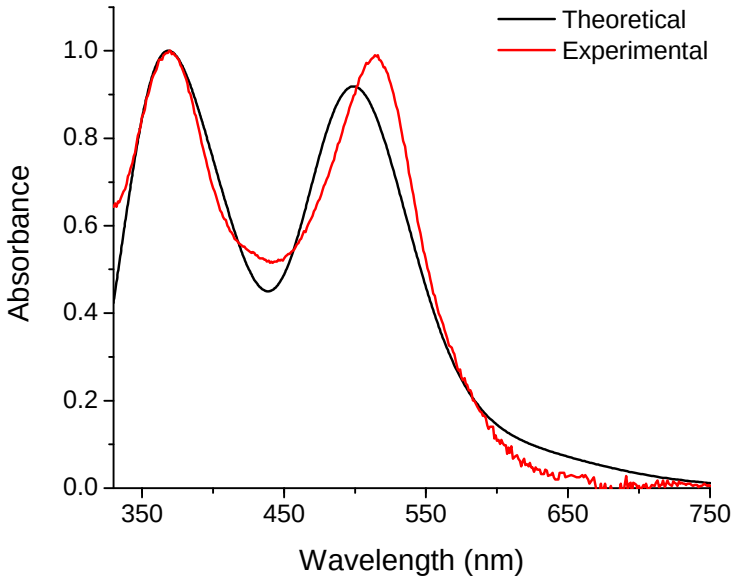

Figure S10. Comparison between calculated and experimental absorption spectra for $Ru(bpy)_2Cl_2$ in water (experimental) and with IEF-PCM (water).

Table S7. Excitation energies and oscillator strengths for $BDCl_4 \times 4H_2O$. The results on each state include: the spin and spatial symmetry, the excitation energy, the oscillator strength, and (on the second line for each state) the largest coefficients in the CI expansion.

Excited State 1:	Singlet-B	0.1282 eV	9669.87 nm	f=0.0001
228 ->229	0.37467			
Excited State 2:	Singlet-A	1.3372 eV	927.21 nm	f=0.0000
226 ->229	0.65143			
Excited State 3:	Singlet-A	1.5587 eV	795.42 nm	f=0.0004
225 ->229	0.65465			
Excited State 4:	Singlet-B	1.5762 eV	786.59 nm	f=0.0027
224 ->229	0.65517			
Excited State 5:	Singlet-B	2.0706 eV	598.78 nm	f=0.3430
226 ->230	0.13271			
227 ->229	0.44420			
228 ->231	-0.40105			
228 ->233	-0.14636			
Excited State 6:	Singlet-A	2.1990 eV	563.82 nm	f=0.0588
228 ->230	0.66736			
228 ->232	0.15805			
Excited State 7:	Singlet-B	2.2872 eV	542.09 nm	f=0.0737
227 ->229	0.18344			
228 ->231	0.50105			
228 ->233	-0.40359			
Excited State 8:	Singlet-A	2.2991 eV	539.28 nm	f=0.0017
228 ->230	-0.13769			
228 ->232	0.67004			
Excited State 9:	Singlet-B	2.3649 eV	524.28 nm	f=0.0344
222 ->229	-0.11381			
227 ->229	0.24695			
228 ->231	0.25581			
228 ->233	0.53515			
Excited State 10:	Singlet-A	2.4592 eV	504.16 nm	f=0.0090
223 ->229	0.69224			
Excited State 11:	Singlet-B	2.5115 eV	493.66 nm	f=0.0097

222 ->229 0.68352

Excited State 12: Singlet-A 2.5960 eV 477.59 nm f=0.0052
221 ->229 0.68644

Excited State 13: Singlet-B 2.6117 eV 474.73 nm f=0.0040
220 ->229 0.68736

Excited State 14: Singlet-B 2.7749 eV 446.81 nm f=0.0013
216 ->229 0.11346
219 ->229 0.68561

Excited State 15: Singlet-A 2.7786 eV 446.22 nm f=0.0000
217 ->229 0.11782
218 ->229 0.68469

Table S8. Excitation energies and oscillator strengths for BS-BD. The results on each state include: the spin and spatial symmetry, the excitation energy, the oscillator strength, and (on the second line for each state) the largest coefficients in the CI expansion.

Excited state symmetry could not be determined.
Excited State 1: ?Spin -?Sym 0.2110 eV 5876.37 nm f=0.0001
191A ->193A -0.12037
192A ->193A -1.10207
192A ->197A 0.15515
191B ->193B 0.12212
192B ->193B 1.10209
192B ->197B 0.15439

Excited state symmetry could not be determined.
Excited State 2: ?Spin -?Sym 0.6436 eV 1926.35 nm f=0.0000
188A ->193A 0.12656
191A ->193A -0.23390
192A ->193A 0.61860
188B ->193B -0.12578
191B ->193B -0.23307
192B ->193B 0.61843

Excited state symmetry could not be determined.
Excited State 3: ?Spin -?Sym 1.0200 eV 1215.51 nm f=0.0001
191A ->193A 0.86253
191A ->197A -0.10292
191B ->193B 0.86136
191B ->197B 0.10248

Excited state symmetry could not be determined.
Excited State 4: ?Spin -?Sym 1.3674 eV 906.70 nm f=0.0005
187A ->193A 0.17683
190A ->193A 0.54412
187B ->193B 0.24649
188B ->193B -0.13447
190B ->193B 0.74183

Excited state symmetry could not be determined.
Excited State 5: ?Spin -?Sym 1.3720 eV 903.67 nm f=0.0001
187A ->193A 0.25751
188A ->193A -0.10654
190A ->193A 0.74010
187B ->193B -0.19114
190B ->193B -0.53912

Excited state symmetry could not be determined.
Excited State 6: ?Spin -?Sym 1.9374 eV 639.96 nm f=0.0000
184A ->193A 0.29797
186A ->193A 0.29228
187A ->193A 0.27130
188A ->193A 0.44215
189A ->193A -0.15173
192A ->193A -0.13791
184B ->193B 0.29080
186B ->193B 0.27619
187B ->193B -0.29951
188B ->193B -0.43740
189B ->193B 0.14524
192B ->193B -0.13876

Excited state symmetry could not be determined.
Excited State 7: ?Spin -?Sym 2.0374 eV 608.54 nm f=0.1641
184A ->193A -0.20001
186A ->193A -0.21542
187A ->193A -0.17952
188A ->193A -0.32625
189A ->193A 0.11306
191A ->193A -0.40746
184B ->193B 0.19631
186B ->193B 0.20627
187B ->193B -0.20186
188B ->193B -0.32688
189B ->193B 0.10943
191B ->193B 0.40936

Excited state symmetry could not be determined.
Excited State 8: ?Spin -?Sym 2.1667 eV 572.22 nm f=0.0174
184A ->193A -0.12877
186A ->193A -0.42549
187A ->193A 0.17872
188A ->193A 0.26215
189A ->193A 0.63637
191A ->193A 0.13056
186B ->193B 0.24773
189B ->193B 0.34716
191B ->193B -0.12408

Excited state symmetry could not be determined.
Excited State 9: ?Spin -?Sym 2.1722 eV 570.78 nm f=0.0018
186A ->193A 0.19408
187A ->193A -0.15383
188A ->193A -0.22738
189A ->193A -0.33498
186B ->193B 0.40602
187B ->193B 0.21929
188B ->193B 0.30843
189B ->193B 0.63929

Excited state symmetry could not be determined.
Excited State 10: ?Spin -?Sym 2.2122 eV 560.47 nm f=0.2072
168A ->193A -0.12521
181A ->193A -0.12187
184A ->193A 0.15419
187A ->193A 0.25883
188A ->193A 0.35965
191A ->193A -0.36466
192A ->195A -0.10857
168B ->193B -0.12485
181B ->193B -0.12462
184B ->193B -0.15005
187B ->193B 0.27769
188B ->193B 0.35093
191B ->193B 0.36576
192B ->195B -0.10905

Excited state symmetry could not be determined.
Excited State 11: ?Spin -?Sym 2.4266 eV 510.93 nm f=0.0002
191A ->198A -0.12873
191A ->199A -0.11958
191A ->205A -0.12298

192A ->194A 0.27518
192A ->197A -0.10538
192A ->198A 0.38883
192A ->199A 0.35920
191B ->198B -0.11354
191B ->199B -0.11217
191B ->205B -0.12103
192B ->194B -0.27974
192B ->197B -0.10878
192B ->198B 0.38792
192B ->199B 0.37550

Excited state symmetry could not be determined.
Excited State 12: ?Spin -?Sym 2.5076 eV 494.44 nm f=0.0024
191A ->198A 0.19833
191A ->199A 0.19217
192A ->194A 0.24838
192A ->197A -0.14920
192A ->198A 0.32830
192A ->199A 0.30927
192A ->200A 0.15552
192A ->204A -0.13729
192A ->205A -0.15787
191B ->198B -0.19366
191B ->199B -0.19849
192B ->194B 0.23855
192B ->197B 0.14659
192B ->198B -0.31167
192B ->199B -0.30585
192B ->200B -0.14866
192B ->204B 0.13627
192B ->205B 0.15794

Excited state symmetry could not be determined.
Excited State 13: ?Spin -?Sym 2.5956 eV 477.68 nm f=0.0005
187A ->193A -0.41351
188A ->193A 0.30284
189A ->196A -0.14345
190A ->193A 0.19815
192A ->196A -0.11682
187B ->193B 0.52485
188B ->193B -0.41674
189B ->196B -0.11247
190B ->193B -0.26138
192B ->196B 0.11140

Excited state symmetry could not be determined.
Excited State 14: ?Spin -?Sym 2.6008 eV 476.72 nm f=0.0053

187A ->193A	0.56461
188A ->193A	-0.40964
189A ->196A	-0.10894
190A ->193A	-0.26947
187B ->193B	0.43806
188B ->193B	-0.34451
189B ->196B	0.14056
190B ->193B	-0.21737

Excited state symmetry could not be determined.
Excited State 15: ?Spin -?Sym 2.6300 eV 471.42 nm f=0.0084

187A ->193A	-0.18232
188A ->193A	0.13625
188A ->199A	0.10120
191A ->198A	0.17039
191A ->199A	0.17483
192A ->194A	-0.18090
192A ->196A	0.20750
192A ->198A	-0.20402
192A ->199A	-0.17942
192A ->200A	0.15136
192A ->204A	-0.17084
192A ->205A	-0.22965
192A ->208A	-0.11090
187B ->193B	0.15508
188B ->193B	-0.12941
188B ->199B	0.10222
191B ->198B	-0.16815
191B ->199B	-0.18138
192B ->194B	-0.18289
192B ->196B	-0.20766
192B ->198B	0.20076
192B ->199B	0.18995
192B ->200B	-0.15495
192B ->204B	0.17056
192B ->205B	0.23028
192B ->208B	0.10816

Table S9. Excitation energies and oscillator strengths for BD - triplet electronic state. The results on each state include: the spin and spatial symmetry, the excitation energy, the oscillator strength, and (on the second line for each state) the largest coefficients in the CI expansion.

Excited State 1: ?Spin -A 0.8214 eV 1509.41 nm f=0.0000
190B ->193B 0.27705
191B ->192B 1.02744
191B ->197B -0.14867
This state for optimization and/or second-order correction.
Total Energy, E(RPA) = -2396.04963507
Copying the excited state density for this state as the 1-particle RhoCI density.

Excited State 2: ?Spin -A 0.8951 eV 1385.18 nm f=0.0002
190B ->192B 0.93453
190B ->194B -0.10686
190B ->197B -0.15950
191B ->193B -0.90688
191B ->196B -0.10793

Excited State 3: ?Spin -A 1.1141 eV 1112.84 nm f=0.0000
190B ->193B 1.01971
191B ->192B 0.22557

Excited State 4: ?Spin -A 1.6077 eV 771.18 nm f=0.0016
187B ->192B 0.18409
188B ->193B -0.39120
189B ->192B 0.82682
189B ->193B -0.26425
189B ->197B -0.11137

Excited State 5: ?Spin -A 1.6184 eV 766.09 nm f=0.0002
186B ->192B 0.17712
188B ->192B 0.81751
188B ->193B 0.26079
188B ->197B -0.11159
189B ->193B -0.41512

Excited State 6: ?Spin -A 1.8964 eV 653.77 nm f=0.0000
187B ->193B 0.18985
188B ->192B 0.37715
188B ->193B 0.16197
189B ->192B 0.31078
189B ->193B 0.81254

Excited State 7: ?Spin -A 1.9034 eV 651.38 nm f=0.0002
186B ->193B 0.18861
188B ->192B -0.31438
188B ->193B 0.82655
189B ->192B 0.34787
189B ->193B -0.15012

Excited State 8: ?Spin -A 2.1843 eV 567.61 nm f=0.4716
192A ->195A -0.14349
190B ->192B 0.55078
190B ->199B 0.12595
191B ->193B 0.59763

Excited State 9: ?Spin -A 2.5678 eV 482.84 nm f=0.0054
184A ->200A 0.11047
184A ->203A 0.14423
185A ->198A -0.10354
188A ->203A 0.11713
192A ->200A -0.12097
192A ->203A -0.13597
193A ->194A -0.32758
193A ->197A -0.23344
193A ->198A 0.76193
193A ->209A 0.12531
191B ->196B -0.10047
191B ->205B -0.16000
191B ->207B -0.14896

Excited State 10: ?Spin -A 2.6085 eV 475.31 nm f=0.0032
184A ->198A -0.16371
185A ->203A 0.11553
186A ->200A 0.10258
186A ->203A 0.12168
192A ->194A -0.26215
192A ->197A -0.20088
192A ->198A 0.68788
192A ->209A 0.11780
193A ->196A -0.15290
193A ->200A -0.20536
193A ->203A -0.24708
193A ->205A -0.11026
190B ->205B -0.10640
191B ->194B -0.12647
191B ->199B 0.19854

Excited State 11: ?Spin -A 2.6711 eV 464.18 nm f=0.0000

184A ->198A -0.18027
188A ->194A 0.12691
188A ->198A -0.16692
192A ->194A 0.14453
192A ->198A -0.36037
193A ->195A -0.10556
193A ->196A -0.15100
193A ->200A -0.19398
193A ->203A -0.23878
193A ->205A -0.10100
185B ->192B -0.16700
191B ->194B -0.46401
191B ->199B 0.53189
191B ->203B -0.10673
191B ->209B 0.12314

Excited State 12: ?Spin -A 2.6952 eV 460.02 nm f=0.0049
190A ->196A 0.12654
191A ->197A -0.16737
186B ->192B -0.17555
186B ->193B -0.12843
187B ->192B 0.85390
187B ->193B -0.19961
189B ->192B -0.20099
189B ->197B -0.10667

Excited State 13: ?Spin -A 2.6995 eV 459.29 nm f=0.0028
190A ->196A -0.11283
190A ->197A -0.15463
191A ->196A 0.13885
186B ->192B 0.84599
186B ->193B 0.20177
187B ->192B 0.17134
187B ->193B -0.13882
188B ->192B -0.19097
188B ->197B -0.10242
189B ->196B -0.10287

Excited State 14: ?Spin -A 2.7301 eV 454.15 nm f=0.0007
185A ->198A -0.12888
186A ->198A -0.15151
187A ->200A -0.16426
187A ->203A -0.20169
188A ->200A -0.10559
188A ->203A -0.12878
189A ->198A -0.25008

189A ->208A -0.12223
190A ->200A -0.16059
190A ->203A -0.20017
191A ->198A -0.27995
191A ->208A -0.12568
186B ->192B -0.11302
187B ->192B 0.12534
188B ->196B 0.14652
188B ->199B -0.16546
188B ->201B -0.10568
188B ->205B 0.26614
188B ->207B 0.26353
188B ->210B -0.10061
189B ->194B -0.11432
189B ->199B 0.40430
189B ->208B -0.16468
189B ->209B 0.15443
190B ->199B 0.12287

Excited State 15: ?Spin -A 2.7338 eV 453.53 nm f=0.0001
187A ->198A -0.27425
187A ->208A -0.12709
188A ->198A -0.16496
189A ->200A -0.18096
189A ->203A -0.21947
190A ->198A -0.27987
190A ->208A -0.12480
191A ->200A -0.17517
191A ->203A -0.21298
186B ->192B 0.14928
187B ->192B 0.10972
188B ->194B -0.11522
188B ->199B 0.41777
188B ->208B -0.16834
188B ->209B 0.15803
189B ->196B 0.14460
189B ->199B 0.13163
189B ->200B 0.10137
189B ->201B -0.12596
189B ->205B 0.27318
189B ->207B 0.26804
189B ->210B -0.10468

Excited State 16: ?Spin -A 2.7552 eV 450.00 nm f=0.0000
185A ->195A 0.14366
186A ->195A -0.15610

187A ->194A 0.10826
188A ->194A -0.20865
188A ->198A -0.12205
193A ->195A 0.29149
193A ->196A -0.14579
193A ->200A -0.15029
193A ->203A -0.15406
184B ->195B 0.20030
185B ->192B 0.59408
185B ->194B 0.17920
191B ->194B 0.33038
191B ->197B 0.24169
191B ->199B 0.27162

Excited State 17: ?Spin -A 2.7605 eV 449.14 nm f=0.0006
185A ->194A 0.11658
186A ->194A -0.19190
187A ->195A 0.11519
188A ->195A -0.22208
189A ->198A -0.12206
192A ->200A 0.15014
192A ->203A 0.12055
193A ->194A 0.27048
193A ->197A -0.10960
193A ->198A 0.12944
182B ->192B -0.12349
184B ->192B 0.55030
184B ->194B 0.18293
185B ->195B 0.19388
190B ->194B 0.21877
190B ->199B -0.28565
191B ->195B 0.36406

Excited State 18: ?Spin -A 2.7707 eV 447.49 nm f=0.0138
185A ->194A -0.11286
185A ->198A 0.14180
186A ->198A 0.20021
188A ->195A 0.13110
189A ->198A -0.20998
192A ->196A 0.21645
192A ->200A 0.23342
192A ->203A 0.30646
192A ->205A 0.12383
193A ->194A -0.25584
184B ->192B -0.20591
184B ->194B -0.10079

190B ->194B	0.32139		
190B ->199B	-0.45135		
190B ->209B	-0.11374		
191B ->195B	-0.32490		
Excited State 19:	?Spin -A	2.8366 eV	437.09 nm f=0.0033
193A ->194A	-0.22218		
193A ->198A	-0.10337		
168B ->192B	-0.19750		
169B ->192B	-0.12022		
181B ->192B	0.17083		
182B ->192B	-0.33314		
183B ->193B	-0.11322		
184B ->192B	0.60223		
190B ->199B	0.10911		
191B ->195B	-0.50937		
191B ->196B	0.18149		
Excited State 20:	?Spin -A	2.8855 eV	429.68 nm f=0.0000
193A ->195A	-0.25049		
193A ->196A	0.10864		
193A ->200A	0.11419		
185B ->192B	0.73053		
191B ->194B	-0.51935		
191B ->197B	-0.16264		

Table S10. Excitation energies and oscillator strengths for optimized $[(bpy)_2(H_2O)RuORu(OH_2)(bpy)_2]^{5+}$ with IEF-PCM (acetonitrile). The results on each state include: the spin and spatial symmetry, the excitation energy, the oscillator strength, and (on the second line for each state) the largest coefficients in the CI expansion.

Excited State 1:	?Spin -B	-0.8652 eV	-1432.99 nm f=-0.0005
171A ->193A	-0.16209		
175A ->193A	-0.23022		
187A ->193A	-0.77554		
189A ->193A	0.26327		
190A ->193A	0.29371		
192A ->193A	0.11119		
170B ->192B	0.15138		
174B ->192B	-0.12521		
176B ->192B	-0.19086		
186B ->192B	0.78256		
188B ->193B	0.12855		
189B ->192B	-0.28835		

This state for optimization and/or second-order correction.
Total Energy, E(RPA) = -2396.59773146
Copying the excited state density for this state as the 1-particle RhoCI density.

Excited State 2: ?Spin -B 0.2143 eV 5785.83 nm f=0.0002
174A ->193A -0.10839
175A ->193A 0.11239
187A ->193A 0.41254
189A ->193A -0.21845
190A ->193A 0.60819
192A ->193A 0.72050
176B ->192B 0.10024
186B ->192B -0.38752
188B ->193B 0.35647
189B ->192B 0.14979

Excited State 3: ?Spin -A 0.5859 eV 2116.19 nm f=0.0001
172B ->192B 0.11721
188B ->192B 0.90927
191B ->192B -0.14043

Excited State 4: ?Spin -A 0.9383 eV 1321.31 nm f=0.0000
176A ->193A -0.13735
177A ->193A -0.10809
184A ->193A 0.13661
186A ->193A -0.38731
191A ->193A -0.13375
174B ->193B 0.14957
177B ->192B 0.23875
184B ->193B 0.41592
185B ->192B 0.76625
191B ->192B 0.21775

Excited State 5: ?Spin -B 0.9436 eV 1313.93 nm f=0.0005
185A ->193A -0.30775
187A ->193A -0.25273
189A ->193A 0.14288
172B ->193B 0.12039
174B ->192B 0.18952
179B ->192B -0.10485
184B ->192B 0.59705
185B ->193B 0.29998
186B ->192B -0.21312
188B ->193B 0.63058
189B ->192B 0.11817
190B ->192B 0.18259

Excited State 6: ?Spin -B 0.9610 eV 1290.19 nm f=0.0001

175A ->193A	-0.11414
185A ->193A	0.25628
187A ->193A	-0.28481
189A ->193A	0.15789
190A ->193A	0.14789
192A ->193A	-0.11952
174B ->192B	-0.12637
177B ->193B	-0.13017
184B ->192B	-0.48740
185B ->193B	-0.31828
186B ->192B	-0.25121
188B ->193B	0.70761
189B ->192B	0.14692
191B ->193B	-0.17083

Excited State 7: ?Spin -A 1.2324 eV 1006.01 nm f=0.0004

184A ->193A	-0.32989
186A ->193A	0.10136
188A ->193A	0.12410
191A ->193A	0.80548
184B ->193B	0.14134
185B ->192B	0.14731
186B ->193B	0.36097
188B ->192B	0.15278
189B ->193B	-0.17267

Excited State 8: ?Spin -B 1.2607 eV 983.42 nm f=0.0003

185A ->193A	0.33530
187A ->193A	0.12620
189A ->193A	-0.14643
190A ->193A	0.62203
192A ->193A	-0.61027
184B ->192B	0.16956
185B ->193B	0.14149

Excited State 9: ?Spin -A 1.2688 eV 977.15 nm f=0.0000

153A ->193A	0.12846
155A ->193A	0.13100
170A ->193A	-0.12858
179A ->193A	-0.11931
184A ->193A	-0.31412
186A ->193A	-0.47411
188A ->193A	0.19452
191A ->193A	-0.36544

185B ->192B -0.11364
186B ->193B 0.63722
188B ->192B 0.25727
189B ->193B -0.30541

Excited State 10: ?Spin -A 1.3847 eV 895.38 nm f=0.0000
176A ->193A 0.16747
177A ->193A 0.13011
184A ->193A -0.19144
186A ->193A 0.64890
188A ->193A 0.15961
191A ->193A -0.39702
184B ->193B 0.10935
186B ->193B 0.16926
188B ->192B 0.14552
190B ->193B 0.10943
191B ->192B 0.46315

Excited State 11: ?Spin -B 1.3928 eV 890.20 nm f=0.0001
173A ->193A 0.12191
175A ->193A -0.12095
178A ->193A 0.13903
185A ->193A 0.70388
189A ->193A 0.13342
190A ->193A -0.22599
192A ->193A 0.28496
185B ->193B 0.10248
190B ->192B 0.49780
191B ->193B 0.14183

Excited State 12: ?Spin -A 1.4512 eV 854.35 nm f=0.0032
186A ->193A -0.31373
188A ->193A -0.16887
191A ->193A 0.17031
184B ->193B -0.18706
185B ->192B -0.25125
190B ->193B 0.14136
191B ->192B 0.81879

Excited State 13: ?Spin -B 1.4518 eV 854.02 nm f=0.0027
185A ->193A -0.34474
189A ->193A -0.28080
192A ->193A -0.13018
184B ->192B -0.22173
185B ->193B -0.17230
190B ->192B 0.79653

191B ->193B 0.12548

Excited State 14: ?Spin -B 1.4640 eV 846.90 nm f=0.0056
185A ->193A -0.16305
187A ->193A 0.36806
189A ->193A 0.86021
190A ->193A 0.15456
188B ->193B -0.10943
190B ->192B 0.18621

Excited State 15: ?Spin -A 1.5273 eV 811.79 nm f=0.0008
186A ->193A -0.10498
188A ->193A 0.93363
186B ->193B -0.24473
187B ->192B 0.11199
188B ->192B -0.12591
189B ->193B 0.11318

Excited State 16: ?Spin -B 1.6112 eV 769.53 nm f=0.0066
186B ->192B 0.34479
187B ->193B -0.16550
189B ->192B 0.91606

Excited State 17: ?Spin -A 1.6205 eV 765.09 nm f=0.0002
170A ->193A 0.13807
172A ->193A 0.11454
176A ->193A -0.10035
179A ->193A -0.13072
184A ->193A 0.72489
186A ->193A 0.12288
186B ->193B 0.29340
187B ->192B 0.37664
188B ->192B 0.15712
189B ->193B -0.28228

Excited State 18: ?Spin -A 1.6763 eV 739.63 nm f=0.0012
184A ->193A -0.31653
188A ->193A -0.12512
186B ->193B -0.19027
187B ->192B 0.89523
188B ->192B -0.10024

Excited State 19: ?Spin -B 1.8801 eV 659.46 nm f=0.0022
184B ->192B -0.18767
185B ->193B 0.15554
188B ->193B 0.15059

190B ->192B -0.19130
191B ->193B 0.93419

Excited State 20: ?Spin -A 1.8891 eV 656.31 nm f=0.0014
184B ->193B 0.16020
185B ->192B -0.16201
190B ->193B 0.94613
191B ->192B -0.18466

Excited State 21: ?Spin -A 2.0723 eV 598.30 nm f=0.0000
184B ->193B 0.28067
185B ->192B -0.16522
186B ->193B 0.38651
187B ->192B 0.18250
189B ->193B 0.83051

Excited State 22: ?Spin -B 2.0836 eV 595.05 nm f=0.0029
177B ->193B 0.15114
184B ->192B -0.46639
185B ->193B 0.72294
187B ->193B -0.39390
191B ->193B -0.22103

Excited State 23: ?Spin -A 2.0989 eV 590.72 nm f=0.0001
174B ->193B 0.15179
184B ->193B 0.75140
185B ->192B -0.47217
186B ->193B -0.20399
189B ->193B -0.26147
190B ->193B -0.22114

Excited State 24: ?Spin -B 2.1219 eV 584.30 nm f=0.0022
184B ->192B -0.17995
185B ->193B 0.32761
186B ->192B 0.10864
187B ->193B 0.89892
189B ->192B 0.12715

Excited State 25: ?Spin -B 2.4556 eV 504.90 nm f=0.5279
171A ->193A -0.11752
175A ->193A -0.23166
178A ->193A -0.14491
187A ->193A 0.43812
172B ->193B -0.10135
176B ->192B 0.17524
186B ->192B 0.42999

188B ->193B 0.38317
188B ->196B 0.12227

Excited State 26: ?Spin -A 2.5057 eV 494.81 nm f=0.0004
153A ->193A -0.21650
155A ->193A -0.23879
161A ->193A 0.10821
163A ->193A -0.12721
164A ->193A -0.15739
176A ->193A 0.12080
179A ->193A 0.74322
152B ->192B 0.26465
154B ->192B 0.12724
178B ->192B -0.39960
179B ->193B 0.15158
186B ->193B 0.19819
188B ->192B 0.12028

Excited State 27: ?Spin -A 2.6215 eV 472.96 nm f=0.0004
180A ->193A 0.11082
182A ->193A 0.93795
184A ->193A -0.12732
182B ->192B -0.24301

Excited State 28: ?Spin -B 2.6260 eV 472.14 nm f=0.0117
181A ->193A 0.13496
183A ->193A 0.94245
183B ->192B -0.24117

Excited State 29: ?Spin -A 2.6359 eV 470.36 nm f=0.0024
182A ->193A 0.11417
184A ->199A 0.16303
184A ->209A 0.13089
190A ->194A 0.35450
190A ->196A 0.46594
190A ->198A 0.26419
192A ->194A 0.36190
192A ->196A 0.47604
192A ->198A 0.25524
186B ->196B 0.13607
188B ->199B -0.15981

Excited State 30: ?Spin -B 2.7101 eV 457.48 nm f=0.0033
173A ->193A -0.10448
175A ->193A -0.16107
178A ->193A 0.59018

183A ->193A -0.12739
185A ->193A -0.11423
155B ->192B 0.11718
163B ->192B 0.11532
165B ->192B 0.10363
174B ->192B 0.10584
179B ->192B 0.66453
183B ->192B -0.16931

Excited State 31: ?Spin -B 2.7401 eV 452.48 nm f=0.0458
178A ->193A 0.14780
181A ->193A 0.11677
183A ->193A 0.21173
179B ->192B 0.11485
181B ->192B 0.11364
182B ->193B -0.22724
183B ->192B 0.90174

Excited State 32: ?Spin -A 2.7406 eV 452.40 nm f=0.0185
180A ->193A 0.13212
182A ->193A 0.23654
180B ->192B 0.10497
182B ->192B 0.91394
183B ->193B -0.22042

Excited State 33: ?Spin -A 2.7729 eV 447.12 nm f=0.0001
176A ->193A 0.35940
177A ->193A 0.30407
179A ->193A -0.19177
180A ->193A 0.81135
186A ->193A -0.16181
180B ->192B -0.11501

Excited State 34: ?Spin -B 2.7840 eV 445.34 nm f=0.0044
173A ->193A -0.21526
174A ->193A 0.15347
175A ->193A 0.14191
178A ->193A -0.40740
181A ->193A 0.74202
185A ->193A 0.17082
179B ->192B 0.31606
181B ->192B -0.11261

Excited State 35: ?Spin -B 2.8012 eV 442.61 nm f=0.0020
178A ->193A 0.55749
181A ->193A 0.56632

183A ->193A -0.12991
179B ->192B -0.52450

Excited State 36: ?Spin -A 2.8497 eV 435.08 nm f=0.0000
176A ->193A 0.42935
177A ->193A 0.65026
179A ->193A -0.12030
180A ->193A -0.51577
182A ->193A 0.12673
184A ->193A 0.13721
186A ->193A -0.19780
177B ->192B -0.12236

Excited State 37: ?Spin -B 2.8701 eV 431.98 nm f=0.0049
173A ->193A -0.13188
175A ->193A 0.25210
178A ->193A 0.13740
181A ->193A -0.13792
184A ->194A -0.15389
184A ->196A -0.21973
184A ->198A -0.10207
184A ->200A -0.10222
190A ->197A -0.13512
190A ->199A -0.35306
192A ->197A -0.19902
192A ->199A -0.33300
186B ->199B -0.14880
188B ->194B -0.28187
188B ->196B 0.45400
188B ->198B 0.29142

Excited State 38: ?Spin -A 2.9037 eV 426.99 nm f=0.0001
176A ->193A 0.11289
191A ->197A 0.10789
172B ->192B 0.14849
175B ->192B -0.13804
177B ->192B 0.36962
180B ->192B 0.77880
181B ->193B -0.17507
185B ->192B -0.13862
191B ->197B -0.12332

Excited State 39: ?Spin -B 2.9134 eV 425.56 nm f=0.0030
181A ->193A 0.13837
185A ->199A -0.13096
186A ->194A -0.10005

186A ->196A -0.14902
190A ->197A -0.11111
174B ->192B -0.32166
176B ->192B 0.10723
180B ->193B -0.17235
181B ->192B 0.72462
184B ->192B 0.11578
184B ->199B 0.15238
185B ->196B 0.15938
190B ->197B 0.14876

Excited State 40: ?Spin -A 2.9210 eV 424.46 nm f=0.0022
172A ->193A 0.13046
176A ->193A 0.11750
179A ->193A 0.39667
172B ->192B 0.12570
177B ->192B -0.11647
178B ->192B 0.78517
179B ->193B 0.24667

Excited State 41: ?Spin -B 2.9312 eV 422.98 nm f=0.0135
173A ->193A -0.18942
175A ->193A 0.51721
185A ->197A 0.10373
185A ->199A 0.20009
186A ->194A 0.14750
186A ->196A 0.20296
186A ->200A 0.12017
174B ->192B 0.11467
176B ->192B 0.31165
181B ->192B 0.40008
184B ->199B -0.23054
185B ->194B 0.13020
185B ->196B -0.20937
185B ->198B -0.12173
185B ->200B -0.12720
186B ->192B 0.10049

Excited State 42: ?Spin -A 2.9352 eV 422.40 nm f=0.0008
176A ->199A -0.13843
177A ->199A -0.10731
185A ->194A -0.20534
185A ->196A -0.28863
185A ->198A -0.11888
185A ->200A -0.20230
186A ->197A -0.14237

186A ->199A -0.30620
191A ->197A -0.13726
174B ->196B 0.10954
177B ->199B 0.14815
178B ->192B -0.17281
180B ->192B 0.28332
184B ->194B -0.20211
184B ->196B 0.34083
184B ->198B 0.18201
184B ->200B 0.20299
185B ->197B 0.15477
185B ->199B 0.36695
190B ->196B 0.11303
191B ->197B 0.13628

Excited State 43: ?Spin -B 2.9370 eV 422.14 nm f=0.0229
173A ->193A 0.40602
174A ->193A -0.20729
175A ->193A -0.36997
181A ->193A 0.16834
184A ->196A -0.13155
185A ->193A -0.14480
185A ->199A 0.22662
186A ->194A 0.11026
186A ->196A 0.15231
186A ->200A 0.12947
192A ->197A -0.13363
174B ->192B -0.20759
176B ->192B -0.10786
181B ->192B 0.12403
184B ->197B -0.10314
184B ->199B -0.25936
185B ->194B 0.13976
185B ->196B -0.24244
185B ->198B -0.13614
185B ->200B -0.14418
191B ->196B -0.10031

Excited State 44: ?Spin -B 2.9509 eV 420.16 nm f=0.0089
173A ->193A 0.52261
174A ->193A -0.46344
175A ->193A 0.38943
181A ->193A 0.14124
187A ->193A -0.10364
176B ->192B 0.35604
178B ->193B 0.11965

179B ->192B 0.15638
181B ->192B -0.26628

Excited State 45: ?Spin -A 2.9875 eV 415.01 nm f=0.0027
172A ->193A 0.24938
176A ->193A 0.40590
177A ->193A -0.21682
180A ->193A -0.10541
188A ->195A 0.10815
189A ->194A 0.10979
191A ->197A 0.14036
192A ->198A 0.11193
172B ->192B -0.14559
177B ->192B 0.55932
179B ->193B -0.11117
180B ->192B -0.30534
184B ->193B -0.10058
185B ->192B -0.11624
185B ->199B 0.12192
187B ->195B 0.10091
190B ->198B 0.13457
191B ->197B -0.14469

Excited State 46: ?Spin -A 2.9924 eV 414.33 nm f=0.0003
172A ->193A -0.13512
176A ->193A -0.44517
177A ->193A 0.45974
188A ->195A -0.17707
189A ->194A -0.19564
175B ->192B -0.14531
177B ->192B 0.49436
180B ->192B -0.28881
185B ->192B -0.13338
187B ->195B -0.17078
189B ->194B -0.18939

Excited State 47: ?Spin -B 3.0002 eV 413.25 nm f=0.0004
180A ->212A -0.10253
181A ->213A -0.10283
185A ->199A 0.13044
190A ->197A -0.27923
191A ->196A -0.22017
191A ->198A 0.39884
191A ->205A -0.10754
192A ->197A 0.34814
192A ->199A -0.14956

180B ->212B 0.10237
181B ->192B -0.17317
181B ->213B 0.10289
184B ->199B -0.14316
185B ->198B -0.11435
190B ->197B 0.43707
190B ->199B -0.11759
190B ->206B -0.10923
191B ->194B -0.13682
191B ->196B 0.19420
191B ->198B -0.38081
191B ->205B 0.10001

Excited State 48: ?Spin -A 3.0012 eV 413.12 nm f=0.0000
176A ->193A -0.18185
177A ->193A 0.13712
190A ->196A 0.14407
190A ->198A -0.21551
191A ->197A 0.42471
191A ->199A -0.12831
191A ->206A -0.12063
192A ->196A -0.16583
192A ->198A 0.31811
177B ->192B -0.29404
185B ->199B 0.10560
190B ->194B 0.14415
190B ->196B -0.19633
190B ->198B 0.35347
191B ->197B -0.41847
191B ->199B 0.11459
191B ->206B 0.10162

Excited State 49: ?Spin -A 3.0129 eV 411.51 nm f=0.0002
172A ->193A -0.25531
176A ->193A -0.20402
177A ->193A 0.22733
188A ->195A 0.37967
189A ->194A 0.42383
189A ->196A -0.17508
189A ->201A 0.12309
172B ->192B 0.16801
177B ->192B 0.10054
178B ->192B 0.12271
179B ->193B 0.10688
187B ->195B 0.38226
187B ->202B 0.11047

189B ->194B 0.41345
189B ->196B 0.16797
189B ->201B -0.11605

Excited State 50: ?Spin -B 3.0142 eV 411.33 nm f=0.0011
173A ->193A 0.12873
188A ->194A 0.41673
188A ->196A -0.20935
188A ->201A 0.14218
189A ->195A 0.50334
173B ->210B -0.10250
176B ->192B -0.10751
187B ->194B -0.41207
187B ->196B -0.19145
187B ->201B 0.13355
189B ->195B -0.50352
189B ->202B -0.11027

Excited State 51: ?Spin -B 3.0376 eV 408.17 nm f=0.0175
173A ->193A 0.24044
174A ->193A -0.11847
173B ->192B 0.13785
174B ->192B 0.70992
176B ->192B -0.33046
177B ->193B 0.17189
181B ->192B 0.34511
184B ->192B -0.19912
185B ->193B -0.14549

Excited State 52: ?Spin -A 3.0658 eV 404.41 nm f=0.0018
169A ->193A -0.16848
172A ->193A 0.63533
176A ->193A -0.34360
177A ->193A 0.28515
184A ->193A -0.12420
169B ->192B 0.11233
172B ->192B -0.42515
175B ->192B 0.12993
179B ->193B -0.11378
180B ->192B 0.16616

Excited State 53: ?Spin -B 3.1043 eV 399.39 nm f=0.0051
171A ->193A -0.19107
173A ->193A 0.54587
174A ->193A 0.69888
175A ->193A 0.26618

174B ->192B -0.11448
176B ->192B -0.16361

Excited State 54: ?Spin -B 3.1319 eV 395.87 nm f=0.0375
171A ->193A 0.42950
173A ->193A 0.10679
174A ->193A 0.39475
175A ->193A -0.25715
170B ->192B 0.11285
174B ->192B 0.26484
176B ->192B 0.59841
178B ->193B 0.17745
182B ->193B -0.10037

Excited State 55: ?Spin -A 3.1348 eV 395.51 nm f=0.0002
172A ->193A -0.44716
169B ->192B 0.10517
172B ->192B -0.53213
175B ->192B 0.55632
177B ->192B 0.16583
178B ->192B 0.19873
180B ->192B 0.15038

Excited State 56: ?Spin -A 3.1697 eV 391.16 nm f=0.0002
172A ->193A -0.12406
184A ->199A 0.14385
187A ->194A 0.32452
187A ->196A 0.41807
187A ->198A 0.24047
189A ->196A -0.22927
189A ->198A -0.11198
190A ->200A 0.22599
192A ->200A 0.21448
172B ->192B -0.11681
175B ->192B -0.32634
186B ->194B 0.19428
186B ->196B -0.31537
186B ->198B -0.20759
188B ->209B 0.12083
189B ->196B 0.17781

Excited State 57: ?Spin -A 3.1834 eV 389.48 nm f=0.0005
155A ->193A 0.10424
172A ->193A 0.15405
179A ->193A 0.14066
187A ->194A 0.13794

187A ->196A 0.21419
169B ->192B -0.12346
172B ->192B 0.46380
173B ->193B -0.10991
175B ->192B 0.65357
179B ->193B -0.11863
183B ->193B -0.10570
186B ->196B -0.13636

Excited State 58: ?Spin -B 3.1992 eV 387.55 nm f=0.0001
184A ->200A 0.16287
190A ->197A 0.14912
190A ->199A 0.32439
192A ->197A 0.16940
192A ->199A 0.34299
174B ->192B -0.13570
182B ->193B -0.28230
186B ->209B -0.12693
188B ->194B -0.29049
188B ->196B 0.42912
188B ->198B 0.29764
188B ->200B -0.31020

Excited State 59: ?Spin -A 3.2019 eV 387.22 nm f=0.0000
184A ->199A 0.17522
184A ->209A -0.11359
190A ->198A -0.10371
190A ->200A 0.49319
192A ->198A -0.11151
192A ->200A 0.46945
183B ->193B -0.11740
186B ->194B -0.15128
186B ->196B 0.23444
186B ->198B 0.13822
186B ->200B 0.15593
188B ->197B -0.16159
188B ->199B -0.42270
189B ->196B -0.11774

Excited State 60: ?Spin -A 3.2149 eV 385.66 nm f=0.0078
153A ->193A -0.16056
155A ->193A -0.17391
161A ->193A 0.10852
163A ->193A -0.13796
164A ->193A -0.13754
169A ->193A -0.35092

172A ->193A 0.16696
179A ->193A -0.32401
155B ->193B 0.10139
172B ->192B 0.14945
174B ->193B 0.13968
175B ->192B 0.13532
177B ->192B 0.10233
179B ->193B 0.66082
183B ->193B -0.18960

Excited State 61: ?Spin -B 3.2183 eV 385.25 nm f=0.0174
192A ->199A 0.11508
173B ->192B -0.34379
178B ->193B 0.12641
182B ->193B 0.80962
183B ->192B 0.22068
188B ->196B 0.15241
188B ->198B 0.10465
188B ->200B -0.11096

Excited State 62: ?Spin -A 3.2249 eV 384.46 nm f=0.0092
175B ->192B 0.11753
179B ->193B 0.17139
181B ->193B 0.10351
182B ->192B 0.24097
183B ->193B 0.90845

Excited State 63: ?Spin -B 3.2438 eV 382.22 nm f=0.0020
173B ->192B 0.86753
174B ->192B -0.13291
175B ->193B -0.19078
177B ->193B -0.10273
182B ->193B 0.35835

Excited State 64: ?Spin -B 3.2750 eV 378.58 nm f=0.0095
171A ->193A 0.75628
175A ->193A 0.12431
170B ->192B -0.42424
172B ->193B -0.22221
176B ->192B -0.17921
178B ->193B -0.26075

Excited State 65: ?Spin -A 3.3038 eV 375.28 nm f=0.0004
170A ->193A 0.92766
172A ->193A -0.12038
184A ->193A -0.17084

171B ->192B -0.21673

Excited State 66: ?Spin -B 3.3385 eV 371.37 nm f=0.0353
171A ->193A 0.14286
152B ->193B -0.13359
170B ->192B -0.18298
174B ->192B -0.13822
176B ->192B -0.26270
177B ->193B 0.10652
178B ->193B 0.85696
182B ->193B -0.11799

Excited State 67: ?Spin -A 3.3788 eV 366.95 nm f=0.0001
169A ->193A 0.70975
172A ->193A 0.18798
152B ->192B -0.13483
169B ->192B -0.28779
172B ->192B -0.20296
174B ->193B -0.14398
178B ->192B -0.15293
179B ->193B 0.40136
181B ->193B 0.10718

Excited State 68: ?Spin -A 3.3955 eV 365.14 nm f=0.0003
170A ->193A 0.14464
170B ->193B -0.14039
171B ->192B 0.67183
176B ->193B -0.34046
180B ->192B -0.13299
181B ->193B -0.50304

Excited State 69: ?Spin -B 3.3973 eV 364.95 nm f=0.0035
172B ->193B 0.11314
174B ->192B -0.12249
175B ->193B -0.12597
177B ->193B 0.23512
178B ->193B -0.17830
180B ->193B 0.88530
181B ->192B 0.19471

Excited State 70: ?Spin -A 3.4096 eV 363.63 nm f=0.0002
169A ->193A -0.23701
170A ->193A 0.10994
172A ->193A -0.11913
171B ->192B 0.42146
174B ->193B -0.14079

176B ->193B -0.13523
180B ->192B 0.16145
181B ->193B 0.77025

Excited State 71: ?Spin -B 3.4345 eV 360.99 nm f=0.0008
171A ->193A 0.15259
185A ->199A 0.10938
170B ->192B 0.57473
171B ->193B -0.18497
172B ->193B -0.17198
174B ->192B -0.17883
175B ->193B -0.10494
177B ->193B 0.52186
180B ->193B -0.21773
185B ->193B -0.13770
185B ->198B 0.10065
188B ->194B 0.14372
188B ->196B 0.10845

Excited State 72: ?Spin -A 3.4668 eV 357.63 nm f=0.0000
153A ->193A -0.14770
155A ->193A -0.17245
164A ->193A -0.13959
169A ->193A 0.31905
179A ->193A -0.13905
152B ->192B 0.19100
170B ->193B -0.10427
171B ->192B 0.29114
172B ->192B 0.13490
174B ->193B 0.52444
176B ->193B 0.29900
177B ->192B -0.10106
179B ->193B -0.18259
181B ->193B 0.18336
184B ->193B -0.10489
184B ->200B 0.11406
186B ->193B 0.15717

Excited State 73: ?Spin -B 3.4779 eV 356.49 nm f=0.0008
184A ->196A 0.27430
184A ->198A 0.11752
186A ->196A 0.22532
186A ->198A 0.10765
186A ->200A -0.16277
187A ->197A 0.14048
187A ->199A 0.26273

189A ->199A -0.11674
190A ->195A -0.23092
190A ->209A 0.19990
192A ->195A -0.24550
192A ->209A 0.18704
172B ->193B 0.25800
180B ->193B -0.15113
185B ->200B 0.11792
186B ->199B -0.24357
188B ->194B -0.19628
188B ->200B 0.30684
188B ->201B -0.10009
189B ->199B 0.11511

Excited State 74: ?Spin -B 3.4920 eV 355.05 nm f=0.0360
171A ->193A -0.21226
185A ->199A -0.11015
190A ->195A 0.10934
192A ->195A 0.12601
170B ->192B -0.44733
171B ->193B 0.15145
174B ->192B -0.11509
176B ->192B 0.14953
177B ->193B 0.67101
180B ->193B -0.15739
185B ->193B -0.13174
185B ->196B -0.15706

Excited State 75: ?Spin -A 3.5036 eV 353.88 nm f=0.0000
176A ->199A -0.10731
185A ->200A -0.35657
186A ->197A -0.12043
186A ->199A -0.26673
186A ->209A 0.14582
171B ->192B 0.12618
174B ->193B -0.34883
176B ->193B 0.40396
177B ->192B 0.10989
179B ->193B 0.14993
181B ->193B -0.14887
184B ->193B 0.13339
184B ->194B 0.17931
184B ->196B -0.24842
184B ->198B -0.20807
184B ->200B 0.13905
185B ->209B -0.16343

Table S11. Excitation energies and oscillator strengths for $Ru(bpy)_2Cl_2$ with IEF-PCM (water). The results on each state include: the spin and spatial symmetry, the excitation energy, the oscillator strength, and (on the second line for each state) the largest coefficients in the CI expansion.

Excited State 1: Singlet-B 1.9758 eV 627.51 nm f=0.0142 <S**2>=0.000
97 -> 98 0.68959
This state for optimization and/or second-order correction.
Total Energy, E(TD-HF/TD-KS) = -1114.55663734
Copying the excited state density for this state as the 1-particle RhoCI density.

Excited State 2: Singlet-A 2.0020 eV 619.31 nm f=0.0020 <S**2>=0.000
95 -> 99 -0.18434
97 -> 99 0.66984

Excited State 3: Singlet-B 2.2315 eV 555.61 nm f=0.0047 <S**2>=0.000
95 -> 98 -0.38997
96 -> 99 0.57863

Excited State 4: Singlet-A 2.2875 eV 542.02 nm f=0.0000 <S**2>=0.000
95 -> 99 -0.39775
96 -> 98 0.57383

Excited State 5: Singlet-B 2.4438 eV 507.35 nm f=0.1560 <S**2>=0.000
95 -> 98 0.57210
96 -> 99 0.37558
97 -> 98 0.11633

Excited State 6: Singlet-A 2.6006 eV 476.76 nm f=0.0097 <S**2>=0.000
95 -> 99 0.51180
96 -> 98 0.35466
97 -> 99 0.19236
97 ->103 0.23482

Excited State 7: Singlet-B 2.8871 eV 429.45 nm f=0.0179 <S**2>=0.000
97 ->100 0.64558
97 ->102 -0.14293
97 ->104 0.21918

Excited State 8: Singlet-B 2.9661 eV 418.00 nm f=0.0162 <S**2>=0.000
95 ->104 0.10862
97 ->100 -0.25243
97 ->102 -0.19246
97 ->104 0.59785

Excited State 9: Singlet-A 3.0997 eV 399.99 nm f=0.0000 <S**2>=0.000
96 ->100 -0.17941
97 ->101 0.65877

Excited State 10: Singlet-A 3.1379 eV 395.11 nm f=0.0046 <S**2>=0.000
96 ->100 0.61393
97 ->101 0.21320
97 ->103 0.24884

Excited State 11: Singlet-B 3.1925 eV 388.36 nm f=0.0270 <S**2>=0.000
95 ->100 -0.35626
95 ->104 0.10770
97 ->102 0.55109
97 ->104 0.19978

Excited State 12: Singlet-B 3.2358 eV 383.17 nm f=0.0585 <S**2>=0.000
95 ->100 0.59668
96 ->101 0.10467
97 ->102 0.31900

Excited State 13: Singlet-A 3.2435 eV 382.25 nm f=0.0188 <S**2>=0.000
95 -> 99 -0.13348
95 ->101 -0.15354
95 ->103 -0.21273
96 ->100 -0.25534
96 ->102 -0.30369
96 ->104 0.24244
97 ->103 0.40648

Excited State 14: Singlet-B 3.3468 eV 370.46 nm f=0.0329 <S**2>=0.000
96 ->103 0.66892
96 ->107 -0.14849

Excited State 15: Singlet-B 3.3742 eV 367.45 nm f=0.0308 <S**2>=0.000
95 ->102 -0.18027
95 ->104 0.24363
96 ->101 0.59749
96 ->103 0.11457
96 ->107 0.10248
97 ->102 -0.11455

Excited State 16: Singlet-A 3.4017 eV 364.47 nm f=0.0116 <S**2>=0.000
95 ->101 0.46461
95 ->103 -0.23967
95 ->107 0.14507

96 ->102 -0.22169
96 ->104 0.22317
97 ->103 -0.26480
97 ->107 -0.14279

Excited State 17: Singlet-A 3.4571 eV 358.64 nm f=0.0149 <S**2>=0.000
95 ->101 -0.22894
95 ->103 -0.37694
95 ->107 0.10758
96 ->102 0.44169
96 ->104 0.25693
97 ->103 -0.12563

Excited State 18: Singlet-B 3.4741 eV 356.89 nm f=0.0232 <S**2>=0.000
95 ->102 -0.10296
95 ->104 0.53151
96 ->101 -0.31829
96 ->107 0.26863

Excited State 19: Singlet-A 3.5073 eV 353.51 nm f=0.0007 <S**2>=0.000
95 ->101 -0.15882
95 ->103 0.46555
95 ->107 0.20385
96 ->104 0.40944
97 ->103 -0.12750
97 ->107 -0.12686

Excited State 20: Singlet-B 3.5193 eV 352.30 nm f=0.0526 <S**2>=0.000
95 ->102 0.65520
95 ->104 0.17366
96 ->101 0.12546

Table S12. Cartesian Coordinates for BD (optimized geometry, strong coupling)

Element	x	y	z
H	-2.29462	-2.45960	-0.71279
H	-6.54091	2.55688	-0.62755
H	4.05373	4.17512	3.82234
H	-5.54382	-2.49042	2.76632
H	-4.06360	2.34967	-0.67864
H	-7.88417	0.82383	0.62555
H	-6.68443	-1.02644	1.77455
H	-0.67761	-2.11229	2.05471
H	-1.56358	-3.99934	3.47100
H	-1.22218	3.39603	0.84830
H	-1.06996	5.37488	-0.69046
H	-1.34172	5.00097	-3.17073
H	-1.73118	2.69040	-4.01323
H	-2.72119	-3.35267	-3.00737
H	-2.66083	-1.75951	-4.96497
H	-2.15667	0.64336	-4.54697
H	2.15671	-0.64333	-4.54697
H	4.06361	-2.34966	-0.67865
H	1.56355	3.99933	3.47099
H	0.67759	2.11229	2.05470
H	1.22217	-3.39604	0.84828
H	-4.05375	-4.17511	3.82233
H	2.29461	2.45961	-0.71278
H	2.72121	3.35268	-3.00735
H	7.88416	-0.82384	0.62559
H	1.34172	-5.00095	-3.17076
H	2.66087	1.75954	-4.96495
H	6.54092	-2.55688	-0.62754
H	6.68442	1.02643	1.77459
H	5.54380	2.49042	2.76633
H	1.06995	-5.37488	-0.69050
H	1.73119	-2.69038	-4.01324
H	2.67709	-1.94942	2.72987
H	1.43107	-1.06294	3.23012
H	-1.43103	1.06291	3.23010
H	-2.67708	1.94937	2.72989

C	-2.25517	-1.80917	-1.57691
C	-6.05495	1.73343	-0.11501
C	-2.24087	-3.28081	3.02125
C	-1.23190	4.37963	-1.09112
C	-2.49153	-2.30164	-2.86713
C	-3.63300	-3.37835	3.21665
C	-1.38301	4.16656	-2.47701
C	-2.45640	-1.41073	-3.95730
C	-6.11848	-0.27649	1.23469
C	-4.47257	-2.42537	2.61747
C	-1.31463	3.28097	-0.22536
C	-2.17282	-0.05561	-3.71836
C	-4.71455	-0.33831	1.17815
C	-3.91613	-1.39398	1.83621
C	-1.68163	1.79352	-2.03665
C	-1.94386	0.39009	-2.40382
C	1.60370	-2.86123	-2.95029
C	-6.80074	0.76726	0.58534
C	-4.65833	1.61945	-0.14675
C	-1.73854	-2.23589	2.23527
C	2.45643	1.41075	-3.95728
C	6.11847	0.27649	1.23472
C	2.24085	3.28081	3.02124
C	4.47255	2.42537	2.61748
C	1.23190	-4.37962	-1.09115
C	1.94387	-0.39007	-2.40382
C	2.49154	2.30165	-2.86711
C	2.17285	0.05563	-3.71836
C	4.65833	-1.61945	-0.14674
C	4.71454	0.33831	1.17817
C	3.91611	1.39398	1.83622
C	1.31463	-3.28097	-0.22538
C	1.68164	-1.79351	-2.03666
C	2.25517	1.80917	-1.57690
C	1.38302	-4.16655	-2.47704
C	1.73853	2.23589	2.23526
C	-1.60369	2.86124	-2.95027
C	6.80074	-0.76726	0.58537
C	6.05495	-1.73343	-0.11499
C	3.63297	3.37835	3.21665

N	-2.55392	-1.31074	1.65211
N	-1.54112	2.01742	-0.68339
N	-1.99421	-0.49284	-1.34248
N	1.54113	-2.01742	-0.68340
N	1.99421	0.49284	-1.34247
N	-3.99029	0.61164	0.48628
N	2.55391	1.31074	1.65211
N	3.99029	-0.61164	0.48628
O	-1.86800	1.47047	2.45621
O	0.00000	0.00001	0.88512
O	1.86802	-1.47048	2.45620
Ru	-1.86067	0.34863	0.52173
Ru	1.86067	-0.34864	0.52173

Table S13. Cartesian Coordinates for BD×4H_2O (optimized geometry, strong coupling)

Element	x	y	z
H	-5.17180	-1.58605	-1.41008
H	-4.56435	-1.81287	-3.84729
H	-2.16197	-1.95828	-4.48691
H	3.84056	-2.26848	-2.99006
H	1.84344	-6.43895	1.44160
H	-0.05778	-2.18096	-4.84475
H	0.05778	2.18096	-4.84475
H	1.78745	4.29870	-1.11187
H	-3.75724	0.96647	3.52485
H	-1.80896	0.35537	2.04749
H	2.41243	-2.40788	-5.06703
H	3.33111	1.55416	0.29040
H	4.37584	-3.39710	3.76895
H	2.72540	-1.93595	-0.78071
H	-1.58235	-6.78199	-1.16227
H	-4.37584	3.39710	3.76895
H	-2.72540	1.93595	-0.78071
H	3.04759	-5.10541	2.55308
H	-1.78745	-4.29870	-1.11187
H	-3.84056	2.26848	-2.99006
H	-0.28484	7.87561	0.13879
H	0.28484	-7.87561	0.13879
H	4.56435	1.81287	-3.84729

H	-2.41243	2.40788	-5.06703
H	1.58235	6.78199	-1.16227
H	-1.84344	6.43895	1.44160
H	1.80896	-0.35537	2.04749
H	3.75724	-0.96647	3.52485
H	-3.04759	5.10541	2.55308
H	-3.33111	-1.55416	0.29040
H	5.17180	1.58605	-1.41008
H	2.16197	1.95828	-4.48691
H	2.27929	2.59986	2.01830
H	-2.27929	-2.59986	2.01830
H	4.38175	3.19590	2.70973
H	-4.38175	-3.19590	2.70973
H	-3.69556	-4.41343	1.93361
H	3.69556	4.41343	1.93361
H	1.00485	2.08188	2.91825
H	-1.00485	-2.08188	2.91825
H	0.13869	3.11381	4.81035
H	0.95334	1.79524	5.21089
H	-0.95334	-1.79524	5.21089
H	-0.13869	-3.11381	4.81035
C	2.14396	-1.98392	-1.69215
C	-0.88285	-6.18971	-0.58186
C	3.20174	-1.73745	3.00147
C	-4.13518	-1.64901	-1.72388
C	2.76227	-2.16690	-2.93541
C	2.12731	-1.38330	2.17339
C	3.54518	-3.09530	3.13896
C	-3.79241	-1.77311	-3.08506
C	1.96330	-2.24135	-4.09278
C	1.03708	-5.98340	0.87921
C	2.79359	-4.05942	2.44850
C	-3.11299	-1.62472	-0.76633
C	0.57096	-2.11465	-3.96439
C	0.86455	-4.58682	0.87506
C	1.72661	-3.65244	1.62731
C	-1.44864	-1.82866	-2.44095
C	0.00000	-1.93326	-2.69106
C	2.43656	1.85721	-3.44314
C	-1.72661	3.65244	1.62731

C	-0.86455	4.58682	0.87506
C	1.00104	4.79344	-0.55728
C	-0.57096	2.11465	-3.96439
C	-2.76227	2.16690	-2.93541
C	-3.20174	1.73745	3.00147
C	0.00000	1.93326	-2.69106
C	-1.00104	-4.79344	-0.55728
C	4.13518	1.64901	-1.72388
C	-2.79359	4.05942	2.44850
C	-1.03708	5.98340	0.87921
C	-1.96330	2.24135	-4.09278
C	0.15860	-6.79738	0.14520
C	3.11299	1.62472	-0.76633
C	1.44864	1.82866	-2.44095
C	-2.14396	1.98392	-1.69215
C	3.79241	1.77311	-3.08506
C	-2.12731	1.38330	2.17339
C	-2.43656	-1.85721	-3.44314
C	-0.15860	6.79738	0.14520
C	0.88285	6.18971	-0.58186
C	-3.54518	3.09530	3.13896
N	0.79285	-1.87989	-1.56270
N	-1.79939	-1.72269	-1.11131
N	1.41506	-2.32097	1.49146
N	-1.41506	2.32097	1.49146
N	-0.79285	1.87989	-1.56270
N	-0.14964	-4.00105	0.15257
N	1.79939	1.72269	-1.11131
N	0.14964	4.00105	0.15257
O	0.00000	0.00000	0.58094
O	-1.44340	-2.03515	2.01210
O	-3.63026	-3.46150	2.14383
O	1.44340	2.03515	2.01210
O	3.63026	3.46150	2.14383
O	0.56266	2.30112	4.47233
O	-0.56266	-2.30112	4.47233
Ru	0.21891	1.86800	0.23423
Ru	-0.21891	-1.86800	0.23423

Table S14. Cartesian Coordinates for $BDCl_4 \times 4H_2O$ (optimized geometry, strong coupling)

Element	x	y	z
H	3.93391	1.95873	-3.22966
H	2.54202	1.96396	-5.33533
H	0.05492	1.90886	-5.13024
H	-5.10076	1.76450	-1.72773
H	-1.71205	6.04030	2.49046
H	-2.04204	2.01883	-4.77204
H	2.04204	-2.01883	-4.77204
H	-0.57710	-4.52403	-1.60878
H	2.94471	-0.22819	4.09336
H	1.54957	0.03211	2.00972
H	-4.45934	1.97985	-4.16534
H	-2.78354	-1.87718	-1.02216
H	-3.48573	2.56016	4.90192
H	-3.28373	1.63602	-0.01773
H	0.41367	6.93377	-1.17905
H	3.48573	-2.56016	4.90192
H	3.28373	-1.63602	-0.01773
H	-2.65885	4.51389	3.59995
H	0.57710	4.52403	-1.60878
H	5.10076	-1.76450	-1.72773
H	0.77995	-7.73839	0.91748
H	-0.77995	7.73839	0.91748
H	-2.54202	-1.96396	-5.33533
H	4.45934	-1.97985	-4.16534
H	-0.41367	-6.93377	-1.17905
H	1.71205	-6.04030	2.49046
H	-1.54957	-0.03211	2.00972
H	-2.94471	0.22819	4.09336
H	2.65885	-4.51389	3.59995
H	2.78354	1.87718	-1.02216
H	-3.93391	-1.95873	-3.22966
H	-0.05492	-1.90886	-5.13024
H	-2.20229	-2.88049	0.87287
H	2.20229	2.88049	0.87287
H	3.23969	4.25156	-0.55827

H	-3.23969	-4.25156	-0.55827
H	-1.25632	-2.51235	2.23599
H	1.25632	2.51235	2.23599
H	-0.63399	-3.75988	3.99394
H	0.63399	3.75988	3.99394
H	1.40510	2.37503	4.41985
H	-1.40510	-2.37503	4.41985
H	-3.88845	-4.24581	0.95823
H	3.88845	4.24581	0.95823
C	-3.05263	1.71964	-1.07148
C	-0.07824	6.24987	-0.49664
C	-2.60517	1.10474	3.55113
C	2.85329	1.90198	-3.19075
C	-4.06123	1.79218	-2.03649
C	-1.83299	0.94247	2.39209
C	-2.91789	2.40339	3.99004
C	2.07347	1.90755	-4.35777
C	-3.69899	1.90779	-3.39360
C	-1.29470	5.73360	1.54020
C	-2.46980	3.50939	3.25025
C	2.21549	1.86314	-1.94231
C	-2.34056	1.92818	-3.73405
C	-1.19902	4.37011	1.22065
C	-1.72220	3.29073	2.07852
C	0.08626	1.86607	-2.96639
C	-1.36196	1.84541	-2.72404
C	-0.67542	-1.89022	-4.24119
C	1.72220	-3.29073	2.07852
C	1.19902	-4.37011	1.22065
C	0.00000	-4.87322	-0.76009
C	2.34056	-1.92818	-3.73405
C	4.06123	-1.79218	-2.03649
C	2.60517	-1.10474	3.55113
C	1.36196	-1.84541	-2.72404
C	0.00000	4.87322	-0.76009
C	-2.85329	-1.90198	-3.19075
C	2.46980	-3.50939	3.25025
C	1.29470	-5.73360	1.54020
C	3.69899	-1.90779	-3.39360
C	-0.73481	6.68296	0.66565

C	-2.21549	-1.86314	-1.94231
C	-0.08626	-1.86607	-2.96639
C	3.05263	-1.71964	-1.07148
C	-2.07347	-1.90755	-4.35777
C	1.83299	-0.94247	2.39209
C	0.67542	1.89022	-4.24119
C	0.73481	-6.68296	0.66565
C	0.07824	-6.24987	-0.49664
C	2.91789	-2.40339	3.99004
N	-1.73111	1.75589	-1.39951
N	0.86475	1.85353	-1.82662
N	-1.40426	2.01687	1.67893
N	1.40426	-2.01687	1.67893
N	1.73111	-1.75589	-1.39951
N	-0.54449	3.95689	0.08009
N	-0.86475	-1.85353	-1.82662
N	0.54449	-3.95689	0.08009
O	0.00000	0.00000	0.26261
O	1.44258	2.29014	1.23896
O	3.32511	3.75534	0.33300
O	-1.44258	-2.29014	1.23896
O	-3.32511	-3.75534	0.33300
O	-1.07747	-2.88948	3.66234
O	1.07747	2.88948	3.66234
Cl	-2.94452	-5.05533	-2.33408
Cl	2.94452	5.05533	-2.33408
Cl	0.27939	-5.32084	4.70475
Cl	-0.27939	5.32084	4.70475
Ru	0.19273	-1.87245	-0.03060
Ru	-0.19273	1.87245	-0.03060

Table S15. Cartesian Coordinates for BS-BD (optimized geometry, broken symmetry state)

Element	x	y	z
H	1.02740	-0.30874	-0.14170
H	-0.78234	0.10034	6.06145
H	4.09156	9.36460	1.26178
H	4.13286	-1.91220	2.92354
H	-0.62323	1.73638	4.18876

H	0.89823	-1.78030	6.17962
H	2.66039	-1.93338	4.43239
H	3.62576	1.73016	-0.36739
H	5.52876	0.09491	-0.63101
H	0.58459	4.84765	3.22107
H	-1.51710	6.03620	3.89697
H	-3.73449	5.09559	3.14460
H	-3.76320	3.03428	1.74878
H	-0.85944	-1.66635	-1.06465
H	-3.22691	-0.89292	-0.65285
H	-3.60429	1.20283	0.63634
H	-2.71083	4.06616	-3.44523
H	1.80301	4.55788	-4.61305
H	3.41044	7.39398	2.67666
H	2.49251	5.34310	1.52644
H	2.95345	1.80775	-2.85785
H	5.76733	-1.75899	1.05845
H	0.09069	6.64957	-0.31179
H	-2.25324	7.40830	-0.74677
H	3.22912	8.48719	-5.69802
H	-0.40385	0.47166	-5.23693
H	-3.67677	6.08717	-2.36006
H	2.33770	6.22710	-6.38555
H	3.55722	8.96933	-3.28158
H	3.84695	9.22268	-1.20688
H	1.99283	0.17997	-4.50313
H	-1.73714	2.35093	-4.29424
H	4.54503	3.88362	-2.43699
H	4.70275	4.15707	-0.86241
H	3.66992	3.22845	2.78546
H	2.56655	3.28636	3.95018
C	0.00000	0.00000	0.00000
C	0.00000	0.00000	5.31664
C	4.82813	0.00000	0.19200
C	-1.56650	5.14254	3.28362
C	-1.06282	-0.75308	-0.51558
C	4.96114	-1.03608	1.13709
C	-2.80303	4.61534	2.86063
C	-2.38226	-0.31843	-0.28478
C	1.93474	-1.12974	4.39059

C	4.03480	-1.12065	2.19003
C	-0.38741	4.48006	2.91323
C	-2.59250	0.86474	0.44409
C	1.98010	-0.17349	3.36034
C	2.99445	-0.17649	2.28343
C	-1.60168	2.82345	1.73780
C	-1.49175	1.58616	0.93996
C	-0.70798	2.21271	-3.98285
C	0.93898	-1.04676	5.38021
C	0.08628	0.92276	4.26543
C	3.77331	0.91327	0.32898
C	-2.66144	5.77738	-2.13186
C	3.17448	8.00234	-3.58607
C	3.31158	7.36298	1.59662
C	3.55197	8.38145	-0.59084
C	1.38098	0.98442	-4.10844
C	-0.78754	4.26089	-2.46286
C	-1.86982	6.51719	-1.23234
C	-2.11308	4.63713	-2.74404
C	2.19034	5.53303	-4.34757
C	2.86292	7.01892	-2.63046
C	3.03513	7.20828	-1.17302
C	1.92590	1.89491	-3.19165
C	-0.10755	3.09894	-3.06892
C	-0.55499	6.10138	-0.98526
C	0.04184	1.14924	-4.51501
C	2.80032	6.21906	0.96771
C	-2.81636	3.44954	2.07481
C	2.98967	7.73348	-4.95412
C	2.49177	6.47486	-5.34069
C	3.69242	8.46428	0.80481
N	2.87308	0.83006	1.34917
N	-0.40031	3.34137	2.16856
N	-0.20488	1.13933	0.71676
N	1.20665	2.93544	-2.68976
N	-0.02015	5.00483	-1.58960
N	1.05314	0.84860	3.30549
N	2.66196	6.13960	-0.38595
N	2.37097	5.78855	-3.01959
O	2.71374	3.29643	2.98203

O	1.71557	3.33648	0.15749
O	4.09806	3.84673	-1.56638
Ru	1.27961	2.18923	1.67312
Ru	1.94894	4.44242	-1.43259

Table S16. Cartesian Coordinates for optimized BD (triplet electronic state).

Element	x	y	z
C	2.505916	1.489464	1.89724
C	6.127657	-0.11612	-1.69829
C	2.047071	-3.10214	3.200659
C	1.277496	1.433552	-4.28564
C	2.838527	2.733736	2.449435
H	2.483445	0.594116	2.504507
C	3.422793	-3.38202	3.317536
C	1.550517	2.785812	-3.9987
C	2.872117	3.864565	1.61149
C	6.075513	-1.51026	0.283681
C	4.313504	-2.81748	2.389373
C	1.333463	0.497762	-3.24283
C	2.55856	3.713068	0.249671
C	4.678286	-1.35816	0.334418
C	3.822443	-1.9859	1.364766
C	1.903404	2.173119	-1.67138
C	2.229649	2.442615	-0.25569
H	6.657867	0.37937	-2.50467
N	2.47384	-1.71585	1.264045
N	1.649752	0.852158	-1.96788
N	2.214145	1.341503	0.576146
O	1.8149	-2.34628	-1.5583
O	-0.00296	-0.52471	-0.00532
H	-3.81259	-3.93222	-4.18659
Ru	1.912947	-0.46956	-0.35573
H	5.372696	-3.03167	2.470094
N	-1.64822	0.816175	1.98384
N	-2.21504	1.358399	-0.54907
O	-1.81503	-2.37818	1.501678
Ru	-1.9202	-0.47173	0.346285
H	4.182462	0.595638	-2.31948
N	4.016867	-0.59786	-0.60905
H	7.890578	-0.99949	-0.78554
H	6.594693	-2.10559	1.025347

H	0.562613	-2.02016	2.030115
H	1.332281	-3.52512	3.89879
C	-1.82338	3.110049	2.734797
N	-2.48611	-1.68272	-1.29681
H	1.13643	-0.55305	-3.42144
H	1.042374	1.109503	-5.29408
H	1.533059	3.532277	-4.78701
H	2.073759	4.193692	-2.44915
C	6.811832	-0.88608	-0.73897
H	3.083646	2.807131	3.50368
H	3.146714	4.838265	2.005681
H	2.590164	4.575811	-0.40577
C	4.735084	0.007233	-1.59862
C	1.609484	-2.26565	2.164295
N	-4.02318	-0.59861	0.599715
H	-2.53923	4.580048	0.490903
C	-2.8423	3.908322	-1.53691
H	-4.18258	0.561665	2.332981
H	-1.35079	-3.44003	-3.96898
C	-6.08536	-1.48948	-0.30661
H	-0.57672	-1.97405	-2.06959
C	-2.06389	-3.03008	-3.26142
C	-4.32902	-2.75839	-2.44146
H	-1.15646	-0.62215	3.412701
C	-1.26874	1.350705	4.311728
H	3.792928	-4.02588	4.109455
C	-2.21079	2.444851	0.301843
C	-2.82927	2.791884	-2.39444
C	-2.52357	3.728584	-0.17967
C	-4.73836	-0.0106	1.601677
C	-4.68808	-1.33915	-0.35726
C	-3.83517	-1.94832	-1.40105
C	-1.33797	0.434458	3.252541
C	-1.88359	2.145666	1.71135
C	-2.51136	1.533632	-1.86575
H	-2.50468	0.64895	-2.48878
C	-1.52078	2.711842	4.048834
C	-1.6238	-2.21543	-2.20886
H	-3.07869	2.887021	-3.44594
H	-7.89733	-0.99536	0.775543
C	1.858657	3.156142	-2.6777
H	-1.4919	3.443877	4.850248
H	-3.10509	4.892566	-1.91253

H	-6.65876	0.348653	2.517798
H	-6.60785	-2.06945	-1.0582
C	-6.81844	-0.88326	0.729072
C	-6.1311	-0.13273	1.701277
H	-5.38874	-2.9687	-2.52457
C	-3.4403	-3.30534	-3.38215
H	-1.03929	1.005249	5.314355
H	-2.0234	4.154548	2.524883
H	-2.49211	-2.54021	2.190555
H	-1.63398	-3.20382	1.008389
H	1.650853	-3.19022	-1.09074
H	2.482866	-2.47634	-2.26244

Table S17. Cartesian Coordinates for BD×12H_2O (optimized geometry, strong coupling).

Element	x	y	z
C	-2.60395	1.034324	2.465118
C	-5.2813	-3.37186	1.062336
C	-2.96853	2.494085	-2.02333
C	0.198	-4.57909	2.009925
C	-2.9642	1.445104	3.754742
C	-2.17758	1.543402	-1.36238
C	-4.36339	2.320275	-2.06477
C	0	-4.40391	3.394262
C	-2.67679	0.602557	4.846245
C	-5.92568	-1.36502	-0.12677
C	-4.92637	1.185026	-1.45848
C	-0.22833	-3.5748	1.131207
C	-2.02418	-0.6168	4.606708
C	-4.57481	-0.97412	-0.15601
C	-4.09138	0.260355	-0.80597
C	-1.02214	-2.24825	2.929783
C	-1.68387	-0.98119	3.290316
C	0.611852	3.226362	3.854808
C	4.091379	-0.26036	-0.80597
C	4.574813	0.974117	-0.15601
C	3.952909	2.929704	1.008897
C	2.024178	0.616797	4.606708
C	2.964195	-1.4451	3.754742
C	2.968526	-2.49409	-2.02333

C	1.683865	0.981185	3.290316
C	-3.95291	-2.9297	1.008897
C	-0.198	4.579094	2.009925
C	4.926371	-1.18503	-1.45848
C	5.92568	1.365015	-0.12677
C	2.676786	-0.60256	4.846245
C	-6.28821	-2.57189	0.492589
C	0.228334	3.574798	1.131207
C	1.022144	2.248246	2.929783
C	2.603949	-1.03432	2.465118
C	0	4.403907	3.394262
C	2.177577	-1.5434	-1.36238
C	-0.61185	-3.22636	3.854808
C	6.288213	2.571893	0.492589
C	5.281296	3.371864	1.062336
C	4.363393	-2.32028	-2.06477
H	0.660758	-5.47693	1.615266
H	0.308162	-5.17078	4.098468
H	-0.7737	-3.08442	4.917215
H	-3.4736	2.392617	3.894865
H	-6.69039	-0.74248	-0.57614
H	-1.80453	-1.28042	5.435217
H	1.804534	1.280419	5.435217
H	3.155294	3.527858	1.426786
H	2.492677	-3.34479	-2.49747
H	1.095991	-1.62134	-1.32188
H	-2.96467	0.882848	5.854708
H	0.116001	3.666031	0.058578
H	-5.00094	3.04551	-2.56119
H	-2.81875	1.64931	1.600616
H	-5.51616	-4.31568	1.542437
H	5.000938	-3.04551	-2.56119
H	2.818745	-1.64931	1.600616
H	-5.99858	1.032387	-1.49295
H	-3.15529	-3.52786	1.426786
H	3.473597	-2.39262	3.894865
H	7.328647	2.879396	0.528885
H	-7.32865	-2.8794	0.528885
H	-0.30816	5.170775	4.098468
H	2.964669	-0.88285	5.854708
H	5.51616	4.315677	1.542437
H	6.69039	0.742479	-0.57614
H	-1.09599	1.621341	-1.32188

H	-2.49268	3.344786	-2.49747
H	5.998583	-1.03239	-1.49295
H	-0.116	-3.66603	0.058578
H	-0.66076	5.476928	1.615266
H	0.773696	3.084422	4.917215
H	1.660548	3.050213	-1.50399
H	-1.66055	-3.05021	-1.50399
N	-1.98757	-0.15612	2.226755
N	-0.83185	-2.4388	1.578257
N	-2.73109	0.460962	-0.75052
N	2.731089	-0.46096	-0.75052
N	1.987568	0.156115	2.226755
N	-3.60105	-1.75332	0.424141
N	0.831851	2.438796	1.578257
N	3.601046	1.753319	0.424141
O	0	0	0.031781
Ru	1.622834	0.958416	0.348771
Ru	-1.62283	-0.95842	0.348771
O	-1.26839	-2.0511	-1.44177
O	-2.21529	-4.31132	-1.65628
O	1.268385	2.051101	-1.44177
O	2.215288	4.311318	-1.65628
O	1.196581	6.717437	-1.14316
O	-4.08579	-4.23602	-3.42413
O	-1.19658	-6.71744	-1.14316
O	4.08579	4.236023	-3.42413
H	1.33321	1.606595	-2.33839
H	-1.33321	-1.6066	-2.33839
O	1.456239	1.212012	-4.03074
O	-1.45624	-1.21201	-4.03074
O	-3.35292	-2.72464	-5.60718
O	1.108888	-1.25118	-4.5726
O	-1.10889	1.251176	-4.5726
O	3.352924	2.724641	-5.60718
H	1.524051	-1.84944	-5.21723
H	0.127339	-1.4306	-4.40824
H	2.92248	3.268724	-6.29928
H	4.065903	2.186435	-6.00934
H	-2.92248	-3.26872	-6.29928
H	-4.0659	-2.18644	-6.00934
H	-0.12734	1.430602	-4.40824
H	-1.52405	1.849436	-5.21723
H	1.695277	7.34798	-0.58786

H	0.631696	7.202814	-1.77544
H	4.885618	4.786978	-3.49282
H	3.89875	3.717224	-4.24722
H	-0.6317	-7.20281	-1.77544
H	-1.69528	-7.34798	-0.58786
H	-4.88562	-4.78698	-3.49282
H	-3.89875	-3.71722	-4.24722
H	-2.99562	-4.34665	-2.30111
H	-1.8109	-5.20424	-1.46708
H	2.995621	4.346651	-2.30111
H	1.810899	5.204238	-1.46708
H	-2.12953	-1.73917	-4.52742
H	-1.48172	-0.21046	-4.26009
H	1.481723	0.210461	-4.26009
H	2.129532	1.739174	-4.52742

Table S18. Cartesian Coordinates for $[(bpy)_2(H_2O)RuORu(OH_2)(bpy)_2]^{5+}$ (optimized geometry). [3,4]-bis-aqua.

Element	x	y	z
C	2.675367	-1.81754	-1.45803
C	0.321702	-6.31355	0.157042
C	3.67822	-0.88882	3.142578
C	-3.57356	-2.68864	-1.51061
C	3.337871	-2.02515	-2.6743
C	2.575838	-0.79855	2.281613
C	4.210446	-2.15902	3.443244
C	-3.18237	-2.92363	-2.84542
C	2.585524	-2.38679	-3.81036
C	2.16476	-5.63518	1.581185
C	3.613777	-3.29862	2.875462
C	-2.59377	-2.33584	-0.57131
C	1.188469	-2.51504	-3.69372
C	1.798154	-4.29189	1.394299
C	2.505554	-3.15632	2.018976
C	-0.88314	-2.4372	-2.21254
C	0.565869	-2.29767	-2.45296
C	1.8261	2.786442	-3.19693
C	-2.50555	3.156324	2.018976
C	-1.79815	4.291892	1.394299
C	0	4.960571	-0.00606
C	-1.18847	2.515039	-3.69372

C	-3.33787	2.025148	-2.6743
C	-3.67822	0.88882	3.142578
C	-0.56587	2.297672	-2.45296
C	0	-4.96057	-0.00606
C	3.573562	2.688635	-1.51061
C	-3.61378	3.298616	2.875462
C	-2.16476	5.635181	1.581185
C	-2.58552	2.38679	-3.81036
C	1.425828	-6.66092	0.960714
C	2.593767	2.335839	-0.57131
C	0.883135	2.437203	-2.21254
C	-2.67537	1.817535	-1.45803
C	3.182369	2.923625	-2.84542
C	-2.57584	0.798547	2.281613
C	-1.8261	-2.78644	-3.19693
C	-1.42583	6.66092	0.960714
C	-0.3217	6.313551	0.157042
C	-4.21045	2.159018	3.443244
H	-4.60947	-2.79156	-1.20321
H	-3.915	-3.2168	-3.59207
H	-1.51903	-2.97123	-4.2204
H	4.417527	-1.92655	-2.72377
H	3.01346	-5.89694	2.202515
H	0.604871	-2.80105	-4.5616
H	-0.60487	2.801048	-4.5616
H	0.843655	4.673672	-0.61789
H	-4.11291	-0.00881	3.570458
H	-2.12813	-0.1552	2.0298
H	3.07552	-2.57619	-4.76135
H	2.855872	2.15095	0.464424
H	5.065353	-2.26069	4.105596
H	3.221476	-1.5566	-0.56093
H	-0.27776	-7.0738	-0.33346
H	-5.06535	2.260687	4.105596
H	-3.22148	1.556601	-0.56093
H	4.013886	-4.27867	3.107995
H	-0.84366	-4.67367	-0.61789
H	-4.41753	1.926549	-2.72377
H	-1.7037	7.701486	1.103182
H	1.703702	-7.70149	1.103182
H	3.915001	3.216799	-3.59207
H	-3.07552	2.576185	-4.76135
H	0.277759	7.073802	-0.33346

H	-3.01346	5.89694	2.202515
H	2.128131	0.155202	2.0298
H	4.112908	0.008806	3.570458
H	-4.01389	4.278673	3.107995
H	-2.85587	-2.15095	0.464424
H	4.609471	2.791564	-1.20321
H	1.519027	2.971227	-4.2204
H	1.429823	2.967511	2.412722
H	0.403742	1.982062	3.157301
H	-0.40374	-1.98206	3.157301
H	-1.42982	-2.96751	2.412722
N	1.322011	-1.95521	-1.3448
N	-1.27788	-2.22334	-0.90719
N	1.999779	-1.90546	1.725563
N	-1.99978	1.905461	1.725563
N	-1.32201	1.95521	-1.3448
N	0.714312	-3.95947	0.596758
N	1.277876	2.223336	-0.90719
N	-0.71431	3.959472	0.596758
O	0.843963	2.188421	2.306157
O	0	0	0.461038
O	-0.84396	-2.18842	2.306157
Ru	-0.30751	1.889156	0.434039
Ru	0.307507	-1.88916	0.434039

Table S19. Cartesian Coordinates for optimized geometry of $[(bpy)_2ClRuORuCl(bpy)_2]^{2+}$.

Element	x	y	z
C	2.947524	-1.90895	-0.58106
C	-0.34089	-6.26278	-0.3326
C	2.028051	-1.36428	4.109978
C	-2.79333	-1.93904	-3.13721
C	4.025349	-1.99202	-1.47043
C	1.447854	-1.13004	2.854154
C	2.13095	-2.68522	4.580794
C	-1.9267	-2.01841	-4.2457
C	3.764442	-2.06812	-2.85277
C	0.631487	-5.85518	1.848131
C	1.668106	-3.73475	3.770349
C	-2.25028	-1.85835	-1.84812
C	2.434235	-2.04163	-3.29736

C	0.617052	-4.47521	1.574816
C	1.10486	-3.44577	2.514751
C	-0.04383	-1.93001	-2.71211
C	1.386725	-1.95182	-2.36103
C	0.540329	2.01143	-4.0273
C	-1.10486	3.445772	2.514751
C	-0.61705	4.475212	1.574816
C	0.329513	4.879644	-0.54974
C	-2.43424	2.041628	-3.29736
C	-4.02535	1.992021	-1.47043
C	-2.02805	1.364275	4.109978
C	-1.38673	1.951815	-2.36103
C	-0.32951	-4.87964	-0.54974
C	2.79333	1.939038	-3.13721
C	-1.66811	3.734752	3.770349
C	-0.63149	5.855183	1.848131
C	-3.76444	2.06812	-2.85277
C	0.147226	-6.759	0.890325
C	2.250276	1.858348	-1.84812
C	0.043826	1.930014	-2.71211
C	-2.94752	1.908949	-0.58106
C	1.926702	2.018405	-4.2457
C	-1.44785	1.130041	2.854154
C	-0.54033	-2.01143	-4.0273
C	-0.14723	6.759	0.890325
C	0.340891	6.262777	-0.3326
C	-2.13095	2.685217	4.580794
N	1.656763	-1.89952	-1.01136
N	-0.90337	-1.85772	-1.63565
N	0.991846	-2.14814	2.077562
N	-0.99185	2.148139	2.077562
N	-1.65676	1.899517	-1.01136
N	0.134151	-4.00322	0.378711
N	0.903368	1.857722	-1.63565
N	-0.13415	4.003222	0.378711
O	0	0	0.510403
Ru	0	1.885067	0.238105
Ru	0	-1.88507	0.238105
Cl	2.128003	2.159445	1.481136
Cl	-2.128	-2.15945	1.481136
H	3.101555	-1.84801	0.488622
H	-0.72827	-6.92681	-1.09756
H	2.389564	-0.52391	4.692525

H	-3.87084	-1.9556	-3.26203
H	5.039289	-2.00244	-1.08536
H	1.355035	-0.13066	2.446456
H	2.567378	-2.89639	5.552103
H	-2.32231	-2.09857	-5.25359
H	4.579547	-2.1488	-3.56523
H	1.005669	-6.22444	2.795415
H	1.749292	-4.75835	4.116344
H	-2.86519	-1.82464	-0.95553
H	2.218008	-2.09925	-4.35803
H	-0.14025	2.08574	-4.86798
H	0.713341	4.459327	-1.47032
H	-2.21801	2.099254	-4.35803
H	-5.03929	2.00244	-1.08536
H	-2.38956	0.523907	4.692525
H	-0.71334	-4.45933	-1.47032
H	3.870839	1.955598	-3.26203
H	-1.74929	4.758347	4.116344
H	-1.00567	6.224439	2.795415
H	-4.57955	2.148798	-3.56523
H	0.14704	-7.82512	1.094568
H	2.865189	1.824637	-0.95553
H	-3.10156	1.848008	0.488622
H	2.32231	2.098568	-5.25359
H	-1.35504	0.13066	2.446456
H	0.140248	-2.08574	-4.86798
H	-0.14704	7.825116	1.094568
H	0.728269	6.926807	-1.09756
H	-2.56738	2.896386	5.552103

Table S20. Cartesian Coordinates for optimized geometry of $[(bpy)_2ClRuORuCl(bpy)_2]^{3+}$.

Element	x	y	z
C	-2.53983	0.370549	-2.70707
C	-6.09067	0.16568	1.447959
C	-1.5004	-4.1169	-1.70589
C	-1.72864	3.455935	2.737899
C	-2.9112	1.153424	-3.80848
C	-1.22947	-2.82708	-1.22641
C	-2.78092	-4.66445	-1.51055
C	-2.08679	4.457744	1.816394

C	-3.07396	2.540075	-3.63165
C	-5.73857	-2.0445	0.520716
C	-3.75868	-3.89197	-0.86165
C	-1.62597	2.128145	2.294292
C	-2.84629	3.100877	-2.36263
C	-4.4083	-1.69299	0.234498
C	-3.44004	-2.59875	-0.41152
C	-2.21304	2.759276	0.082232
C	-2.47004	2.27207	-1.29113
C	2.32799	4.104402	-0.47582
C	3.440075	-2.59864	0.411449
C	4.408163	-1.693	-0.23498
C	4.75668	0.461955	-1.14517
C	2.847348	3.100515	2.362838
C	2.912314	1.152941	3.808512
C	1.500677	-4.11662	1.706422
C	2.470636	2.271866	1.291369
C	-4.75712	0.462256	1.143913
C	1.727912	3.45639	-2.73722
C	3.758819	-3.89178	0.86176
C	5.738328	-2.04461	-0.52156
C	3.075282	2.539574	3.631746
C	-6.59049	-1.11156	1.133537
C	1.625267	2.128547	-2.29377
C	2.213224	2.759277	-0.08183
C	2.540502	0.370222	2.707136
C	2.086532	4.458019	-1.8157
C	1.229641	-2.82689	1.226795
C	-2.32779	4.104358	0.476373
C	6.590048	-1.11186	-1.13496
C	6.090114	0.16527	-1.44963
C	2.781188	-4.66417	1.510963
N	-2.32912	0.914499	-1.47915
N	-1.86463	1.790956	0.998735
N	-2.17414	-2.08715	-0.58481
N	2.174194	-2.08706	0.584888
N	2.32956	0.914296	1.479312
N	-3.93076	-0.44156	0.550873
N	1.86438	1.79113	-0.99835
N	3.93053	-0.44164	-0.55151
O	-1.6E-05	-0.13913	0.000252
Ru	1.853928	-0.17503	-0.24461
Ru	-1.85403	-0.17509	0.244735

Cl	1.672923	-1.21879	-2.45376
Cl	-1.67367	-1.21931	2.453692
H	-2.40741	-0.69953	-2.79908
H	-6.71365	0.913329	1.926413
H	-0.72225	-4.66677	-2.224
H	-1.55214	3.687711	3.782765
H	-3.07357	0.683567	-4.77243
H	-0.26118	-2.36677	-1.37918
H	-3.01851	-5.66291	-1.86401
H	-2.19073	5.490449	2.135194
H	-3.37565	3.170853	-4.46221
H	-6.11187	-3.03253	0.279862
H	-4.75378	-4.29567	-0.71885
H	-1.38417	1.308933	2.961948
H	-2.97284	4.167365	-2.21736
H	2.617327	4.867996	0.236886
H	4.336619	1.425541	-1.39682
H	2.974019	4.166997	2.217634
H	3.074838	0.682972	4.772375
H	0.722632	-4.66643	2.224749
H	-4.33716	1.425928	1.395391
H	1.551039	3.688336	-3.78198
H	4.753906	-4.29549	0.718869
H	6.11169	-3.03258	-0.28057
H	3.377301	3.170236	4.462272
H	-7.61743	-1.37666	1.364545
H	1.383146	1.309461	-2.96146
H	2.407924	-0.69984	2.799109
H	2.1905	5.490758	-2.13438
H	0.261362	-2.36656	1.379653
H	-2.61675	4.868087	-0.23634
H	7.616899	-1.37705	-1.36626
H	6.712908	0.912756	-1.92858
H	3.018868	-5.66256	1.864554

Table S21. Cartesian Coordinates for $Ru(bpy)_2Cl_2$ (optimized geometry).

Element	x	y	z
Ru	0	0	0.532821
N	0.572083	1.982683	0.511597
C	1.020042	4.755154	0.542165
C	-0.21201	2.819617	-0.25203

C	1.557327	2.511449	1.290303
C	1.808888	3.888638	1.325788
C	0	4.211801	-0.25158
H	2.103777	1.790987	1.89089
H	2.597169	4.268933	1.967445
H	-0.62977	4.862095	-0.84897
H	1.189403	5.827973	0.559633
N	-0.57208	-1.98268	0.511597
C	-1.02004	-4.75515	0.542165
C	0.212013	-2.81962	-0.25203
C	-1.55733	-2.51145	1.290303
C	-1.80889	-3.88864	1.325788
C	0	-4.2118	-0.25158
H	-2.10378	-1.79099	1.89089
H	-2.59717	-4.26893	1.967445
H	0.629773	-4.8621	-0.84897
H	-1.1894	-5.82797	0.559633
N	-1.29982	0.764532	-0.85557
C	-3.094	2.030902	-2.61837
C	-2.22857	0.042308	-1.54352
C	-1.25126	2.133051	-1.03371
C	-2.14238	2.77876	-1.91257
C	-3.13449	0.633853	-2.42831
H	-2.23741	-1.0237	-1.35217
H	-2.09588	3.855013	-2.03788
H	-3.85913	0.014024	-2.94662
H	-3.78932	2.52046	-3.29373
N	1.299819	-0.76453	-0.85557
C	3.094002	-2.0309	-2.61837
C	1.251261	-2.13305	-1.03371
C	2.228567	-0.04231	-1.54352
C	3.134489	-0.63385	-2.42831
C	2.142376	-2.77876	-1.91257
H	2.237414	1.023701	-1.35217
H	3.859134	-0.01402	-2.94662
H	2.095879	-3.85501	-2.03788
H	3.78932	-2.52046	-3.29373
Cl	1.697236	-0.67459	2.237535
Cl	-1.69724	0.674589	2.237535

REFERENCES

1. Frisch, M. J. ; Trucks, G. W.; Schlegel, H. B.; Scuseria, G. E.; Robb, M. A.; Cheeseman, J. R.; J.A. Montgomery, J.; Vreven, T.; Kudin, K. N.; Burant, J. C.; Millam, J. M.; Iyengar, S. S.; Tomasi, J.; Barone, V.; Mennucci, B.; Cossi, M.; Scalmani, G.; Rega, N.; Petersson, G. A.; Nakatsuji, H.; Hada, M.; Ehara, M.; Toyota, K.; Fukuda, R.; Hasegawa, J.; Ishida, M.; Nakajima, T.; Honda, Y.; Kitao, O.; Nakai, H.; Klene, M.; Li, X.; Knox, J. E.; Hratchian, H. P.; Cross, J. B.; Bakken, V.; Adamo, C.; Jaramillo, J.; Gomperts, R.; Stratmann, R. E.; Yazyev, O.; Austin, A. J.; Cammi, R.; Pomelli, C.; Ochterski, J. W.; Ayala, P. Y.; Morokuma, K.; Voth, G. A.; Salvador, P.; Dannenberg, J. J.; Zakrzewski, V. G.; Dapprich, S.; Daniels, A. D.; Strain, M. C.; Farkas, O.; Malick, D. K.; Rabuck, A. D.; Raghavachari, K.; Foresman, J. B.; Ortiz, J. V.; Cui, Q.; Baboul, A. G.; Clifford, S.; Cioslowski, J.; Stefanov, B. B.; Liu, G.; Liashenko, A.; Piskorz, P.; Komaromi, I.; Martin, R. L.; Fox, D. J.; Keith, T.; Al-Laham, M. A.; Peng, C. Y.; Nanayakkara, A.; Challacombe, M.; Gill, P. M. W.; Johnson, B.; Chen, W.; Wong, M. W.; Gonzalez, C.; Pople, J. A. *Gaussian 03*, revision D.01; Gaussian Inc., Wallingford, CT, 2004.

2. Becke, A. D. *Phys. Rev., Ser. A* **1988**, *38*, 3098-3100.

3. Becke, A. D. *J. Chem. Phys.* **1993**, *98*, 1372-1377.

4. Becke, A. D. *J. Chem. Phys.* **1993**, *98*, 5648-5652.

5. Stevens, P. J.; Devlin, F. J.; Chablowski, C. F.; Frisch, M. J. *J. Phys. Chem.* **1994**, *98*, 11623-11627.

6. Lee, C.; Yang, W.; Parr, R. G. *Phys. Rev.* **1988**, *B37*, 785-789.

7. Stratmann, R. E.; Scuseria, G. E.; Frisch, M. J. *J. Chem. Phys.* **1998**, *109*, 8218-8224.

8. Bauernschmitt, R.; Ahlrichs, R. *Chem. Phys. Lett.* **1996**, *256*, 454-464.

9. Casida, M. E. ; Jamorski, C.; Casida, K. C.; Salahub, D. R. *J. Chem. Phys.* **1998**, *108*, 4439-4449.

10. Barone, V.; Cossi, M. *J. Phys. Chem. A* **1998**, *102*, 1995-2001.

11. Cossi, M.; Rega, N.; Scalmani, G.; Barone, V. *J. Comp. Chem.* **2003**, *24*, 669-681.

12. Tomasi, J.; Mennucci, B.; Cammi, R. *Chem. Rev.* **2005**, *105* (8), 2999-3093.

13. Cance`s, E.; Mennucci, B.; Tomasi, J. *J. Chem. Phys.* **1997**, *107*, 3032.

14. Mennucci, B.; Cance`s, E.; Tomasi, J. *J. Phys. Chem. B* **1997**, *101*, 10506.

15. Cance`s, E.; Mennucci, B. *J. Math. Chem.* **1998**, *23*, 309.

16. Nazeeruddin, M. K.; Wang, Q.; Cevey, L.; Aranyos, V.; Liska, P.; Figgemeier, E.; Klein, C.; Hirata, N.; Koops, S.; Haque, S. A.; Durrant, J. R.; Hagfeldt, A.; Lever, A. B. P.; Graetzel, M. *Inorg. Chem.* **2006**, *45*(2), 787-797.

17. Baik, M.-H.; Friesner, R. A. *J. Phys. Chem. A* **2002**, *106*(32), 7407-7412.

18. Yang, X.; Baik, M.-H. *J. Am. Chem. Soc.* **2004**, *126*(41), 13222-13223.

19. Yang, X.; Baik, M.-H. *J. Am. Chem. Soc.* **2006**, *128*(23), 7476-7485.

20. Gilbert, J. A.; Eggleston, D. S.; Murphy, W. R. Jr.; Geselowitz, D. A.; Gersten, S. W.; Hodgson, D. J.; Meyer, T. J. *J. Am. Chem. Soc.* **1985**, *107*(13), 3855-3864.

21. Ishitani, O.; White, P. S.; Meyer, T. J. *Inorg. Chem.* **1996**, *35*, 2167-2168.

22. Phelps, D. W.; Kahn, E. M.; Hodgson, D. J. *Inorg. Chem.* **1975**, *14*, 2486.

23. Concepcion, J. J.; Meyer, T. J. *Unpublished Results*.

24. Batista, E. R.; Martin, R. L. *J. Am. Chem. Soc.* **2007**, *129*(23), 7224-7225.

APPENDIX B

Mechanism of Water Oxidation by the Blue Dimer, *cis,cis*-$[(bpy)_2(H_2O)RuORu(OH_2)(bpy)_2]^{4+}$

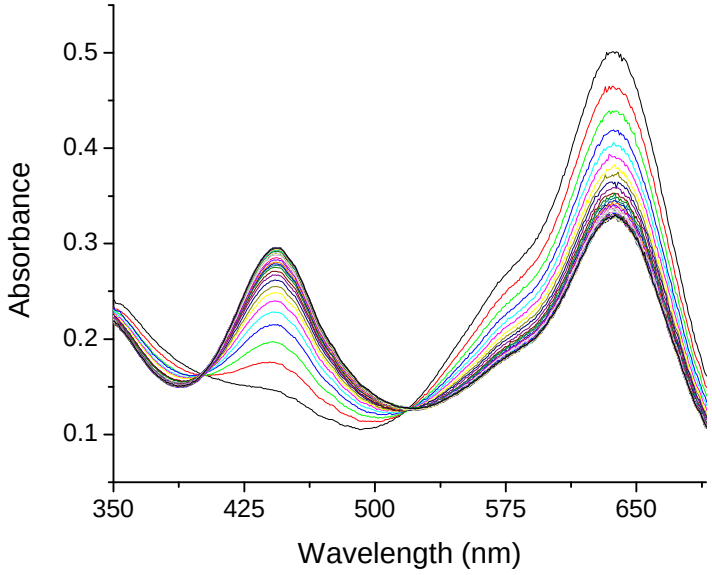

Figure S1. Addition of 5.4 x 10^{-5} M Ce(IV) to 1.48 x 10^{-4} M $[(H_2O)Ru^{III}ORu^{III}(OH_2)]^{4+}$ in 1.0 M $HClO_4$. First scan with maximum absorbance at 637 nm taken 0.0131 s after Ce(IV) addition, last scan with maximum absorbance at 445 nm measured at 4.7631 s, with 0.095 s between scans.

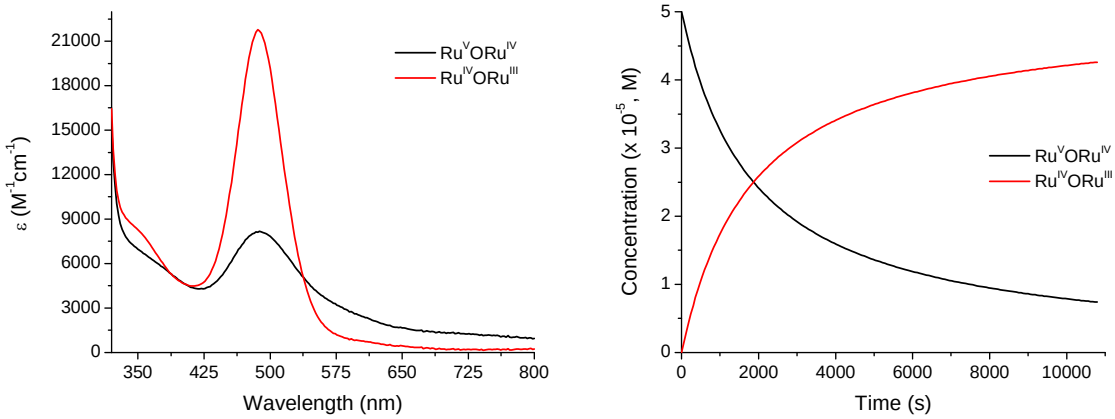

Figure S2. Decay of electrolytically-prepared 5.0 x 10^{-5} M $[(O)Ru^{V}ORu^{IV}(O)]^{3+}$ in 0.1 M pH 5.8 phosphate buffer at 25 °C. Left: Calculated spectra of species. Right: Concentration (x 10^{-5} M) vs. time (s) of the species.

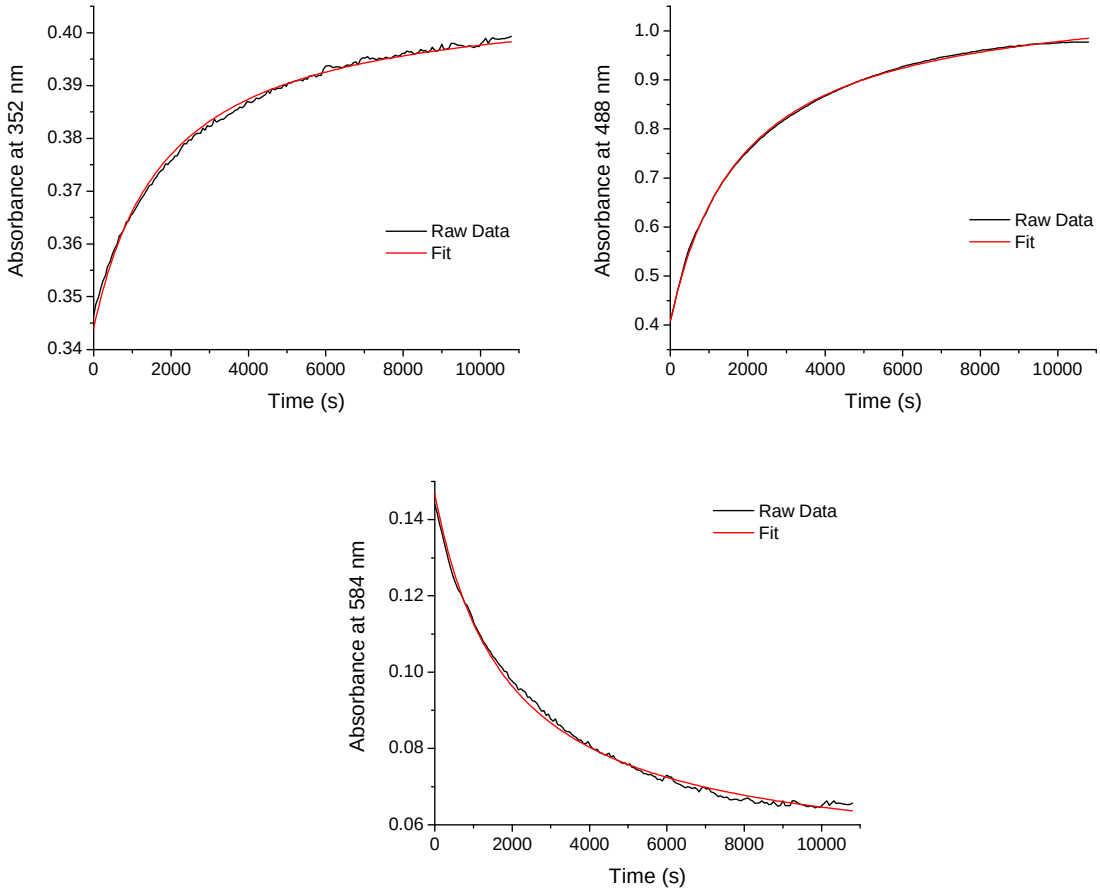

Figure S3. Decay of electrolytically-prepared 5.0 x 10^{-5} M $[(O)Ru^{V}ORu^{IV}(O)]^{3+}$ in 0.1 M pH 5.8 phosphate buffer at 25 °C. Single wavelength fits.

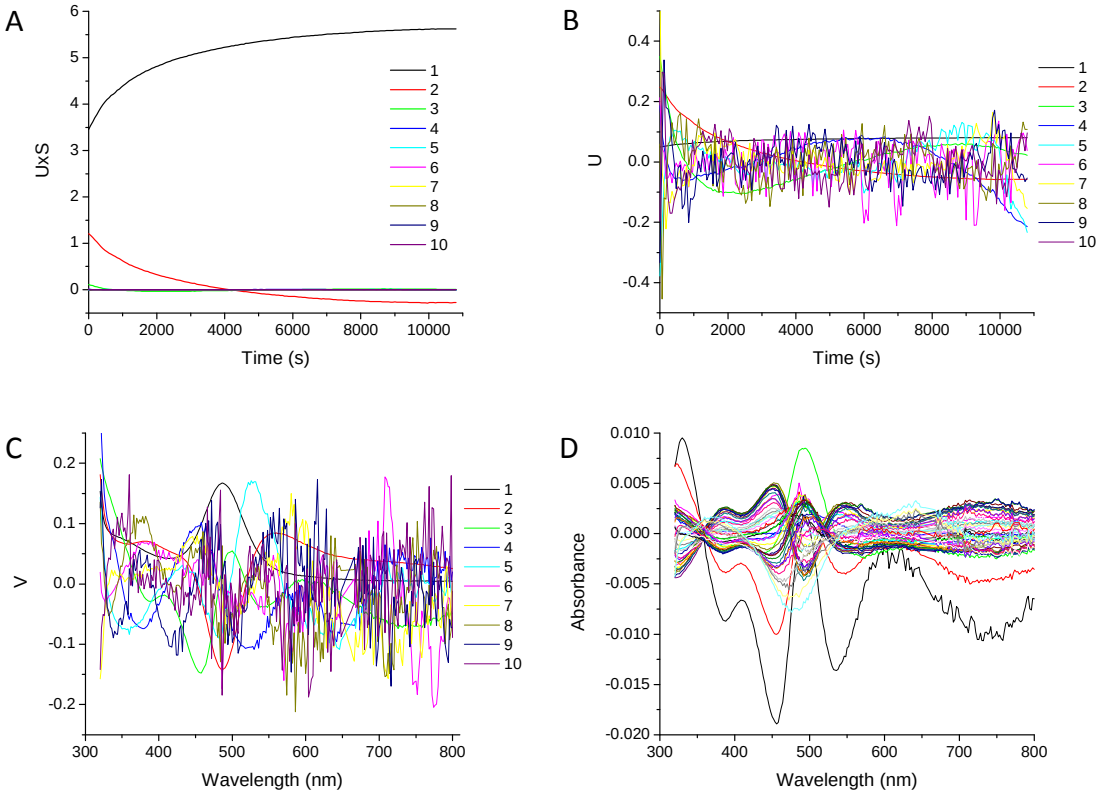

Figure S4. Decay of electrolytically-prepared 5.0 x 10^{-5} M $[(O)Ru^{V}ORu^{IV}(O)]^{3+}$ in 0.1 M pH 5.8 phosphate buffer at 25 °C. (A) Concentration eigenvectors scaled by their eigenvalues, (B) Concentration eigenvectors, (C) Spectroscopic eigenvectors, (D) Residuals of the fit at all points.

[TYPE]
Second Order, A + A -> B + B

[SPECIES]	[INIT.CONC]	[COLORED]	[FIXED]	[SPECTRUM]
A	5.000E-05	True	False	
B	0.000E+00	True	False	

[NAME]	[FIXED]	[PARAMETER]		[ERROR]	[UNITS]
k1	False	5.34865E+00	+/-	6.16970E-02	/M/sec

[TIME ZERO]
Tzero = 0

[CONVERGENCE]
Iterations = 3
Convergence Limit = 1.000E-03
Convergence Found = 0.000E+00
Marquardt Parameter = 0.0
Sum(Y-y)^2 Residuals = 1.69965E-01
Std. Deviation of Fit(Y) = 1.97395E-03

[STATISTICS]
Experimental Noise = 7.057E-05
Relative Error Of Fit = 0.5863%
Durbin-Watson Factor = 0.0427
Goodness Of Fit, Chi^2 = 7.824E+02
Durbin-Watson Factor (raw data) = 0.0442

Fitting Report 1. Decay of electrolytically prepared 5.0 x 10^{-5} M $[(O)Ru^{V}ORu^{IV}(O)]^{3+}$ in pH 5.8 phosphate buffer at 25 °C.

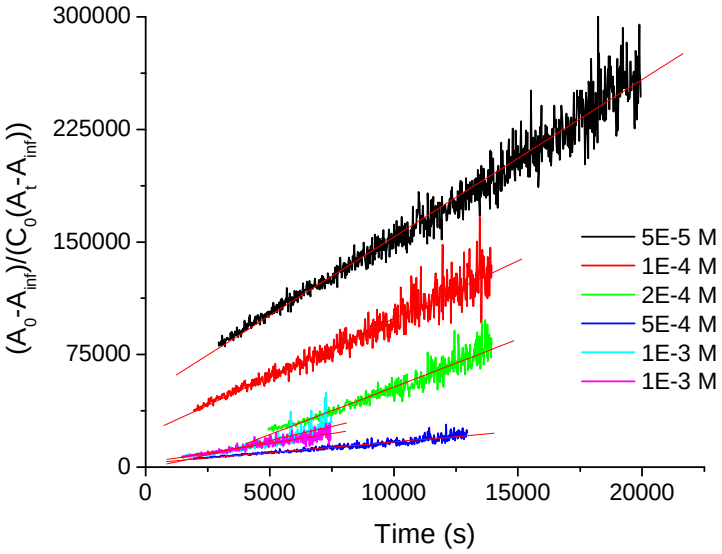

Figure S5. Decay kinetics of $[(O)Ru^{V}ORu^{IV}(O)]^{3+}$ in 0.1 M HNO_3 at 23 ± 2 °C, prepared by addition of 2 eq. of Ce(IV) to $[(HO)Ru^{IV}ORu^{III}(OH_2)]^{4+}$, measured by following the growth of $Ru^{IV}ORu^{III}$ at 495 nm. The second order equal concentration kinetics are shown for different concentrations of complex. Rate constants had modest variations from 1.4 $M^{-1}s^{-1}$ to 10.5 $M^{-1}s^{-1}$.

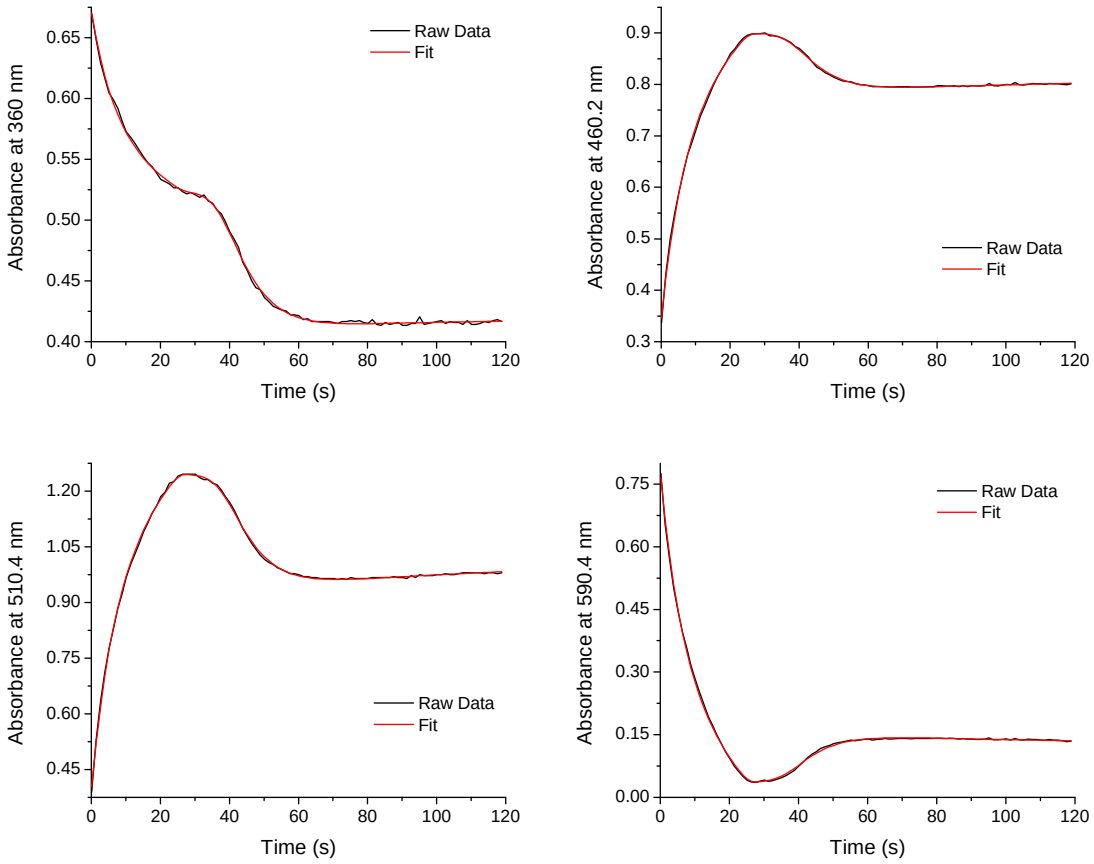

Figure S6. Addition of 3 eq. of Ce(IV) to 6.5 x 10^{-5} M $[(H_2O)Ru^{III}ORu^{III}(OH_2)]^{4+}$ in 0.1 M $HClO_4$. Single wavelength fits.

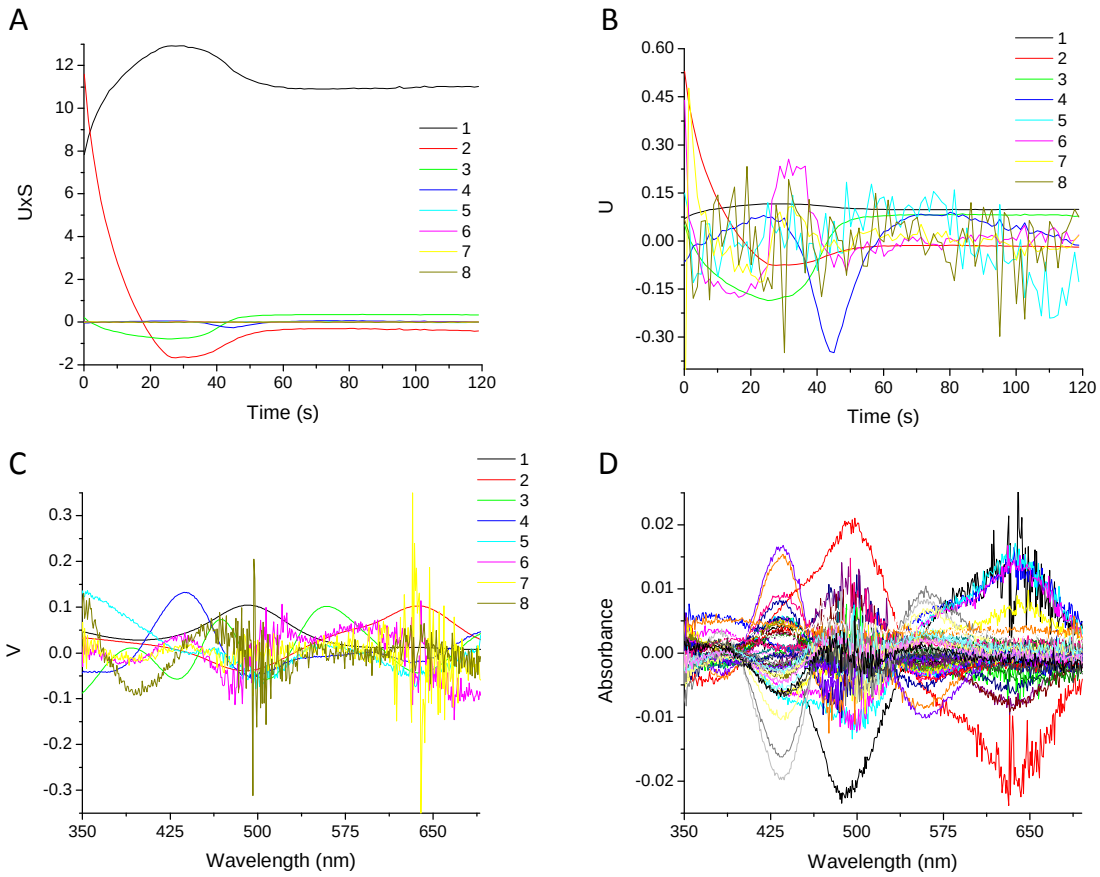

Figure S7. Addition of 3 eq. of Ce(IV) to 6.5 x 10^{-5} M $[(H_2O)Ru^{III}ORu^{III}(OH_2)]^{4+}$ in 0.1 M $HClO_4$. (A) Concentration eigenvectors scaled by their eigenvalues, (B) Concentration eigenvectors, (C) Spectroscopic eigenvectors, (D) Residuals of the fit at all points.

[SPECIES]	[INIT.CONC]	[BUFFERED]	[COLORED]		[FIXED] [SPECTRUM]
Ce4	1.950E-04	False	True	True	CE4C.FIX
3,3	5.600E-05	False	True	False	
Ce3	0.000E+00	False	False	False	
3,4	0.000E+00	False	True	False	
4,4	0.000E+00	False	True	False	
4,5	0.000E+00	False	True	False	
5,5	0.000E+00	False	True	False	

[NAME]	[REACTION]
k1	Ce4 + 3,3 --> Ce3 + 3,4
k2	Ce4 + 3,4 --> Ce3 + 4,4
k3	Ce4 + 4,4 --> Ce3 + 4,5
k4	Ce4 + 4,5 --> Ce3 + 5,5
k5	5,5 --> 3,3
k6	5,5 --> 4,4
k7	4,4 --> 3,3
k8	3,3 + 4,4 --> 2*3,4
k-8	2*3,4 --> 3,3 + 4,4
k9	3,3 + 4,5 --> 3,4 + 4,4
k10	3,4 + 4,5 --> 2*4,4
k-10	2*4,4 --> 3,4 + 4,5
k11	4,4 + 5,5 --> 2*4,5
k-11	2*4,5 --> 4,4 + 5,5

[NAME]	[TYPE]	[LINK]	[PARAMETER]	[ERROR]	[RATIO]
k1	FIX	0	6.25000E+02 +/-	0.00000E+00	
k2	FIX	0	1.50000E+01 +/-	0.00000E+00	
k3	FIX	0	7.50000E+03 +/-	0.00000E+00	
k4	FIX	0	1.40000E+02 +/-	0.00000E+00	
k5	FIX	0	3.00000E-03 +/-	0.00000E+00	
k6	FIX	0	0.00000E+00 +/-	0.00000E+00	
k7	FIX	0	0.00000E+00 +/-	0.00000E+00	
k8	VAR	0	2.68424E+04 +/-	1.29746E+03	
k-8	FIX	0	0.00000E+00 +/-	0.00000E+00	
k9	FIX	0	1.00000E+06 +/-	0.00000E+00	
k10	VAR	0	1.03370E+04 +/-	1.98209E+02	
k-10	FIX	11	1.03370E+04 +/-	1.98209E+02	1.000E+00
k11	VAR	0	4.12382E-01 +/-	1.14631E+03	
k-11	FIX	13	4.12382E-01 +/-	1.14631E+03	1.000E+00

[CONVERGENCE]

Iterations = 3
Convergence Limit = 1.000E-03
Convergence Found = 8.030E-05
Marquardt Parameter = 0.0
Sum(Y-y)^2 Residuals = 6.08202E-01
Std. Deviation of Fit(Y) = 3.83402E-03

[STATISTICS]
Experimental Noise = 9.221E-04
Relative Error Of Fit = 0.6911%
Durbin-Watson Factor = 0.5346
Goodness Of Fit, Chi^2 = 1.729E+01
Durbin-Watson Factor (raw data) = 0.5954

Fitting Report 2. Addition of 3 eq. of Ce(IV) to 6.5 x 10^{-5} M $[(H_2O)Ru^{III}ORu^{III}(OH_2)]^{4+}$ in 0.1 M $HClO_4$.

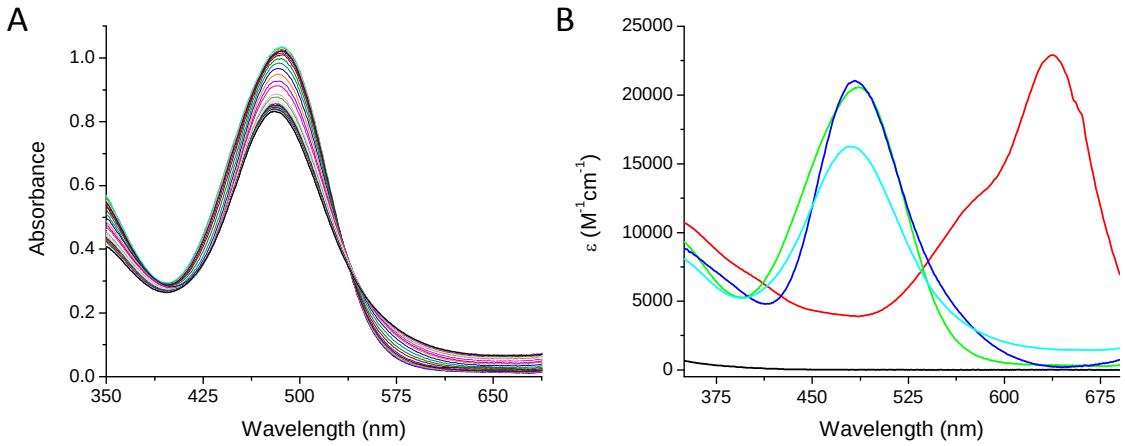

Figure S8. Addition of 2.8 eq. (1.4 x 10^{-4} M) of Ce(IV) to 5.0 x 10^{-5} M $[(HO)Ru^{IV}ORu^{III}(OH_2)]^{4+}$ in 0.1 M $HClO_4$. Left: Raw data. Right: Calculated spectra of species.

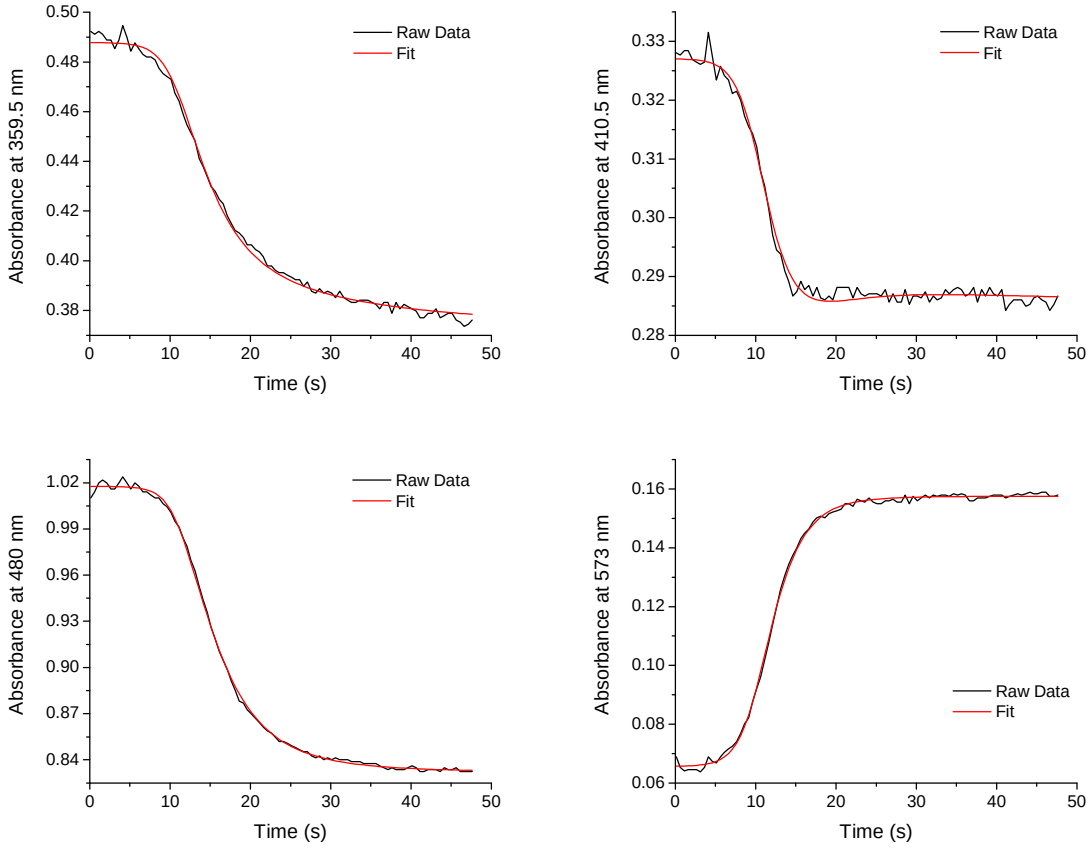

Figure S9. Addition of 2.8 eq. (1.4 x 10^{-4} M) of Ce(IV) to 5.0 x 10^{-5} M $[(HO)Ru^{IV}ORu^{III}(OH_2)]^{4+}$ in 0.1 M $HClO_4$. Single wavelength fits.

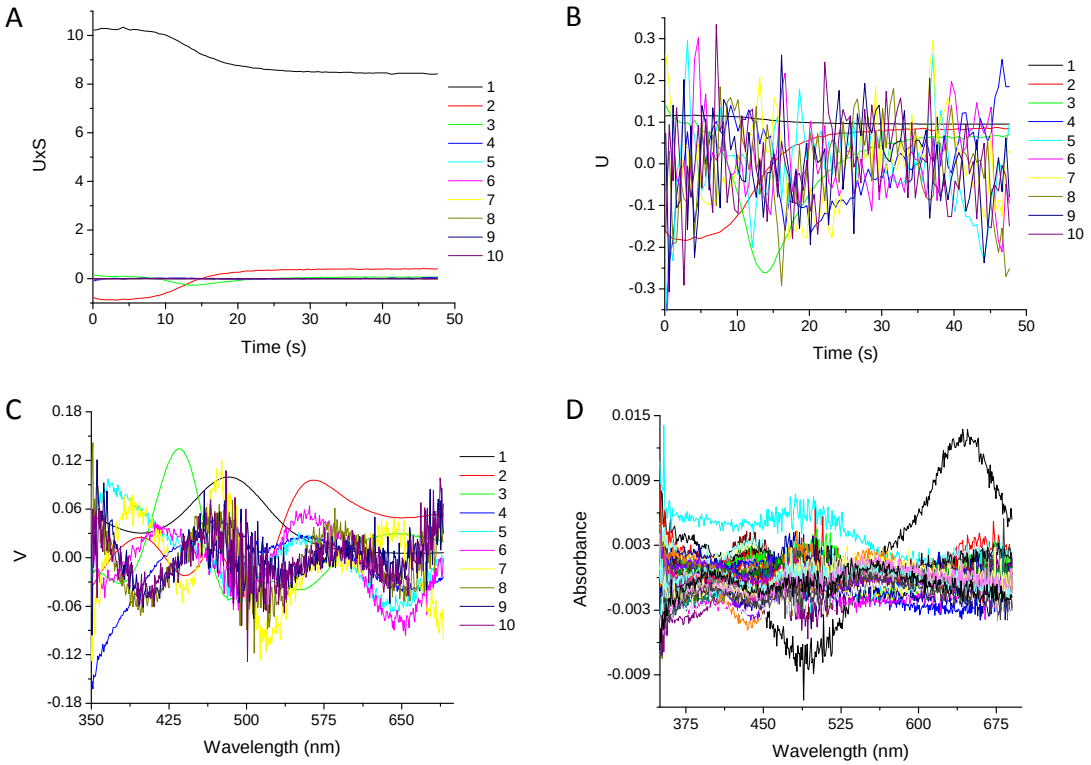

Figure S10. Addition of 2.8 eq. (1.4 x 10^{-4} M) of Ce(IV) to 5.0 x 10^{-5} M $[(HO)Ru^{IV}ORu^{III}(OH_2)]^{4+}$ in 0.1 M $HClO_4$. (A) Concentration eigenvectors scaled by their eigenvalues, (B) Concentration eigenvectors, (C) Spectroscopic eigenvectors, (D) Residuals of the fit at all points.

[SPECIES]	[INIT.CONC]	[BUFFERED]	[COLORED]		[FIXED] [SPECTRUM]
Ce4	1.400E-04	False	True	True	CE4C.FIX
3,3	0.000E+00	False	True	True	33.FIX
Ce3	0.000E+00	False	False	False	
3,4	5.000E-05	False	True	False	
4,4	0.000E+00	False	True	False	
4,5	0.000E+00	False	True	False	
5,5	0.000E+00	False	False	False	

[NAME]	[REACTION]
k1	Ce4 + 3,3 --> Ce3 + 3,4
k2	Ce4 + 3,4 --> Ce3 + 4,4
k3	Ce4 + 4,4 --> Ce3 + 4,5
k4	Ce4 + 4,5 --> Ce3 + 5,5
k5	5,5 --> 3,3
k6	5,5 --> 4,4
k7	4,4 --> 3,3
k8	3,3 + 4,4 --> 2*3,4
k-8	2*3,4 --> 3,3 + 4,4
k9	3,3 + 4,5 --> 3,4 + 4,4
k10	3,4 + 4,5 --> 2*4,4
k-10	2*4,4 --> 3,4 + 4,5
k11	4,4 + 5,5 --> 2*4,5
k-11	2*4,5 --> 4,4 + 5,5

[NAME]	[TYPE]	[LINK]		[PARAMETER]	[ERROR]	[RATIO]
k1	FIX	0	6.25000E+02	+/-	0.00000E+00	
k2	VAR	0	3.23676E+00	+/-	1.23367E-01	
k3	FIX	0	7.50000E+03	+/-	0.00000E+00	
k4	FIX	0	2.00000E+02	+/-	0.00000E+00	
k5	FIX	0	5.00000E+00	+/-	0.00000E+00	
k6	FIX	0	0.00000E+00	+/-	0.00000E+00	
k7	FIX	0	0.00000E+00	+/-	0.00000E+00	
k8	FIX	0	0.00000E+00	+/-	0.00000E+00	
k-8	FIX	0	0.00000E+00	+/-	0.00000E+00	
k9	FIX	0	1.00000E+05	+/-	0.00000E+00	
k10	FIX	0	5.86600E+04	+/-	0.00000E+00	
k-10	FIX	11	5.86600E+04	+/-	0.00000E+00	1.000E+00
k11	FIX	0	5.52500E-02	+/-	0.00000E+00	
k-11	FIX	13	5.52500E-02	+/-	0.00000E+00	1.000E+00

[CONVERGENCE]

Iterations = 3
Convergence Limit = 1.000E-03
Convergence Found = 1.151E-04
Marquardt Parameter = 0.0
Sum(Y-y)^2 Residuals = 9.90931E-02
Std. Deviation of Fit(Y) = 1.55481E-03

[STATISTICS]
Experimental Noise = 6.972E-04
Relative Error Of Fit = 0.3574%
Durbin-Watson Factor = 0.6723
Goodness Of Fit, Chi^2 = 4.974E+00
Durbin-Watson Factor (raw data) = 0.8308

Fitting Report 3. Addition of 2.8 eq. (1.4×10^{-4} M) of Ce(IV) to 5.0×10^{-5} M $[(HO)Ru^{IV}ORu^{III}(OH_2)]^{4+}$ in 0.1 M $HClO_4$. Details provided in supporting information.

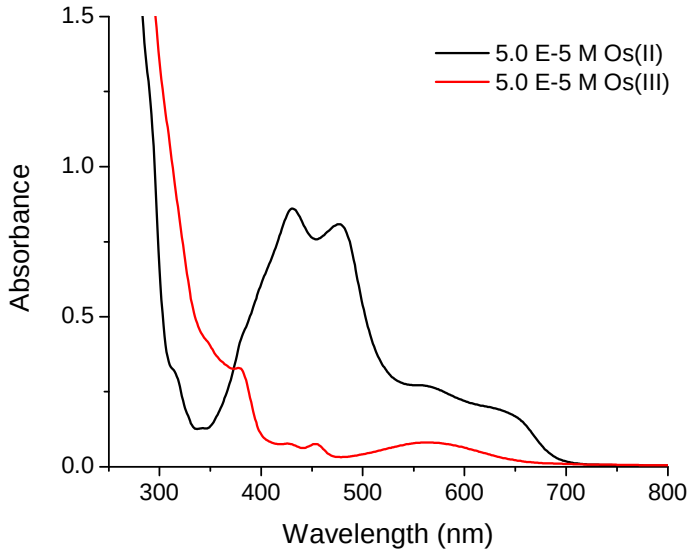

Figure S11. Spectra of $[Os^{II}(phen)_3](NO_3)_2$ and $[Os^{III}(phen)_3](NO_3)_3$ in 0.1 M HNO_3 for comparison with redox titration shown in Figure S12 below.

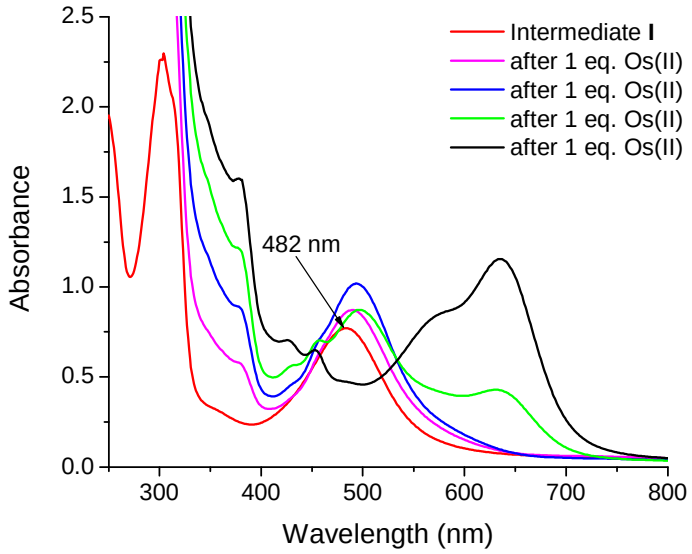

Figure S12. Redox titration of intermediate II, λ_{max} = 482 nm, with $[Os^{II}(phen)_3](NO_3)_2$ in 0.1 M HNO_3, generated by addition of 3 eq. of Ce(IV) to 5.0 x 10^{-5} M $[(HO)Ru^{IV}ORu^{III}(OH_2)]^{4+}$.

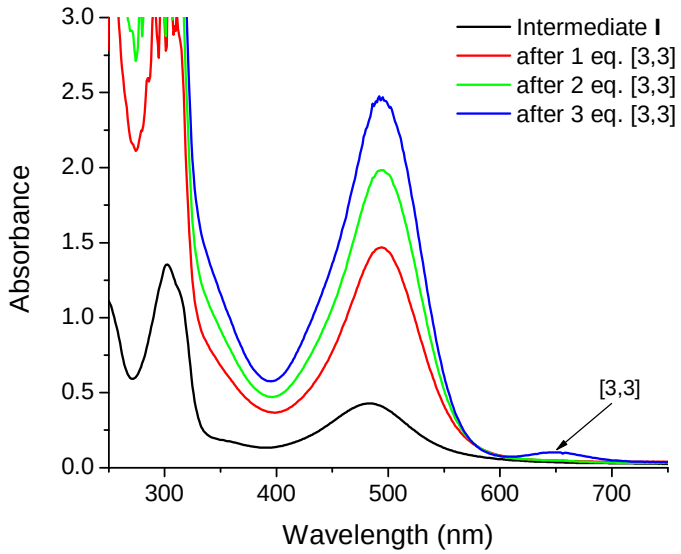

Figure S13. Redox titration of intermediate **II** (prepared in same way as described in Figure S12) with $[(H_2O)Ru^{III}ORu^{III}(OH_2)]^{4+}$ in 0.1 M HNO_3.

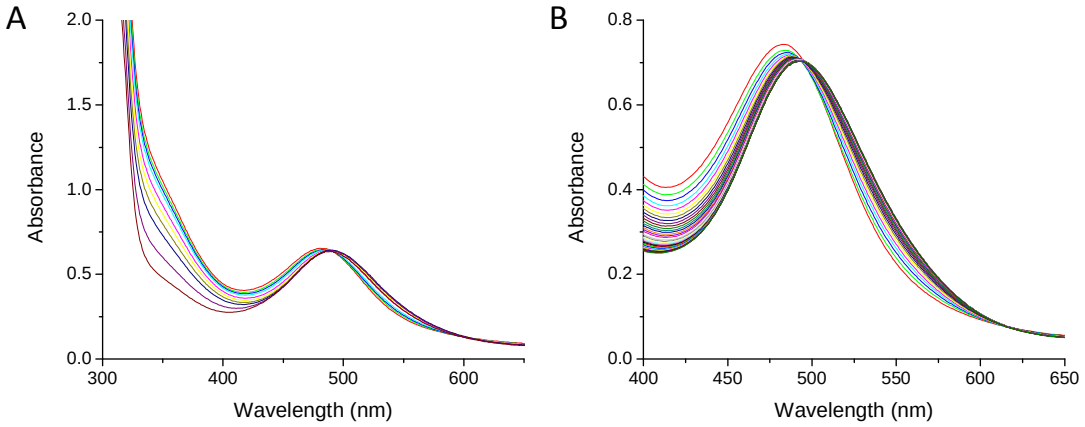

Figure S14. Addition of 30 eq. of Ce(IV) to 5.0 x 10^{-5} M blue dimer. (A) 0.1 M $HClO_4$ (B) 0.1 M CF_3SO_3H.

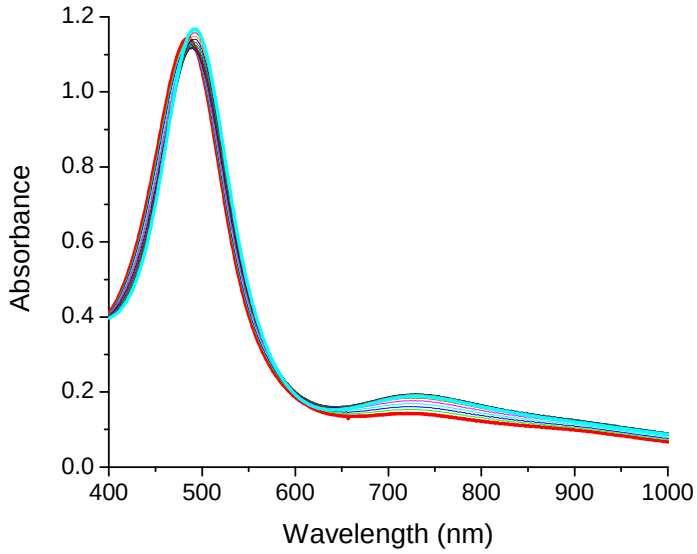

Figure S15. Addition of 3 eq. of Ce(IV) to 0.0094 M $[(HO)Ru^{IV}ORu^{III}(OH_2)]^{4+}$ in 0.1 M HNO_3.

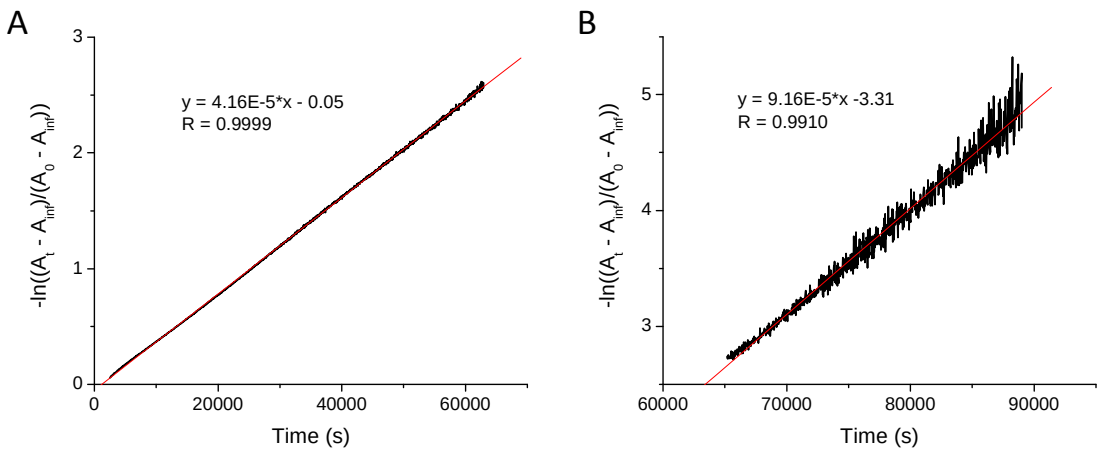

Figure S16. First order kinetic plot, $-\ln((A_t - A_\infty)/(A_0 - A_\infty))$ vs. time (s) for absorbance at 495 nm following the decay of intermediate **II** by the appearance of $[(HO)Ru^{IV}ORu^{III}(OH_2)]^{4+}$ at its lmax. Fits of two first order kinetic regions (Figure 18B): (A) First stage of decay (B) second stage of decay.

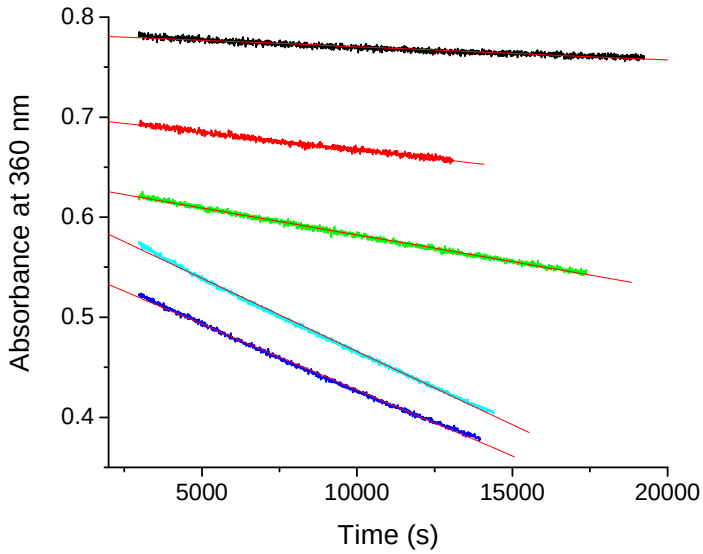

Figure S17. Long stage of Ce(IV) consumption, zero order in Ce(IV), in dilute blue dimer, 0.1 M HNO_3. Legend: Concentrations of blue dimer, 1.0 x 10^{-6} M (black), 5.0 x 10^{-6} M (red), 1.0 x 10^{-5} M (green), 1.73 x 10^{-5} M (blue), 2.5 x 10^{-5} M (cyan).

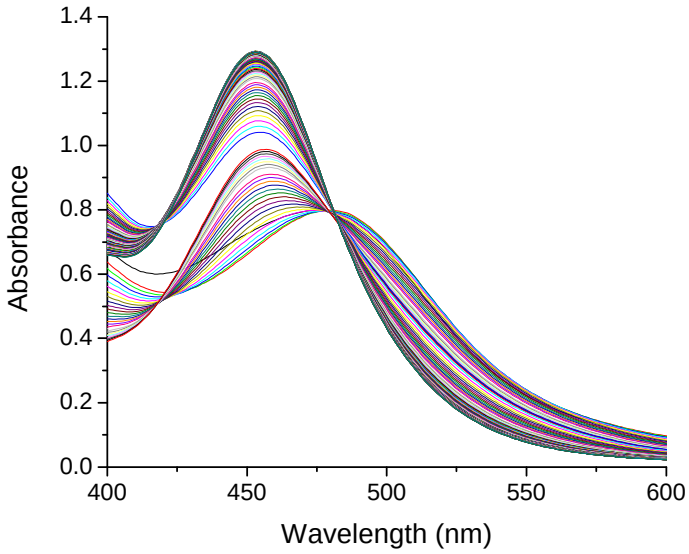

Figure S18. Addition of 30 eq. of Ce(IV) to 5.0 x 10^{-5} M $[(H_2O)Ru^{III}ORu^{III}(OH_2)]^{4+}$ in 1.0 M HNO_3, followed by a second addition of 30 eq. of Ce(IV) after formation of intermediate **III** with λ_{max} = 455 nm.

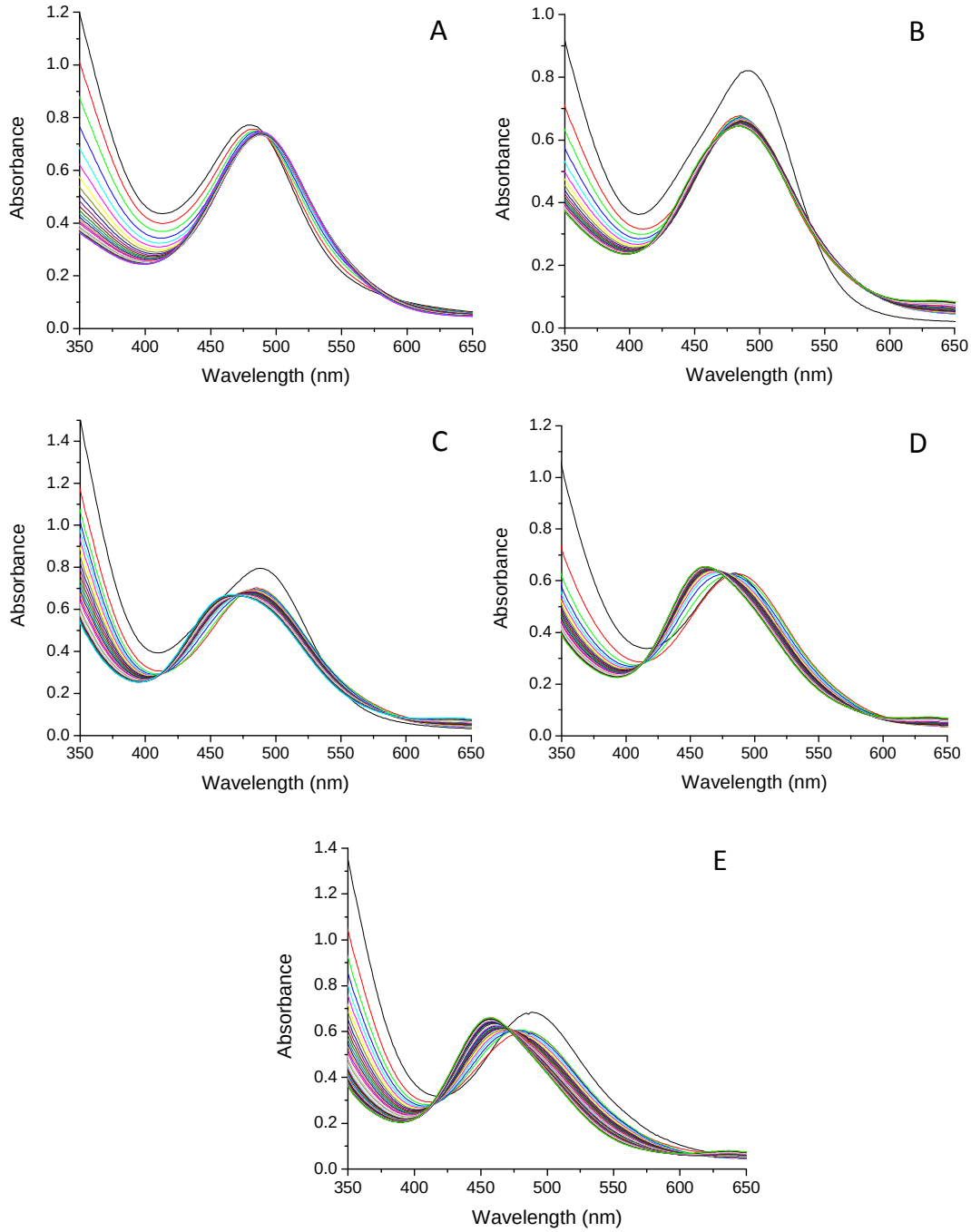

Figure S19. Addition of 30 eq. of Ce(IV) to 5.0 x 10^{-5} M blue dimer in 0.1 M HNO_3 with different amounts of added KNO_3. (A) no KNO_3, (B) 0.1 M KNO_3, (C) 0.4 M KNO_3, (D) 0.9 M KNO_3, (E) 1.4 M KNO_3.

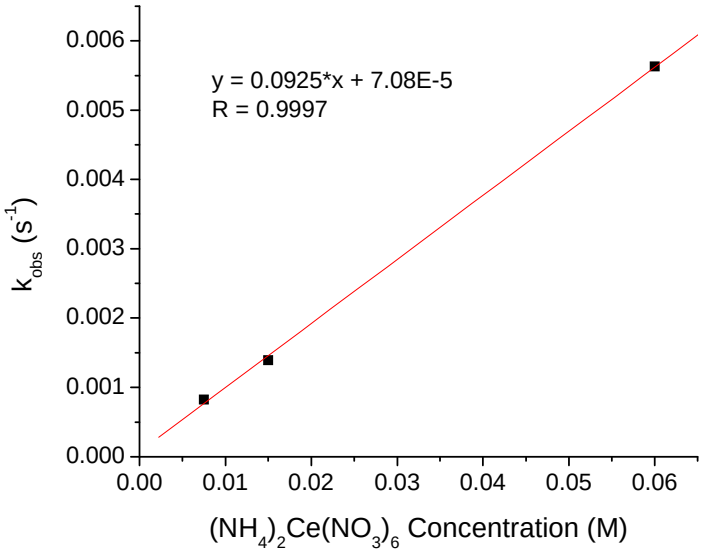

Figure S20. Second order rate constant for growth of intermediate **III**, monitored at 455 nm. k_{obs} (s^{-1}) is plotted as a function of Ce(IV) concentration corresponding to different amounts of Ce(IV) added to 0.001 M $[(H_2O)Ru^{III}ORu^{III}(OH_2)]^{4+}$ in 0.1 M HNO_3.

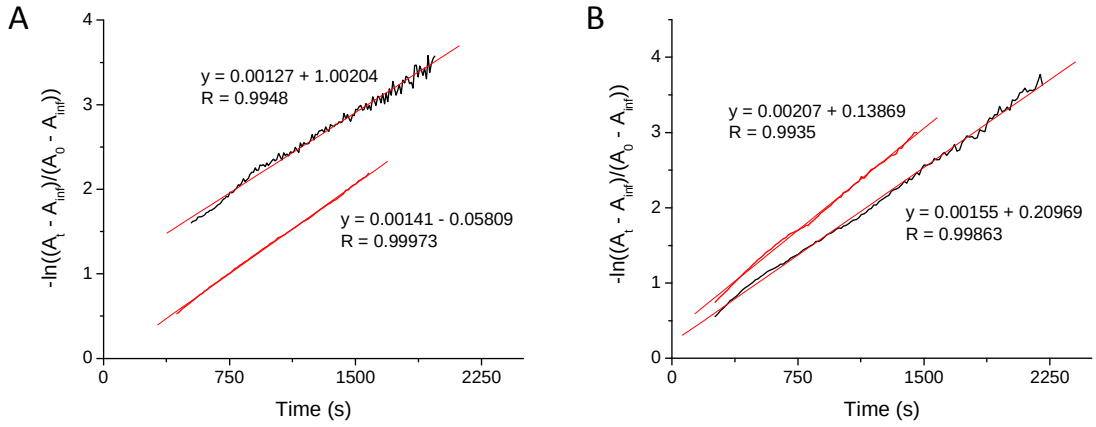

Figure S21. The same amount of Ce(IV) added to different concentrations of blue dimer in 0.1 M HNO_3. Saturation kinetics are observed. (A) Addition of 15 eq. of Ce(IV) added to 0.001 M blue dimer and 30 eq. of Ce(IV) added to 5.0 x 10^{-4} M blue dimer, (B) 30 eq. of Ce(IV) added to 0.001 M blue dimer and 60 eq. of Ce(IV) added to 5.0 x 10^{-4} M blue dimer.

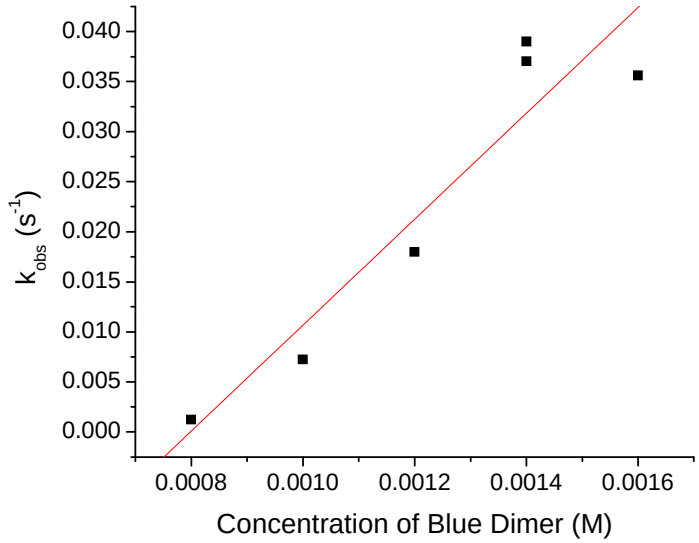

Figure 22. Excess Ce(IV) consumption by the Blue Dimer in 0.1 M HNO_3, monitoring at 360 nm. The addition of Ce(IV) has been kept constant at 30 eq. of Ce(IV) with respect to 8.0 x 10^{-4} M catalyst.

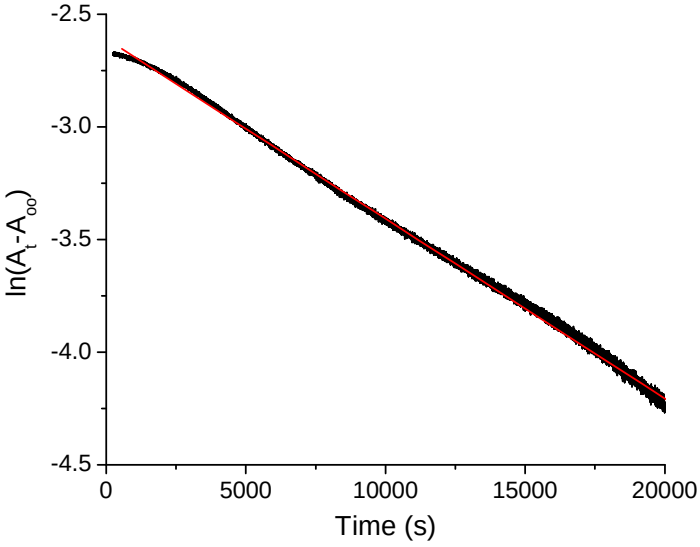

Figure S23. First order decay of $[(O_2NO)Ru^{IV}ORu^{IV}(OH)]^{4+}$ in 1.0 M HNO_3, measured by monitoring growth of $[(H_2O)Ru^{IV}ORu^{III}(OH_2)]^{5+}$ at 445 nm. k = 8.0 x 10^{-5} s^{-1}.

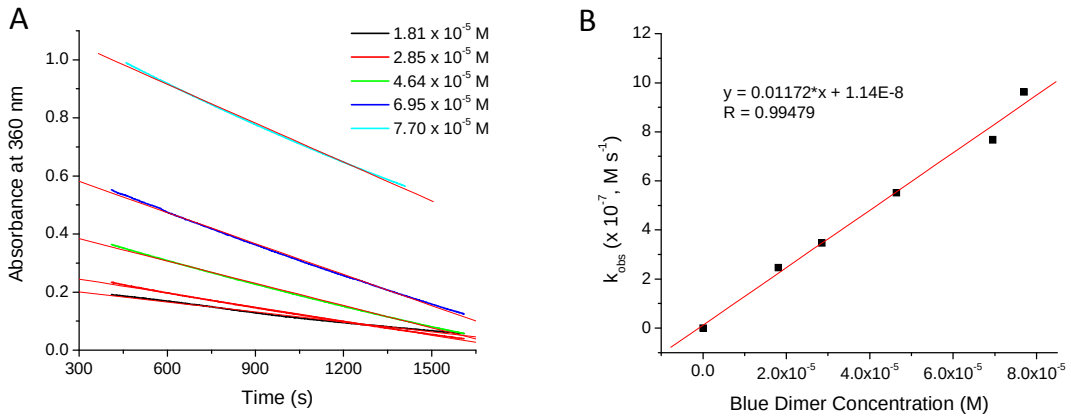

Figure S24. (A) Absorbance at 360 nm vs. time for second stage of Ce(IV) consumption following 30 eq. of Ce(IV) with respect to 5.0 x 10^{-5} M blue dimer to different concentrations of catalyst in 1.0 M CF_3SO_3H. (B) Kinetic plot of second stage of Ce(IV) consumption. k_{obs} (M s^{-1}), zero-order in Ce(IV) vs. Blue Dimer concentration (M) showing first order dependence on catalyst, k = 0.012 s^{-1}.

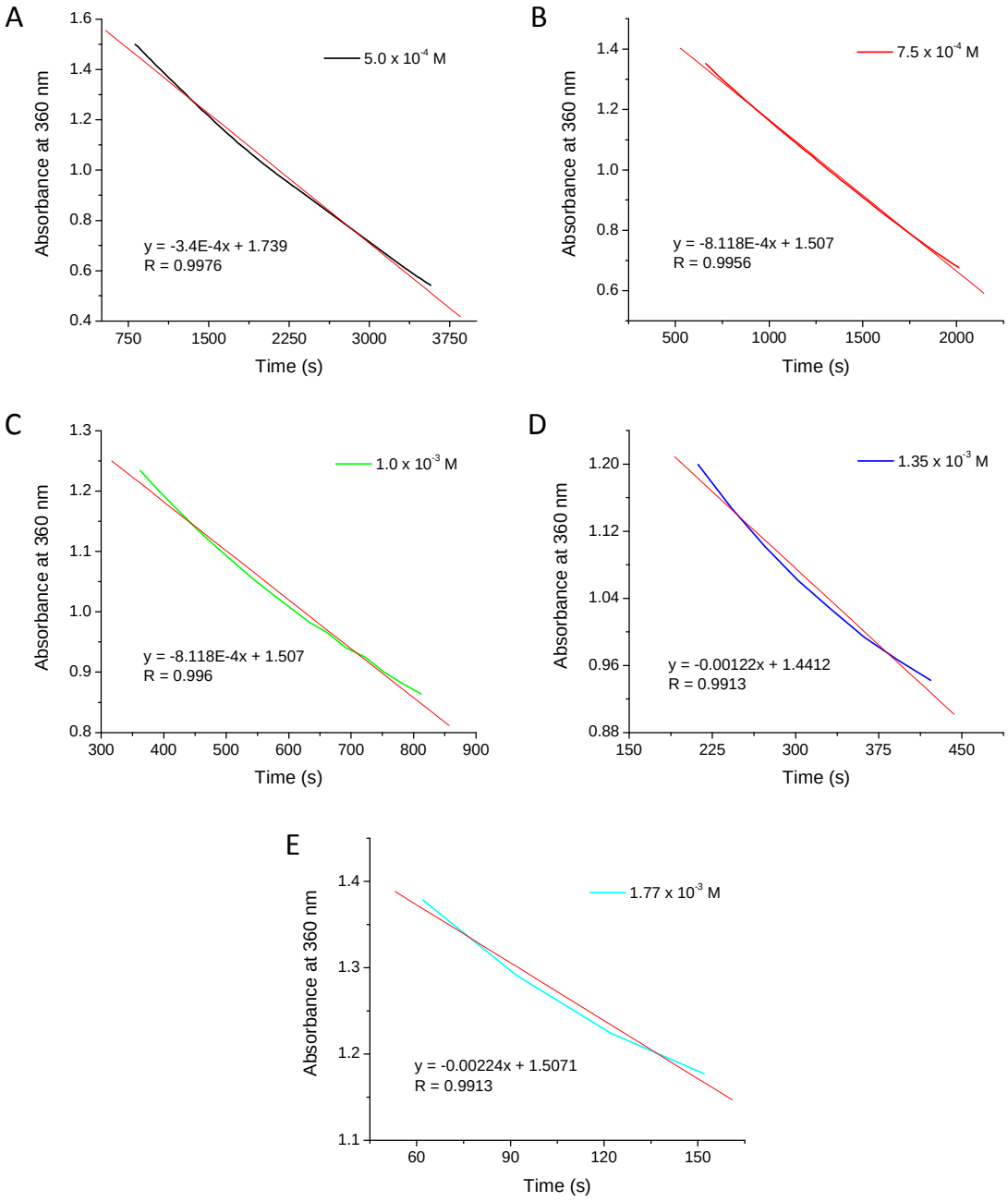

Figure S25. Linear fits of the pseudo-zero order Ce(IV) consumption, followed at 360 nm, for the addition of 30 eq. of Ce(IV) with respect to 0.001 M blue dimer to different catalyst concentrations, ranging from 5.0 x 10^{-4} M to 1.77 x 10^{-3} M.

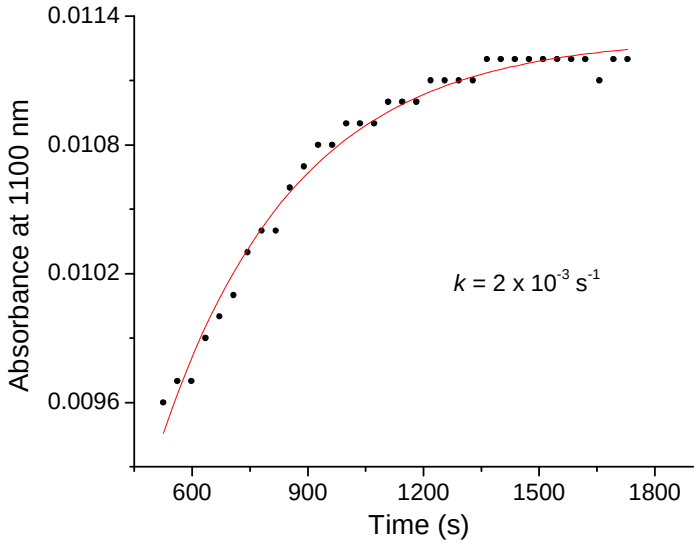

Figure S26. Decay of $[(CF_3O_2SO)Ru^{IV}ORu^{IV}(OH)]^{4+}$ and $[(O)Ru^{V}ORu^{IV}(O)]^{3+}$ in 1.0 M CF_3SO_3H after Ce(IV) consumption following the addition of 30 eq. of Ce(IV) to 5.0 x 10^{-5} M blue dimer. The reappearance of $[(H_2O)Ru^{IV}ORu^{III}(OH_2)]^{5+}$ was monitored at 1100 nm.

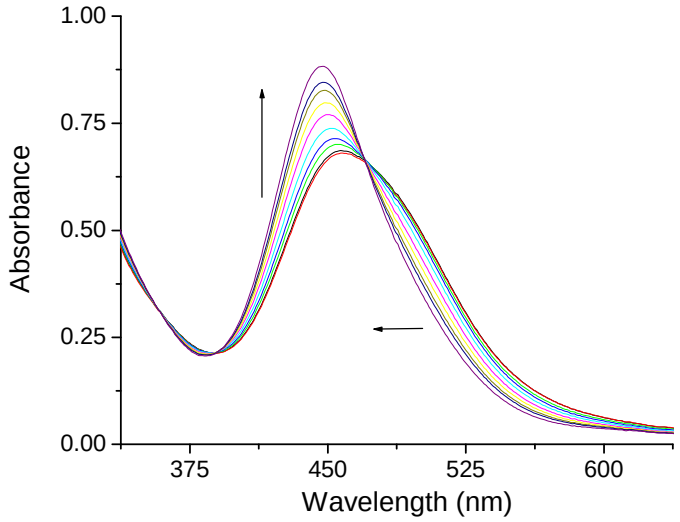

Figure S27. Decay of oxidized blue dimer species to $[(H_2O)Ru^{IV}ORu^{III}(OH_2)]^{5+}$ (λ_{max} = 445 nm) after Ce(IV) consumption of 30 eq. of Ce(IV) to 5.0 x 10^{-5} M blue dimer in 1.0 M $HClO_4$. First spectrum (red) at time = 920 s after Ce(IV) addition, last spectrum (purple) at time = 6180 s.

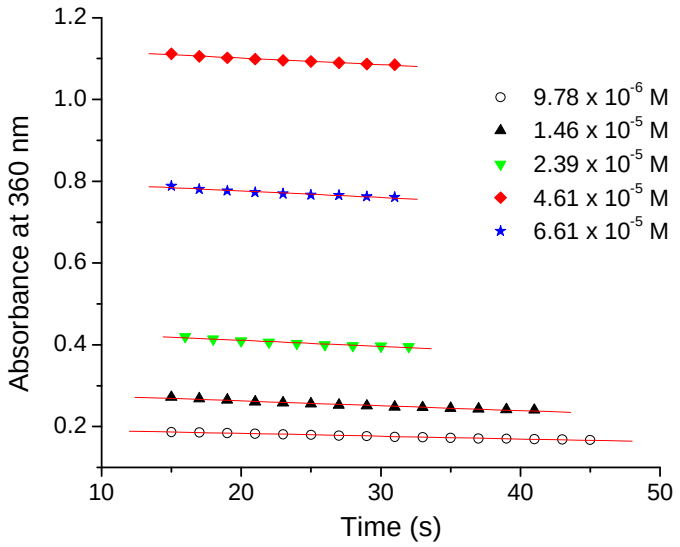

Figure S28. First stage of Ce(IV) consumption, monitored at 360 nm, following addition of 30 eq. of Ce(IV) with respect to 5.0 x 10^{-5} M to different concentrations of catalyst in 1.0 M $HClO_4$.

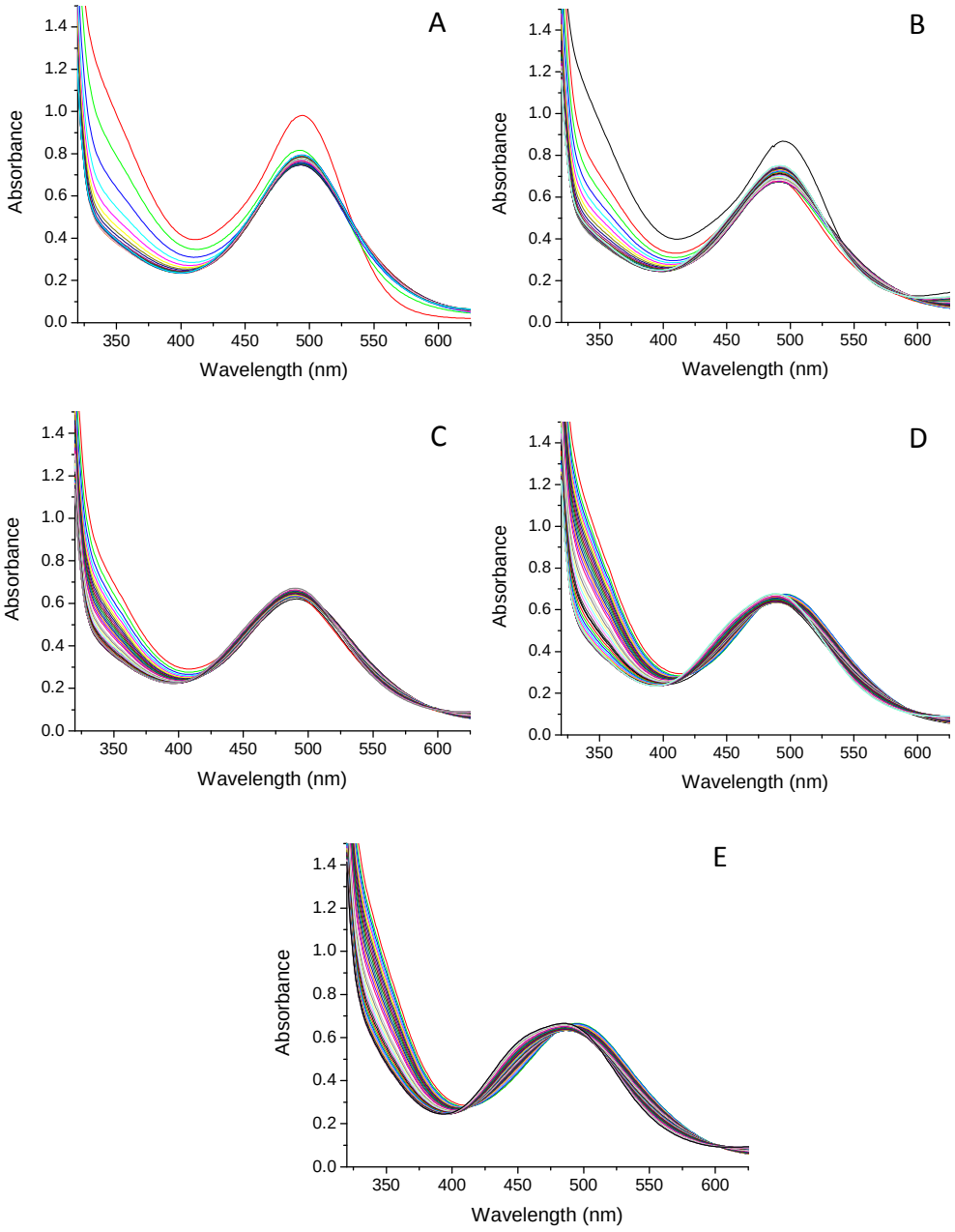

Figure S29. Addition of 30 eq. of Ce(IV) to 5 x 10^{-5} M blue dimer in 0.1 M CF_3SO_3H with different amounts of added CF_3SO_3Li. (A) no CF_3SO_3Li, (B) 0.1 M CF_3SO_3Li, (C) 0.4 M CF_3SO_3Li, (D) 0.9 M CF_3SO_3Li, (E) 1.4 M CF_3SO_3Li.

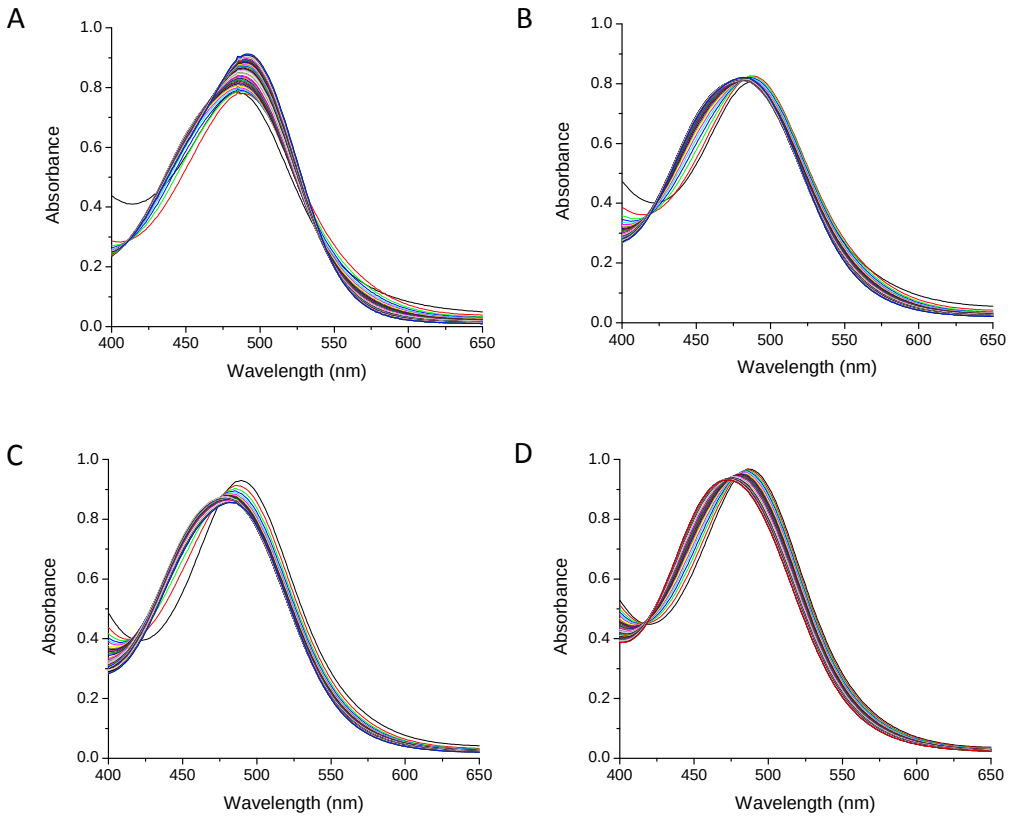

Figure S30. Addition of 30 eq. of Ce(IV) to 5.0 x 10^{-5} M $[(H_2O)Ru^{III}ORu^{III}(OH_2)]^{4+}$ in 0.1 M HNO_3 with added $Ce^{III}(NO_3)_6^{3-}$. (A) 0.0167 M Ce(III), spectra from 10 to 60640 s, 1213 s between spectra, B) 0.0667 M Ce(III), spectra from 10 to 19260 s, 385 s between spectra, (C) 0.15 M Ce(III), spectra from 10 to 62160 s, 1243 s between spectra, (D) 0.233 M Ce(III), spectra from 10 to 16520 s, 330 s between spectra.

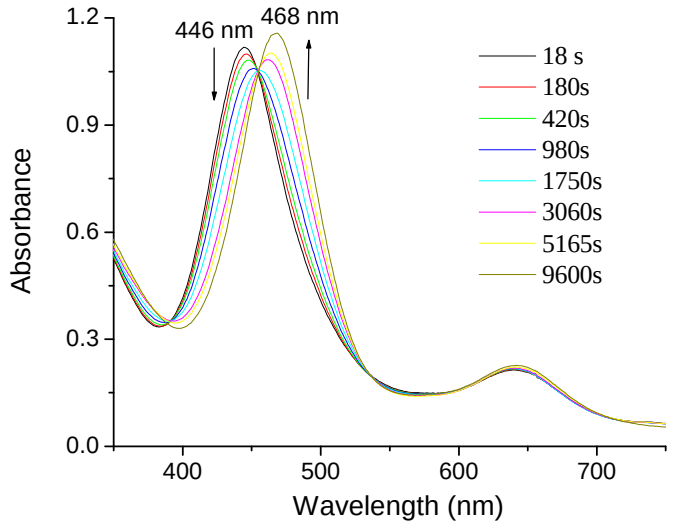

Figure S31. $[(H_2O)Ru^{III}ORu^{III}(OH_2)]^{4+}$ (1.0 x 10^{-5} M) and $[(H_2O)Ru^{IV}ORu^{III}(OH_2)]^{5+}$ (5.0 x 10^{-5} M) in 1.0 M CF_3SO_3H, then 1.0 M H_2SO_4 is added. Times refer to after H_2SO_4 was added.

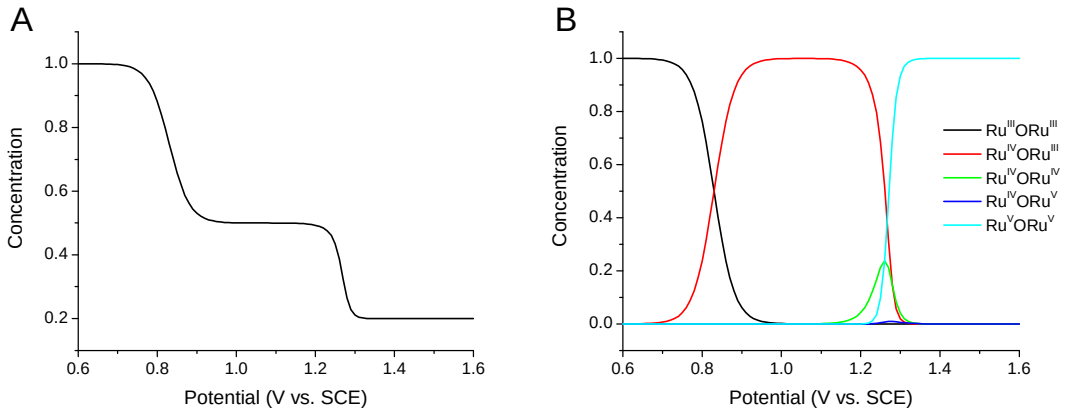

Figure S32. Concentration vs. potential (V vs. SCE) profiles for Nernst simulation in SpecFit of reported redox potentials, assuming 1 e^- couples.

[TYPE]
4 E°, A = B = C = D = E

[SPECIES]	[INIT.CONC]	[COLORED]		[FIXED]	[SPECTRUM]
A	1.000E+00	True	False		
B	0.000E+00	True	False		
C	0.000E+00	True	False		
D	0.000E+00	True	False		
E	0.000E+00	True	False		

[ELECTRON]	[FIXED]	[PARAMETER]		[ERROR]
1	True	8.30000E-01	+/-	0.00000E+00
1	True	1.28000E+00	+/-	0.00000E+00
1	True	1.35000E+00	+/-	0.00000E+00
1	True	1.17000E+00	+/-	0.00000E+00

[TEMPERATURE]
Temp(K) = 298.15

[CONVERGENCE]
Iterations = 0
Convergence Limit = 1.000E-03
Convergence Found = 0.000E+00
Marquardt Parameter = 0.0
Sum(Y-y)^2 Residuals = 0.00000E+00
Std. Deviation of Fit(Y) = 0.00000E+00

[STATISTICS]
Experimental Noise = None
Relative Error Of Fit = None
Durbin-Watson Factor = 2.0476
Goodness Of Fit, Chi^2 = None
Durbin-Watson Factor (raw data) = 2.0476

Fitting Report 4. Nernst simulation in SpecFit of reported redox potentials, assuming 1 e^- couples.

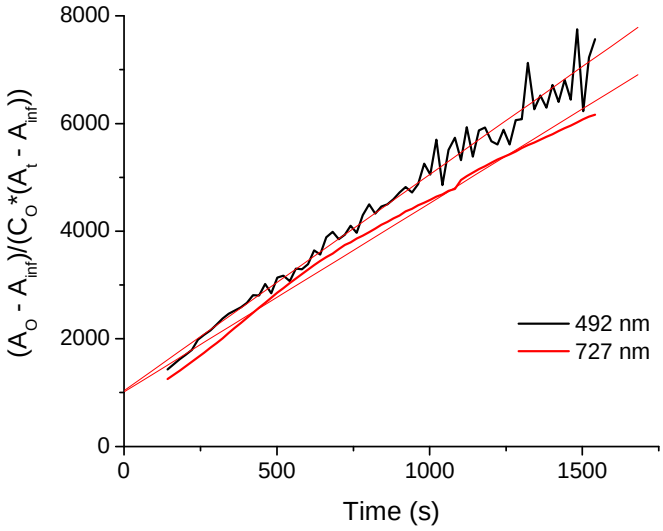

Figure S33. Second order kinetics following the change in absorption spectrum of intermediate **I** generated by addition of 3 eq. of Ce(IV) to 0.0012 M $[(HO)Ru^{IV}ORu^{III}(OH_2)]^{4+}$ in 0.1 M HNO_3, 1 mm path length cell, 23 °C.

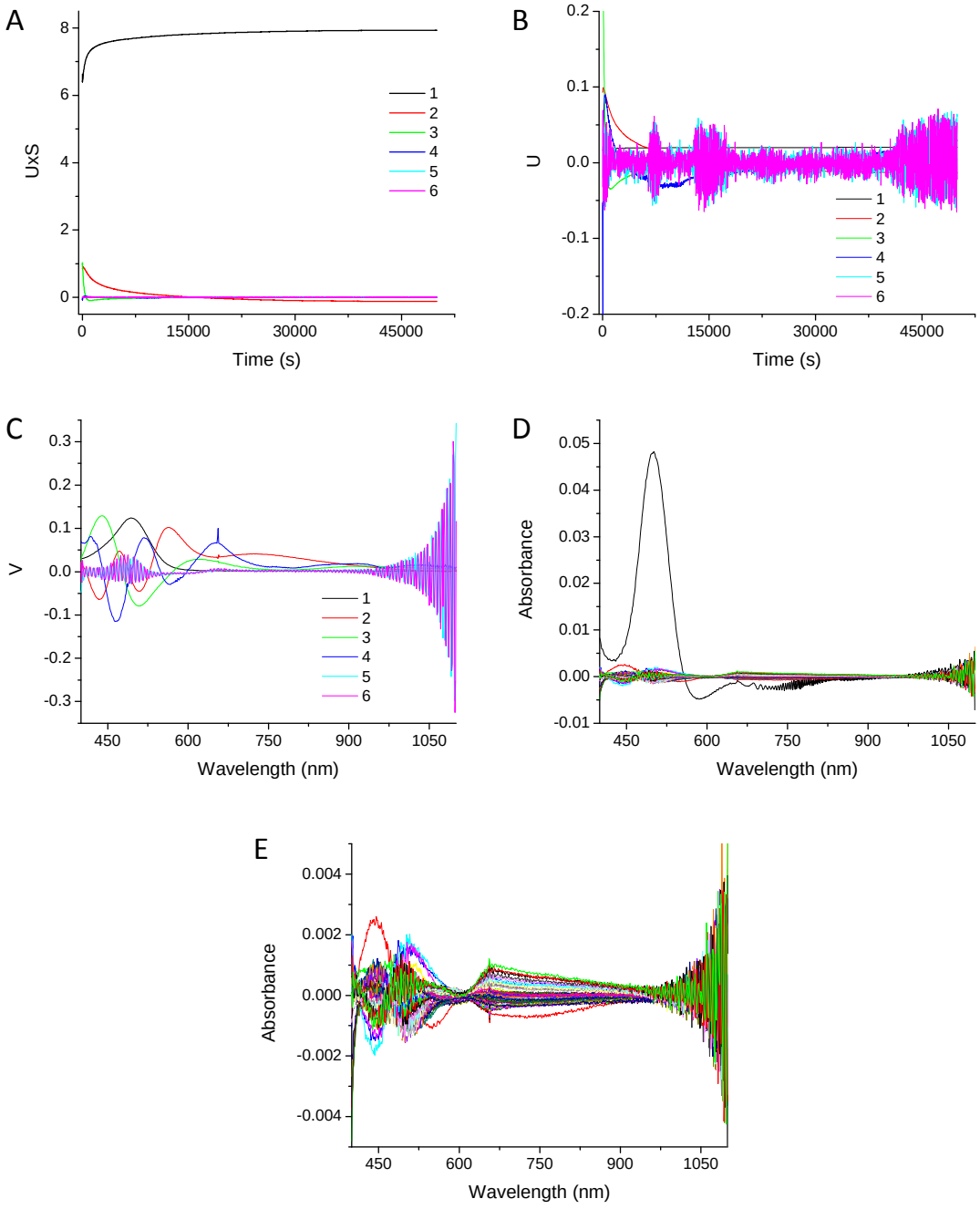

Figure S34. Decay of intermediate **I** after generation by adding 3 eq. of Ce(IV) to 5.0 x 10^{-5} M $[(HO)Ru^{IV}ORu^{III}(OH_2)]^{4+}$ in 0.1 M HNO_3. (A) Concentration eigenvectors scaled by their eigenvalues, (B) Concentration eigenvectors, (C) Spectroscopic eigenvectors, (D) Residuals of the fit at all points. (E) Residuals minus the first outlier.

[SPECIES]	[INIT.CONC]	[BUFFERED]	[COLORED]	[FIXED]
	[SPECTRUM]			
A	5.000E-05	False	True	False
B	0.000E+00	False	True	False
C	0.000E+00	False	True	False
D	0.000E+00	False	True	False

[NAME]	[REACTION]
k1	2*A --> B + C
k2	B --> D
k3	C > D

[NAME]	[TYPE]	[LINK]	[PARAMETER]	[ERROR]	[RATIO]
k1	VAR	0	2.75646E+01	+/-	4.07328E-01
k2	VAR	0	8.67350E-05	+/-	2.84851E-07
k3	VAR	0	1.11315E-03	+/-	9.59992E-06

[CONVERGENCE]
Iterations = 3
Convergence Limit = 1.000E-03
Convergence Found = 1.470E-05
Marquardt Parameter = 0.0
Sum(Y-y)^2 Residuals = 3.69981E-01
Std. Deviation of Fit(Y) = 4.59474E-04

[STATISTICS]
Experimental Noise = 4.475E-04
Relative Error Of Fit = 0.1555%
Durbin-Watson Factor = 0.7100
Goodness Of Fit, Chi^2 = 1.054E+00
Durbin-Watson Factor (raw data) = 0.8900

Fitting Report 5. Decay of intermediate **I** after generation by adding 3 eq. of Ce(IV) to 5.0 x 10^{-5} M $[(HO)Ru^{IV}ORu^{III}(OH_2)]^{4+}$ in 0.1 M HNO_3.

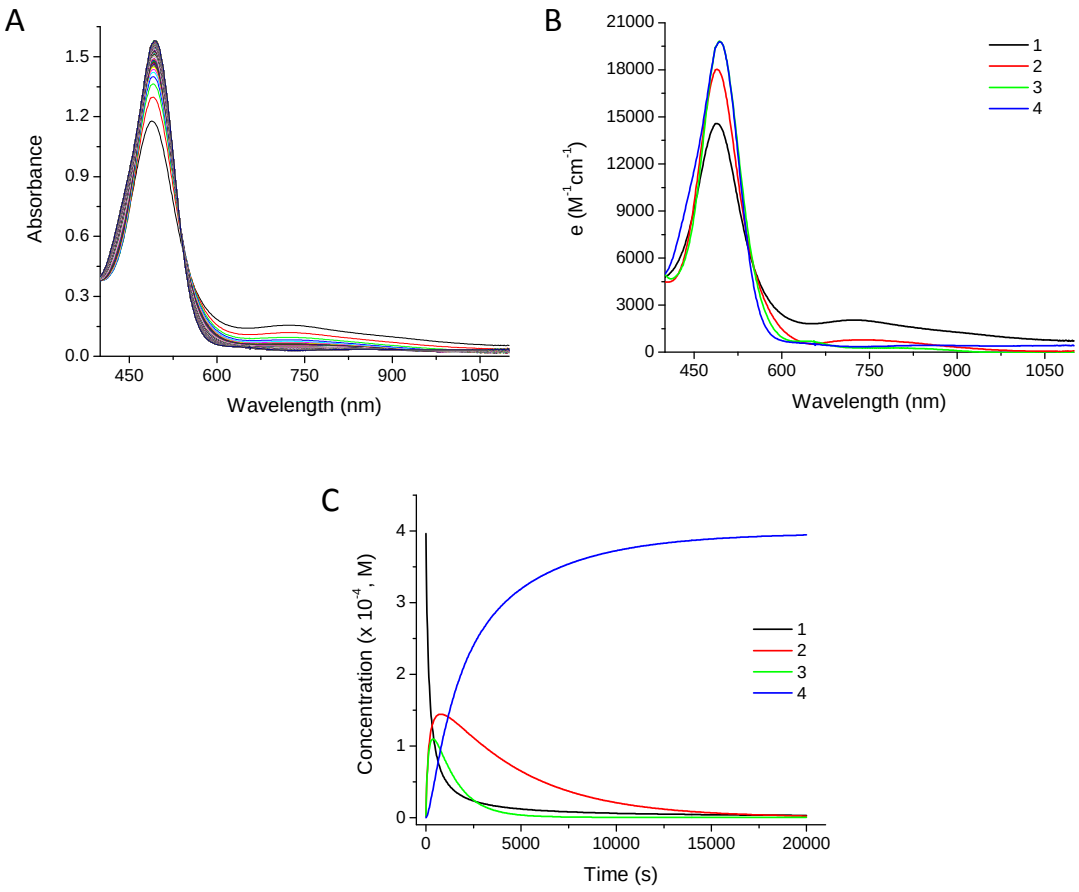

Figure S35. Decay of intermediate **I** after generation by adding 3 eq. of Ce(IV) to 4.0 x 10^{-4} M $[(HO)Ru^{IV}ORu^{III}(OH_2)]^{4+}$ in 0.1 M HNO_3. (A) Raw data, (B) Calculated spectra of each species, (C) Concentration (x 10^{-4} M) vs. Time (s) profiles of each species.

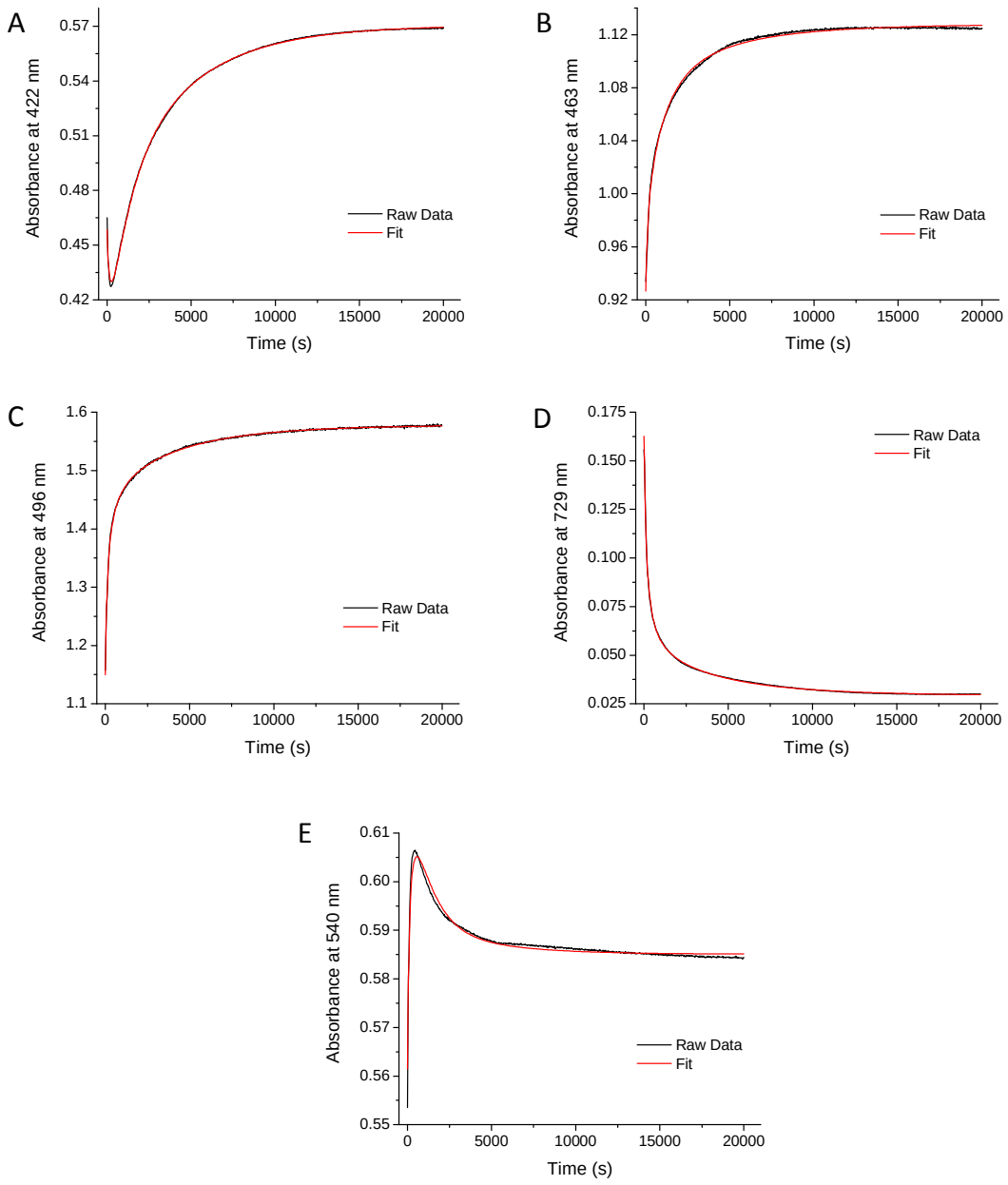

Figure S36. Decay of intermediate **I** after generation by adding 3 eq. of Ce(IV) to 4.0 x 10^{-4} M $[(HO)Ru^{IV}ORu^{III}(OH_2)]^{4+}$ in 0.1 M HNO_3. Single wavelength fits.

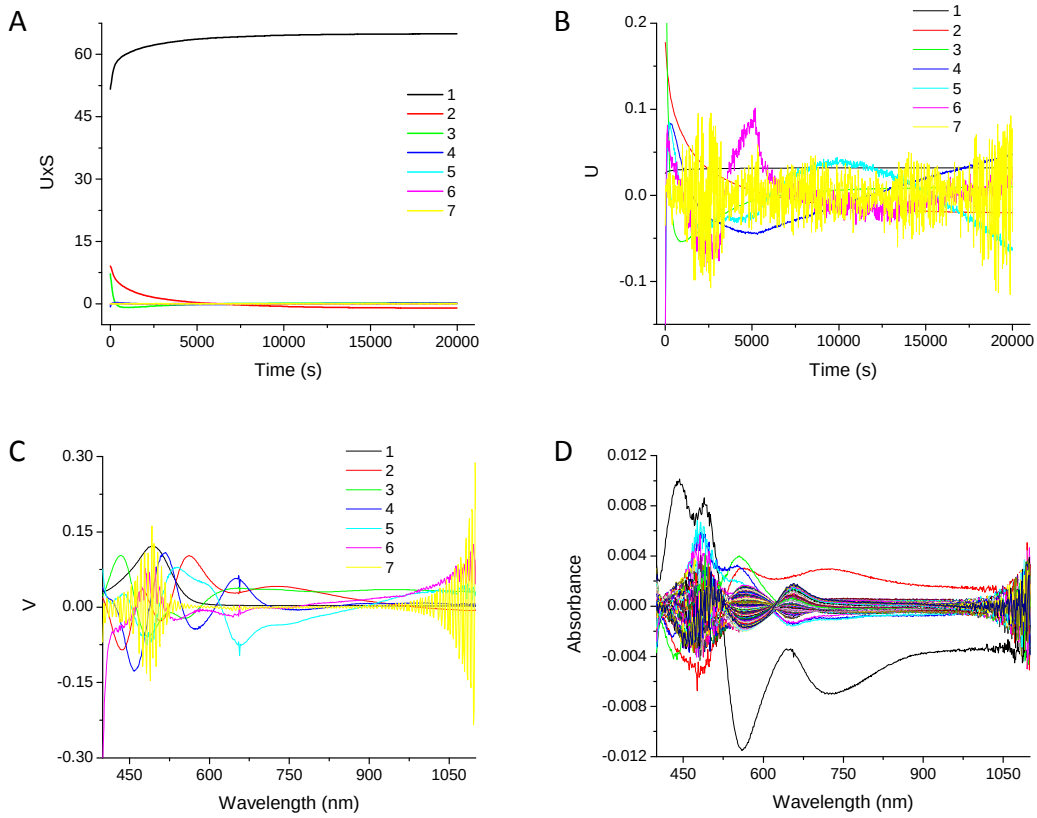

Figure S37. Decay of intermediate **I** after generation by adding 3 eq. of Ce(IV) to 4.0 x 10^{-4} M $[(HO)Ru^{IV}ORu^{III}(OH_2)]^{4+}$ in 0.1 M HNO_3. (A) Concentration eigenvectors scaled by their eigenvalues, (B) Concentration eigenvectors, (C) Spectroscopic eigenvectors, (D) Residuals of the fit at all points.

[SPECIES]	[INIT.CONC]	[BUFFERED]	[COLORED]	[FIXED]
	[SPECTRUM]			
A	4.000E-04	False	True	False
B	0.000E+00	False	True	False
C	0.000E+00	False	True	False
D	0.000E+00	False	True	False

[NAME]	[REACTION]
k1	2*A > B + C
k2	B > D
k3	C > D

[NAME]	[TYPE]	[LINK]		[PARAMETER]	[ERROR]
[RATIO]					
k1	VAR	0	8.05502E+00	+/-	8.30819E-02
k2	VAR	0	2.41863E-04	+/-	1.76865E-06
k3	VAR	0	9.94136E-04	+/-	1.28151E-05

[CONVERGENCE]
Iterations = 3
Convergence Limit = 1.000E-03
Convergence Found = 4.329E-05
Marquardt Parameter = 0.0
Sum(Y-y)^2 Residuals = 2.72791E-01
Std. Deviation of Fit(Y) = 6.23816E-04

[STATISTICS]
Experimental Noise = 4.133E-04
Relative Error Of Fit = 0.1292%
Durbin-Watson Factor = 0.1755
Goodness Of Fit, Chi^2 = 2.278E+00
Durbin-Watson Factor (raw data) = 0.5219

Fitting Report 6. Decay of intermediate **I** after generation by adding 3 eq. of Ce(IV) to 4.0 x 10^{-4} M $[(HO)Ru^{IV}ORu^{III}(OH_2)]^{4+}$ in 0.1 M HNO_3.

APPENDIX C

One Site is Enough: Monomeric Water Oxidation Catalysts

Synthesis and characterization.

Ligands.

2,6-bis(1-methylbenzimidazol-2-yl)pyridine (Mebimpy). This ligand was prepared by a modification of the procedure reported for 2,6-bis(benzimidazol-2-yl)pyridine.[1] A mixture of pyridine-2,6-dicarboxylic acid (3.35 g, 20 mmol) and N-methyl-1,2-phenylenediamine (5.38 g, 44 mmol) in 40 mL of 85% phosphoric acid was stirred at ca 230 ºC for 4 h. The dark green melt was poured into 1L of vigorously stirred cold water. After it was cooled to room temperature, the blue precipitate was collected by filtration, then slurried into 300 mL of hot aqueous sodium carbonate solution (10%). The resulting solid was filtered off and recrystallized from methanol to give a white solid. Yield: 5.77 g, 85%. ^{1}H NMR ($CDCl_3$): δ 8.42 (d, 2H), 8.05 (t, 1H), 7.86–7.89 (m, 2H), 7.44–7.48 (m, 2H), 7.33–7.41 (m, 4H), 4.25 (s, 6H, $2CH_3$). This ligand was pure by ^{1}H-NMR and was used without further purification.

2,6-bis(dimethylaminomethyl)pyridine (DMAP). This ligand was prepared by a literature procedure.[2]

***N*-Methyl-*N'*-2-pyridylimidazolium hexafluorophosphate (MeIm-py$^+$PF6$^-$).** This ligand was synthesized by a modification of a literature procedure.[3] A mixture of 2-bromopyridine (3.16 g, 20.0 mmol) and 1-methylimidazole (1.64 g, 20.0 mmol) was kept neat at 160 °C for 48 h. After cooling to ca 50 ºC, acetone was added and the resulting solid was filtered and washed with acetone and ether. The solid was dissolved in water, filtered and added to aqueous ammonium hexafluorophosphate. Upon standing for 2 hours the solid was isolated by filtration and washed with water and ether. Yield: 4.27 g (70%). ^{1}H NMR (CD_3CN): δ 9.25 (s, 1H, NCHN), 8.59 (d, 1H), 8.08-8.12 (dt, 1H), 8.06 (t, 1H), 7.72 (d, 1H), 7.56-7.59

(dd, 1H), 7.54 (t, 1H), 3.96 (s, 3H, CH_3). This ligand was pure by ^{1}H-NMR and was used without further purification.

***N*-Methyl-*N'*-2-pyridylbenzimidazolium iodide (Mebim-py$^+$I$^-$).** A mixture of 2-iodopyridine (2.0 g, 9.8 mmol) and 1-methylbenzimidazole (1.29 g, 9.8 mmol) was kept neat at 140 °C for 72 h. After cooling to ca 50 ºC, acetone was added and the resulting solid was filtered and washed with acetone and ether. Yield: 826 mg (25%). ^{1}H NMR (DMSO-d_6): δ 10.48 (s, 1H, NCHN), 8.79 (d, 1H), 8.47-8.49 (m, 1H), 8.27-8.32 (dt, 1H), 8.14-8.16 (m, 1H), 8.04 (d, 1H), 7.77-7.82 (m, 2H), 7.71-7.74 (dd, 1H), 4.20 (s, 3H, CH_3). This ligand was pure by ^{1}H-NMR and was used without further purification.

***N*-Methyl-*N'*-2-pyrazylbenzimidazolium iodide (Mebim-pz$^+$I$^-$).** A mixture of 2-iodopyrazine (2.0 g, 9.7 mmol) and 1-methylbenzimidazole (1.28 g, 9.7 mmol) was kept neat at 135 °C for 72 h. After cooling to ca 50 ºC, acetone was added and the resulting solid was filtered and washed with acetone and ether. Yield: 1.1 g (34%). ^{1}H NMR (DMSO-d_6): δ 10.59 (s, 1H, NCHN), 9.36 (s, 1H, pz), 8.97 (d, 1H), 8.88-8.90 (m, 1H), 8.47-8.49 (m, 1H), 8.17-8.19 (m, 1H), 7.79-7.85 (m, 2H), 4.23 (s, 3H, CH_3). This ligand was pure by ^{1}H-NMR and was used without further purification.

4,4'-Bis(diethylmethylphosphonate)-2,2'-bipyridine (4,4'-($H_2O_3PCH_2$)$_2$-bpy). This ligand was prepared by a literature procedure.[4]

Complexes.

Synthesis of $[Ru(tpy)(bpm)(OH_2)]^{2+}$ or $[Ru(tpy)(bpz)(OH_2)]^{2+}$.

Method A.$Ru(tpy)(C_2O_4)(OH_2)\cdot 2H_2O$ (500 mg, 1.05 mmol) and 1.25 mmol of the ligand (bpz or bpm) were refluxed in 0.1 M $HClO_4$ for 2 hours. Purification was achieved by

column chromatography (Sephadex LH-20) with 0.1 M HNO_3 as the eluant. The red fractions with λ_{max} = 483 nm (bpm monomer) or λ_{max} = 493 nm (bpz monomer) were combined and isolated as the corresponding hexafluorophosphate or perchlorate salts by addition of saturated aqueous NH_4PF_6 or $NaClO_4$, respectively.

Method B. 500 mg (0.80 mmol) of Ru(tpy)(L)(Cl)(ClO_4) (L is bpm or bpz) and 340 mg (2.0 mmol) of $AgNO_3$ were heated at reflux in 40 mL of 1:1 H_2O-MeOH for 2 hours. The reaction mixture was filtered hot through a bed of Celite and left standing in the fume hood. Crystals of the monomers formed after evaporation of the MeOH and were isolated by filtration and rinsed with cold water.

Elemental analysis. a) [Ru(tpy)(bpz)(OH_2)](ClO_4)$_2$•2H_2O: Anal. Calcd for $C_{23}H_{23}Cl_2N_7O_{11}Ru$: C, 37.06; N, 13.15; H, 3.11. Found: C, 37.03; N, 13.19; H, 2.88. b) [Ru(tpy)(bpm)(OH_2)](PF_6)$_2$•H_2O: Anal. Calcd for $C_{23}H_{21}F_{12}N_7O_2P_2Ru$: C, 33.75; N, 11.98; H, 2.59. Found: C, 33.72; N, 12.09; H, 2.54.

Ru(Mebimpy)Cl$_3$. This complex was synthesized as reported for Ru(tpy)Cl_3[5] using Mebimpy intead of tpy. In a typical experiment $RuCl_3$×3H_2O (1.00 g, 3.83 mmol) and Mebimpy (1.30 g, 3.83 mmol) were mixed in 400 mL of ethanol and the mixture refluxed for 3 hours. Upon cooling to room temperature, the brown solid was filtered, washed with ethanol until the ethanol came out clear and finally with ether. Yield: 1.6 g, 76%. This compound was used without further purification.

Ru(DMAP)Cl$_3$. This complex was synthesized by a modification of a literature procedure.[2] $RuCl_3$×3H_2O (2.0 g, 7.66 mmol) and DMAP (1.48 g, 7.66 mmol) were refluxed in ethanol (50 mL) for 3 hours. Upon cooling the green solid was filtered and washed with ethanol and ether. This solid was refluxed in 30 mL of concentrated HCl for ~ 30 min to yield the product

as an orange powder that was collected by filtration and washed with water and ether. This compound was used without further purification.

((Mebimpy)(Cl)Ru)$_2$Cl$_2$. Ru(Mebimpy)Cl$_3$ (500 mg,) was suspended in ethanol (40 mL) and the mixture degassed by bubbling argon trough it. Triethylamine (1.5 mL) was added and the mixture refluxed for 2 hours and filtered hot. The purple solid obtained was washed with ethanol and ether to remove [Ru(Mebimpy)$_2$]Cl$_2$, which is soluble in ethanol. This impurity is the result of reduction of [Ru(Mebimpy)$_2$]Cl$_3$ that forms as a byproduct in the synthesis of Ru(Mebimpy)Cl$_3$. [((Mebimpy)(Cl)Ru)$_2$Cl$_2$] was used without further purification.

Ru(tpy)(bpy)(OH$_2$)(ClO$_4$)$_2$. This complex was prepared as reported in the literature.[6]

Ru(tpy)(Mebim-py)(OH$_2$)(ClO$_4$)$_2$•2H$_2$O. Ru(tpy)Cl$_3$ (500 mg, 1.13 mmol) and Mebim-py$^+$I$^-$ (382 mg, 1.13 mmol) were suspended in ethyleneglycol and degassed by bubbling argon. Triethylamine (1.0 mL) was added with a syringe and the mixture was heated at 150 ºC for 3 hours. The crude product was isolated by addition of aqueous ammonium hexafluorophosphate and washed with water and ether. The brown solid obtained was dissolved in acetone and aqueous potassium nitrate was added. The solvents were removed by rotary evaporation and a small amount of 0.1 M HNO$_3$ was added. The mixture was filtered to remove undissolved materials and the filtrate was loaded on a column (Sephadex LH-20) and eluted with 0.1 M HNO$_3$. The yellow-orange band was collected and added to saturated aqueous sodium perchlorate. Upon standing in the refrigerator overnight crystals of Ru(tpy)(Mebim-py)(OH$_2$)(ClO$_4$)$_2$•2H$_2$O formed. The product was isolated by filtration, washed with ice-cold water and air-dried. Yield: 315 mg, 35%. Anal. Found (Calc.) for C$_{28}$H$_{28}$Cl$_2$N$_6$O$_{11}$Ru: C, 42.25 (42.22); N, 10.68 (10.55); H, 3.45 (3.54). ^{1}H NMR (CD$_3$CN, as Ru(tpy)(Mebim-py)(CD$_3$CN)$^{2+}$): δ 9.44 (d, 1H), 8.52 (d, 3H), 8.40 (d, 2H), 8.35-8.39 (dt,

1H), 8.27-8.31 (t, 1H), 8.16 (d, 1H), 7.99-8.03 (dt, 2H), 7.73-7.76 (m, 1H), 7.59 (d, 2H), 7.41-7.45 (dt, 1H), 7.35-7.39 (dt, 1H), 7.30-7.34 (m, 2H), 7.27 (d, 1H), 2.90 (s, 3H, CH_3).

Ru(tpy)(Mebim-pz)(OH_2)(NO_3)(PF_6)•$2H_2O$. Ru(tpy)Cl_3 (500 mg, 1.13 mmol) and Mebim-pz$^+I^-$ (382 mg, 1.13 mmol) were suspended in ethyleneglycol and degassed by bubbling argon. Triethylamine (1.0 mL) was added with a syringe and the mixture was heated at 150 ºC for 2 hours. The crude product was isolated by addition of aqueous ammonium hexafluorophosphate and washed with water and ether. The brown solid obtained was dissolved in acetone and aqueous potassium nitrate was added. The mixture was filtered to remove undissolved materials and the filtrate was allowed to stand for several days. The dark red crystals of Ru(tpy)(Mebim-pz)(OH_2)(NO_3)(PF_6)•$2H_2O$ were isolated by filtration, washed with ice-cold water, ether and air-dried. Yield: 450 mg, 49%. Anal. Found (Calc.) for $C_{27}H_{27}F_6N_8O_6PRu$: C, 40.81 (40.25); N, 13.58 (13.91); H, 3.28 (3.38). ^{1}H NMR (CD_3CN, as Ru(tpy)(Mebim-pz)(CD_3CN)$^{2+}$): δ 10.2 (d, 1H), 9.72 (s, 1H, pz) 8.80 (d, 1H), 8.49 (d, 2H), 8.6 (d, 2H), 8.19-8.23 (t, 2H), 7.90-7.94 (t, 2H), 7.54 (d, 2H), 7.34-7.43 (m, 2H), 7.21-7.24 (dd, 3H), 2.96 (s, 3H, CH_3).

Ru(tpy)(MeIm-py)(OH_2)(ClO_4)$_2$. Ru(tpy)Cl_3 (500 mg, 1.13 mmol) and MeIm-py$^+PF_6^-$ (345 mg, 1.13 mmol) were suspended in ethyleneglycol and degassed by bubbling argon. Triethylamine (1.0 mL) was added with a syringe and the mixture was heated at 150 ºC for 2 hours. Aqueous sodium perchlorate was added and the mixture was filtered. The filtrate was allowed to stand for several hours and a black microcrystalline solid formed. It was isolated by filtration, washed with ice-cold water and air-dried. Yield: 520 mg, 65%. Anal. Found (Calc.) for $C_{24}H_{22}Cl_2N_6O_9Ru$: C, 40.50 (40.57); N, 11.72 (11.83); H, 3.12 (3.13). ^{1}H NMR (CD_3CN, as Ru(tpy)(MeIm-py)(CD_3CN)$^{2+}$): δ 9.36 (d, 1H), 8.49 (d, 2H) 8.39 (d, 2H), 8.26-

8.30 (t, 1H), 8.21-8.25 (t, 1H), 8.00-8.06 (m, 3H), 7.90 (d, 1H), 7.70-7.74 (t, 1H), 7.60 (d, 2H), 7.34-7.37 (t, 2H), 6.85 (d, 1H), 2.71 (s, 3H, CH_3).

Ru(tpy)(acac)(OH_2)(PF_6). This complex was prepared as reported in the literature.[7]

[Ru(Mebimpy)(bpy)(Cl)](Cl). [((Mebimpy)(Cl)Ru)$_2Cl_2$] (300 mg, 0.29 mmol) and bpy (92 mg, 59 mmol) were suspended in 45 mL of 2:1 EtOH:H_2O and the mixture was degassed by argon bubbling. The suspension was heated at reflux for 4 hours and 10 mL of 20% aqueous LiCl were added. After an additional 20 min the mixture was filtered hot and the filtrate was allowed to cool overnight. The brown microcrystalline solid formed was isolated by filtration and washed with water and ether. Yield: 329 mg, 85%. ^{1}H-NMR (CD_3OD): δ 10.68 (d, 1H), 8.83 (d, 1H), 8.71 (d, 2H), 8.44-8.48 (td, 1H), 8.36 (d, 1H), 8.20-8.24 (t, 1H), 8.09-8.12 (td, 1H), 7.69 (d, 2H), 7.56-7.60 (td, 1H), 7.46 (d, 1H), 7.38-7.42 (t, 2H), 4.51 (s, 6H, $2CH_3$). This compound was used without further purification.

[Ru(Mebimpy)(bpy)(OTf)](OTf)•4H_2O (OTf is the triflate anion). A mixture of [Ru(Mebimpy)(bpy)(Cl)](Cl) (267 mg, 0.40 mmol) and AgOTf (218 mg, 0.85 mmol) in MeOH (20 mL) were stirred under argon at room temperature overnight. The silver chloride was removed by filtration using a bed of Celite and the filtrate was taken to dryness by rotary evaporation. Diethyl ether was added and the solid was filtered, washed with ether and air dried. Yield: 348 mg, 90%. Anal. Found (Calc.) for $C_{33}H_{33}F_6N_7O_{10}RuS_2$: C, 41.09 (40.99); N, 10.13 (10.14); H, 2.86 (3.44). ^{1}H-NMR (CD_3CN, 400 MHz, as [Ru(Mebimpy)(bpy)(CD_3CN)](OTf)$_2$) δ 10.10 (d, 1H), 8.70 (d, 1H), 8.67 (d, 2H), 8.49 (td, 1H), 8.36 (t, 1H), 8.28 (d, 1H), 8.07-8.10 (m, 1H), 7.72 (td, 2H), 7.69 (d, 2H), 7.44-7.48 (m, 2H), 7.41 (d, 1H), 7.13-7.17 (m, 2H), 7.07-7.10 (m, 1H), 6.20 (d, 2H), 4.44 (s, 6H, $2CH_3$).

[Ru(Mebimpy)(bpy)(OH_2)]($OTf)_2$. This complex was prepared in-situ dissolving [Ru(Mebimpy)(bpy)(OTf)](OTf) in water. UV-Vis (0.1 M HNO_3) λ_{max}, nm (ε, $M^{-1}cm^{-1}$): 487 (12600), 358 (40460), 343 (34700), 315 (27150), 290 (46300), 253 (sh, 32000), 245 (34700). UV-Vis (0.01 M NaOH) λ_{max}, nm (ε, $M^{-1}cm^{-1}$): 600 (sh, 3970), 518 (11620), 357 (39500), 342 (33050), 315 (24450), 292 (50500), 255 (sh, 26650), 241 (31770).

[Ru(Mebimpy)(bpm)(Cl)](Cl). [Ru(Mebimpy)Cl_3] (700 mg, 1.28 mmol) and bpm (203 mg, 1.28 mmol) were suspended in 60 mL of 2:1 EtOH:H_2O and the mixture was degassed by argon bubbling. Triethylamine (2.5 mL) was added with a syringe and the suspension was heated at reflux for 4 hours. 20 mL of 20% aqueous LiCl were added and the brown microcrystalline solid formed was isolated by filtration and washed with water and ether. Yield: 728 mg, 85%. ^{1}H-NMR (CD_3CN): δ 10.89-10.91 (dd, 1H), 9.42-9.44 (dd, 1H), 8.58 (d, 3H), 8.13-8.18 (m, 2H), 7.70-7.72 (dd, 1H), 7.63 (d, 2H), 7.39-7.44 (td, 2H), 7.09-7.13 (t, 2H), 6.99-7.02 (t, 1H), 6.24 (d, 2H), 4.40 (s, 6H, $2CH_3$). This compound was used without further purification.

[Ru(Mebimpy)(bpm)(OTf)](OTf)•5H_2O (OTf is the triflate anion). A mixture of [Ru(Mebimpy)(bpm)(Cl)](Cl) (268 mg, 0.40 mmol) and AgOTf (218 mg, 0.85 mmol) in MeOH (20 mL) were stirred under argon at room temperature overnight. The silver chloride was removed by filtration using a bed of Celite and the filtrate was taken to dryness by rotary evaporation. Diethyl ether was added and the solid was filtered, washed with ether and air dried. Yield: 359 mg, 91%. Anal. Found (Calc.) for $C_{31}H_{23}F_6N_9O_6RuS_2$•$5H_2O$: C, 37.63 (37.73); N, 12.59 (12.77); H, 2.77 (3.37). ^{1}H-NMR (D_2O, 400 MHz, as [Ru(Mebimpy)(bpy)(D_2O)]($OTf)_2$) δ 10.27 (dd, 1H); 9.42 (d, 1H); 8.64 (d, 2H); 8.45 (dd,

1H); 8.26 (t, 2H); 8.24 (d, 1H); 7.74 (dd, 1H); 7.61 (d, 2H); 7.37 (t, 2H); 7.06 (t, 2H); 6.99 (t, 1H); 6.23 (d, 2H); 4.40 (s, 6H, $2CH_3$).

[Ru(Mebimpy)(bpm)(OH_2)](OTf)$_2$. This complex was prepared in-situ dissolving [Ru(Mebimpy)(bpm)(OTf)](OTf) in water. UV-Vis (0.1 M HNO_3) λ_{max}, nm (ε, $M^{-1}cm^{-1}$): 526 (sh, 4120), 439 (9070), 359 (34180), 345 (28140), 316 (21700), 245 (37640). UV-Vis (0.01 M NaOH) λ_{max}, nm (ε, $M^{-1}cm^{-1}$): 572 (sh, 4840), 494 (8360), 358 (31400), 344 (25950), 315 (20350), 302 (18300), 262 (sh, 29650), 245 (33600).

[Ru(Mebimpy)(bpz)(Cl)](Cl). [Ru(Mebimpy)Cl_3] (700 mg, 1.28 mmol) and bpz (203 mg, 1.28 mmol) were suspended in 25 mL of 4:1 ethyleneglycol:H_2O and the mixture was degassed by argon bubbling. Triethylamine (2.5 mL) was added with a syringe and the suspension was heated at 140 ºC for 3 hours. 20 mL of 20% aqueous LiCl were added and the black microcrystalline solid formed was isolated by filtration and washed with water and ether. Yield: 745 mg, 87%. ^{1}H-NMR (DMSO-d_6): δ 10.62 (d, 1H), 10.23 (s, 1H), 9.75 (s, 1H), 9.27 (d, 1H), 8.81 (d, 2H), 8.35-8.39 (t, 1H), 8.17 (d, 1H), 7.87 (d, 2H), 7.76 (d, 1H), 7.38-7.42 (t, 2H), 7.11-7.15 (t, 2H), 6.04 (d, 2H), 4.50 (s, 6H, $2CH_3$). This compound was used without further purification.

[Ru(Mebimpy)(bpz)(OTf)](OTf)•4H_2O (OTf is the triflate anion). A mixture of [Ru(Mebimpy)(bpz)(Cl)](Cl) (268 mg, 0.40 mmol) and AgOTf (218 mg, 0.85 mmol) in MeOH (20 mL) were stirred under argon at room temperature overnight. The silver chloride was removed by filtration using a bed of Celite and the filtrate was taken to dryness by rotary evaporation. Diethyl ether was added and the solid was filtered, washed with ether and air dried. Yield: 359 mg, 91%. Anal. Found (Calc.) for $C_{31}H_{31}F_6N_9O_{10}RuS_2$: C, 38.13 (38.43); N, 13.26 (13.01); H, 2.97 (3.23). ^{1}H-NMR (CD_3CN, 400 MHz, as

[Ru(Mebimpy)(bpz)(CD_3CN)]$(OTf)_2$) δ 10.20 (d, 1H), 9.90 (s, 1H), 9.47 (s, 1H), 9.18 (d, 1H), 8.70 (d, 2H), 8.43-8.47 (t, 1H), 8.21 (d, 1H), 7.68 (d, 2H), 7.59 (d, 1H), 7.43-7.47 (t, 2H), 7.14-7.18 (t, 2H), 6.18 (d, 2H), 4.42 (s, 6H, $2CH_3$).

[Ru(Mebimpy)(bpz)(OH_2)]$(OTf)_2$. This complex was prepared in-situ dissolving [Ru(Mebimpy)(bpz)(OTf)](OTf) in water. UV-Vis (0.1 M HNO_3) λ_{max}, nm (ε, $M^{-1}cm^{-1}$): 509 (6760), 428 (6450), 357 (27230), 343 (sh, 22880), 308 (32550).

Ru(Mebimpy)(Mebim-py)(OH_2)$(OTf)_2$•H_2O. Ru(Mebimpy)Cl_3 (618 mg, 1.13 mmol) and Mebim-py^+I^- (382 mg, 1.13 mmol) were suspended in ethyleneglycol and degassed by bubbling argon. Triethylamine (1.0 mL) was added with a syringe and the mixture was heated at 150 ºC for 3 hours. The crude product was isolated by addition of aqueous lithium triflate and washed with water and ether. The brown solid obtained was dissolved in 1:1 MeOH:H_2O, filtered to remove undissolved materials and the filtrate was loaded on a column (Sephadex LH-20) and eluted with 1:1 MeOH:H_2O. The yellow-orange band was collected and added to saturated aqueous lithium triflate. Upon standing in the refrigerator overnight Ru(Mebimpy)(Mebim-py)(OH_2)$(OTf)_2$•H_2O formed. The product was isolated by filtration, washed with ice-cold water and air-dried. Yield: 450 mg, 40%. Anal. Found (Calc.) for $C_{36}H_{32}F_6N_8O_8RuS_2$: C, 43.79 (43.95); N, 11.32 (11.39); H, 3.14 (3.28). ^{1}H NMR (CD_3CN, as Ru(Mebimpy)(Mebim-py)(CD_3CN)$^{2+}$): δ 9.83-9.85 (dd, 1H), 8.58-8.62 (t, 3H), 8.49-8.53 (dt, 1H), 8.30-8.34 (t, 1H), 8.12 (d, 1H), 7.81-7.84 (dt, 1H), 7.67 (d, 2H), 7.40-7.43 (t, 2H), 7.33-7.37 (dt, 1H), 7.28-7.32 (t, 1H), 7.20 (d, 1H), 7.08-7.12 (t, 2H), 6.09 (d, 2H), 4.39 (s, 6H, $2CH_3$, Mebimpy), 2.99 (s, 3H, CH_3, Mebim-py).

Ru(Mebimpy)(MeIm-py)(OH_2)$(OTf)_2$•$2H_2O$. Ru(Mebimpy)Cl_3 (618 mg, 1.13 mmol) and MeIm-$py^+PF_6^-$ (345 mg, 1.13 mmol) were suspended in ethyleneglycol and degassed by

bubbling argon. Triethylamine (1.0 mL) was added with a syringe and the mixture was heated at 150 ºC for 3 hours. The crude product was isolated by addition of aqueous lithium triflate and washed with water and ether. The brown solid obtained was dissolved in 1:1 MeOH:H_2O, filtered to remove undissolved materials and the filtrate was loaded on a column (Sephadex LH-20) and eluted with 1:1 MeOH:H_2O. The yellow-orange band was collected and added to saturated aqueous lithium triflate. Upon standing in the refrigerator overnight Ru(Mebimpy)(MeIm-py)$(OH_2)(OTf)_2$•$2H_2O$ formed. The product was isolated by filtration, washed with ice-cold water and air-dried. Yield: 484 mg, 45%. Anal. Found (Calc.) for $C_{36}H_{32}F_6N_8O_8RuS_2$: C, 40.36 (40.38); N, 11.74 (11.77); H, 3.25 (3.39). ^{1}H NMR (CD_3CN, as Ru(Mebimpy)(MeIm-py)$(CD_3CN)^{2+}$): δ 9.77 (d, 1H), 8.58 (d, 2H), 8.39-8.43 (t, 1H), 8.24-8.28 (t, 1H), 8.10 (d, 1H), 7.84 (d, 1H), 7.78-7.82 (t, 1H), 7.69 (d, 2H), 7.43-7.47 (t, 2H), 7.11-7.15 (t, 2H), 6.77 (d, 1H), 6.10 (d, 2H), 4.40 (s, 6H, $2CH_3$, Mebimpy), 2.80 (s, 3H, CH_3, MeIm-py).

Ru(Mebimpy)(acac)$(OH_2)(OTf)$•H_2O. Neat triflic acid (2.0 mL) was added to 300 mg (0.29 mmol) of [((Mebimpy)(Cl)Ru)$_2Cl_2$] and the mixture was stirred for 1 hour. Addition of ether causes precipitation of a red solid which was filtered and washed with ether. This solid is presumably Ru(Mebimpy)$(OTf)_3$ and was used in the next step without further characterization. The obtained Ru(Mebimpy)$(OTf)_3$, acetylacetone (71 mg, 0.645 mmol) and methanol (40 mL) were degassed by argon bubbling and triethylamine (2.0 mL) was added with a syringe. The mixture was heated at reflux for 3 hours and water was added, followed by 10% aqueous lithium triflate. The purple solid was filtered and washed with water and ether and dried under vacuum. Yield: 400 mg, 94%. Anal. Found (Calc.) for $C_{36}H_{32}F_6N_8O_8RuS_2$: C, 44.89 (44.75); N, 9.69 (9.66); H, 3.87 (3.89).

Ru(Mebimpy)(4,4'-($H_2O_3PCH_2$)$_2$-bpy)(OH_2)(OTf)$_2$. Ru(Mebimpy)Cl_3 (618 mg, 1.13 mmol), 4,4'-((OEt)$_2$$OPCH_2$)$_2$-bpy (516 mg, 1.13 mmol) and LiCl (100 mg) were suspended in 45 mL of 2:1 EtOH:H_2O and degassed by bubbling argon. Triethylamine (1.0 mL) was added with a syringe and the mixture was heated at reflux for 5 hours. 10% aqueous lithium chloride (20 mL) was added and the precipitate of Ru(Mebimpy)(4,4'-((OEt)$_2$$OPCH_2$)$_2$-bpy)(Cl)(Cl) was isolated by filtration and washed with water and ether. This solid was refluxed in 60 mL of 4.0 M aqueous HCl for 5 days to hydrolyze the phosphonate esther groups. After cooling to room temperature, the purple precipitate of Ru(Mebimpy)(4,4'-($H_2O_3PCH_2$)$_2$-bpy)(Cl)(Cl) was isolated by filtration and washed with water and ether. To this solid, triflic acid (3.0 mL) was added, and the mixture was stirred at room temperature for 2 hours. Hydroquinone (124 mg, 1.13 mmol) dissolved in 10 mL of water was added to reduce any Ru(III) species and after a few minutes aqueous lithium triflate was added to complete precipitation of the product. The maroon solid was isolated by filtration, washed with water, ether and air-dried. Yield: 896 mg, 72%. Anal. Found (Calc.) for $C_{35}H_{33}F_6N_7O_{13}P_2RuS_2$: C, 38.73 (38.19); N, 9.19 (8.91); H, 3.95 (3.02). ^{1}H NMR (CD_3OD): δ 9.83-9.91 (dd, 1H), 8.81 (d, 2H), 8.77 (d, 2H), 8.33-8.37 (t, 1H), 8.28-8.32 (t, 1H), 8.12-8.18 (dd, 1H), 7.70-7.74 (t, 2H), 7.42 (d, 1H), 7.39 (d, 1H), 7.11-7.20 (m, 2H), 6.92 (d, 1H), 6.31-6.35 (t, 2H), 4.56 (s, 6H, 2CH_3, Mebimpy), 3.66 (d, 2H, CH_2), 2.97 (d, 2H, CH_2).

Ru(DMAP)(bpy)(OH_2)(PF_6)$_2$•1.5H_2O. This complex was prepared by a modification of a literature procedure for Ru(DMAP)(bpy)(OH_2)(ClO_4)$_2$•2H_2O.[2] Ru(DMAP)Cl_3 (500 mg, 1.25 mmol), bpy (195 mg, 1.25 mmol) and zinc powder (1.00 g) were suspended in water (60 mL) and degassed by bubbling argon. The mixture was heated at reflux for 1 hour and filtered hot through a bed of Celite. The crude product was isolated by addition of aqueous ammonium

hexafluorophosphate and washed with water and ether. The red solid obtained was dissolved in MeOH, filtered to remove undissolved materials and added to aqueous ammonium hexafluorophosphate. The MeOH was removed by rotary evaporation and the dark red needles of Ru(DMAP)(bpy)(OH_2)(PF_6)$_2$•1.5H_2O formed were filtered and washed with cold water and ether. Yield: 589 mg, 60%. Anal. Found (Calc.) for $C_{21}H_{32}F_{12}N_5O_{2.5}P_2Ru$: C, 32.10 (32.11); N, 8.90 (8.92); H, 4.03 (4.11). ^{1}H NMR (CD_3CN, as Ru(DMAP)(bpy)(CD_3CN)$^{2+}$): δ 9.49 (d, 1H), 8.55 (d, 1H), 8.51 (d, 1H), 8.10-8.14 (dt, 1H), 8.05-8.09 (dt, 1H), 7.98-8.02 (t, 1H), 7.93 (d, 1H), 7.75-7.78 (dt, 1H), 7.64 (d, 2H), 7.47-7.51 (dt, 1H), 4.11 (d, 2H, H CH_2(1), H CH_2(2)), 3.92 (d, 2H, H CH_2(2), H CH_2(1)), 2.36 (s, 6H, 3H CH_3(1), 3H CH_3(2)), 1.49 (s, 6H, 3H CH_3(2), 3H CH_3(1)).

Ru(DMAP)(MeIm-py)(OH_2)(PF_6)$_2$•0.5H_2O. Ru(DMAP)Cl_3 (250 mg, 0.63 mmol) and MeIm-py$^+PF_6^-$ (191 mg, 0.63 mmol) were suspended in ethyleneglycol and degassed by bubbling argon. Triethylamine (1.0 mL) was added with a syringe and the mixture was heated at 150 ºC for 3 hours. The product was isolated by addition of aqueous ammonium hexafluorophosphate and washed with water and ether and air-dried. Yield: 290 mg, 60%. Anal. Found (Calc.) for $C_{20}H_{31}F_{12}N_6O_{1.5}P_2Ru$: C, 31.11 (31.18); N, 12.02 (10.91); H, 4.02 (4.06). ^{1}H NMR (CD_3CN, as Ru(DMAP)(MeIm-py)(CD_3CN)$^{2+}$): δ 9.29 (d, 2H), 8.01 (d, 1H), 7.96 (d, 1H), 7.79-7.82 (t, 1H), 7.50-7.53 (t, 1H), 7.44 (d, 2H), 6.48 (s, 1H), 3.95 (d, 2H, H CH_2(1), H CH_2(2)), 3.89 (d, 2H, H CH_2(2), H CH_2(1)), 3.81 (s, 3H, CH_3, MeIm-py), 2.26 (s, 6H, 3H CH_3(1), 3H CH_3(2)), 1.67 (s, 6H, 3H CH_3(2), 3H CH_3(1)).

Ru(DMAP)(Mebim-py)(OH_2)(PF_6)$_2$•2H_2O. Ru(DMAP)Cl_3 (250 mg, 0.63 mmol) and Mebim-py$^+I^-$ (212 mg, 0.63 mmol) were suspended in ethyleneglycol and degassed by bubbling argon. Triethylamine (1.0 mL) was added with a syringe and the mixture was

heated at 150 ºC for 3 hours. The product was isolated by addition of aqueous ammonium hexafluorophosphate and washed with water and ether and air-dried. Yield: 281 mg, 55%. Anal. Found (Calc.) for $C_{24}H_{36}F_{12}N_6O_3P_2Ru$: C, 33.92 (34.01); N, 9.83 (9.92); H, 4.19 (4.28). ^{1}H NMR (CD_3CN, as Ru(DMAP)(MeIm-py)$(CD_3CN)^{2+}$): δ 9.29 (d, 1H), 8.46 (d, 1H), 8.23-8.26 (m, 1H), 8.15-8.20 (dt, 1H), 7.97-8.00 (t, 1H), 7.62 (d, 2H), 7.50-7.58 (m, 4H), 4.22 (d, 2H, H CH_2(1), H CH_2(2)), 3.93 (d, 2H, H CH_2(2), H CH_2(1)), 3.34 (s, 3H, CH_3, Mebim-py), 2.36 (s, 6H, 3H CH_3(1), 3H CH_3(2)), 1.77 (s, 6H, 3H CH_3(2), 3H CH_3(1)).

Representative ^{1}H-NMR spectra.

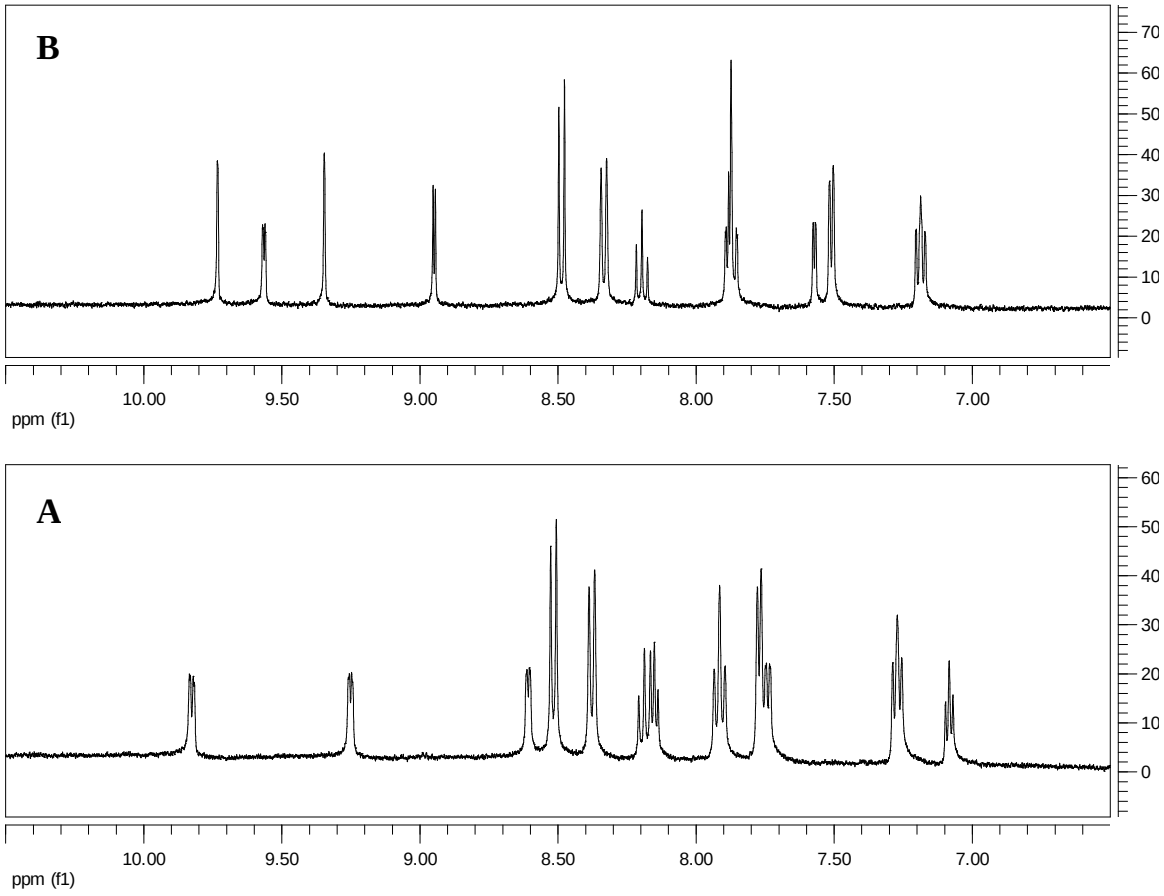

Figure S1. ^{1}H-NMR spectrum (400 MHz) for Ru(tpy)(bpm)$(OH_2)(PF_6)_2$ (A) and for Ru(tpy)(bpz)$(OH_2)(PF_6)_2$ (B) in D_2O. Integration gives a total of 17 protons in both cases: 11 protons from the tpy ligand and 6 protons from the bidentate ligand (bpm or bpz).

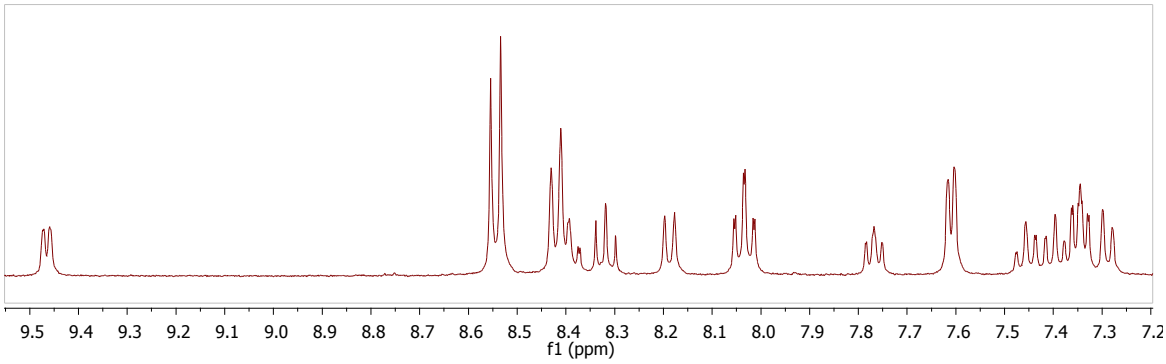

Figure S2. ^{1}H-NMR spectrum for [Ru(tpy)(Mebim-py)(OH_2)](NO_3)$_2$ in CD_3CN as [Ru(tpy)(Mebim-py)(CD_3CN)](NO_3)$_2$.

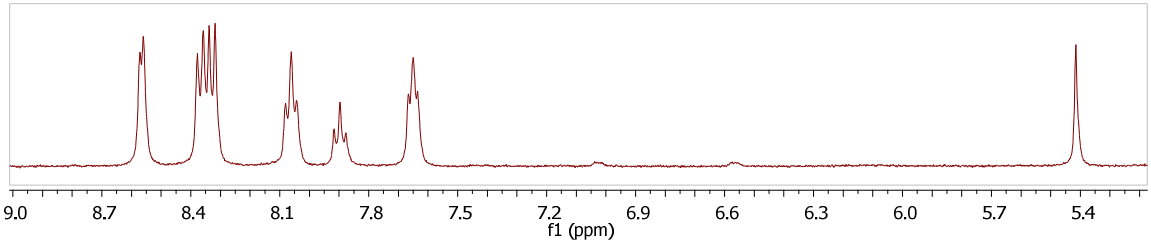

Figure S3. ^{1}H-NMR spectrum for [Ru(tpy)(acac)(OH_2)](PF_6) in CD_3CN as [Ru(tpy)(acac)(CD_3CN)](PF_6).

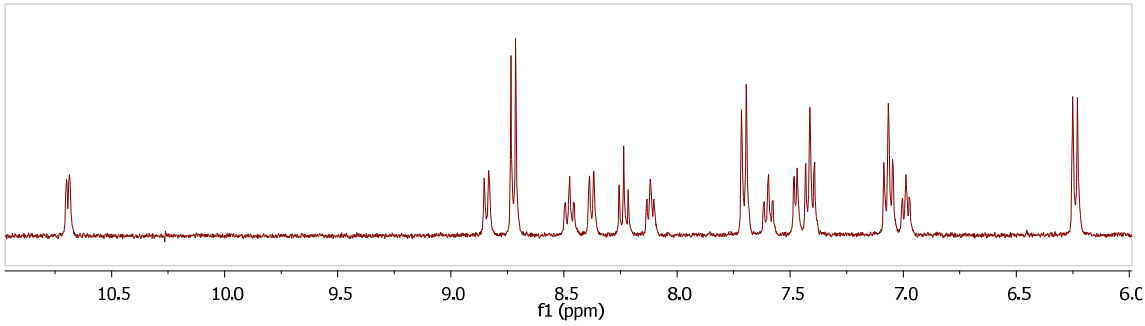

Figure S4. ^{1}H-NMR spectrum for [Ru(Mebimpy)(bpy)(Cl)]Cl in CD_3OD.

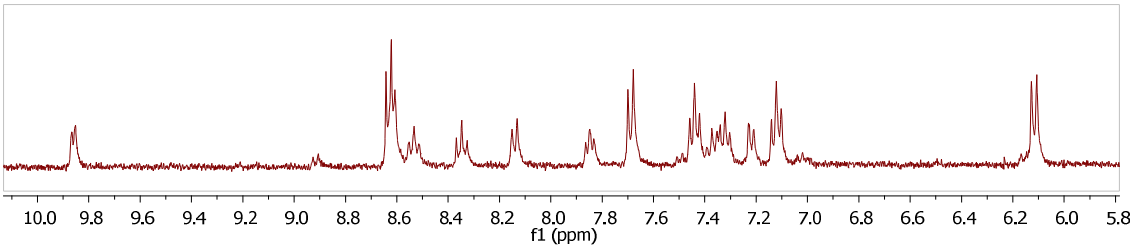

Figure S5. ^{1}H-NMR spectrum for [Ru(Mebimpy)(Mebim-py)(OH_2)]($OTf)_2$ as [Ru(Mebimpy)(Mebim-py)(CD_3CN)]($OTf)_2$.

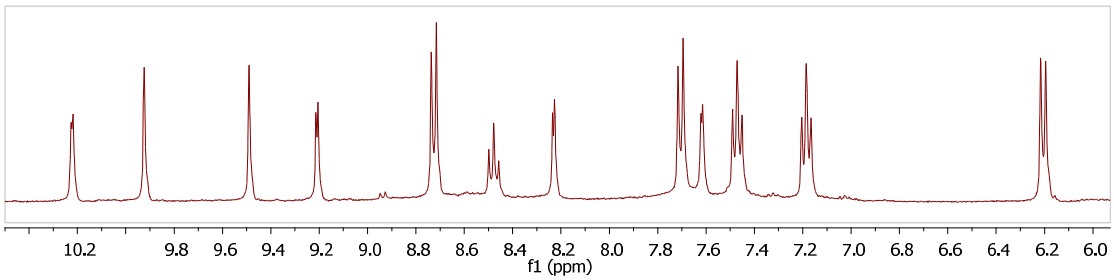

Figure S6. ^{1}H-NMR spectrum for [Ru(Mebimpy)(bpz)(OH_2)]($OTf)_2$ as [Ru(Mebimpy)(bpz)(CD_3CN)]($OTf)_2$.

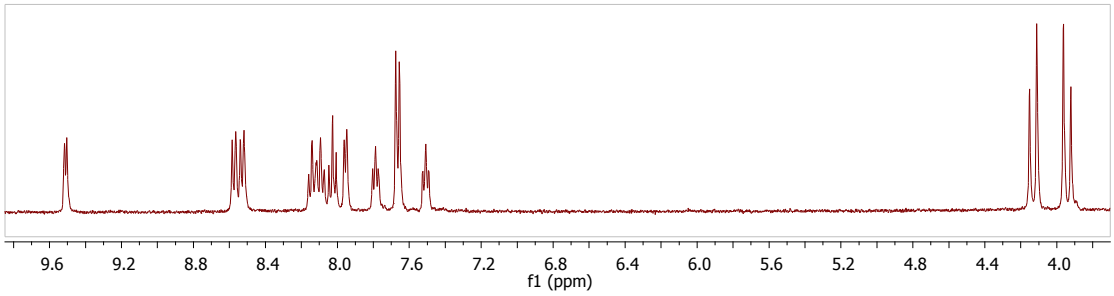

Figure S7. ^{1}H-NMR spectrum for [Ru(DMAP)(bpy)(OH_2)]($PF_6)_2$ as [Ru(DMAP)(bpy)(CD_3CN)]($PF_6)_2$.

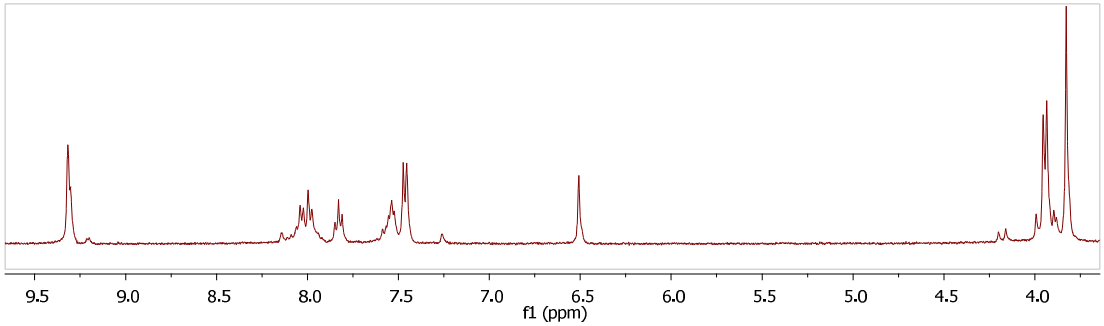

Figure S8. ^{1}H-NMR spectrum for [Ru(DMAP)(MeIm-py)(OH_2)](PF_6)$_2$ as [Ru(DMAP)(MeIm-py)(CD_3CN)](PF_6)$_2$.

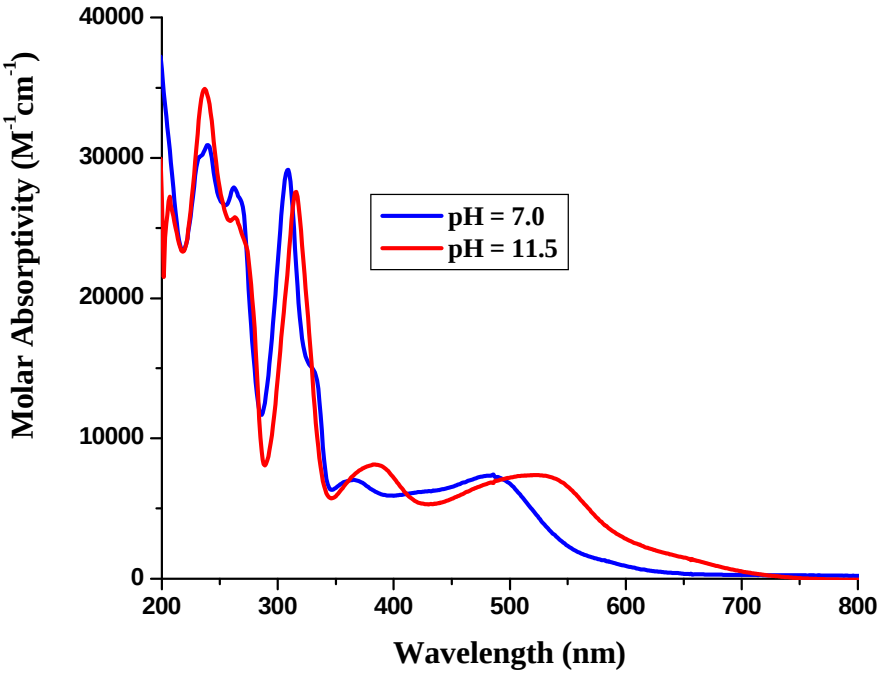

(A)

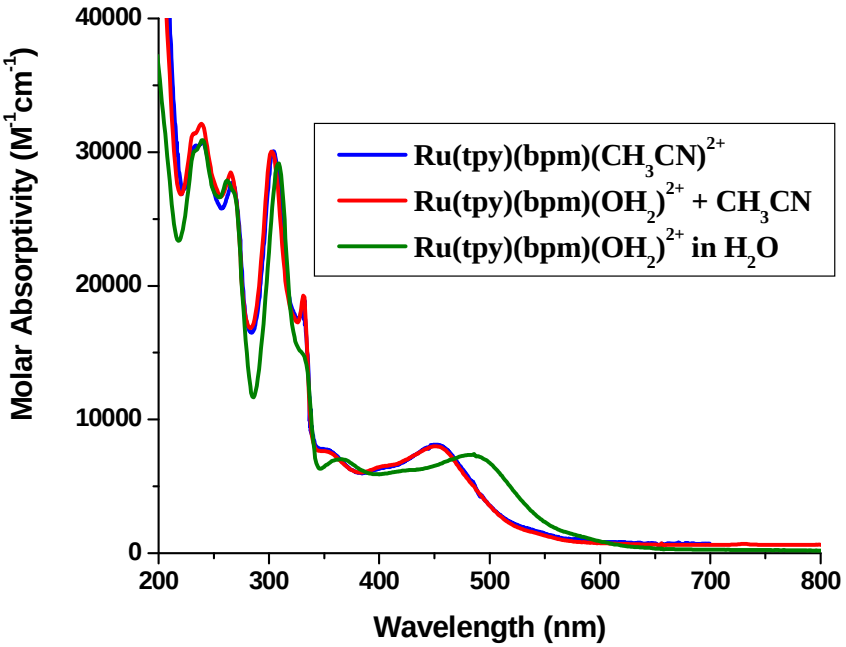

(B)

Figure S9. (A) Absorption spectra of Ru(tpy)(bpm)$(OH_2)^{2+}$and Ru(tpy)(bpm)$(OH)^{+}$. (B) Absorption spectra of Ru(tpy)(bpm)$(OH_2)^{2+}$ in CH_3CN and in H_2O, and absorption spectra of Ru(tpy)(bpm)$(CH_3CN)^{2+}$ in CH_3CN.[8] The concentration of complex is 5.1×10^{-5} M in all cases.

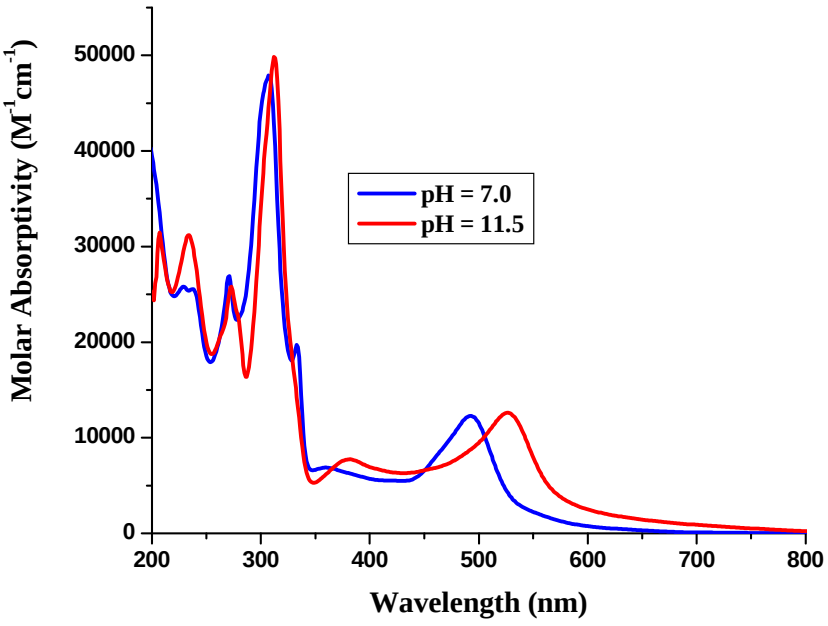

Figure S10. Absorption spectra of Ru(tpy)(bpz)$(OH_2)^{2+}$and Ru(tpy)(bpz)$(OH)^{+}$. The concentration of complex is 5.1×10^{-5} M.

Determination of pK_a for Ru(tpy)(bpm)$(OH_2)^{2+}$ spectrophotometrically. The absorption spectrum of Ru(tpy)(bpm)$(OH_2)^{2+}$ was measured from pH = 6.5 to pH = 13. Figure S11 shows a plot of absorbance vs. pH at 309 and 316 nm. From the plot, pK_a = 9.7 is obtained for Ru(tpy)(bpm)$(OH_2)^{2+}$. The same value is obtained from the Pourbaix diagram shown in Figure 1.

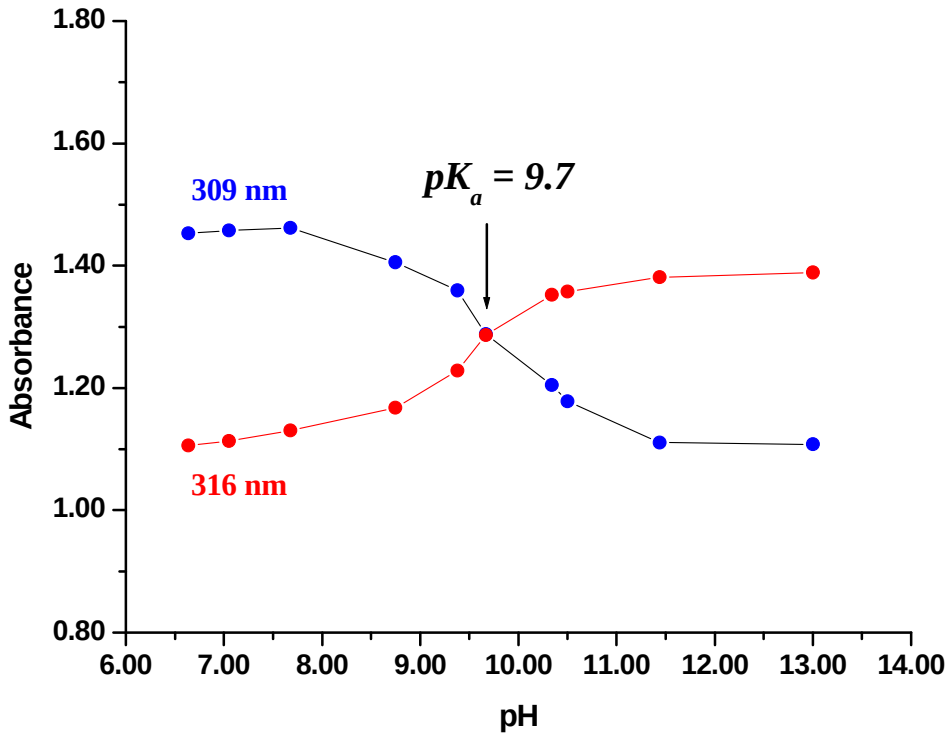

Figure S11. Absorbance *vs* pH at 309 and 316 nm for Ru(tpy)(bpm)$(OH_2)^{2+}$.

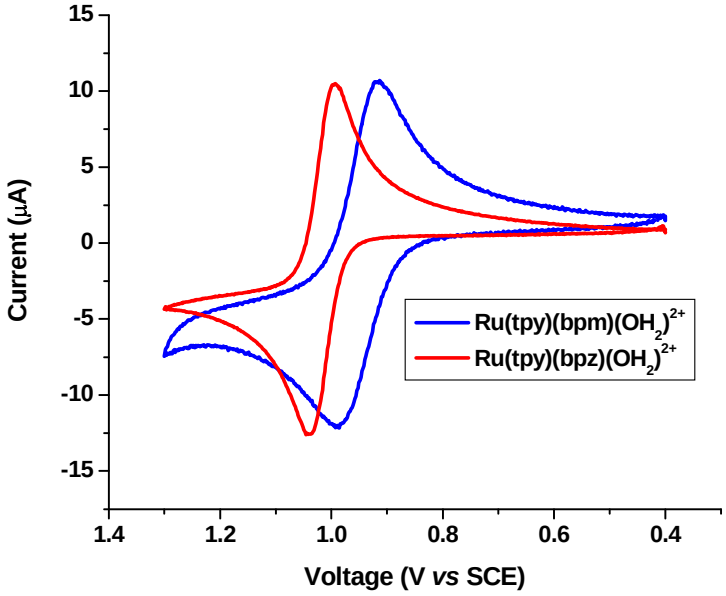

(A)

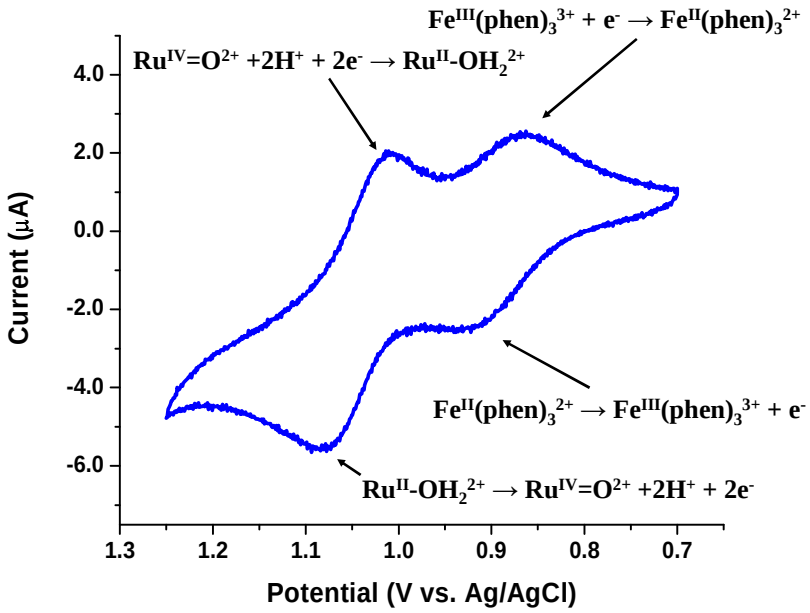

(B)

Figure S12. (A) Cyclic voltammograms for 1 mM Ru(tpy)(bpm)$(OH_2)^{2+}$ and 1 mM Ru(tpy)(bpz)$(OH_2)^{2+}$ in 0.1 M HNO_3 showing the two-electron waves for the corresponding $Ru^{IV}=O^{2+}/Ru^{II}$-OH_2^{2+} couples (glassy carbon working electrode, 50 mV/s). (B) Cyclic voltammogram for 1 mM Ru(tpy)(bpz)$(OH_2)^{2+}$ and 1 mM $Fe(phen)_3^{2+}$ in 0.1 M HNO_3 showing the two-electron wave for the $Ru^{IV}=O^{2+}/Ru^{II}$-OH_2^{2+} couple (Ru(tpy)(bpz)$(OH_2)^{2+}$) and the one-electron wave for the Fe^{III}/Fe^{II} couple (glassy carbon working electrode, 10 mV/s).

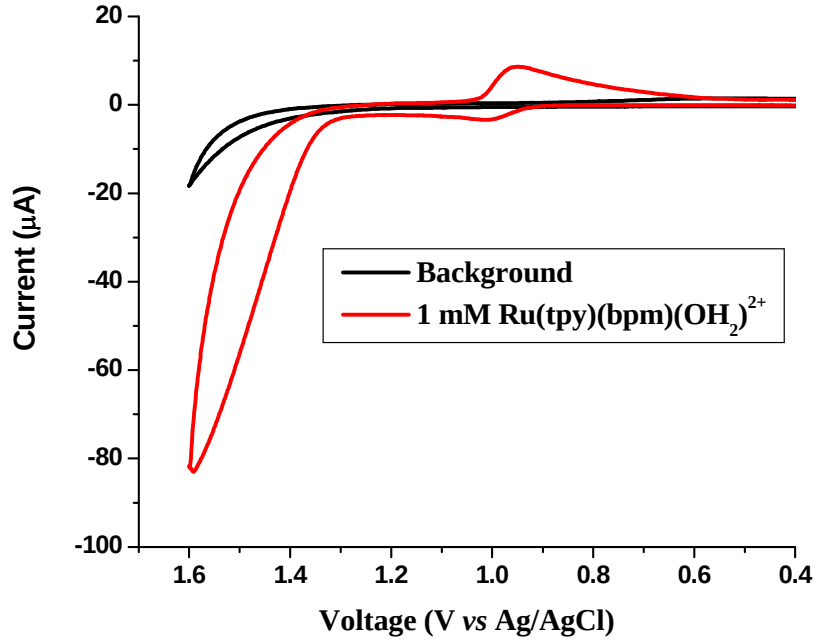

(A)

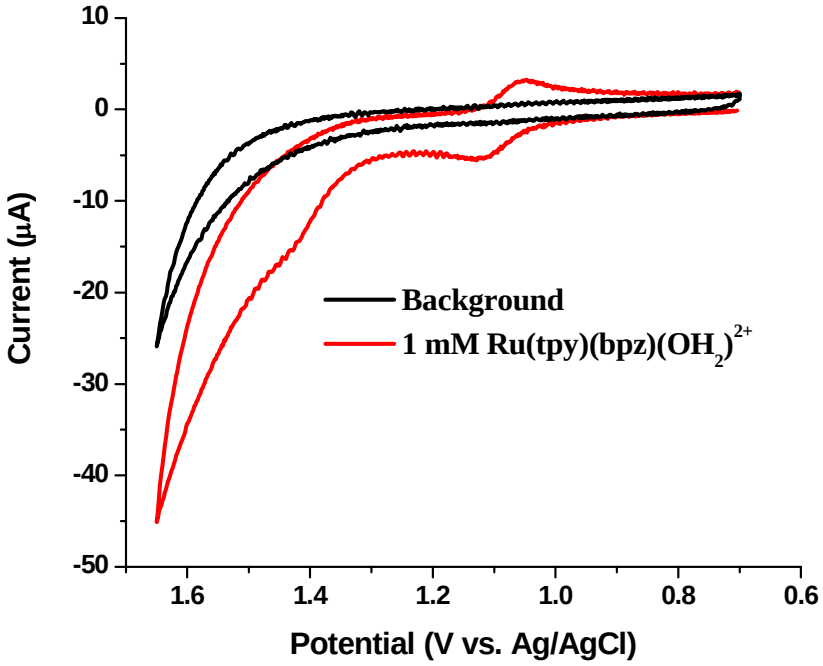

(B)

Figure S13. (A) Cyclic voltammogram for 1 mM $Ru(tpy)(bpm)(OH_2)^{2+}$ in 0.1 M $HClO_4$ (glassy carbon working electrode, 10 mV/s). (B) Cyclic voltammogram for 1 mM $Ru(tpy)(bpz)(OH_2)^{2+}$ in 1.0 M HNO_3 (glassy carbon working electrode, 10 mV/s).

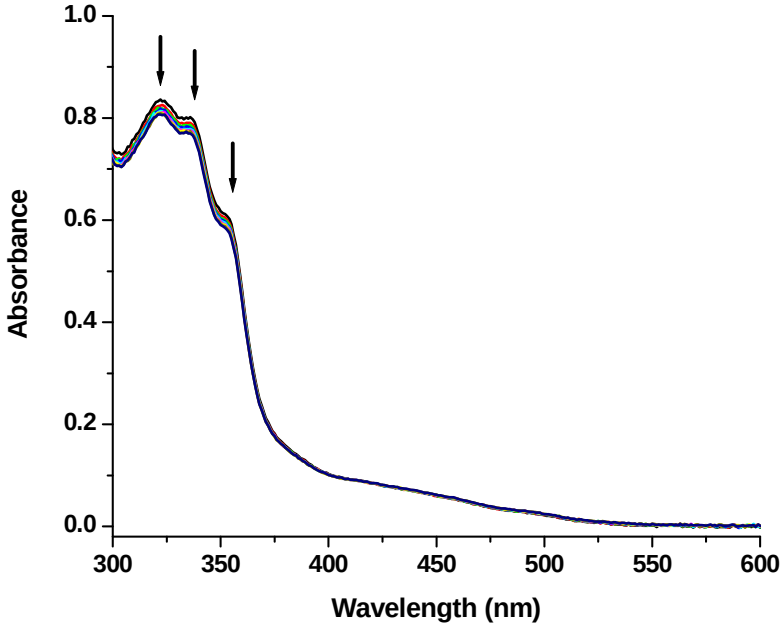

Figure S14. Spectral changes (120 s intervals) upon addition of 1 equivalent of Ce(IV) to 5.1×10^{-5} M $Ru^{IV}(tpy)(bpm)(O)^{2+}$ to form $Ru^{V}(tpy)(bpm)(O)^{3+}$ in 0.1 M $HClO_4$.

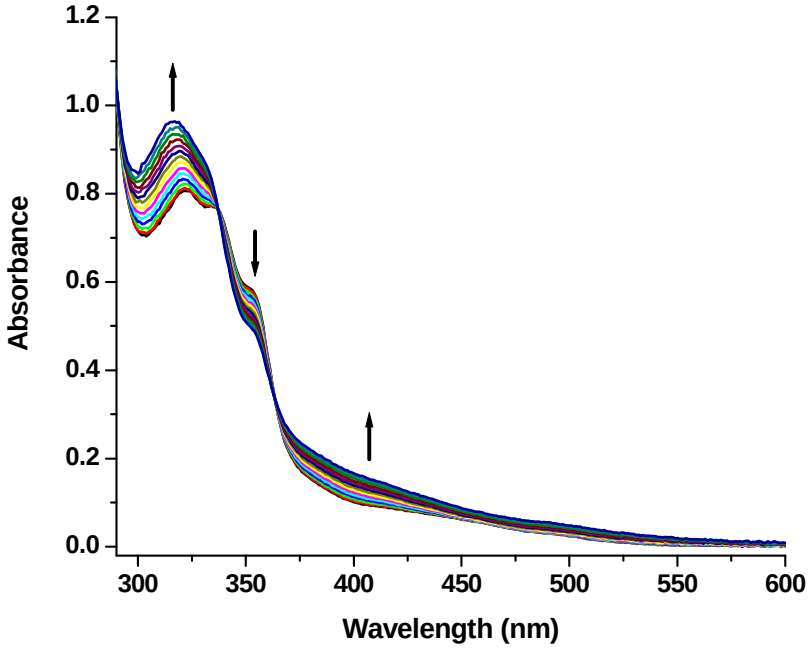

Figure S15. Spectral changes (120 s intervals) showing the formation of $Ru^{III}(tpy)(bpm)(OOH)^{2+}$ from $Ru^{V}(tpy)(bpm)(O)^{3+}$ in 0.1 M $HClO_4$. The concentration of complex is 5.1×10^{-5} M.

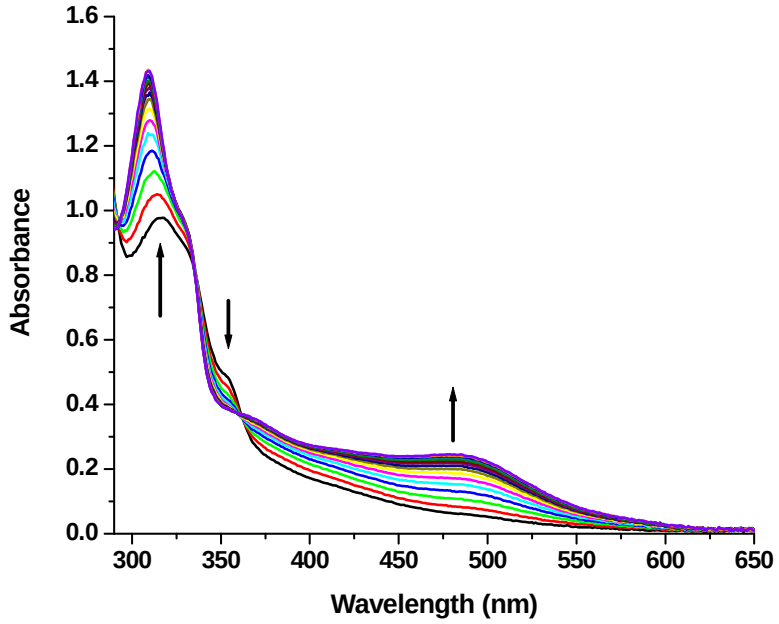

Figure S16. Spectral changes (120 s intervals) showing the decomposition of $Ru^{III}(tpy)(bpm)(OOH)^{2+}$ in 0.1 M $HClO_4$. The concentration of complex is 5.1×10^{-5} M.

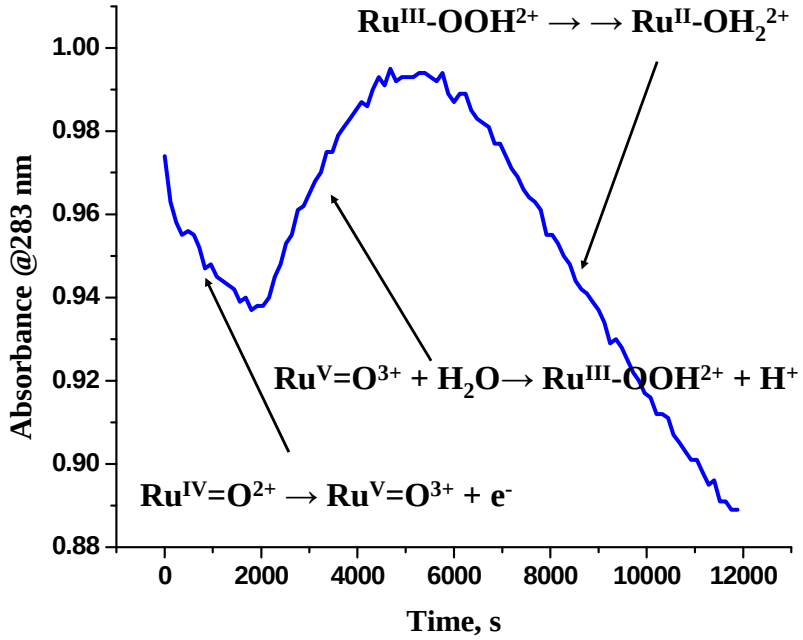

Figure S17. Absorbance changes at 283 nm upon addition of 1 equivalent of Ce(IV) to 5.1×10^{-5} M $Ru^{IV}(tpy)(bpm)(O)^{2+}$ in 0.1 M $HClO_4$. Three different regions are clearly observed and correspond to the spectral changes shown in figures S14, S15 and S16.

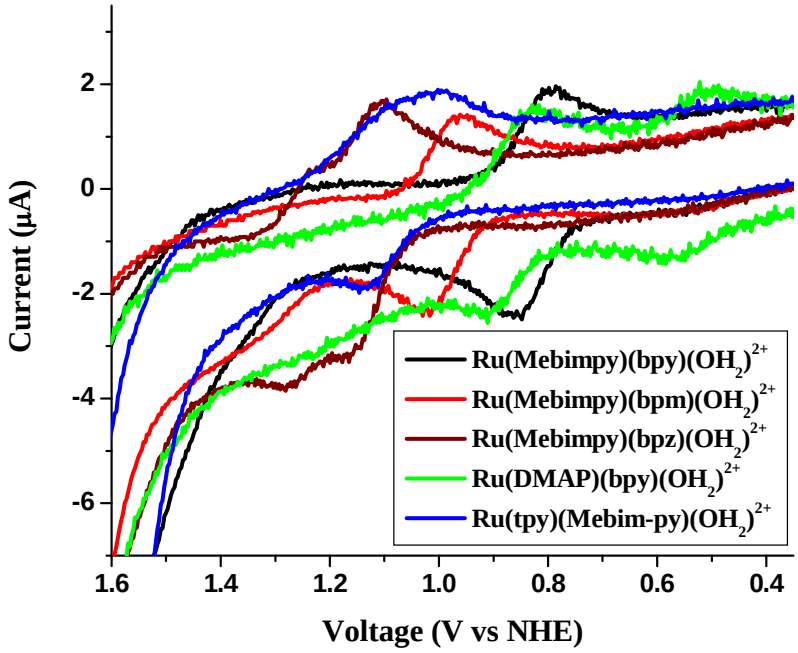

Figure S18. Representative cyclic voltammograms for monomeric catalysts. Conditions: 1.0 mM complex in 0.1 M HNO_3; glassy carbon working electrode; scan rate: 10 mV/s.

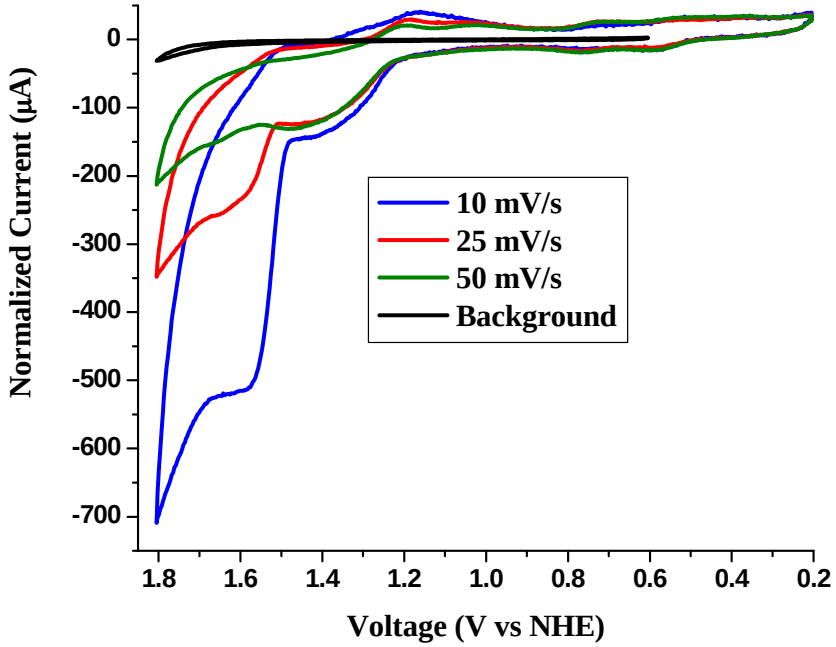

Figure S19. Cyclic voltammograms for $[Ru(tpy)(acac)(OH_2)]^+$. Conditions: 1.0 mM complex in 0.1 M HNO_3; glassy carbon working electrode.

Kinetics.

For a zeroth-order reaction: $\frac{dC}{dt} = k$ (C is concentration, t is time and k is the rate constant).

Integration gives $C\text{-}C_0 = kt$ with k having units of M•s^{-1}. Since $C = \frac{A}{\varepsilon b}$ (A is absorbance, ε is molar absorptivity and b is the path length of the cell), $\frac{A}{\varepsilon b} - \frac{A_0}{\varepsilon b} = kt$. From a plot of $\frac{A}{\varepsilon b}$ versus t the zeroth-order rate constant can be obtained.

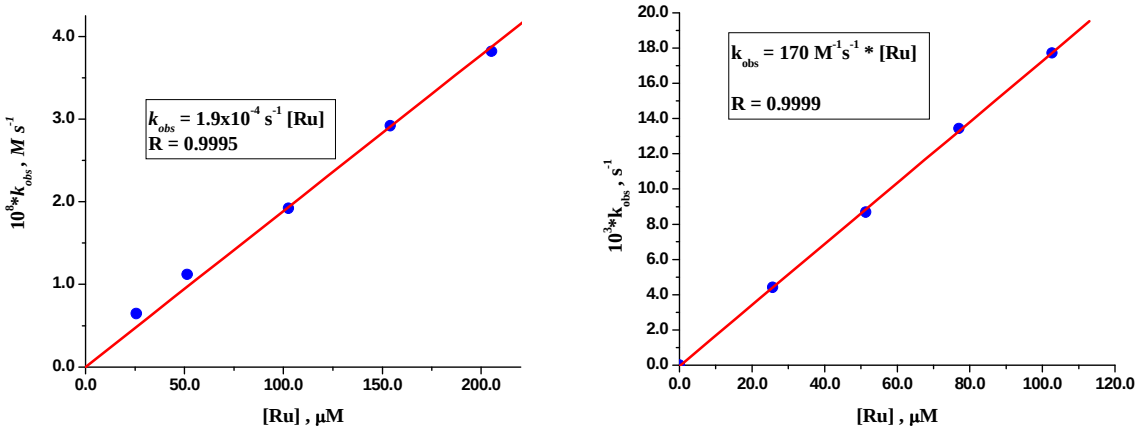

A **B**

Figure S20. Representative examples for determination of rate constants for the rate limiting step in the water oxidation cycle for the two pathways. **A**) The rate limiting step for [Ru(tpy)(bpy)(OH$_2$)]$^{2+}$ in 0.1 M HNO_3 is first order in catalyst and zeroth-order in Ce(IV). **B**) The rate limiting step for [Ru(Mebimpy)(Mebim-pz)(OH$_2$)]$^{2+}$ in 0.1 M HNO_3 is first order in catalyst and first order in Ce(IV).

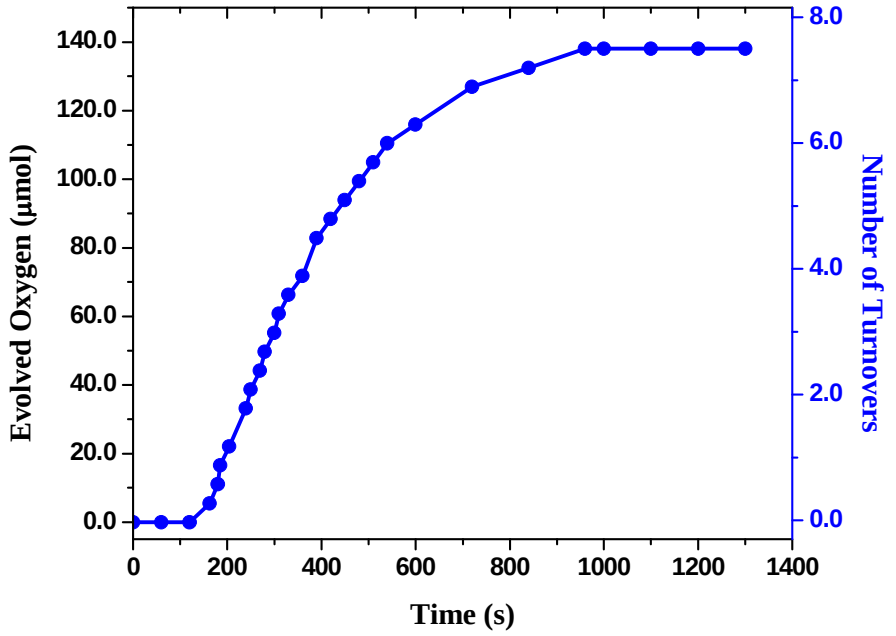

Figure S21. Oxygen evolution/number of turnovers *vs* time plot for the addition of 30 equivalents of Ce(IV) to 6.5 mL of 2.9×10^{-3} M $[Ru(tpy)(bpm)(OH_2)](PF_6)_2$ in 1.0 M HNO_3 at 298 K.

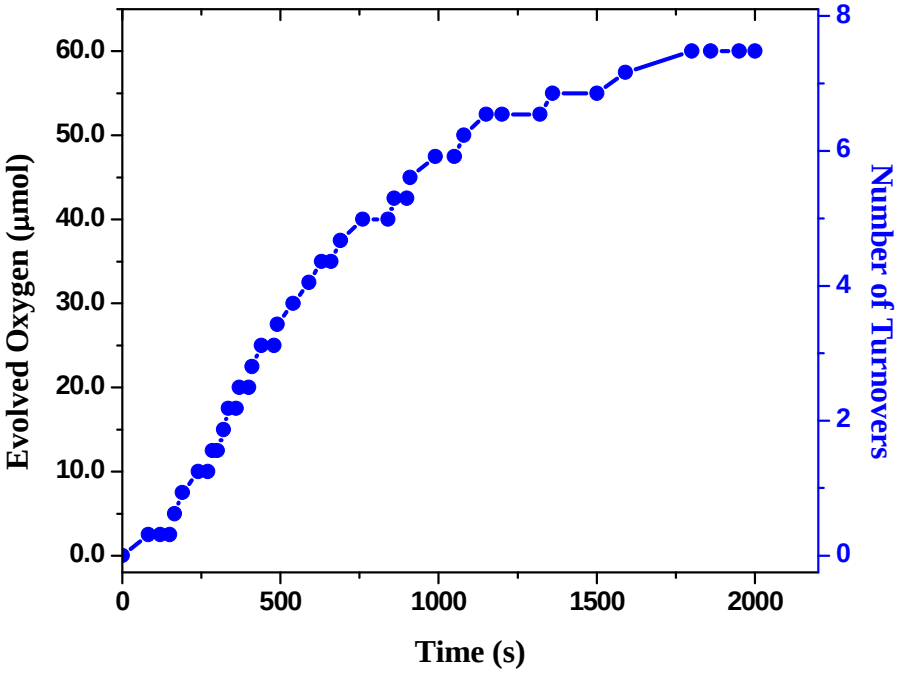

Figure S22. Oxygen evolution/number of turnovers *vs* time plot for the addition of 30 equivalents of Ce(IV) to 8.0 mL of 1.0×10^{-3} M $[Ru(Mebimpy)(bpy)(OH_2)](OTf)_2$ in 1.0 M HNO_3 at 298 K.

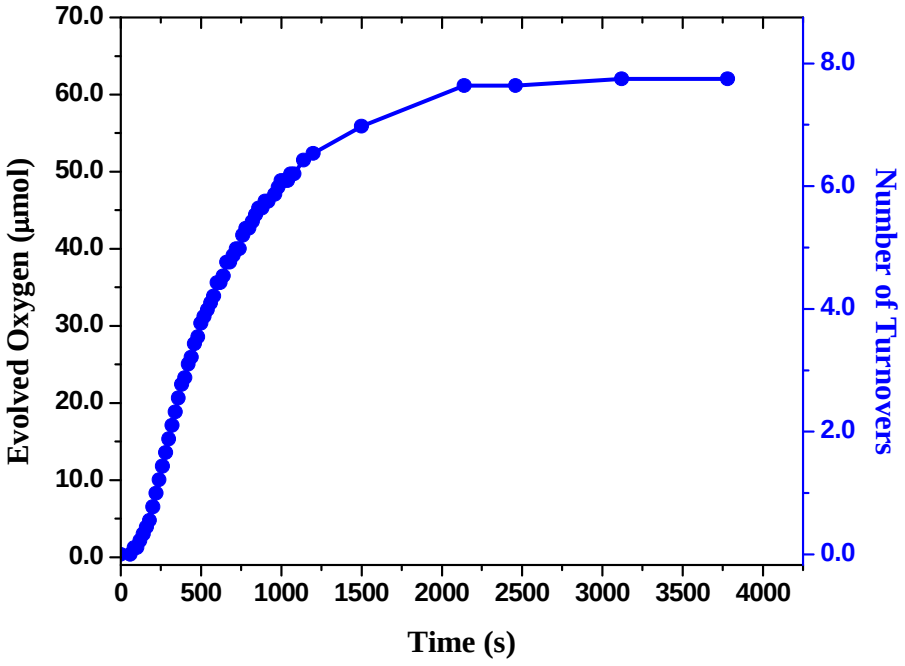

Figure S23. Oxygen evolution/number of turnovers *vs* time plot for the addition of 30 equivalents of Ce(IV) to 8.0 mL of 1.0×10^{-3} M $[Ru(tpy)(Mebim\text{-}py)(OH_2)](ClO_4)_2$ in 0.1 M HNO_3 at 298 K.

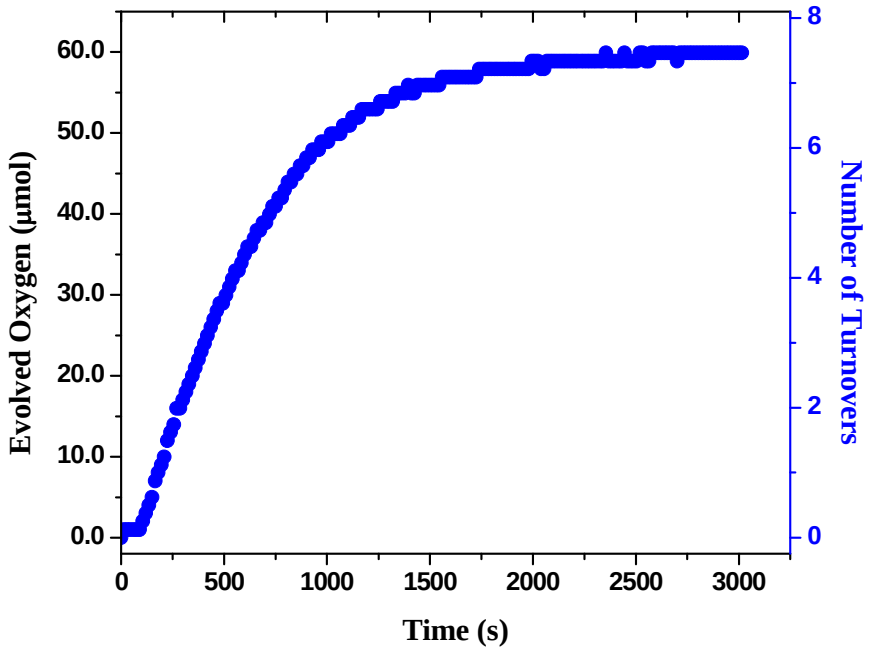

Figure S24. Oxygen evolution/number of turnovers *vs* time plot for the addition of 30 equivalents of Ce(IV) to 8.0 mL of 1.0×10^{-3} M $[Ru(tpy)(Mebim\text{-}pz)(OH_2)](PF_6)_2$ in 0.1 M HNO_3 at 298 K.

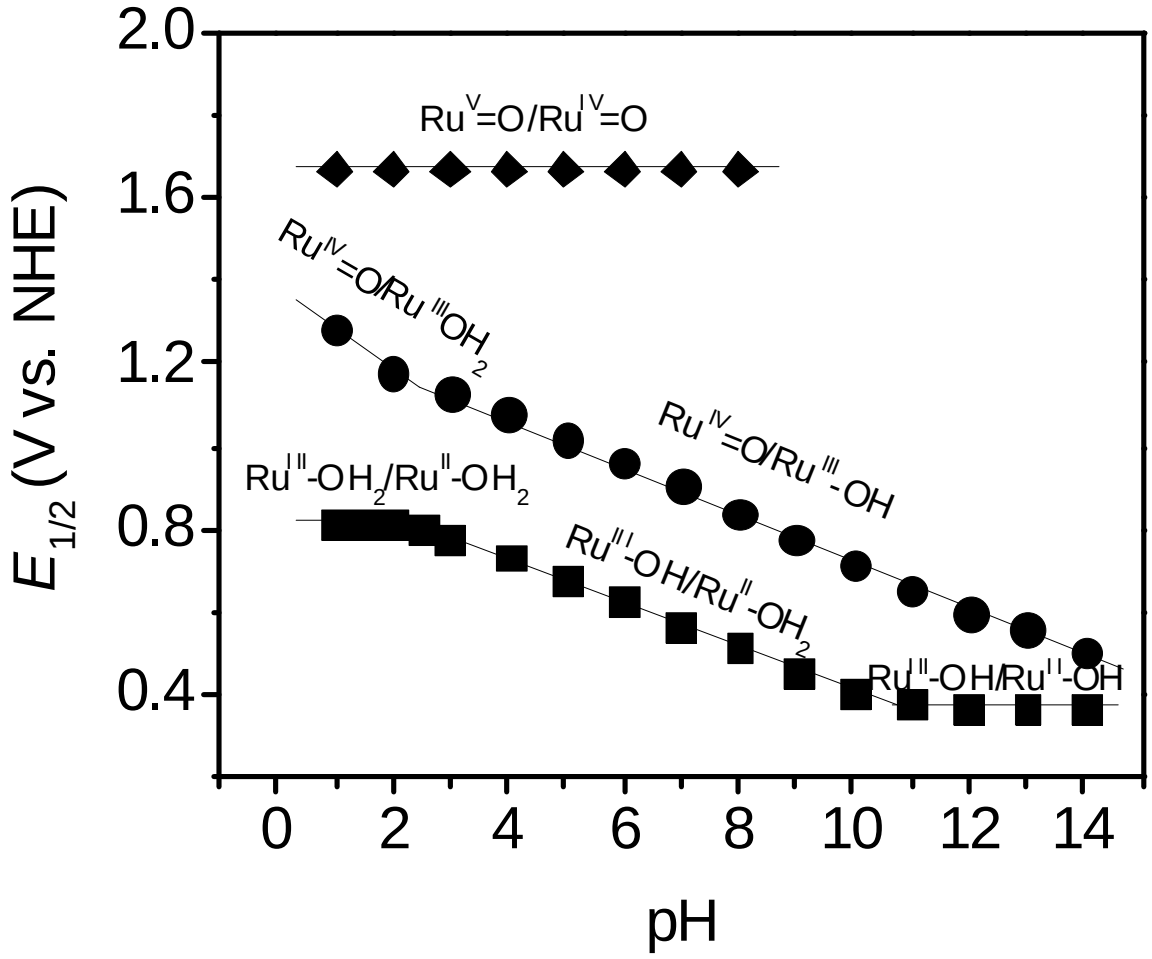

Figure S25. Plots of $E_{1/2}$ vs pH for the Ru(III/II), Ru(IV/III), and Ru(V/IV) couples of $[Ru(Mebimpy)(bpy)(OH_2)]^{2+}$ at GC working electrode. I = 0.1 M; scan rate, 100 mV/s.

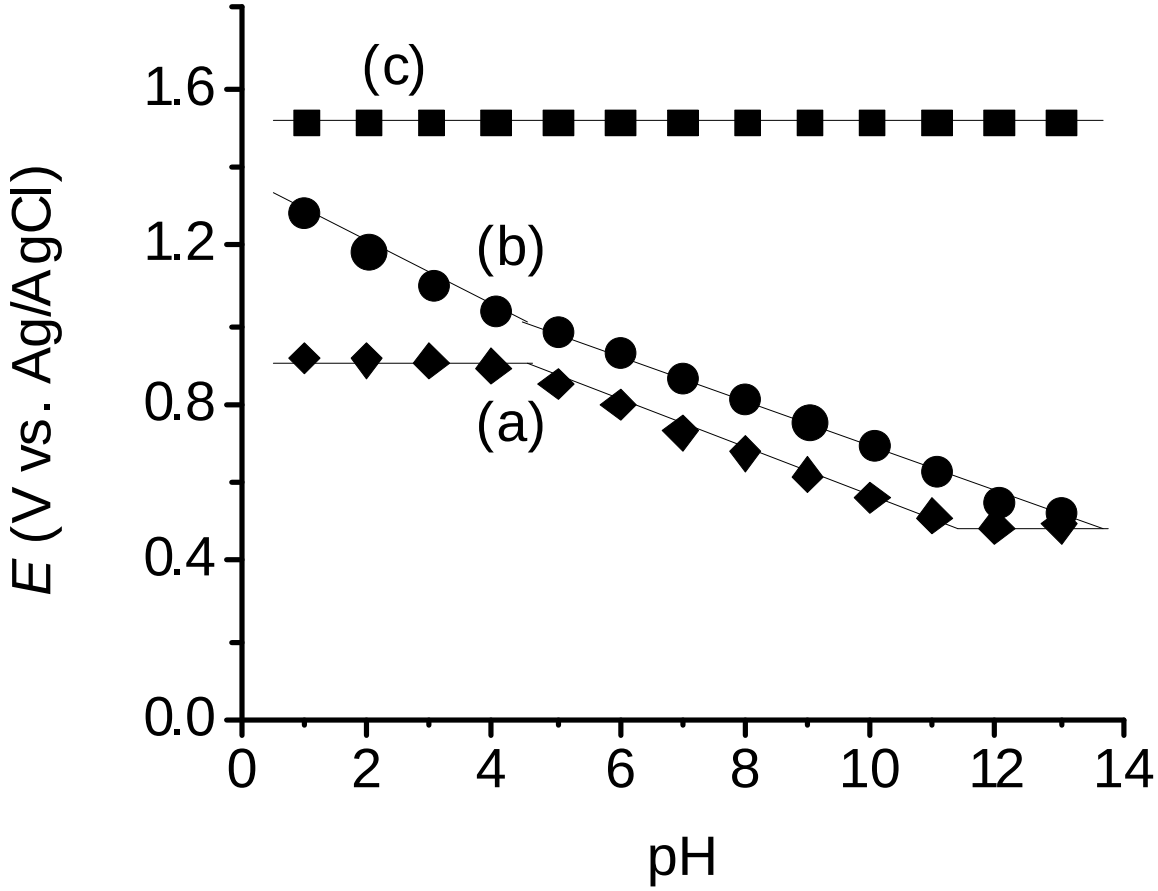

Figure S26. Plots of $E_{1/2}$ (V vs Ag/AgCl) vs pH for the Ru(III/II) (a), Ru(IV/III) (b), and (c) Ru(V/IV) redox couples of *trans*-$[Ru(tpy)(Mebim\text{-}py)(OH_2)]^{2+}$ (I = 0.1 M; GC working electrode; scan rate, 100 mV/s).

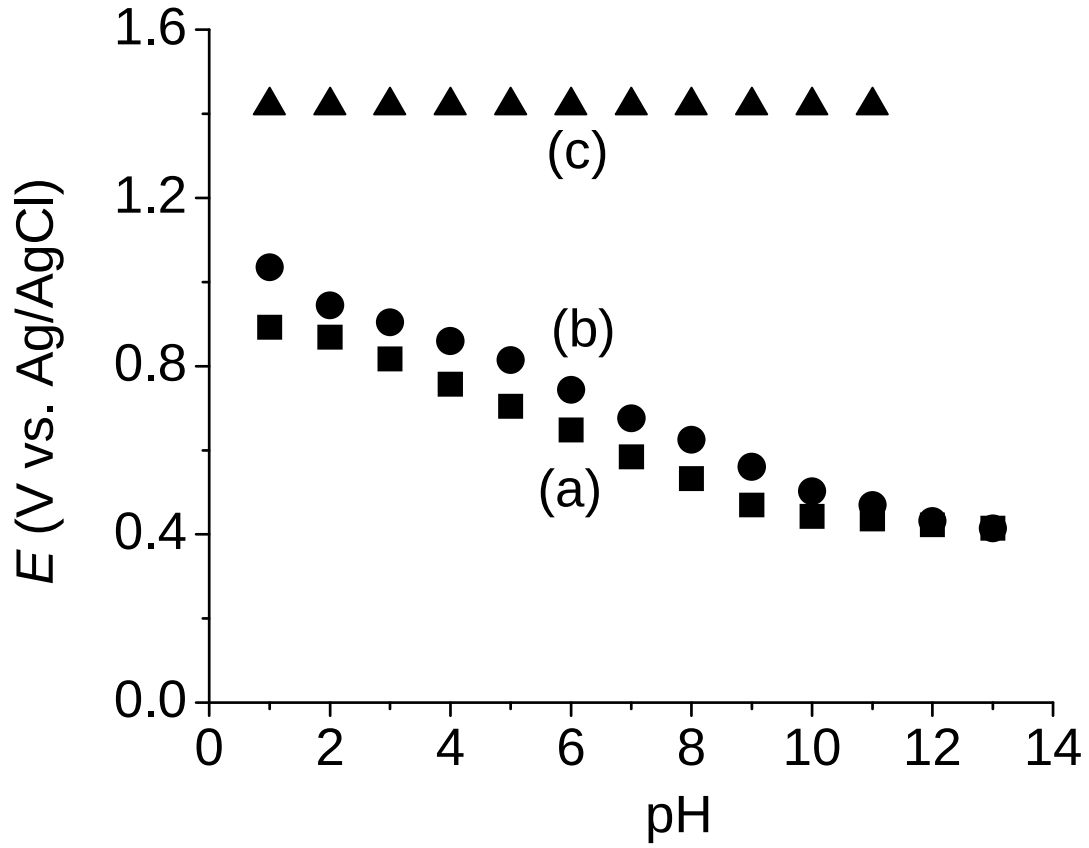

Figure S27. Plots of $E_{1/2}$ (V vs Ag/AgCl) vs pH for the Ru(III/II) (a), Ru(IV/III) (b), and (c) Ru(V/IV) couples of $[Ru(Mebimpy)(bpy)(OH_2)]^{2+}$ (I = 0.1 M; GC working electrode; scan rate, 100 mV/s).

Crystal Structure Report for *trans*-[Ru(tpy)(Mebim-py)(OH_2)](ClO_4)$_2$. Abbreviated: c09291.

A purple block-like specimen of $C_{28}H_{28}Cl_2N_6O_{11}Ru$, approximate dimensions 0.05 mm x 0.10 mm x 0.10 mm, was used for the X-ray crystallographic analysis. The X-ray intensity data were measured. The total exposure time was 40.28 hours. The frames were integrated with the Bruker SAINT software package using a narrow-frame algorithm. The integration of the data using a triclinic unit cell yielded a total of 21471 reflections to a maximum θ angle of 69.67° (0.82 Å resolution), of which 10228 were independent (average redundancy 2.099, completeness = 98.6%, R_{int} = 12.61%, R_{sig} = 14.76%) and 5893 (57.62%) were greater than $2\sigma(F^2)$. The final cell constants of a = 13.8740(10) Å, b = 15.2143(11) Å, c = 16.5727(13) Å, α = 103.936(6)°, β = 110.074(6)°, γ = 94.635(6)°, volume = 3137.3(4) Å^3, are based upon the refinement of the XYZ-centroids of 3493 reflections above 20 σ(I) with 6.084° < 2θ < 136.0°. Data were corrected for absorption effects using the multi-scan method (SADABS). The ratio of minimum to maximum apparent transmission was 0.715. The calculated minimum and maximum transmission coefficients (based on crystal size) are 0.5745 and 0.7457. The structure was solved and refined using the Bruker SHELXTL Software Package, using the space group P -1, with Z = 4 for the formula unit, $C_{28}H_{28}Cl_2N_6O_{11}Ru$. The final anisotropic full-matrix least-squares refinement on F^2 with 915 variables converged at R1 = 5.97%, for the observed data and wR2 = 15.37% for all data. The goodness-of-fit was 0.964. The largest peak in the final difference electron density synthesis was 0.910 e^-/Å^3 and the largest hole was -0.634 e^-/Å^3 with an RMS deviation of 0.117 e^-/Å^3. On the basis of the final model, the calculated density was 1.686 g/cm^3 and F(000), 1616 e^-.

Table S1. Sample and crystal data for c09291.

Identification code	c09291	
Chemical formula	$C_{28}H_{28}Cl_2N_6O_{11}Ru$	
Formula weight	796.53	
Temperature	100(2) K	
Wavelength	1.54178 Å	
Crystal size	0.05 x 0.10 x 0.10 mm	
Crystal habit	purple block	
Crystal system	triclinic	
Space group	P -1	
Unit cell dimensions	a = 13.8740(10) Å	α = 103.936(6)°
	b = 15.2143(11) Å	β = 110.074(6)°
	c = 16.5727(13) Å	γ = 94.635(6)°
Volume	3137.3(4) $Å^3$	
Z	4	
Density (calculated)	1.686 Mg/cm^3	
Absorption coefficient	6.234 mm^{-1}	
F(000)	1616	

Table S2. Data collection and structure refinement for c09291.

Theta range for data collection	2.96 to 69.67°
Index ranges	-16<=h<=9, -17<=k<=18, -19<=l<=19
Reflections collected	21471
Independent reflections	10228 [R(int) = 0.1261]
Coverage of independent reflections	98.6%
Absorption correction	multi-scan
Max. and min. transmission	0.7457 and 0.5745
Structure solution technique	direct methods
Structure solution program	SHELXS-97 (Sheldrick, 2008)

Refinement method	Full-matrix least-squares on F^2	
Refinement program	SHELXL-97 (Sheldrick, 2008)	
Function minimized	$\Sigma\, w(F_o^2 - F_c^2)^2$	
Data / restraints / parameters	10228 / 12 / 915	
Goodness-of-fit on F^2	0.964	
Δ/σ_{max}	0.005	
Final R indices	5893 data; $I>2\sigma(I)$	R1 = 0.0597, wR2 = 0.1251
	all data	R1 = 0.1244, wR2 = 0.1537
Weighting scheme	$w=1/[\sigma^2(F_o^2)+(0.0482P)^2+0.0000P]$ where $P=(F_o^2+2F_c^2)/3$	
Largest diff. peak and hole	0.910 and -0.634 eÅ^{-3}	
R.M.S. deviation from mean	0.117 eÅ^{-3}	

Table S3. Atomic coordinates and equivalent isotropic atomic displacement parameters (Å^2) for c09291.

U(eq) is defined as one third of the trace of the orthogonalized U_{ij} tensor.

	x/a	y/b	z/c	U(eq)
Ru1	0.38453(5)	0.85148(4)	0.13528(4)	0.03105(17)
O1	0.3110(5)	0.8213(4)	0.9895(4)	0.0386(14)
N2	0.2593(5)	0.7735(5)	0.1443(5)	0.0323(16)
C3	0.1746(5)	0.7237(5)	0.0771(5)	0.037(2)
C4	0.0968(5)	0.6695(5)	0.0892(5)	0.035(2)
C5	0.1097(7)	0.6671(5)	0.1730(7)	0.044(2)
C6	0.1964(7)	0.7179(5)	0.2447(5)	0.040(2)
C7	0.2715(5)	0.7699(5)	0.2282(5)	0.0324(18)
N8	0.3656(5)	0.8226(5)	0.2933(5)	0.0354(16)
C9	0.4109(7)	0.8370(5)	0.3869(5)	0.035(2)

	x/a	y/b	z/c	U(eq)
C10	0.3779(8)	0.8064(5)	0.4471(5)	0.043(2)
C11	0.4454(8)	0.8332(7)	0.5354(7)	0.047(2)
C12	0.5443(7)	0.8882(7)	0.5633(7)	0.046(2)
C13	0.5768(7)	0.9181(7)	0.5027(5)	0.046(2)
C14	0.5082(7)	0.8898(5)	0.4137(5)	0.038(2)
N15	0.5193(5)	0.9089(5)	0.3398(5)	0.0343(16)
C16	0.4336(5)	0.8685(5)	0.2631(5)	0.032(2)
C17	0.6114(7)	0.9626(7)	0.3404(7)	0.046(2)
N18	0.3377(5)	0.9801(5)	0.1409(5)	0.0376(17)
C19	0.2478(5)	0.0024(5)	0.1406(5)	0.038(2)
C20	0.2212(7)	0.0860(5)	0.1341(7)	0.043(2)
C21	0.2932(7)	0.1514(5)	0.1273(7)	0.043(2)
C22	0.3867(7)	0.1293(5)	0.1293(5)	0.042(2)
C23	0.4092(5)	0.0433(5)	0.1335(5)	0.0323(18)
C24	0.5047(7)	0.0111(5)	0.1295(5)	0.037(2)
C25	0.5897(7)	0.0633(5)	0.1248(5)	0.038(2)
C26	0.6717(7)	0.0191(7)	0.1176(7)	0.046(2)
C27	0.6666(7)	0.9269(7)	0.1103(7)	0.044(2)
C28	0.5806(7)	0.8769(5)	0.1131(5)	0.035(2)
N29	0.5049(5)	0.9218(5)	0.1278(5)	0.0338(16)
C30	0.5591(7)	0.7769(5)	0.1041(5)	0.038(2)
C31	0.6251(5)	0.7184(5)	0.0887(5)	0.035(2)
C32	0.6013(7)	0.6257(5)	0.0814(5)	0.042(2)
C33	0.5091(7)	0.5963(7)	0.0915(7)	0.045(2)
C34	0.4445(7)	0.6577(5)	0.1058(5)	0.035(2)
N35	0.4691(5)	0.7490(5)	0.1135(5)	0.0347(16)

	x/a	y/b	z/c	U(eq)
Ru2	0.80485(5)	0.67144(4)	0.47736(4)	0.02794(16)
O41	0.7990(4)	0.5228(4)	0.4389(4)	0.0326(13)
N42	0.8369(5)	0.6792(4)	0.3647(4)	0.0294(14)
C43	0.8412(5)	0.6073(5)	0.3010(5)	0.033(2)
C44	0.8576(5)	0.6180(5)	0.2281(5)	0.035(2)
C45	0.8732(7)	0.7055(5)	0.2186(5)	0.037(2)
C46	0.8707(7)	0.7799(5)	0.2838(5)	0.035(2)
C47	0.8502(5)	0.7631(5)	0.3560(5)	0.0267(16)
N48	0.8434(5)	0.8325(4)	0.4260(4)	0.0281(14)
C49	0.8604(5)	0.9290(5)	0.4471(5)	0.0303(17)
C50	0.8787(5)	0.9899(5)	0.4027(5)	0.035(2)
C51	0.8875(5)	0.0833(5)	0.4448(7)	0.039(2)
C52	0.8785(7)	0.1122(5)	0.5259(5)	0.040(2)
C53	0.8624(7)	0.0522(5)	0.5729(5)	0.037(2)
C54	0.8522(5)	0.9583(5)	0.5298(5)	0.0320(18)
N55	0.8310(5)	0.8821(4)	0.5568(5)	0.0298(15)
C56	0.8249(5)	0.8033(5)	0.4935(5)	0.0253(16)
C57	0.8215(7)	0.8855(5)	0.6410(5)	0.0315(18)
N58	0.6404(5)	0.6426(5)	0.4190(5)	0.0318(15)
C59	0.5790(7)	0.6281(5)	0.3335(5)	0.036(2)
C60	0.4739(7)	0.5994(5)	0.3022(5)	0.041(2)
C61	0.4278(7)	0.5898(5)	0.3625(5)	0.039(2)
C62	0.4897(7)	0.6061(5)	0.4501(5)	0.037(2)
C63	0.5974(7)	0.6325(5)	0.4785(5)	0.034(2)
C64	0.6698(5)	0.6451(5)	0.5707(5)	0.0292(17)
C65	0.6455(7)	0.6369(5)	0.6441(5)	0.0332(18)

	x/a	y/b	z/c	U(eq)
C66	0.7245(7)	0.6457(5)	0.7240(5)	0.040(2)
C67	0.8280(7)	0.6628(5)	0.7320(5)	0.036(2)
C68	0.8500(7)	0.6741(5)	0.6604(5)	0.034(2)
N69	0.7715(5)	0.6642(4)	0.5818(5)	0.0305(15)
C70	0.9533(7)	0.6873(5)	0.6544(5)	0.032(2)
C71	0.0463(7)	0.7026(5)	0.7282(5)	0.036(2)
C72	0.1406(7)	0.7094(5)	0.7141(7)	0.044(2)
C73	0.1394(7)	0.7015(5)	0.6303(5)	0.037(2)
C74	0.0438(7)	0.6900(5)	0.5614(5)	0.038(2)
N75	0.9527(5)	0.6849(4)	0.5726(4)	0.0288(14)
Cl1	0.19889(16)	0.43789(14)	0.05262(14)	0.0388(5)
O80	0.1443(7)	0.4600(5)	0.9724(5)	0.066(2)
O81	0.2789(5)	0.5102(5)	0.1112(5)	0.081(3)
O82	0.2377(5)	0.3560(5)	0.0309(5)	0.068(2)
O83	0.1272(5)	0.4205(5)	0.0943(5)	0.0534(18)
Cl2	0.57769(17)	0.37129(14)	0.25381(17)	0.0452(5)
O84	0.4683(5)	0.3615(5)	0.2073(5)	0.0543(18)
O85	0.6336(5)	0.4351(5)	0.2270(5)	0.058(2)
O86	0.6027(5)	0.4058(5)	0.3490(5)	0.0507(17)
O87	0.6097(5)	0.2844(5)	0.2346(5)	0.059(2)
Cl3	0.86921(17)	0.42899(13)	0.62103(14)	0.0386(5)
O88	0.7625(5)	0.4315(5)	0.5741(5)	0.069(2)
O89	0.9324(5)	0.4749(4)	0.5850(4)	0.0407(14)
O90	0.8987(5)	0.4748(5)	0.7137(5)	0.058(2)
O91	0.8859(5)	0.3358(4)	0.6114(5)	0.058(2)
Cl4	0.97000(16)	0.93282(13)	0.15968(14)	0.0362(5)

	x/a	y/b	z/c	U(eq)
O92	0.9355(5)	0.9854(4)	0.2253(5)	0.0515(17)
O93	0.8904(5)	0.8532(4)	0.1018(4)	0.0467(16)
O94	0.0650(5)	0.9024(4)	0.2018(4)	0.0446(15)
O95	0.9888(5)	0.9887(5)	0.1067(5)	0.0548(18)
O96	0.0556(5)	0.2229(4)	0.0505(4)	0.0443(15)
O97	0.7159(5)	0.3563(5)	0.0938(5)	0.0486(16)
O98	0.1175(5)	0.8620(5)	0.9341(5)	0.0486(16)
O99	0.9233(5)	0.4155(5)	0.1293(5)	0.0560(18)

Table S4. Bond lengths (Å) for c09291.

Ru1-C16	1.933(9)	Ru1-N29	1.966(6)
Ru1-N35	2.063(8)	Ru1-N2	2.093(6)
Ru1-N18	2.102(7)	Ru1-O1	2.188(6)
N2-C3	1.322(11)	N2-C7	1.357(11)
C3-C4	1.404(11)	C4-C5	1.349(13)
C5-C6	1.373(13)	C6-C7	1.397(12)
C7-N8	1.399(11)	N8-C9	1.413(12)
N8-C16	1.418(10)	C9-C14	1.381(12)
C9-C10	1.387(13)	C10-C11	1.377(14)
C11-C12	1.412(14)	C12-C13	1.383(14)
C13-C14	1.389(13)	C14-N15	1.380(12)
N15-C16	1.369(11)	N15-C17	1.456(11)
N18-C19	1.318(11)	N18-C23	1.381(10)
C19-C20	1.371(13)	C20-C21	1.404(13)
C21-C22	1.358(13)	C22-C23	1.382(12)

C23-C24	1.466(12)	C24-N29	1.353(11)
C24-C25	1.402(12)	C25-C26	1.393(13)
C26-C27	1.373(14)	C27-C28	1.383(12)
C28-N29	1.358(11)	C28-C30	1.487(12)
C30-N35	1.357(11)	C30-C31	1.370(13)
C31-C32	1.389(12)	C32-C33	1.398(13)
C33-C34	1.381(13)	C34-N35	1.367(11)
Ru2-C56	1.943(7)	Ru2-N69	1.964(7)
Ru2-N75	2.073(7)	Ru2-N42	2.089(7)
Ru2-N58	2.110(6)	Ru2-O41	2.184(6)
N42-C47	1.324(10)	N42-C43	1.346(11)
C43-C44	1.349(12)	C44-C45	1.386(12)
C45-C46	1.377(12)	C46-C47	1.395(12)
C47-N48	1.405(10)	N48-C56	1.390(10)
N48-C49	1.404(10)	C49-C50	1.373(12)
C49-C54	1.381(12)	C50-C51	1.398(12)
C51-C52	1.362(14)	C52-C53	1.385(12)
C53-C54	1.406(12)	C54-N55	1.386(10)
N55-C56	1.364(10)	N55-C57	1.436(10)
N58-C59	1.332(11)	N58-C63	1.347(11)
C59-C60	1.361(12)	C60-C61	1.387(14)
C61-C62	1.358(13)	C62-C63	1.395(12)
C63-C64	1.468(12)	C64-N69	1.357(10)
C64-C65	1.399(12)	C65-C66	1.366(13)
C66-C67	1.393(12)	C67-C68	1.368(12)
C68-N69	1.345(11)	C68-C70	1.471(12)
C70-N75	1.344(11)	C70-C71	1.395(13)

C71-C72	1.406(13)	C72-C73	1.358(14)
C73-C74	1.386(13)	C74-N75	1.337(11)
Cl1-O81	1.390(8)	Cl1-O82	1.413(8)
Cl1-O80	1.421(8)	Cl1-O83	1.432(7)
Cl2-O84	1.423(7)	Cl2-O87	1.426(7)
Cl2-O85	1.437(8)	Cl2-O86	1.442(7)
Cl3-O90	1.421(7)	Cl3-O88	1.425(8)
Cl3-O91	1.435(7)	Cl3-O89	1.441(6)
Cl4-O95	1.429(7)	Cl4-O92	1.432(7)
Cl4-O94	1.435(7)	Cl4-O93	1.451(6)

Table S5. Bond angles (°) for c09291.

C16-Ru1-N29	100.1(3)	C16-Ru1-N35	93.7(3)
N29-Ru1-N35	79.4(3)	C16-Ru1-N2	79.2(3)
N29-Ru1-N2	178.2(3)	N35-Ru1-N2	99.0(3)
C16-Ru1-N18	95.5(3)	N29-Ru1-N18	79.6(3)
N35-Ru1-N18	158.2(3)	N2-Ru1-N18	102.1(3)
C16-Ru1-O1	172.6(3)	N29-Ru1-O1	87.3(3)
N35-Ru1-O1	87.4(3)	N2-Ru1-O1	93.4(2)
N18-Ru1-O1	86.0(3)	C3-N2-C7	117.8(7)
C3-N2-Ru1	126.8(6)	C7-N2-Ru1	115.2(5)
N2-C3-C4	122.9(9)	C5-C4-C3	118.5(8)
C4-C5-C6	120.4(8)	C5-C6-C7	118.3(9)
N2-C7-C6	122.0(8)	N2-C7-N8	112.6(7)
C6-C7-N8	125.4(8)	C7-N8-C9	131.9(7)
C7-N8-C16	117.2(7)	C9-N8-C16	110.8(7)

C14-C9-C10	121.6(8)	C14-C9-N8	105.2(8)
C10-C9-N8	133.2(8)	C11-C10-C9	117.0(9)
C10-C11-C12	121.5(10)	C13-C12-C11	121.1(9)
C12-C13-C14	116.7(9)	N15-C14-C9	108.5(7)
N15-C14-C13	129.4(8)	C9-C14-C13	122.0(9)
C16-N15-C14	111.9(7)	C16-N15-C17	122.8(8)
C14-N15-C17	125.2(7)	N15-C16-N8	103.6(7)
N15-C16-Ru1	140.6(6)	N8-C16-Ru1	115.7(6)
C19-N18-C23	119.0(8)	C19-N18-Ru1	128.4(6)
C23-N18-Ru1	112.2(6)	N18-C19-C20	123.3(8)
C19-C20-C21	118.5(9)	C22-C21-C20	118.2(9)
C21-C22-C23	121.3(8)	N18-C23-C22	119.6(8)
N18-C23-C24	115.4(7)	C22-C23-C24	125.1(8)
N29-C24-C25	120.2(8)	N29-C24-C23	113.9(7)
C25-C24-C23	125.9(8)	C26-C25-C24	117.3(8)
C27-C26-C25	121.1(8)	C26-C27-C28	120.1(9)
N29-C28-C27	118.6(8)	N29-C28-C30	113.1(7)
C27-C28-C30	128.3(8)	C24-N29-C28	122.2(7)
C24-N29-Ru1	118.8(6)	C28-N29-Ru1	118.7(5)
N35-C30-C31	123.0(8)	N35-C30-C28	114.1(8)
C31-C30-C28	122.8(8)	C30-C31-C32	120.4(8)
C31-C32-C33	117.0(8)	C34-C33-C32	120.4(9)
N35-C34-C33	121.9(8)	C30-N35-C34	117.2(8)
C30-N35-Ru1	114.7(6)	C34-N35-Ru1	128.1(6)
C56-Ru2-N69	101.5(3)	C56-Ru2-N75	90.7(3)
N69-Ru2-N75	79.0(3)	C56-Ru2-N42	78.4(3)
N69-Ru2-N42	178.8(3)	N75-Ru2-N42	102.2(3)

C56-Ru2-N58	98.4(3)	N69-Ru2-N58	79.5(3)
N75-Ru2-N58	158.0(3)	N42-Ru2-N58	99.2(3)
C56-Ru2-O41	167.7(3)	N69-Ru2-O41	90.3(2)
N75-Ru2-O41	88.4(2)	N42-Ru2-O41	89.8(2)
N58-Ru2-O41	86.8(2)	C47-N42-C43	119.1(7)
C47-N42-Ru2	115.1(5)	C43-N42-Ru2	125.8(5)
N42-C43-C44	121.9(8)	C43-C44-C45	119.7(8)
C46-C45-C44	119.1(8)	C45-C46-C47	117.9(8)
N42-C47-C46	122.3(7)	N42-C47-N48	114.1(7)
C46-C47-N48	123.6(7)	C56-N48-C49	111.0(6)
C56-N48-C47	115.8(6)	C49-N48-C47	133.0(7)
C50-C49-C54	121.7(8)	C50-C49-N48	133.5(8)
C54-C49-N48	104.8(7)	C49-C50-C51	116.7(9)
C52-C51-C50	121.6(8)	C51-C52-C53	122.7(8)
C52-C53-C54	115.5(9)	C49-C54-N55	108.9(7)
C49-C54-C53	121.7(8)	N55-C54-C53	129.4(8)
C56-N55-C54	110.2(7)	C56-N55-C57	124.9(7)
C54-N55-C57	124.9(7)	N55-C56-N48	105.2(6)
N55-C56-Ru2	138.2(6)	N48-C56-Ru2	116.5(5)
C59-N58-C63	119.3(7)	C59-N58-Ru2	128.5(6)
C63-N58-Ru2	112.1(5)	N58-C59-C60	122.8(8)
C59-C60-C61	118.9(8)	C62-C61-C60	118.7(8)
C61-C62-C63	120.4(8)	N58-C63-C62	120.0(8)
N58-C63-C64	116.5(7)	C62-C63-C64	123.4(8)
N69-C64-C65	118.8(7)	N69-C64-C63	113.4(7)
C65-C64-C63	127.8(8)	C66-C65-C64	119.3(8)
C65-C66-C67	120.2(9)	C68-C67-C66	119.5(8)

N69-C68-C67	119.6(8)	N69-C68-C70	112.7(8)
C67-C68-C70	127.4(8)	C68-N69-C64	122.5(7)
C68-N69-Ru2	119.0(6)	C64-N69-Ru2	118.4(5)
N75-C70-C71	121.6(8)	N75-C70-C68	115.5(7)
C71-C70-C68	122.9(8)	C70-C71-C72	118.3(9)
C73-C72-C71	119.9(8)	C72-C73-C74	118.1(9)
N75-C74-C73	123.7(9)	C74-N75-C70	118.3(7)
C74-N75-Ru2	128.0(6)	C70-N75-Ru2	113.6(5)
O81-Cl1-O82	111.3(5)	O81-Cl1-O80	110.5(5)
O82-Cl1-O80	109.1(5)	O81-Cl1-O83	109.5(5)
O82-Cl1-O83	107.5(5)	O80-Cl1-O83	108.8(5)
O84-Cl2-O87	110.0(4)	O84-Cl2-O85	110.4(5)
O87-Cl2-O85	108.9(5)	O84-Cl2-O86	109.5(4)
O87-Cl2-O86	109.4(5)	O85-Cl2-O86	108.6(4)
O90-Cl3-O88	109.8(5)	O90-Cl3-O91	108.7(4)
O88-Cl3-O91	110.8(5)	O90-Cl3-O89	109.4(4)
O88-Cl3-O89	108.7(4)	O91-Cl3-O89	109.4(4)
O95-Cl4-O92	109.4(4)	O95-Cl4-O94	108.5(4)
O92-Cl4-O94	110.9(4)	O95-Cl4-O93	109.2(4)
O92-Cl4-O93	109.8(4)	O94-Cl4-O93	109.1(4)

Table S6. Torsion angles (°) for c09291.

C16-Ru1-N2-C3	-176.7(8)	N29-Ru1-N2-C3	-108.(9)
N35-Ru1-N2-C3	-84.5(7)	N18-Ru1-N2-C3	90.0(7)
O1-Ru1-N2-C3	3.3(7)	C16-Ru1-N2-C7	-1.5(6)
N29-Ru1-N2-C7	67.(10)	N35-Ru1-N2-C7	90.6(6)

N18-Ru1-N2-C7	-94.9(6)	O1-Ru1-N2-C7	178.5(6)
C7-N2-C3-C4	1.5(12)	Ru1-N2-C3-C4	176.5(7)
N2-C3-C4-C5	-1.0(14)	C3-C4-C5-C6	1.0(14)
C4-C5-C6-C7	-1.5(14)	C3-N2-C7-C6	-2.0(12)
Ru1-N2-C7-C6	-177.6(7)	C3-N2-C7-N8	177.7(7)
Ru1-N2-C7-N8	2.1(9)	C5-C6-C7-N2	2.1(13)
C5-C6-C7-N8	-177.6(8)	N2-C7-N8-C9	-178.4(8)
C6-C7-N8-C9	1.3(14)	N2-C7-N8-C16	-1.7(10)
C6-C7-N8-C16	178.0(8)	C7-N8-C9-C14	175.3(8)
C16-N8-C9-C14	-1.6(9)	C7-N8-C9-C10	-1.7(16)
C16-N8-C9-C10	-178.6(10)	C14-C9-C10-C11	1.7(13)
N8-C9-C10-C11	178.3(9)	C9-C10-C11-C12	-0.8(14)
C10-C11-C12-C13	0.6(15)	C11-C12-C13-C14	-1.2(14)
C10-C9-C14-N15	179.4(8)	N8-C9-C14-N15	2.0(9)
C10-C9-C14-C13	-2.5(14)	N8-C9-C14-C13	-179.9(8)
C12-C13-C14-N15	179.7(9)	C12-C13-C14-C9	2.1(14)
C9-C14-N15-C16	-1.8(10)	C13-C14-N15-C16	-179.7(9)
C9-C14-N15-C17	-179.6(8)	C13-C14-N15-C17	2.5(15)
C14-N15-C16-N8	0.7(9)	C17-N15-C16-N8	178.6(8)
C14-N15-C16-Ru1	-175.4(8)	C17-N15-C16-Ru1	2.6(14)
C7-N8-C16-N15	-176.8(7)	C9-N8-C16-N15	0.6(9)
C7-N8-C16-Ru1	0.4(10)	C9-N8-C16-Ru1	177.8(5)
N29-Ru1-C16-N15	-2.0(10)	N35-Ru1-C16-N15	77.9(10)
N2-Ru1-C16-N15	176.3(10)	N18-Ru1-C16-N15	-82.4(10)
O1-Ru1-C16-N15	176.3(18)	N29-Ru1-C16-N8	-177.7(6)
N35-Ru1-C16-N8	-97.9(6)	N2-Ru1-C16-N8	0.6(6)
N18-Ru1-C16-N8	101.9(6)	O1-Ru1-C16-N8	1.(3)

C16-Ru1-N18-C19	-86.5(8)	N29-Ru1-N18-C19	174.3(8)
N35-Ru1-N18-C19	158.9(7)	N2-Ru1-N18-C19	-6.3(8)
O1-Ru1-N18-C19	86.3(8)	C16-Ru1-N18-C23	101.4(6)
N29-Ru1-N18-C23	2.1(6)	N35-Ru1-N18-C23	-13.2(11)
N2-Ru1-N18-C23	-178.4(6)	O1-Ru1-N18-C23	-85.9(6)
C23-N18-C19-C20	-0.6(14)	Ru1-N18-C19-C20	-172.3(7)
N18-C19-C20-C21	0.1(15)	C19-C20-C21-C22	-1.3(14)
C20-C21-C22-C23	3.1(14)	C19-N18-C23-C22	2.3(13)
Ru1-N18-C23-C22	175.2(7)	C19-N18-C23-C24	-176.8(8)
Ru1-N18-C23-C24	-3.8(9)	C21-C22-C23-N18	-3.6(14)
C21-C22-C23-C24	175.4(9)	N18-C23-C24-N29	4.0(11)
C22-C23-C24-N29	-175.1(8)	N18-C23-C24-C25	-177.9(9)
C22-C23-C24-C25	3.1(15)	N29-C24-C25-C26	0.6(14)
C23-C24-C25-C26	-177.4(8)	C24-C25-C26-C27	3.6(14)
C25-C26-C27-C28	-2.3(15)	C26-C27-C28-N29	-3.4(15)
C26-C27-C28-C30	178.3(9)	C25-C24-N29-C28	-6.5(13)
C23-C24-N29-C28	171.8(8)	C25-C24-N29-Ru1	179.7(7)
C23-C24-N29-Ru1	-2.1(10)	C27-C28-N29-C24	7.8(13)
C30-C28-N29-C24	-173.6(8)	C27-C28-N29-Ru1	-178.3(7)
C30-C28-N29-Ru1	0.3(10)	C16-Ru1-N29-C24	-93.7(7)
N35-Ru1-N29-C24	174.3(7)	N2-Ru1-N29-C24	-162.(9)
N18-Ru1-N29-C24	0.0(6)	O1-Ru1-N29-C24	86.5(7)
C16-Ru1-N29-C28	92.1(7)	N35-Ru1-N29-C28	0.2(6)
N2-Ru1-N29-C28	24.(10)	N18-Ru1-N29-C28	-174.1(7)
O1-Ru1-N29-C28	-87.6(6)	N29-C28-C30-N35	-0.9(11)
C27-C28-C30-N35	177.5(10)	N29-C28-C30-C31	179.7(8)
C27-C28-C30-C31	-1.8(15)	N35-C30-C31-C32	0.3(14)

C28-C30-C31-C32	179.6(9)	C30-C31-C32-C33	-0.8(14)
C31-C32-C33-C34	1.7(14)	C32-C33-C34-N35	-2.2(14)
C31-C30-N35-C34	-0.8(13)	C28-C30-N35-C34	179.9(7)
C31-C30-N35-Ru1	-179.6(7)	C28-C30-N35-Ru1	1.1(10)
C33-C34-N35-C30	1.7(12)	C33-C34-N35-Ru1	-179.7(7)
C16-Ru1-N35-C30	-100.3(6)	N29-Ru1-N35-C30	-0.7(6)
N2-Ru1-N35-C30	-180.0(6)	N18-Ru1-N35-C30	14.6(11)
O1-Ru1-N35-C30	87.0(6)	C16-Ru1-N35-C34	81.1(7)
N29-Ru1-N35-C34	-179.4(8)	N2-Ru1-N35-C34	1.4(8)
N18-Ru1-N35-C34	-164.0(7)	O1-Ru1-N35-C34	-91.6(7)
C56-Ru2-N42-C47	-2.6(5)	N69-Ru2-N42-C47	84.(12)
N75-Ru2-N42-C47	-90.7(6)	N58-Ru2-N42-C47	94.1(6)
O41-Ru2-N42-C47	-179.1(5)	C56-Ru2-N42-C43	179.8(7)
N69-Ru2-N42-C43	-94.(12)	N75-Ru2-N42-C43	91.6(7)
N58-Ru2-N42-C43	-83.5(7)	O41-Ru2-N42-C43	3.3(7)
C47-N42-C43-C44	-0.7(12)	Ru2-N42-C43-C44	176.9(6)
N42-C43-C44-C45	1.6(13)	C43-C44-C45-C46	-0.6(13)
C44-C45-C46-C47	-1.2(13)	C43-N42-C47-C46	-1.3(12)
Ru2-N42-C47-C46	-179.1(6)	C43-N42-C47-N48	179.6(7)
Ru2-N42-C47-N48	1.8(8)	C45-C46-C47-N42	2.2(12)
C45-C46-C47-N48	-178.7(8)	N42-C47-N48-C56	0.6(10)
C46-C47-N48-C56	-178.6(7)	N42-C47-N48-C49	174.1(7)
C46-C47-N48-C49	-5.0(13)	C56-N48-C49-C50	-177.9(9)
C47-N48-C49-C50	8.3(15)	C56-N48-C49-C54	0.3(9)
C47-N48-C49-C54	-173.5(8)	C54-C49-C50-C51	-0.7(12)
N48-C49-C50-C51	177.3(8)	C49-C50-C51-C52	0.1(13)
C50-C51-C52-C53	1.4(14)	C51-C52-C53-C54	-2.2(13)

C50-C49-C54-N55	178.4(7)	N48-C49-C54-N55	-0.1(9)
C50-C49-C54-C53	-0.1(13)	N48-C49-C54-C53	-178.6(7)
C52-C53-C54-C49	1.5(12)	C52-C53-C54-N55	-176.7(8)
C49-C54-N55-C56	-0.1(9)	C53-C54-N55-C56	178.3(8)
C49-C54-N55-C57	177.3(7)	C53-C54-N55-C57	-4.3(13)
C54-N55-C56-N48	0.3(8)	C57-N55-C56-N48	-177.2(7)
C54-N55-C56-Ru2	176.9(6)	C57-N55-C56-Ru2	-0.6(13)
C49-N48-C56-N55	-0.3(8)	C47-N48-C56-N55	174.6(6)
C49-N48-C56-Ru2	-177.8(5)	C47-N48-C56-Ru2	-2.9(8)
N69-Ru2-C56-N55	7.8(9)	N75-Ru2-C56-N55	-71.2(9)
N42-Ru2-C56-N55	-173.5(9)	N58-Ru2-C56-N55	88.7(9)
O41-Ru2-C56-N55	-156.9(9)	N69-Ru2-C56-N48	-175.9(5)
N75-Ru2-C56-N48	105.2(6)	N42-Ru2-C56-N48	2.8(5)
N58-Ru2-C56-N48	-94.9(6)	O41-Ru2-C56-N48	19.4(16)
C56-Ru2-N58-C59	83.4(7)	N69-Ru2-N58-C59	-176.3(8)
N75-Ru2-N58-C59	-163.3(7)	N42-Ru2-N58-C59	3.9(7)
O41-Ru2-N58-C59	-85.4(7)	C56-Ru2-N58-C63	-101.4(6)
N69-Ru2-N58-C63	-1.1(6)	N75-Ru2-N58-C63	11.9(11)
N42-Ru2-N58-C63	179.1(6)	O41-Ru2-N58-C63	89.8(6)
C63-N58-C59-C60	-2.9(13)	Ru2-N58-C59-C60	172.0(7)
N58-C59-C60-C61	3.9(14)	C59-C60-C61-C62	-2.5(14)
C60-C61-C62-C63	0.4(13)	C59-N58-C63-C62	0.7(12)
Ru2-N58-C63-C62	-175.0(6)	C59-N58-C63-C64	177.1(7)
Ru2-N58-C63-C64	1.4(9)	C61-C62-C63-N58	0.6(13)
C61-C62-C63-C64	-175.6(8)	N58-C63-C64-N69	-0.9(11)
C62-C63-C64-N69	175.4(7)	N58-C63-C64-C65	-178.9(8)
C62-C63-C64-C65	-2.6(13)	N69-C64-C65-C66	-1.9(12)

C63-C64-C65-C66	176.0(8)	C64-C65-C66-C67	0.2(13)
C65-C66-C67-C68	2.4(14)	C66-C67-C68-N69	-3.2(13)
C66-C67-C68-C70	-176.3(8)	C67-C68-N69-C64	1.4(12)
C70-C68-N69-C64	175.5(7)	C67-C68-N69-Ru2	-175.4(6)
C70-C68-N69-Ru2	-1.4(9)	C65-C64-N69-C68	1.1(12)
C63-C64-N69-C68	-177.0(7)	C65-C64-N69-Ru2	178.0(6)
C63-C64-N69-Ru2	-0.1(9)	C56-Ru2-N69-C68	-85.8(6)
N75-Ru2-N69-C68	2.6(6)	N42-Ru2-N69-C68	-170.(60)
N58-Ru2-N69-C68	177.7(6)	O41-Ru2-N69-C68	91.0(6)
C56-Ru2-N69-C64	97.2(6)	N75-Ru2-N69-C64	-174.4(6)
N42-Ru2-N69-C64	11.(13)	N58-Ru2-N69-C64	0.7(6)
O41-Ru2-N69-C64	-86.0(6)	N69-C68-C70-N75	-1.7(11)
C67-C68-C70-N75	171.8(8)	N69-C68-C70-C71	177.4(8)
C67-C68-C70-C71	-9.0(14)	N75-C70-C71-C72	-4.3(13)
C68-C70-C71-C72	176.6(8)	C70-C71-C72-C73	0.4(13)
C71-C72-C73-C74	2.2(13)	C72-C73-C74-N75	-1.0(13)
C73-C74-N75-C70	-2.8(12)	C73-C74-N75-Ru2	178.2(6)
C71-C70-N75-C74	5.5(12)	C68-C70-N75-C74	-175.3(7)
C71-C70-N75-Ru2	-175.4(6)	C68-C70-N75-Ru2	3.8(9)
C56-Ru2-N75-C74	-82.8(7)	N69-Ru2-N75-C74	175.6(7)
N42-Ru2-N75-C74	-4.6(7)	N58-Ru2-N75-C74	162.5(7)
O41-Ru2-N75-C74	84.9(7)	C56-Ru2-N75-C70	98.1(6)
N69-Ru2-N75-C70	-3.5(5)	N42-Ru2-N75-C70	176.4(5)
N58-Ru2-N75-C70	-16.5(10)	O41-Ru2-N75-C70	-94.1(6)

Table S7. Anisotropic atomic displacement parameters (Å^2) for c09291.

The anisotropic atomic displacement factor exponent takes the form: $-2\pi^2[h^2 a^{*2} U_{11} + ... + 2 h k a^* b^* U_{12}]$

	U_{11}	U_{22}	U_{33}	U_{23}	U_{13}	U_{12}
Ru1	0.0267(2)	0.0343(2)	0.0348(4)	0.0111(2)	0.0148(2)	0.0013(2)
O1	0.032(3)	0.046(3)	0.039(4)	0.012(3)	0.016(3)	0.003(3)
N2	0.022(3)	0.035(4)	0.041(4)	0.012(3)	0.014(3)	0.001(3)
C3	0.033(5)	0.040(4)	0.041(5)	0.015(4)	0.018(4)	-0.001(4)
C4	0.024(4)	0.042(5)	0.044(6)	0.018(4)	0.014(4)	0.005(4)
C5	0.035(5)	0.041(5)	0.056(7)	0.021(4)	0.016(4)	-0.008(4)
C6	0.048(5)	0.043(5)	0.035(5)	0.018(4)	0.018(4)	0.000(4)
C7	0.028(4)	0.034(4)	0.040(5)	0.016(4)	0.014(4)	0.010(4)
N8	0.035(4)	0.038(4)	0.042(5)	0.021(3)	0.019(3)	0.005(3)
C9	0.041(5)	0.034(4)	0.031(5)	0.006(4)	0.017(4)	0.007(4)
C10	0.044(5)	0.044(5)	0.042(6)	0.014(4)	0.015(4)	0.012(4)
C11	0.054(6)	0.045(5)	0.044(6)	0.015(4)	0.019(5)	0.009(5)
C12	0.037(5)	0.058(6)	0.044(6)	0.013(4)	0.014(4)	0.022(5)
C13	0.036(5)	0.066(6)	0.039(6)	0.012(5)	0.019(4)	0.015(5)
C14	0.038(5)	0.041(5)	0.037(5)	0.010(4)	0.014(4)	0.015(4)
N15	0.021(3)	0.046(4)	0.036(4)	0.010(3)	0.013(3)	0.007(3)
C16	0.027(4)	0.032(4)	0.042(5)	0.002(4)	0.023(4)	0.005(4)
C17	0.030(5)	0.058(6)	0.044(6)	0.009(4)	0.012(4)	-0.002(4)
N18	0.033(4)	0.039(4)	0.042(5)	0.011(3)	0.016(3)	-0.001(3)
C19	0.029(4)	0.045(5)	0.040(5)	0.011(4)	0.015(4)	0.005(4)
C20	0.030(5)	0.044(5)	0.050(6)	0.006(4)	0.015(4)	0.002(4)
C21	0.040(5)	0.035(4)	0.050(6)	0.008(4)	0.015(4)	0.008(4)

	U_{11}	U_{22}	U_{33}	U_{23}	U_{13}	U_{12}
C22	0.039(5)	0.039(5)	0.046(6)	0.010(4)	0.015(4)	0.000(4)
C23	0.033(4)	0.029(4)	0.035(5)	0.009(3)	0.014(4)	-0.002(4)
C24	0.030(4)	0.040(5)	0.039(5)	0.009(4)	0.011(4)	0.006(4)
C25	0.038(5)	0.039(4)	0.043(6)	0.017(4)	0.019(4)	0.001(4)
C26	0.036(5)	0.059(6)	0.046(6)	0.015(5)	0.022(4)	-0.009(5)
C27	0.037(5)	0.053(5)	0.052(6)	0.022(5)	0.023(4)	0.013(5)
C28	0.033(5)	0.036(4)	0.041(5)	0.011(4)	0.018(4)	0.010(4)
N29	0.024(3)	0.035(4)	0.044(5)	0.015(3)	0.015(3)	-0.005(3)
C30	0.043(5)	0.043(5)	0.026(5)	0.008(4)	0.013(4)	0.001(4)
C31	0.030(4)	0.036(4)	0.044(6)	0.010(4)	0.022(4)	0.004(4)
C32	0.043(5)	0.045(5)	0.045(6)	0.008(4)	0.024(4)	0.020(4)
C33	0.033(5)	0.043(5)	0.049(6)	0.011(4)	0.007(4)	0.005(4)
C34	0.031(4)	0.037(4)	0.033(5)	0.012(4)	0.009(4)	0.003(4)
N35	0.028(4)	0.039(4)	0.033(4)	0.010(3)	0.010(3)	-0.011(3)
Ru2	0.0299(2)	0.0281(2)	0.0281(4)	0.0091(2)	0.0136(2)	0.0023(2)
O41	0.037(3)	0.030(3)	0.034(4)	0.011(2)	0.016(3)	0.003(3)
N42	0.030(4)	0.031(3)	0.024(4)	0.007(3)	0.006(3)	0.006(3)
C43	0.044(5)	0.035(4)	0.024(4)	0.009(3)	0.019(4)	-0.004(4)
C44	0.035(5)	0.035(4)	0.037(5)	0.006(4)	0.018(4)	0.009(4)
C45	0.042(5)	0.039(4)	0.035(5)	0.009(4)	0.021(4)	0.003(4)
C46	0.040(5)	0.036(4)	0.039(5)	0.019(4)	0.022(4)	0.009(4)
C47	0.025(4)	0.033(4)	0.018(4)	0.001(3)	0.008(3)	0.002(3)
N48	0.028(3)	0.031(3)	0.027(4)	0.007(3)	0.012(3)	0.007(3)
C49	0.033(4)	0.028(4)	0.033(5)	0.012(3)	0.014(4)	0.005(4)
C50	0.031(4)	0.032(4)	0.048(6)	0.016(4)	0.019(4)	0.013(4)
C51	0.030(4)	0.034(4)	0.054(6)	0.017(4)	0.016(4)	-0.002(4)

	U_{11}	U_{22}	U_{33}	U_{23}	U_{13}	U_{12}
C52	0.036(5)	0.022(4)	0.048(6)	0.007(4)	0.006(4)	-0.008(4)
C53	0.037(5)	0.032(4)	0.040(5)	0.010(4)	0.013(4)	0.003(4)
C54	0.018(4)	0.035(4)	0.040(5)	0.008(4)	0.007(3)	0.009(3)
N55	0.028(3)	0.029(3)	0.031(4)	0.007(3)	0.011(3)	0.003(3)
C56	0.025(4)	0.026(4)	0.025(4)	0.008(3)	0.010(3)	0.001(3)
C57	0.044(5)	0.029(4)	0.021(4)	0.003(3)	0.015(4)	0.004(4)
N58	0.023(3)	0.035(4)	0.035(4)	0.011(3)	0.009(3)	0.000(3)
C59	0.046(5)	0.036(4)	0.031(5)	0.015(4)	0.019(4)	0.003(4)
C60	0.030(5)	0.044(5)	0.036(5)	0.010(4)	-0.001(4)	0.005(4)
C61	0.031(4)	0.037(4)	0.050(6)	0.017(4)	0.015(4)	0.002(4)
C62	0.038(5)	0.032(4)	0.052(6)	0.018(4)	0.028(4)	0.013(4)
C63	0.037(5)	0.028(4)	0.038(5)	0.010(4)	0.014(4)	0.006(4)
C64	0.035(4)	0.028(4)	0.029(5)	0.010(3)	0.015(4)	0.005(4)
C65	0.035(4)	0.033(4)	0.040(5)	0.012(4)	0.022(4)	0.008(4)
C66	0.045(5)	0.047(5)	0.038(5)	0.012(4)	0.029(4)	0.013(4)
C67	0.042(5)	0.035(4)	0.033(5)	0.011(4)	0.014(4)	0.003(4)
C68	0.037(5)	0.035(4)	0.032(5)	0.004(3)	0.020(4)	0.008(4)
N69	0.035(4)	0.028(3)	0.036(4)	0.014(3)	0.018(3)	0.014(3)
C70	0.039(5)	0.033(4)	0.027(5)	0.011(3)	0.015(4)	0.002(4)
C71	0.040(5)	0.034(4)	0.039(5)	0.012(4)	0.019(4)	0.003(4)
C72	0.034(5)	0.040(5)	0.047(6)	0.007(4)	0.009(4)	0.000(4)
C73	0.035(5)	0.038(4)	0.042(6)	0.014(4)	0.017(4)	0.005(4)
C74	0.045(5)	0.030(4)	0.041(5)	0.013(4)	0.016(4)	0.010(4)
N75	0.029(3)	0.030(3)	0.030(4)	0.010(3)	0.013(3)	0.003(3)
Cl1	0.0342(11)	0.0452(11)	0.0386(11)	0.0144(9)	0.0147(9)	0.0035(10)
O80	0.100(6)	0.062(4)	0.046(5)	0.029(4)	0.028(4)	0.014(5)

	U_{11}	U_{22}	U_{33}	U_{23}	U_{13}	U_{12}
O81	0.053(5)	0.073(5)	0.089(7)	0.025(5)	-0.003(4)	-0.022(4)
O82	0.076(5)	0.060(5)	0.096(7)	0.031(4)	0.055(5)	0.031(4)
O83	0.057(4)	0.050(4)	0.058(5)	0.011(3)	0.033(4)	-0.002(3)
Cl2	0.0351(11)	0.0419(11)	0.0534(15)	0.0018(10)	0.0192(10)	0.0023(10)
O84	0.034(4)	0.064(4)	0.055(5)	0.002(3)	0.015(3)	0.010(3)
O85	0.053(4)	0.055(4)	0.062(5)	0.004(3)	0.028(4)	0.001(4)
O86	0.044(4)	0.056(4)	0.047(4)	0.006(3)	0.020(3)	-0.009(3)
O87	0.034(4)	0.045(4)	0.080(6)	-0.004(3)	0.016(3)	0.002(3)
Cl3	0.0490(11)	0.0350(10)	0.0386(11)	0.0123(9)	0.0236(10)	0.0075(10)
O88	0.048(4)	0.104(7)	0.070(6)	0.043(5)	0.029(4)	0.006(4)
O89	0.047(4)	0.035(3)	0.052(4)	0.021(3)	0.028(3)	0.006(3)
O90	0.092(6)	0.043(4)	0.044(4)	0.010(3)	0.033(4)	0.014(4)
O91	0.100(6)	0.039(3)	0.062(5)	0.021(3)	0.058(4)	0.020(4)
Cl4	0.0353(11)	0.0393(10)	0.0388(11)	0.0136(9)	0.0189(9)	0.0026(9)
O92	0.056(4)	0.045(4)	0.049(4)	-0.003(3)	0.028(3)	-0.003(3)
O93	0.037(3)	0.049(4)	0.045(4)	0.005(3)	0.013(3)	-0.002(3)
O94	0.046(4)	0.043(3)	0.050(4)	0.016(3)	0.021(3)	0.016(3)
O95	0.052(4)	0.053(4)	0.080(6)	0.040(4)	0.034(4)	0.011(3)
O96	0.042(4)	0.048(4)	0.039(4)	0.006(3)	0.014(3)	0.007(3)
O97	0.050(4)	0.053(4)	0.043(4)	0.010(3)	0.021(3)	0.006(3)
O98	0.050(4)	0.050(4)	0.053(5)	0.020(3)	0.023(3)	0.013(3)
O99	0.062(5)	0.051(4)	0.068(5)	0.021(4)	0.038(4)	0.011(4)

Table S8. Hydrogen atomic coordinates and isotropic atomic displacement parameters (Å^2) for c09291.

	x/a	y/b	z/c	U(eq)
H1A	0.306(12)	0.758(3)	-0.042(9)	0.12(6)
H1B	0.241(2)	0.832(5)	-0.034(5)	0.02(2)
H3	0.1661	0.7246	0.0179	0.044
H4	0.0363	0.6353	0.0394	0.042
H5	0.0584	0.6301	0.1825	0.053
H6	0.2052	0.7177	0.3041	0.048
H10	0.3116	0.7687	0.4283	0.052
H11	0.4249	0.8141	0.5786	0.057
H12	0.5894	0.9051	0.6246	0.055
H13	0.6427	0.9561	0.5211	0.055
H17A	0.6498	0.9212	0.3135	0.069
H17B	0.6563	0.9963	0.4023	0.069
H17C	0.5902	1.0064	0.3058	0.069
H19	0.1988	0.9582	0.1450	0.045
H20	0.1556	1.0994	0.1343	0.052
H21	0.2769	1.2096	0.1215	0.052
H22	0.4377	1.1738	0.1278	0.051
H25	0.5912	1.1263	0.1264	0.046
H26	0.7322	1.0533	0.1177	0.056
H27	0.7222	0.8974	0.1033	0.053
H31	0.6874	0.7415	0.0830	0.042
H32	0.6457	0.5840	0.0700	0.05
H33	0.4908	0.5338	0.0886	0.054
H34	0.3810	0.6359	0.1104	0.041

	x/a	y/b	z/c	U(eq)
H41A	0.739(6)	0.475(6)	0.407(8)	0.09(4)
H41B	0.842(6)	0.524(7)	0.499(3)	0.05(3)
H43	0.8324	0.5472	0.3077	0.04
H44	0.8585	0.5658	0.1834	0.042
H45	0.8855	0.7140	0.1677	0.045
H46	0.8825	0.8409	0.2798	0.041
H50	0.8850	0.9697	0.3462	0.041
H51	0.9001	1.1276	0.4162	0.047
H52	0.8834	1.1763	0.5513	0.048
H53	0.8586	1.0730	0.6304	0.045
H57A	0.7686	0.8338	0.6327	0.047
H57B	0.8006	0.9436	0.6635	0.047
H57C	0.8887	0.8815	0.6844	0.047
H59	0.6097	0.6383	0.2927	0.043
H60	0.4329	0.5861	0.2401	0.049
H61	0.3543	0.5722	0.3428	0.046
H62	0.4594	0.5995	0.4923	0.044
H65	0.5748	0.6255	0.6385	0.04
H66	0.7088	0.6401	0.7742	0.048
H67	0.8830	0.6666	0.7868	0.044
H71	1.0459	0.7084	0.7864	0.043
H72	1.2051	0.7194	0.7631	0.052
H73	1.2022	0.7038	0.6193	0.045
H74	1.0428	0.6855	0.5029	0.046
H96A	0.086(5)	0.185(4)	0.014(4)	0.02(2)
H96B	0.020(8)	0.271(5)	0.069(8)	0.08(4)

	x/a	y/b	z/c	U(eq)
H97A	0.7897(13)	0.376(6)	0.113(6)	0.03(2)
H97B	0.688(10)	0.380(10)	0.138(7)	0.12(6)
H98A	0.090(7)	0.911(4)	0.912(6)	0.04(3)
H98B	0.078(6)	0.843(6)	0.966(5)	0.05(3)
H99A	0.989(6)	0.407(11)	0.125(11)	0.13(7)
H99B	0.925(8)	0.458(6)	0.095(6)	0.06(3)

Theoretical calculations

Theoretical calculations were carried out by using Density Functional Theory (DFT) as implemented in Gaussian03, revision D.02.[9] Becke's three-parameter hybrid functional[10-13] with the LYP correlation functional[14] (B3LYP) was used with Los Alamos effective core potential LanL2DZ basis set. The transition state was located with the *Synchronous Transit-Guided Quasi-Newton* (STQN) Method, developed by H. B. Schlegel and coworkers.[15,16] The solvent was modeled by means of the Integral Equation Formalism Polarizable Continum Model (IEF-PCM),[17-20] as implemented in Gaussian03.

The geometries of $Ru^{IV}(tpy)(bpm)(\eta^2\text{-}O_2)^{2+}$ and $Ru^{IV}(tpy)(bpm)(O\text{-}O)^{2+}$ were fully optimized. Frequency calculations were performed on the optimized geometries to verify that they correspond to minima in the potential energy surface. The transition state for the reaction $Ru^{IV}(tpy)(bpm)(\eta^2\text{-}O_2)^{2+} \rightarrow Ru^{IV}(tpy)(bpm)(O\text{-}O)^{2+}$ was found using the QST3 option of the STQN method, as implemented in Gaussian03. The initial structure for the transition state was the geometry with the highest energy from a relaxed coordinate scan of the Ru-O distance from the equilibrium geometry for $Ru^{IV}(tpy)(bpm)(\eta^2\text{-}O_2)^{2+}$ to the

equilibrium geometry of $Ru^{IV}(tpy)(bpm)(O\text{-}O)^{2+}$. A frequency calculation returned one negative frequency and animation of the corresponding vibration shows that it corresponds to the coordinate that interconvert $Ru^{IV}(tpy)(bpm)(\eta^2\text{-}O_2)^{2+}$ and $Ru^{IV}(tpy)(bpm)(O\text{-}O)^{2+}$. Single-point calculations were carried out on the optimized geometries with the solvent (water) modeled by means of IEF-PCM. Pictures of the structures with significant distances and angles, total and relatives energies and Cartesian coordinates are shown below.

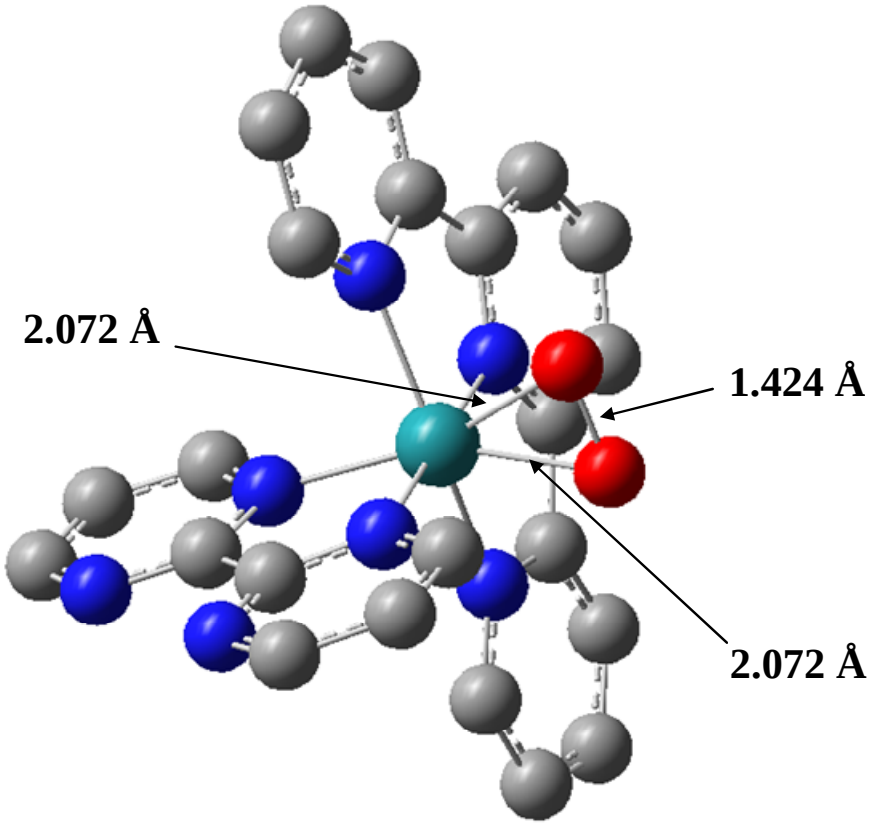

Figure S28. Optimized structure for $Ru(tpy)(bpm)(\eta^2\text{-}O_2)^{2+}$; <(O1RuO2) = 40.2 º.

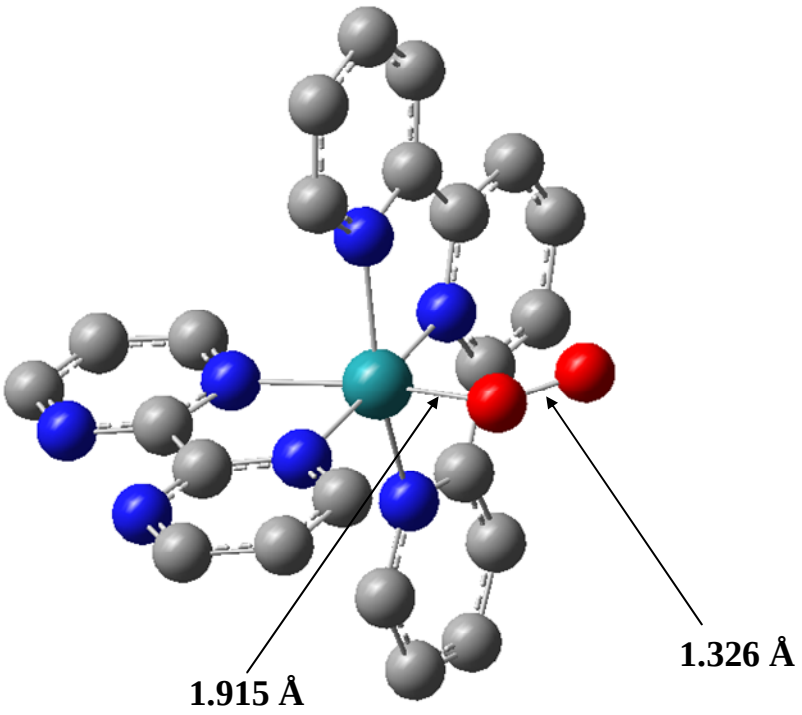

Figure S29. Optimized structure for Ru(tpy)(bpm)(O-O)$^{2+}$; <(RuO1O2) = 126.1 º.

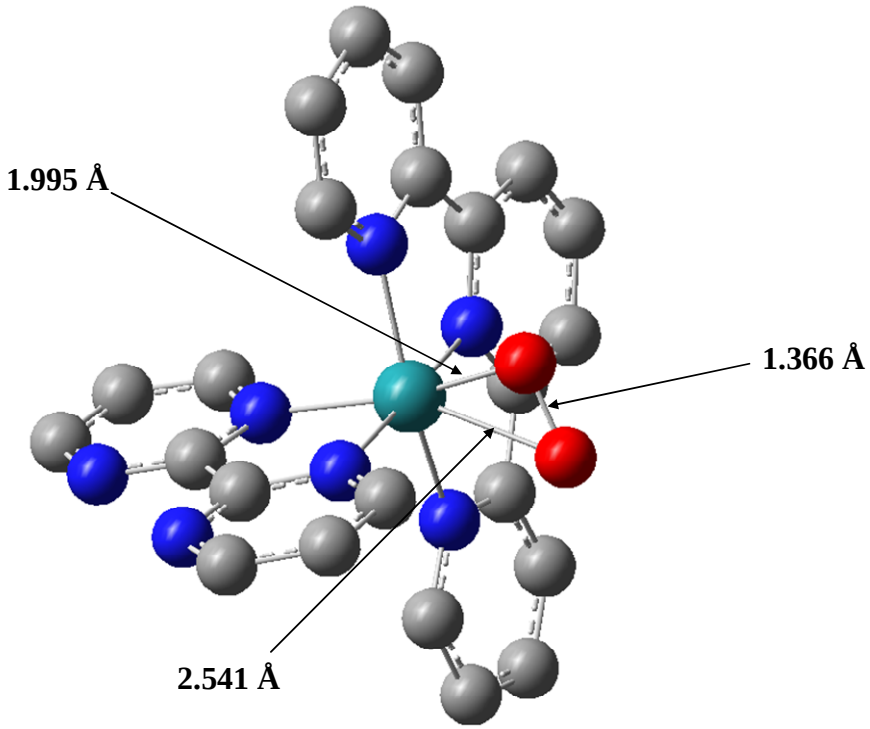

Figure S30. Optimized structure for the transition state for the reaction Ru^{IV}(tpy)(bpm)(η^2-O_2)$^{2+}$ → Ru^{IV}(tpy)(bpm)(O-O)$^{2+}$; <(RuO1O2) = 96.4 º.

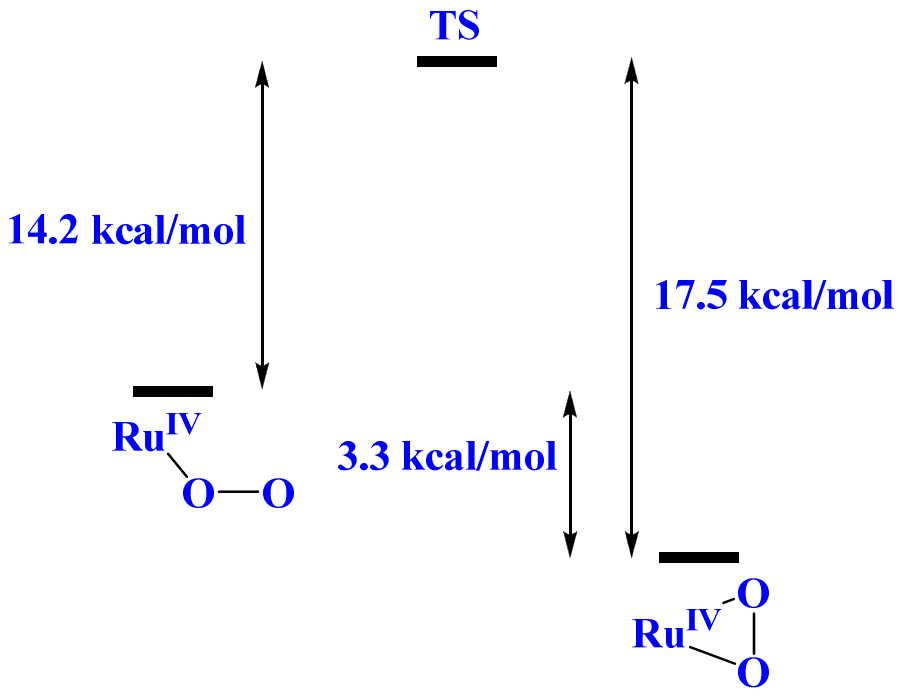

Figure S31. Relative energies and activation barriers for the interconversion between $Ru^{IV}(tpy)(bpm)(\eta^2\text{-}O_2)^{2+}$ and $Ru^{IV}(tpy)(bpm)(O\text{-}O)^{2+}$.

Table S9. Cartesian coordinates for $Ru^{IV}(tpy)(bpm)(\eta^2\text{-}O_2)^{2+}$.

Element	X	Y	Z
N	-0.93274	-0.000089	1.474086
Ru	-0.01779	0.000043	-0.44244
N	0.350576	2.072931	-0.26093
N	0.351226	-2.07258	-0.26067
N	-2.07308	-0.00023	-0.9408
N	1.931216	0.00043	0.082781
C	4.63941	0.000888	0.575348
C	2.569962	1.199537	0.19406
C	2.57034	-1.19846	0.194224
C	3.952836	-1.22227	0.448981
C	3.952448	1.223814	0.448808

H	4.49229	-2.15808	0.537524
H	4.491609	2.159808	0.537229
H	5.708099	0.00107	0.764726
C	1.187242	-4.74397	-0.10958
C	1.679778	-2.36742	0.005532
C	-0.53953	-3.08236	-0.43969
C	-0.15881	-4.43049	-0.37228
C	2.110806	-3.70055	0.082272
H	-1.56413	-2.80035	-0.65066
H	-0.89924	-5.2075	-0.52787
H	3.151053	-3.92992	0.284037
H	1.512678	-5.77815	-0.05657
C	1.185721	4.744602	-0.11012
C	1.679019	2.368223	0.005264
C	-0.5405	3.082396	-0.44008
C	-0.16022	4.430661	-0.37283
C	2.109621	3.701485	0.081866
H	-1.565	2.800027	-0.65102
H	-0.90089	5.20742	-0.52851
H	3.14979	3.931215	0.283632
H	1.510827	5.778886	-0.05721
C	-4.80879	-0.00054	-1.24699
C	-2.59708	-0.00025	-2.20056
C	-2.94693	-0.00038	0.122256
C	-3.98614	-0.00045	-2.39385
H	-4.4082	-0.00054	-3.3922
C	-2.44823	-0.00021	3.773868
C	-2.31119	-0.00033	1.465319
C	-0.30615	-4.8E-05	2.683559
C	-1.04089	-0.00018	3.876246
H	0.777667	0.000032	2.680685

H	-0.54433	-0.00025	4.839535
H	-3.08879	-0.00049	4.650281
H	-5.89193	-0.00077	-1.31641
H	-1.89129	-0.00016	-3.0242
O	0.398116	-0.00042	-2.31149
N	-3.07327	-0.0004	2.570236
N	-4.28405	-0.00055	0.004521
O	1.61401	-0.00246	-2.84101

Table S10. Cartesian coordinates for $Ru^{IV}(tpy)(bpm)(O\text{-}O)^{2+}$.

Element	X	Y	Z
N	-0.932737	-0.000089	1.474086
Ru	-0.017794	0.000043	-0.442444
N	0.350576	2.072931	-0.260927
N	0.351226	-2.072580	-0.260668
N	-2.073077	-0.000225	-0.940796
N	1.931216	0.000430	0.082781
C	4.639410	0.000888	0.575348
C	2.569962	1.199537	0.194060
C	2.570340	-1.198458	0.194224
C	3.952836	-1.222267	0.448981
C	3.952448	1.223814	0.448808
H	4.492290	-2.158079	0.537524
H	4.491609	2.159808	0.537229
H	5.708099	0.001070	0.764726
C	1.187242	-4.743974	-0.109578
C	1.679778	-2.367424	0.005532
C	-0.539527	-3.082359	-0.439686
C	-0.158810	-4.430488	-0.372280
C	2.110806	-3.700547	0.082272

H	-1.564125	-2.800351	-0.650656
H	-0.899235	-5.207502	-0.527872
H	3.151053	-3.929919	0.284037
H	1.512678	-5.778149	-0.056570
C	1.185721	4.744602	-0.110124
C	1.679019	2.368223	0.005264
C	-0.540499	3.082396	-0.440083
C	-0.160219	4.430661	-0.372827
C	2.109621	3.701485	0.081866
H	-1.565004	2.800027	-0.651020
H	-0.900892	5.207420	-0.528510
H	3.149790	3.931215	0.283632
H	1.510827	5.778886	-0.057209
C	-4.808788	-0.000536	-1.246987
C	-2.597083	-0.000253	-2.200555
C	-2.946925	-0.000379	0.122256
C	-3.986139	-0.000450	-2.393845
H	-4.408198	-0.000541	-3.392200
C	-2.448227	-0.000213	3.773868
C	-2.311186	-0.000326	1.465319
C	-0.306150	-0.000048	2.683559
C	-1.040887	-0.000181	3.876246
H	0.777667	0.000032	2.680685
H	-0.544331	-0.000250	4.839535
H	-3.088786	-0.000493	4.650281
H	-5.891931	-0.000769	-1.316408
H	-1.891294	-0.000156	-3.024203
O	0.398116	-0.000416	-2.311488
N	-3.073266	-0.000403	2.570236
N	-4.284046	-0.000548	0.004521
O	1.614010	-0.002455	-2.841005

Table S11. Cartesian coordinates for the transition state for the reaction $Ru^{IV}(tpy)(bpm)(\eta^2\text{-}O_2)^{2+} \rightarrow Ru^{IV}(tpy)(bpm)(O\text{-}O)^{2+}$.

Symbol	X	Y	Z
N	0.836803	0.004542	1.459393
Ru	-0.012432	-0.009470	-0.449332
N	-0.482920	-2.066824	-0.175360
N	-0.301283	2.072225	-0.270540
N	2.093452	-0.091602	-0.870820
N	-1.982126	0.071072	-0.016919
C	-4.716939	0.198283	0.301152
C	-2.682723	-1.097405	0.079129
C	-2.575533	1.300325	0.034771
C	-3.969815	1.386643	0.199388
C	-4.077369	-1.055835	0.243292
H	-4.470535	2.346904	0.240378
H	-4.660212	-1.966512	0.317658
H	-5.794463	0.248070	0.421554
C	-1.024159	4.778167	-0.201527
C	-1.628473	2.427528	-0.102479
C	0.644217	3.036685	-0.400022
C	0.320917	4.401301	-0.368091
C	-2.004696	3.779549	-0.066548
H	1.665246	2.706662	-0.547982
H	1.104591	5.142370	-0.481539
H	-3.045181	4.057195	0.059082
H	-1.305046	5.826395	-0.180959
C	-1.424111	-4.699748	-0.033676
C	-1.833994	-2.307365	-0.010825
C	0.383723	-3.107294	-0.257680
C	-0.050762	-4.439621	-0.191836
C	-2.322129	-3.620436	0.059389

H	1.430431	-2.865618	-0.396905
H	0.670834	-5.245432	-0.269922
H	-3.383276	-3.807991	0.179100
H	-1.790039	-5.720521	0.014970
C	4.849005	-0.174506	-1.024643
C	2.690914	-0.131312	-2.099762
C	2.914069	-0.092199	0.233818
C	4.088990	-0.172989	-2.212130
H	4.562344	-0.205104	-3.186658
C	2.204044	0.040373	3.847704
C	2.210682	-0.036054	1.536020
C	0.133958	0.072990	2.625495
C	0.793397	0.089679	3.860259
H	-0.946419	0.109316	2.554025
H	0.237184	0.139242	4.789069
H	2.788525	0.050064	4.762383
H	5.933793	-0.207360	-1.033308
H	2.044208	-0.143980	-2.968015
O	-0.317090	0.475339	-2.359978
N	2.900834	-0.019638	2.686776
N	4.254601	-0.133168	0.194214
O	-0.091634	-0.770820	-2.872115

REFERENCES

(1) Xu, X. J.; Xi, Z. X.; Chen, W. Z.; Wang, D. Q. *Journal of Coordination Chemistry* **2007**, *60*, 2297.

(2) Welch, T. W.; Ciftan, S. A.; White, P. S.; Thorp, H. H. *Inorganic Chemistry* **1997**, *36*, 4812.

(3) Grundemann, S.; Kovacevic, A.; Albrecht, M.; Faller, J. W.; Crabtree, R. H. *Journal of the American Chemical Society* **2002**, *124*, 10473.

(4) Will, G.; Boschloo, G.; Rao, S. N.; Fitzmaurice, D. *Journal of Physical Chemistry B* **1999**, *103*, 8067.

(5) Sullivan, B. P.; Calvert, J. M.; Meyer, T. J. *Inorganic Chemistry* **1980**, *19*, 1404.

(6) Takeuchi, K. J.; Thompson, M. S.; Pipes, D. W.; Meyer, T. J. *Inorganic Chemistry* **1984**, *23*, 1845.

(7) Adeyemi, S. A.; Dovletoglou, A.; Guadalupe, A. R.; Meyer, T. J. *Inorganic Chemistry* **1992**, *31*, 1375.

(8) Swavey, S.; Fang, Z. L.; Brewer, K. J. *Inorganic Chemistry* **2002**, *41*, 2598.

(9) Frisch, M. J.; Trucks, G. W.; Schlegel, H. B.; Scuseria, G. E.; Robb, M. A.; Cheeseman, J. R.; Montgomery, J., J. A.; Vreven, T.; Kudin, K. N.; Burant, J. C.; Millam, J. M.; Iyengar, S. S.; Tomasi, J.; Barone, V.; Mennucci, B.; Cossi, M.; Scalmani, G.; Rega, N.; Petersson, G. A.; Nakatsuji, H.; Hada, M.; Ehara, M.; Toyota, K.; Fukuda, R.; Hasegawa, J.; Ishida, M.; Nakajima, T.; Honda, Y.; Kitao, O.; Nakai, H.; Klene, M.; Li, X.; Knox, J. E.; Hratchian, H. P.; Cross, J. B.; Bakken, V.; Adamo, C.; Jaramillo, J.; Gomperts, R.; Stratmann, R. E.; Yazyev, O.; Austin, A. J.; Cammi, R.; Pomelli, C.; Ochterski, J. W.; Ayala, P. Y.; Morokuma, K.; Voth, G. A.; Salvador, P.; Dannenberg, J. J.; Zakrzewski, V. G.; Dapprich, S.; Daniels, A. D.; Strain, M. C.; Farkas, O.; Malick, D. K.; Rabuck, A. D.; Raghavachari, K.; Foresman, J. B.; Ortiz, J. V.; Cui, Q.; Baboul, A. G.; Clifford, S.; Cioslowski, J.; Stefanov, B. B.; Liu, G.; Liashenko, A.; Piskorz, P.; Komaromi, I.; Martin, R. L.; Fox, D. J.; Keith, T.; Al-Laham, M. A.; Peng, C. Y.; Nanayakkara, A.; Challacombe, M.; Gill, P. M. W.; Johnson, B.; Chen, W.; Wong, M. W.; Gonzalez, C.; Pople, J. A.; Gaussian, Inc.: Wallingford, CT, 2004.

(10) Becke, A. D. *Physical Review A* **1988**, *38*, 3098.

(11) Becke, A. D. *Journal of Chemical Physics* **1993**, *98*, 1372.

(12) Becke, A. D. *Journal of Chemical Physics* **1993**, *98*, 5648.

(13) Stephens, P. J.; Devlin, F. J.; Chabalowski, C. F.; Frisch, M. J. *Journal of Physical Chemistry* **1994**, *98*, 11623.

(14) Lee, C. T.; Yang, W. T.; Parr, R. G. *Physical Review B* **1988**, *37*, 785.

(15) Peng, C. Y.; Schlegel, H. B. *Israel Journal of Chemistry* **1993**, *33*, 449.

(16) Peng, C. Y.; Ayala, P. Y.; Schlegel, H. B.; Frisch, M. J. *Journal of Computational Chemistry* **1996**, *17*, 49.

(17) Cances, E.; Mennucci, B.; Tomasi, J. *Journal of Chemical Physics* **1997**, *107*, 3032.

(18) Mennucci, B.; Cances, E.; Tomasi, J. *Journal of Physical Chemistry B* **1997**, *101*, 10506.

(19) Cances, E.; Mennucci, B. *Journal of Mathematical Chemistry* **1998**, *23*, 309.

(20) Tomasi, J.; Mennucci, B.; Cammi, R. *Chemical Reviews* **2005**, *105*, 2999.

APPENDIX D

Diffusional and Surface-adsorbed Electron Transfer Mediators

Synthesis.

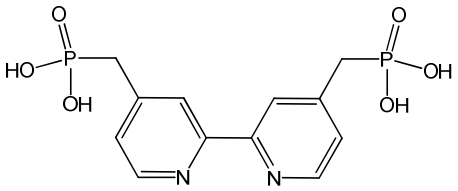

4,4'-$((HO)_2P(O)CH_2)_2$-bpy

4,4’-bis(diethoxyphosphorylmethyl)-2,2’-bipyridine was synthesized from 4,4’-dimethyl-2,2’-bipyridine by the scheme below:

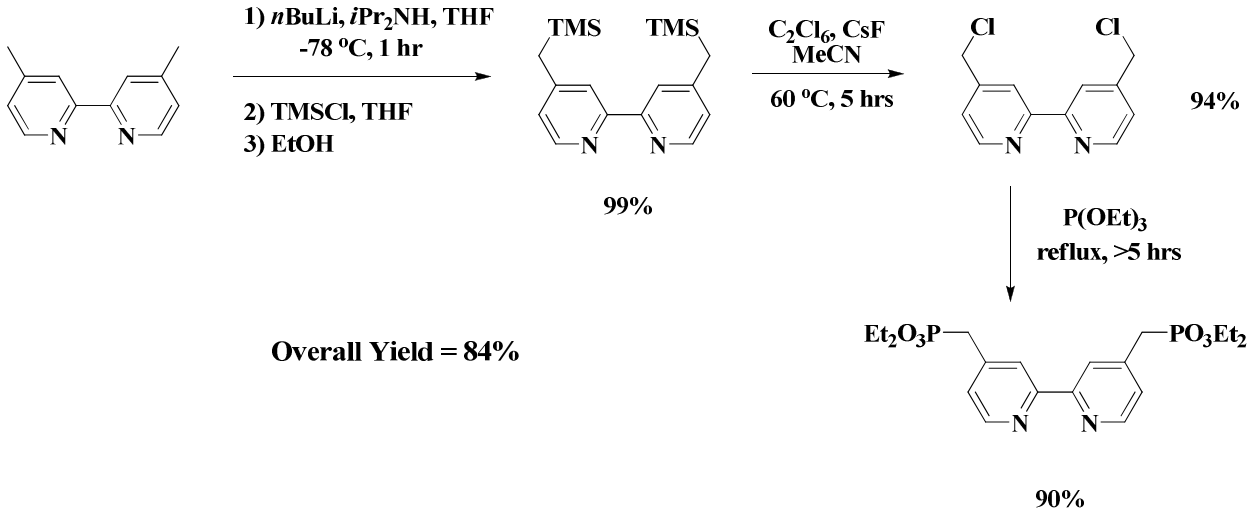

4,4’-bis[(trimethylsilyl)methyl]-2,2’-bipyridine and 4,4’-bis(chloromethyl)-2,2’-bipyridine were synthesized as detailed in reference 1 with the following caveat. After collection of the product following silica gel chromatography, undissolved hexachloroethane remained. The orangish-brown solid was stirred in a flask with 2 M HCl for ~15 minutes, followed by filtration on a medium frit to remove hexachloroethane, rinsing with 2 M HCl (3 x 20 mL). The filtrate with added to a separatory funnel and the solution pH was increased to ~pH 9

with ammonium hydroxide which caused a voluminous white precipitate to form. The solid was extracted with ethyl acetate and dried over $MgSO_4$, resulting in pure product.

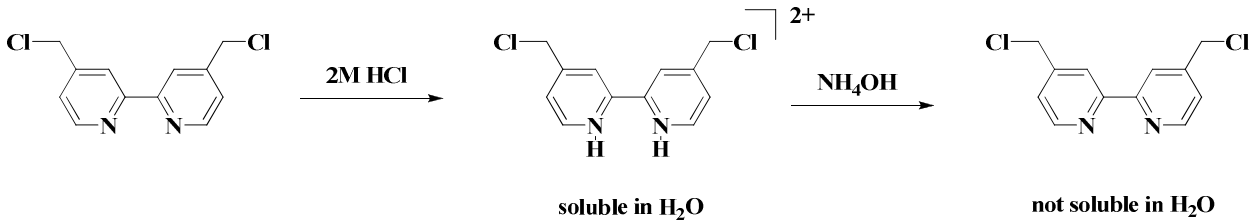

Synthesis of 4,4'-bis(diethoxyphosphorylmethyl)-2,2'-bipyridine. To a 250-mL three neck round bottom flask equipped with a stir bar and reflux condenser was added 6.0 g (23.7 mmol) 4,4'-bis(chloromethyl)-2,2'-bipyridine. The reaction flask was purged and evacuated (x3) under argon, then 40 mL (230 mmol) of triethylphosphite was added. The solution was heated at reflux overnight at 160 °C with stirring and cooled to room temperature. The reflux condenser was removed and the volatiles and excess triethylphosphite removed under reduced pressure utilizing an intermediate liquid nitrogen trap. The product was purified on a silica gel column with a 4:4:1 toluene:hexanes:triethylamine eluent to yield 7.47 g (21.3 mmol) product. The ^{1}H NMR was in agreement with reference 2.

Synthesis of $[Ru(4,4'-((HO)_2P(O)CH_2)_2bpy)_2(bpy)]Cl_2$. This salt was prepared by the procedure described in reference 3.

Electrode Preparation:

Pre-cut ITO (Delta Technologies, Ltd., 15 Ω/□) substrates were cleaned by sonication for 20 minutes in 2-propanol followed by sonication in Milli-Q purified water for 20 minutes (x 2). The slides were allowed to air dry.

Electrode Working Area. The working area of the electrode was defined by applying polyimide Kapton® tape with the electrode immersed to the level of the tape for electrochemical measurements.

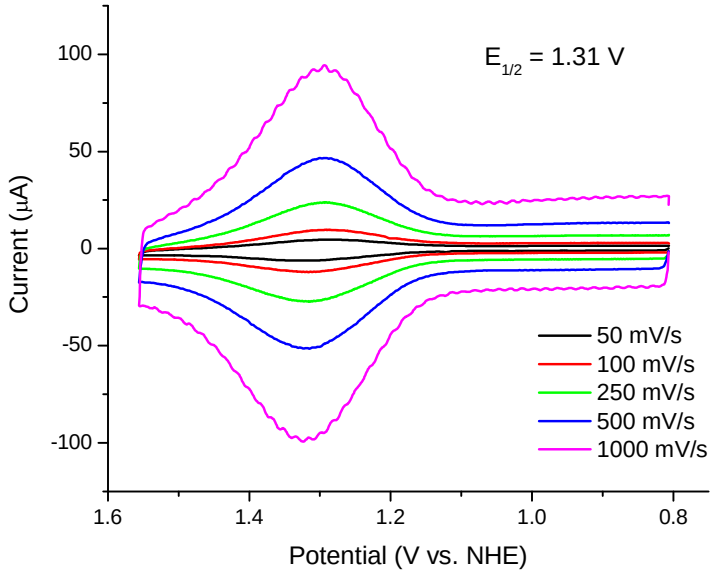

Figure S1: Cyclic voltammograms of surface-adsorbed $[Ru(4,4'\text{-}((HO_2)_2P(O)CH_2)_2bpy)_2(bpy)]^{2+}$ on ITO ($\Gamma \sim 1x10^{-10}$ mol/cm^2; 1.55 cm^2) in 0.1 M HOTf at 23 ± 2 ^oC.

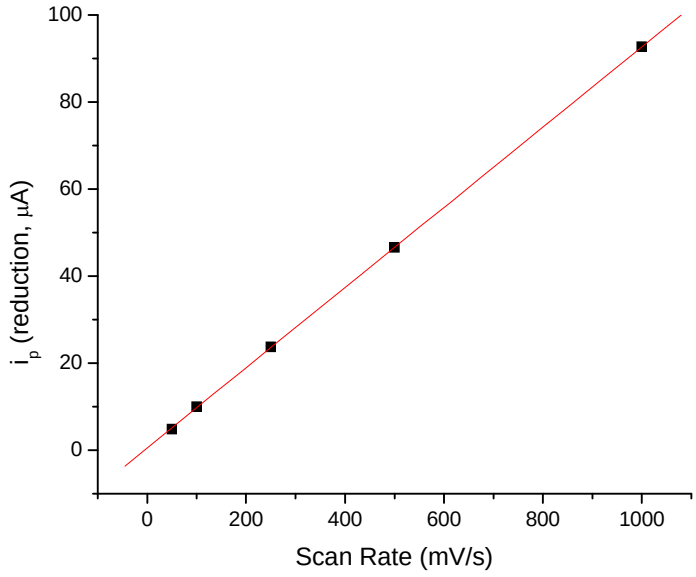

Figure S2: Scan rate dependence for surface-adsorbed $[Ru(4,4'\text{-}((HO_2)_2P(O)CH_2)_2bpy)_2(bpy)]^{2+}$ on ITO ($\Gamma \sim 1x10^{-10}$ mol/cm^2; 1.55 cm^2). i_p(reduction, μA) vs. Scan Rate (mV/s). The cyclic voltammograms are shown in Figure S1.

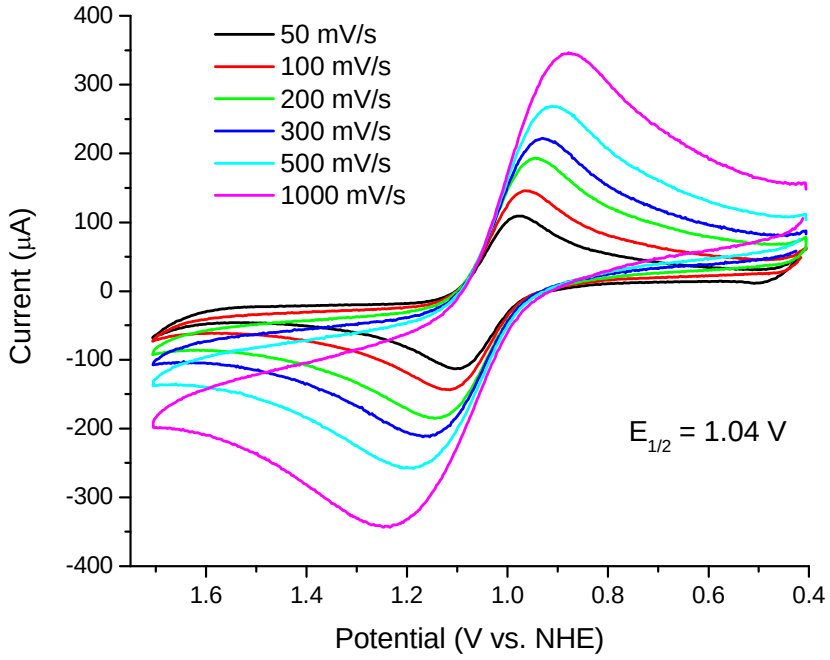

Figure S3. Scan rate dependent cyclic voltammograms of 1 mM Blue dimer in 0.1 M HNO_3 at an ITO electrode (1.6 cm^2).

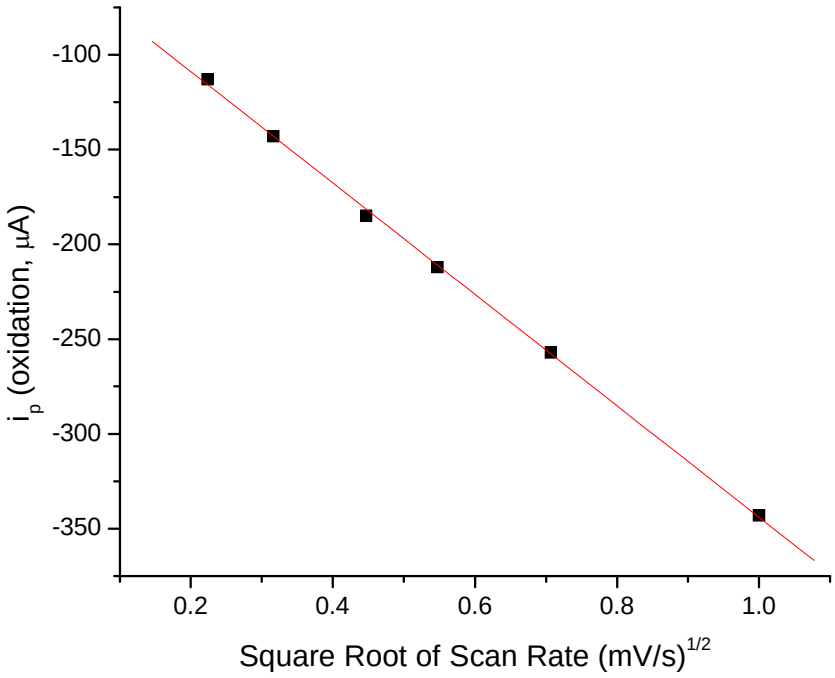

Figure S4. Scan rate dependence for 1 mM Blue dimer in 0.1 M HNO_3 at an ITO electrode (1.6 cm^2) illustrating the dependence of i_p(oxidation, μA) vs. square root of the scan rate, $(mV/s)^{1/2}$. The cyclic voltammograms are shown in Figure S3.

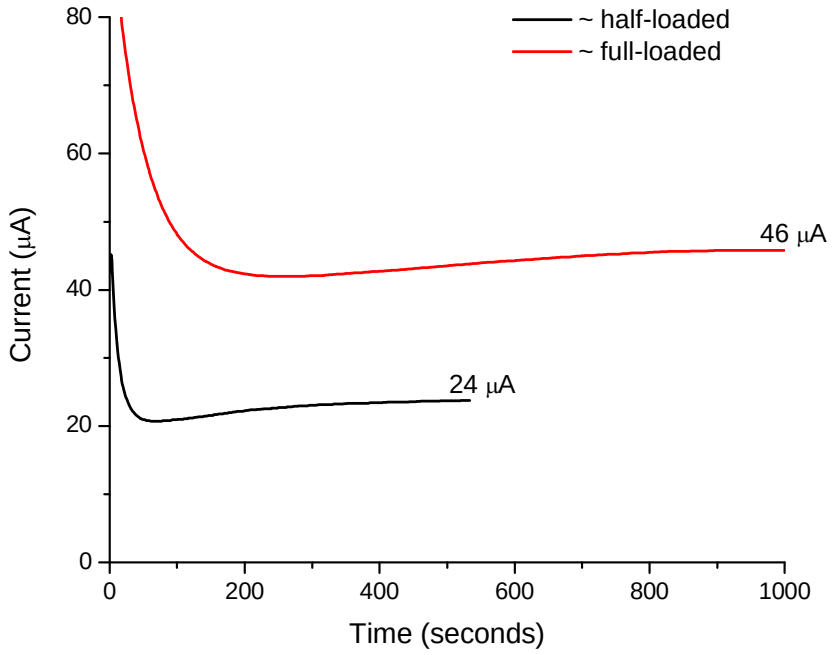

Figure S5: Controlled potential electrolysis of water oxidation for a still solution of 1.0 x 10^{-4} M $[(bpy)_2(H_2O)Ru^{III}ORu^{IV}(OH)(bpy)_2]^{4+}$ in 0.1 M HOTf at ITO-$[Ru(4,4'-((HO_2)_2P(O)CH_2)_2bpy)_2(bpy)]^{2+}$ electrodes of two different surface coverages (~ half-loaded: Γ = 4.8 x 10^{-11} mol/cm^2, 1.52 cm^2; and ~ full-loaded: Γ = 1.1 x10^{-10} mol/cm^2, 1.47 cm^2). The potential was held at 1.66 V versus NHE. This demonstrates the first order dependence of surface mediator in surface catalysis of blue dimer water oxidation.

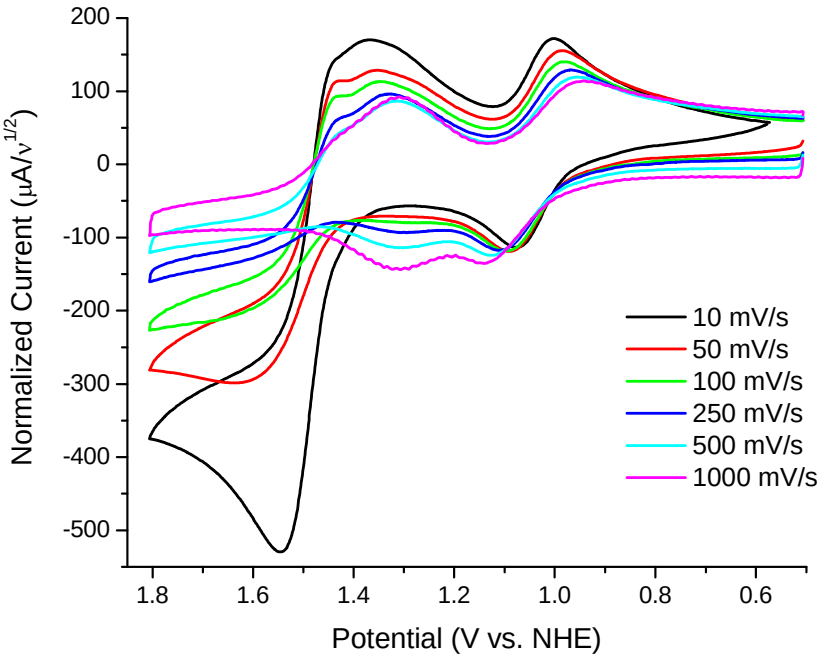

Figure S6: Scan rate normalized cyclic voltammograms of 2.5 x 10^{-4} M Blue dimer in 0.1 M HOTf at ITO-$[Ru(4,4'-((HO_2)_2P(O)CH_2)_2bpy)_2(bpy)]^{2+}$ (Γ ~ 1x10^{-10} mol/cm^2; 1.40 cm^2).

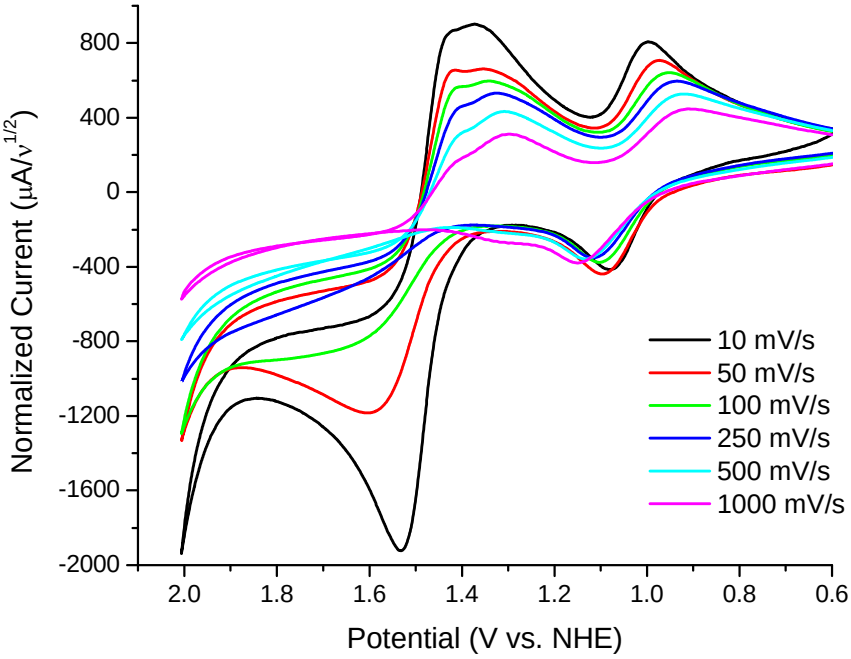

Figure S7: Scan rate normalized cyclic voltammograms of 1 mM Blue Dimer in 0.1 M HOTf at ITO-$[Ru(4,4'\text{-}((HO_2)_2P(O)CH_2)_2bpy)_2(bpy)]^{2+}$ on ITO ($\Gamma \sim 1x10^{-10}$ mol/cm^2; 1.43 cm^2).

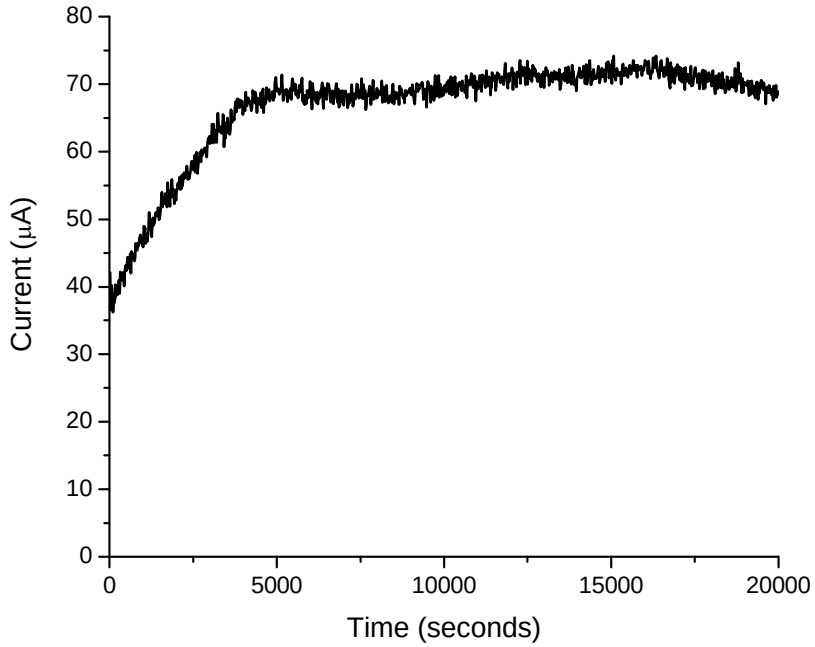

Figure S8: Controlled potential electrolysis (1.46 V vs NHE) of a stirred solution of 0.5 mM $[(bpy)_2(H_2O)Ru^{III}ORu^{IV}(OH)(bpy)_2]^{4+}$ in 0.1 M HOTf with 2.5 x 10^{-5} M $[Ru(4,4'\text{-}((HO_2)_2P(O)CH_2)_2bpy)_2(bpy)]^{2+}$ in the external solution at ITO-$[Ru(4,4'\text{-}((HO_2)_2P(O)CH_2)_2bpy)_2(bpy)]^{2+}$ ($\Gamma \sim 1x10^{-10}$ mol/cm^2; 1.55 cm^2). Note: this specific run was not used to measure evolved O_2.

Synthesis of Previous Standard for $[Ru(4,4'-((HO)_2P(O)CH_2)_2bpy)_2(bpy)]Cl_2$. The intermediate $[Ru(4,4'-((EtO)_2P(O)CH_2)_2bpy)_2Cl_2$ was prepared with minor modification according to a reported procedure.[4] After the reaction was finished, diethyl ether was added to precipitate the product which was subsequently isolated by vacuum filtration. In a 100-mL three neck round bottom flask containing 0.150 g (0.138 mmol) of $[Ru(4,4'-((EtO)_2P(O)CH_2)_2bpy)_2Cl_2$ and 0.033 g (0.207 mmol) of 2,2'-bipyridine was added 20 mL of 9:1 methanol: water. The reaction mixture was degassed with argon and shielded from light before being heated at reflux overnight. The reaction mixture was taken to dryness by rotary evaporation and 15 mL of 4 M HCl was added and the reaction mixture was heated for 3 days at 110 °C. The solvent was removed by rotary evaporation. The solid was dissolved in a minimum amount of water and chromatographed on LH-20 Sephadex eluting with pure water. The purity of each fraction was determined by UV-vis spectroscopy. Pure fractions were combined and taken to dryness yielding 0.126 g (90 %). Characterization of the complex was in agreement with reference [5].

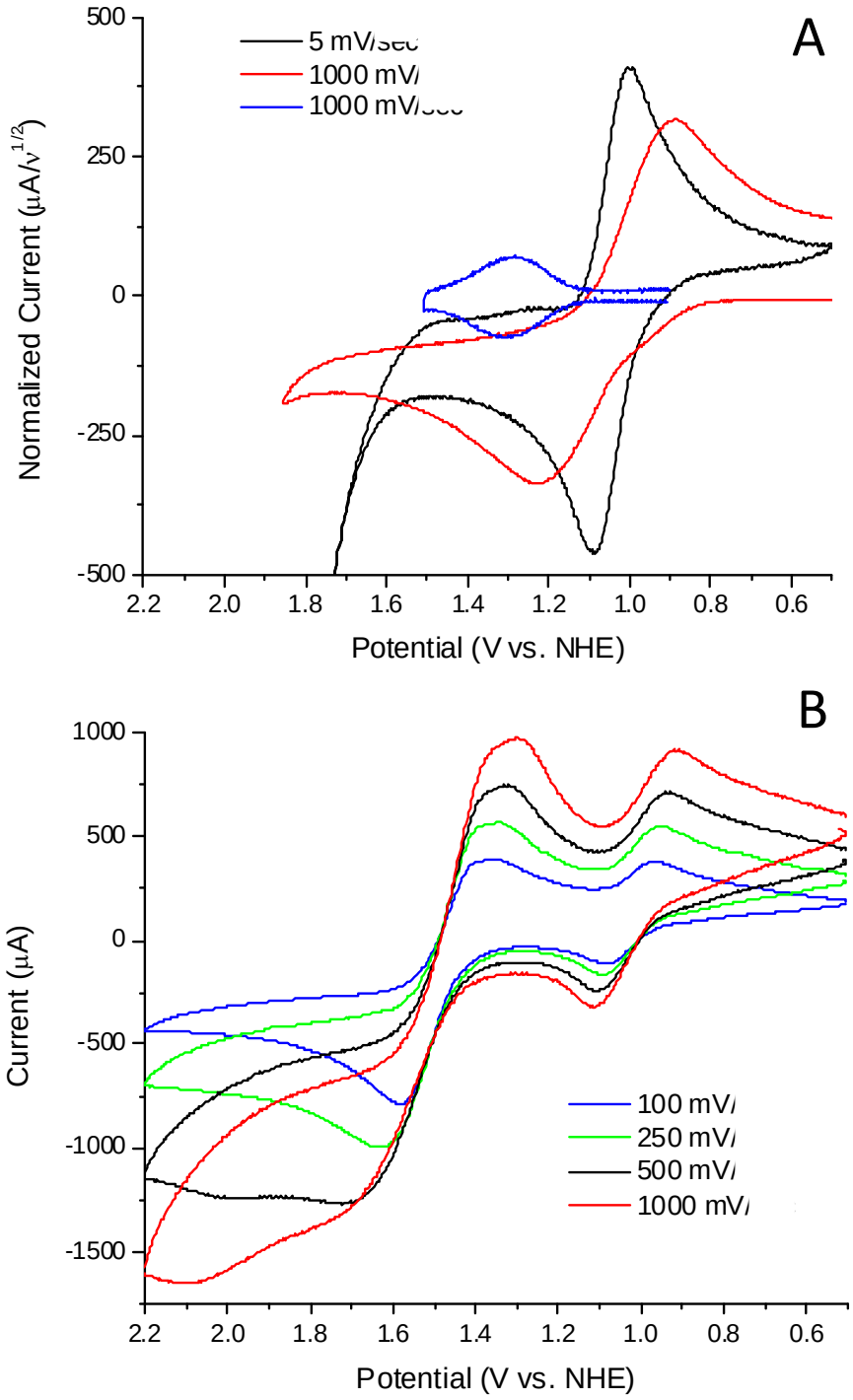

Figure S9: A). Cyclic voltammograms of 1 mM Blue dimer in 0.10 M HNO_3 at an ITO electrode (1.2 cm^2) at scan rates of 5 and 1000 mV/s. A CV of surface-adsorbed $[Ru(4,4'\text{-}((HO_2)_2P(O)CH_2)_2bpy)_2(bpy)]^{2+}$ on ITO, $\Gamma = 1.0 \times 10^{-10}$ mol/cm^2, 1.5 cm^2, is also shown; note the difference in current scales. B). 1 mM Blue dimer in 0.10 M HOTf (triflic acid) at an ITO electrode with surface adsorbed $[Ru(4,4'\text{-}((HO_2)_2P(O)CH_2)_2bpy)_2(bpy)]^{2+}$, ITO-$Ru^{2+}$, $\Gamma \sim 1 \times 10^{-10}$ mol/cm^2; 1.6 cm^2.

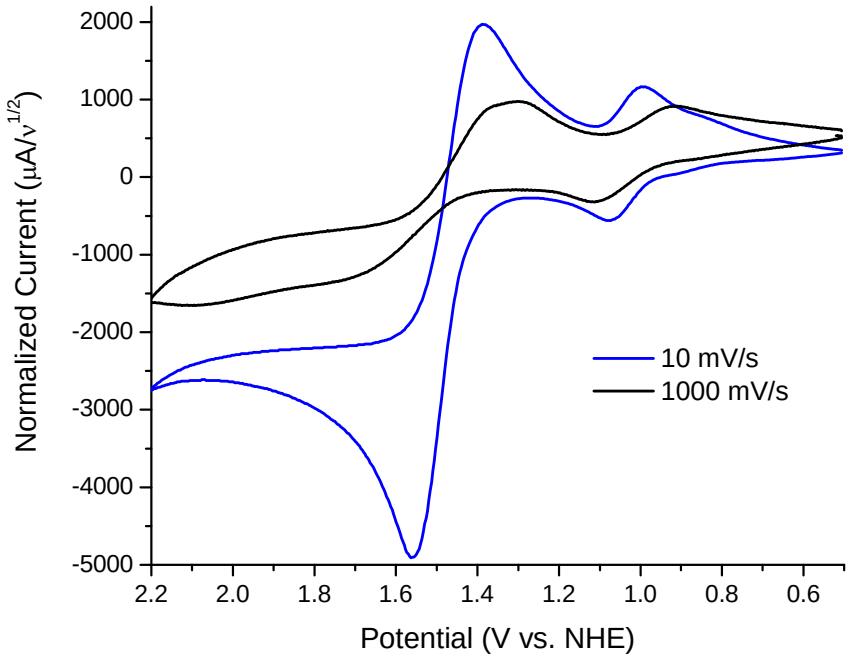

Figure S10: Cyclic voltammograms of 1 mM Blue dimer in 0.10 M HOTf (triflic acid) at an ITO electrode with surface adsorbed $[Ru(4,4'\text{-}((HO_2)_2P(O)CH_2)_2bpy)_2(bpy)]^{2+}$, ITO-$Ru^{2+}$, $\Gamma \sim 1 \times 10^{-10}$ mol/cm^2; 1.6 cm^2.

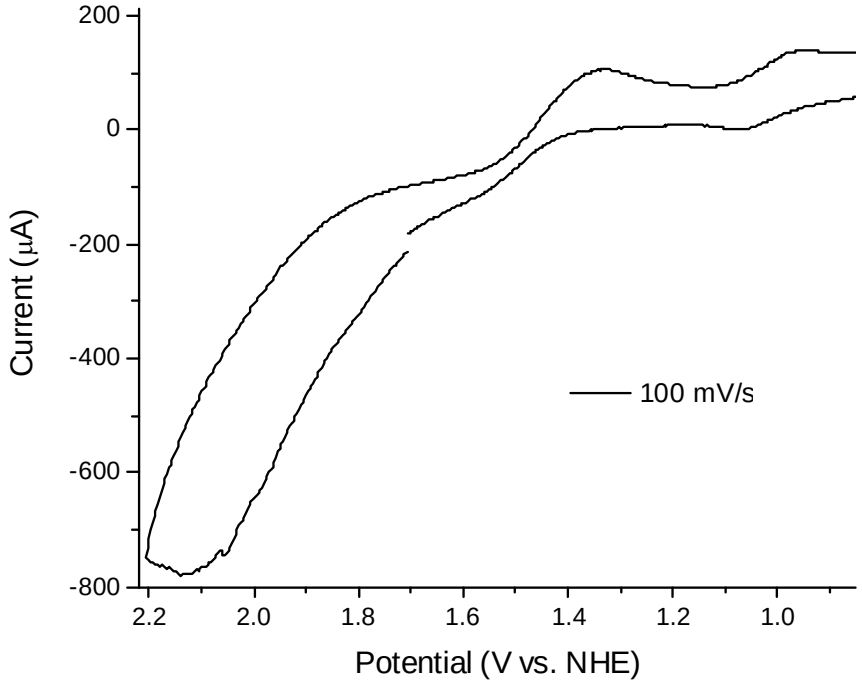

Figure S11. A CV of the peroxido intermediate formed by addition of x3 Ce(IV) to $[(bpy)_2(H_2O)Ru^{III}ORu^{IV}(OH)(bpy)_2]^{4+}$ in 0.1 M HNO_3 with surface adsorbed $[Ru(4,4'\text{-}((HO_2)_2P(O)CH_2)_2bpy)_2(bpy)]^{2+}$ on ITO ($\Gamma \sim 1 \times 10^{-10}$ mol/cm^2; 1.5 cm^2).

REFERENCES

(1) Fraser, C. L.; Anastasi, N. R.; Lamba, J. J. S. *Journal of Organic Chemistry* **1997**, *62*, 9314.

(2) Yan, S. G.; Hupp, J. T. *Journal of Physical Chemistry* **1996**, *100*, 6867.

(3) Norris, M. R.; Glasson, C. R.; Concepcion, J. J.; Jurss, J. W.; Brennaman, M. K.; Hull, J. F.; Song, W.; Templeton, J. L.; Meyer, T. J. *Manuscript in preparation.*

(4) Will, G.; Boschloo, G.; Rao, S. N.; Fitzmaurice, D. *Journal of Physical Chemistry B* **1999**, *103*, 8067.

(5) Park, H.; Bae, E.; Lee, J. J.; Park, J.; Choi, W. *Journal of Physical Chemistry B* **2006**, *110*, 8740.

APPENDIX E

Electron Transfer Mediators-Chromophore/Catalyst Assemblies

Surface coverage. Surface coverages in mol/cm^2 of electroactive molecules on ITO or FTO were estimated from cyclic voltammograms. After correction for the background charging current for both the positive and negative scans, the areas under voltammetric waves were integrated and divided by the scan rate and electron charge. The moles oxidized and reduced were the same (~ 7 x 10^{-10} mol/cm^2 for **1-(PO_3H_2)** and ~ 3 x 10^{-10} mol/cm^2 for **2-(PO_3H_2)**), within the accuracy of the base-line correction, and were independent of scan rate from 50 to 250 mV/s. Electrode areas were between 1.95 and 2.0 cm^2 without correction for surface roughness.[1] The extent of surface loading on FTO|TiO_2 in mol/cm^2 was calculated from UV-visible measurements by using $\Gamma = A(\lambda) / (10^3 \times \varepsilon(\lambda))$, with $A(\lambda)$ and $\varepsilon(\lambda)$ the absorbance and molar absorptivities at λ.[2]

Synthesis of [$(bpy)_2Ru^{II}(bpm)Ru^{II}(LLL)(OH_2)](OTf)_4$ {LLL is tpy (1) or Mebimpy (2)}. A mixture of [$Ru^{II}(bpy)_2Cl_2]\times2H_2O$ (250 mg, 0.48 mmol) and [Ru^{II}(LLL)(bpm)Cl](Cl) (0.45 mmol) was refluxed in 1:1 EtOH:H_2O (30 mL) for 24 hours. The ethanol and the water were removed on a rotary evaporator to give crude [$(bpy)_2Ru^{II}(bpm)Ru^{II}$(LLL)Cl]$Cl_3$. Triflic acid (2.0 mL) was added and the mixture was stirred for 2 hours with evolution of HCl. Addition of an excess of diethyl ether resulted in precipitation of crude [$(bpy)_2Ru^{II}(bpm)Ru^{II}$(LLL)(OTf)]$(OTf)_3$ which was dissolved in 1:1 MeOH:H_2O. The methanol was removed in a rotary evaporator and the remaining solution was filtered and loaded on a Sephadex LH-20 column. Upon elution with water the dark green fraction was collected and the water removed under rotary evaporation. **1**: UV-Vis (pH = 1.0) λ_{max} = 281 (ε = 83,700 $M^{-1}cm^{-1}$), 413 (ε = 27,300 $M^{-1}cm^{-1}$) and 610 nm (ε = 8,800 $M^{-1}cm^{-1}$). ^{1}H-NMR (D_2O) δ 9.77 (d, 1H), 8.50-8.55 (dd, 4H), 8.37-8.45 (m, 5H), 8.23 (t, 1H), 8.18 (d, 1H), 7.92-8.12 (m, 8H), 7.80 (d, 1H), 7.76 (d, 1H), 7.71 (d, 1H), 7.56-7.60 (m, 3H), 7.49 (t, 1H), 7.43

(t, 1H), 7.38 (t, 1H), 7.28-7.33 (dd, 2H), 7.24 (t, 1H), 6.96 (t, 1H). High resolution MS (ESI, *m/z*): 543.5382 ([M + $CF_3SO_3^-$ + CH_3OH]$^{2+}$); 528.0289 ([M + $CF_3SO_3^-$]$^{2+}$); 469.0470 ([M + CH_3OH]$^{2+}$). **2**: This complex was precipitated after column chromatography by addition of saturated aqueous sodium perchlorate. UV-Vis (pH = 7.0) λ_{max} = 284 (ε = 73,600 $M^{-1}cm^{-1}$), 359 (ε = 36,900 $M^{-1}cm^{-1}$), 421 (ε = 26,100 $M^{-1}cm^{-1}$) and 629 nm (ε = 7,100 $M^{-1}cm^{-1}$). ^{1}H-NMR (D_2O) δ 10.23 (d, 1H), 8.60-8.63 (dd, 2H), 8.49-8.56 (m, 3H), 8.25-8.35 (m, 3H), 7.96-8.11 (m, 4H), 7.74-7.89 (m, 4H), 7.59-7.65 (dd, 2H), 7.31-7.51 (m, 6H), 7.10-7.23 (m, 3H), 6.85 (t, 1H), 6.63-6.68 (dd, 2H), 6.57 (d, 1H), 5.64 (d, 1H), 4.37 (s, 3H, CH_3), 4.33 (s, 3H, CH_3). High resolution MS (ESI, *m/z*): 531.5560 ([M' + OH_2 + CH_3OH]$^{2+}$); 563.4931 ([M'=O + ClO_4^-]$^{2+}$).

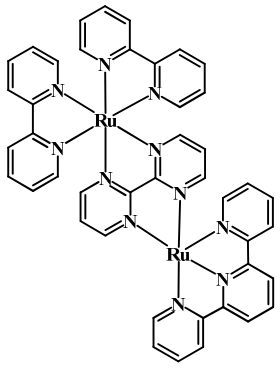

M for MS

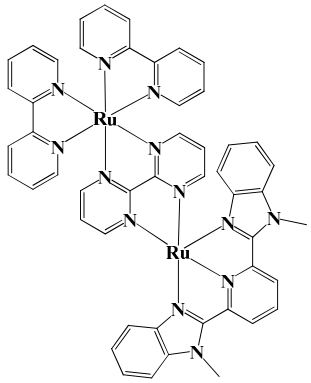

M' for MS

Synthesis of [((4,4'-$(HO)_2OPCH_2)_2$bpy)$_2$$Ru^{II}(bpm)Ru^{II}(LLL)(OH_2)$]$(OTf)_4$ {LLL is tpy (1-(PO_3H_2)) or Mebimpy (2-(PO_3H_2))}. A mixture of [Ru^{II}((4,4'-$(EtO)_2OPCH_2)_2$bpy)$_2$$Cl_2$] (520 mg, 0.48 mmol) and [Ru^{II}(LLL)(bpm)Cl](Cl) (0.45 mmol) were refluxed in 1:1 EtOH:H_2O (30 mL) for 24 hours. Ethanol and water were removed with a rotary evaporator to give crude [((4,4'-$(EtO)_2OPCH_2)_2$bpy)$_2$$Ru^{II}(bpm)Ru^{II}$(LLL)Cl]$Cl_3$. Hydrochloric acid (4.0 M , 30 mL) was added and the mixture refluxed for 48 hours to hydrolyze the ethyl esther groups. The hydrochloric acid was removed on a rotary evaporator to give crude [((4,4'-

$(HO)_2OPCH_2)_2bpy)_2Ru^{II}(bpm)Ru^{II}(LLL)Cl]Cl_3$. Triflic acid (2.0 mL) was added and the mixture was stirred for 2 hours with evolution of HCl. Addition of an excess of diethyl ether resulted in precipitation of crude [((4,4'-$(HO)_2OPCH_2)_2bpy)_2Ru^{II}(bpm)Ru^{II}(LLL)(OTf)](OTf)_3$ which was dissolved in 1:1 MeOH:H_2O. The methanol was removed in a rotary evaporator and the remaining solution was filtered and loaded on a Sephadex LH-20 column. Upon elution with water the dark green fraction was collected and the water removed under rotary evaporation. **1-(PO_3H_2)**: Anal. Found (Calc.) for $C_{49}H_{45}F_6N_{11}O_{19}P_4Ru_2S_2 \cdot 4H_2O$ ([(4-((HO)(O^-)$OPCH_2$)-4'-$((HO)_2OPCH_2)bpy)_2Ru^{II}(bpm)Ru^{II}(tpy)(OH_2)](OTf)_2 \cdot 4H_2O$) C, 35.28 (35.17); H, 3.20 (4.59); N, 9.24 (9.36). UV-Vis (pH = 1.0) λ_{max} = 285 (ε = 74,800 $M^{-1}cm^{-1}$), 314 (ε = 45,600 $M^{-1}cm^{-1}$), 360 (ε = 36,000 $M^{-1}cm^{-1}$), 423 (ε = 24,500 $M^{-1}cm^{-1}$) and 629 nm (ε = 6,300 $M^{-1}cm^{-1}$). ^{1}H-NMR (D_2O) δ 9.74-9.78 (nr, 1H), 7.15-8.55 (nr, 27H), 6.84-6.99 (nr, 1H), 3.00-3.28 (nr, 8H, $4CH_2$). ^{31}P-NMR (D_2O) δ 16.5 (s). **2-(PO_3H_2)**: Anal. Found (Calc.) for $C_{55}H_{51}F_6N_{13}O_{19}P_4Ru_2S_2 \cdot 5H_2O$ ([(4-((HO)(O^-)$OPCH_2$)-4'-$((HO)_2OPCH_2)bpy)_2Ru^{II}(bpm)Ru^{II}(Mebimpy)(OH_2)](OTf)_2 \cdot 5H_2O$) C, 36.86 (36.87); H, 3.43 (4.43); N, 10.16 (10.38).UV-Vis (pH = 1.0) λ_{max} = 285 (ε = 74,800 $M^{-1}cm^{-1}$), 314 (ε = 45,600 $M^{-1}cm^{-1}$), 360 (ε = 36,000 $M^{-1}cm^{-1}$), 423 (ε = 24,500 $M^{-1}cm^{-1}$) and 629 nm (ε = 6,300 $M^{-1}cm^{-1}$). ^{1}H-NMR (D_2O) δ 10.21-10.24 (nr, 1H), 8.60-8.63 (dd, 2H), 8.49-8.56 (m, 3H), 8.25-8.35 (m, 3H), 7.96-8.11 (m, 4H), 7.74-7.89 (m, 4H), 7.59-7.65 (dd, 2H), 7.31-7.51 (m, 6H), 7.10-7.23 (m, 3H), 6.85 (t, 1H), 6.63-6.68 (dd, 2H), 6.57 (d, 1H), 5.65 (d, 1H), 4.39 (s, 3H, CH_3), 4.36 (s, 3H, CH_3), 2.99-3.28 (nr, 8H, $4CH_2$). ^{31}P-NMR (D_2O) δ 16.5 (s).

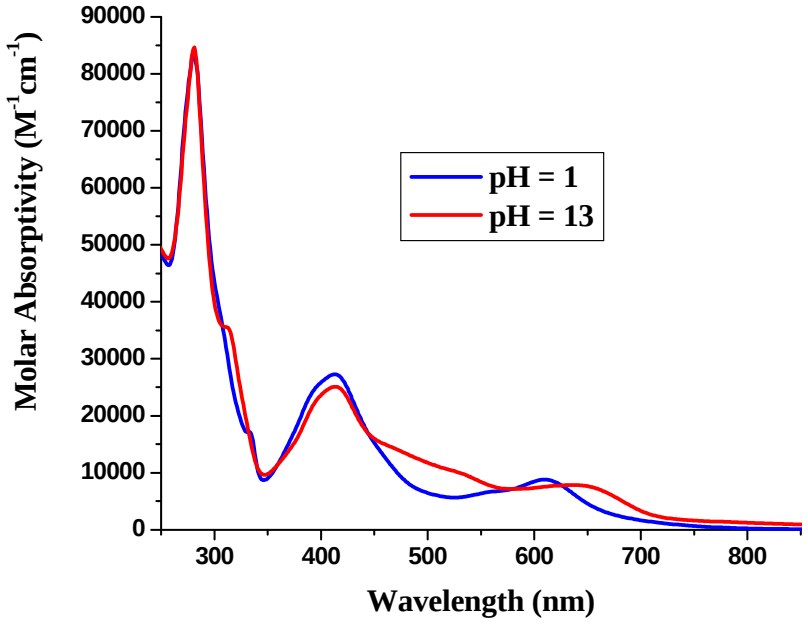

(A)

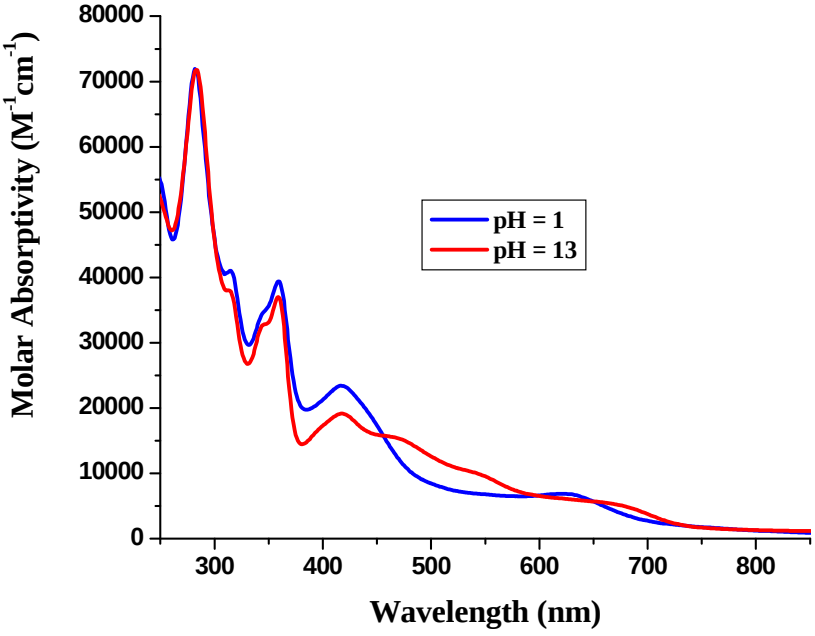

(B)

Figure S1. (A) Absorption spectra of **1** at pH = 1 and 13. (B) Absorption spectra of **2** at pH = 1 and 13.

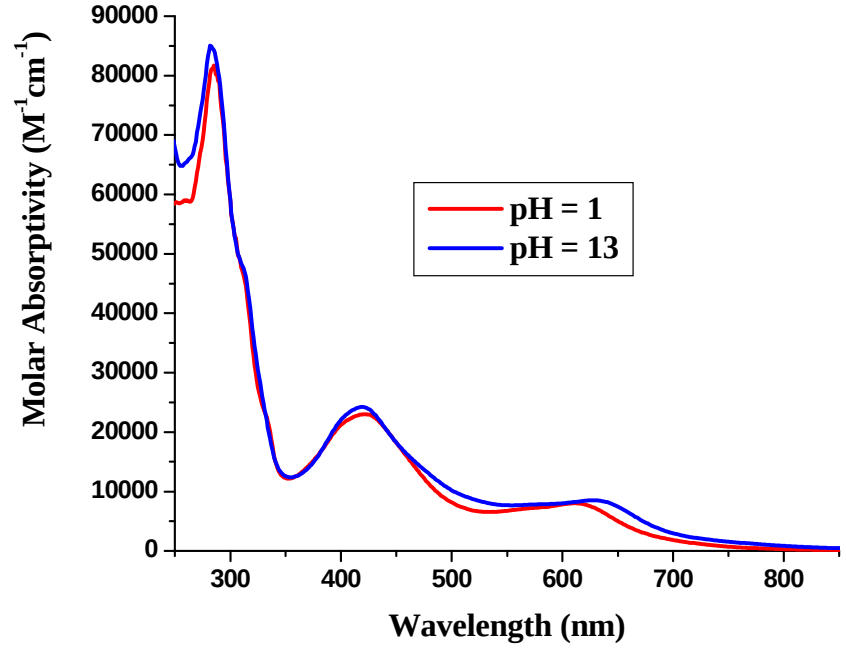

(A)

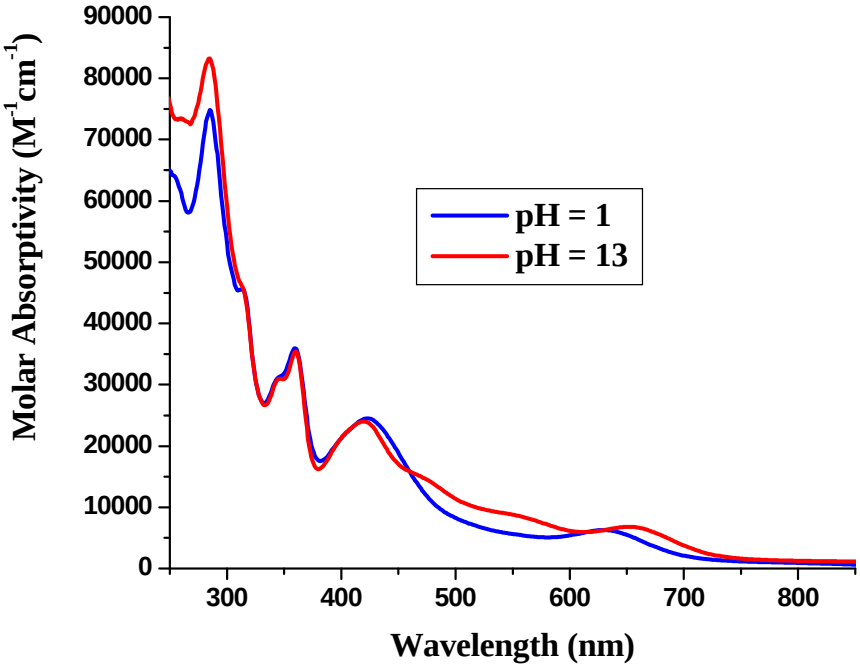

(B)

Figure S2. (A) Absorption spectra of **1-(PO_3H_2)** at pH = 1 and 13. (B) Absorption spectra of **2-(PO_3H_2)** at pH = 1 and 13.

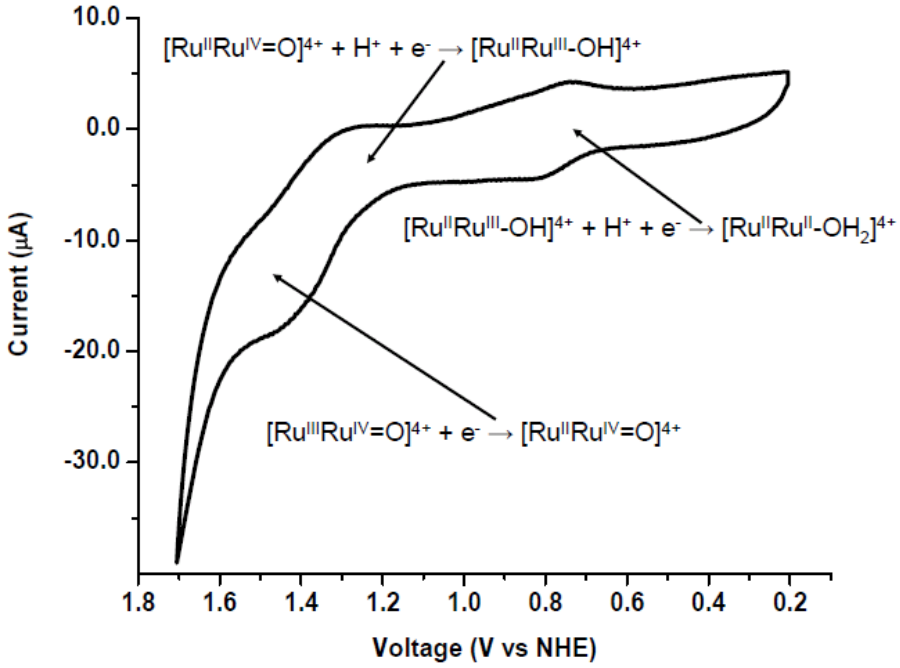

(A)

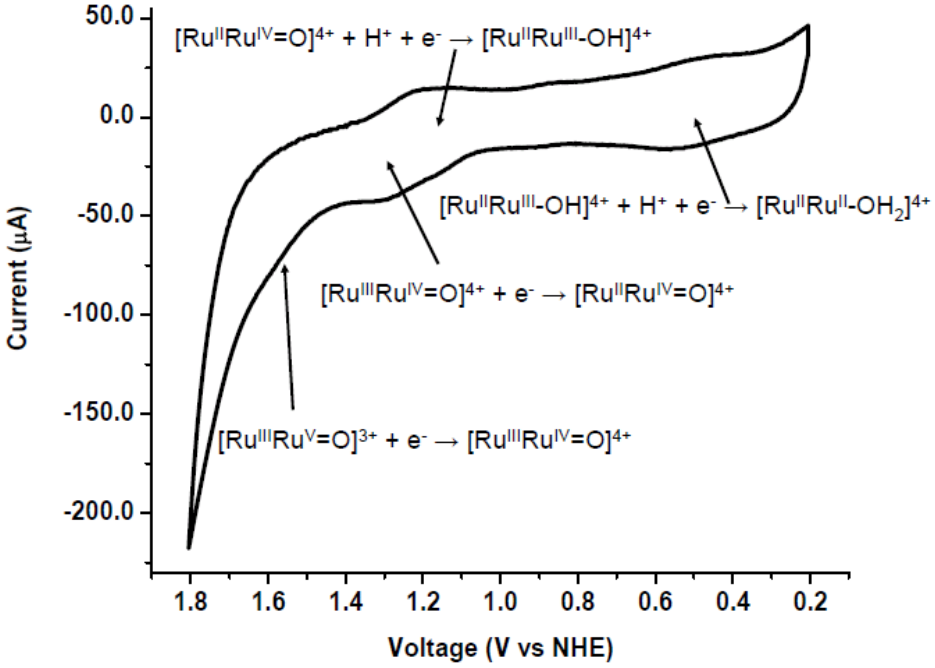

(B)

Figure S3. (A) Cyclic voltammogram for **1** at pH = 4.0 (1.0 mM, 100 mV/s, glassy carbon working electrode). (B) Cyclic voltammogram for **2** at pH = 4.0 (1.0 mM, 100 mV/s, glassy carbon working electrode).

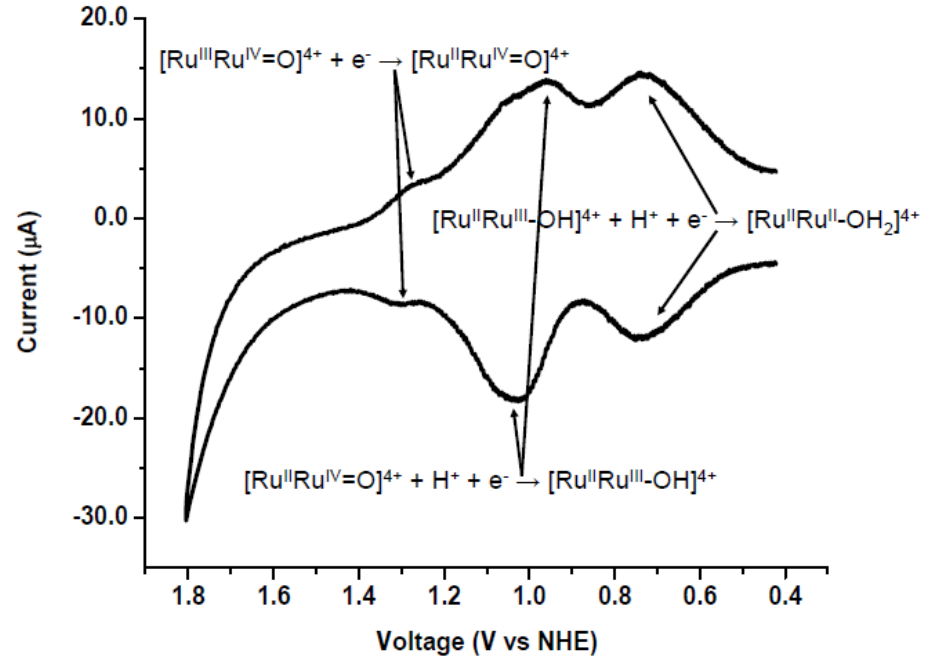

(A)

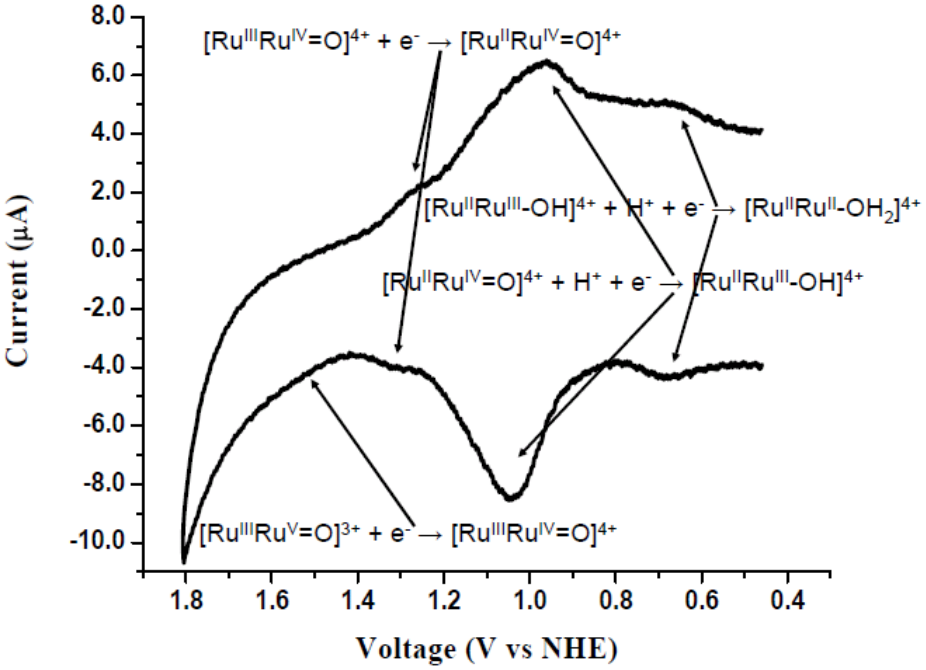

(B)

Figure S4. (A) Cyclic voltammogram for **1-(PO_3H_2)** anchored to ITO at pH = 4.0 (100 mV/s; $\Gamma \sim 7\times10^{-10}$ mol/cm^2; A = 1.95 cm^2). (B) Cyclic voltammogram for **2-(PO_3H_2)** anchored to ITO at pH = 4.0 (100 mV/s; $\Gamma \sim 3\times10^{-10}$ mol/cm^2; A = 1.95 cm^2).

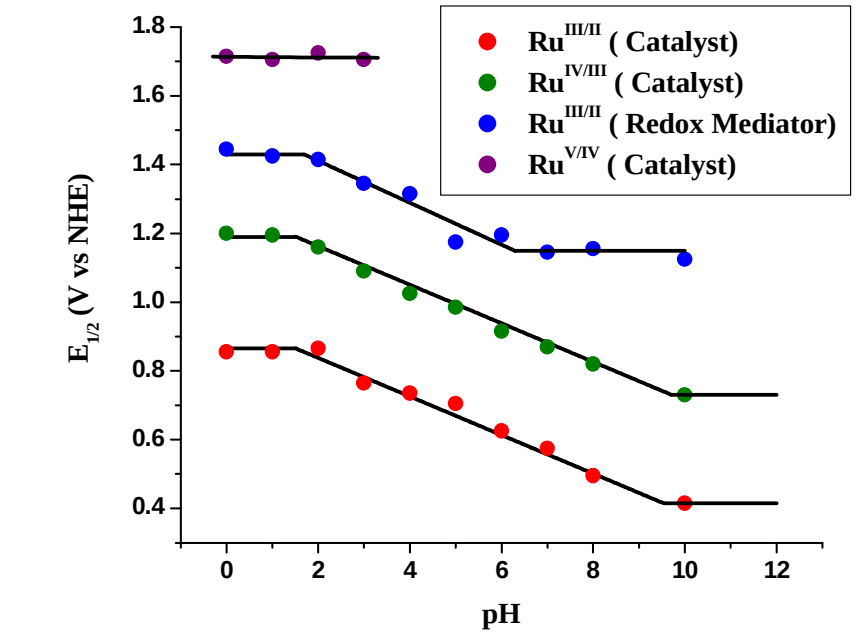

(A)

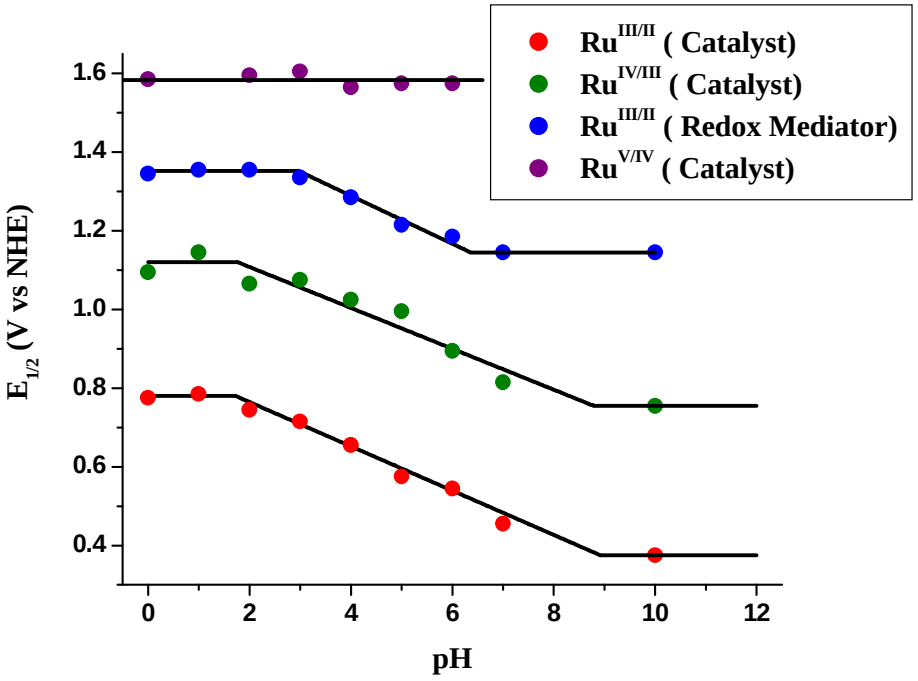

(B)

Figure S5. (A) Pourbaix diagram for **1-(PO_3H_2)** anchored to ITO ($\Gamma \sim 7\times10^{-10}$ mol/cm^2; A = 1.95 cm^2). (B) Pourbaix diagram for **2-(PO_3H_2)** anchored to ITO ($\Gamma \sim 3\times10^{-10}$ mol/cm^2; A = 1.95 cm^2).

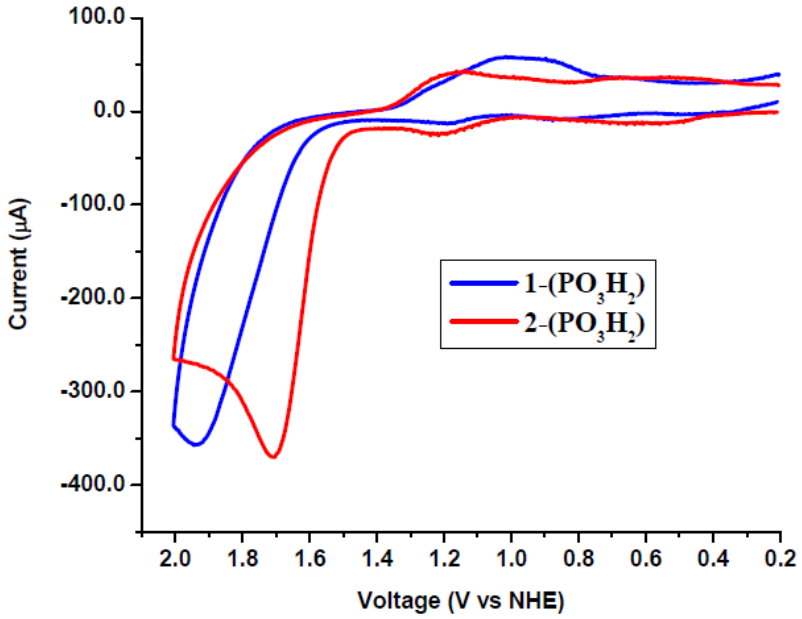

Figure S6. (A) Cyclic voltammogram for **1-(PO_3H_2)** anchored to ITO at pH = 1.0 showing the electrocatalytic wave for water oxidation (0.1 M HOTf, 50 mV/s; $\Gamma \sim 7\times10^{-10}$ mol/cm^2; A = 1.95 cm^2). (B) Cyclic voltammogram for **2-(PO_3H_2)** anchored to ITO at pH = 1.0 showing the electrocatalytic wave for water oxidation (0.1 M HOTf, 50 mV/s; $\Gamma \sim 3\times10^{-10}$ mol/cm^2; A = 1.95 cm^2).

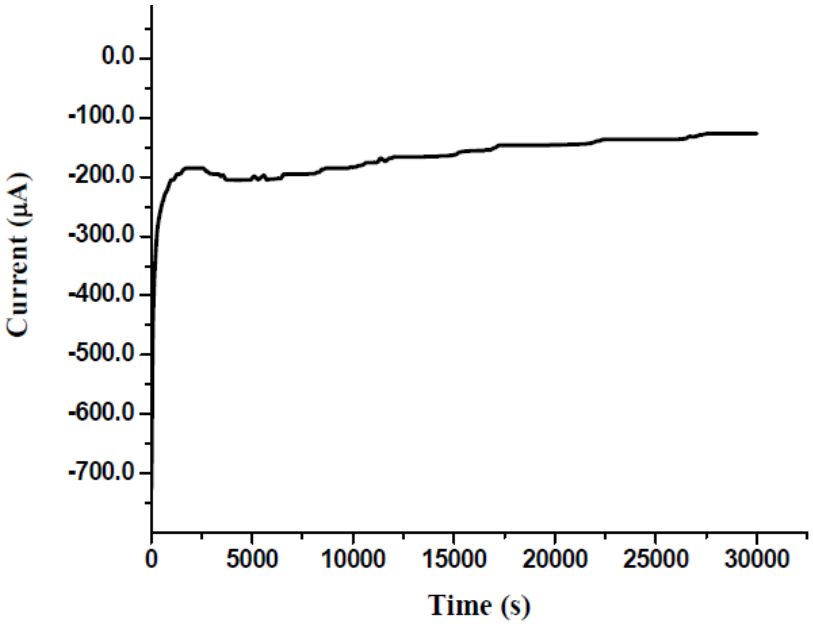

Figure S7. Electrolysis of **1-(PO_3H_2)** anchored to FTO|TiO_2 at 1.8 V in 0.1 M HNO_3. Number of turnovers: ~ 82; TOF = 2.7×10^{-3} s^{-1}; current density ~ 83 μA/cm^2; $\Gamma \sim 8.5\times10^{-8}$ mol/cm^2; A = 1.8 cm^2.

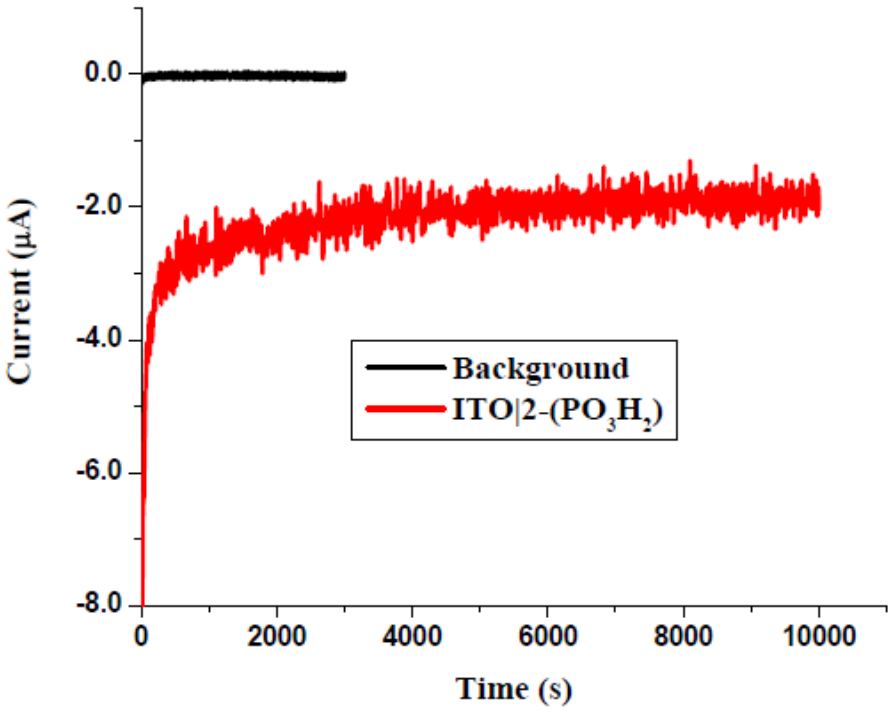

Figure S8. Electrolysis of **2-(PO_3H_2)** anchored to ITO at 1.50 V in 0.1 M $HClO_4$. Number of turnovers: ~ 70; TOF = 7×10^{-3} s^{-1}; current density ~ 1.5 μA/cm^2; Γ ~ 5.7×10^{-10} mol/cm^2; A = 1.3 cm^2.

REFERENCES

(1) Meyer, T. J.; Meyer, G. J.; Pfennig, B. W.; Schoonover, J. R.; Timpson, C. J.; Wall, J. F.; Kobusch, C.; Chen, X. H.; Peek, B. M.; Wall, C. G.; Ou, W.; Erickson, B. W.; Bignozzi, C. A. *Inorganic Chemistry* **1994**, *33*, 3952.

(2) Trammell, S. A.; Meyer, T. J. *Journal of Physical Chemistry B* **1999**, *103*, 104.

APPENDIX F

pH Dependence of Phosphonic Acid Derivatized $[Ru(bpy)_3]^{2+}$ and Electrostatic Synthesis of Redox Mediator-Chromophore/Catalyst Assemblies

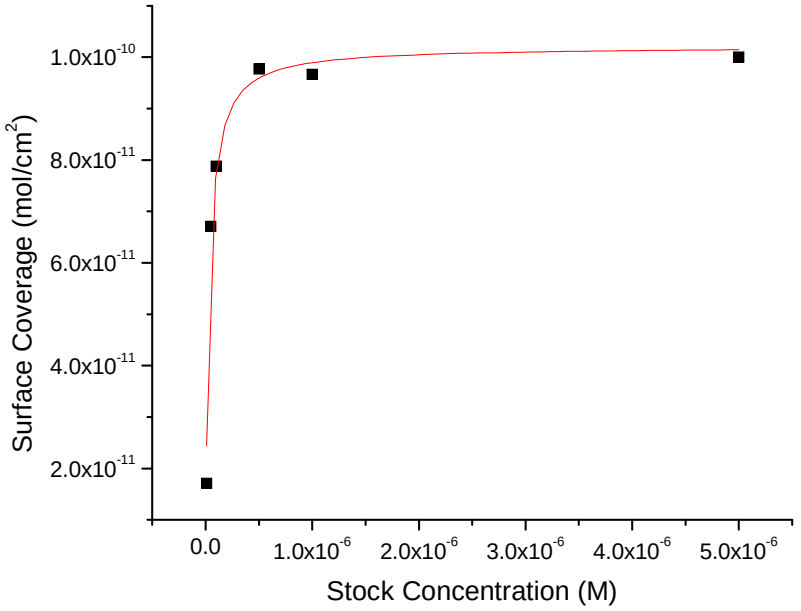

Figure S1. Isotherm (surface coverage (mol/cm^2) vs. concentration of stock solution (M)) of [Ru(bpy)$_2$(4,4'-(H_2O_3P)$_2$-bpy)]Cl_2 loaded from 0.1 M HNO_3. Surface coverages determined from CVs obtained in 0.1 M $HClO_4$.

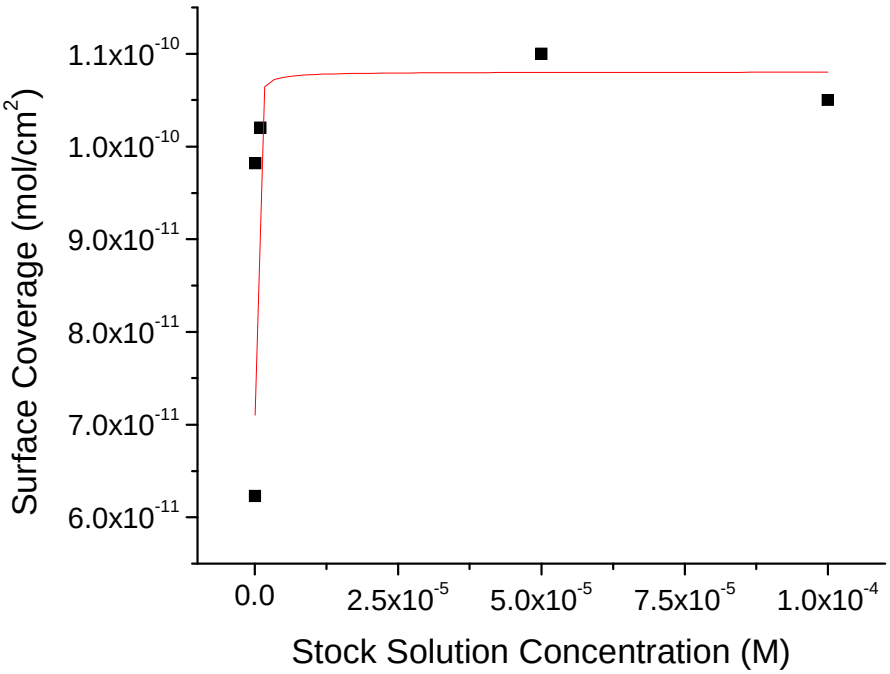

Figure S2. Isotherm (surface coverage (mol/cm^2) vs. concentration of stock solution (M)) of [Ru(bpy)$_2$(4,4'-($H_2O_3PCH_2$)$_2$-bpy)]Cl_2 loaded from 0.1 M HNO_3. Surface coverages determined from CVs obtained in 0.1 M $HClO_4$.

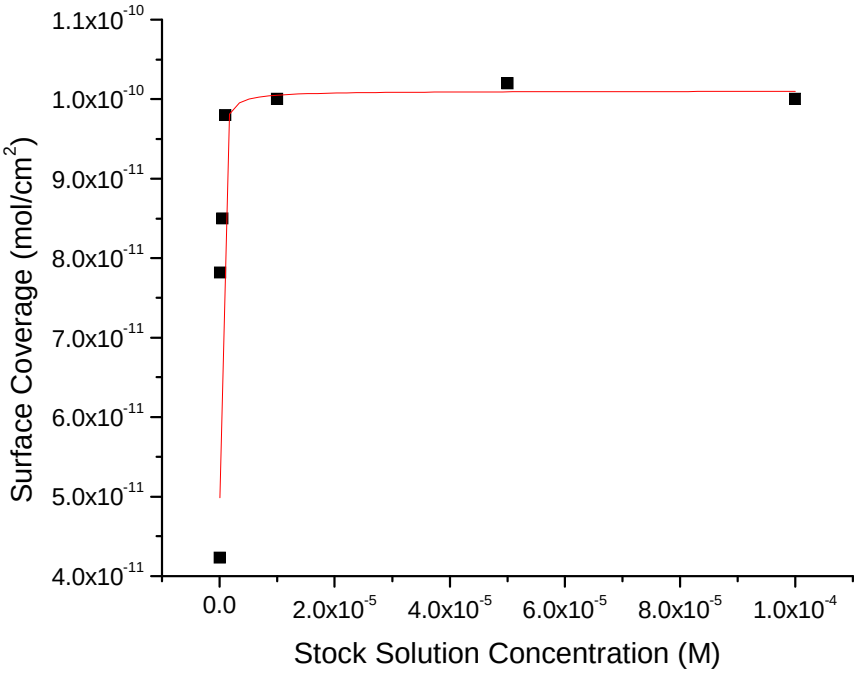

Figure S3. Isotherm (surface coverage (mol/cm^2) vs. concentration of stock solution (M)) of [Ru(bpy)$_2$(4,4'-($H_2O_3PCH_2$)$_2$-bpy)]Cl_2 loaded from 0.1 M HNO_3. Surface coverages determined from CVs obtained in 0.1 M $HClO_4$.

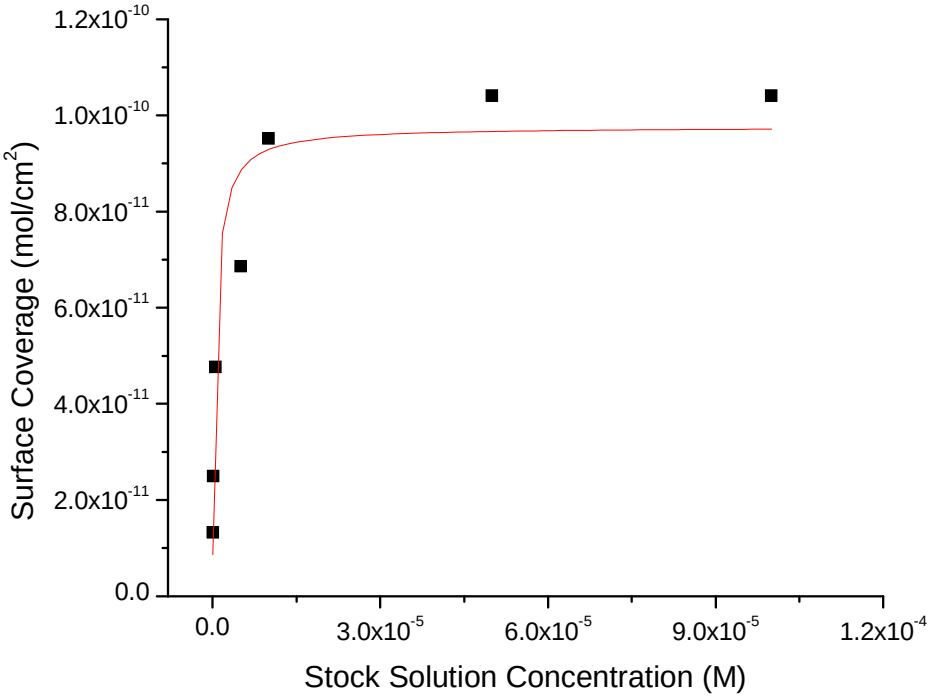

Figure S4. Isotherm (surface coverage (mol/cm^2) vs. concentration of stock solution (M)) of [Ru(4,4'-($H_2O_3PCH_2$)$_2$-bpy)$_3$]Cl_2 loaded from 0.1 M HNO_3. Surface coverages determined from CVs obtained in 0.1 M $HClO_4$.

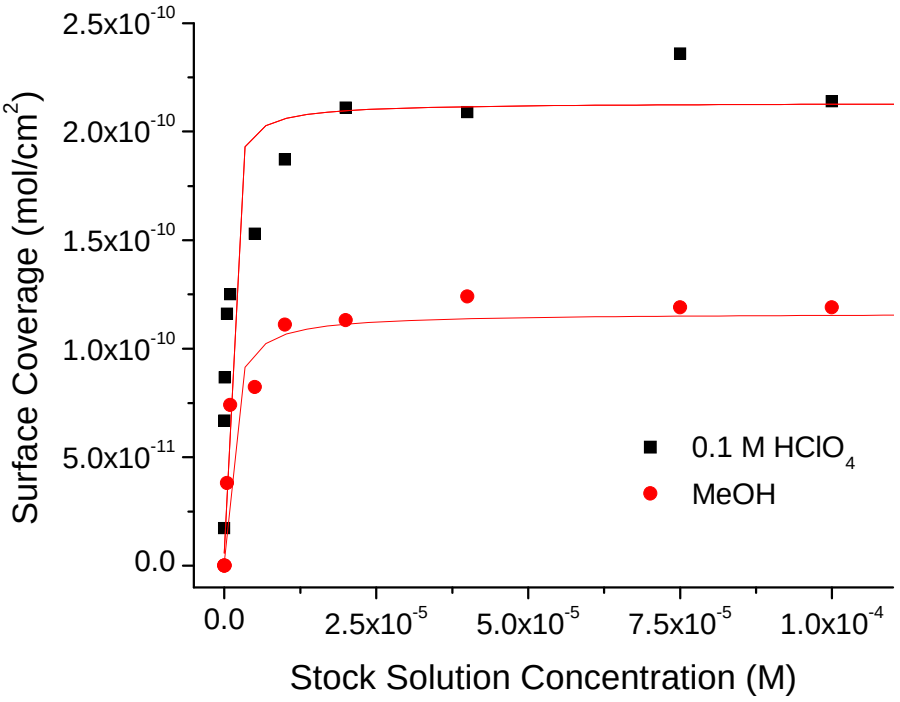

Figure S5: Surface coverage isotherm for surface-adsorbed $[Ru(4,4'\text{-}(H_2O_3PCH_2)_2\text{-}bpy)_2(bpy)]Cl_2$ on ITO, determined by cyclic voltammetry in 0.1 M HNO_3 at 23 ± 2°C.

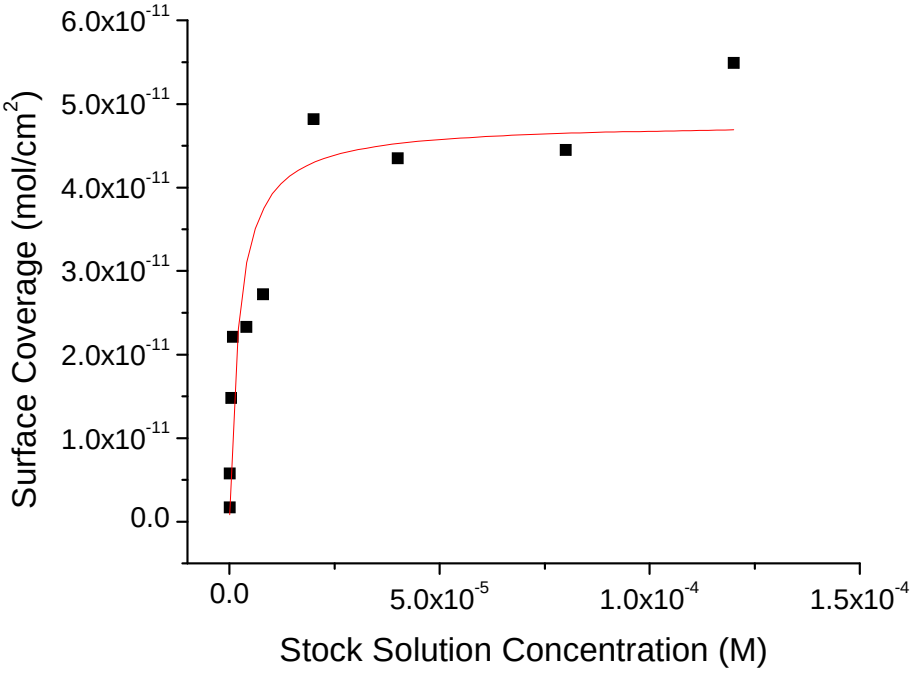

Figure S6. Isotherm (surface coverage (mol/cm^2) vs. concentration of stock solution (M)) of $[Ru(bpy)_2(4,4'\text{-}(H_2O_3PCH_2)_2\text{-}bpy)]Cl_2$ loaded from methanol. Surface coverages determined from CVs obtained in 0.1 M $HClO_4$.

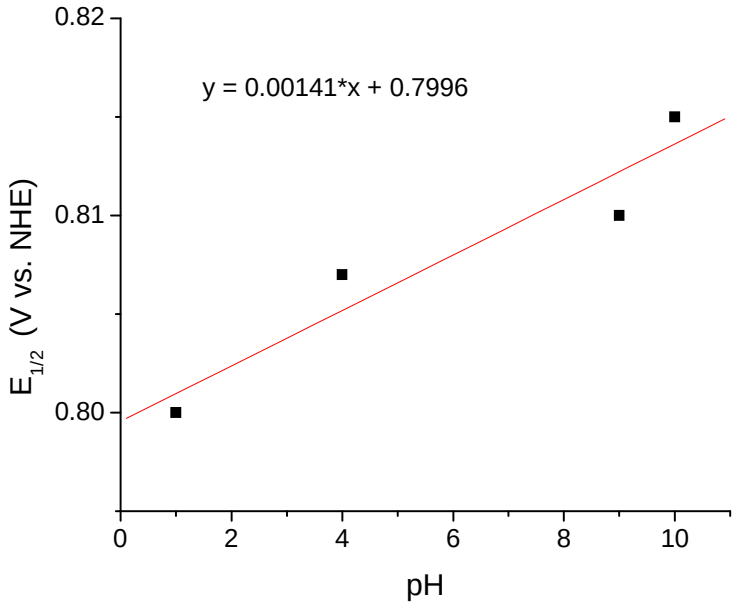

Figure S7. $E_{1/2}$ vs. pH diagram for 0.001 M $[Os(phen)_3]Cl_2$ (phen = 1,10-phenanthroline) at a bare ITO electrode with 1.0 M NaCl. (pH = 1 obtained with 0.1 M HNO_3, remaining pH data points were obtained from 0.1 M phosphate buffer.)

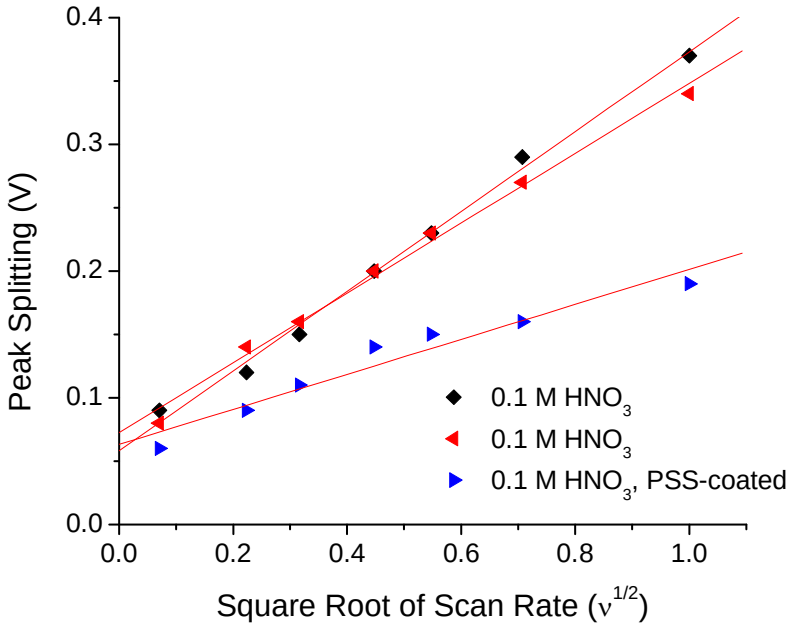

Figure S8. Peak splitting of oxidative and reductive waves associated with the $1e^-$ couple, $([(HO)Ru^{IV}ORu^{III}(OH_2)]^{4+}/[(H_2O)Ru^{III}ORu^{III}(OH_2)]^{4+})$ of the blue dimer, $[(bpy)2(H_2O)RuORu(OH_2)(bpy)_2](ClO_4)_4$, (0.001 M) at a bare ITO electrode and at an ITO electrode-coated with a monolayer of polystyrenesulfonate (PSS), cyclic voltammograms measured in 0.1 M HNO_3, electrode area ~1.5 cm^2, 23 ± 2 °C.

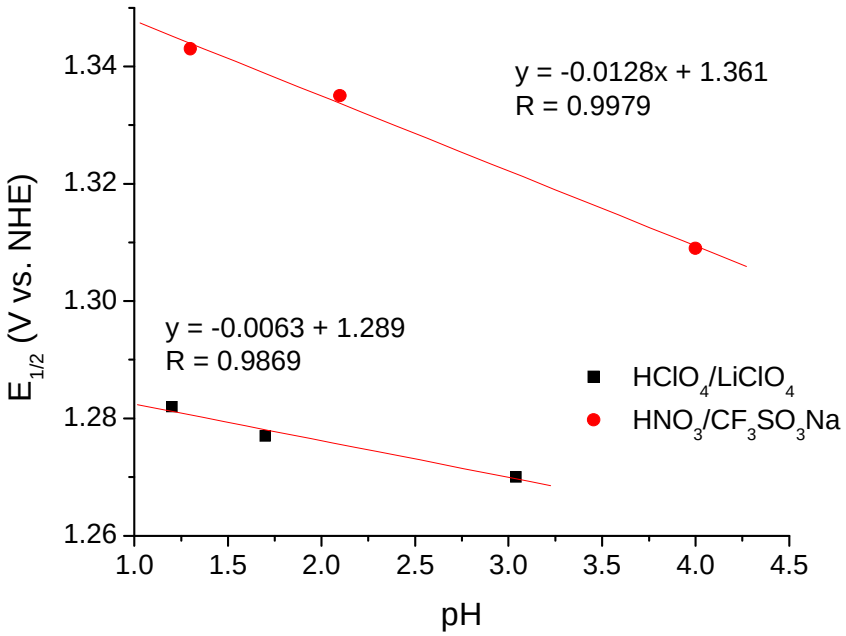

Figure S9. $E_{1/2}$-pH diagram of $[Ru(bpy)_2(4,4'\text{-}(H_2O_3P)_2\text{-}bpy)]^{2+}$ on ITO at 1.0 M constant ionic strength, 23 °C, Γ = 1.0 x 10^{-10} mol/cm^2. The data points in black were measured from cyclic voltammograms various pHs with 1.0 M $LiClO_4$ and $HClO_4$, while the points in red were measured in 1.0 M CF_3SO_3Na and HNO_3.

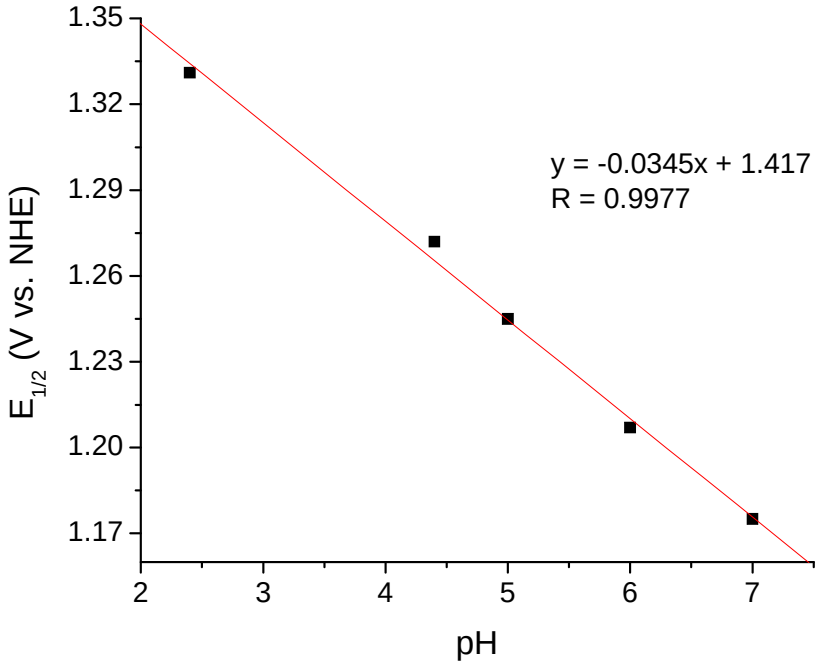

Figure S10. $E_{1/2}$-pH diagram of $[Ru(4,4'\text{-}(H_2O_3P)_2\text{-}bpy)_2(bpy)]^{2+}$ on ITO (Γ = 1.0 x 10^{-10} mol/cm^2) in 0.1 M phosphate buffer. Cyclic voltammograms measured at 23 °C.

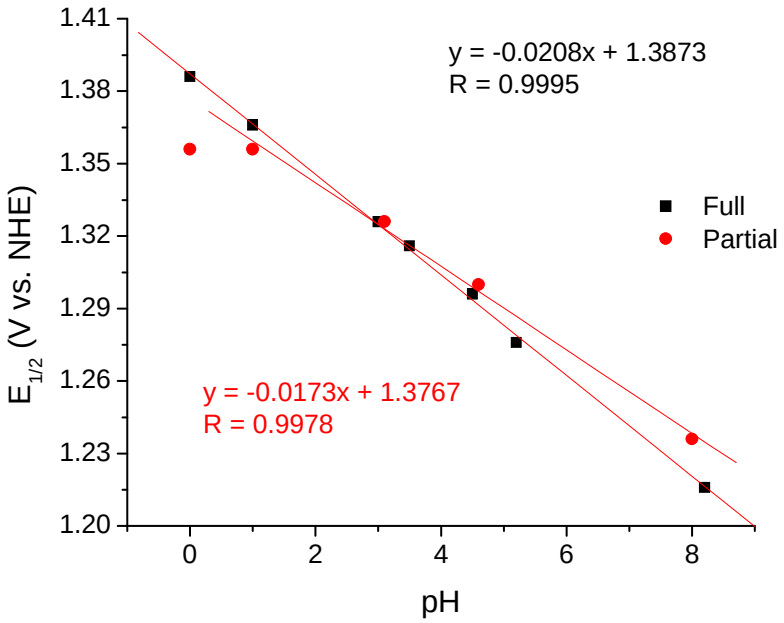

Figure S11. $E_{1/2}$-pH diagram of $[Ru(4,4'\text{-}(H_2O_3P)_2\text{-}bpy)_2(bpy)]^{2+}$ on ITO. Cyclic voltammograms measured at 23 °C. The ionic strength was kept constant with 0.95 M $LiClO_4$. The black data points were with full-loaded slides (Γ = 1.0 x 10^{-10} mol/cm^2) and the red points were measured with partially-loaded slides (Γ ~ 0.3 x 10^{-10} mol/cm^2).

[CONVERGENCE]
Iterations = 10
Convergence Limit = 1.000E-05
Convergence Found = 6.140E-06
Marquardt Parameter = 0.0
Sum(Y-y)^2 Residuals = 4.43684E-03
Std. Deviation of Fit(Y) = 2.82689E-04

Fitting Report 1. $[Ru(bpy)_2(4,4'\text{-}(H_2O_3P)_2\text{-}bpy)]^{2+}$ (1.0 x 10^{-4} M) in 0.1 M H_3PO_4 acidified to pH 1 with HNO_3 containing 0.9 M $NaClO_4$ supporting electrolyte.

[CONVERGENCE]
Iterations = 21
Convergence Limit = 1.000E-05
Convergence Found = 9.453E-06
Marquardt Parameter = 0.0
Sum(Y-y)^2 Residuals = 1.11258E-02
Std. Deviation of Fit(Y) = 4.46080E-04

Fitting Report 2. $[Ru(4,4'\text{-}(H_2O_3P)_2\text{-}bpy)_2(bpy)]^{2+}$ (1.0 x 10^{-4} M) in 0.1 M H_3PO_4 acidified to pH 1 with HNO_3 containing 0.9 M $NaClO_4$ supporting electrolyte.

[CONVERGENCE]
Iterations = 20
Convergence Limit = 1.000E-05
Convergence Found = 2.856E-06
Marquardt Parameter = 0.0
Sum(Y-y)^2 Residuals = 2.35737E-02
Std. Deviation of Fit(Y) = 6.57791E-04

Fitting Report 3. $[Ru(bpy)_2(4,4'\text{-}(H_2O_3PCH_2)_2\text{-}bpy)]^{2+}$ (2.0×10^{-4} M) in 0.1 M H_3PO_4 acidified to pH 1 with HNO_3 containing 0.9 M $NaClO_4$ supporting electrolyte.

[CONVERGENCE]
Iterations = 9
Convergence Limit = 1.000E-05
Convergence Found = 5.264E-06
Marquardt Parameter = 0.0
Sum(Y-y)^2 Residuals = 1.21072E-02
Std. Deviation of Fit(Y) = 4.71987E-04

Fitting Report 4. $[Ru(4,4'\text{-}(H_2O_3PCH_2)_2\text{-}bpy)_2(bpy)]^{2+}$ (1.13×10^{-4} M) in 0.1 M H_3PO_4 acidified to pH 1 with HNO_3 containing 0.9 M NaCl supporting electrolyte.

[CONVERGENCE]
Iterations = 12
Convergence Limit = 1.000E-05
Convergence Found = 5.929E-06
Marquardt Parameter = 0.0
Sum(Y-y)^2 Residuals = 3.94381E-02
Std. Deviation of Fit(Y) = 7.54763E-04

Fitting Report 5. $[Ru(4,4'\text{-}(H_2O_3PCH_2)_2\text{-}bpy)_3]^{2+}$ (1.1×10^{-4} M) in 0.1 M H_3PO_4 acidified to pH 1 with HNO_3 containing 0.9 M $NaClO_4$ supporting electrolyte.

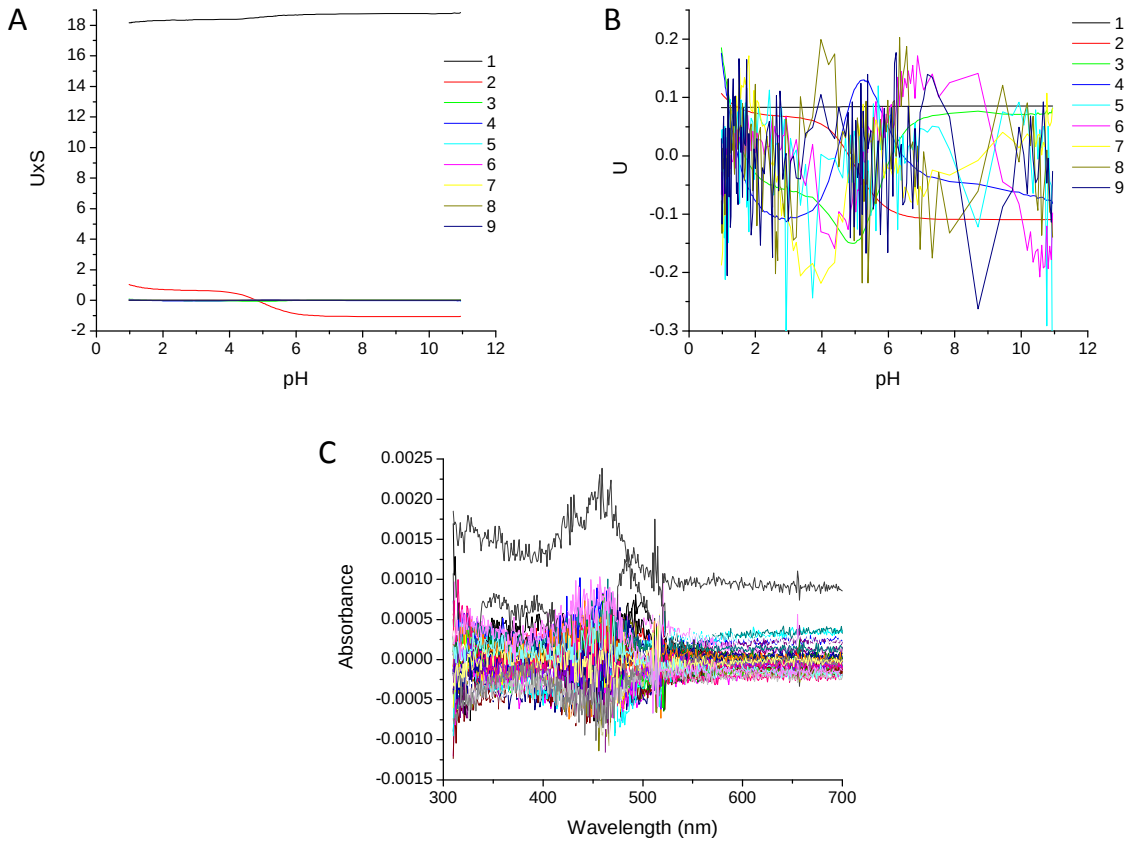

Figure S12. $[Ru(bpy)_2(4,4'\text{-}(H_2O_3P)_2\text{-}bpy)]^{2+}$ (1.0×10^{-4} M) in 0.1 M H_3PO_4 acidified to pH 1 with HNO_3 containing 0.9 M $NaClO_4$ supporting electrolyte. (A) Concentration eigenvectors scaled by their eigenvalues, (B) Concentration eigenvectors (C) Residuals of the fit at all points.

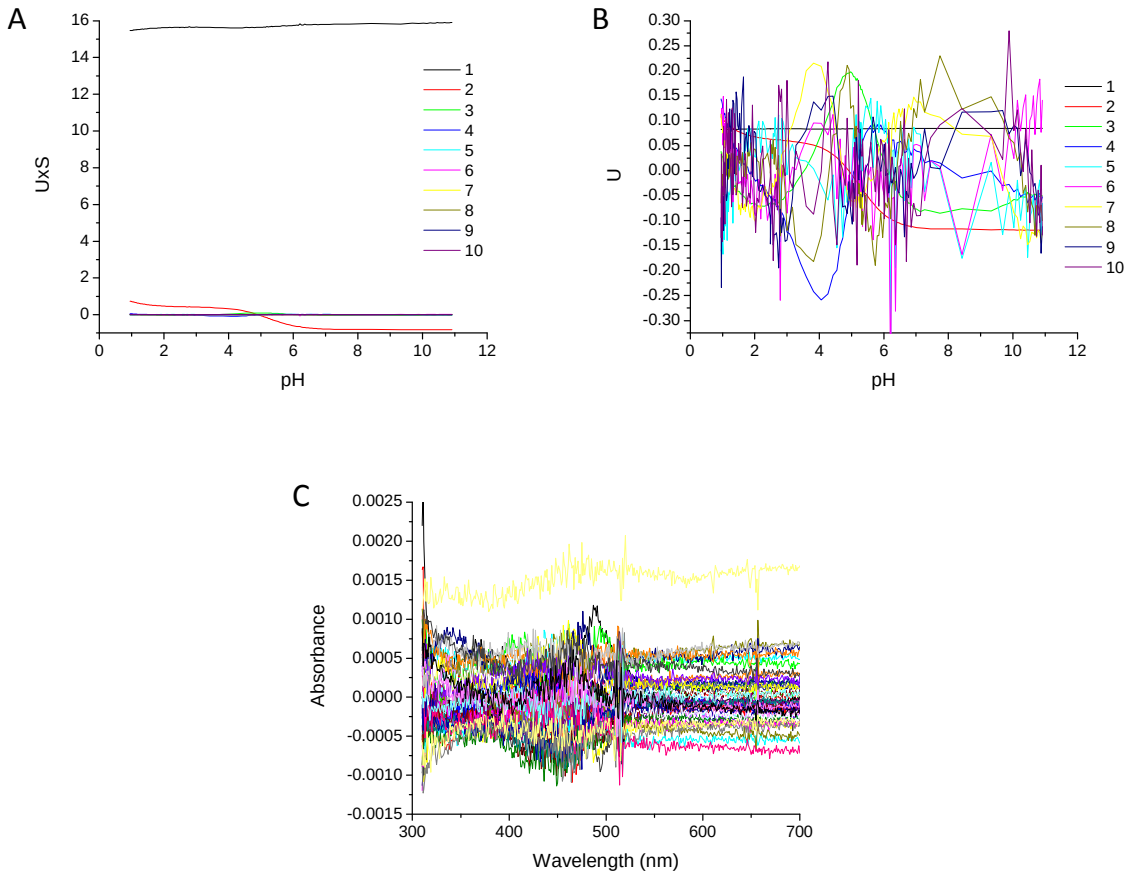

Figure S13. $[Ru(4,4'\text{-}(H_2O_3P)_2\text{-}bpy)_2(bpy)]^{2+}$ (1.0×10^{-4} M) in 0.1 M H_3PO_4 acidified to pH 1 with HNO_3 containing 0.9 M $NaClO_4$ supporting electrolyte. (A) Concentration eigenvectors scaled by their eigenvalues, (B) Concentration eigenvectors (C) Residuals of the fit at all points.

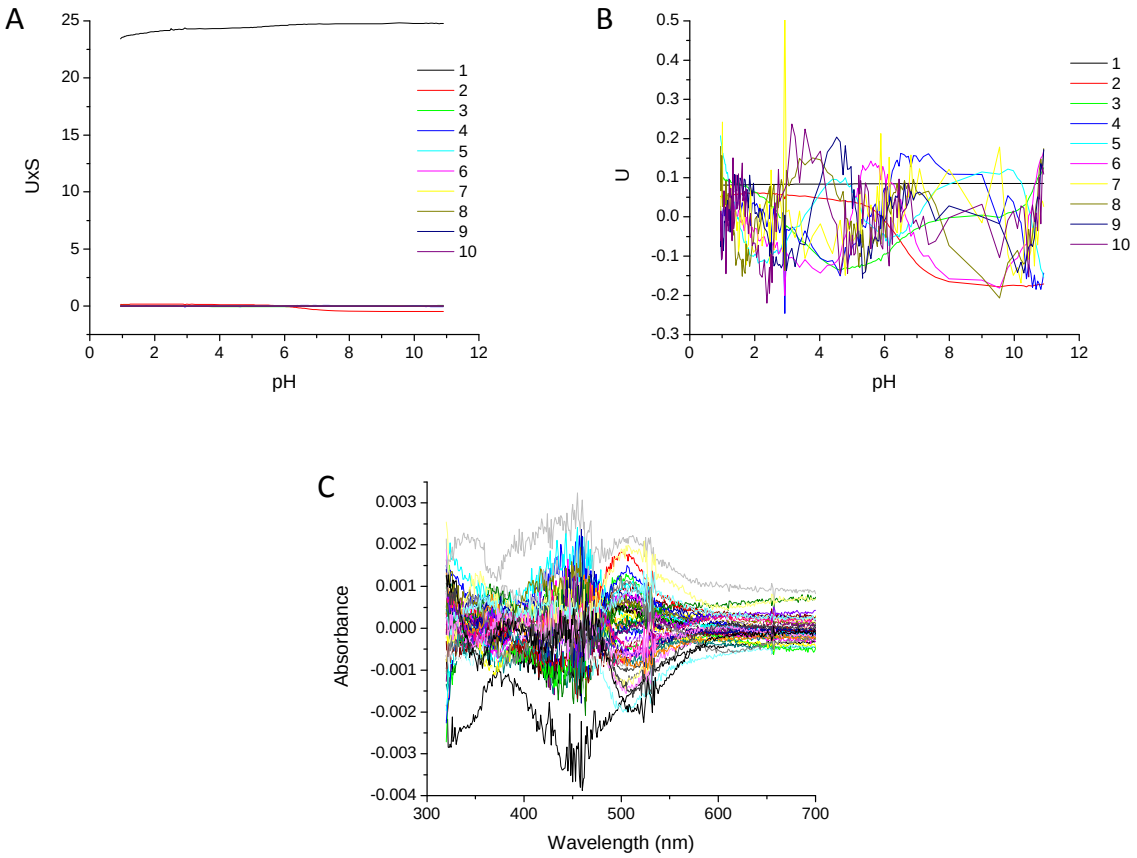

Figure S14. $[Ru(bpy)_2(4,4'\text{-}(H_2O_3PCH_2)_2\text{-}bpy)]^{2+}$ (2.0×10^{-4} M) in 0.1 M H_3PO_4 acidified to pH 1 with HNO_3 containing 0.9 M $NaClO_4$ supporting electrolyte. (A) Concentration eigenvectors scaled by their eigenvalues, (B) Concentration eigenvectors (C) Residuals of the fit at all points.

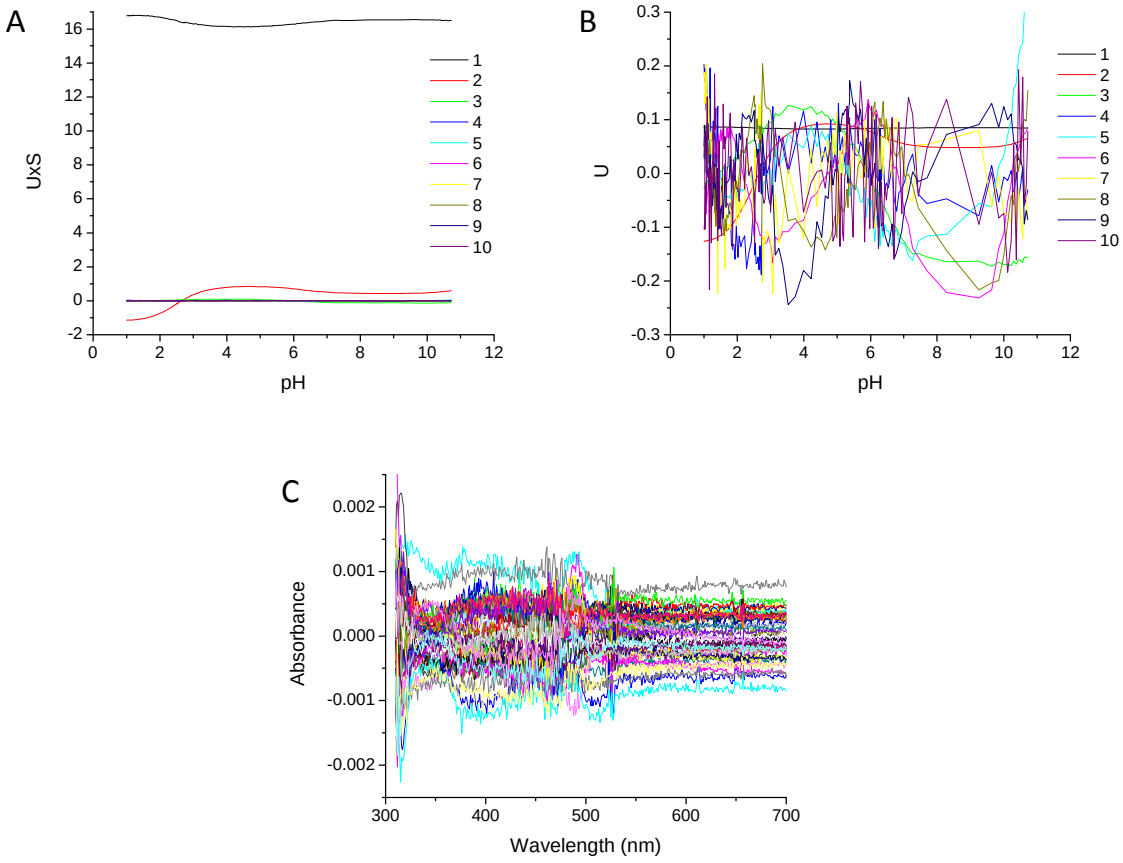

Figure S14. $[Ru(4,4'\text{-}(H_2O_3PCH_2)_2\text{-}bpy)_2(bpy)]^{2+}$ (1.13×10^{-4} M) in 0.1 M H_3PO_4 acidified to pH 1 with HNO_3 containing 0.9 M NaCl supporting electrolyte. (A) Concentration eigenvectors scaled by their eigenvalues, (B) Concentration eigenvectors (C) Residuals of the fit at all points.

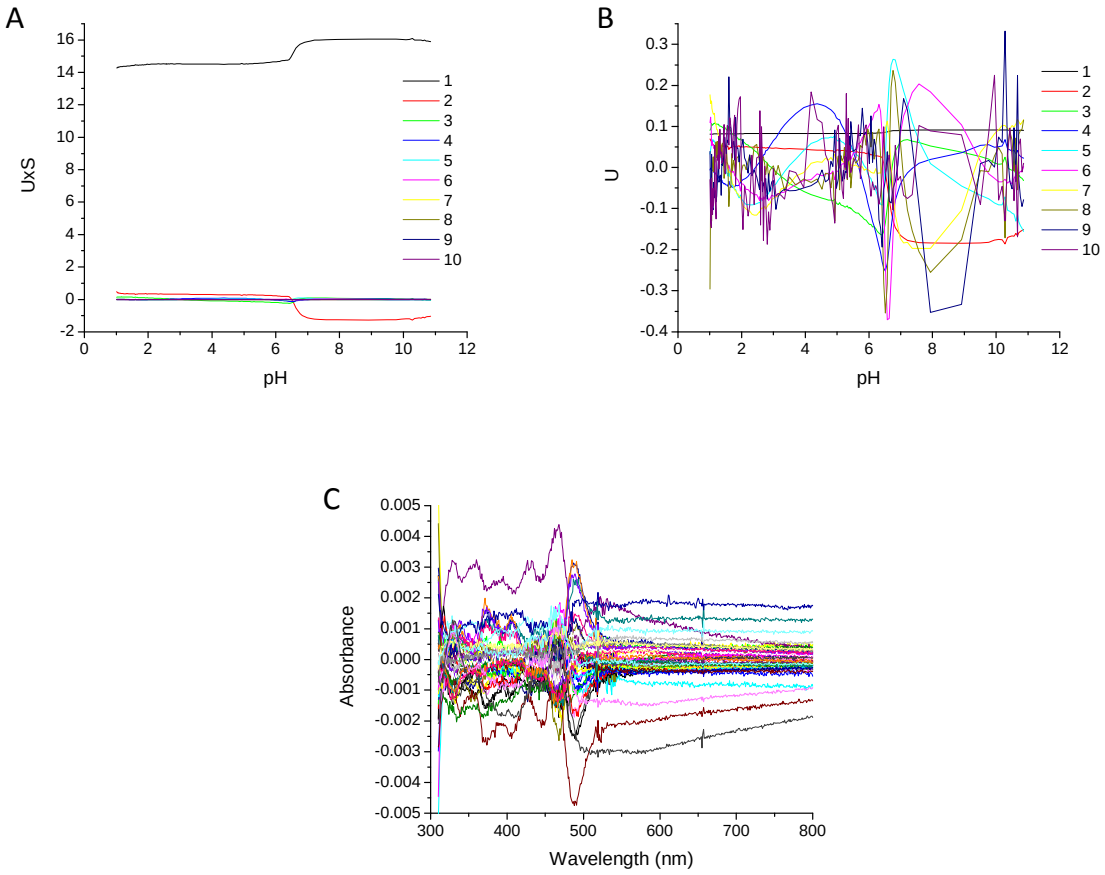

Figure S15. $[Ru(4,4'\text{-}(H_2O_3PCH_2)_2\text{-}bpy)_3]^{2+}$ (1.1 x 10^{-4} M) in 0.1 M H_3PO_4 acidified to pH 1 with HNO_3 containing 0.9 M $NaClO_4$ supporting electrolyte. (A) Concentration eigenvectors scaled by their eigenvalues, (B) Concentration eigenvectors (C) Residuals of the fit at all points.

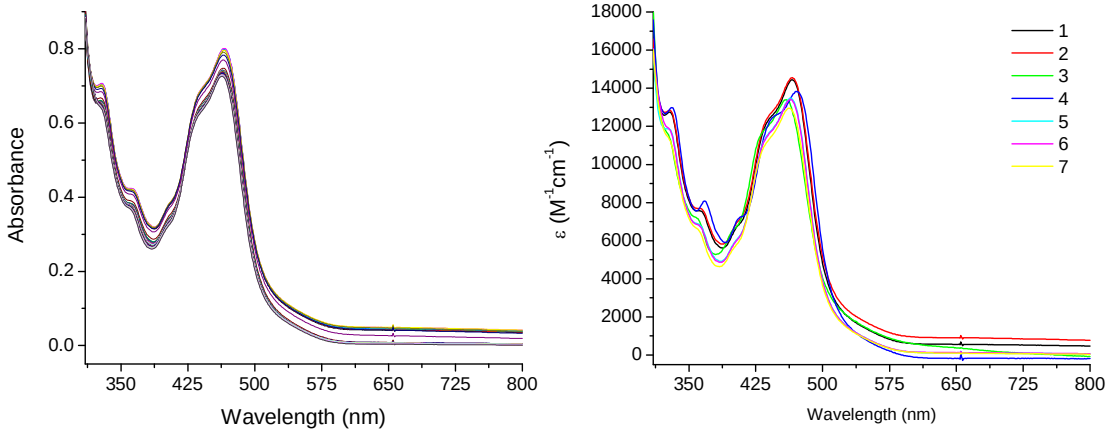

Figure S16. $[Ru(4,4'\text{-}(H_2O_3PCH_2)_2\text{-}bpy)_3]^{2+}$ (1.1 x 10^{-4} M) in 0.1 M H_3PO_4 acidified to pH 1 with HNO_3. Left: dilution corrected raw data. Right: contributing species.

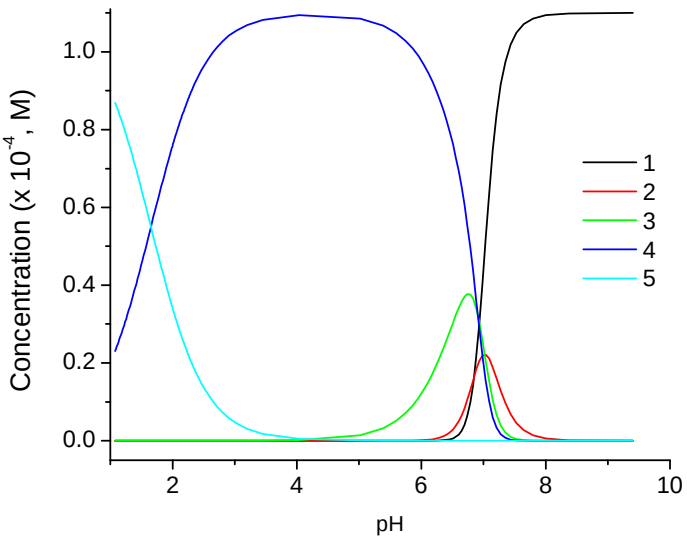

Figure S17. Concentration vs. pH curves for different acid-base forms of $[Ru(4,4'-(H_2O_3PCH_2)_2\text{-}bpy)_3]^{2+}$ (1.1×10^{-4} M) in 0.1 M H_3PO_4 acidified to pH 1 with HNO_3.

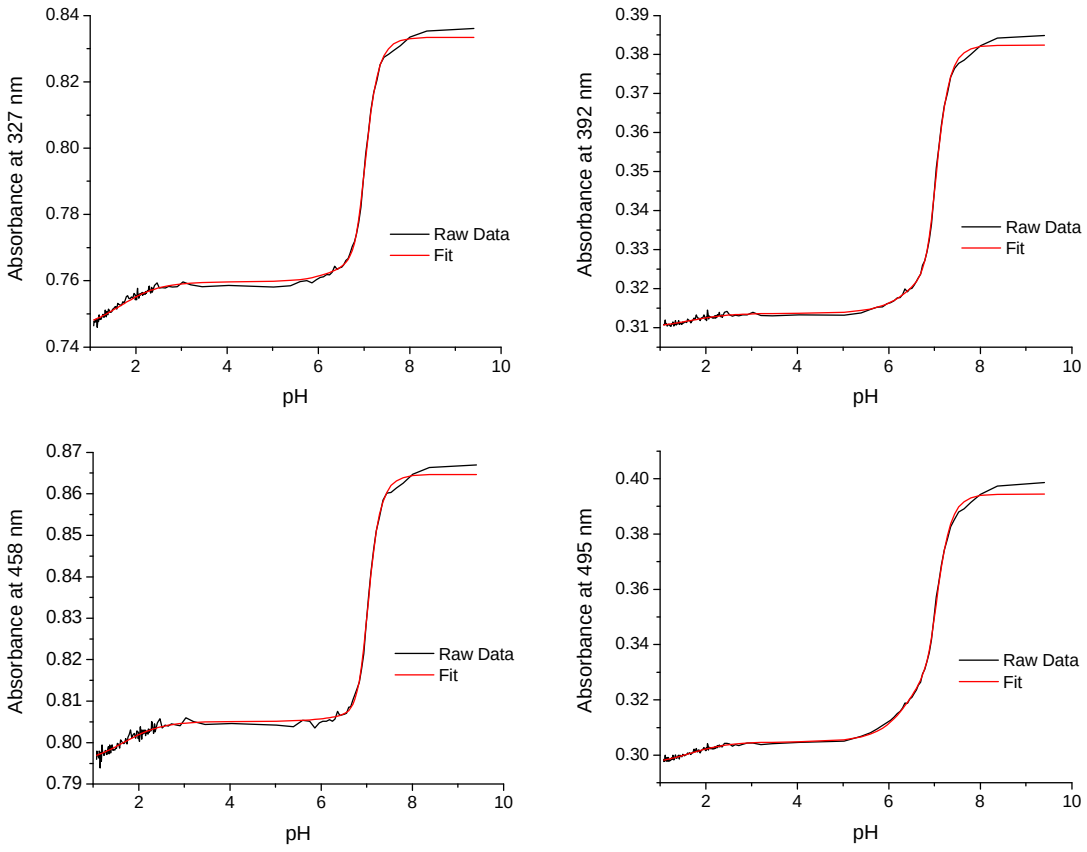

Figure S18. $[Ru(4,4'-(H_2O_3PCH_2)_2\text{-}bpy)_3]^{2+}$ (1.1×10^{-4} M) in 0.1 M H_3PO_4 acidified to pH 1 with HNO_3. Single wavelength fits.

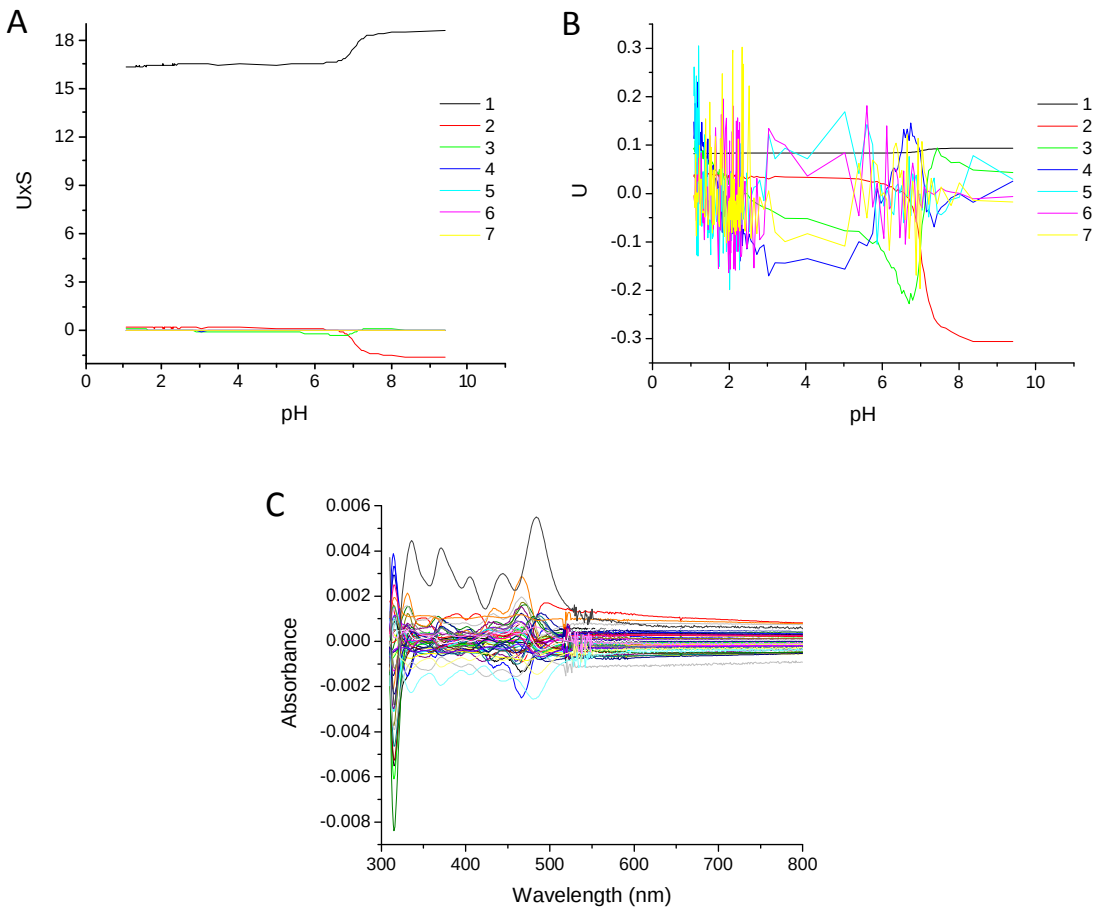

Figure S19. $[Ru(4,4'\text{-}(H_2O_3PCH_2)_2\text{-}bpy)_3]^{2+}$ (1.1×10^{-4} M) in 0.1 M H_3PO_4 acidified to pH 1 with HNO_3. (A) Concentration eigenvectors scaled by their eigenvalues, (B) Concentration eigenvectors (C) Residuals of the fit at all points.

[SPECIES]	[FIXED]	[PARAMETER]		[ERROR]
1 0	True	0.00000E+00	+/-	0.00000E+00
1 2	False	1.36989E+01	+/-	3.20188E-02
1 4	False	2.77365E+01	+/-	5.98009E-02
1 5	False	3.46453E+01	+/-	4.56741E-02
1 6	False	3.63001E+01	+/-	6.22735E-02

[CONVERGENCE]
Iterations = 21
Convergence Limit = 1.000E-04
Convergence Found = 2.594E-06
Marquardt Parameter = 0.0
Sum(Y-y)^2 Residuals = 3.41719E-02
Std. Deviation of Fit(Y) = 7.02566E-04

[STATISTICS]
Experimental Noise = 3.494E-05
Relative Error Of Fit = 0.1869%
Durbin-Watson Factor = 1.1193
Goodness Of Fit, Chi^2 = 4.043E+02
Durbin-Watson Factor (raw data) = 1.1208

Fitting Report 6. $[Ru(4,4'\text{-}(H_2O_3PCH_2)_2\text{-}bpy)_3]^{2+}$ (1.1 x 10^{-4} M) in 0.1 M H_3PO_4 acidified to pH 1 with HNO_3.

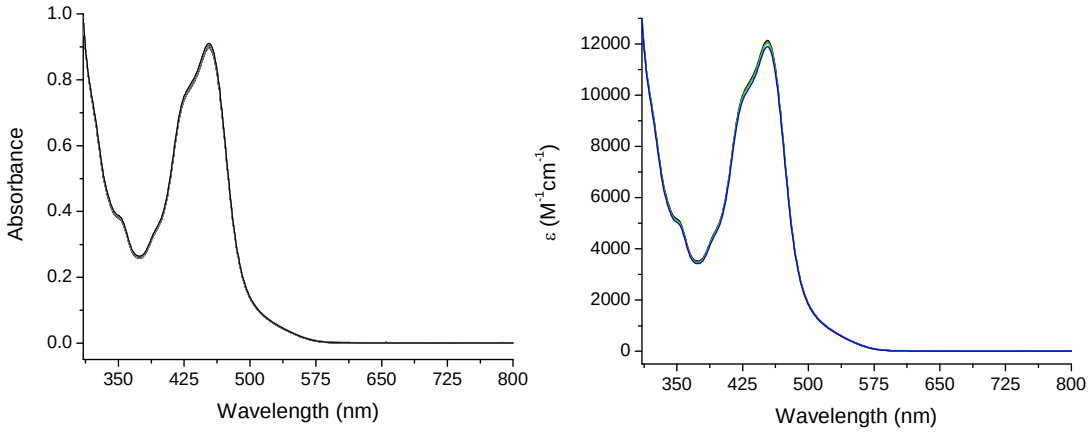

Figure S20. $[Ru(bpy)_3]^{2+}$ (1.5 x 10^{-4} M) in 0.1 M H_3PO_4 acidified to pH 1 with HNO_3 containing 0.9 M NaCl. Left: dilution corrected raw data. Right: contributing species.

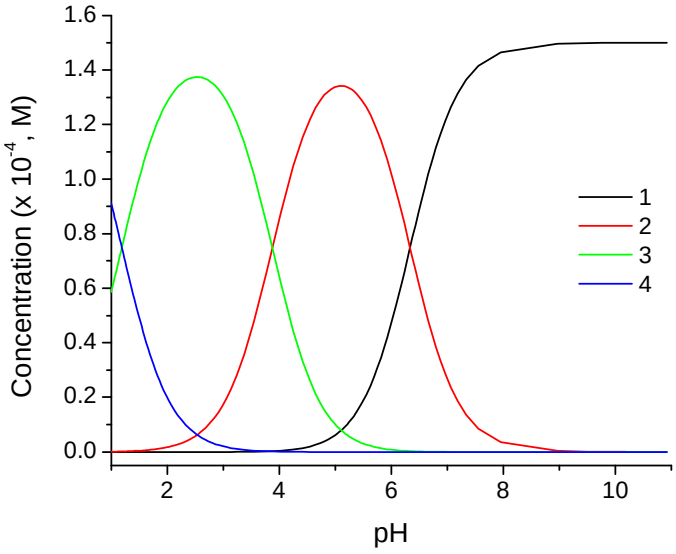

Figure S21. Concentration vs. pH curves for different acid-base forms of $[Ru(bpy)_3]^{2+}$ (1.5 x 10^{-4} M) in 0.1 M H_3PO_4 acidified to pH 1 with HNO_3 containing 0.9 M NaCl.

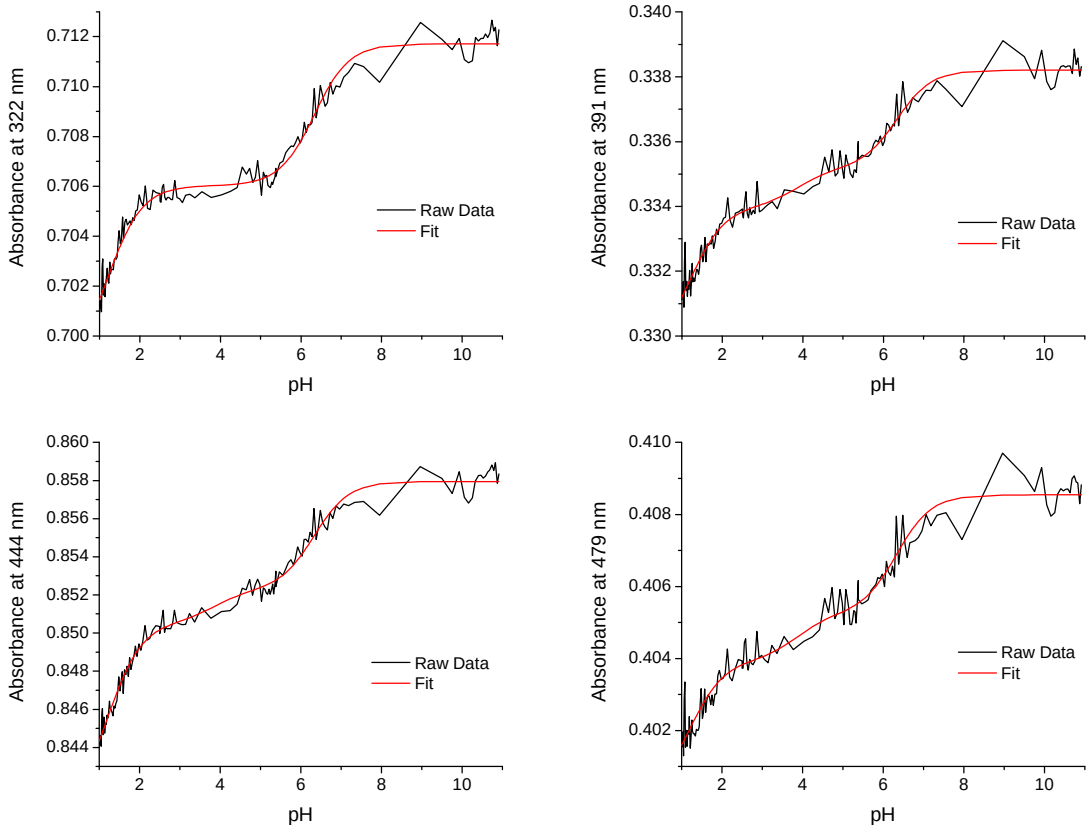

Figure S22. $[Ru(bpy)_3]^{2+}$ (1.5×10^{-4} M) in 0.1 M H_3PO_4 acidified to pH 1 with HNO_3 containing 0.9 M NaCl. Single wavelength fits.

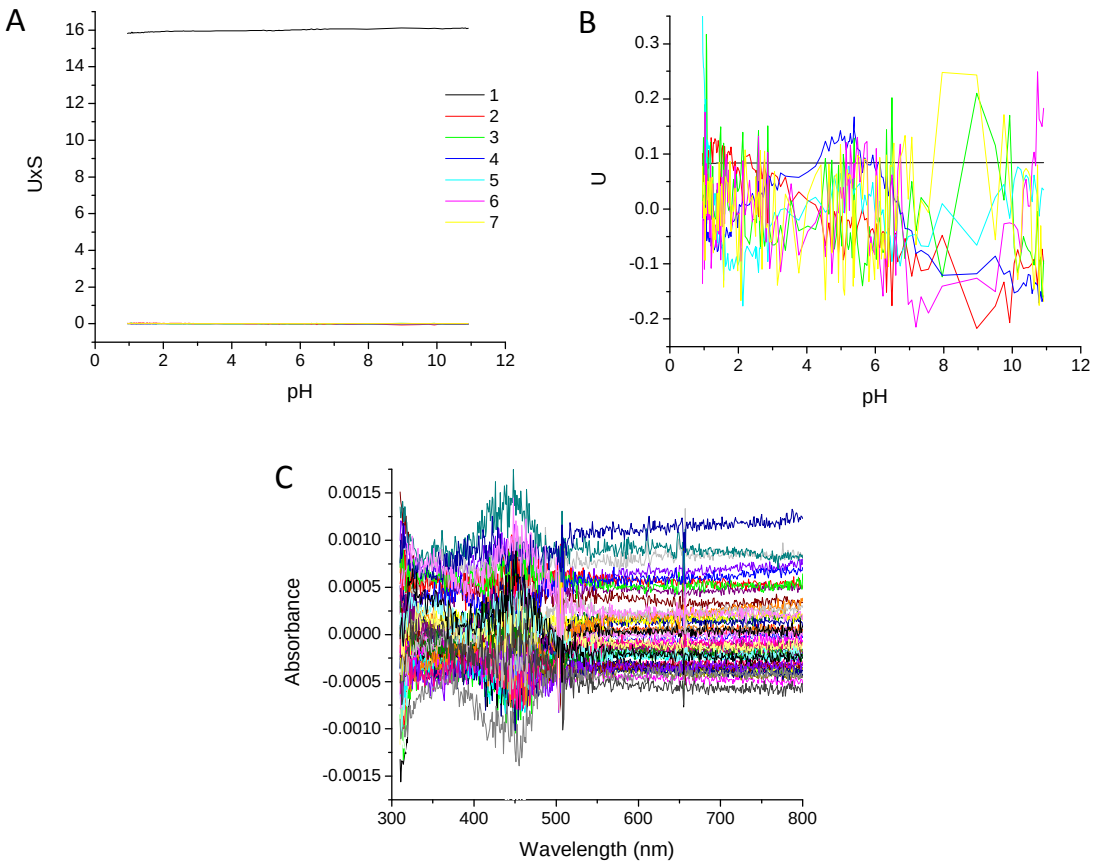

Figure S23. $[Ru(bpy)_3]^{2+}$ (1.5×10^{-4} M) in 0.1 M H_3PO_4 acidified to pH 1 with HNO_3 containing 0.9 M NaCl. (A) Concentration eigenvectors scaled by their eigenvalues, (B) Concentration eigenvectors (C) Residuals of the fit at all points.

[SPECIES]	[FIXED]	[PARAMETER]		[ERROR]
1 0	True	0.00000E+00	+/-	0.00000E+00
1 1	False	6.33399E+00	+/-	4.24682E-02
1 2	False	1.02074E+01	+/-	1.78231E-01
1 3	False	1.13954E+01	+/-	1.98836E-01

[CONVERGENCE]
Iterations = 11
Convergence Limit = 1.000E-03
Convergence Found = 1.661E-04
Marquardt Parameter = 0.0
Sum(Y-y)^2 Residuals = 1.00318E-02
Std. Deviation of Fit(Y) = 3.77993E-04

[STATISTICS]
Experimental Noise = 9.069E-05
Relative Error Of Fit = 0.1049%
Durbin-Watson Factor = 1.5996
Goodness Of Fit, Chi^2 = 1.737E+01
Durbin-Watson Factor (raw data) = 1.6154

Fitting Report 7. $[Ru(bpy)_3]^{2+}$ (1.5×10^{-4} M) in 0.1 M H_3PO_4 acidified to pH 1 with HNO_3 containing 0.9 M NaCl.

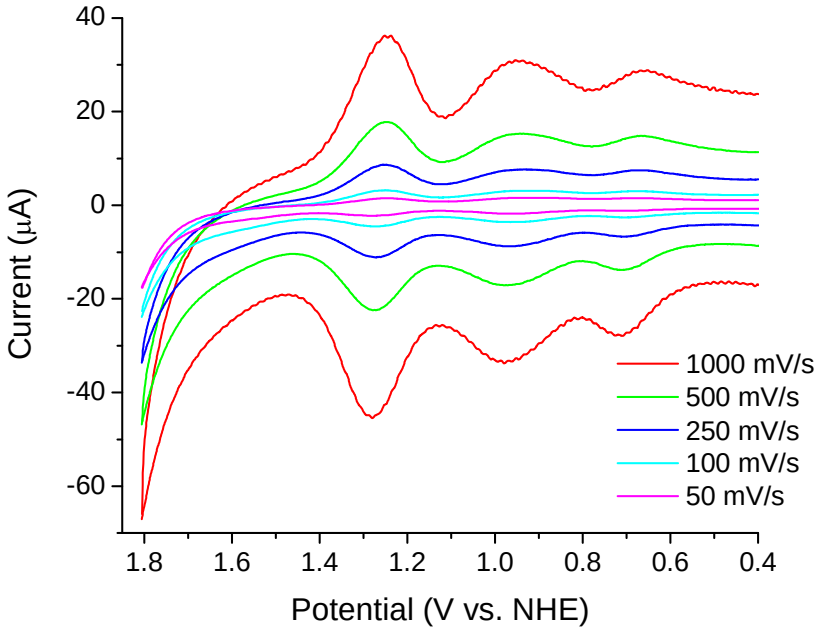

Figure S24. $[Ru(4,4'\text{-}(H_2O_3P)_2\text{-}bpy)_2(bpy)]^{2+}$ on ITO ($\Gamma = 1.0 \times 10^{-10}$ mol/cm^2), soaked in 0.001 M $[Ru(Mebimpy)(bpy)(OH_2)]^{2+}$ in 0.025 M pH 5 acetate buffer (~4 h)
CV measured in clean 0.1 M pH 5 acetate buffer. Scan rates are shown.

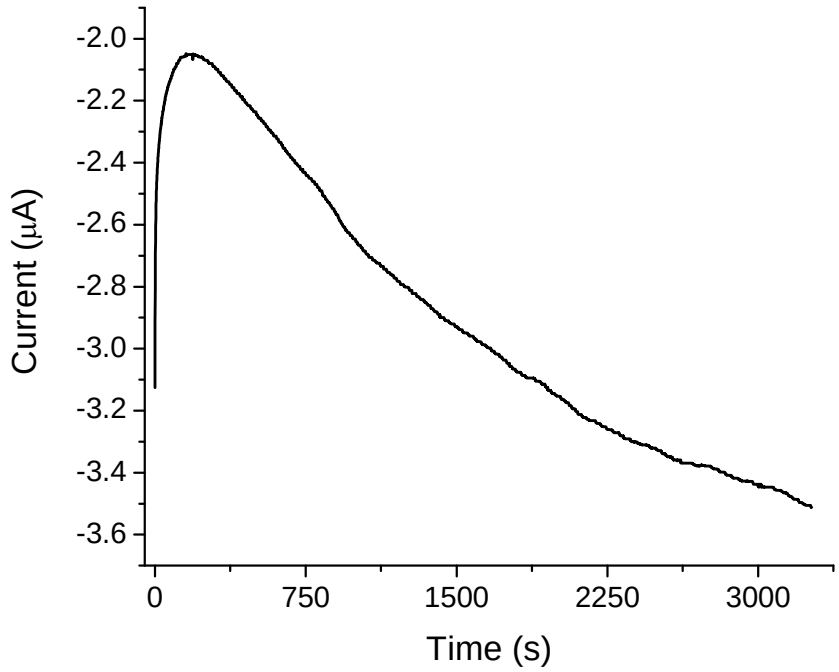

Figure S25. $[Ru(4,4'\text{-}(H_2O_3P)_2\text{-}bpy)_2(bpy)]^{2+}$ on ITO, soaked in 0.001 M $[Ru(Mebimpy)(bpy)(OH_2)]^{2+}$ in 0.025 M pH 5 acetate buffer (~4 h). CPE at 1.71 V vs. NHE.

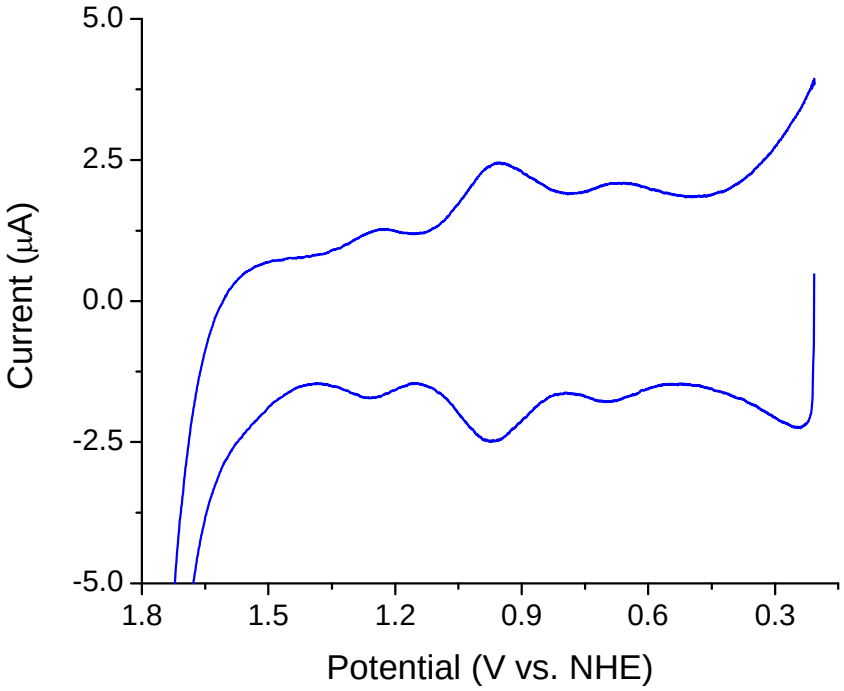

Figure S26. $[Ru(4,4'\text{-}(H_2O_3P)_2\text{-}bpy)_2(bpy)]^{2+}$ on ITO, soaked in 0.001 M $[Ru(Mebimpy)(bpy)(OH_2)]^{2+}$ in 0.025 M pH 5 acetate buffer. CVs in 0.1 M pH 5 acetate buffer following CPE at 1.71 V vs. NHE for ~3100 s.

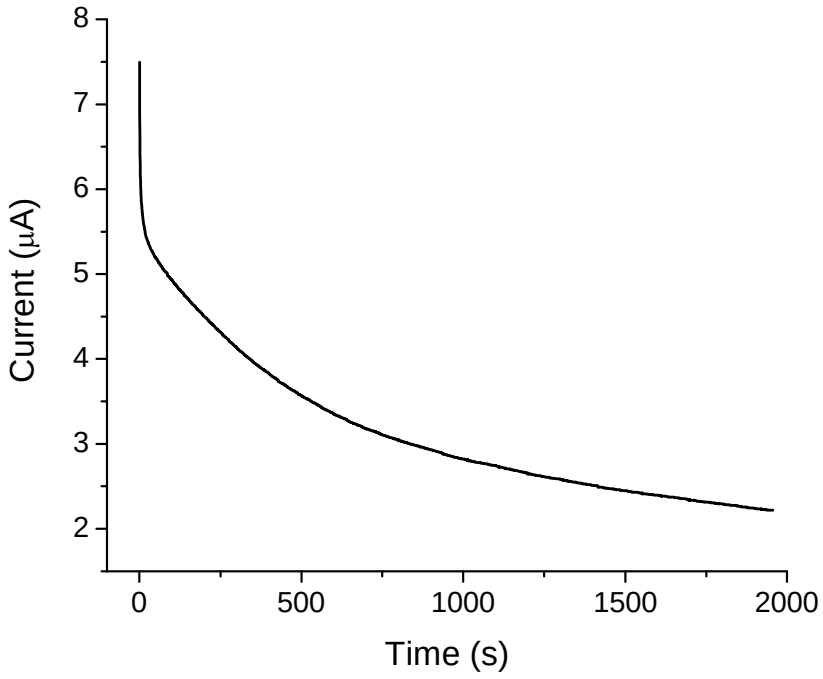

Figure S27. $[Ru(4,4'\text{-}(H_2O_3P)_2\text{-}bpy)_2(bpy)]^{2+}$ on ITO, soaked in 0.001 M $[Ru(Mebimpy)(bpy)(OH_2)]^{2+}$ in 0.025 M pH 5 acetate buffer. CPE at 0.0 V vs. NHE for ~2000 s.